

UNIVERSITAT POLITÈCNICA DE VALÈNCIA  
INSTITUTO DE TECNOLOGÍA QUÍMICA (UPV-CSIC)



INSTITUTO DE  
TECNOLOGÍA  
QUÍMICA



**CSIC**  
CONSEJO SUPERIOR DE INVESTIGACIONES CIENTÍFICAS



UNIVERSITAT  
POLITÈCNICA  
DE VALÈNCIA

# **INNOVATIVE DESIGN OF HETEROGENEOUS CATALYSTS WITH IMPROVED CO<sub>2</sub> HYDROGENATION PERFORMANCE**

**DOCTORAL THESIS**

**International Mention**

**Presented by:**

Jorge Cored Bandrés

**Supervised by:**

Dr. Patricia Concepción Heydorn

Valencia, March 2022



Dr. PATRICIA CONCEPCIÓN HEYDORN, Research Scientist (CSIC) at the "Instituto de Tecnología Química (UPV-CSIC)"

CERTIFIES that the PhD thesis entitled "**Innovative design of heterogeneous catalysts with improved CO<sub>2</sub> hydrogenation performance**" has been developed by the PhD student Jorge Cored Bandrés under her supervision at "the Instituto de Tecnología Química (UPV-CSIC)", located in Valencia (Spain).

Dr. Patricia Concepción Heydorn



*"We need leaders that want to collaborate and can create networks.  
That are constant learners and flexible thinkers.  
That have the necessary courage to face a challenge and to present their ideas."*

(António Mexia, former CEO of EDP Group)



*A Mari Carmen, mi madre,*

*mi faro, ahora mi luz*





## AGRADECIMIENTOS – ACKNOWLEDGEMENTS

En primer lugar, me gustaría agradecer al **proyecto RTI2018-099668-B-C21 financiado por MCIN/AEI/10.13039/501100011033/ y por FEDER Una manera de hacer Europa** por el soporte económico durante estos años, a través del cual además se han sufragado los gastos de impresión de las copias físicas de esta tesis. También agradezco al Gobierno de España (MINECO) y al Instituto de Tecnología Química por la concesión de mi contrato predoctoral Severo Ochoa (**BES-2015-075748**), que me ha permitido “gozar” de una posición de privilegio científico en España costeando, además de los recursos para investigar, los congresos, publicaciones, experimentos de sincrotrón sin apoyo económico, la totalidad de la estancia en Estados Unidos y otras actividades formativas.

Tras este primer párrafo de “agradecimientos institucionales” me gustaría seguir compartiendo mis pensamientos con vosotros:

Todas las historias, tanto las mejores como las peores avenidas, tienen su final. En 2016 emprendí un proyecto científico que supuso un cambio total en mi vida. Abandoné mi zona de confort cambiando el Ebro por el Mediterráneo, y comencé en Valencia una nueva etapa. Desde entonces han pasado casi seis años. Seis años de muchas luces, también de muchas sombras. Seis años que ni el mejor guionista de Hollywood hubiera podido escribir: un largometraje que ha contenido Ciencia (de “no ficción”), amor, desamor, comedia, suspense, drama, fantasía, tragedia... lo ha tenido todo, hasta una pandemia mundial... y quién sabe si una Guerra.

Si tuviese que quedarme con una palabra que definiese todo este tiempo sería “increíble”. Por una parte, ha sido una etapa intensa, de aprendizaje, de puesta a prueba, de superar límites que no conocía y de cruzar líneas rojas... También ha

sido increíble en su otra acepción: todavía me cuesta echar la vista atrás y creer que todo lo conseguido es real... que he disfrutado haciendo Ciencia, que he podido viajar por sincrotrones del mundo para poder investigar a un altísimo nivel, que he dispuesto de todos los medios a mi alcance para ir "tejiendo" el contenido de esta tesis en España (que "tantísimo" apuesta por la Ciencia y por el talento joven...). Incluso tuve la gran suerte de vivir en Nueva York durante unos meses, impregnándome de una cultura científica diferente (y también aprovechando para pasear entre inmensos rascacielos, metáfora de que los sueños, aunque sean ambiciosos y elevados, se cumplen).

Evidentemente nada de esto ha sido gratis. De hecho, aunque el precio que he pagado estaba fuera de mercado, en ningún momento me planteé coger el ticket y devolverme a mi antigua realidad. La dedicación prácticamente total a este proyecto ha supuesto mucho esfuerzo, muchísimas renunciaciones y sobre todo mucho tiempo... el más preciado de nuestros recursos existenciales, ya que es el único que, lamentablemente, no se puede recuperar.

Pero más allá de la narrativa épica, uno de los elementos más importantes de esta etapa ha sido, sin duda, la compañía. Llega el momento de los "otros" agradecimientos, probablemente las líneas más leídas de esta tesis:

Querría comenzar agradeciendo al Profesor Avelino Corma su implicación y su interés. Disfruté infinitamente las reuniones con él. Ha sido un privilegio poder compartir Ciencia con una figura como la suya y discutir acerca de "mis rutenios". Por otra parte, mi agradecimiento a la Dra. Patricia Concepción, mi Directora de Tesis. Con el tiempo me di cuenta de que era complicado ser más diferentes... pero si este proyecto ha llegado a buen puerto creo que es porque compartimos

algo fundamental: una pasión desmedida por la Ciencia. Gracias por llamarme aquel día, por confiar en mis manos un contrato predoctoral de Excelencia Severo Ochoa, y por ser sincera y transparente desde el principio. Hemos pasado infinitas horas en tu despacho viendo datos, elucubrando, fantaseando... hemos disfrutado viajando por el mundo en busca de un rayo de luz (sincrotrónica) con el que iluminar a nuestros materiales... ha sido una experiencia única e inolvidable. También me gustaría agradecerte de corazón todo el apoyo y la predisposición durante estos últimos meses. Han sido tremendamente difíciles, pero siempre estuviste ahí (incluso durante las "vacaciones" de Navidad, para corregir la tesis). Hazle el agradecimiento extensivo también a "tu" Javier por haber estado siempre al borde del cañón con el reactor y toda la instrumentación. Los mejores pilotos de F1 cuentan también con el mejor apoyo mecánico y técnico. Asimismo, me gustaría agradecer a la Profesora Sara Iborra su atención, su amabilidad y su ayuda en la parte final del proceso, que nos ha permitido llegar con garantías hasta el día de hoy. Por último, dentro de la sección dedicada a los "jefes" me gustaría agradecer enormemente a Anibal Boscoboinik la oportunidad que me brindó para llevar a cabo mi estancia internacional en el "Brookhaven National Laboratory" de Nueva York. Esos meses fueron fundamentales para poder tomar oxígeno y enfrentarme al final de mi tesis. Estoy plenamente convencido de que, sin ese *break* en el extranjero, no estaríais hoy leyendo estas palabras. Gracias de verdad por compartir tu Ciencia conmigo, y también un poco de tu vida. Fue increíble pelear en la "cancha" y golpear a algunos de los científicos más relevantes de EE.UU., así como disfrutar de una cena de Acción de Gracias junto a tu familia.

Tras "los dineros y los jefes", toca dar las gracias a los grandes guerreros del escuadrón "Amapola Roja", esas personas que tuvieron el mérito de aguantarme diariamente mientras deambulaba cual Fantasma de la Ópera por el ITQ. Gracias a Pepemi (Pepel, hijo \*\*\*\*) por tanto y tan bueno. Desde el principio fuiste un apoyo y un gran escudero experimental. Hemos pasado miles de horas en "tu" laboratorio de IR riendo, disfrutando, trabajando, aprendiendo de literatura contemporánea... Afortunadamente hemos disfrutado del negocio y también del ocio. Hasta que nos dejó el bicho pudimos aprovechar los mejores descuentos en cenas, discotecas, carreras de karts, cines, fines de semana "rurales"... Ha sido un placer amigo (por cierto, me debes un paseo en moto). Suerte con lo tuyo. Avisa para descorchar el champán. También querría acordarme de otra de las culpables de que yo haya acabado siendo Doctor: Cris. ¡Ay Cristinita, hija! (con acento postizo del sur). Qué importante fue que aparecieras... el mejor SMSI de la historia. Allí donde no llegaba yo estabas tú, parcheando, cubriendo, escuchando... "No queda ya na', en un plissss lo tienes". Gracias por ser como eres y por tu coherencia. Mucha suerte en tu nueva vida científica. Eres excelente. Demuéstralo, que seguro que esta vez te dejan. La siguiente de la tropa se encuentra también "alojada" en la planta baja: Dolo. Cuánto nos ha cambiado la vida desde 2016 y cuánto lo hemos ido comentando en el laboratorio de XPS... Gracias por tu apoyo y tu ayuda cuando el rutenio llamaba a la puerta y gracias por haberme dejado incordiar y estar por ahí para aprender y toquetear el equipo. Espero que hayas encontrado alguien de confianza para apagarlo a última hora y para ayudarte a montar la "falla del *bake*". Subiendo al primer piso, me encuentro a la teniente de la "bat-cueva" (ahora ya pequeño imperio de la espectroscopía tras las obras de ampliación): Adelina. Muchísimas gracias por tus consejos, tus

enseñanzas científicas, tu paciencia y nuestras conversaciones... no sé si fuimos capaces de arreglar el mundo en medio de la oscuridad, pero a mí sí me sirvieron para continuar apretando el acelerador. He conocido pocas personas con la vocación que muestras. Ojalá nunca la pierdas, porque motiva mucho a la gente que tienes alrededor. No me olvido de mis "herederos": José y Carmen. Muchísimas gracias José por cuidar de nuestros CZGs (o CPs, o JSs... jajaja) y de haber sido mis manos en más de una ocasión durante estos últimos meses de proyecto. Enhorabuena por la parte que te toca. Gracias a ti también Carmen por tu alegría, tu naturalidad y tus "miguelitos". Fue un placer compartir mis últimos momentos de reactor contigo... En tus manos se queda el legado del rutenio (y creo que no podría haber quedado en mejores). A los dos mucha fuerza para seguir en el camino. No os rindáis. Todo acaba llegando. Querría terminar este bloque acordándome de la gente que "resucitó" antes que yo: el Becario 1 que se transformó en Doctor 1 y la Doctora Primigenia. Dani... ¿qué decirte que no te haya dicho ya? Hemos pasado tanto juntos... Fuimos pareja de baile muchas noches bajo la brillante luz de sincrotrón, compartimos hogar durante un tiempo, y muchas horas de trabajo y confesiones. Cuando te vi defender a través de la pantalla pensé que quedaba un mundo para que yo estuviera en tu situación y aquí estoy... ¿Cómo es posible? Vaya tela, nene (con el tono de voz característico). Seguro que en nada podemos celebrarlo por "Barna" y gritar al unísono que lo conseguimos. Y, por último: Saray. Primero, no quiero escuchar ni una sola crítica al formato de estos agradecimientos. No sé si le faltan comas, le sobran puntos, hay comillas que no van donde están y este tipo de detalles que captan las escritoras de éxito pero que mi mente no llega a acabar de procesar. Pasando de la advertencia, muchas gracias por todo, por siempre. Por estar ahí cuando todo

era campo. Cuando lo de los clústeres me sonaba a chino, y estaba más perdido que un pulpo en mitad de un laboratorio de raman. Ahí estuviste, acompañándome cuando ya la Ciencia para ti era probablemente lo de menos... Qué pena no haber coincidido ambos en plenas "facultades científicas". No nos hubiéramos aburrido. No me olvido de una miembro de los "Patricios originales" que huyó descaradamente a la capital en busca de nuevos *escape rooms*, porque aquí los agotamos todos. Gracias Bea (y también a José Luis) por todo lo vivido. Por las risas entre juegos de mesa y chuches terapéuticas, que ayudaron a olvidarse de los quebraderos de cabeza que nos daba la investigación.

Justo en la interfaz de los "Patricios originales" se encuentra Fany, turolense (que no maña, que maños son solo los de Zaragoza), compañera de piso y de trabajo con la que me veía más en el ITQ que en casa (vaya panorama). Gracias por todo este tiempo, por haber estado ahí y perdón por haber aguantado a mi versión más pobre y esclava... En un universo paralelo se hubiera liado mucho más, pero así fueron las cosas y así se las tuvimos que contar. ¡Mucho ánimo con la tesis! Vales muchísimo y seguro que va a ir de lujo. En nada lo tienes. Un beso para Anabel también. ¡Torreta de Miramar *forever!*

También en el día a día (incluidos horarios diario, nocturno y de fin de semana) he tenido la enorme suerte de coincidir con grandes científicos y sobre todo enormes personas. Seres especiales con las mismas incertidumbres que yo, que han sido un apoyo fundamental durante todo este tiempo. Gracias a Sergio, Hijo Predilecto de Extremadura, por todo. Por tu templanza, tu sentido común, tu afecto. Suerte para tu aventura. Cuida los carbohidratos, que se echan a la barriga. Merci beaucoup Jordan, el investigador "mejor-humorado" del ITQ. Qué importante es tener gente positiva, trabajadora (y que aguante las noches como

Dios manda). ¡Leña con esa tesis! Gracias también a Javi "Ceuta", nuestro africano favorito. La excepción que confirma la regla. El hombre de acero que desafió a la Ciencia. Ha sido un placer compartir esta experiencia tanto en el ITQ como en el Sincrotrón... Diría que disfruté también del "gym" contigo, pero solo duré una semana... Gracias a Silvia, mi clúster favorito. La mujer que mejor convoca los cafés y resuelve enigmas en habitaciones cerradas. Gracias por tu predisposición y tus ganas de ayudar siempre (trasládaselas a José también. PD: necesito la receta del "Redonet"). Especial agradecimiento a Jaime, que además de compartir mesa, cerveza y cacao más de una vez en el "Coffee", compartimos proyecto científico. Eres un crack. Lo noté desde el segundo cero que te escuché hablar de "lo nuestro". Mucho éxito en tu nueva etapa. Gracias también a la recién "estrenada" Dra. Cumplido, ese huracán llamado Pili. Además de alegrarme más de un café vespertino con tu risa, fuiste clave en la gestión de mi periplo internacional. Si alguien necesita conseguir un visado para los "States", que contrate sus servicios. Grazie mille Alice a ti también por tu simpatía y por los buenos momentos vividos (incluido el último fin de semana costero sorpresa). Moltes gràcies Ferran, vecino de Lleida y segundo máximo accionista de Renfe+. Gracias también a los "gonzaleros" (Iván, Eva, Elena y Marcos). Ha sido un placer haber traspasado las paredes del ITQ con vosotros y de haberme divertido tanto. Por favor, si es posible dejad, aunque sea, los laboratorios de la planta baja sin conquistar. Gracias "Marcs" de forma especial para ti. El Cubo fue un entorno menos hostil en tu compañía. Gracias a Ximet por las risas en la planta baja, los menús del "Coffee" y del Bocalinda, el pádel, y tantas otras historias. Eres un tío con un gran corazón. Gracias Nuria por abrirme de par en par las puertas de tu laboratorio (con permiso del gurú Vicent) y de los momentos vividos fuera de él

(recuerdo especialmente el curso de Santander, con concierto "gratuito" de Luis Fonsi).

Me gustaría nombrar también a compañeros con los que coincidí y de los que guardo un gran recuerdo: Óscar, Mauri, Christian, Francine, Irene, José Cerrillo, María, Miguel, Andrea, Lichen, Andrés, Sebas, Agustín, Vicent(e), Eli, "la Millet", Aroa, Pablo, Carmen y Álvaro. Gracias a todos y también a todo el personal técnico y científico del ITQ que de una u otra forma me han allanado el camino.

I would also like to thank my colleagues at the CFN: Calley, Lesli, Burcu, Mark, Zubin, and especially Angie) for their support. It was an amazing and unforgettable experience. Many thanks to Dr. Dario Stacchiola for hosting me in your group (Interface Science and Catalysis) during my stay.

También me gustaría agradecer la colaboración y el soporte técnico de todo el personal de los sincrotrones en los que hemos tenido el privilegio de realizar nuestros experimentos. Especialmente, querría darle las gracias a la Dra. Virginia Pérez-Dieste de CIRCE (ALBA) por todo lo vivido estos años. Hemos tenido la suerte de coincidir muchas veces y de que me fuera descubriendo poco a poco los misterios del XPS. Gracias también a la Dra. Laura Simonelli, al Dr. Vlad Diaconescu y al Dr. Giovanni Agostini por su colaboración en nuestra investigación.

Para cerrar esta sección de agradecimientos científicos, me gustaría acordarme de la Catedrática Anabel Elduque de la Facultad de Ciencias de la Universidad de Zaragoza. Muchas gracias Anabel por tu apoyo y tu confianza "desde mis inicios". Gracias por "convencerme" para cursar el Máster de Química Industrial, que me abrió las puertas de esta tesis. Fue un placer y un honor formarme en una



Universidad como la nuestra. Ojalá el futuro me permita algún día “volver a casa”.  
No hay nada que me haría más feliz.

Por último (pero no por ello menos importante), me gustaría dirigirme a mi familia. Afortunadamente, tengo la inmensa suerte de sentirme acompañado en la vida por gente increíble, que ha estado ahí en las buenas y en las no tan buenas.

Por ello mi primer recuerdo es para mi familia de “Quimipandi”. Gracias por estos casi 13 años de vida conjunta. Es técnicamente imposible resumir en unas pocas líneas lo que significáis para mí... así que simplemente: Badía (hermano), Fer (el diseñador con más experiencia en química del mundo), Alba (mucho más que una líder emérita), Aitor (el bróker), Amaya (*best feminist ever*), Anamar (más dulce que un croissant, cuando quiere), Llori (tu guardameta de confianza), Diego Royo (el que nunca te saluda con la mano izquierda), Javi (buen support, mejor escalador), José (Antonio, el del humor elaborado xD), Juanico (el ciudadano más carismático de Jaca eres tú, que no te engañen con lo de Georgina), Lorena (no te oigo), Marcos (son de amores), Pablo (amores que matan), Rebeca (la magnate de la industria química pirenaica) y Regina (mi pizza preferida). A todos, gracias por todo. Sois para mí una inspiración, un espejo en el que fijarme, un ejemplo a seguir. ¡Os quiero!

Si subimos 75 km al norte, nos encontramos con mi segunda rama familiar: “Bufetes y allegados”. No tengo palabras suficientes de agradecimiento. Aunque cada uno va confeccionando su propio camino, siempre encontramos momentos para seguir formando parte de la misma historia, nuestra historia. Gracias Geljo (porque la mayor riqueza es tenerte a ti), Loren (Mr. Huesca 2022 y Mr. Bondad Absoluta 1991), Borja (el triunfador de Malasaña), Pablo (el tío más feliz del

planeta Tierra), Alberto (el culpable de la contraportada de esta Tesis), Fran (un templario de valor incalculable), Clara (hasta el infinito y más allá), Raluca (mucho más que una abogada risueña y vital), Aleha (la gallega soñadora), Coral (nos debemos un abrazo) y Lucía (la doctora que sí cura). Os llevo grabados a fuego.

Me gustaría acordarme también de "las gentes" de La Pasión Huesca y del Teatro de Robres, y en especial de Don Luis (Casaus), que me lleva acompañando desde el 2004 sobre las tablas y también en la vida. Parte de lo que soy hoy también es culpa tuya. Gracias por todo y por haber visto "algo" en mí.

Finalmente, me gustaría acordarme de mi familia (los Cored y los Bandrés). En especial de mis abuelos, que siguen con nosotros alegrándonos la vida y preocupándose por nosotros: Yaya Achón y Yayo Salvador. Aunque el COVID nos tenga un poco alejados, en nada os estoy enseñando esta dedicatoria. Gracias también a mi hermano Sergio por los ánimos... por los pelos no me has adelantado por la derecha (aunque ya veremos jajajaja). Aprieta, que en nada tenemos el doblote. Gracias también a mi padre por apoyarme siempre en todas las etapas y por confiar ciegamente en que esto iba a terminar saliendo bien.

El penúltimo agradecimiento va dirigido a otra Patricia (la que me aguanta todos los días, concretamente). Gracias por estos cinco años. Como describía al inicio, ha sido una etapa dura, compleja mentalmente, donde ha habido que saber jugar las cartas. Hemos vivido cosas inolvidables y cosas perfectamente olvidables. Gracias por compartir conmigo el camino. Desde el día 3 de febrero de 2020, la suerte no ha caído demasiado de mi lado, pero estoy seguro de que, tras esta etapa, llegarán grandes momentos. Nos lo merecemos. Gracias también a Luci y Luis por vuestro cariño y por hacerme sentir parte de vuestra familia.

Y para finalizar, querría dedicar estas últimas líneas a la persona más especial de mi vida: Mi madre. Siempre estuviste ahí en la distancia protegiéndome, preocupándote por mí. Desde la primera vez que me tuviste en brazos hasta el día en que te fuiste. Como dice una de tus canciones preferidas de IL DIVO: "Gracias por ser quien soy, y gracias también por lo que no soy". Fuiste siempre una luchadora, y me enseñaste a serlo. Por ello, nunca he dado ninguna batalla por perdida (ni la daré). Me entristece tremendamente que no vayas a disfrutar de esto, más después de sufrir conmigo durante toda la tesis. Vivo desde hace unos meses en una tiniebla que me ha puesto las cosas muy difíciles. He tenido que hacer un esfuerzo sobrehumano para poder terminar lo que empecé en 2016. Y lo he hecho por ti, por tu memoria y porque nos lo merecemos. Gracias por la energía que me has mandado y me seguirás mandando. Espero que estés orgullosa, porque por fin lo hemos conseguido. Te quiero. Mucho. Esta Tesis que ahora comienza va por ti.



## ABSTRACT

Climate change is one of the existential threats of our times. Greenhouse gases (GHG), such as carbon dioxide, are primary drivers of this phenomenon, and their emissions need to be urgently reduced. In 2019, the European Commission presented the European Green Deal, which will help the EU to attain an ambitious goal for our region: to become carbon-neutral by 2050. The decarbonization strategies included in the roadmap towards net-zero emissions will imply the energy transition from fossil fuels to renewable energies, with a massive reduction of CO<sub>2</sub> deliverance. In this sense, the development of effective Carbon Capture and Storage (CCS) and Carbon Capture and Utilization (CCU) technologies will allow the valorization of CO<sub>2</sub>, evolving into a circular carbon economy.

The present Doctoral Thesis focuses on the design, synthesis and characterization of innovative heterogeneous metal-based systems, which are able to transform CO<sub>2</sub> into value-added products. Among a wide catalogue of reactions that "connects" CO<sub>2</sub> with various carbon-based compounds, this thesis will be devoted to the synthesis of two C<sub>1</sub> platform chemicals of industrial interest: methanol and methane.

Chapters 3 and 4 are dedicated to methanol synthesis, a highly hampered exothermic process due to the inherent stability of the CO<sub>2</sub> molecule and the presence of the competitive reverse water-gas shift reaction (RWSG). On the one hand, Chapter 3 is focused on the promoting effect of gallium on the structural, electronic, and catalytic properties of Cu/ZnO based materials (CZG systems). In particular, the promoting effect of Ga<sup>3+</sup>-doped in the wurtzite ZnO lattice of a Cu/ZnO/Ga<sub>2</sub>O<sub>3</sub> catalyst is compared to that of a zinc gallate (ZnGa<sub>2</sub>O<sub>4</sub>) phase

following a multimodal spectroscopic-catalytic approach. In Chapter 4, a bifunctional catalyst containing 2 nm Cu nanoparticles and Cu<sup>+</sup> species is presented, to overcome the “assumed” low activity of small copper particles that prevents obtaining high atom efficiency and competitive catalytic results in the CO<sub>2</sub> hydrogenation to methanol. A detailed spectroscopic study (combined with theoretical calculations and catalytic tests) performed on a Cu-Mg-Al mixed oxide catalyst derived from a hydrotalcite precursor by calcination and further reduction (CuHT-230) highlights the key role of doped Cu<sup>+</sup> ions in methanol production.

The success of CCU technologies in the medium-long term will depend not only on the development of competitive catalysts but also on their ability to operate under milder reaction conditions, which will make these processes economically viable. Consequently, the energy efficiency issue will be addressed in Chapter 5 with the innovative design of a core-shell structure formed by a core of metallic ruthenium and a shell of ruthenium carbide, synthesized via hydrothermal treatment. This catalyst (Ru@EDTA-20) exhibits exceptional high activity for CO<sub>2</sub> hydrogenation to methane (Sabatier reaction) at low temperatures (160-200 °C) with 100% selectivity to CH<sub>4</sub>, outperforming the state of the art catalysts operating at 400-500 °C.

Finally, Chapter 6 covers the investigation carried out on a model ruthenium-based catalyst composed of a 2D-bilayered aluminosilicate grown over a Ru(0001) surface during my international short-term stay at Brookhaven National Laboratory (New York, USA). The combination of these materials in a composite allows the creation of a confined nano-space that can be exploited as a nano-reactor. In this project, water formation reaction (WFR) was selected as model reaction, which was fundamentally explored at NSLS-II synchrotron.

## RESUMEN

El cambio climático es una de las amenazas de nuestro tiempo. Los gases de efecto invernadero, como el dióxido de carbono, son los principales causantes de este fenómeno, siendo necesario disminuir urgentemente sus emisiones. En 2019, la Comisión Europea presentó el "Pacto Verde Europeo", que será clave para alcanzar un objetivo tremendamente ambicioso para nuestra región: la neutralidad climática de aquí a 2050. Las estrategias de descarbonización incluidas en su hoja de ruta van a implicar necesariamente la transición energética de los combustibles fósiles a las energías renovables, reduciendo de forma masiva la liberación de CO<sub>2</sub>. En este sentido, el desarrollo de tecnologías efectivas de Captura, Almacenamiento y Uso del Carbono (CAUC) permitirá la valorización del CO<sub>2</sub>, evolucionando hacia una economía de carbono circular.

La presente Tesis Doctoral se enmarca en el diseño, síntesis y caracterización de sistemas catalíticos heterogéneos innovadores basados en metales capaces de transformar el CO<sub>2</sub> en otros productos de valor añadido. Entre un amplio catálogo de reacciones que "conectan" el CO<sub>2</sub> con diversos compuestos basados en carbono, esta Tesis se centrará principalmente en la síntesis de dos moléculas C<sub>1</sub> plataforma de interés industrial: el metanol y el metano.

Los Capítulos 3 y 4 están dedicados a la síntesis de metanol, un proceso exotérmico limitado termodinámicamente debido a la estabilidad inherente de la molécula de CO<sub>2</sub>, así como a la presencia de la reacción competitiva RWGS. Por un lado, el Capítulo 3 se centra en el efecto promotor del galio sobre las propiedades estructurales, electrónicas y catalíticas de materiales basados en Cu/ZnO (sistemas CZG). Mediante un enfoque espectroscópico-catalítico

multidisciplinar se ha comparado el efecto promotor del  $\text{Ga}^{3+}$  dopado en la red de un ZnO tipo wurtzita presente en un catalizador Cu/ZnO/ $\text{Ga}_2\text{O}_3$  con el de una fase de galato de zinc ( $\text{ZnGa}_2\text{O}_4$ ). Por otro lado, en el Capítulo 4 se muestra un catalizador bifuncional que contiene nanopartículas de Cu de 2 nm y especies  $\text{Cu}^+$ , con el objetivo de enfrentarse a la inherente baja actividad de estas pequeñas partículas, hecho que impide mejorar la eficiencia atómica de los catalizadores, dificultando así la obtención de resultados catalíticos competitivos en la hidrogenación de  $\text{CO}_2$ . La realización de un estudio espectroscópico detallado (combinado con cálculo teórico y ensayos catalíticos) sobre un catalizador óxido mixto de Cu-Mg-Al derivado de un precursor de hidrotalcita tras calcinación y posterior reducción (CuHT-230) pone de manifiesto el papel clave de los iones  $\text{Cu}^+$  dopados en estructura en la producción de metanol.

El éxito de las tecnologías CAUC a medio-largo plazo dependerá no solo del desarrollo de catalizadores competitivos, sino también de su capacidad para operar en condiciones de reacción más suaves, permitiendo que estos procesos sean viables económicamente. Por ello, el concepto de eficiencia energética se abordará en el Capítulo 5, a través de un innovador diseño de catalizador tipo "shell/core" formado por un núcleo de rutenio metálico y una envoltura de carburo de rutenio, sintetizado mediante tratamiento hidrotermal. Este sistema (Ru@EDTA-20) exhibe una actividad excepcionalmente alta para la hidrogenación de  $\text{CO}_2$  a metano a bajas temperaturas (160-200 °C) con una selectividad a  $\text{CH}_4$  del 100%, superando a catalizadores de bibliografía que normalmente operan a mayores temperaturas (400-500 °C).

Por último, en el Capítulo 6 se estudia un catalizador modelo compuesto por un alumino-silicato bidimensional sintetizado sobre una superficie de Ru(0001),



investigación realizada durante mi estancia internacional en el Laboratorio Nacional de Brookhaven (Nueva York, Estados Unidos). La combinación de estos dos materiales en el mismo composite permite la creación de un nanoespacio confinado que puede emplearse como nanorreactor. En este proyecto, se seleccionó la reacción de formación de agua como modelo, que se exploró a nivel fundamental en el sincrotrón NSLS-II.

## RESUM

El canvi climàtic és una de les amenaces del nostre temps. Els gasos d'efecte d'hivernacle, com el diòxid de carboni, són els principals causants d'aquest fenomen, sent necessari reduir urgentment les seues emissions. En 2019, la Comissió Europea va presentar el "Pacte Verd Europeu", que serà clau per a aconseguir un objectiu tremendament ambiciós per a la nostra regió: la neutralitat climàtica d'ací a 2050. Les estratègies de descarbonització incloses en el seu full de ruta implicaran necessàriament la transició energètica dels combustibles fòssils a les energies renovables, reduint de manera massiva l'alliberament de CO<sub>2</sub>. En aquest sentit, el desenvolupament de tecnologies efectives de Captura, Emmagatzematge i Ús del Carboni (CEUC) permetrà la valorització del CO<sub>2</sub>, evolucionant cap a una economia de carboni circular.

La present Tesi Doctoral s'emmarca en el disseny, síntesi i caracterització de sistemes catalítics heterogenis innovadors basats en metalls capaços de transformar el CO<sub>2</sub> en altres productes de valor afegit. Entre un ampli catàleg de reaccions que "connecten" el CO<sub>2</sub> amb diversos compostos basats en carboni, aquesta Tesi se centrarà principalment en la síntesi de dues molècules C<sub>1</sub> plataforma d'interés industrial: el metanol i el metà.

Els Capítols 3 i 4 estan dedicats a la síntesi de metanol, un procés exotèrmic limitat degut tant a l'estabilitat inherent de la molècula de CO<sub>2</sub> com a la presència de la reacció competitiva RWGS. D'una banda, el Capítol 3 se centra en l'efecte promotor del gal·li sobre les propietats estructurals, electròniques i catalítiques de materials basats en Cu/ZnO (sistemes CZG). Mitjançant un enfocament espectroscòpic-catalític multidisciplinari s'ha comparat l'efecte promotor del Ga<sup>3+</sup>

dopat en la xarxa d'un ZnO (wurtzita) present en un catalitzador Cu/ZnO/Ga<sub>2</sub>O<sub>3</sub> amb el d'una fase de ZnGa<sub>2</sub>O<sub>4</sub>. D'altra banda, en el Capítol 4 es mostra un catalitzador bifuncional que conté nanopartícules de Cu de 2 nm i espècies Cu<sup>+</sup>, amb l'objectiu d'enfrontar-se a la inherent baixa activitat d'aquestes petites partícules, fet que impedeix millorar l'eficiència atòmica dels catalitzadors, dificultant així l'obtenció de resultats catalítics competitius en la hidrogenació de CO<sub>2</sub>. La realització d'un estudi espectroscòpic detallat (combinat amb càlcul teòric i assajos catalítics) sobre un catalitzador òxid mixt de Cu-Mg-Al derivat d'un precursor de hidrotalcita després de calcinació i posterior reducció (CuHT-230) posa de manifest el paper clau dels ions Cu<sup>+</sup> dopats en estructura en la producció de metanol.

L'èxit de les tecnologies CEUC a mig-llarg termini dependrà no solament del desenvolupament de catalitzadors competitius, sinó també de la seua capacitat per a operar en condicions de reacció més suaus, permetent que aquests processos siguen viables econòmicament. Per això, el concepte d'eficiència energètica s'abordarà en el Capítol 5, a través un innovador disseny de catalitzador tipus "shell/core" format per un nucli de ruteni metàl·lic i un embolcall de carbur de ruteni, sintetitzat mitjançant tractament hidrotermal. Aquest sistema (Ru@EDTA-20) exhibeix una activitat excepcionalment alta per a la hidrogenació de CO<sub>2</sub> a metà a baixes temperatures (160-200 °C) amb una selectivitat a CH<sub>4</sub> del 100%, superant a catalitzadors de bibliografia que normalment operen a majors temperatures (400-500 °C).

Finalment, en el Capítol 6 s'estudia un catalitzador model compost per un alumino-silicat bidimensional sintetitzat sobre una superfície de Ru(0001), investigació realitzada durant la meua estada internacional en el Laboratori

Nacional de Brookhaven (Nova York, els Estats Units). La combinació d'aquests dos materials en el mateix "composite" permet la creació d'un nano-espai confinat que pot emprar-se com nano-reactor. En aquest projecte, es va seleccionar la reacció de formació d'aigua com a model, que es va explorar a nivell fonamental en el sincrotró NSLS-II.

## **TABLE OF CONTENTS**

<b>CHAPTER 1: Introduction</b> .....	<b>1</b>
1.1. Climate change.....	3
1.2. Greenhouse effect and global warming .....	4
1.3. Greenhouse gas emissions.....	5
1.4. EU International action on climate change .....	9
1.4.1. A glimpse into the past.....	9
1.4.2. Horizon 2050: towards climate neutrality .....	10
1.5. CO <sub>2</sub> remediation technologies.....	14
1.5.1. Physico-chemical properties of CO <sub>2</sub> .....	15
1.5.2. CO <sub>2</sub> capture.....	16
1.5.3. CO <sub>2</sub> transportation.....	18
1.5.4. CO <sub>2</sub> storage.....	18
1.5.5. Carbon Capture and Utilization.....	19
1.5.6. Thermocatalytic CO <sub>2</sub> hydrogenation to value-added products .....	23
1.5.7. Methanol synthesis.....	24
1.5.8. CO <sub>2</sub> hydrogenation to methane.....	37
1.6. References .....	58
<b>CHAPTER 2: PhD Thesis Objectives</b> .....	<b>81</b>
<b>CHAPTER 3: CO<sub>2</sub> hydrogenation to methanol over gallium promoted Cu/ZnO commercial-like catalysts</b> .....	<b>89</b>
3.1. Introduction .....	91
3.2. Materials and methods .....	93
3.2.1. Preparation of catalytic samples and references .....	93
3.2.2. Characterization techniques .....	97

3.3. Results and discussion.....	103
3.3.1. Synthesis and physico-chemical properties of calcined and reduced CZG catalysts.....	103
3.3.2. Catalytic activity in the CO <sub>2</sub> hydrogenation to methanol.....	109
3.3.3. Determination of catalytic sites involved in MeOH synthesis.....	113
3.4. Conclusions .....	123
3.5. Supporting Information .....	125
3.5.1. Physico-chemical properties of calcined and reduced CZG catalysts .....	125
3.5.2. Catalytic activity in the CO <sub>2</sub> hydrogenation to methanol .....	134
3.5.3. Determination of catalytic sites involved in MeOH synthesis.....	141
3.6. References.....	160
<b>CHAPTER 4: Enhanced methanol production over non-promoted 2 nm Cu particles on Cu-MgO-Al<sub>2</sub>O<sub>3</sub> materials .....</b>	<b>169</b>
4.1. Introduction.....	171
4.2. Materials and methods.....	174
4.2.1. Preparation of catalytic samples and references.....	174
4.2.2. Characterization techniques.....	177
4.3. Results and discussion.....	185
4.3.1. Synthesis, characterization and catalytic properties of calcined-reduced catalysts.....	185
4.3.2. Spectroscopic catalyst characterization.....	192
4.4. Conclusions .....	201
4.5. Supporting Information .....	203
4.5.1. Physico-chemical properties of calcined-reduced catalysts.....	203
4.5.2. Catalytic activity in the CO <sub>2</sub> hydrogenation to methanol .....	210
4.5.3. X-ray photoelectron spectroscopy (XPS) characterization .....	220

4.5.4. Infrared characterization: Identification of Cu <sup>+</sup> species .....	221
4.5.5. Assignment of the IR band at 2137 cm <sup>-1</sup> to Cu <sup>+</sup> ions in metal oxide lattice positions.....	228
4.5.6. Operando Infrared studies and structural-activity correlations.....	236
4.6. References .....	249
<b>CHAPTER 5: Low-temperature carbon dioxide hydrogenation to methane over hydrothermal Ru@C catalysts .....</b>	<b>261</b>
5.1. Introduction .....	263
5.2. Materials and methods .....	265
5.2.1. Preparation of catalytic samples and references .....	265
5.2.2. Characterization techniques .....	268
5.3. Results and discussion.....	272
5.3.1. Synthesis and characterization of Ru@C-EDTA catalysts .....	272
5.3.2. Catalytic properties and active site elucidation in the Sabatier reaction.....	277
5.4. Conclusions.....	282
5.5. Supporting Information.....	283
5.5.1. Synthesis and characterization of Ru@C-EDTA catalysts.....	283
5.5.2. Catalytic properties and active site elucidation in the Sabatier reaction.....	291
5.6. References .....	297
<b>CHAPTER 6: Water formation reaction under interfacial confinement over AlSiO<sub>2</sub>/Ru(0001) model system.....</b>	<b>303</b>
6.1. Introduction .....	305
6.2. Materials and methods .....	311
6.2.1. Material synthesis.....	311
6.2.2. Water formation reaction procedure .....	311
6.2.3. Computational methods.....	312

6.3. Results and discussion.....	313
6.3.1. Kinetic study of the water formation reaction at constant pressure (0.1 Torr H <sub>2</sub> ) by (NAP)-XPS.....	313
6.3.2. DFT calculations.....	316
6.3.3. Reaction order with respect to H <sub>2</sub> .....	319
6.4. Conclusions .....	321
6.5. Supporting Information .....	322
6.6. References.....	323
<b>CHAPTER 7: General Conclusions .....</b>	<b>331</b>
<b>CHAPTER 8: Appendices .....</b>	<b>337</b>
8.1. List of abbreviations and acronyms .....	339
8.2. List of Figures.....	343
8.3. List of Tables .....	353
8.4. Fundamentals of selected characterization techniques .....	356
8.4.1. X-ray diffraction (XRD).....	356
8.4.2. Infrared spectroscopy (IR).....	357
8.4.3. X-ray photoelectron spectroscopy (XPS).....	360
8.4.4. X-ray absorption spectroscopy (XAS).....	365
8.4.5. Catalytic tests in the fixed-bed reactor.....	370
8.4.6. References (for Section 8.4).....	372
8.5. Scientific production.....	373
8.5.1. Publications .....	373
8.5.2. Patents.....	374
8.5.3. Conference contributions.....	374
8.6. Synchrotron projects.....	375



8.6.1. ALBA Synchrotron (Cerdanyola del Vallès, Barcelona, Spain).....	376
8.6.2. NSLS-II (Brookhaven National Laboratory, Upton, NY, United States).....	378
8.6.3. European Synchrotron Radiation Facility, ESRF (Grenoble, France).....	378
8.6.4. DIAMOND Light Source Ltd. (Didcot, Oxfordshire, United Kingdom) .....	378
8.6.5. BESSY II Photon Source, HZB (Berlin, Germany).....	378
8.7. Scientific dissemination .....	379
8.8. Dr. Patricia Concepción's group.....	380



# CHAPTER 1

## Introduction





*“A goal without a plan is just a wish”*

(Antoine de Saint-Exupéry)

## 1.1. Climate change

Climate change is one of the existential threats of our times. Direct observations made on the Earth’s surface since the mid-20<sup>th</sup> century reveal that the planet’s climate is significantly changing. These scientific evidences (as changes in temperature and precipitation patterns, sea level and acidity, or the characteristics of extreme weather events) are proceeding at a rate that is unprecedented over millennia.<sup>[1]</sup>

The Intergovernmental Panel on Climate Change (IPCC, 1988), the United Nations body for assessing the science related to this topic, defines the term as a *“change in the state of the climate that can be identified (e.g., by using statistical tests) by changes in the mean and/or the variability of its properties and that persists for an extended period, typically decades or longer. Climate change may be due to natural internal processes or external forcings such as modulations of the solar cycles, volcanic eruptions and persistent anthropogenic changes in the composition of the atmosphere or in land use”*.<sup>[2]</sup> Although the IPCC’s experts considered “natural processes” as potential sources of the phenomenon, their Fifth Assessment Report concluded in 2014 that *“there is a more than 95 percent probability that human activities over the past 50 years have warmed our planet”*<sup>[3]</sup>. In line with this affirmation, Figure 1.1 demonstrates that there is no correlation between the solar irradiance profile (yellow line, left) that is received from the Sun since 1880 and the global surface temperature changes over the same period (red

line, right). In the last 70 years, no net increase is found for the solar energy reception, whereas the global temperature has risen markedly.<sup>[4]</sup>

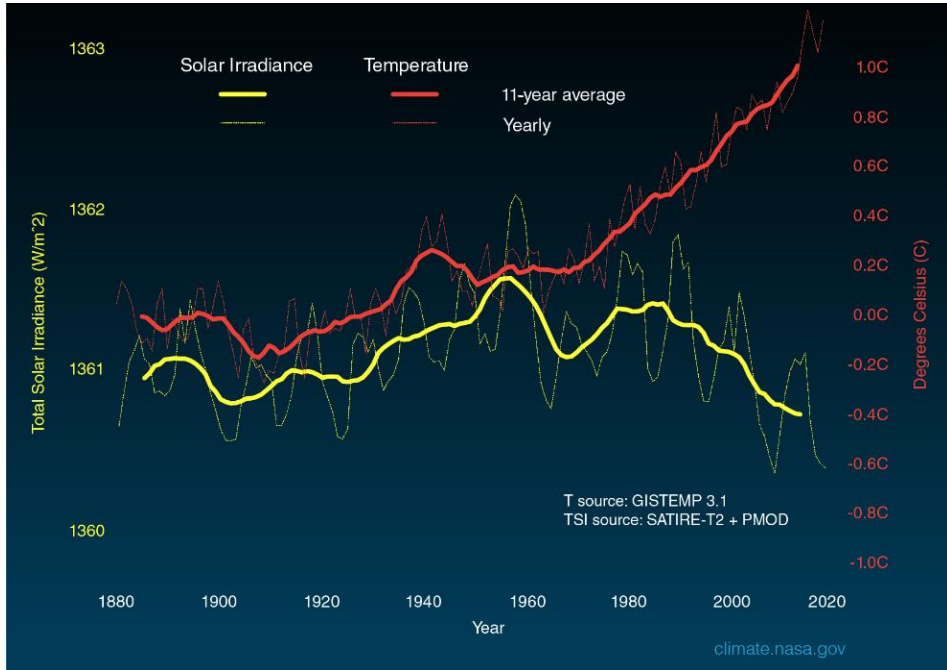


**Figure 1.1** Total Solar Irradiance (in watts per square meter) received from the Sun compared with global surface temperature changes since 1880. Thinner lines correspond to yearly levels. Thicker lines show the 11-year average trends. *Author credits: NASA/JPL-Caltech. No copyright intended.*<sup>[4]</sup>

## 1.2. Greenhouse effect and global warming

The “greenhouse effect” is the natural phenomenon responsible for regulating the Earth’s temperature, enabling life on our planet. It is caused by the so-called greenhouse gases (GHG), which act as a blanket, radiating back toward the Earth’s surface the infrared heat that are able to absorb. The most relevant GHG present in the atmosphere are water vapor, carbon dioxide, methane, nitrous oxide, and the rigidly regulated chloroflouorocarbons (CFCs).

The massive increase in the GHG emissions since the Industrial Revolution due to anthropogenic activities has unbalanced the natural greenhouse effect. Table 1.1 shows a comparison between the current atmospheric concentration of CO<sub>2</sub>, CH<sub>4</sub> and N<sub>2</sub>O and their levels in the 18<sup>th</sup> century.

**Table 1.1** Effect of human activities on the molar concentration of GHG in the Earth's atmosphere before the Industrial Revolution and nowadays.

GHG	Pre-industrial level	These days
CO <sub>2</sub>	280 ppm <sup>[5]</sup>	417 ppm <sup>[6]</sup>
CH <sub>4</sub>	722 ppb <sup>[5]</sup>	1901 ppb <sup>[7]</sup>
N <sub>2</sub> O	270 ppb <sup>[5]</sup>	334 ppb <sup>[8]</sup>

Furthermore, the IPCC's 2018 Special Report stated that the 1.0 °C of global warming occurred since the 18<sup>th</sup> century (Figure 1.1) could be followed by an additional 1.5 °C increase between 2030 and 2052.<sup>[2]</sup> This estimation was done according to the contemporary scenario and the environmental policies that ruled at the time.

### 1.3. Greenhouse gas emissions

GHG are primary drivers of global climate change and need to be urgently reduced. In this section, some trends related to GHG at a global and European levels will be reviewed. This brief analysis will help us size up our present point in terms of emissions, and how the environmental responsibility is shared between regions.

The official standard metric used to quantify the GHG emissions is the "carbon dioxide-equivalent (CO<sub>2</sub>e) tonne. Today, about 50 billion tonnes of carbon dioxide equivalents (CO<sub>2</sub>e) are emitted each year.<sup>[9]</sup> As observed in Figure 1.2, carbon

dioxide is the largest contributor with almost three-quarters of total emissions, but not the only one. Actually, methane and nitrous oxide play a leading role in global warming.

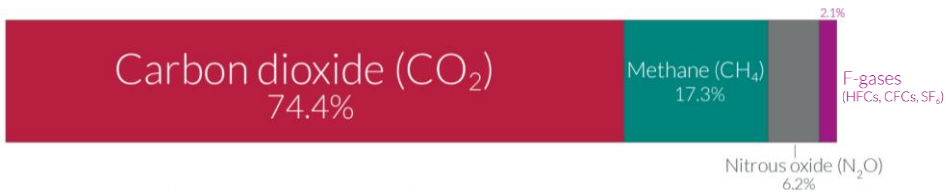


**Figure 1.2** Global greenhouse gas emissions by gas in 2016 (converted to CO<sub>2</sub>e). *Author credits: Ritchie, H. Open access under a CC-BY License.*<sup>[9]</sup>

Moreover, Figure 1.3 displays a visualization of annual CO<sub>2</sub> emissions (2017) by country and region. The relative area of rectangles is proportional to the emissions of each country.

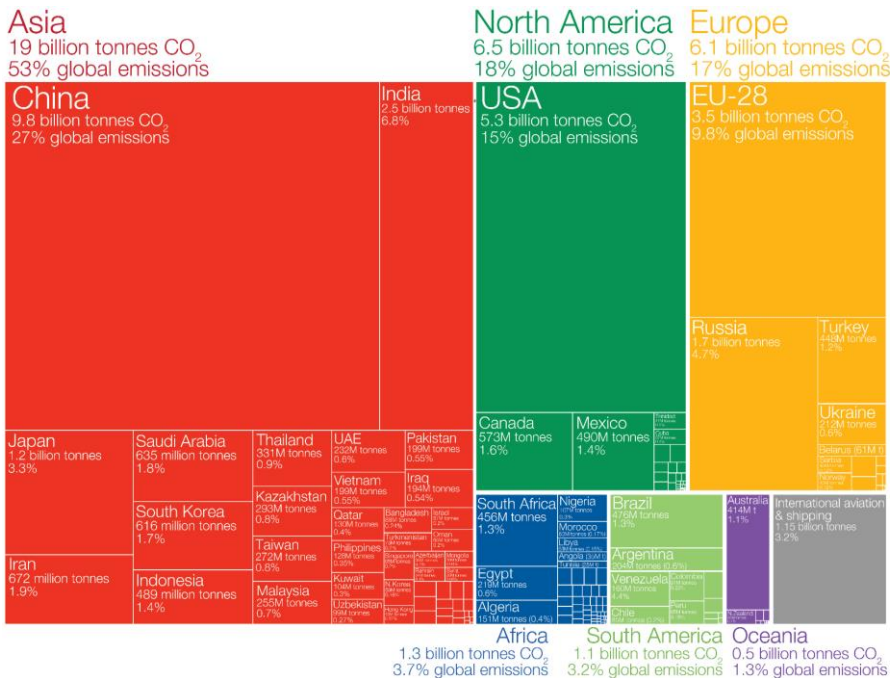


**Figure 1.3** Global CO<sub>2</sub> production-based emissions in 2017. *Author credits: Ritchie, H. Open access under a CC-BY License.*<sup>[10]</sup>



On the one hand, notice that most of the world's GHG emissions come from a small group of countries: China (red, 27%), US (green, 15%), and the European Union + United Kingdom (EU-28, yellow, ~10%). Furthermore, Asia (red) is by far the largest emitter (53%). South America (light green), Africa (blue) and Oceania (purple) account for less than 10% of the emissions, together. The contribution of international aviation and shipping (gray), are not included in national or regional emissions.

Continuing with a historical analysis, Figure 1.4 exhibits the evolution of GHG emissions in the last 30 years.<sup>[11]</sup>

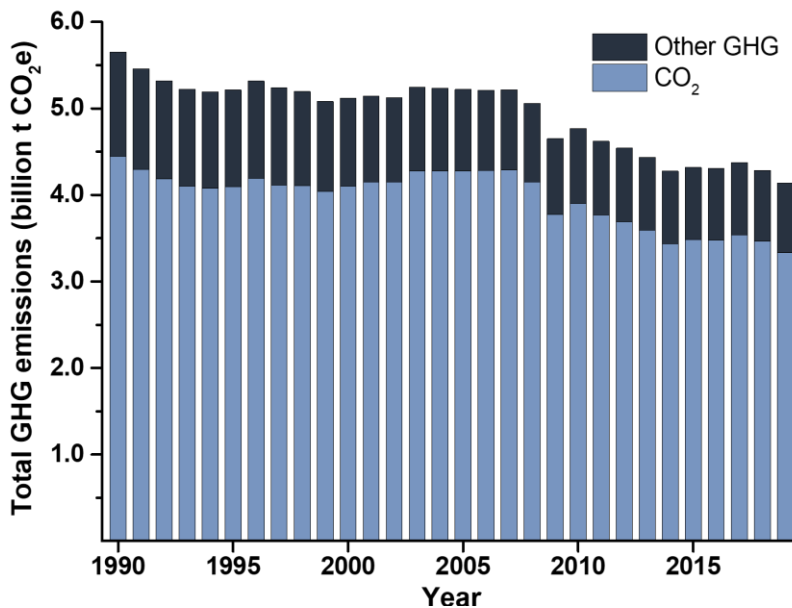


**Figure 1.4** Total GHG emissions (EU-27+UK) over the period 1990-2019 in billion tCO<sub>2</sub>e. International transport contribution is included.<sup>[11]</sup> Author credits: Coreid, J.; No copyright intended.

The first feature noticed almost instantly in this graph is the decrease of total emissions over the period. In fact, a reduction of about 27% is observed. Another

important point, in line with the global trend reviewed in Figure 1.2, is the major contribution of CO<sub>2</sub> (lighter blue bars in Figure 1.4), which accounted for 82.2% of total emissions in 2019 (the last year that has been officially reported). It was followed by CH<sub>4</sub> (10.0%), N<sub>2</sub>O (5.5%) and fluorinated gases (2.3%).

Complementing the evolution of GHG emissions in the last three decades, Figure 1.5 shows a comparison of the CO<sub>2</sub> emissions distribution according to the “environment” (or sector) where they were produced.<sup>[12]</sup> The doughnut chart confronts two temporal situations: i.e., the first and the last year of the selected period in Figure 1.4 (1990, outer ring; 2019, inner ring).

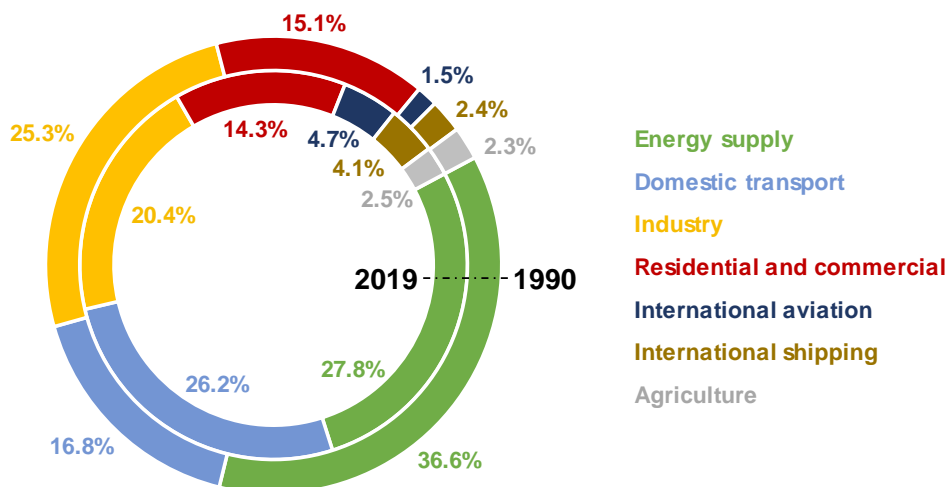


**Figure 1.5** Distribution of CO<sub>2</sub> emissions by origin (EU-27+UK). Comparison of 1990 (outer ring) and 2019 (inner ring) situations.<sup>[12]</sup> Author credits: Cored, J.; No copyright intended.

Here, three sectors clearly stand out: Energy supply, industry and domestic transport. Their percentages varied a lot over the period. Firstly, energy supply (green) and industry (yellow) sectors have diminished their importance today (from 36.6 to 27.8% and 25.3 to 20.4%, respectively), as a consequence of strong environmental regulations. On the other hand, domestic transport (light blue) has

become more relevant (16.8 to 26.2%) because of a continuous growing in the global car fleet and a strengthening of emerging markets (especially China). This latter trend is likely to change in the near future due to the introduction of electrification in the sector. Indeed, electric cars only accounted for 2.6% of global car sales in 2019.<sup>[13]</sup> Once an effective electrification will arrive to two/three-wheelers, buses and trucks, the market is expected to expand significantly, minimizing CO<sub>2</sub> emissions. On the other hand, residential and commercial emissions contribution (red) remained stable over time (15.1 to 14.3%). This trend is also found for agriculture (gray), with a small portion of total emissions (~2.5%). Finally, an increase is observed in the other minority sectors: international aviation (dark blue) tripled its percentage (4.7% in 2019 versus 1.5% in 1990) whereas international shipping (gold) almost doubled its value (2.4 to 4.1%).

## **1.4. EU International action on climate change**

### **1.4.1. A glimpse into the past**

Nowadays, the European Union and its 27 Members take part in international efforts to fight climate change under the United Nations Framework Convention on Climate Change (UNFCCC). This international treaty was agreed in 1992 during the “Rio Earth Summit”, held on the occasion of the 20<sup>th</sup> anniversary of the first Human Environment Conference in Stockholm (Sweden, 1972). Now, the UNFCCC is ratified by 197 Parties. Furthermore, this body is also responsible for two landmark environmental agreements:

One the one hand, the Kyoto Protocol (1997), which was the first global legally binding instrument for cutting GHG.<sup>[14]</sup> After signing this protocol, the EU achieved a 18% reduction of its emissions by 2012 (the target was an 8%). In view

of the good results, the European Commission reset in 2007 an ambitious 20% target by 2020, milestone that was finally surpassed two years before.<sup>[15]</sup>

After Kyoto, the Paris Agreement (2016), that is the first-ever universal, legally binding global climate change treaty, was adopted at the Paris climate conference (COP21, 2015),<sup>[16]</sup> entering into force the year after. Its long-term goal was clear: limiting global warming to well below 2 °C (preferably to 1.5 °C), compared to pre-industrial levels.<sup>[17]</sup> Likewise, countries aimed to achieve a climate neutral world by mid-century by balancing the CO<sub>2</sub> emissions and removals.

#### **1.4.2. Horizon 2050: towards climate neutrality**





Europe's future depends on a healthy planet. Current climate and environmental challenges require an urgent response... and, once again, the EU has picked up the gauntlet. Indeed, in December 2019, European Commission President Ursula Von der Layen presented the European Green Deal, a roadmap for legislative and non-legislative initiatives which will help the EU to attain an ambitious goal for Europe: to become carbon-neutral by 2050. This idea goes beyond the traditional concept of "fighting against climate change". It is about an integral transformation of Europe so that it can be the first continent to reach net zero emissions. To do so, the European Climate Law was formally adopted on 29 July 2021, which will translate the EU's political commitments on climate into legal obligations.<sup>[18]</sup> This law also sets a short-term target of an (at least) 55% reduction in GHG emissions by 2030.<sup>[19]</sup>

The decarbonization strategies and all the policies included in the roadmap towards net-zero emissions imply a major challenge that countries will have to face, sooner or later: the energy transition from fossil fuels to renewable energies.

It will require a huge collaborative effort between governments, energy companies and the scientific and investment communities in the next years.

This transition will bring with it a new reality full of opportunities. For example, renewable energies are expected to shake the current geopolitical landscape, dominated last 200 years by the control of oil, natural gas, coal and global sea routes.<sup>[15]</sup> Some countries such as China are strongly investing in new technologies related to renewables, to reinforce its global influence in the sector. Indeed, it is the world's largest producer, exporter and installer of solar panels, wind turbines, batteries and electric vehicles, taking the lead in renewable energy patents.<sup>[15,20]</sup> In this renewed context, the EU has the opportunity to reposition itself globally, profiting the enormous potential that offer these energy alternatives.

Finally, within the EU decarbonization strategies, we can find the so-called "Hydrogen strategy", which underlines its potential as a future fuel. However, decarbonizing hydrogen before its use is mandatory because the current industrial generation and use of this energy carrier are responsible for ~2% global CO<sub>2</sub> emissions.<sup>[21]</sup> Each year, ~120 million tonnes of hydrogen are produced globally, mostly based on natural gas and coal (~95%). The remaining 5% is obtained as a by-product from electrolytic chlorine production. Furthermore, there is no significant hydrogen production from renewable sources yet. Hydrogen is usually used for crude oil refining, and for ammonia and methanol synthesis, which together, represent a ~75% of H<sub>2</sub> demand. As this energetic vector can be produced from multiple processes and energy sources, a color code has been recently created to classify its origin (see Figure 1.6).

Color	GREY HYDROGEN	BLUE HYDROGEN	TURQUOISE HYDROGEN	GREEN HYDROGEN
Process	SMR or gasification	SMR or gasification with carbon capture (85-95%)	Pyrolysis	Electrolysis
Source	Methane or coal 	Methane or coal 	Methane 	Renewable electricity 

**Figure 1.6** Color code nomenclature commonly used to denominate the way hydrogen is produced. (SMR = Steam methane reforming). *Author credits: International Renewable Energy Agency (IRENA). No copyright intended.*<sup>[22]</sup>

On the one hand, gray hydrogen (grey, in British English) is produced from fossil fuels, such as methane (through steam methane reforming, SMR) or coal gasification. These methods entail substantial CO<sub>2</sub> emissions, making them undesirable for the carbon-neutral scenario by 2050. As an “intermediate stage” through clean hydrogen, blue H<sub>2</sub> appears as the most realistic option in early stages of the energy transition. It consists of producing gray H<sub>2</sub> and sequestering the CO<sub>2</sub> emitted during production via Carbon Capture and Storage technologies (discussed later). Although blue H<sub>2</sub> presents some technical limitations (fossil fuel price fluctuations, additional costs for CO<sub>2</sub> transport and storage or carbon capture inefficiencies), it is considered the most suitable option for a fully sustainable energy transition towards green hydrogen production. An intermediate shade between blue and green H<sub>2</sub> appears, noted in Figure 1.6 as turquoise hydrogen. This sort of H<sub>2</sub> is obtained through methane pyrolysis, where carbon is permanently stored in form of solid carbon black. This approach, little-known until now, is still at the pilot stage. Finally, the most advanced technology for producing green H<sub>2</sub> is water electrolysis fueled by renewable energy. Through

this green method, the International Energy Agency (IEA) estimates that the full substitution of gray H<sub>2</sub> would mean 3000 TWh of additional renewable production per year, equivalent to Europe's current electricity demand. Furthermore, this technology has different characteristics (both positive and negative) that we must take into account: Firstly, green H<sub>2</sub> production is (ideally) 100% sustainable, since there is no emission of pollutant gases during the process. Moreover, hydrogen is easily storable, which means that it is not necessary to be used instantly after production. In addition, it could be transported through methane pipelines with minor modifications in structural elements if necessary, too. Another advantage of this molecular gas is its versatility: For instance, it can be transformed into electricity or synthetic fuels, for domestic, industrial or mobility purposes. In contrast, critical disadvantages are now the higher energy consumption to produce green H<sub>2</sub> compared to other fuels, together with the high price of this energy coming from renewable and intermittent sources. Additionally, due to its volatility and flammability, safety issues will have to be addressed to avoid leaks or explosions. Because of these reasons, the EU is planning to install hydrogen electrolyzers (6 GW) by 2024, power that is expected to be increased to 40 GW by 2030, and to 500 GW by the mid-century.<sup>[15]</sup>

Despite these promising perspectives, we have to be cautious and realistic... At this moment, the production of green H<sub>2</sub> is (still) not economically viable. With the current scenario, where the price of gray hydrogen is ~1.5 €/kg, the prices estimated by the EU for blue H<sub>2</sub> (2.4 €/kg) and green H<sub>2</sub> (up to 5.5 €/kg) are not competitive enough.<sup>[15]</sup> However, with more mature hydrogen technologies and

infrastructure, a stable regulatory framework and a new financial paradigm, this tough road can turn into an exciting journey very soon.

## **1.5. CO<sub>2</sub> remediation technologies**

Throughout the above sections, we have reviewed the issue of climate change, its causes and consequences, and how global and regional organizations are working to develop integral environmental policies and setting different targets by 2050. The main goal is clear: to achieve net-zero emissions... but how to reduce CO<sub>2</sub> deliverance? We can adopt two different approaches: On the one hand, avoiding its production. Although this option may sound obvious at first glance, we have to take into account that the current chemical paradigm, based on fossil fuels and a mature industry, presents a limited operational flexibility. To get a realistic and effective differentiation in emissions, we will have to redesign reactions, to find new synthetic procedures and separation processes, developing advanced technologies... and this important transition will take time (and investment). On the other hand, the second group of strategies is focused on CO<sub>2</sub> management. If these emissions cannot be completely reduced, then they will have to be removed in a certain way: to do so, this gas has to be captured, transported, and finally stored or transformed in other chemical compounds. These technologies, known as Carbon Capture and Storage (CCS) and Carbon Capture and Utilization (CCU) will be described next. But before starting with CO<sub>2</sub> remediation technologies, it is indispensable to briefly detail the characteristics of this molecule.



### 1.5.1. Physico-chemical properties of CO<sub>2</sub>

Carbon dioxide is an odorless, colorless and non-flammable gas. It is a linear 16 e<sup>-</sup> molecule belonging to the D<sub>∞h</sub> geometry group, which features very short C-O bond lengths in its ground state (1.16 Å).<sup>[23]</sup> This double C=O confers high stability to CO<sub>2</sub> ( $\Delta G_f^0 = -394.4 \text{ kJ}\cdot\text{mol}^{-1}$ ), considering it as an “inert” compound. Although CO<sub>2</sub> is a non-polar molecule, the electronegativity difference between C (2.5) and O (3.5) imparts a partial electrophilic character on the carbon center and a weak nucleophilic character on the terminal oxygen atoms. Therefore, CO<sub>2</sub> is considered as a bifunctional (or amphoteric) molecule, with two distinct reaction sites. In addition, CO<sub>2</sub> can react with bases since it is a weak Brønsted acid in water (forming H<sub>2</sub>CO<sub>3</sub>). Moreover, the physical state of CO<sub>2</sub> is temperature/pressure dependent (Figure 1.7),<sup>[24]</sup> which makes it suitable for diverse applications:

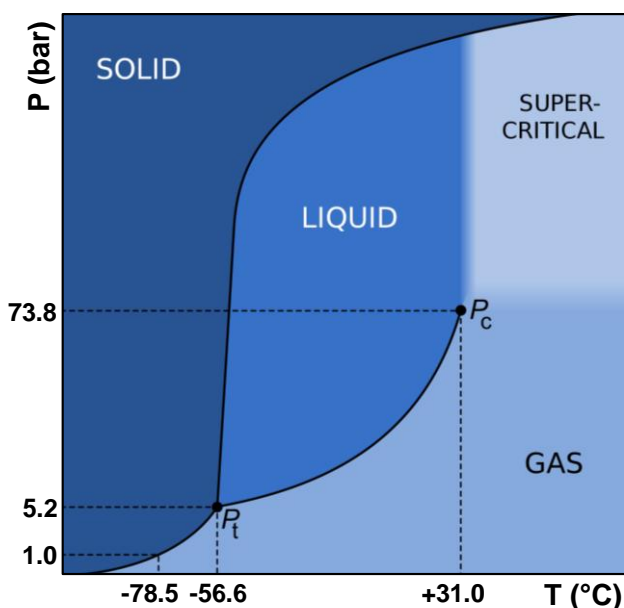


**Figure 1.7** The phase diagram of carbon dioxide. *Author credits: Rothwild-Wikimedia Commons. No copyright intended.*<sup>[25]</sup>

For instance, CO<sub>2</sub> becomes solid at low temperature (-78.5 °C) and atmospheric pressure ("dry ice"), and is used as a cooling agent in this phase, sublimating directly below ~5 bar. In its supercritical state (exceeding the critical point at 31 °C and ~74 bar), it is applied in the pharmaceutical industry and in other sectors to extract selectively some substances (e.g., caffeine). Moreover, supercritical and liquid CO<sub>2</sub> is also utilized in the field of heterogeneous catalysis, since it can act simultaneously as reactant and/or solvent in a high-pressure reaction setup, overcoming thermodynamic limitations.<sup>[26-29]</sup>

### 1.5.2. CO<sub>2</sub> capture

Historically, oil and gas industries have used carbon capture as a way to enhance the recovery of oil and gas from dried oil rigs. Some of these technologies were already available one century ago and were used to separate CO<sub>2</sub> from methane extracted from natural gas reserves.<sup>[30]</sup>

The objective of CO<sub>2</sub> capture is to remove selectively this gas from a mixture to produce a concentrated CO<sub>2</sub> stream. There are two main types of carbon dioxide sources: The ambient air and the so-called stationary points (industrial plants). Depending on the sort of facility, the gas composition, impurities or working conditions can differ.<sup>[31]</sup> For instance, CO<sub>2</sub>/N<sub>2</sub> mixtures are usually produced in coal power plants and in cement or steel industries, whereas CO<sub>2</sub>/CH<sub>4</sub> mixtures are found in natural gas wells. In addition, CO<sub>2</sub>/H<sub>2</sub> mixtures are produced in gasification plants. Some common impurities are H<sub>2</sub>O, N<sub>2</sub>, O<sub>2</sub>, NO<sub>x</sub> and SO<sub>x</sub>. Depending on the specific characteristics of each process, the carbon capture is combined with different strategies, such as post-combustion, pre-combustion and oxy-fuel combustion.<sup>[30]</sup>

A wide range of technologies are being developed for capturing CO<sub>2</sub>, and we will focus on three approaches applied in stationary points:<sup>[31]</sup>

- Conventional solvents: CO<sub>2</sub> capture is carried out by physical or chemical absorption. The former procedure depends on temperature and pressure differences, and the latter takes advantage of the acidic character of CO<sub>2</sub> in water to neutralize it in basic media. Generally, monoethanolamine (MEA) has been the standard absorber for post-combustion capture. However, physical solvents (such as chilled methanol or N-methylpyrrolidone) are used for pre-combustion capture, due to the lower partial pressure of CO<sub>2</sub> in the mixture.
- Solid sorbents: These materials are able to bind selectively CO<sub>2</sub> from gas mixtures and concentrate it through the mediation of pressure or temperature. Depending on the solid characteristics, the CO<sub>2</sub> uptake capacity, selectivity and stability can vary. For instance, zeolites, metal organic frameworks (MOFs), and amine-grafted solid materials are applied in this approach.
- Membranes: This option is fabricated using (semi)permeable materials, which are good candidates for selective CO<sub>2</sub> separation. Inorganic membranes based on ceramics, metal oxides, graphene oxide, zeolites or MOFs are employed. Another promising options are polymeric membranes (presenting excellent mechanical properties and low fabrication costs) or mixed matrix membranes (a combination of a homogeneously distributed inorganic phase and a bulk polymeric phase).

In the future, critical issues like long-term stability, high CO<sub>2</sub> purity or tolerance to impurities (such as water) have to be improved. In addition, some scalability issues, long regeneration times and environmental impacts derived from advances organic synthesis are problems to be addressed.

### **1.5.3. CO<sub>2</sub> transportation**

After CO<sub>2</sub> capture, the next step is its transportation (in liquid or supercritical state) to a remote location, where it can be stored. Depending on the volume of gas and the compression applied during the capture stage, several options are available, such as roads, ships, or pipelines. The latter is recommended if long distances are involved. In addition, pipelines are always accompanied by recompression stations, to solve any pressure drop that might occur during the process.

### **1.5.4. CO<sub>2</sub> storage**

CO<sub>2</sub> storage is the final step on CCS technologies, where the gas is stored in large-scale geological formations with high porosity. Different sites can be selected, depending on pore fluid dynamics, local mineralogy and geochemistry. With a depth of at least ~1 km, the area must have a proper temperature and pressure so that CO<sub>2</sub> can be safely injected, remaining trapped into a reservoir in liquid or supercritical state for a long time. Then, saline aquifers, the deep ocean and depleted oil reserves are usual locations. Related to the third place, CO<sub>2</sub> can be used to extract more oil from existing wells or reservoirs (enhanced oil recovery, EOR).

Over the past five decades, CCS technologies have demonstrated that are able to reduce CO<sub>2</sub> emissions consistently and safely (~300 million tonnes of CO<sub>2</sub> stored

to date).<sup>[32]</sup> CCS can eliminate fossil-fired CO<sub>2</sub> emissions from power plants, supporting renewable approaches that will become a reality in the near future, addressed to the total decarbonization. Today, there are 65 commercial CCS facilities worldwide: 26 are currently operating, storing about 40 Mt of CO<sub>2</sub> per year (~90% CO<sub>2</sub> capture rate is currently achieved).<sup>[32]</sup> The others are in different stages (under construction and/or development, operating at a demonstration scale...). The global distribution of these facilities is depicted in Figure 1.8, where the US is found as central node.



**Figure 1.8** Current CCS commercial facilities in the world. *Author credits: Global CCS Institute. Open access under a CC BY-NC-ND 4.0 License.*<sup>[33]</sup>

### 1.5.5. Carbon Capture and Utilization

Carbon capture and utilization (CCU) is a broad term that covers innovative industrial processes that aim at capturing carbon dioxide (from previously mentioned stationary points or directly from the air) and at transforming this GHG into a variety of value-added products, such as chemicals, fuels or building

materials. By following this approach, and in combination with CCS technologies, the linear carbon cycle will progressively evolve to a circular carbon cycle.

Nevertheless, the chemical utilization of CO<sub>2</sub> is not (only) a 21<sup>st</sup> century trending topic. Industrial processes developed at the end of 19<sup>th</sup> century such as the synthesis of urea,<sup>[34]</sup> the soda Solvay process,<sup>[35]</sup> and the production of salicylic acid<sup>[36]</sup> already included CO<sub>2</sub> as a reactant. In the 1900s, CO<sub>2</sub> was eclipsed by the “golden era” of CO chemistry to obtain chemicals and fuels. However, from the 1970s, a renewed interest in CO<sub>2</sub> exploitation arose, coinciding with its use as additive in the CO hydrogenation to methanol,<sup>[37]</sup> and its utilization in organic applied chemistry (e.g., formation of organic carbonates from epoxides).<sup>[38]</sup> Despite this, it has not been widely used as raw material in industrial processes because of its high stability. The reason of this inertness lies in the high oxidation state of carbon atom in CO<sub>2</sub> molecule (i.e., 4+), which means that a considerable energy input is required to transform the molecule into higher-valued chemicals (see Subsection 1.5.1).

In view of near-future environmental perspectives, the introduction of renewable energy into a catalytic process is of particular interest, since it comprises ~25% of the current global electricity capacity.<sup>[39]</sup> However, we need to understand that electricity-driven CO<sub>2</sub> transformation processes are in early stages of development, presenting different barriers or limitations. Electricity could be utilized directly in the CO<sub>2</sub>R transformation (where, “R” means reductive), or indirectly to obtain an energy carrier (such as H<sub>2</sub>). Now, different accessible approaches will be briefly discussed and compared with the traditional thermocatalysis (which is a more mature and well established field).<sup>[40]</sup>

- Direct electrochemical pathway: An external voltage is applied across two electrodes (separated by a selective ionic membrane) in an electrolyzer, where  $\text{CO}_2$  can be reduced to  $\text{C}_1$ - $\text{C}_2$  products such as CO, formic acid, ethylene, ethanol, and other oxygenates. Although this technology could be commercially deployed for  $\text{C}_1$  compounds with 100% theoretical  $\text{CO}_2$  conversion and high energy conversion efficiency, the current selectivity to products involving a chain growth ( $\text{C}_{2+}$ ) is low, presenting deactivation issues that affect the long-term stability of the process. In order to improve the catalytic features of this pathway (selectivity to certain products,  $\text{CO}_2$  conversion per pass) or solving technical problems such as scaling up the synthesis or the cell overpotential, new catalytic materials and membranes have to be investigated, together with a systematic optimization of the reaction conditions (electrolytes, pH, mass transport, etc.). In line with this, it is possible to complement this pathway by using microorganisms (i.e., microbial electrosynthesis, MES). The idea would be to perform the  $\text{CO}_2$  reduction under milder conditions in a bio-cathode inoculated with anaerobic microorganisms, which are able to fix carbon in a very high selective way to obtain mainly methane and acetate (and potentially other  $\text{C}_1$ - $\text{C}_6$  species). Despite the low productivity obtained, the ~100% selectivity and the possibility of tuning the microorganism characteristics via genetic engineering turn this approach very appealing. This will need a better understanding of reaction mechanisms, a further development in bio-compatible electrodes, and an optimization of electrical properties (e.g., current density) without damaging the inoculated cultures.

- Photo-electrochemical approach: the combination of electricity and light in the same process has also appeared as a promising option because the application of an electric field allows the physical separation of the photogenerated charge carriers (electrons and holes) on two electrodes, increasing the lifetime of these carriers, and consequently, the catalytic activity.<sup>[41]</sup> However, due to the multi-electronic transfer process and the similarity of the chemical potentials needed to synthesize different C<sub>1</sub> products (such as CO, MeOH, CH<sub>4</sub>, or formic acid), obtaining a high selectivity in this dual process is still a challenge.
- Non-thermal plasma (NTP): Also known as cold plasma, is the state of matter comprising ionized gaseous species that are not under thermodynamic equilibrium. The electron temperature in NTP is higher compared to that of other molecules in the ionized gas. In those conditions, the electrons possess an energy of about 1-10 eV, which is in the suitable range to activate and break chemical bonds (5.5 eV for C=O bond in CO<sub>2</sub> molecule). Depending on the reactor configuration (dielectric barrier, microwave, or gliding arc) and the feedstock composition (including CO<sub>2</sub> and other compounds such as H<sub>2</sub> or H<sub>2</sub>O), different saturated and unsaturated C<sub>2</sub>-C<sub>3</sub> hydrocarbons and oxygenates (ethanol or acetic acid) can be obtained. Although a high power demand and low selectivity to C<sub>2+</sub> products are now important limitations, it is possible to obtain a 100% theoretical CO<sub>2</sub> conversion with a flexible feedstock. This approach has a long way to go, since commercially viable reactor designs presenting high CO<sub>2</sub> conversions (and being energetically efficient) are still far.



- Indirect thermochemical approach: By combining heat, pressure, and heterogeneous catalysts, thermocatalytic hydrogenation of CO<sub>2</sub> offers diverse mature routes to obtain products of industrial interest. Despite the availability of existing industrial infrastructure and knowledge of these transformations, some technical challenges have to be addressed. For instance, most of CO<sub>2</sub>R pathways are reversible, presenting thermodynamic constraints that limit the single-pass conversion of CO<sub>2</sub>. Lower product yields signify additional costs related to downstream purification. Moreover, the conventional routes are usually multistage processes, where critical impurities (such as H<sub>2</sub>O) are removed in between stages to minimize catalyst deactivation. Then, the overall goal must be the development of stable multifunctional catalytic formulations, which allow the process intensification. In addition, the thermodynamic limitations can be overcome by using improved reactor designs or by optimizing the operational conditions. Finally, the integration of green H<sub>2</sub> and captured CO<sub>2</sub> in these highly energy-demanding processes will help to reduce the environmental impact, leading the transition to a more sustainable circular carbon economy.

### **1.5.6. Thermocatalytic CO<sub>2</sub> hydrogenation to value-added products**

As it has been discussed above, a pivotal task for us, as scientists that investigate in the field of heterogeneous catalysis, is to find active, selective, and stable catalysts that assist the transformation of CO<sub>2</sub>. Accordingly, thermocatalytic CO<sub>2</sub> hydrogenation has been extensively studied,<sup>[42,43]</sup> obtaining a wide “catalogue” of processes and materials that “connects” CO<sub>2</sub> with various chemicals, as depicted in Figure 1.9.

Among all these possibilities, this thesis will be focused on the synthesis of methanol and methane. Both  $C_1$  compounds are platform chemicals (and precursors for further synthesis of industrial interest).

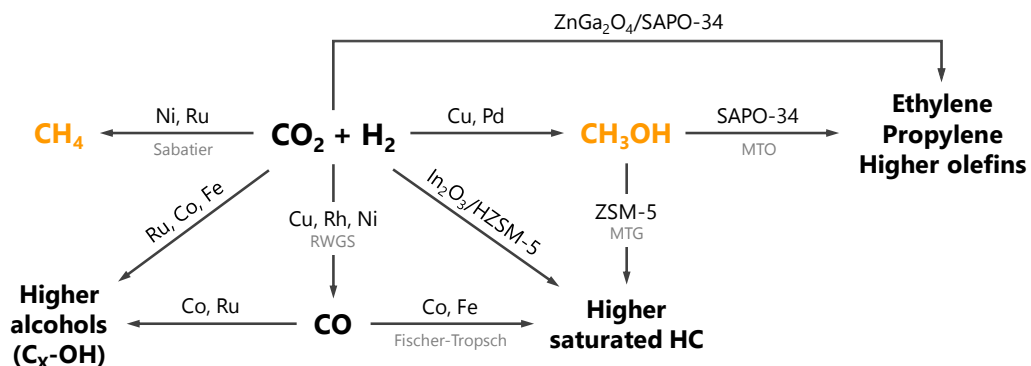


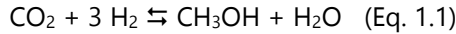
**Figure 1.9**  $CO_2$  chemical network to obtain diverse products of industrial interest via thermocatalytic hydrogenation. *Author credits: Concepción, P. and Cored, J.; No copyright intended.*

### 1.5.7. Methanol synthesis

Methanol is one of the most important commodities in the chemical industry and represents a promising energetic vector for a sustainable economy with an annual production of about 95 million tonnes.<sup>[44,45]</sup> Nowadays, almost all methanol is produced from natural gas and coal in a two-step process. The first step, which is the syngas ( $CO + H_2$ ) production, accounts for ~60% of the total cost.<sup>[42]</sup> Moreover, this commodity attracts widespread interest because of its various applications: it is used as common solvent, fuel additive, is employed in fuel cells, or as intermediate for the industrial production of DME, olefins, gasolines, formaldehyde, methyl *tert*-butyl ether (MTBE), among others. Most of these compounds are also building blocks to obtain products in our daily life, such as plastics, adhesives, resins, paints...

### *Thermodynamic considerations*

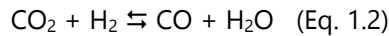
In view of thermodynamics, CO<sub>2</sub> hydrogenation to methanol is a highly hampered exothermic process (Eq. 1.1):<sup>[24]</sup>



$$\Delta H^0_{298\text{K}} = -49.5 \text{ kJ/mol}$$

$$\Delta G^0_{298\text{K}} = -9.0 \text{ kJ/mol}$$

Methanol synthesis competes with reverse water-gas shift reaction (RWGS, Eq. 1.2), and it is also possible that CO, formed via RWGS, undergoes toward methanol (Eq. 1.3):<sup>[24]</sup>



$$\Delta H^0_{298\text{K}} = +41.1 \text{ kJ/mol}$$

$$\Delta G^0_{298\text{K}} = -20.1 \text{ kJ/mol}$$



$$\Delta H^0_{298\text{K}} = -90.6 \text{ kJ/mol}$$

$$\Delta G^0_{298\text{K}} = -29.1 \text{ kJ/mol}$$

According to Le Châtelier's principle, working at low temperatures and increasing the reaction pressure favors methanol synthesis (Eq. 1.1), due to the exothermic nature of the process and a decrease in the number of molecules, respectively. These modifications does not positively affect RWGS (Eq. 1.2), since this competing reaction is endothermic and there is no change in the number of total molecules between reactants and products. Moreover, altering the stoichiometry of the feed gases (i.e., high H<sub>2</sub>/CO<sub>2</sub> molar ratio) also favors methanol formation. Figure 1.10 illustrates the thermodynamic limitations of CO<sub>2</sub> to methanol reaction

at stoichiometric conditions (left panels) and at increased  $\text{H}_2/\text{CO}_2$  molar ratio (right panels).

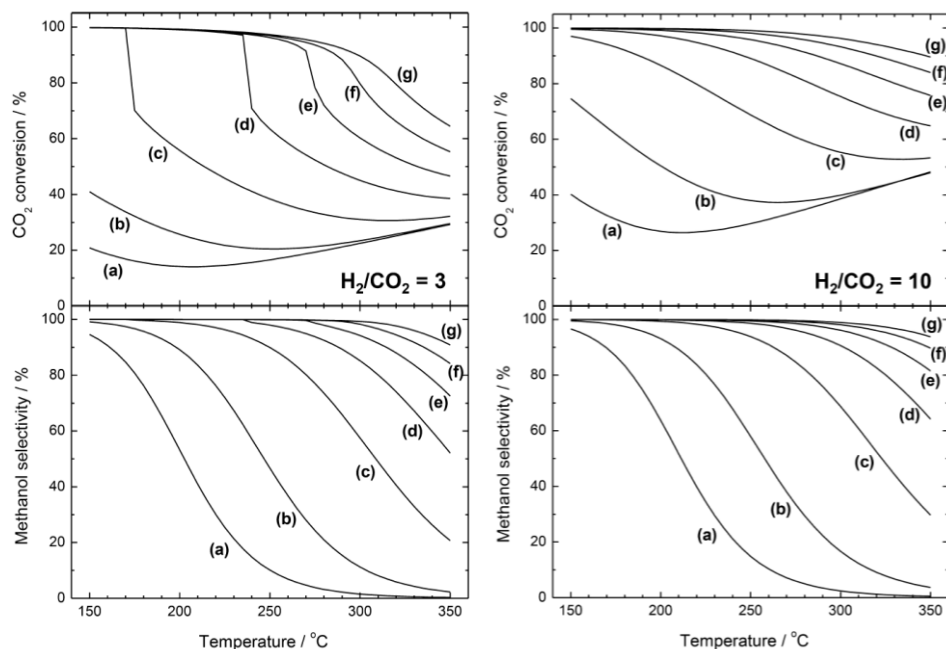


**Figure 1.10** Equilibrium  $\text{CO}_2$  conversion and methanol selectivity at different temperatures and at increasing pressures: (a) 10 bar, (b) 30 bar, (c) 100 bar, (d) 200 bar, (e) 300 bar, (f) 400 bar, and (g) 500 bar. Initial  $\text{H}_2/\text{CO}_2$  molar ratio mixtures of 3 (left panels) and 10 (right panels) are used. *Reprinted with permission from ACS Catal. 2020, 10, 14147-14185. Copyright 2020 American Chemical Society.*<sup>[43]</sup>

As observed in Figure 1.10, operational pressure is a key factor to shift the equilibrium conversion at any stoichiometry in the 150–350 °C temperature range. Indeed, an abrupt change is observed when the pressure is increased from 30 (“b” line) to 200 bar (“d” line), caused by the formation of a liquid phase.<sup>[24]</sup> Indeed, at 200 bar, ~240 °C, and under stoichiometric conditions ( $\text{H}_2/\text{CO}_2=3$ ), it is already possible to overcome thermodynamic limitations, obtaining a theoretical value of 100%  $\text{CO}_2$  conversion (see Figure 1.7). Regarding to methanol selectivity, two

trends are highlighted: Firstly, at relatively low temperatures (i.e.,  $<250\text{ }^{\circ}\text{C}$ ), where methanol synthesis predominates over RWGS, the selectivity to MeOH increases at increasing the working pressure. On the other hand, methanol selectivity dramatically drops with rising temperature at low pressure ( $<100\text{ bar}$ ), which is caused by the enhancement of endothermic RWGS reaction.

### *Catalyst development*

The very first industrial syngas-based (i.e.,  $\text{CO}+\text{H}_2$ ) process for methanol synthesis was developed by BASF in the 1920s. By using  $\text{ZnO}-\text{Cr}_2\text{O}_3$  catalysts, the reaction was operated under harsh conditions ( $300\text{-}400\text{ }^{\circ}\text{C}$  and  $250\text{-}300\text{ bar}$ ).<sup>[46]</sup> In the 1960s, ICI introduced a highly selective  $\text{Cu}/\text{ZnO}/\text{Al}_2\text{O}_3$  system, operating at milder reaction conditions ( $220\text{-}300\text{ }^{\circ}\text{C}$  and  $50\text{-}100\text{ bar}$ ). Since then, research has been mainly focused on copper-based materials (in particular in  $\text{Cu}-\text{ZnO}$  combinations), but there are three more groups of solids that have appealed chemists last 20 years: palladium-based, bimetallic, and oxide catalysts (see Table 1.2 below for a summary of representative catalysts operating in the  $\text{CO}_2$  hydrogenation to MeOH).

- Cu-based systems: Typically, commercial-like catalysts are prepared by a co-precipitation method with a 60 wt % Cu, 30 wt % ZnO, and 10 wt %  $\text{Al}_2\text{O}_3$  composition. This preparation method consist of precipitating metallic hydroxycarbonates or hydroxides mixing a metal precursor solution (i.e., nitrates, acetates...) with a basic precipitating agent ( $\text{CO}_3^{2-}$ ,  $\text{HCO}_3^-$ ,  $\text{OH}^-$ ). Temperature and pH are key parameters that need to be controlled in this step. Precipitation is followed by an aging period, where the usually amorphous formed precipitates evolve towards crystalline phases, such as aurichalcite or zincian malachite. To obtain the final

catalyst, the solution is dried, and the resulting solid is firstly calcined, and then reduced (sometimes, reduction step is carried out in situ in the catalytic reactor). In addition to co-precipitation, another approaches such as sol-gel synthesis,<sup>[47]</sup> citrate decomposition,<sup>[48-50]</sup> and impregnations<sup>[51,52]</sup> have also been reported. In Cu/ZnO commercial formulations, alumina ( $\text{Al}_2\text{O}_3$ ) acts as a structural promoter, facilitating the dispersion of copper particles and conferring mechanical and thermal stability to the catalyst. ZnO also acts as a geometric spacer between CuNPs. However, it has an additional role, modulating the electron properties owing to the metal/support interaction (i.e., SMSI effect). Moreover, zirconia ( $\text{ZrO}_2$ ) is another support that accompanies Cu in catalysts for  $\text{CO}_2$  hydrogenation to methanol. Indeed, due to the excellent mechanical and thermal stabilities, high specific surface area, low hydrophilicity and semiconductor properties, Cu/ $\text{ZrO}_2$  based catalysts usually exhibit higher catalytic performance than Cu/ZnO/ $\text{Al}_2\text{O}_3$ .<sup>[53-55]</sup> Additionally,  $\text{ZrO}_2$  possesses two crystallographic phases (i.e., monoclinic and tetragonal) with distinctive  $\text{CO}_2$  to methanol catalytic behavior. Monoclinic phase (m- $\text{ZrO}_2$ ) exhibits a higher amount of Zr-OH Brønsted groups, together with both stronger Lewis acidity of  $\text{Zr}^{4+}$  and basicity of  $\text{O}^{2-}$  ions than tetragonal phase. These features explain the superior activity and improved MeOH selectivity, compared to its tetragonal analogous.<sup>[56,57]</sup> The level of nanocrystallinity is also a decisive property since the lower is the particle size, the higher is the number of exposed surface sites, resulting in higher activity and atomic efficiency of the catalytic system. However, methanol synthesis has been reported as a structure-sensitivity reaction, where a drop in activity is found

for Cu particles smaller than  $\sim 8$  nm.<sup>[58]</sup> This issue will be addressed in Chapter 4, where a rational design of a 2 nm copper-based catalyst will allow obtaining competitive catalytic results. More recently, a variety of materials such as CeO<sub>2</sub> (with its peculiar Ce<sup>3+</sup>/Ce<sup>4+</sup> reversible valence change and oxygen vacancies),<sup>[59,60]</sup> SiO<sub>2</sub>,<sup>[61]</sup> carbon derived materials,<sup>[62]</sup> and graphene oxide<sup>[63,64]</sup> have been developed for this reaction. It is also worth mentioning MOFs as potential materials for methanol synthesis. Indeed, the confinement/encapsulation of CuNPs into MOFs cavities displays a new sort of opportunities: for instance, synergy between Cu and Zr metal centers in Cu@UiO-66,<sup>[65]</sup> or an improved rate of methanol formation caused by electron donating functional groups in organic linkers interacting with intermediates.<sup>[66]</sup> Additionally, the incorporation of other metal oxides as additives (e.g., Ga<sub>2</sub>O<sub>3</sub>,<sup>[67-69]</sup> La<sub>2</sub>O<sub>3</sub>,<sup>[70]</sup> Y<sub>2</sub>O<sub>3</sub>,<sup>[71]</sup> TiO<sub>2</sub><sup>[72]</sup>) or noble metals as dopants (e.g., Pd<sup>[73]</sup> and Au<sup>[74]</sup>) is a recurring strategy to improve the catalytic performance. Indeed, their inclusion in the catalytic formulation improves certain characteristics such as Cu dispersion or reducibility, modifies acid-base, redox and electrical properties, enhancing the activity (and the selectivity to desired products). The effect of gallium promotion in methanol synthesis will be investigated in Chapter 3, where we will deepen into the phenomenon at a catalytic and fundamental level. Finally, although Cu-based systems are widespread used because of their superior performance, they occasionally suffer from low thermal and temporal stability caused by copper sintering (under reductive conditions), copper partial oxidation or ZnO agglomeration accelerated by water

formation (as by-product).<sup>[75]</sup> To mitigate this feature, new catalytic compositions (and reactor configurations) are being investigated.

- Pd-based catalysts: Due to the superior stability and resistance to sintering and poisoning, Pd-based catalysts have been studied as alternatives of Cu-based systems. Similarly to copper, different types of supports, including oxides (ZnO,<sup>[76,77]</sup> CeO<sub>2</sub>,<sup>[78,79]</sup> Ga<sub>2</sub>O<sub>3</sub>,<sup>[80,81]</sup> In<sub>2</sub>O<sub>3</sub><sup>[82]</sup>), mesoporous silica,<sup>[83,84]</sup> and carbon materials<sup>[85,86]</sup> have been formulated in combination with palladium by following diverse synthetic procedures, such as co-precipitation,<sup>[87]</sup> incipient wetness impregnation,<sup>[85,88]</sup> sol-immobilization,<sup>[88]</sup> and citrate decomposition.<sup>[78]</sup>
- Bimetallic systems: These catalysts, presenting unique structural and electronic properties, derived from the synergistic effect of two metals, can be divided into alloys (such as Cu-X, X=Zn,<sup>[69,89]</sup> Pd,<sup>[90,91]</sup> Ni,<sup>[92]</sup> Ag,<sup>[93]</sup> Pd-Zn<sup>[78,88]</sup> and Pd-Ga;<sup>[80]</sup> Pt-Co,<sup>[94]</sup> Rh-W<sup>[95]</sup>) and the so-called intermetallic compounds, where both elements are homogeneously distributed (e.g., Ni-Ga,<sup>[96]</sup> Cu-In;<sup>[97]</sup> Pd-X, X=Ga,<sup>[98]</sup> Zn,<sup>[98]</sup> In<sup>[99]</sup>).
- Oxides and hybrid oxide systems: Novel catalytic formulations with singular structures, such a core-shell MnO<sub>x</sub>/m-Co<sub>3</sub>O<sub>4</sub> and a ZnO-ZrO<sub>2</sub> solid solution exhibit competitive catalytic activity.<sup>[100]</sup> Indeed, Li et al. reported for the latter solid solution that the strong synergy between Zn and Zr allows the catalyst activating both H<sub>2</sub> (adsorbed and dissociated on Zn sites) and CO<sub>2</sub> (activated onto Zr sites).<sup>[101]</sup> Moreover, the oxygen-deficient "metal-free" In<sub>2</sub>O<sub>3</sub> has been identified as a suitable catalysts for methanol synthesis. Despite the good selectivity exhibited by this type of



catalysts, their activity is still improvable, fact that can be solved through the combination with acid functionalities to obtain dimethyl ether (DME) or olefins.

### Reaction mechanism

Knowledge about reaction mechanisms at a molecular level is essential to guide the rational design of catalysts with improved catalytic performance. As will be further discussed in Chapters 3 and 4, many aspects in MeOH synthesis are still under debate, some of them related to active centers and reaction mechanisms. A combination between experimental and theoretical approaches has been needed to unravel this reaction at a fundamental level.

The three proposed pathways for methanol formation over Cu-based catalysts are illustrated in Figure 1.11.<sup>[102]</sup>

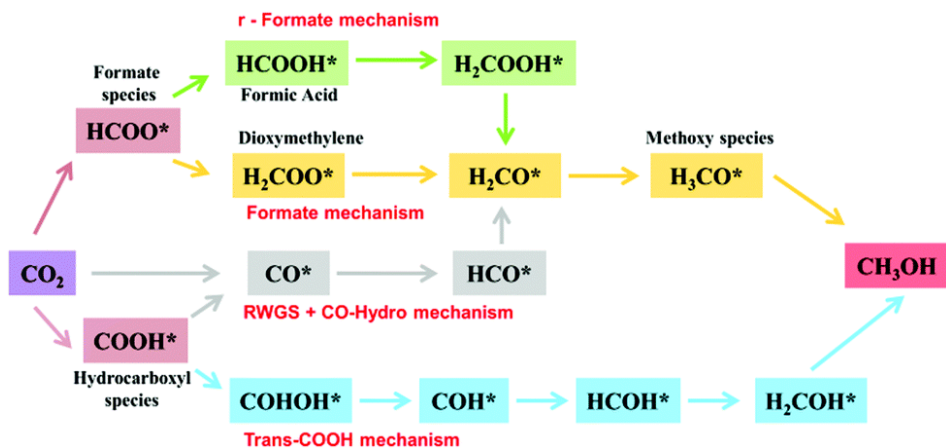


**Figure 1.11** Proposed reaction network for methanol synthesis from CO<sub>2</sub> hydrogenation. (\*) indicates adsorbed species. *Reproduced from Chem. Soc. Rev. 2020, 49, 1325-1616 with permission from the Royal Society of Chemistry (Copyright 2020).*

The most conventional and accepted mechanism occurs via formate (HCOO\*, yellow route). After CO<sub>2</sub> adsorption through the Eley-Rideal or Langmuir-

Hinshelwood mechanisms, dioxymethylene ( $\text{H}_2\text{COO}^*$ ) intermediate is formed from formate, that is further hydrogenated to formaldehyde ( $\text{H}_2\text{CO}^*$ ), methoxy ( $\text{H}_3\text{CO}^*$ ), and finally methanol ( $\text{CH}_3\text{OH}^*$ ). The overall reaction rate of this route is limited by both  $\text{HCOO}^*$  and  $\text{H}_2\text{COO}^*$  hydrogenations, being the latter the rate-determining step.<sup>[103]</sup> An alternative (revised) formate pathway has also been reported,<sup>[104]</sup> where formate is ( $\text{HCOO}^*$ ) preferentially hydrogenated to formic acid ( $\text{HCOOH}^*$ , green route). Then, formic acid is hydrogenated to  $\text{H}_2\text{COOH}^*$  and the C-O is split to form formaldehyde ( $\text{H}_2\text{CO}^*$ ).

The second pathway is called *trans*-COOH mechanism (blue route). This pathway starts with the formation of hydrocarboxyl intermediate ( $\text{COOH}^*$ ), which isomerizes to dihydroxycarbene ( $\text{COHOH}^*$ , similarly expressed as  $=\text{C}(\text{OH})_2$ ). Hydroxymethylidyne species ( $\text{COH}^*$ ) are formed via OH scission from  $\text{COHOH}^*$ , that is transformed to hydroxymethylene ( $\text{HCOH}^*$ ) after H addition. Then,  $\text{HCOH}^*$  is further hydrogenated to hydroxymethyl ( $\text{H}_2\text{COH}^*$ ), and finally to methanol.

The third possibility is the RWGS + CO-hydro pathway (gray route), beginning similarly to the *trans*-COOH mechanism (blue).  $\text{CO}_2$  is firstly converted to  $\text{CO}^*$  via hydrocarboxyl ( $\text{COOH}^*$ ) intermediate. Then,  $\text{CO}^*$  is hydrogenated to methanol through formyl ( $\text{HCO}^*$ ), formaldehyde ( $\text{H}_2\text{CO}^*$ ) and methoxy ( $\text{H}_3\text{CO}$ ) intermediates. This mechanism allows us to understand the CO formation as by-product. Additionally, CO could be formed by direct  $\text{CO}_2$  dissociation ( $\text{CO}_2^* \rightarrow \text{CO}^* + \text{O}^*$ ) without the intervention of hydrocarboxyl intermediate ( $\text{COOH}^*$ ).

### *Industrial perspective*

As it will be shown in the thesis chapters devoted to methanol formation (Chapters 3 and 4), the methanol yield is strongly dependent on the reaction

conditions. In fact, it is possible to optimize the methanol production by increasing the pressure, the space velocity or the  $H_2/CO_2$  ratio.<sup>[101,105]</sup>

Although our focus is on the rational design of new catalytic formulations with improved  $CO_2$  hydrogenation performance, the development of innovative reactors is of particular relevance at industrial level. A critical point to control at “large-scale” is the efficient removal of heat generated on stream due to the high exothermicity of the process. Then, several types of reactors are commonly used to this purpose. For instance:<sup>[42,102]</sup>

- Tubular boiling-water reactor: The heat of reaction is removed from the catalyst-loaded tubes by boiling water. The feed gas enters axially, following a nearly isothermal trajectory, due to the good temperature regulation. This minimizes the sintering rate of active centers, stabilizing the conversion. Companies such as Lurgi and Haldor Topsøe use this usual design, with a maximum capacity of about 1500-2200 t/d.
- Multi-stage radial flow (MRF) reactor: In this design by Toyo and MTC, the gas flows radially across the shell, where the catalysts is placed. A concentric cooling zone dissipates the heat generated.
- Multi-stage adiabatic fixed-bed reactor: Until 10000 t/d can be obtained through this large capacity design of cylindrical reactors by Haldor Topsøe (with internal cooling). This type of unit has a spherical version, with thinner walls, lower pressure drop, and higher methanol production rate.
- Liquid-phase methanol synthesis process (LPMEOH):<sup>[29,102]</sup> The low one-pass  $CO_2$  conversion (because of the thermodynamic limitations), the

above discussed catalyst deactivation, and the exothermicity of the process aimed at developing this alternative configuration. There, an inert mineral oil solvent (e.g., DMF, 1,4-dioxane, *n*-hexadecane, etc.) is introduced in a slurry bubble column reactor (SBCR), absorbing the heat released during the reaction. The catalyst slurry (in the solvent) is kept in suspension by the bubbles produced by the reactant gases. After synthesis, the products (mainly methanol and water) are separated from the solvent, and the latter recirculated to the SBCR unit. The LPMEOH approach allows for an exceptional reactor temperature control due to a very efficient transfer of the heat delivered during the process. Moreover, the higher conversion per pass diminishes the recycling ratio of unreacted gas. On the other hand, working under less severe temperature conditions means minimizing the occurrence of hot-spots, which is one of the main causes of catalyst deactivation in a fixed-bed reactor.

Additionally, new innovative designs such as membrane reactors are being developed to overcome the thermodynamic constraints or to improve reaction rates. This setup facilitates the removal of water vapors from the feed gas, increasing the methanol yield.<sup>[106]</sup> Different materials have been studied, such as perfluorinated cation exchange materials, ceramic (silica/alumina) composites, and zeolites.

Moreover, it is worth mentioning that several companies and institutions are currently producing sustainable methanol (some of them even on a commercial level) applying three types of processes (see Figure 1.12).<sup>[107]</sup>

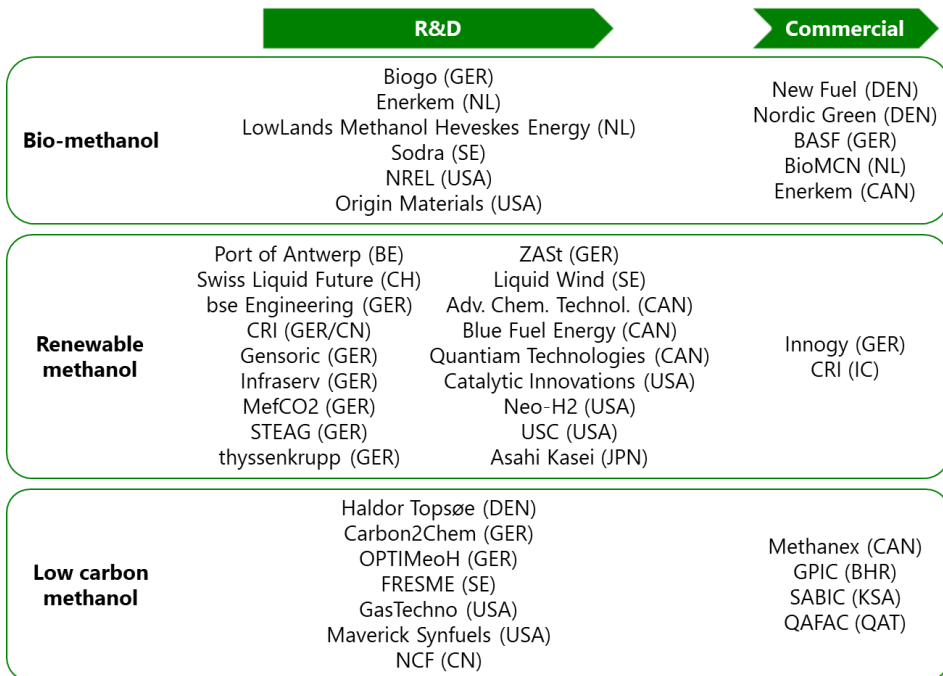


**Figure 1.12** Companies and institutions involved in the production of sustainable MeOH. Adapted from reference [107]. Author credits: Methanol Institute/ATA insights. No copyright intended.

Firstly, the so-called “bio-methanol” is obtained from biomass. In this approach, organic matter coming from forestry residues, agriculture or municipal solid waste undergoes anaerobic fermentation or gasification at high temperature to produce syngas, which is subsequently transformed into bio-methanol. The second option is producing “renewable methanol” by catalytically reacting captured CO<sub>2</sub> (from a stationary point) with green hydrogen (obtained from the electrolysis of water by using renewable electricity). This is the case of the famous “G. A. Olah Renewable Methanol Plant” in Iceland (CRI), which currently produces ~5 million liters of high purity renewable methanol per year (sold as gasoline additive, Vulcanol™). CRI Company is now working in the first CO<sub>2</sub> to methanol

plant ever that will recycle industrial waste gases (located in Henan, China). Actually, commissioning phase was initiated last year (2021) and it is expected to operate soon. Thirdly, we find “low carbon methanol (LCM)” production. For instance, Methanex Corporation generates LCM by injecting sequestered CO<sub>2</sub> from a neighboring industrial facility into the methanol synthesis process. On the other hand, Qatar Fuel Additives Company Limited (QAFAC) have developed CO<sub>2</sub> recovery plants to extract CO<sub>2</sub> from the exhaustion gases, reinjecting it into the methanol production.

To end with this subsection, the integral process (from the CO<sub>2</sub> capture to the final methanol obtention) will be briefly analyzed from an economic point of view. Firstly, it is remarkable that the CCUs plants capital costs are lower than in a conventional MeOH facility, whereas the variable operational costs are significantly higher. Recently, Meunier et al. performed the simulation of an optimized process which would be able to treat ~2500 t/d CO<sub>2</sub>, obtaining ~1550 t/d MeOH (~90% CO<sub>2</sub> conversion).<sup>[108]</sup> The catalytic reaction would be performed at 250 °C and 80 bar over a Cu/ZnO/Al<sub>2</sub>O<sub>3</sub> commercial catalyst. The global capital expenditures of the facility was estimated to 47M €, with ~28M € dedicated to the installed equipment costs of both CO<sub>2</sub> capture and conversion processes. Indeed, approximately 40% of the costs of the aforementioned category would be associated with compressors in the CO<sub>2</sub> conversion unit and a 30% related to heat exchangers. Considering a current average electricity price of 70 €/MWh, the process would not be economically viable. However, with a cost of 34 €/MWh, it could be considered as realistic in some countries such as Iceland. This simulation is in agreement with the techno-economic evaluation reported by Szima and Cormos for a hypothetical plant that would transform ~425 t/d CO<sub>2</sub> (running 8000

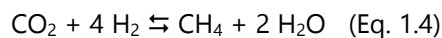
h in a year).<sup>[109]</sup> In fact, both publications agree that the price of electricity to generate green hydrogen is the economic bottleneck, and it should drop to half in order to be a project “financially attractive”.

### 1.5.8. CO<sub>2</sub> hydrogenation to methane

The CO<sub>2</sub> methanation (so-called Sabatier reaction) has gained renewed interest in the last years due to its application in the power-to-gas technology (P2G).<sup>[110]</sup> P2G process consists of harnessing the excess of energy from renewable sources to produce H<sub>2</sub>, transforming it, together with captured CO<sub>2</sub>, into CH<sub>4</sub>, which can be easily stored, transported, and used in the actual industrial infrastructure.<sup>[111]</sup>

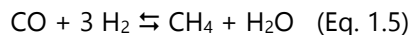
#### *Thermodynamic considerations*

CO<sub>2</sub> methanation is a strongly exothermic reaction (Eq. 1.4), thermodynamically favored at low temperatures. The global reaction can be expressed as a combination of RWGS (Eq. 1.2) and CO methanation (Eq. 1.5):<sup>[111,112]</sup>



$$\Delta H_{298\text{K}}^0 = -164.6 \text{ kJ/mol}$$

$$\Delta G_{298\text{K}}^0 = -130.8 \text{ kJ/mol}$$



$$\Delta H_{298\text{K}}^0 = -206.1 \text{ kJ/mol}$$

$$\Delta G_{298\text{K}}^0 = -141.9 \text{ kJ/mol}$$

Figure 1.13 summarizes the influence of some operational conditions in the Sabatier reaction. The first remarkable feature in CO<sub>2</sub> methanation, contrary to methanol synthesis situation, is the possibility to operate at atmospheric pressure and relatively low temperatures (i.e., 200-250 °C) without thermodynamic limitation. Indeed, as observed in Figure 1.13a, theoretical values of ~100% CO<sub>2</sub>

conversion and 100% selectivity to methane in the pressure range 1-100 atm at stoichiometric conditions can be obtained. At higher temperatures, CO<sub>2</sub> conversion starts decreasing, but this loss of activity can be attenuated by increasing the working pressure.

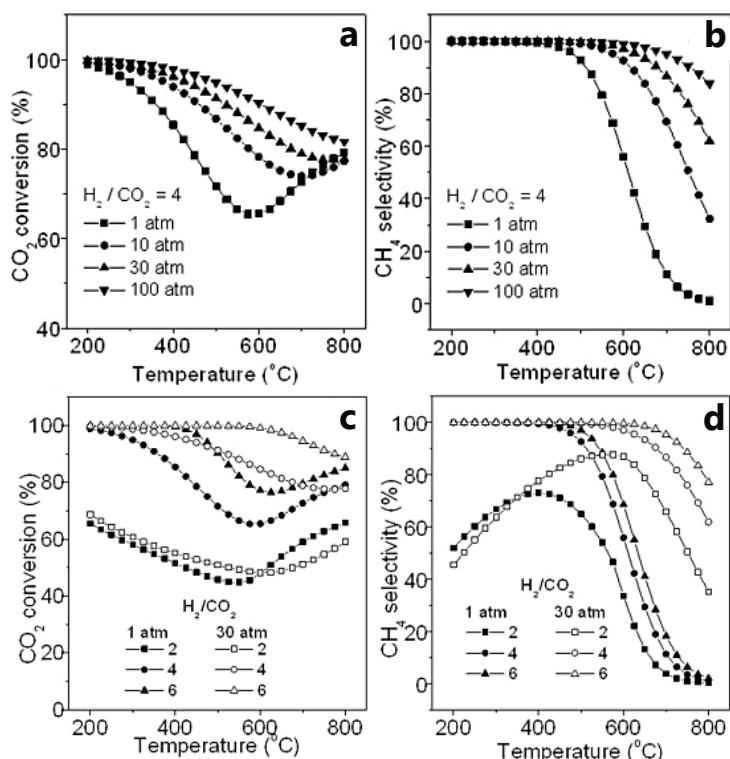


**Figure 1.13** Effect of pressure and temperature in CO<sub>2</sub> conversion (a) and CH<sub>4</sub> selectivity (b) at a H<sub>2</sub>/CO<sub>2</sub> molar ratio of 4; and influence of H<sub>2</sub>/CO<sub>2</sub> molar ratio and temperature at 1 atm (1.013 bar) and 30 atm (30.397 bar) in CO<sub>2</sub> conversion (c) and CH<sub>4</sub> selectivity (d). *Reproduced from RSC Advances 2012, 2, 2358-2368 with permission from the Royal Society of Chemistry (Copyright 2012).*

Furthermore, 100% CH<sub>4</sub> selectivity can be achieved until ~450 °C, where it decreases progressively due to RWGS, forming CO as by-product (see Figure 1.13b). Again, we can maintain an important selectivity to methane at a certain



high temperature by increasing the pressure. This pressure effect should not be surprising since a decrease in the number of molecules participating in the reaction (from reactants to products) is taking place. On the other hand, lower panels in Figure 1.13 describe the effect of  $\text{H}_2/\text{CO}_2$  molar ratio variation. It can be seen that higher  $\text{CO}_2$  conversion and  $\text{CH}_4$  selectivity is obtained at either 1 or 30 atm by using a high  $\text{H}_2/\text{CO}_2$  ratio (i.e., 6), whereas much less competitive results are achieved under sub-stoichiometric conditions (i.e.,  $\text{H}_2/\text{CO}_2=2$ ).

### *Catalyst development*

Although  $\text{CO}_2$  methanation is not thermodynamically limited at mild conditions, obtaining complete  $\text{CO}_2$  conversion with high selectivity values, the effective eight-electron reduction of  $\text{CO}_2$  to  $\text{CH}_4$  is difficult to achieve, presenting kinetic limitations.<sup>[113]</sup> This can be solved by operating at 350-500 °C. Nevertheless, working at high temperature range entails certain drawbacks: For instance, reaction temperatures above 500 °C can cause sintering of particles, leading to catalyst deactivation. Another critical phenomenon is high temperature carbon deposition, which causes active center coverage, with a subsequent loss of activity. Carbon coverage can be minimized by increasing the pressure and by working under stoichiometric or over-stoichiometric  $\text{H}_2/\text{CO}_2$  molar ratio.<sup>[112]</sup>

Since the discovery of this reaction more than a century ago, numerous catalysts have been tested and developed, predominating supported transition-metal of groups 8, 9 and 10. In particular, Yaccato et al. carried out a high-throughput screening of more than 500 catalytic formulations, concluding that Ru, Rh and Ni are the most active metals for  $\text{CO}_2$  methanation.<sup>[114]</sup> Additionally, Younas et al. ranked potential transition-metal centers according to their activity and selectivity, obtaining:<sup>[115]</sup>

CO<sub>2</sub> conversion: **Ru** > Rh > Ni > Fe > Co > Os > Pt > Ir > Mo > Pd > Ag > Au

CH<sub>4</sub> selectivity: Pd > Pt > Ir > Ni > Rh > Co > Fe > **Ru** > Mo > Ag > Au

Among them, nickel arises as one of the top-ranked metals, exhibiting high catalytic performance. Although this element is less resistant to deactivation than other more noble metals (such as Pd, Pt, or Ru) over a wide temperature range due to carbon deposition, its lower cost and non-noble nature justify its utilization for industrial application. In fact, Ni/Al<sub>2</sub>O<sub>3</sub> based catalysts are usually supplied by catalyst manufacturers, such as Johnson Matthey, Topsøe, and Clariant-Süd Chemie.<sup>[116]</sup> On the other hand, non-noble metals such as Co and Fe, together with Ni, have been studied in CO<sub>2</sub> methanation.<sup>[117]</sup> Pure Fe/Al<sub>2</sub>O<sub>3</sub> catalysts have been found less competitive, but in combination with the other two forming alloys (i.e., Ni and Co), boosts its selectivity to CH<sub>4</sub>.<sup>[118]</sup>

However, the performance of the metal is strongly dependent on support-metal interface interactions and physico-chemical properties. Then, the use of a certain support affects key catalytic features such as metal dispersion, reducibility of the metal center, surface activation of CO<sub>2</sub>, etc. Among oxides, CeO<sub>2</sub> arose as the best support combined with Ni and Ru, compared to SiO<sub>2</sub>, ZrO<sub>2</sub> or Ytria-stabilized ZrO<sub>2</sub>, TiO<sub>2</sub>, MgO or Al<sub>2</sub>O<sub>3</sub>.<sup>[119-124]</sup> Indeed, Ni/CeO<sub>2</sub> reduced catalyst, that is able to generate oxygen vacancies, exhibits high CO<sub>2</sub> adsorption and oxygen exchange capacities, increasing the CO<sub>2</sub> hydrogenation activity.<sup>[125-127]</sup> Furthermore, Ocampo et al. reported that Ni/CeO<sub>2</sub> performance can be further improved by combining CeO<sub>2</sub>-ZrO<sub>2</sub>(60/40) supports, obtaining an outstanding value of 80.5% CO<sub>2</sub> conversion and >99% CH<sub>4</sub> selectivity at 350 °C, operating at atmospheric

pressure.<sup>[128]</sup> Finally, several important factors that have a clear influence on catalysis are commented below:

- Metallic content in Ni catalysts varies from 10-25 wt %, whereas Ru materials are normally prepared in a lower range (i.e., 0.1-5 wt %), proof of the higher inherently activity of Ru in CO<sub>2</sub> methanation. Metal content variation typically leads to a change in the degree of metal dispersion. Thus, low metal loadings would result in higher dispersions which implies that metal atoms are distributed in small NPs, or even clusters. In order to obtain the best atomic efficiency, high dispersions are needed. However, in CO<sub>2</sub> methanation, several studies have demonstrated that CH<sub>4</sub> yield is higher for bigger metallic particles (Ru,<sup>[129]</sup> Ni,<sup>[130]</sup> Rh,<sup>[131,132]</sup> Pd<sup>[133]</sup>) than for highly dispersed systems, mainly yielding CO as reaction product. This catalytic behavior would be explained in the basis of the interaction between solids and species participating in the process. Indeed, bigger particles, where metal atoms are massively surrounded by other metals, are able to effectively dissociate H<sub>2</sub> and to strongly react with CO, avoiding its desorption as product. Nevertheless, the interaction between adsorbed CO and "more" isolated metal centers in small NPs or clusters is more labile, facilitating CO desorption.<sup>[132]</sup>
- The addition of promoters has been widely studied as a way to increase the catalytic efficiency. In particular, two types of promoters have been used: transition-metals, and alkali and alkaline-earth metals. The first group of promoters (e.g., Ce, La, Zr...) are added to increase the metal dispersion, to alter the electronics into the active center, or to modulate the basicity of the material. For instance, Ce promotion (2 wt %) on Ni

catalysts favors the metal dispersion and introduces oxygen vacancies after reduction.<sup>[134]</sup> Furthermore, Wierzbicki et al. reported the effect of La addition (2-4 wt %) in the basicity of a Ni-hydrotalcite derived material.<sup>[135]</sup> In particular, the incorporation of La led to an increase in medium-strength basic centers, promoting CO<sub>2</sub> methanation. Moreover, they found that La promotion consisted of hindering the interaction between Ni and the support, favoring its reducibility. On the other hand, it is possible to add noble metals in small amounts (typically less than 0.5-1.0 wt %) as promoters. As an example, Ocampo et al. reported the addition of 0.5 wt % of Ru or Rh to a Ni/ZrO<sub>2</sub>-CeO<sub>2</sub> catalyst.<sup>[128]</sup> Non-promoted sample displayed as-prepared NiO particles of about 26 nm, whereas particle size in Ru and Rh promoted as-prepared samples was ~19 and 16 nm, respectively, which means an important increase in nickel dispersion. Moreover, an enhanced reducibility of CeO<sub>2</sub> was found. On the other hand, the addition of alkali (Cs<sup>+</sup>, Na<sup>+</sup>, Li<sup>+</sup>, K<sup>+</sup>) and alkaline-earth metals (Mg<sup>2+</sup>, Ca<sup>2+</sup>, Ba<sup>2+</sup>) also implies a positive effect in catalysis. Normally, the addition of these promoters does not affect textural properties or Ni reducibility, but it improves the CO<sub>2</sub> adsorption capacity, as well as the basicity of the material.

To give an insight into the performance of catalytic systems operating in the Sabatier reaction, Table 1.3 is placed at the end of the chapter.

### *Reaction mechanism*

As previously seen in methanol synthesis mechanism, one fundamental feature to take into account is the complexity of the reaction network for CO<sub>2</sub> hydrogenations. The existence of several reaction paths, that sometimes are

common for different products, as well as the stabilization of certain intermediates on the catalyst surface, critically modulate the final selectivity of the transformation. Although the specific mechanism of  $\text{CO}_2$  methanation over a catalyst depends on multiple factors (such as metal/oxide interaction, interfaces, structural or electronic effects...) and there is still no consensus on the kinetics and mechanisms, Figure 1.14 depicts the possible reaction pathways to obtain  $\text{CH}_4$  ( $\text{CO}$  and methanol can also be obtained following the same network).<sup>[122]</sup>

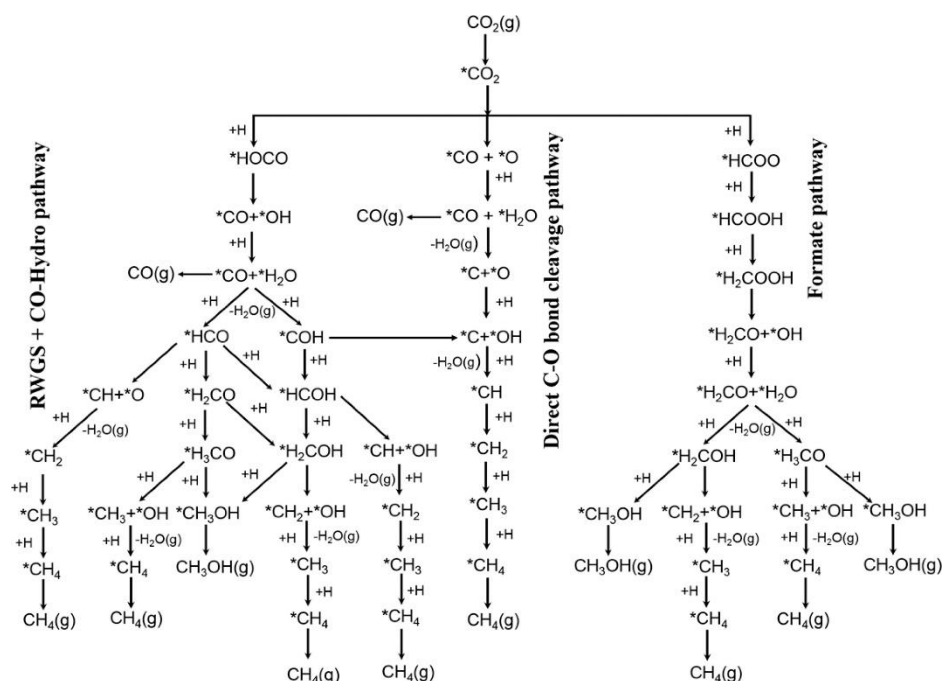


**Figure 1.14** Reaction pathways of  $\text{CO}_2$  hydrogenation to  $\text{CH}_4$  ( $\text{CH}_3\text{OH}$  and  $\text{CO}$  products are also included). (\*) indicates adsorbed species. *Reprinted with permission of J. Am. Chem. Soc. 2017, 139, 9739-9754. Copyright 2017 American Chemical Society.*

Methane formation can occur via RWGS + CO-hydro pathway (left branch in Figure 1.14). In this route,  $^*\text{CO}_2$  is associatively transformed to  $^*\text{CO}$  through hydrocarboxyl intermediate ( $^*\text{HOCO}$ , labeled as  $\text{COOH}^*$  in Figure 1.11). Then,  $^*\text{CO}$

can evolve to formyl ( $^*\text{HCO}$ ) or to hydroxymethylidyne ( $^*\text{COH}$ ) species, obtaining hydroxymethylene ( $^*\text{HCOH}$ ), hydroxymethyl ( $^*\text{H}_2\text{COH}$ ) or methoxy ( $^*\text{H}_3\text{CO}$ ). Finally, C-O bond scission of these intermediates leads to the formation of  $^*\text{CH}_x$  species, undergoing progressive hydrogenations to yield  $\text{CH}_4$ .

Next mechanism takes place via direct C-O bond cleavage, which is a dissociative mechanism (center branch in Figure 1.14). Along this pathway,  $^*\text{CO}_2$  dissociates twice: firstly to  $^*\text{CO}$  and  $^*\text{O}$ , and then to “naked”  $^*\text{C}$  and  $^*\text{O}$ . Thereupon,  $^*\text{C}$  is subsequently hydrogenated to  $\text{CH}_4$ .

The third option is the associative formate pathway (the revised one, according to Figure 1.11, occurring via formic acid,  $^*\text{HCOOH}$ ; right branch in Figure 1.14). After formic acid formation, it is hydrogenated to  $^*\text{H}_2\text{COOH}$ , that later dissociates to formaldehyde ( $^*\text{H}_2\text{CO}$ ) and  $^*\text{OH}$ . Then, formaldehyde can be transformed to hydroxymethyl ( $^*\text{H}_2\text{COH}$ ) or methoxy ( $^*\text{H}_3\text{CO}$ ) intermediates, where the C-O scission takes place. The resulting  $^*\text{CH}_x$  species will be finally hydrogenated to  $\text{CH}_4$ . Notice that along all pathways, the competition between C-O bond cleavage in  $^*\text{H}_x\text{CO}$  species and their consecutive hydrogenations ultimately determines the global  $\text{CH}_4$  selectivity in Sabatier reaction.

On  $\text{Ni}/\text{Al}_2\text{O}_3$  catalysts,  $\text{CO}_2$  methanation usually occurs via direct C-O bond cleavage pathway, where the rate-limiting step was found in  $^*\text{CO}$  dissociation to  $^*\text{C} + ^*\text{O}$ .<sup>[136]</sup> On the other hand, DFT calculations combined with micro-kinetic modelling concluded that  $\text{CO}_2$  methanation over  $\text{Ru}(0001)$  system followed a mixed mechanism (combining RWGS + CO-hydro and direct C-O bond cleavage pathways), where  $^*\text{CO}_2$  direct dissociation to  $^*\text{CO}$  and  $\text{O}^*$  was followed by  $^*\text{CO}$  hydrogenation to formyl intermediate ( $^*\text{HCO}$ ). Moreover, formyl was dissociated

to  $*O + *CH$  (being the rate-limiting step), that was consecutively hydrogenated upon  $CH_4$ .<sup>[137]</sup>

### *Industrial perspective*

As it already happened in the methanol synthesis process, different reactor configurations have been investigated to effectively remove the released heat produced in the Sabatier reaction. Here, preventing hot spots is a priority, so proper selection of the cooling equipment (and the catalytic unit) is required.<sup>[42]</sup>

Whereas wall-cooled fixed-bed reactors have been extensively used in the  $CO_2$  methanation process at a commercial level, structured or fluidized-bed reactors are still in previous development stages. For instance:

- Multichannel mini-reactors: This is one type of structured reactor design by Technical Research and Innovation to operate at 200-400 °C and 15 bar pressure.<sup>[138]</sup> The use of this configuration with smaller channel diameter favors the catalyst/gas contact, enhancing heat transfer. Nevertheless, the appearance of hot spots is inevitable, which is not acceptable from a safety point of view. For this reason, the development of reactors in series (permitting catalyst dilution) or advanced temperature control methods are needed.
- Another possibility explored by different groups<sup>[139,140]</sup> is coupling two-fixed bed reactors:  $CO_2$  is adsorbed in the first unit using a hydrotalcite-based material, which is subsequently hydrogenated at low pressure (2.5 bar) in the second unit. This is a very promising approach, but the selectivity to methane (<40% at 350 °C) is still low.<sup>[141]</sup> This issue can be addressed by an improved design of both the sorbent (in the first unit) and the Ni-based catalyst (in the hydrogenation unit).

- Three-phase methanation SBCR: the introduction of a liquid phase in the methanation allows for an effective reactor temperature control. This unit presents several advantages, such as working under isothermal conditions and at elevated pressures, or the possibility to replace the catalyst during operation.<sup>[142]</sup> However, the reaction temperature is limited by the evaporation/decomposition of the fluid (e.g., dibenzyltoluene, DBZ), and mass transfer limitations could be found depending on the operational conditions and the reactor characteristics.

Over the last decade, many companies, research institutions, and public-private partnerships have been involved in scaling up the Sabatier reaction at industrial level, with a leading role of Europe (and, particularly, Germany). In Figure 1.15, most relevant projects concerning CO<sub>2</sub> methanation (from development to commercial application) are summarized:<sup>[115,143-150]</sup>



**Figure 1.15** CO<sub>2</sub> methanation projects under different stages of development. Numbers in brackets refer to the capacity/power of the plant, expressed in kW. <sup>a</sup>First module will go into operation in 2022, full capacity in 2028. <sup>b</sup>This plant will start operations in 2024. *Author credits: Cored, J.; No copyright intended.*



From this list, it is worth mentioning the ambitious plan of INPEX and Osaka Gas companies, which will launch the world's largest-scale Sabatier plant at Nagaoka (Japan) by 2025-2026.<sup>[151]</sup> The production of synthetic methane is expected to be  $\sim 400 \text{ m}^3$  of  $\text{CH}_4$  per hour. After achieving this milestone, the companies will be focus in developing an outstanding production of  $60000 \text{ m}^3_{\text{CH}_4} \cdot \text{h}^{-1}$  by 2030 in a new plant, with the aim of exporting their technology to neighboring countries, such as Australia.

Finally, an aspect to understand when performing an economic analysis is that the "industrial Sabatier reaction" would take place in a two-process plant (namely, electrolysis to obtain green  $\text{H}_2$  + methanation). Considering the efficiencies of process steps (such as green electricity generation, electrolysis,  $\text{CO}_2$  methanation and subsequent  $\text{CH}_4$  compression, transportation, etc.) the estimated net energy efficiency for a current process would be of  $\sim 35\text{-}50\%$ .<sup>[115]</sup>

Moreover, the official "Report on experience curves and economies of scale" (STORE&GO project, 2018) calculated the initial costs of the electrolysis (1100-2500 €/kW) and the catalytic methanation (600 €/kW) processes. This estimation was made assuming a 5 MW electrolyzer and a 5 MW methanation units.<sup>[152]</sup> The operational conditions considered to calculate the price of the methanation step were: 300-350 °C, 20-50 bar, and 1000-10000  $\text{h}^{-1}$  GHSV (performed in a honeycomb structured reactor). This means that an adequate catalytic design able to operate efficiently at milder conditions (e.g.,  $\sim 200$  °C and atmospheric pressure) would help to significantly reduce the operating costs of this step. This issue will be address in Chapter 5, where the design of a novel ruthenium-based catalyst is reported.

In addition, CO<sub>2</sub> capture technologies were also evaluated: “Traditional” CO<sub>2</sub> capture costs in different industrial sectors (e.g., refineries, iron and steel factories, paper production, etc.) are typically in the range of 20-100 €/t<sub>CO<sub>2</sub></sub>, whereas direct air capture costs are much elevated (~100-500 €/t<sub>CO<sub>2</sub></sub>).<sup>[152]</sup>

Together with the initial investment, another limiting factor when analyzing the variable operational costs is the electricity price (as we already discussed in the methanol synthesis). In this sense, Brouwer et al.<sup>[153]</sup> reported that the theoretical variable cost of CH<sub>4</sub> production in a facility located in California would be of about 60 \$/MWh. Assuming 100% renewable electricity as the input energy source, the analysis revealed that CH<sub>4</sub> could be produced at costs comparable to those of the conventional fuel.

**Table 1.2** Performance of representative catalytic systems in the CO<sub>2</sub> hydrogenation to methanol.

Catalyst	H <sub>2</sub> /CO <sub>2</sub> mol ratio	T (°C)	P (Bar)	GHSV or WHSV	Space velocity <sup>a</sup>	X <sub>CO2</sub> (%)	S <sub>MeOH</sub> (%)	STY (mol <sub>MeOH</sub> ·g <sub>cat</sub> <sup>-1</sup> ·h <sup>-1</sup> )	REF
Cu(1)ZnO	9:1	225	7	W	2000	4.8	21	8.3·10 <sup>-5</sup>	[154]
Cu(15)ZnO	9:1	225	7	W	2000	3.9	61	1.9·10 <sup>-4</sup>	[154]
CuO-ZnO	3:1	250	20	G	1000	8.6	45	1.2·10 <sup>-3</sup>	[155]
Cu@ZnO <sub>x</sub> (core-shell)	3:1	250	30	W	18000	2.3	100	4.6·10 <sup>-3</sup>	[156]
Cu/ZrO <sub>2</sub>	3:1	240	20	G	5400	6.3	48.8	1.1·10 <sup>-2</sup>	[51]
Cu(12.4%)@ZrO <sub>x</sub>	3:1	260	45	W	21600	13.1	78.8	2.5·10 <sup>-2</sup>	[157]
40%Cu/TiO <sub>2</sub>	3:1	260	30	W	3600	-	64.7	2.1·10 <sup>-3</sup>	[158]
C <sub>35</sub> Z <sub>33</sub> A <sub>32</sub> G66A Süd Chemie	3:1	200	10	W	4400	5.5	53.8	1.4·10 <sup>-3</sup>	[159]
Cu/ZnO/Al <sub>2</sub> O <sub>3</sub> (6:3:1)	3:1	240	20	G	6000	14.4	35.0	3.2·10 <sup>-3</sup>	[160]
Cu/ZnO/Al <sub>2</sub> O <sub>3</sub> (15:7:78)	3:1	210	22.5	W	10800	10.8	77.1	9.2·10 <sup>-3</sup>	[161]
Cu/ZnO/Al <sub>2</sub> O <sub>3</sub> -FHI (68:29:3)	3.5:1	240	30	G	37000	10.5	44.0	2.4·10 <sup>-2</sup>	[162]
Cu(42%)Zn(19%)Al-HiFuel	3:1	250	45	W	21600	20.3	55	2.7·10 <sup>-2</sup>	[163]
Cu/ZnO/Al <sub>2</sub> O <sub>3</sub>	3:1	250	50	W	18000	19.7	48.1	2.0·10 <sup>-2</sup>	[164]
Cu-ZnO/Al <sub>2</sub> O <sub>3</sub>	10:1	260	360	G	182000	65.8	77.3	2.4·10 <sup>-1</sup>	[165]
Cu/ZnO/ZrO <sub>2</sub> (5:2:3)	3:1	220	30	W	6000	18.9	80.2	9.3·10 <sup>-3</sup>	[166]
M-CZZ (16)	3:1	240	30	W	6000	9.7	91.4	5.4·10 <sup>-3</sup>	[166]
50-Cu <sub>0.5</sub> Zn <sub>0.2</sub> Zr <sub>0.3</sub>	3:1	240	30	G	3600	17.0	56.2	1.8·10 <sup>-3</sup>	[167]

<sup>a</sup>GHSV is expressed in h<sup>-1</sup>; WHSV is expressed in mL·g<sub>cat</sub><sup>-1</sup>·h<sup>-1</sup>.

Catalyst	H <sub>2</sub> /CO <sub>2</sub> mol ratio	T (°C)	P (Bar)	GHSV or WHSV	Space velocity <sup>a</sup>	X <sub>CO2</sub> (%)	S <sub>MeOH</sub> (%)	STY (mol <sub>MeOH</sub> ·g <sub>cat</sub> <sup>-1</sup> ·h <sup>-1</sup> )	REF
Cu-ZnO-ZrO <sub>2</sub>	3:1	240	30	G	80000	9.0	-	3.8·10 <sup>-2</sup>	[168]
Cu-ZnO-ZrO <sub>2</sub> (5:2:3)	3:1	240	30	W	3600	12.1	54.1	2.1·10 <sup>-3</sup>	[169]
Cu-ZnO-ZrO <sub>2</sub> /LDH (6:3:1)	3:1	250	30	W	2000	4.9	78.3	1.2·10 <sup>-3</sup>	[170]
(Cu/ZnO/ZrO <sub>2</sub> )@SBA-15	3:1	250	30	G	44000	19.1	26.4	1.0·10 <sup>-2</sup>	[171]
Cu-ZnO-ZrO <sub>2</sub>	3:1	240	50	W	55000	9.7	62	3.8·10 <sup>-2</sup>	[172]
Cu(62.5%)/ZnO/ZrO <sub>2</sub>	3:1	220	80	G	3300	21	68	5.7·10 <sup>-3</sup>	[173]
Cu/Ga/ZnO	3:1	270	20	W	18000	6.0	88.0	1.2·10 <sup>-2</sup>	[67]
CuZnLDH30Ga	3:1	270	45	W	18000	18.8	47.8	1.8·10 <sup>-2</sup>	[105]
CuZnZrGaY	3:1	240	20	W	30000	-	-	1.7·10 <sup>-2</sup>	[174]
Cu/Ga <sub>2</sub> O <sub>3</sub> /ZrO <sub>2</sub>	3:1	250	20	G	2500	13.7	75.6	1.9·10 <sup>-3</sup>	[52]
Cu/Ba <sub>2</sub> O <sub>3</sub> /ZrO <sub>2</sub>	3:1	250	20	G	2500	15.8	67.3	2.0·10 <sup>-3</sup>	[52]
Cu/Zn/Ga/hydrophobic SiO <sub>2</sub>	3:1	270	20	W	18000	5.6	99.5	1.1·10 <sup>-2</sup>	[175]
Cu(10)/ZnCr-3.5	3:1	300	20	W	6000	25.1	31.1	4.7·10 <sup>-3</sup>	[176]
Cu <sub>0.25</sub> -In <sub>0.75</sub> -Zr <sub>0.5</sub> -O	3:1	250	25	W	18000	~1.5	79.7	~2.4·10 <sup>-3</sup>	[177]
La(10%)-Cu/ZrO <sub>2</sub>	3:1	220	30	W	3600	5.8	72	1.4·10 <sup>-3</sup>	[70]
Cu(28%)/Zn/SiO <sub>2</sub>	3:1	220	30	W	2000	14.1	57.2	1.7·10 <sup>-3</sup>	[172]
CZA-r@CZM	3:1	240	30	W	32000	11.7	73.0	2.3·10 <sup>-2</sup>	[179]
(10%)Cu <sub>1</sub> La <sub>0.2</sub> /SBA-15	3:1	240	30	W	12000	5.7	81.2	6.0·10 <sup>-3</sup>	[180]
C <sub>5</sub> Z <sub>2</sub> Z <sub>2.8</sub> W <sub>0.2</sub>	3:1	240	30	W	2400	19.7	49.3	2.2·10 <sup>-3</sup>	[181]

<sup>a</sup>GHSV is expressed in h<sup>-1</sup>; WHSV is expressed in mL·g<sub>cat</sub><sup>-1</sup>·h<sup>-1</sup>.

Catalyst	H <sub>2</sub> /CO <sub>2</sub> mol ratio	T (°C)	P (Bar)	GHSV or WHSV	Space velocity <sup>a</sup>	X <sub>CO2</sub> (%)	S <sub>MeOH</sub> (%)	STY (mol <sub>MeOH</sub> ·g <sub>cat</sub> <sup>-1</sup> ·h <sup>-1</sup> )	REF
C <sub>5</sub> Z <sub>2</sub> ZrW <sub>2</sub>	3:1	240	30	W	2400	5.6	64.0	8.3·10 <sup>-4</sup>	[181]
CuZnAlZr (1.5:1.0:0.8:0.2)	3:1	250	30	W	4000	25.9	49.2	7.3·10 <sup>-3</sup>	[182]
Cu <sub>11</sub> In <sub>9</sub> -In <sub>2</sub> O <sub>3</sub>	3:1	280	30	W	7500	11.4	80.5	6.1·10 <sup>-3</sup>	[97]
Cu <sub>8</sub> -In <sub>6.6</sub> @SiO <sub>2</sub>	3:1	280	30	W	20000	9.8	78.1	1.4·10 <sup>-2</sup>	[183]
Cu/Zn/Al/ZrO <sub>2</sub>	3:1	240	40	G	9742	18.8	47.2	-	[184]
Cu(33.5%)-LDHGa(30%)	3:1	270	45	W	18000	~20	~49	1.8·10 <sup>-2</sup>	[105]
Cu/ZnO/Al <sub>2</sub> O <sub>3</sub> /ZrO <sub>2</sub>	3:1	190	50	G	4000	10.7	81.8	2.7·10 <sup>-3</sup>	[185]
Cu(51)/ZnO/Al <sub>2</sub> O <sub>3</sub> /Y <sub>2</sub> O <sub>3</sub> (0.2)	3:1	230	50	W	10000	17.8	70.5	1.1·10 <sup>-2</sup>	[71]
Cu/Zn/Al/Y	3:1	250	50	W	12000	26.9	52.4	1.6·10 <sup>-2</sup>	[186]
La <sub>0.8</sub> Zr <sub>0.2</sub> Cu <sub>0.7</sub> Zn <sub>0.3</sub> O <sub>x</sub>	3:1	250	50	G	3600	12.6	52.5	3.1·10 <sup>-3</sup>	[187]
LCZ-173 (La-Cu-ZnO <sub>x</sub> )	3:1	250	50	G	3600	6.4	57.9	1.6·10 <sup>-3</sup>	[187]
Ga-Cu-ZnO-ZrO <sub>2</sub>	3:1	250	70	W	15000	22	72	2.2·10 <sup>-2</sup>	[188]
Cu/ZnO/ZrO <sub>2</sub> /Ga <sub>2</sub> O <sub>3</sub>	3:1	250	80	G	3300	-	70	1.2·10 <sup>-2</sup>	[50]
Cu/ZnO/ZrO <sub>2</sub> /Ga <sub>2</sub> O <sub>3</sub>	3:1	250	80	G	3300	-	75	1.0·10 <sup>-2</sup>	[50]
Cu-K/Al <sub>2</sub> O <sub>3</sub>	4:1	200	100	G	4000	3.6	4.2	1.3·10 <sup>-4</sup>	[189]
Cu-Ba/Al <sub>2</sub> O <sub>3</sub>	4:1	200	100	G	4000	2.8	62.4	1.5·10 <sup>-3</sup>	[189]
Cu/Al <sub>2</sub> O <sub>3</sub>	4:1	200	100	G	4000	2.4	46.2	9.6·10 <sup>-4</sup>	[189]
Cu@UiO-bpy	3:1	250	40	G	1600	5.6	51.9	4.5·10 <sup>-4</sup>	[190]
CuZn@UiO-bpy	3:1	250	40	G	18000	3.3	100	5.8·10 <sup>-3</sup>	[190]

<sup>a</sup>GHSV is expressed in h<sup>-1</sup>; WHSV is expressed in mL·g<sub>cat</sub><sup>-1</sup>·h<sup>-1</sup>.

Catalyst	H <sub>2</sub> /CO <sub>2</sub> mol ratio	T (°C)	P (Bar)	GHSV or WHSV	Space velocity <sup>a</sup>	X <sub>CO2</sub> (%)	S <sub>MeOH</sub> (%)	STY (mol <sub>MeOH</sub> ·g <sub>cat</sub> <sup>-1</sup> ·h <sup>-1</sup> )	REF
Cu(10%)Zn/rGO	3:1	250	15	G	2400	26.0	5.1	1.3·10 <sup>-2</sup>	[191]
Cu(30%)Zn/rGO	3:1	250	15	G	2400	20.0	15.6	7.6·10 <sup>-3</sup>	[191]
Cu/ZrO <sub>2</sub> /CNTs	3:1	260	30	G	3600	16.3	43.5	2.6·10 <sup>-3</sup>	[192]
Pd/ZnO	3:1	250	20	W	3600	10.7	60	2.4·10 <sup>-3</sup>	[88]
Pd(9.2%)-Zn(5.2%)/CeO <sub>2</sub>	3:1	220	20	W	3600	14.1	97.2	5.2·10 <sup>-3</sup>	[79]
5%Pd <sub>1</sub> -Zn <sub>5</sub> /TiO <sub>2</sub>	3:1	250	20	W	3600	10.1	40	1.7·10 <sup>-3</sup>	[193]
5%Pd <sub>1</sub> -Zn <sub>5</sub> /Al <sub>2</sub> O <sub>3</sub>	3:1	250	20	W	3600	8.6	19	6.4·10 <sup>-4</sup>	[193]
Pd(5%)/ZnO-Al <sub>2</sub> O <sub>3</sub>	3:1	180	30	W	3600	2.9	79.4	7.8·10 <sup>-4</sup>	[76]
Pd/Zn/CNTs	3:1	250	30	W	1800	6.3	99.6	1.2·10 <sup>-3</sup>	[85]
Pd <sub>5</sub> -Zn <sub>5</sub> -Ca <sub>0.5</sub> /CeO <sub>2</sub>	3:1	220	30	W	2400	7.7	100	2.1·10 <sup>-3</sup>	[78]
Pd(2.5%)/ZnO-3.93Al	3:1	250	30	W	6000	14.2	51.6	4.9·10 <sup>-3</sup>	[194]
PdZn-400	3:1	270	45	W	21600	15.1	56.2	2.0·10 <sup>-2</sup>	[195]
Pd(5%)/plate Ga <sub>2</sub> O <sub>3</sub>	3:1	250	50	W	6000	17.3	51.6	5.5·10 <sup>-3</sup>	[81]
Pd(0.91%)-P/In <sub>2</sub> O <sub>3</sub>	4:1	300	50	W	21000	20	70	2.8·10 <sup>-2</sup>	[82]
Pd-In <sub>2</sub> O <sub>3</sub> CP	4:1	280	50	W	48000	9.7	78.0	3.2·10 <sup>-2</sup>	[196]
Pd(10%)/In <sub>2</sub> O <sub>3</sub> /SBA-15	4:1	260	50	W	15000	12.6	83.9	1.1·10 <sup>-2</sup>	[197]
Pd <sub>8.7</sub> -Cu <sub>10</sub> /SBA-15	3:1	250	41	W	3600	6.5	23	7.2·10 <sup>-4</sup>	[198]
Pd <sub>8.7</sub> -Cu <sub>10</sub> /SiO <sub>2</sub>	3:1	250	41	W	3600	6.6	34	1.1·10 <sup>-3</sup>	[198]
Pd-Cu/CeO <sub>2</sub>	3:1	250	41	W	3600	9.9	28.4	1.4·10 <sup>-3</sup>	[199]

<sup>a</sup>GHSV is expressed in h<sup>-1</sup>; WHSV is expressed in mL·g<sub>cat</sub><sup>-1</sup>·h<sup>-1</sup>.

Catalyst	H <sub>2</sub> /CO <sub>2</sub> mol ratio	T (°C)	P (Bar)	GHSV or WHSV	Space velocity <sup>a</sup>	X <sub>CO2</sub> (%)	S <sub>MeOH</sub> (%)	STY (mol <sub>MeOH</sub> ·g <sub>cat</sub> <sup>-1</sup> ·h <sup>-1</sup> )	REF
Pd-Cu/ZrO <sub>2</sub>	3:1	250	41	W	3600	15.8	26.8	1.9·10 <sup>-3</sup>	[199]
Pd-Cu/Al <sub>2</sub> O <sub>3</sub>	3:1	250	41	W	3600	12.4	31.4	1.7·10 <sup>-3</sup>	[199]
15.7%(Pd <sub>1</sub> Cu <sub>3</sub> )/SiO <sub>2</sub>	3:1	250	50	W	30000	2.8	18.5	1.6·10 <sup>-3</sup>	[90]
Au/ZnO	3:1	240	5	G	4800	0.3	82	1.5·10 <sup>-4</sup>	[200]
Au(62.5%)/Zn/ZrO <sub>2</sub>	3:1	220	80	G	3300	1.5	100	4.1·10 <sup>-4</sup>	[173]
NiGa/SiO <sub>2</sub>	3:1	200	1	G	6000	-	-	(2.8-3.9)·10 <sup>-3</sup>	[96]
LaCr <sub>0.5</sub> Cu <sub>0.5</sub> O <sub>3</sub>	3:1	250	20	W	9000	10.4	90.8	8.7·10 <sup>-3</sup>	[201]
Cu <sub>11</sub> In <sub>9</sub> -In <sub>2</sub> O <sub>3</sub>	3:1	280	30	W	7500	11.4	80.5	6.1·10 <sup>-3</sup>	[97]
Pd(1.46%)ZnAl	3:1	250	30	W	15000	0.6	60	5.5·10 <sup>-4</sup>	[98]
In(56%)@Co	4:1	300	50	W	27500	15.7	~80	2.7·10 <sup>-2</sup>	[202]
Ni(9.7%)/In <sub>2</sub> O <sub>3</sub>	4:1	300	50	W	21000	18.5	54.0	1.7·10 <sup>-2</sup>	[203]
20-MnO <sub>x</sub> -Co <sub>3</sub> O <sub>4</sub>	3:1	250	10	G	88800	45.1	22.1	9.8·10 <sup>-2</sup>	[204]
In <sub>2</sub> O <sub>3</sub> (9%)/ZrO <sub>2</sub>	4:1	300	50	W	20000	5.2	99.8	1.0·10 <sup>-2</sup>	[205]
ZnO-ZrO <sub>2</sub>	4:1	320	50	W	24000	10	91	2.3·10 <sup>-2</sup>	[101]
Ga/ZrO <sub>x</sub>	3:1	300	50	W	24000	4.3	80	8.1·10 <sup>-3</sup>	[206]
5%In <sub>2</sub> O <sub>3</sub> /m-ZrO <sub>2</sub>	4:1	280	50	W	24000	4.8	84.0	8.4·10 <sup>-3</sup>	[207]
5%In <sub>2</sub> O <sub>3</sub> /t-ZrO <sub>2</sub>	4:1	280	50	W	24000	0.5	82.0	1.3·10 <sup>-3</sup>	[207]
In <sub>5</sub> /ZrO <sub>2</sub>	4:1	280	50	G	24000	1.8	68.2	2.2·10 <sup>-3</sup>	[208]
In <sub>0.1</sub> /ZrO <sub>2</sub>	4:1	280	50	G	24000	1.1	21.3	4.4·10 <sup>-4</sup>	[208]
CdZrO <sub>x</sub>	3:1	312	50	G	24000	12.4	80	2.3·10 <sup>-2</sup>	[206]

<sup>a</sup>GHSV is expressed in h<sup>-1</sup>; WHSV is expressed in mL·g<sub>cat</sub><sup>-1</sup>·h<sup>-1</sup>.

**Table 1.3** Performance of representative catalytic systems in the CO<sub>2</sub> hydrogenation to methane.

Catalyst	H <sub>2</sub> /CO <sub>2</sub> mol ratio	T (°C)	P (Bar)	GHSV or WHSV	Space velocity <sup>a</sup>	X <sub>CO2</sub> (%)	S <sub>MeOH</sub> (%)	REF
10Ni@MOF-5	4:1	280	1	G	2000	47.2	~100	[244]
3wt%Ni-MCM-41	4.2:1	300	1	W	5760	16.8	96.1	[222]
10Ni/CeO <sub>2</sub>	4:1	300	1	G	10000	~80	~100	[234]
NiMgO <sub>x</sub>	4:1	300	1	G	40000	70	99	[237]
20%Ni/Al <sub>2</sub> O <sub>3</sub>	4:1	325	1	W	120000	90	100	[218]
Ni/ZrO <sub>2</sub>	4:1	350	1	G	60000	79.1	96.71	[210]
15%Ni/SiO <sub>2</sub>	4:1	350	1	W	60000	55	96.1	[216]
20Ni/Al <sub>2</sub> O <sub>3</sub>	3.5:1	350	1	W	9000	82.4	~100	[233]
10Ni/MSN	4:1	350	1	W	50000	85	100	[239]
12Ni/CNT	4:1	350	1	W	30000	61.1	96.6	[243]
Ni/Al <sub>2</sub> O <sub>3</sub> -HT	4:1	380	1	W	75000	84	99.35	[228]
20%Ni/ZrO <sub>2</sub>	4:1	400	1	W	43500	50	100	[211]
10%Ni/SiO <sub>2</sub>	4:1	400	1	G	2400	68	66	[217]
10%Ni/Al <sub>2</sub> O <sub>3</sub>	4:1	400	1	W	15000	68	97.5	[219]
14Ni/USY	4:1	400	1	G	43000	65.5	94.2	[241]
5Ni/USY	4:1	400	1	G	43000	24.7	61.4	[241]
Ni/SiO <sub>2</sub>	4:1	450	1	W	6120	36.8	81.8	[225]
Ni/ZrO <sub>2</sub>	4:1	250	5	G	10000	90	90	[226]

<sup>a</sup>GHSV is expressed in h<sup>-1</sup>; WHSV is expressed in mL·g<sub>cat</sub><sup>-1</sup>·h<sup>-1</sup>.



Catalyst	H <sub>2</sub> /CO <sub>2</sub> mol ratio	T (°C)	P (Bar)	GHSV or WHSV	Space velocity <sup>a</sup>	X <sub>CO2</sub> (%)	S <sub>MeOH</sub> (%)	REF
20Ni@UiO-66	3:1	300	10	W	9000	57.6	100	[209]
Fe-Ni/Al <sub>2</sub> O <sub>3</sub>	24:1	250	1	W	32000	22.1	99.5	[227]
40Ni-Ce <sub>0.9</sub> Zr <sub>0.1</sub> O <sub>2</sub>	4:1	275	1	W	3000	98	100	[212]
21Ni.0.4La-HT(Mg,Al)	4:1	300	1	G	12000	~80	~99	[238]
21Ni-HT(Mg,Al)	4:1	300	1	G	12000	~65	~99	[238]
Ni/CeAl-p	4:1	300	1	W	30000	81	99	[232]
NiRu/CeZr	4:1	300	1	W	24000	53	93	[215]
NiWMgO <sub>x</sub>	4:1	300	1	G	40000	86	~100	[237]
10Ni-10Co/Al <sub>2</sub> O <sub>3</sub>	4:1	350	1	W	133000	61.5	95	[218]
10Ni10La <sub>2</sub> O <sub>3</sub> /Na-BETA	4:1	350	1	G	10000	65	99	[242]
12Ni4.5Ce/CNT	4:1	350	1	W	30000	83.8	99.8	[243]
5Ni/CZ(60-40)	4:1	350	1	G	43000	80.5	-	[128]
5Ni/CZ(80-20)	4:1	350	1	G	43000	71.5	98.5	[128]
5Ni-0.5Rh/CZ(80-20)	4:1	350	1	G	43000	77.8	99.2	[128]
K-Ni/Al <sub>2</sub> O <sub>3</sub> -HT	4:1	380	1	W	75000	87	99.76	[228]
10%Ni-1%Cu/SiO <sub>2</sub>	4:1	400	1	W	60000	39.5	44.4	[216]
23wt%Ni/CaO-Al <sub>2</sub> O <sub>3</sub>	4:1	400	1	G	15000	81	98	[223]
5%Ni/Zr/CNT-SEQ	5:1	400	1	W	75000	55	98	[213]
5Ni15Ce/USY	4:1	400	1	G	43000	55	86.2	[241]

<sup>a</sup>GHSV is expressed in h<sup>-1</sup>; WHSV is expressed in mL·g<sub>cat</sub><sup>-1</sup>·h<sup>-1</sup>.

Catalyst	H <sub>2</sub> /CO <sub>2</sub> mol ratio	T (°C)	P (Bar)	GHSV or WHSV	Space velocity <sup>a</sup>	X <sub>CO2</sub> (%)	S <sub>MeOH</sub> (%)	REF
8%Ni-2%Co/Al <sub>2</sub> O <sub>3</sub>	4:1	400	1	W	15000	80	98.3	[219]
Ni-Co/Al <sub>2</sub> O <sub>3</sub>	4:1	400	1	W	10000	78	99	[221]
Ni-Ru/CZ/15CNF <sub>f</sub>	4:1	400	1	G	10000	65.1	96.2	[214]
Ni-Ru/CZ <sub>p</sub>	4:1	400	1	G	10000	82.2	99.3	[214]
Ni-Ru/SiC <sub>p</sub>	4:1	400	1	G	10000	76.2	98.4	[214]
Pd-Ni/SiO <sub>2</sub>	4:1	450	1	W	6120	50.5	89	[225]
Co-Ni/ZrO <sub>2</sub>	4:1	250	5	G	10000	93	90	[226]
Cu-Ni/ZrO <sub>2</sub>	4:1	250	5	G	10000	55	70	[226]
Fe-Ni/ZrO <sub>2</sub>	4:1	250	5	G	10000	96	92	[226]
35Ni5Fe0.6RuAx	4:1	220	10	W	9600	68.2	98.9	[224]
Ni-La <sub>2</sub> O <sub>3</sub> /SBA-15	4:1	320	10	W	6000	90.7	99.5	[231]
Co/KIT-6	4.6:1	280	1	W	22000	48.9	100	[240]
Co/CeO <sub>2</sub> -nanorods	4:1	400	1	G	20000	62.8	91.1	[230]
Co/(0.01)PC-600	4:1	270	30	W	72000	52.5	99.2	[245]
10Co/Al <sub>2</sub> O <sub>3</sub>	4:1	400	30	W	3600	77.8	96.5	[220]
10Co/SiO <sub>2</sub>	4:1	400	30	W	3600	80.1	97.8	[220]
10Co/AC	4:1	400	30	W	3600	40.5	90.8	[220]
10Co/SiC	4:1	400	30	W	3600	77.5	96.4	[220]
10Co/ZrO <sub>2</sub>	4:1	400	30	W	3600	92.5	99.9	[220]

<sup>a</sup>GHSV is expressed in h<sup>-1</sup>; WHSV is expressed in mL·g<sub>cat</sub><sup>-1</sup>·h<sup>-1</sup>.

Catalyst	H <sub>2</sub> /CO <sub>2</sub> mol ratio	T (°C)	P (Bar)	GHSV or WHSV	Space velocity <sup>a</sup>	X <sub>CO2</sub> (%)	S <sub>MeOH</sub> (%)	REF
10Co/TiO <sub>2</sub>	4:1	400	30	W	3600	30.9	4.2	[220]
Ru/TiO <sub>2</sub>	4:1	180	1	W	864	100	100	[236]
Fe/Al <sub>2</sub> O <sub>3</sub>	24:1	250	1	W	32000	11.4	96.5	[227]
0.5Ru0.2Na/TiO <sub>2</sub>	4:1	350	1	G	56000	~40	~97	[235]
0.5Ru/TiO <sub>2</sub>	4:1	350	1	G	56000	~20	~85	[235]
Rh-Ba/Al <sub>2</sub> O <sub>3</sub>	4:1	400	1	G	6000	40	95	[229]
Pd/SiO <sub>2</sub>	4:1	450	1	W	6120	40.8	10.4	[225]
Pd-Fe/SiO <sub>2</sub>	4:1	450	1	W	6120	44.7	2.8	[225]
Mg/SiO <sub>2</sub>	4:1	450	1	W	6120	0.8	10.3	[225]
Pd-Mg/SiO <sub>2</sub>	4:1	450	1	W	6120	59.2	95.3	[225]
5Ru/CeO <sub>2</sub>	4.8:1	300	-	G	7640	83	99	[120]

<sup>a</sup>GHSV is expressed in h<sup>-1</sup>; WHSV is expressed in mL·g<sub>cat</sub><sup>-1</sup>·h<sup>-1</sup>.

## 1.6. References

- [1] *Sixth Assessment Report: Summary for Policymakers*. Intergovernmental Panel on Climate Change, 2021. <https://www.ipcc.ch/report/ar6/wg1/#SPM> (accessed 2022-01-16).
- [2] *Special report: Global Warming of 1.5 °C, Glossary*. Intergovernmental Panel on Climate Change, 2018. <https://www.ipcc.ch/sr15/chapter/glossary/> (accessed 2022-01-16).
- [3] *Fifth Assessment Report: AR5 Climate Change: Impacts, Adaptation, and Vulnerability*. Intergovernmental Panel on Climate Change, 2014. <https://www.ipcc.ch/report/ar5/wg2/> (accessed 2022-01-16).
- [4] *The Causes of Climate Change - NASA website*. <https://climate.nasa.gov/causes/> (accessed 2022-01-16).
- [5] *Climate change 2013: The Physical Science Basis. Contribution of Working Group I contribution to the Fifth Assessment Report of the Intergovernmental Panel on Climate Change*. Intergovernmental Panel on Climate Change, 2013. <https://www.ipcc.ch/report/ar5/wg1/> (accessed 2022-01-16).
- [6] *Trends in Atmospheric Carbon Dioxide - National Oceanic and Atmospheric Administration website*. <https://gml.noaa.gov/ccgg/trends/mlo.html> (accessed 2022-01-16).
- [7] *Trends in Atmospheric Methane - National Oceanic and Atmospheric Administration website*. [https://gml.noaa.gov/ccgg/trends\\_ch4/](https://gml.noaa.gov/ccgg/trends_ch4/) (accessed 2022-01-16).
- [8] *Trends in Atmospheric Nitrous Oxide - National Oceanic and Atmospheric Administration website*. [https://gml.noaa.gov/ccgg/trends\\_n2o/](https://gml.noaa.gov/ccgg/trends_n2o/) (accessed 2022-01-16).
- [9] *CO<sub>2</sub> and Greenhouse Gas Emissions - Our World in Data website*. <https://ourworldindata.org/greenhouse-gas-emissions?country=> (accessed 2022-01-16).
- [10] *Who emits the most CO<sub>2</sub> today? - Our World in Data website*. <https://ourworldindata.org/annual-co2-emissions> (accessed 2022-01-16).
- [11] *EEA greenhouse gases - Eurostat website*. <https://ec.europa.eu/eurostat> (accessed 2022-01-16).
- [12] *Greenhouse gas emissions by source sector - Eurostat website*. <https://ec.europa.eu/eurostat> (accessed 2022-01-16).
- [13] *Global EV Outlook 2020: Entering the decade of electric drive?* International Energy Agency, 2020. <https://www.iea.org/reports/global-ev-outlook-2020> (accessed 2022-01-16).
- [14] *Climate Action - European Commission website*. [https://ec.europa.eu/clima/policies/international/negotiations\\_en](https://ec.europa.eu/clima/policies/international/negotiations_en) (accessed 2022-01-16).

- [15] Freitas, J.; Dabrowski, J.; Silva, S. *The journey to net zero: 12 perspectives from the frontline of the energy transition in Europe*, 1st ed.; European University Institute, 2021. DOI: 10.2870/587688.
- [16] *The road to Paris (Climate Action) - European Commission website*. [https://ec.europa.eu/clima/policies/international/negotiations/progress\\_en](https://ec.europa.eu/clima/policies/international/negotiations/progress_en) (accessed 2022-01-16).
- [17] *The Paris Agreement - United Nations Framework Convention on Climate Change website*. <https://unfccc.int/process-and-meetings/the-paris-agreement/the-paris-agreement> (accessed 2022-01-16).
- [18] *European Climate Law - European Commission website*. [https://ec.europa.eu/clima/policies/eu-climate-action/law\\_en](https://ec.europa.eu/clima/policies/eu-climate-action/law_en) (accessed 2022-01-16).
- [19] Bouzarovski, S.; Thomson, H.; Cornelis, M.; Varo, A.; Guyet, R. *Towards an inclusive energy transition in the European Union: Confronting energy poverty amidst a global crisis*, 1st ed.; Publications Office (European Commission), 2020. DOI: 10.2833/103649.
- [20] Norhasyima, R. S.; Mahlia, T. M. I. Advances in CO<sub>2</sub> utilization technology: A patent landscape review. *J. CO<sub>2</sub> Util.* **2018**, *26*, 323-335. DOI: 10.1016/j.jcou.2018.05.022.
- [21] *Energía limpia: ¿Qué es el hidrógeno verde? - Revista PQ.com website*. [https://www.revistapq.com/file/view/25822#your\\_book\\_name/1](https://www.revistapq.com/file/view/25822#your_book_name/1) (accessed 2022-01-16).
- [22] *Green Hydrogen: A guide to policy making*. International Renewable Energy Agency, 2020. [https://www.irena.org//media/Files/IRENA/Agency/Publication/2020/Nov/IRENA\\_Green\\_hydrogen\\_policy\\_2020.pdf](https://www.irena.org//media/Files/IRENA/Agency/Publication/2020/Nov/IRENA_Green_hydrogen_policy_2020.pdf) (accessed 2022-01-16).
- [23] Aresta, M.; Dibenedetto, A.; Quaranta, E. State of the art and perspectives in catalytic processes for CO<sub>2</sub> conversion into chemicals and fuels: The distinctive contribution of chemical catalysis and biotechnology. *J. Catal.* **2016**, *343*, 2-45. DOI: 10.1016/j.jcat.2016.04.003.
- [24] Sha, F.; Han, Z.; Tang, S.; Wang, J.; Li, C. Hydrogenation of Carbon Dioxide to Methanol over Non-Cu-based Heterogeneous Catalysts. *ChemSusChem* **2020**, *13*, 6160-6181. DOI: 10.1002/cssc.202002054.
- [25] *The phase diagram of carbon dioxide - Wikimedia website*. [https://commons.wikimedia.org/wiki/File:Colored\\_phase\\_diagram\\_of\\_carbon\\_dioxide\\_\(multi\\_language\).svg](https://commons.wikimedia.org/wiki/File:Colored_phase_diagram_of_carbon_dioxide_(multi_language).svg) (accessed 2022-01-16).
- [26] Olmos, A.; Asensio, G.; Pérez, P. J. Homogeneous Metal-Based Catalysis in Supercritical Carbon Dioxide as Reaction Medium. *ACS Catal.* **2016**, *6*, 4265-4280. DOI: 10.1021/acscatal.6b00848.
- [27] Bektesevic, S.; Kleman, A. M.; Marteel-Parrish, A. E.; Abraham, M. A. Hydroformylation in supercritical carbon dioxide: Catalysis and benign solvents. *J. Supercrit. Fluids* **2006**, *38*, 232-241. DOI: 10.1016/j.supflu.2006.01.019.

- [28] Gothe, M. L.; Pérez-Sanz, F. J.; Braga, A. H.; Borges, L. R.; Abreu, T. F.; Bazito, R. C.; Gonçalves, R. V.; Rossi, L. M.; Vidinha, P. Selective CO<sub>2</sub> hydrogenation into methanol in a supercritical flow process. *J. CO<sub>2</sub> Util.* **2020**, *40*, 101195. DOI: 10.1016/j.jcou.2020.101195.
- [29] Xie, S.; Zhang, W.; Lan, X.; Lin, H. CO<sub>2</sub> Reduction to Methanol in the Liquid Phase: A Review. *ChemSusChem* **2020**, *13*, 6141-6159. DOI: 10.1002/cssc.202002087.
- [30] Tri, P. N.; Wu, H.; Nguyen, T. A.; Barnabé, S.; Bénard, P. *Nanomaterials for CO<sub>2</sub> capture, storage, conversion, and utilization*; Elsevier, 2021. ISBN: 978-0-12-822894-4.
- [31] Yuan, Z.; Eden, M. R.; Gani, R. Toward the Development and Deployment of Large-Scale Carbon Dioxide Capture and Conversion Processes. *Ind. Eng. Chem. Res.* **2016**, *55*, 3383-3419. DOI: 10.1021/acs.iecr.5b03277.
- [32] Loria, P.; Bright, M. B. H. Lessons captured from 50 years of CCS projects. *Electr. J.* **2021**, *34*, 106998. DOI: 10.1016/j.tej.2021.106998.
- [33] *Global status of CCS 2020*. Global CCS Institute, 2020. <https://www.globalccsinstitute.com/wp-content/uploads/2021/03/Global-Status-of-CCS-Report-English.pdf> (accessed 2022-01-16).
- [34] Bazarov, A. I. Obtaining urea directly from Carbon dioxide and Ammonia. *J. Prakt. Chem.* **1870**, *2*, 283-312.
- [35] Steinhauser, G. *J. Cleaner Prod.* **2008**, *16*, 833-841. DOI: 10.1016/j.jclepro.2007.04.005.
- [36] Kolbe, H. On a new method of preparation and some remarkable properties of salicylic acid. *J. Prakt. Chem.* **1874**, 89-112. DOI: 10.1002/prac.18740100106.
- [37] Liu, X. M.; Lu, G. Q.; Yan, Z. F.; Beltrami, J. Recent Advances in Catalysts for Methanol Synthesis via Hydrogenation of CO and CO<sub>2</sub>. *Ind. Eng. Chem. Res.* **2003**, *42*, 6518-6530. DOI: 10.1021/ie020979s.
- [38] Tsuda, T.; Chujo, Y.; Saegusa, T. Copper (I) cyanoacetate as a carrier of activated carbon dioxide. *J. Chem. Soc. Chem. Commun.* **1976**, 415-416. DOI: 10.1039/C39760000415.
- [39] *Renewable Power Generation Costs in 2017*. International Renewable Energy Agency, 2018. <https://www.irena.org/publications/2018/jan/renewable-power-generation-costs-in-2017> (accessed 2022-01-16).
- [40] Grim, R. G.; Huang, Z.; Guarnieri, M. T.; Ferrell III, J. R.; Tao, L.; Schaidle, J. A. Transforming the carbon economy: challenges and opportunities in the convergence of low-cost electricity and reductive CO<sub>2</sub> utilization. *Energy Environ. Sci.* **2020**, *13*, 472-494. DOI: 10.1039/c9ee02410g.
- [41] Tountas, A. A.; Peng, X.; Tavasoli, A. V.; Duchesne, P. N.; Dingle, T. L.; Dong, Y.; Hurtado, L.; Mohan, A.; Sun, W.; Ulmer, U.; Wang, L.; Wood, T. E.; Maravelias, C. T.; Sain, M. M.; Ozin, G. A. Towards Solar Methanol: Past, Present, and Future. *Adv. Sci.* **2019**, *6*, 1801903. DOI: 10.1002/adv.201801903.

- [42] Saeidi, S.; Najari, S.; Hessel, V.; Wilson, K.; Keil, F. J.; Concepción, P.; Suib, S. L.; Rodrigues, A. E. Recent advances in CO<sub>2</sub> hydrogenation to value-added products: Current challenges and future directions. *Prog. Energy Combust. Sci.* **2021**, *85*, 100905. DOI: 10.1016/j.pecs.2021.100905.
- [43] De, S.; Dokania, A.; Ramirez, A.; Gascon, J. Advances in the Design of Heterogeneous Catalysts and Thermocatalytic Processes for CO<sub>2</sub> Utilization. *ACS Catal.* **2020**, *10*, 14147-14185. DOI: 10.1021/acscatal.0c04273.
- [44] Kajaste, R.; Hurme, M.; Oinas, P. Methanol-Managing greenhouse gas emissions in the production chain by optimizing the resource base. *AIMS Energy* **2018**, *6*, 1074-1102. DOI: 10.3934/energy.2018.6.1074.
- [45] Sheldon, D. Methanol Production - A Technical History. *Johnson Matthey Technol. Rev.* **2017**, *61*, 172-182. DOI: 10.1595/205651317X695622.
- [46] Álvarez, A.; Bansode, A.; Urakawa, A.; Bavykina, A. V.; Wezendonk, T. A.; Makkee, M.; Gascon, J.; Kapteijn, F. Challenges in the Greener Production of Formates/Formic Acid, Methanol, and DME by Heterogeneously Catalyzed CO<sub>2</sub> Hydrogenation Processes. *Chem. Rev.* **2017**, *117*, 9804-9838. DOI: 10.1021/acs.chemrev.6b00816.
- [47] Carnes, C. L.; Klabunde, K. J. The catalytic methanol synthesis over nanoparticle metal oxide catalysts. *J. Mol. Catal. A: Chem.* **2003**, *194*, 227-236. DOI: 10.1016/S1381-1169(02)00525-3.
- [48] Słoczynski, J.; Grabowski, R.; Kozłowska, A.; Olszewski, P.; Lachowska, M.; Skrzypek, J.; Stoch, J. Effect of Mg and Mn oxide additions on structural and adsorptive properties of Cu/ZnO/ZrO<sub>2</sub> catalysts for the methanol synthesis from CO<sub>2</sub>. *Appl. Catal. A: Gen.* **2003**, *249*, 129-138. DOI: 10.1016/S0926-860X(03)00191-1.
- [49] Karelovic, A.; Bargibant, A.; Fernández, C.; Ruiz, P. Effect of the structural and morphological properties of Cu/ZnO catalysts prepared by citrate method on their activity toward methanol synthesis from CO<sub>2</sub> and H<sub>2</sub> under mild reaction conditions. *Catal. Today* **2012**, *197*, 109-118. DOI: 10.1016/j.cattod.2012.07.029.
- [50] Słoczynski, J.; Grabowski, R.; Olszewski, P.; Kozłowska, A.; Stoch, J.; Lachowska, M.; Skrzypek, J. Effect of metal oxide additives on the activity and stability of Cu/ZnO/ZrO<sub>2</sub> catalysts in the synthesis of methanol from CO<sub>2</sub> and H<sub>2</sub>. *Appl. Catal. A: Gen.* **2006**, *310*, 127-137. DOI: 10.1016/j.apcata.2006.05.035.
- [51] Liu, J.; Shi, J.; He, D.; Zhang, Q.; Wu, X.; Liang, Y.; Zhu, Q. Surface active structure of ultra-fine Cu/ZrO<sub>2</sub> catalysts used for the CO<sub>2</sub>+H<sub>2</sub> to methanol reaction. *Appl. Catal. A: Gen.* **2001**, *218*, 113-119. DOI: 10.1016/S0926-860X(01)00625-1.
- [52] Liu, X. M.; Lu, G. Q.; Yan, Z. F. Nanocrystalline zirconia as catalyst support in methanol synthesis. *Appl. Catal. A: Gen.* **2005**, *279*, 241-245. DOI: 10.1016/j.apcata.2004.10.040.

- [53] Frei, E.; Schaadt, A.; Ludwig, T.; Hillebrecht, H.; Krossing, I. The Influence of the Precipitation/ Ageing Temperature on a Cu/ZnO/ZrO<sub>2</sub> Catalyst for Methanol Synthesis from H<sub>2</sub> and CO<sub>2</sub>. *ChemCatChem* **2014**, *6*, 1721-1730. DOI: 10.1002/cctc.201300665.
- [54] Li, K.; Chen, J. G. CO<sub>2</sub> Hydrogenation to Methanol over ZrO<sub>2</sub>-Containing Catalysts: Insights into ZrO<sub>2</sub> Induced Synergy. *ACS Catal.* **2019**, *9*, 7840-7861. DOI: 10.1021/acscatal.9b01943.
- [55] Wambach, J.; Baiker, A.; Wokaun, A. CO<sub>2</sub> hydrogenation over metal/zirconia catalysts. *Phys. Chem. Chem. Phys.* **1999**, *1*, 5071-5080. DOI: 10.1039/A904923A.
- [56] Guo, X.; Mao, D.; Lu, G.; Wang, S.; Wu, G. CO<sub>2</sub> hydrogenation to methanol over Cu/ZnO/ZrO<sub>2</sub> catalysts prepared via a route of solid-state reaction. *Catal. Commun.* **2011**, *12*, 1095-1098. DOI: 10.1016/j.catcom.2011.03.033.
- [57] Jung, K. T.; Bell, A. T. Effects of Zirconia Phase on the Synthesis of Methanol over Zirconia-Supported Copper. *Catal. Lett.* **2002**, *80*, 63-68. DOI: 10.1023/A:1015326726898.
- [58] Van der Berg, R.; Prieto, G.; Korpershoek, G.; Van der Wal, L. I.; Van Bunningen, A. J.; Laegsgaard-Jorgensen, S.; De Jongh, P. E.; De Jong, K. P. Structure sensitivity of Cu and CuZn catalysts relevant to industrial methanol synthesis. *Nat. Commun.* **2016**, *7*, 13057. DOI: 10.1038/ncomms13057.
- [59] Campbell, C. T.; Peden, C. H. F. Oxygen Vacancies and Catalysis on Ceria Surfaces. *Science* **2005**, *309*, 713-714. DOI: 10.1126/science.1113955.
- [60] Rodriguez, J. A.; Grinter, D. C.; Liu, Z.; Palomino, R. M.; Senanayake, S. D. Ceria-based model catalysts: fundamental studies on the importance of the metal-ceria interface in CO oxidation, the water-gas shift, CO<sub>2</sub> hydrogenation, and methane and alcohol reforming. *Chem. Soc. Rev.* **2017**, *46*, 1824-1841. DOI: 10.1039/C6CS00863A.
- [61] Wang, Z. Q.; Xu, Z. N.; Peng, S. Y.; Zhang, M. J.; Lu, G.; Chen, Q. S.; Chen, Y.; Guo, G. C. High-Performance and Long-Lived Cu/SiO<sub>2</sub> Nanocatalyst for CO<sub>2</sub> Hydrogenation. *ACS Catal.* **2015**, *5*, 4255-4259. DOI: 10.1021/acscatal.5b00682.
- [62] Din, I. U.; Shaharun, M. S.; Subbarao, D.; Naeem, A. Synthesis, characterization and activity pattern of carbon nanofibers based copper/zirconia catalysts for carbon dioxide hydrogenation to methanol: Influence of calcination temperature. *J. Power Sources* **2015**, *274*, 619-628. DOI: 10.1016/j.jpowsour.2014.10.087.
- [63] Witoon, T.; Numpilai, T.; Phongamwong, T.; Donphai, W.; Boonyuen, C.; Warakulwit, C.; Chareonpanich, M.; Limtrakul, J. Enhanced activity, selectivity and stability of a CuO-ZnO-ZrO<sub>2</sub> catalyst by adding graphene oxide for CO<sub>2</sub> hydrogenation to methanol. *Chem. Eng. J.* **2018**, *334*, 1781-1791. DOI: 10.1016/j.cej.2017.11.117.
- [64] Fan, Y. J.; Wu, S. F. Graphene-supported copper-based catalyst for the hydrogenation of carbon dioxide to form methanol. *J. CO<sub>2</sub> Util.* **2016**, *16*, 150-156. DOI: 10.1016/j.jcou.2016.07.001.



- [65] Rungtaweeworanit, B.; Baek, J.; Araujo, J. R.; Archanjo, B. S.; Choi, K. M.; Yaghi, O. M.; Somotjai, G. A. Copper Nanocrystals Encapsulated in Zr-based Metal-Organic Frameworks for Highly Selective CO<sub>2</sub> Hydrogenation to Methanol. *Nano Lett.* **2016**, *16*, 7645-7649. DOI: 10.1021/acs.nanolett.6b03637.
- [66] Kobayashi, H.; Taylor, J. M.; Mitsuka, Y.; Ogiwara, N.; Yamamoto, T.; Toriyama, T.; Matsumura, S.; Kitagawa, H. Charge transfer dependence on CO<sub>2</sub> hydrogenation activity to methanol in Cu nanoparticles covered with metal-organic framework systems. *Chem. Sci.* **2019**, *10*, 3289-3294. DOI: 10.1039/C8SC05441J.
- [67] Toyir, J.; Ramírez de la Piscina, P.; Fierro, J. L. G.; Homs, N. Catalytic performance for CO<sub>2</sub> conversion to methanol of gallium-promoted copper-based catalysts: influence of metallic precursors. *Appl. Catal. B: Environ.* **2001**, *34*, 255-266. DOI: 10.1016/S0926-3373(01)00203-X.
- [68] Schumann, J.; Eichelbaum, M.; Lunkenbein, T.; Thomas, N.; Álvarez Galván, M. C.; Schlögl, R.; Behrens, M. Promoting Strong Metal Support Interaction: Doping ZnO for Enhanced Activity of Cu/ZnO:M (M = Al, Ga, Mg) Catalysts. *ACS Catal.* **2015**, *5*, 3260-3270. DOI: 10.1021/acscatal.5b00188.
- [69] Li, M. M. J.; Zeng, Z.; Liao, F.; Hong, X.; Tsang, S. C. E. Enhanced CO<sub>2</sub> hydrogenation to methanol over CuZn nanoalloy in Ga modified Cu/ZnO catalysts. *J. Catal.* **2016**, *343*, 157-167. DOI: 10.1016/j.jcat.2016.03.020.
- [70] Guo, X.; Mao, D.; Lu, G.; Wang, S.; Wu, G. The influence of La doping on the catalytic behavior of Cu/ZrO<sub>2</sub> for methanol synthesis from CO<sub>2</sub> hydrogenation. *J. Mol. Catal. A: Chem.* **2011**, *345*, 60-68. DOI: 10.1016/j.molcata.2011.05.019.
- [71] Gao, P.; Zhong, L.; Zhang, L.; Wang, H.; Zhao, N.; Wei, W.; Sun, Y. Yttrium oxide modified Cu/ZnO/Al<sub>2</sub>O<sub>3</sub> catalysts via hydrotalcite-like precursors for CO<sub>2</sub> hydrogenation to methanol. *Catal. Sci. Technol.* **2015**, *5*, 4365-4377. DOI: 10.1039/C5CY00372E.
- [72] Zhang, L.; Zhang, Y.; Chen, S. Effect of promoter SiO<sub>2</sub>, TiO<sub>2</sub> or SiO<sub>2</sub>-TiO<sub>2</sub> on the performance of CuO-ZnO-Al<sub>2</sub>O<sub>3</sub> catalyst for methanol synthesis from CO<sub>2</sub> hydrogenation. *Appl. Catal. A: Gen.* **2012**, *415*, 118-123. DOI: 10.1016/j.apcata.2011.12.013.
- [73] Choi, E. J.; Lee, Y. H.; Lee, D. W.; Moon, D. J.; Lee, K. Y. Hydrogenation of CO<sub>2</sub> to methanol over Pd-Cu/CeO<sub>2</sub> catalysts. *Mol. Catal.* **2017**, *434*, 146-153. DOI: 10.1016/j.mcat.2017.02.005.
- [74] Martin, O.; Mondelli, C.; Curulla-Ferré, D.; Drouilly, C.; Hauert, R.; Pérez-Ramírez, J. Zinc-Rich Copper Catalysts Promoted by Gold for Methanol Synthesis. *ACS Catal.* **2015**, *5*, 5607-5616. DOI: 10.1021/acscatal.5b00877.
- [75] Fichtl, M. B.; Schlereth, D.; Jacobsen, N.; Kasatkin, I.; Schumann, J.; Behrens, M.; Schlögl, R.; Hinrichsen, O. Kinetics of deactivation on Cu/ZnO/Al<sub>2</sub>O<sub>3</sub> methanol synthesis catalysts. *Appl. Catal. A: Gen.* **2015**, *502*, 262-270. DOI: 10.1016/j.apcata.2015.06.014.

- [76] Xu, J.; Su, X.; Liu, X.; Pan, X.; Pei, G.; Huang, Y.; Wang, X.; Zhang, T.; Geng, H. Methanol synthesis from CO<sub>2</sub> and H<sub>2</sub> over Pd/ZnO/Al<sub>2</sub>O<sub>3</sub>: Catalyst structure dependence of methanol selectivity. *Appl. Catal. A: Gen.* **2016**, *514*, 51-59. DOI: 10.1016/j.apcata.2016.01.006.
- [77] Iwasa, N.; Suzuki, H.; Terashita, M.; Arai, M.; Takezawa, N. Methanol Synthesis from CO<sub>2</sub> Under Atmospheric Pressure over Supported Pd Catalysts. *Catal. Lett.* **2004**, *96*, 75-78. DOI: 10.1023/B:CATL.0000029533.41604.13.
- [78] Malik, A. S.; Zaman, S. F.; Al-Zahrani, A. A.; Daous, M. A.; Driss, H.; Petrov, L. A. Development of highly selective PdZn/CeO<sub>2</sub> and Ca-doped PdZn/CeO<sub>2</sub> catalysts for methanol synthesis from CO<sub>2</sub> hydrogenation. *Appl. Catal. A: Gen.* **2018**, *560*, 42-53. DOI: 10.1016/j.apcata.2018.04.036.
- [79] Ojelade, O. A.; Zaman, S. F.; Daous, M. A.; Al-Zahrani, A. A.; Malik, A. S.; Driss, H.; Shterk, G.; Gascon, J. Optimizing Pd:Zn molar ratio in PdZn/CeO<sub>2</sub> for CO<sub>2</sub> hydrogenation to methanol. *Appl. Catal. A: Gen.* **2019**, *584*, 117185. DOI: 10.1016/j.apcata.2019.117185.
- [80] Qu, J.; Zhou, X.; Xu, F.; Gong, X. Q.; Tsang, S. C. E. Shape Effect of Pd-Promoted Ga<sub>2</sub>O<sub>3</sub> Nanocatalysts for Methanol Synthesis by CO<sub>2</sub> Hydrogenation. *J. Phys. Chem. C* **2014**, *118*, 24452-24466. DOI: 10.1021/jp5063379.
- [81] Zhou, X.; Qu, J.; Xu, F.; Hu, J.; Foord, J. S.; Zeng, Z.; Hong, X.; Tsang, S. C. E. Shape selective plate-form Ga<sub>2</sub>O<sub>3</sub> with strong metal-support interaction to overlying Pd for hydrogenation of CO<sub>2</sub> to CH<sub>3</sub>OH. *Chem. Commun.* **2013**, *49*, 1747-1749. DOI: 10.1039/C3CC38455A.
- [82] Rui, N.; Wang, Z.; Sun, K.; Ye, J.; Ge, Q.; Liu, C. J. CO<sub>2</sub> hydrogenation to methanol over Pd/In<sub>2</sub>O<sub>3</sub>: effects of Pd and oxygen vacancy. *Appl. Catal. B: Environ.* **2017**, *218*, 488-497. DOI: 10.1016/j.apcatb.2017.06.069.
- [83] Koizumi, N.; Jiang, X.; Kugai, J.; Song, C. S. Effects of mesoporous silica supports and alkaline promoters on activity of Pd catalysts in CO<sub>2</sub> hydrogenation for methanol synthesis. *Catal. Today* **2012**, *194*, 16-24. DOI: 10.1016/j.cattod.2012.08.007.
- [84] Song, Y.; Liu, X.; Xiao, L.; Wu, W.; Zhang, J.; Song, X. Pd-Promoter/MCM-41: A Highly Effective Bifunctional Catalyst for Conversion of Carbon Dioxide. *Catal. Lett.* **2015**, *145*, 1272-1280. DOI: 10.1007/s10562-015-1529-0.
- [85] Liang, X. L.; Dong, X.; Lin, G. D.; Zhang, H. B. Carbon nanotube-supported Pd-ZnO catalyst for hydrogenation of CO<sub>2</sub> to methanol. *Appl. Catal. B: Environ.* **2009**, *88*, 315-322. DOI: 10.1016/j.apcatb.2008.11.018.
- [86] Díez-Ramírez, J.; Sánchez, P.; Rodríguez-Gómez, A.; Valverde, J. L.; Dorado, F. Carbon Nanofiber-Based Palladium/Zinc Catalysts for the Hydrogenation of Carbon Dioxide to Methanol at Atmospheric Pressure. *Ind. Eng. Chem. Res.* **2016**, *55*, 3556-3567. DOI: 10.1021/acs.iecr.6b00170.

- [87] Liang, X. L.; Xie, J. R.; Liu, Z. M. A Novel Pd-decorated Carbon Nanotubes-promoted Pd-ZnO Catalyst for CO<sub>2</sub> Hydrogenation to Methanol. *Catal. Lett.* **2015**, *145*, 1138-1147. DOI: 10.1007/s10562-015-1505-8.
- [88] Bahruji, H.; Bowker, M.; Hutchings, G.; Dimitratos, N.; Wells, P.; Gibson, E.; Jones, W.; Brookes, C.; Morgan, D.; Lalev, G. Pd/ZnO catalysts for direct CO<sub>2</sub> hydrogenation to methanol. *J. Catal.* **2016**, *343*, 133-146. DOI: 10.1016/j.jcat.2016.03.017.
- [89] Grunwaldt, J. D.; Molenbroek, A. M.; Topsøe, N. Y.; Topsøe, H.; Clausen, B. S. In Situ Investigations of Structural Changes in Cu/ZnO Catalysts. *J. Catal.* **2000**, *194*, 452-460. DOI: 10.1006/jcat.2000.2930.
- [90] Nie, X.; Jiang, X.; Wang, H.; Luo, W.; Janik, M. J.; Chen, Y.; Guo, X.; Song, C. Mechanistic Understanding of Alloy Effect and Water Promotion for Pd-Cu Bimetallic Catalysts in CO<sub>2</sub> Hydrogenation to Methanol. *ACS Catal.* **2018**, *8*, 4873-4892. DOI: 10.1021/acscatal.7b04150.
- [91] Jiang, X.; Nie, X.; Wang, X.; Wang, H.; Koizumi, N.; Chen, Y.; Guo, X.; Song, C. Origin of Pd-Cu bimetallic effect for synergetic promotion of methanol formation from CO<sub>2</sub> hydrogenation. *J. Catal.* **2019**, *369*, 21-32. DOI: 10.1016/j.jcat.2018.10.001.
- [92] Tan, Q.; Shi, Z.; Wu, D. CO<sub>2</sub> Hydrogenation to Methanol over a Highly Active Cu-Ni/CeO<sub>2</sub>-Nanotube Catalyst. *Ind. Eng. Chem. Res.* **2018**, *57*, 10148-10158. DOI: 10.1021/acs.iecr.8b01246.
- [93] Tada, S.; Watanabe, F.; Kiyota, K.; Shimoda, N.; Hayashi, R.; Takahashi, M.; Nariyuki, A.; Igarashi, A.; Satokawa, S. Ag addition to CuO-ZrO<sub>2</sub> catalysts promotes methanol synthesis via CO<sub>2</sub> hydrogenation. *J. Catal.* **2017**, *351*, 107-118. DOI: 10.1016/j.jcat.2017.04.021.
- [94] Bai, S.; Shao, Q.; Feng, Y.; Bu, L.; Huang, X. Highly Efficient Carbon Dioxide Hydrogenation to Methanol Catalyzed by Zigzag Platinum-Cobalt Nanowires. *Small* **2017**, *13*, 1604311. DOI: 10.1002/smll.201604311.
- [95] Zhang, W.; Wang, L.; Liu, H.; Hao, Y.; Li, H.; Khan, M. U.; Zeng, J. Integration of Quantum Confinement and Alloy Effect to Modulate Electronic Properties of RhW Nanocrystals for Improved Catalytic Performance toward CO<sub>2</sub> Hydrogenation. *Nano Lett.* **2017**, *17*, 788-793. DOI: 10.1021/acs.nanolett.6b03967.
- [96] Studt, F.; Sharafutdinov, I.; Abild-Pedersen, F.; Elkjaer, C. F.; Hummelshøj, J. S.; Dahl, S.; Chorkendorff, I.; Nørskov, J. K. Discovery of a Ni-Ga catalyst for carbon dioxide reduction to methanol. *Nat. Chem.* **2014**, *6*, 320-324. DOI: 10.1038/nchem.1873.
- [97] Shi, Z.; Tan, Q.; Tian, C.; Pan, Y.; Sun, X.; Zhang, J.; Wu, D. CO<sub>2</sub> hydrogenation to methanol over Cu-In intermetallic catalysts: Effect of reduction temperature. *J. Catal.* **2019**, *379*, 78-89. DOI: 10.1016/j.jcat.2019.09.024.
- [98] Ota, A.; Kunkes, E. L.; Kasatkin, I.; Groppo, E.; Ferri, D.; Poceiro, B.; Navarro-Yerga, R. M.; Behrens, M. Comparative study of hydrotalcite-derived supported Pd<sub>2</sub>Ga and PdZn intermetallic

- nanoparticles as methanol synthesis and methanol steam reforming catalysts. *J. Catal.* **2012**, *293*, 27-38. DOI: 10.1016/j.jcat.2012.05.020.
- [99] Snider, J. L.; Streibel, V.; Hubert, M. A.; Choksi, T. S.; Valle, E.; Upham, D. C.; Schumann, J.; Duyar, M. S.; Gallo, A.; Abild-Pedersen, F.; Jaramillo, T. F. Revealing the Synergy between Oxide and Alloy Phases on the Performance of Bimetallic In-Pd Catalysts for CO<sub>2</sub> Hydrogenation to Methanol. *ACS Catal.* **2019**, *9*, 3399-3412. DOI: 10.1021/acscatal.8b04848.
- [100] Li, C. S.; Melaet, G.; Ralston, W. T.; An, K.; Brooks, C.; Ye, Y. F.; Liu, Y. S.; Zhu, J. F.; Guo, J. H.; Alayoglu, S.; Somorjai, G. A. High-performance hybrid oxide catalyst of manganese and cobalt for low-pressure methanol synthesis. *Nat. Commun.* **2015**, *6*, 6538. DOI: 10.1038/ncomms7538.
- [101] Wang, J.; Li, G.; Li, Z.; Tang, C.; Feng, Z.; An, H.; Liu, H.; Liu T.; Li, C. A highly selective and stable ZnO-ZrO<sub>2</sub> solid solution catalyst for CO<sub>2</sub> hydrogenation to methanol. *Sci. Adv.* **2017**, *3*, e1701290. DOI: 10.1126/sciadv.1701290.
- [102] Zhong, J.; Yang, X.; Wu, Z.; Liang, B.; Huang, Y.; Zhang, T. State of the art and perspectives in heterogeneous catalysis of CO<sub>2</sub> hydrogenation to methanol. *Chem. Soc. Rev.* **2020**, *49*, 1325-1616. DOI: 10.1039/C9CS00614A.
- [103] Yang, Y.; Evans, J.; Rodriguez, J. A.; White, M. G.; Liu. Fundamental studies of methanol synthesis from CO<sub>2</sub> hydrogenation on Cu(111), Cu clusters, and Cu/ZnO(0001). *P. Phys. Chem. Chem. Phys.* **2010**, *12*, 9909-9917. DOI: 10.1039/C001484B.
- [104] Li, Y. W.; Chan, S. H.; Sun, Q. Heterogeneous catalytic conversion of CO<sub>2</sub>: a comprehensive theoretical review. *Nanoscale* **2015**, *7*, 8663-8683. DOI: 10.1039/C5NR00092K.
- [105] Li, M. M. J.; Chen, C.; Ayvali, T.; Suo, H.; Zheng, J.; Teixeira, I. F.; Ye, L.; Zou, H.; O'Hare, D.; Tsang, S. C. E. CO<sub>2</sub> Hydrogenation to Methanol over Catalysts Derived from Single Cationic Layer CuZnGa LDH Precursors. *ACS Catal.* **2018**, *8*, 4390-4401. DOI: 10.1021/acscatal.8b00474.
- [106] Gallucci, F.; Paturzo, L.; Basile, A. An experimental study of CO<sub>2</sub> hydrogenation into methanol involving a zeolite membrane reactor. *Chem. Eng. Process.: Process Intensif.* **2004**, *43*, 1029-1036. DOI: 10.1016/j.cep.2003.10.005.
- [107] *Renewable Methanol Report*. Methanol Institute and ATA insights, 2018. <https://www.methanol.org/wp-content/uploads/2019/01/MethanolReport.pdf> (accessed 2022-01-16).
- [108] Meunier, N.; Chauvy, R.; Mouhoubi, S.; Thomas, D.; De Weireld, G. Alternative production of methanol from industrial CO<sub>2</sub>. *Renew. Energy* **2020**, *146*, 1192-1203. DOI: 10.1016/j.renene.2019.07.010.
- [109] Szima, S.; Cormos, C. C. Improving methanol synthesis from carbon-free H<sub>2</sub> and captured CO<sub>2</sub>: A techno-economic and environmental evaluation. *J. CO<sub>2</sub> Util.* **2018**, *24*, 555-563. DOI: 10.1016/j.jcou.2018.02.007.

- [110] Aziz, M. A. A.; Jalil, A. A.; Triwahyono, S.; Ahmad, A. CO<sub>2</sub> methanation over heterogeneous catalysts: recent progress and future prospects. *Green Chem.* **2015**, *17*, 2647-2663. DOI: 10.1039/c5gc00119f.
- [111] Stangeland, K.; Kalai, D.; Li, H.; Yu, Z. CO<sub>2</sub> Methanation: The Effect of Catalysts and Reaction Conditions. *Energy Procedia* **2017**, *105*, 2022-2027. DOI: 10.1016/j.egypro.2017.03.577.
- [112] Gao, J.; Wang, Y.; Ping, Y.; Hu, D.; Xu, G.; Gu, F.; Su, F. A thermodynamic analysis of methanation reactions of carbon oxides for the production of synthetic natural gas. *RSC Adv.* **2012**, *2*, 2358-2368. DOI: 10.1039/c2ra00632d.
- [113] Thampi, K. R.; Kiwi, J.; Gratzel, M. Methanation and photo-methanation of carbon dioxide at room temperature and atmospheric pressure. *Nature* **1987**, *327*, 506-508. DOI: 10.1038/327506a0.
- [114] Yaccato, K.; Carhart, R.; Hagemeyer, A.; Lesik, A.; Strasser, P.; Volpe Jr., A. F.; Turner, H.; Weinberg, H.; Grasselli, R. B.; Brooks, C. Competitive CO and CO<sub>2</sub> methanation over supported noble metal catalysts in high throughput scanning mass spectrometer. *Appl. Catal. A: Gen.* **2005**, *296*, 30-48. DOI: 10.1016/j.apcata.2005.07.052.
- [115] Younas, M.; Kong, L. L.; Bashir, M. J. K.; Nadeem, H.; Shehzad, A.; Sethupathi, S. Recent Advancements, Fundamental Challenges, and Opportunities in Catalytic Methanation of CO<sub>2</sub>. *Energy Fuels* **2016**, *30*, 8815-8831. DOI: 10.1021/acs.energyfuels.6b01723.
- [116] Garbarino, G.; Bellotti, D.; Riani, P.; Magistri, L.; Busca, G. Methanation of carbon dioxide on Ru/Al<sub>2</sub>O<sub>3</sub> and Ni/Al<sub>2</sub>O<sub>3</sub> catalysts at atmospheric pressure: Catalysts activation, behaviour and stability. *Int. J. Hydrog. Energy* **2015**, *40*, 9171-9182. DOI: 10.1016/j.ijhydene.2015.05.059.
- [117] Gao, J.; Liu, Q.; Gu, F.; Liu, B.; Zhong, Z.; Su, F. Recent advances in methanation catalysts for the production of synthetic natural gas. *RSC Adv.* **2015**, *5*, 22759-22776. DOI: 10.1039/C4RA16114A.
- [118] Sandupatla, A. S.; Banerjee, A.; Deo, G. Optimizing CO<sub>2</sub> hydrogenation to methane over CoFe bimetallic catalyst: experimental and density functional theory studies. *Appl. Surf. Sci.* **2019**, *485*, 441-449. DOI: 10.1016/j.apsusc.2019.04.217.
- [119] Le, T. A.; Kim, M. S.; Lee, S. H.; Kim, T. W.; Park, E. D. CO and CO<sub>2</sub> methanation over supported Ni catalysts. *Catal. Today* **2017**, *293-294*, 89-96. DOI: 10.1016/j.cattod.2016.12.036.
- [120] Dreyer, J. A. H.; Li, P.; Zhang, L.; Beh, G. K.; Zhang, R.; Sit, P. H. L.; Teoh, W. Y. Influence of the oxide support reducibility on the CO<sub>2</sub> methanation over Ru-based catalysts. *Appl. Catal. B: Environ.* **2017**, *219*, 715-726. DOI: 10.1016/j.apcatb.2017.08.011.
- [121] Jangam, A.; Das, S.; Dewangan, N.; Hongmanorom, P.; Hui, W. M.; Kawi, S. Conversion of CO<sub>2</sub> to C<sub>1</sub> chemicals: catalyst design, kinetics and mechanism aspects of the reactions. *Catal. Today* **2020**, *358*, 3-29. DOI: 10.1016/j.cattod.2019.08.049.

- [122] Kattel, S.; Liu, P.; Chen, J. G. Tuning Selectivity of CO<sub>2</sub> Hydrogenation Reactions at the Metal/Oxide Interface *J. Am. Chem. Soc.* **2017**, *139*, 9739-9754. DOI: 10.1021/jacs.7b05362.
- [123] Garbarino, G.; Cavattoni, T.; Riani, P.; Busca, G. Support effects in metal catalysis: a study of the behavior of unsupported and silica-supported cobalt catalysts in the hydrogenation of CO<sub>2</sub> at atmospheric pressure. *Catal. Today* **2020**, *345*, 213-219. DOI: 10.1016/j.cattod.2019.10.016.
- [124] Martin, N. M.; Hemmingsson, F.; Schaefer, A.; Ek, M.; Merte, L. R.; Hejral, U.; Gustafson, J.; Skoglundh, M.; Dippel, A. C.; Gutowski, O.; Bauer, M.; Carlsson, P. A. Structure-function relationship for CO<sub>2</sub> methanation over ceria supported Rh and Ni catalysts under atmospheric pressure conditions. *Catal. Sci. Technol.* **2019**, *9*, 1644-1653. DOI: 10.1039/C8CY02097C.
- [125] Zhu, M.; Tian, P.; Cao, X.; Chen, J.; Pu, T.; Shi, B.; Xu, J.; Moon, J.; Wu, Z.; Han, Y. F. Vacancy engineering of the nickel-based catalysts for enhanced CO<sub>2</sub> methanation. *Appl. Catal. B: Environ.* **2021**, *282*, 119561. DOI: 10.1016/j.apcatb.2020.119561.
- [126] Boaro, M.; Colussi, S.; Trovarelli, A. Ceria-Based Materials in Hydrogenation and Reforming Reactions for CO<sub>2</sub> Valorization. *Front. Chem.* **2019**, *7*, 28. DOI: 10.3389/fchem.2019.00028.
- [127] Lee, S. M.; Lee, Y. H.; Moon, D. Y.; Ahn, J. Y.; Nguyen, D. D.; Chang, S. W.; Kim, S. S. Reaction Mechanism and Catalytic Impact of Ni/CeO<sub>2-x</sub> Catalyst for Low-Temperature CO<sub>2</sub> Methanation. *Ind. Eng. Chem. Res.* **2019**, *58*, 8656-8662. DOI: 10.1021/acs.iecr.9b00983.
- [128] Ocampo, F.; Louis, B.; Kiwi-Minsker, L.; Roger, A. C. Effect of Ce/Zr composition and noble metal promotion on nickel based Ce<sub>x</sub>Zr<sub>1-x</sub>O<sub>2</sub> catalysts for carbon dioxide methanation. *Appl. Catal. A: Gen.* **2011**, *392*, 36-44. DOI: 10.1016/j.apcata.2010.10.025.
- [129] Kwak J. H.; Kovarik, L.; Szanyi, J. CO<sub>2</sub> Reduction on Supported Ru/Al<sub>2</sub>O<sub>3</sub> Catalysts: Cluster Size Dependence of Product Selectivity. *ACS Catal.* **2013**, *3*, 2449-2455. DOI: 10.1021/cs400381f.
- [130] Wu, H. C.; Chang, Y. C.; Wu, J. H.; Lin, J. H.; Lin, I. K.; Chen, C. S. Methanation of CO<sub>2</sub> and reverse water gas shift reactions on Ni/SiO<sub>2</sub> catalysts: the influence of particle size on selectivity and reaction pathway. *Catal. Sci. Technol.* **2015**, *5*, 4154-4163. DOI: 10.1039/C5CY00667H.
- [131] Karelavic, A.; Ruiz, P. CO<sub>2</sub> hydrogenation at low temperature over Rh/ $\gamma$ -Al<sub>2</sub>O<sub>3</sub> catalysts: Effect of the metal particle size on catalytic performances and reaction mechanism. *Appl. Catal. B: Environ.* **2012**, *113-114*, 237-249. DOI: 10.1016/j.apcatb.2011.11.043.
- [132] Matsubu, J. C.; Yang, V. N.; Christopher, P. Isolated Metal Active Site Concentration and Stability Control Catalytic CO<sub>2</sub> Reduction Selectivity. *J. Am. Chem. Soc.* **2015**, *137*, 3076-3084. DOI: 10.1021/ja5128133.
- [133] Kwak, J. H.; Kovarik, L.; Szanyi, J. Heterogeneous Catalysis on Atomically Dispersed Supported Metals: CO<sub>2</sub> Reduction on Multifunctional Pd Catalysts. *ACS Catal.* **2013**, *3*, 2094-2100. DOI: 10.1021/cs4001392.

- [134] Rahmani, S.; Rezaei, M.; Meshkani, F. Preparation of promoted nickel catalysts supported on mesoporous nanocrystalline gamma alumina for carbon dioxide methanation reaction. *J. Ind. Eng. Chem.* **2014**, *20*, 4176-4182. DOI: 10.1016/j.jiec.2014.01.017.
- [135] Wierzbicki, D.; Debek, R.; Motak, M.; Grzybek, T.; Gálvez, M. E.; Da Costa, P. Novel Ni-La-hydrotralcite derived catalysts for CO<sub>2</sub> methanation. *Catal. Commun.* **2016**, *83*, 5-8. DOI: 10.1016/j.catcom.2016.04.021.
- [136] Lim, J. Y.; McGregor, J.; Sederman, A. J.; Dennis, J. S. Kinetic studies of CO<sub>2</sub> methanation over a Ni/γ-Al<sub>2</sub>O<sub>3</sub> catalyst using a batch reactor. *Chem. Eng. Sci.* **2016**, *141*, 28-45. DOI: 10.1016/j.ces.2015.10.026.
- [137] Avanesian, T.; Gusmao, G. S.; Christopher, P. Mechanism of CO<sub>2</sub> reduction by H<sub>2</sub> on Ru(0001) and general selectivity descriptors for late-transition metal catalysts. *J. Catal.* **2016**, *343*, 86-96. DOI: 10.1016/j.jcat.2016.03.016.
- [138] Pérez, S.; Aragón, J. J.; Peciña, I.; García-Suárez, E. J. Enhanced CO<sub>2</sub> Methanation by New Microstructured Reactor Concept and Design. *Top. Catal.* **2019**, *62*, 518-523. DOI: 10.1007/s11244-019-01139-4.
- [139] Wu, H.; Yuan, Q.; Zhu, B. An experimental investigation of optimal active catalyst distribution in nonisothermal pellets. *Ind. Eng. Chem. Res.* **1988**, *27*, 1169-1174. DOI: 10.1021/ie00079a014.
- [140] Veselovskaya, J. V.; Parunin, P. D.; Kunev, A. G. Catalytic process for methane production from atmospheric carbon dioxide utilizing renewable energy. *Catal. Today* **2017**, *298*, 117-123. DOI: 10.1016/j.cattod.2017.05.044.
- [141] Miguel, C.; Soria, M.; Mendes, A.; Madeira, L. A sorptive reactor for CO<sub>2</sub> capture and conversion to renewable methane. *Chem. Eng. J.* **2017**, *322*, 590-602. DOI: 10.1016/j.cej.2017.04.024.
- [142] Lefebvre, J.; Götz, M.; Bajohr, S.; Reimert, R.; Kolb, T. Improvement of three-phase methanation reactor performance for steady-state and transient operation. *Fuel Process Technol.* **2015**, *132*, 83-90. DOI: 10.1016/j.fuproc.2014.10.040.
- [143] *Power to Gas - Wikipedia website.* <https://de.wikipedia.org/wiki/Power-to-Gas> (accessed 2022-01-16).
- [144] *Sufire GmbH partner - Helmeth project website.* <http://www.helmeth.eu/index.php/partners/sunfire> (accessed 2022-01-16).
- [145] *Proyecto Renovagas - Centro Nacional de Hidrógeno website.* <https://www.cnh2.es/cnh2/renovagas/> (accessed 2022-01-16).
- [146] *Proyecto RIS3CAT CoSin - Naturgy website.* [https://www.naturgy.com/conocenos/innovacion\\_y\\_futuro/plan\\_de\\_innovacion\\_tecnologica/ris3cat\\_cosin\\_combustibles\\_sinteticos](https://www.naturgy.com/conocenos/innovacion_y_futuro/plan_de_innovacion_tecnologica/ris3cat_cosin_combustibles_sinteticos) (accessed 2022-01-16).

- [147] Bailera, M.; Lisbona, P.; Romeo, L. M.; Espatolero, S. Power to Gas projects review: Lab, pilot and demo plants for storing renewable energy and CO<sub>2</sub>. *Renew. Sust. Energy Rev.* **2017**, *69*, 292-313. DOI: 10.1016/j.rser.2016.11.130.
- [148] *Results of the STORE&GO Project - Store&GO website*. <https://www.storeandgo.info/about-the-project/goals-approach/> (accessed 2022-01-16).
- [149] Hashimoto, K. *Prototype Plant and Pilot Plant, Global Carbon Dioxide Recycling: For Global Sustainable Development by Renewable Energy*; Springer Singapore, 2019.
- [150] *INPEX, Osaka Gas set for world's largest-scale methanation plant, eye LNG production - S&P Global Platts website*. <https://www.spglobal.com/platts/en/market-insights/latest-news/energy-transition/101521-inpex-osaka-gas-set-for-worlds-largest-scale-methanation-planteye-lng-production> (accessed 2022-01-16).
- [151] *Hydrogen: Beyond the Hype - S&P Global Platts website*. <https://www.spglobal.com/platts/en/market-insights/topics/hydrogen> (Accessed 2022-01-16).
- [152] *Experience curves and economies of scale*. Store&GO Project, 2018. [https://www.storeandgo.info/fileadmin/downloads/deliverables\\_2019/20190801-STOREandGO-D7.5-EILReport\\_on\\_experience\\_curves\\_and\\_economies\\_of\\_scale.pdf](https://www.storeandgo.info/fileadmin/downloads/deliverables_2019/20190801-STOREandGO-D7.5-EILReport_on_experience_curves_and_economies_of_scale.pdf) (accessed 2022-01-16).
- [153] *Power-to-Gas: The case for Hydrogen (White Paper)*. California Hydrogen Business Council, 2015. <https://www.californiahydrogen.org/wp-content/uploads/2018/01/CHBC-HydrogenEnergy-Storage-White-Paper-FINAL.pdf> (accessed 2022-01-16).
- [154] Karelavic, A.; Ruiz, P. The role of copper particle size in low pressure methanol synthesis via CO<sub>2</sub> hydrogenation over Cu/ZnO catalysts. *Catal. Sci. Technol.* **2015**, *5*, 869-881. DOI: 10.1039/C4CY00848K.
- [155] Kondrat, S. A.; Smith, P. J.; Carter, J. H.; Hayward, J. S.; Pudge, G. J.; Shaw, G.; Spencer, M. S.; Bartley, J. K.; Taylor, S. H.; Hutchings, G. J. The effect of sodium species on methanol synthesis and water-gas shift Cu/ZnO catalysts: utilising high purity zincian georgeite. *Faraday Discuss* **2017**, *197*, 287-307. DOI: 10.1039/C6FD00202A.
- [156] Le Valant, A.; Comminges, C.; Tisseraud, C.; Canaff, C.; Pinard, L.; Pouilloux, Y. The Cu-ZnO synergy in methanol synthesis from CO<sub>2</sub>, Part 1: Origin of active site explained by experimental studies and a sphere contact quantification model on Cu+ZnO mechanical mixtures. *J. Catal.* **2015**, *324*, 41-49. DOI: 10.1016/j.jcat.2015.01.021.
- [157] Liu, T.; Hong, X.; Liu, G. In Situ Generation of the Cu@3DZrO<sub>x</sub> Framework Catalyst for Selective Methanol Synthesis from CO<sub>2</sub>/H<sub>2</sub>. *ACS Catal.* **2020**, *10*, 93-102. DOI: 10.1021/acscatal.9b03738.
- [158] Bao, Y.; Huang, C.; Chen, L.; Zhang, Y.; Liang, L.; Wen, J.; Fu, M.; Wu, J.; Ye, D. Highly efficient Cu/anatase TiO<sub>2</sub> {001}-nanosheets catalysts for methanol synthesis from CO<sub>2</sub>. *J. Energy Chem.* **2018**, *27*, 381-388. DOI: 10.1016/j.jechem.2017.12.015.



- [159] Arena, F.; Barbera, K.; Italiano, G.; Bonura, G.; Spadaro, L.; Frusteri, F. Synthesis, characterization and activity pattern of Cu-ZnO/ZrO<sub>2</sub> catalysts in the hydrogenation of carbon dioxide to methanol. *J. Catal.* **2007**, *249*, 185-194. DOI: 10.1016/j.jcat.2007.04.003.
- [160] Pori, M.; Arcon, I.; Dasireddy, V. D. B. C.; Likozar, B.; Orel, Z. C.; Marinsek, M. Photo-Chemically-Deposited and Industrial Cu/ZnO/Al<sub>2</sub>O<sub>3</sub> Catalyst Material Surface Structures During CO<sub>2</sub> Hydrogenation to Methanol: EXAFS, XANES and XPS Analyses of Phases After Oxidation, Reduction, and Reaction. *Catal. Lett.* **2021**, *151*, 3114-3134. DOI: 10.1007/s10562-021-03556-1.
- [161] Halim, N. S. A.; Zabidi, N. A. M. Z.; Tasfy, S. F. H.; Shaharun, M. S. Morphology and performance of Cu/ZnO based catalyst: Comparison between Al<sub>2</sub>O<sub>3</sub> and SiC support. *AIP Conf. Proc.* **2016**, *1787*, 030008. DOI: 10.1063/1.4968073.
- [162] Bukhtiyarova, M.; Lunkenbein, T.; Kähler, K.; Schlögl, R. Methanol Synthesis from Industrial CO<sub>2</sub> Sources: A Contribution to Chemical Energy Conversion. *Catal. Lett.* **2017**, *147*, 416-427. DOI: 10.1007/s10562-016-1960-x.
- [163] Hu, B.; Yin, Y.; Zhong, Z.; Wu, D.; Liu, G.; Hong, X. Cu@ZIF-8 derived inverse ZnO/Cu catalyst with sub-5 nm ZnO for efficient CO<sub>2</sub> hydrogenation to methanol. *Catal. Sci. Technol.* **2019**, *9*, 2673-2681. DOI: 10.1039/C8CY02546K.
- [164] Fujitani, T.; Saito, M.; Kanai, Y.; Takeuchi, M.; Moriya, K.; Watanabe, T.; Kawai, M.; Kakumoto, T. Methanol Synthesis from CO<sub>2</sub> and H<sub>2</sub> over Cu/ZnO/Ga<sub>2</sub>O<sub>3</sub> Catalyst. *Chem. Lett.* **1993**, *22*, 1079-1080. DOI: 10.1246/cl.1993.1079.
- [165] Bansode, A.; Urakawa, A. Towards full one-pass conversion of carbon dioxide to methanol and methanol-derived products. *J. Catal.* **2014**, *309*, 66-70. DOI: 10.1016/j.jcat.2013.09.005.
- [166] Wang, Y.; Kattel, S.; Gao, W.; Li, K.; Liu, P.; Chen, J. G.; Wang, H. Exploring the ternary interactions in Cu-ZnO-ZrO<sub>2</sub> catalysts for efficient CO<sub>2</sub> hydrogenation to methanol. *Nat. Commun.* **2019**, *10*, 1166. DOI: 10.1038/s41467-019-09072-6.
- [167] Guo X. M.; Mao, D. S.; Wang, S.; Wu, G. S.; Lu, G. Z. Combustion synthesis of CuO-ZnO-ZrO<sub>2</sub> catalysts for the hydrogenation of carbon dioxide to methanol. *Catal. Commun.* **2009**, *10*, 1661-1664. DOI: 10.1016/j.catcom.2009.05.004.
- [168] Bonura, G.; Cordaro, M.; Cannilla, C.; Arena, F.; Frusteri, F. The changing nature of the active site of Cu-Zn-Zr catalysts for the CO<sub>2</sub> hydrogenation reaction to methanol. *Appl. Catal. B: Environ.* **2014**, *152*, 152-161. DOI: 10.1016/j.apcatb.2014.01.035.
- [169] Li, L.; Mao, D. S.; Yu, J.; Guo, X. M. Highly selective hydrogenation of CO<sub>2</sub> to methanol over CuO-ZnO-ZrO<sub>2</sub> catalysts prepared by a surfactant-assisted co-precipitation method *J. Power Sources* **2015**, *279*, 394-404. DOI: 10.1016/j.jpowsour.2014.12.142.
- [170] Fang, X.; Men, Y.; Wu, F.; Zhao, Q.; Singh, R.; Xiao, P.; Du, T.; Webley, P. A. Improved methanol yield and selectivity from CO<sub>2</sub> hydrogenation using a novel Cu-ZnO-ZrO<sub>2</sub> catalyst supported on

- Mg-Al layered double hydroxide (LDH). *J. CO<sub>2</sub> Util.* **2019**, *29*, 57-64. DOI: 10.1016/j.jcou.2018.11.006.
- [171] Mureddu, M.; Ferrara, F.; Pettinau, A. Highly efficient CuO/ZnO/ZrO<sub>2</sub>@SBA-15 nanocatalysts for methanol synthesis from the catalytic hydrogenation of CO<sub>2</sub>. *Appl. Catal. B: Environ.* **2019**, *258*, 117941. DOI: 10.1016/j.apcatb.2019.117941.
- [172] Arena, F.; Mezzatesta, G.; Zafarana, G.; Trunfio, G.; Frusteri, F.; Spadaro, L. Effects of oxide carriers on surface functionality and process performance of the Cu-ZnO system in the synthesis of methanol via CO<sub>2</sub> hydrogenation. *J. Catal.* **2013**, *300*, 141-151. DOI: 10.1016/j.jcat.2012.12.019.
- [173] Słoczynski, J.; Grabowski, R.; Kozłowska, A.; Olszewski, P.; Stoch, J.; Skrzypek, J.; Lachowska, M. Catalytic activity of the M/(3ZnO-ZrO<sub>2</sub>) system (M=Cu, Ag, Au) in the hydrogenation of CO<sub>2</sub> to methanol. *Appl. Catal. A: Gen.* **2004**, *278*, 11-23. DOI: 10.1016/j.apcata.2004.09.014.
- [174] Natesakhawat, S.; Lekse, J. W.; Baltrus, J. P.; Ohodnicki Jr., P. R.; Howard, B. H.; Deng, X.; Matranga, C. Active Sites and Structure-Activity Relationships of Copper-Based Catalysts for Carbon Dioxide Hydrogenation to Methanol. *ACS Catal.* **2012**, *2*, 1667-1676. DOI: 10.1021/cs300008g.
- [175] Toyir, J.; Ramírez de la Piscina, P.; Fierro, J. L. G.; Homs, N. Highly effective conversion of CO<sub>2</sub> to methanol over supported and promoted copper-based catalysts: influence of support and promoter. *Appl. Catal. B: Environ.* **2001**, *29*, 207-215. DOI: 10.1016/S0926-3373(00)00205-8.
- [176] Xiong, S.; Lian, Y.; Xie, H.; Liu, B. Hydrogenation of CO<sub>2</sub> to methanol over Cu/ZnCr catalyst. *Fuel* **2019**, *256*, 115975. DOI: 10.1016/j.fuel.2019.115975.
- [177] Yao, L.; Shen, X.; Pan, Y.; Peng, Z. Synergy between active sites of Cu-In-Zr-O catalyst in CO<sub>2</sub> hydrogenation to methanol. *J. Catal.* **2019**, *372*, 74-85. DOI: 10.1016/j.jcat.2019.02.021.
- [178] Jiang, Y.; Yang, H.; Gao, P.; Li, X.; Zhang, J.; Liu, H.; Wang, H.; Wei, W.; Sun, Y. Slurry methanol synthesis from CO<sub>2</sub> hydrogenation over micro-spherical SiO<sub>2</sub> support Cu/ZnO catalysts. *J. CO<sub>2</sub> Util.* **2018**, *26*, 642-651. DOI: 10.1016/j.jcou.2018.06.023.
- [179] Guo, Y.; Guo, X.; Song, C.; Han, X.; Liu, H.; Zhao, Z. Capsule-Structured Copper-Zinc Catalyst for Highly Efficient Hydrogenation of Carbon Dioxide to Methanol. *ChemSusChem* **2019**, *12*, 4916-4926. DOI: 10.1002/cssc.201902485.
- [180] Chen, K.; Fang, H.; Wu, S.; Liu, X.; Zheng, J.; Zhou, S.; Duan, X.; Zhuang, Y.; Tsang, S. C. E.; Yuan, Y. CO<sub>2</sub> hydrogenation to methanol over Cu catalysts supported on La-modified SBA-15: The crucial role of Cu-LaO<sub>x</sub> interfaces. *Appl. Catal. B: Environ.* **2019**, *251*, 119-129. DOI: 10.1016/j.apcatb.2019.03.059.
- [181] Wang, G.; Mao, D.; Guo, X.; Yu, J. Enhanced performance of the CuO-ZnO-ZrO<sub>2</sub> catalyst for CO<sub>2</sub> hydrogenation to methanol by WO<sub>3</sub> modification. *Appl. Surf. Sci.* **2018**, *456*, 403-409. DOI: 10.1016/j.apsusc.2018.06.090.

- [182] Hou, X. X.; Xu, C. H.; Liu, Y. L.; Li, J. J.; Hu, X. D.; Liu, J.; Liu, J. Y.; Xu, Q. Improved methanol synthesis from CO<sub>2</sub> hydrogenation over CuZnAlZr catalysts with precursor pre-activation by formaldehyde. *J. Catal.* **2019**, *379*, 147-153. DOI: 10.1016/j.jcat.2019.09.025.
- [183] Shi, Z.; Tan, Q.; Wu, D. A novel Core-Shell structured CuIn@SiO<sub>2</sub> catalyst for CO<sub>2</sub> hydrogenation to methanol. *AIChE J.* **2019**, *65*, 1047-1058. DOI: 10.1002/aic.16490.
- [184] An, X.; Li, J.; Zuo, Y.; Zhang, Q.; Wang, D.; Wang, J. A Cu/Zn/Al/Zr fibrous catalyst that is an improved CO<sub>2</sub> hydrogenation to methanol catalyst. *Catal. Lett.* **2007**, *118*, 264-269. DOI: 10.1007/s10562-007-9182-x.
- [185] Xiao, S.; Zhang, Y.; Gao, P.; Zhong, L.; Li, X.; Zhang, Z.; Wang, H.; Wei, W.; Sun, Y. Highly efficient Cu-based catalysts via hydrotalcite-like precursors for CO<sub>2</sub> hydrogenation to methanol. *Catal. Today* **2017**, *281*, 327-336. DOI: 10.1016/j.cattod.2016.02.004.
- [186] Gao, P.; Li, F.; Zhao, N.; Xiao, F. K.; Wei, W.; Zhong, L. S.; Sun, Y. H. Influence of modifier (Mn, La, Ce, Zr and Y) on the performance of Cu/Zn/Al catalysts via hydrotalcite-like precursors for CO<sub>2</sub> hydrogenation to methanol. *Appl. Catal. A: Gen.* **2013**, *468*, 442-452. DOI: 10.1016/j.apcata.2013.09.026.
- [187] Zhan, H. J.; Li, F.; Gao, P.; Zhao, N.; Xiao, F. K.; Wei, W.; Zhong, L. S.; Sun, Y. H. Methanol synthesis from CO<sub>2</sub> hydrogenation over La-M-Cu-Zn-O (M = Y, Ce, Mg, Zr) catalysts derived from perovskite type precursors. *J. Power Sources* **2014**, *251*, 113-121. DOI: 10.1016/j.jpowsour.2013.11.037.
- [188] Ladera, R.; Pérez-Alonso, F. J.; González-Carballo, J. M.; Ojeda, M.; Rojas, S.; Fierro, J. L. G. Catalytic valorization of CO<sub>2</sub> via methanol synthesis with Ga-promoted Cu-ZnO-ZrO<sub>2</sub> catalysts. *Appl. Catal. B: Environ.* **2013**, *142-143*, 241-248. DOI: 10.1016/j.apcatb.2013.05.019.
- [189] Bansode, A.; Tidona, B.; von Rohr, P. R.; Urakawa, A. Impact of K and Ba promoters on CO<sub>2</sub> hydrogenation over Cu/Al<sub>2</sub>O<sub>3</sub> catalysts at high pressure. *Catal. Sci. Technol.* **2013**, *3*, 767-778. DOI: 10.1039/C2CY20604H.
- [190] An, B.; Zhang, J. Z.; Cheng, K.; Ji, P. F.; Wang, C.; Lin, W. B. Confinement of Ultrasmall Cu/ZnO<sub>x</sub> Nanoparticles in Metal-Organic Frameworks for Selective Methanol Synthesis from Catalytic Hydrogenation of CO<sub>2</sub>. *J. Am. Chem. Soc.* **2017**, *139*, 3834-3840. DOI: 10.1021/jacs.7b00058.
- [191] Deerattrakul, V.; Dittanet, P.; Sawangphruk, M.; Kongkachuichay, P. CO<sub>2</sub> hydrogenation to methanol using Cu-Zn catalyst supported on reduced graphene oxide nanosheets. *J. CO<sub>2</sub> Util.* **2016**, *16*, 104-113. DOI: 10.1016/j.jcou.2016.07.002.
- [192] Wang, G.; Chen, L.; Sun, Y.; Wu, J.; Fu, M.; Ye, D. Carbon dioxide hydrogenation to methanol over Cu/ZrO<sub>2</sub>/CNTs: effect of carbon surface chemistry. *RSC Adv.* **2015**, *5*, 45320-45330. DOI: 10.1039/C5RA04774A.

- [193] Bahruji, H.; Bowker, M.; Jones, W.; Hayward, J.; Ruiz Esquiús, J.; Morgan, D. J.; Hutchings, G. J. PdZn catalysts for CO<sub>2</sub> hydrogenation to methanol using chemical vapour impregnation (CVI). *Faraday Discuss.* **2017**, *197*, 309-324. DOI: 10.1039/C6FD00189K.
- [194] Song, J.; Liu, S.; Yang, C.; Wang, G.; Tian, H.; Zhao, Z.; Mu, R.; Gong, J. The role of Al doping in Pd/ZnO catalyst for CO<sub>2</sub> hydrogenation to methanol. *Appl. Catal. B: Environ.* **2020**, *263*, 118367. DOI: 10.1016/j.apcatb.2019.118367.
- [195] Yin, Y. Z.; Hu, B.; Li, X. L.; Zhou, X. H.; Hong, X. L.; Liu, G. L. Pd@zeolitic imidazolate framework-8 derived PdZn alloy catalysts for efficient hydrogenation of CO<sub>2</sub> to methanol. *Appl. Catal. B: Environ.* **2018**, *234*, 143-152. DOI: 10.1016/j.apcatb.2018.04.024.
- [196] Frei, M. S.; Mondelli, C.; García-Muelas, R.; Kley, K. S.; Puértolas, B.; López, N.; Safonova, O. V.; Stewart, J. A.; Curulla Ferré, D.; Pérez-Ramírez, J. Atomic-scale engineering of indium oxide promotion by palladium for methanol production via CO<sub>2</sub> hydrogenation. *Nat. Commun.* **2019**, *10*, 3377. DOI: 10.1038/s41467-019-11349-9.
- [197] Jiang, H.; Lin, J.; Wu, X.; Wang, W.; Chen, Y.; Zhang, M. Efficient hydrogenation of CO<sub>2</sub> to methanol over Pd/In<sub>2</sub>O<sub>3</sub>/SBA-15 catalysts. *J. CO<sub>2</sub> Util.* **2020**, *36*, 33-39. DOI: 10.1016/j.jcou.2019.10.013.
- [198] Jiang, X.; Koizumi, N.; Guo, X. W.; Song, C. S. Bimetallic Pd-Cu catalysts for selective CO<sub>2</sub> hydrogenation to methanol. *Appl. Catal. B: Environ.* **2015**, *170*, 173-185. DOI: 10.1016/j.apcatb.2015.01.010.
- [199] Lin, F.; Jiang, X.; Boreriboon, N.; Wang, Z.; Song, C.; Cen, K. Effects of supports on bimetallic Pd-Cu catalysts for CO<sub>2</sub> hydrogenation to methanol. *Appl. Catal. A: Gen.* **2019**, *585*, 117210. DOI: 10.1016/j.apcata.2019.117210.
- [200] Hartadi, Y.; Widmann, D.; Behm, R. J. CO<sub>2</sub> Hydrogenation to Methanol on Supported Au Catalysts under Moderate Reaction Conditions: Support and Particle Size Effects. *ChemSusChem* **2015**, *8*, 456-465. DOI: 10.1002/cssc.201402645.
- [201] Jia, L.; Gao, J.; Fang, W.; Li, Q. Carbon dioxide hydrogenation to methanol over the pre-reduced LaCr<sub>0.5</sub>Cu<sub>0.5</sub>O<sub>3</sub> catalyst. *Catal. Commun.* **2009**, *10*, 2000-2003. DOI: 10.1016/j.catcom.2009.07.017.
- [202] Bavykina, A.; Yarulina, I.; Al Abdulghani, A. J.; Gevers, L.; Hedhili, M. N.; Miao, X.; Galilea, A. R.; Pustovarenko, A.; Dikhtiarenko, A.; Cadiau, A.; Aguilar-Tapia, A.; Hazemann, J. L.; Kozlov, S. M.; Oud-Chikh, S.; Cavallo, L.; Gascon, J. Turning a Methanation Co Catalyst into an In-Co Methanol Producer. *ACS Catal.* **2019**, *9*, 6910-6918. DOI: 10.1021/acscatal.9b01638.
- [203] Jia, X.; Sun, K.; Wang, J.; Shen, C.; Liu, C. Selective hydrogenation of CO<sub>2</sub> to methanol over Ni/In<sub>2</sub>O<sub>3</sub> catalyst. *J. Energy Chem.* **2020**, *50*, 409-415. DOI: 10.1016/j.jechem.2020.03.083.

- [204] Stangeland, K.; Kalai, D. Y.; Ding, Y.; Yu, Z. Mesoporous manganese-cobalt oxide spinel catalysts for CO<sub>2</sub> hydrogenation to methanol. *J. CO<sub>2</sub> Util.* **2019**, *32*, 146-154. DOI: 10.1016/j.jcou.2019.04.018.
- [205] Martin, O.; Martín, A. J.; Mondelli, C.; Mitchell, S.; Segawa, T. F.; Hauert, R.; Drouilly, C.; Curulla-Ferré, D.; Pérez-Ramírez, J. Indium Oxide as a Superior Catalyst for Methanol Synthesis by CO<sub>2</sub> Hydrogenation. *Angew. Chem. Int. Ed.* **2016**, *55*, 6261-6265. DOI: 10.1002/anie.201600943.
- [206] Wang, J.; Tang, C.; Li, G.; Han, Z.; Li, Z.; Liu, H.; Cheng, F.; Li, C. High-performance M<sub>a</sub>ZrO<sub>x</sub> (M<sub>a</sub>= Cd, Ga) solid-solution catalysts for CO<sub>2</sub> hydrogenation to methanol. *ACS Catal.* **2019**, *9*, 10253-10259. DOI: 10.1021/acscatal.9b03449.
- [207] Frei, M. S.; Mondelli, C.; Cesarini, A.; Krumeich, F.; Hauert, R.; Stewart, J. A.; Curulla Ferré, D.; Pérez-Ramírez, J. Role of Zirconia in Indium Oxide-Catalyzed CO<sub>2</sub> Hydrogenation to Methanol. *ACS Catal.* **2020**, *10*, 1133-1145. DOI: 10.1021/acscatal.9b03305.
- [208] Chen T. Y.; Cao, C.; Chen, T. B.; Ding, X.; Huang, H.; Shen, L.; Cao, X.; Zhu, M.; Xu, J.; Gao, J.; Han, Y. F. Unraveling highly tunable selectivity in CO<sub>2</sub> hydrogenation over bimetallic In-Zr oxide catalysts. *ACS Catal.* **2019**, *9*, 8785-8797. DOI: 10.1021/acscatal.9b01869.
- [209] Zhao, Z. W.; Zhou, X.; Liu, Y. N.; Shen, C. C.; Yuan, C. Z.; Jiang, Y. F.; Zhao, S. J.; Ma, L. B.; Cheang, T. Y.; Xu, A. W. Ultrasmall Ni nanoparticles embedded in Zr-based MOFs provide high selectivity for CO<sub>2</sub> hydrogenation to methane at low temperatures. *Catal. Sci. Technol.* **2018**, *8*, 3160-3165. DOI: 10.1039/C8CY00468D.
- [210] Jia, X.; Zhang, X.; Rui, N.; Hu, X.; Liu, C. J. Structural effect of Ni/ZrO<sub>2</sub> catalyst on CO<sub>2</sub> methanation with enhanced activity. *Appl. Catal. B: Environ.* **2019**, *244*, 159-169. DOI: 10.1016/j.apcatb.2018.11.024.
- [211] Martínez, J.; Hernández, E.; Alfaro, S.; López Medina, R.; Valverde Aguilar, G.; Albiter, E.; Valenzuela, M. A. High Selectivity and Stability of Nickel Catalysts for CO<sub>2</sub> Methanation: Support Effects. *Catalysts* **2019**, *9*, 24. DOI: 10.3390/catal9010024.
- [212] Nie, W.; Zou, X.; Chen, C.; Wang, X.; Ding, W.; Lu, X. Methanation of Carbon Dioxide over Ni-Ce-Zr Oxides Prepared by One-Pot Hydrolysis of Metal Nitrates with Ammonium Carbonate. *Catalysts* **2019**, *7*, 104. DOI: 10.3390/catal7040104.
- [213] Romero-Sáez, M.; Dongil, A. B.; Benito, N.; Espinoza-González, R.; Escalona, N.; Gracia, F. CO<sub>2</sub> methanation over nickel-ZrO<sub>2</sub> catalyst supported on carbon nanotubes: A comparison between two impregnation strategies. *Appl. Catal. B: Environ.* **2018**, *237*, 817-825. DOI: 10.1016/j.apcatb.2018.06.045.
- [214] Frey, M.; Édouard, D.; Roger, A. C. Optimization of structured cellular foam-based catalysts for low-temperature carbon dioxide methanation in a platelet milli-reactor. *C. R. Chim.* **2015**, *18*, 283-292. DOI: 10.1016/j.crci.2015.01.002.

- [215] Le Saché, E.; Pastor-Pérez, L.; Haycock, B. J.; Villora-Picó, J. J.; Sepúlveda-Escribano, A.; Reina, T. R. Switchable Catalysts for Chemical CO<sub>2</sub> Recycling: A Step Forward in the Methanation and Reverse Water-Gas Shift Reactions. *ACS Sustainable Chem. Eng.* **2020**, *8*, 4614-4622. DOI: 10.1021/acssuschemeng.0c00551.
- [216] Dias, Y. R.; Perez-Lopez, O. W. Carbon dioxide methanation over Ni-Cu/SiO<sub>2</sub> catalysts. *Energy Convers. Manag.* **2020**, *203*, 112214. DOI: 10.1016/j.enconman.2019.112214.
- [217] Guo, X.; Traitangwong, A.; Hu, M.; Zuo, C.; Meeyoo, V.; Peng, Z.; Li, C. Carbon Dioxide Methanation over Nickel-Based Catalysts Supported on Various Mesoporous Material. *Energy Fuels* **2018**, *32*, 3681-3689. DOI: 10.1021/acs.energyfuels.7b03826.
- [218] Alrafei, B.; Polaert, I.; Ledoux, A.; Azzolina-Jury, F. Remarkably stable and efficient Ni and Ni-Co catalysts for CO<sub>2</sub> methanation. *Catal. Today* **2020**, *346*, 23-33. DOI: 10.1016/j.cattod.2019.03.026.
- [219] Xu, L.; Lian, X.; Chen, M.; Cui, Y.; Wang, F.; Li, W.; Huang, B. CO<sub>2</sub> methanation over Co-Ni bimetal-doped ordered mesoporous Al<sub>2</sub>O<sub>3</sub> catalysts with enhanced low-temperature activities. *Int. J. Hydrog. Energy* **2018**, *43*, 17172-17184. DOI: 10.1016/j.ijhydene.2018.07.106.
- [220] Li, W.; Nie, X.; Jiang, X.; Zhang, A.; Ding, F.; Liu, M.; Liu, Z.; Guo, X.; Song, C. ZrO<sub>2</sub> support imparts superior activity and stability of Co catalysts for CO<sub>2</sub> methanation. *Appl. Catal. B: Environ.* **2018**, *220*, 397-408. DOI: 10.1016/j.apcatb.2017.08.048.
- [221] Liu, Q.; Bian, B.; Fan, J.; Yang, J. Cobalt doped Ni based ordered mesoporous catalysts for CO<sub>2</sub> methanation with enhanced catalytic performance. *Int. J. Hydrog. Energy* **2018**, *43*, 4893-4901. DOI: 10.1016/j.ijhydene.2018.01.132.
- [222] Du, G.; Lim, S.; Yang, Y.; Wang, C.; Pfefferle, L.; Haller, G. L. Methanation of carbon dioxide on Ni-incorporated MCM-41 catalysts: The influence of catalyst pretreatment and study of steady-state reaction. *J. Catal.* **2007**, *249*, 370-379. DOI: 10.1016/j.jcat.2007.03.029.
- [223] Mutz, B.; Carvalho, H. W. P.; Mangold, S.; Kleist, W.; Grunwaldt, J. D. Methanation of CO<sub>2</sub>: Structural response of a Ni-based catalyst under fluctuating reaction conditions unraveled by operando spectroscopy. *J. Catal.* **2015**, *327*, 48-53. DOI: 10.1016/j.jcat.2015.04.006.
- [224] Hwang, S.; Lee, J.; Hong, U. G.; Baik, J. H.; Koh, D. J.; Lim, H.; Song, I. K. Methanation of carbon dioxide over mesoporous Ni-Fe-Ru-Al<sub>2</sub>O<sub>3</sub> xerogel catalysts: Effect of ruthenium content. *J. Ind. Eng. Chem.* **2013**, *19*, 698-703. DOI: 10.1016/j.jiec.2012.10.007.
- [225] Park, J. N.; McFarland, E. W. A highly dispersed Pd-Mg/SiO<sub>2</sub> catalyst active for methanation of CO<sub>2</sub>. *J. Catal.* **2009**, *266*, 92-97. DOI: 10.1016/j.jcat.2009.05.018.
- [226] Ren, J.; Qin, X.; Yang, J. Z.; Qin, Z. F.; Guo, H. L.; Lin, J. Y.; Li, Z. Methanation of carbon dioxide over Ni-M/ZrO<sub>2</sub> (M = Fe, Co, Cu) catalysts: Effect of addition of a second metal. *Fuel Process. Technol.* **2015**, *137*, 204-211. DOI: 10.1016/j.fuproc.2015.04.022.

- [227] Pandey, D.; Deo, G. Effect of support on the catalytic activity of supported Ni-Fe catalysts for the CO<sub>2</sub> methanation reaction. *J. Ind. Eng. Chem.* **2016**, *33*, 99-107. DOI: 10.1016/j.jiec.2015.09.019.
- [228] He, L.; Lin, Q.; Liu, Y.; Huang, Y. Unique catalysis of Ni-Al hydrotalcite derived catalyst in CO<sub>2</sub> methanation: cooperative effect between Ni nanoparticles and a basic support. *J. Energy Chem.* **2014**, *23*, 587-592. DOI: 10.1016/S2095-4956(14)60144-3.
- [229] Büchel, R.; Baiker, A.; Pratsinis, S. E. Effect of Ba and K addition and controlled spatial deposition of Rh in Rh/Al<sub>2</sub>O<sub>3</sub> catalysts for CO<sub>2</sub> hydrogenation. *Appl. Catal. A: Gen.* **2014**, *477*, 93-101. DOI: 10.1016/j.apcata.2014.03.010.
- [230] Konsolakis, M.; Lykaki, M.; Stefa, S.; Carabineiro, S. A. C.; Varvoutis, G.; Papista, E.; Marnellos, G. E. CO<sub>2</sub> Hydrogenation over Nanoceria-Supported Transition Metal Catalysts: Role of Ceria Morphology (Nanorods versus Nanocubes) and Active Phase Nature (Co versus Cu). *Nanomaterials*, **2019**, *9*, 1739. DOI: 10.3390/nano9121739.
- [231] Wang, X.; Zhu, L.; Zhuo, Y.; Zhu, Y.; Wang, S. Enhancement of CO<sub>2</sub> Methanation over La-Modified Ni/SBA-15 Catalysts Prepared by Different Doping Methods. *ACS Sustain. Chem. Eng.* **2019**, *7*, 14647-14660. DOI: 10.1021/acssuschemeng.9b02563.
- [232] Bian, L.; Zhang, L.; Xia, R.; Li, Z. Enhanced low-temperature CO<sub>2</sub> methanation activity on plasma-prepared Ni-based catalyst. *J. Nat. Gas Sci. Eng.* **2015**, *27*, 1189-1194. DOI: 10.1016/j.jngse.2015.09.066.
- [233] Rahmani, S.; Rezaei, M.; Meshkani, F. Preparation of highly active nickel catalysts supported on mesoporous nanocrystalline  $\gamma$ -Al<sub>2</sub>O<sub>3</sub> for CO<sub>2</sub> methanation. *J. Ind. Eng. Chem.* **2014**, *20*, 1346-1352. DOI: 10.1016/j.jiec.2013.07.017.
- [234] Tada, S.; Shimizu, T.; Kameyama, H.; Haneda, T.; Kikuchi, R. Ni/CeO<sub>2</sub> catalysts with high CO<sub>2</sub> methanation activity and high CH<sub>4</sub> selectivity at low temperatures. *Int. J. Hydrog. Energy* **2012**, *37*, 5527-5531. DOI: 10.1016/j.ijhydene.2011.12.122.
- [235] Petala, A.; Panagiotopoulou, P. Methanation of CO<sub>2</sub> over alkali-promoted Ru/TiO<sub>2</sub> catalysts: I. Effect of alkali additives on catalytic activity and selectivity. *Appl. Catal. B: Environ.* **2018**, *224*, 919-927. DOI: 10.1016/j.apcatb.2017.11.048.
- [236] Abe, T.; Tanizawa, M.; Watanabe, K.; Taguchi, A. CO<sub>2</sub> methanation property of Ru nanoparticle-loaded TiO<sub>2</sub> prepared by a polygonal barrel-sputtering method. *Energy Environ. Sci.* **2009**, *2*, 315-321. DOI: 10.1039/B817740F.
- [237] Yan, Y.; Dai, Y.; He, H.; Yu, Y.; Yang, Y. A novel W-doped Ni-Mg mixed oxide catalyst for CO<sub>2</sub> methanation. *Appl. Catal. B: Environ.* **2016**, *196*, 108-116. DOI: 10.1016/j.apcatb.2016.05.016.
- [238] Wierzbicki, D.; Motak, M.; Grzybek, T.; Gálvez, M. E.; Da Costa, P. The influence of lanthanum incorporation method on the performance of nickel-containing hydrotalcite-derived catalysts

- in CO<sub>2</sub> methanation reaction. *Catal. Today* **2018**, *307*, 205-211. DOI: 10.1016/j.cattod.2017.04.020.
- [239] Aziz, M. A. A.; Jalil, A. A.; Triwahyono, S.; Saad, M. W. A. CO<sub>2</sub> methanation over Ni-promoted mesostructured silica nanoparticles: Influence of Ni loading and water vapor on activity and response surface methodology studies. *Chem. Eng. J.* **2015**, *260*, 757-764. DOI: 10.1016/j.cej.2014.09.031.
- [240] Zhou, G.; Wu, T.; Xie, H.; Zheng, X. Effects of structure on the carbon dioxide methanation performance of Co-based catalysts. *Int. J. Hydrog. Energy* **2013**, *38*, 10012-10018. DOI: 10.1016/j.ijhydene.2013.05.130.
- [241] Graça, I.; González, L. V.; Bacariza, M. C.; Fernandes, A.; Henriques, C.; Lopes, J. M.; Ribeiro, M. F. CO<sub>2</sub> hydrogenation into CH<sub>4</sub> on NiHNaUSY zeolites. *Appl. Catal. B: Environ.* **2014**, *147*, 101-110. DOI: 10.1016/j.apcatb.2013.08.010.
- [242] Quindimil, A.; De La Torre, U.; Pereda-Ayo, B.; González-Marcos, J. A.; González-Velasco, J. R. Ni catalysts with La as promoter supported over Y- and BETA- zeolites for CO<sub>2</sub> methanation. *Appl. Catal. B: Environ.* **2018**, *238*, 393-403. DOI: 10.1016/j.apcatb.2018.07.034.
- [243] Wang, W.; Chu, W.; Wang, N.; Yang, W.; Jiang, C. Mesoporous nickel catalyst supported on multi-walled carbon nanotubes for carbon dioxide methanation. *Int. J. Hydrog. Energy* **2016**, *41*, 967-975. DOI: 10.1016/j.ijhydene.2015.11.133.
- [244] Zhen, W.; Li, B.; Lu, G.; Ma, J. Enhancing catalytic activity and stability for CO<sub>2</sub> methanation on Ni@MOF-5 via control of active species dispersion. *Chem. Commun.* **2015**, *51*, 1728-1731. DOI: 10.1039/C4CC08733J.
- [245] Li, W.; Zhang, A.; Jiang, X.; Chen, C.; Liu, Z.; Song, C.; Guo, X. Low Temperature CO<sub>2</sub> Methanation: ZIF-67-Derived Co-Based Porous Carbon Catalysts with Controlled Crystal Morphology and Size. *ACS Sustainable Chem. Eng.* **2017**, *5*, 7824-7831. DOI: 10.1021/acssuschemeng.7b01306.







# CHAPTER 2

## PhD Thesis Objectives





The overall goal of the present Doctoral Thesis focuses on the design, synthesis and characterization of innovative heterogeneous metal-based catalysts, as well as the in-depth study of their reactivity in chemical processes of industrial interest. As pointed out in Chapter 1, the catalytic systems that are able to transform CO<sub>2</sub> into methanol and methane present several recurring problems reported in the literature, which are: stability, atomic efficiency and energy efficiency. Therefore, the aim of this thesis will be to address these weaknesses in order to improve the catalytic performance, as illustrated in Table 2.1:

**Table 2.1** Global strategy to be followed to accomplish the thesis objectives.

Issues	Actions
Catalyst stability	- Use of promoters (Chapter 3) - Study of model systems (Chapter 6)
Atom efficiency	- Bifunctionality M <sup>n+</sup> /M <sup>0</sup> (Chapter 4)
Energy efficiency	- New formulations for low-temperature reactions (Chapter 5)

Along this thesis, the selective CO<sub>2</sub> hydrogenation reactions to methanol and methane will be studied from a multidisciplinary perspective, combining catalytic and advanced spectroscopic studies, to find out structure-activity correlations.

In particular, the objectives of this thesis are the following:

- In Chapter 3, we will try to **increase the catalytic efficiency of commercial-like catalysts operating in the methanol synthesis via addition of gallium promoters**. Our motivation is trying to extrapolate the results obtained with Ga<sup>3+</sup>-doped ZnO materials in photo/electrocatalysis to “our” thermocatalysis field, resulting in a Ga-doped

Cu/ZnO system with enhanced catalytic properties (compared to conventional Ga<sub>2</sub>O<sub>3</sub>-promoted Cu/ZnO catalysts). A deeper understanding of this phenomenon, unravelling the interactions among active catalyst components, will be done. Hence, catalytic performance carried out in a fixed-bed reactor will be correlated with catalysts microstructure using a multimodal spectroscopic approach, involving: synchrotron radiation techniques such as (NAP)-XPS and XAS, laboratory operando spectroscopies (IR and XPS) and other characterization techniques (H<sub>2</sub>D<sub>2</sub> isotopic exchange, electrochemical impedance spectroscopy, or TPD-CO<sub>2</sub>). These systems will be also evaluated from an industrial point of view in terms of efficiency, scalability, and long-term stability.

- In Chapter 4, we will try to overcome the **low-activity of small copper particles (2 nm) that prevents obtaining high atom efficiency and competitive catalytic results in the CO<sub>2</sub> hydrogenation to methanol.**

The approach carried out in this chapter is based in our group's previous knowledge of hydrotalcite-derived materials, together with the widely discussed promoter effect of Cu<sup>+</sup> in the literature. In this direction, bifunctional catalysts containing ex-solved CuNPs of 2 nm and Cu<sup>+</sup> species (stabilized in the metal lattice of the support) are easily prepared starting from Mg/Al/Cu layered double hydroxides. Then, a detailed spectroscopic study (temperature-resolved and operando IR experiments at variable pressures) combined with theoretical calculations and catalytic tests will be conducted on a Cu-MgO-Al<sub>2</sub>O<sub>3</sub> mixed oxide derived from a hydrotalcite precursor. Existing ambiguities in the literature related to the role of specific active sites and other catalytic features, such as the type of

intermediates that are formed along the process, will be cleared up. Special attention will be paid to the thermal and temporal catalytic stabilities of the systems under study (in comparison with the commercial-like Cu/ZnO/Al<sub>2</sub>O<sub>3</sub> catalyst), features of significant interest for a potential industrial implementation.

- After two chapters devoted to methanol formation, we will proceed to CO<sub>2</sub> methanation in Chapter 5. The introductory chapter have shown that an **improvement in the energy efficiency** is necessary in order to make this process economically feasible. In this sense, being able to work at much lower temperatures in the methanation reaction would be a proper solution. To do this, a novel catalytic approach that let modulating the electronics of the active center (via metallic carbide formation) is proposed. Although several studies in the literature have demonstrated appealing catalytic properties of metal carbides, very few are related to RuC, being ruthenium an active component in the CO<sub>2</sub> methanation reaction at temperatures above ~230 °C. Then, we will present an innovative Ru-RuC core-shell structure synthesized via a mild hydrothermal treatment with unprecedented activity in a non-usual reactivity window for the Sabatier reaction (i.e., below 200 °C and at atmospheric pressure). We will cover synthesis, structure determination (by advanced techniques such as synchrotron XPS and NEXAFS), low-temperature catalysis in a fixed-bed reactor, and active center elucidation.

Together with the studies conducted over “real” (or bulk) heterogeneous catalysts in Chapters 3-5 for CO<sub>2</sub> hydrogenation reactions, this thesis contains an additional experimental chapter that will cover the investigation on “model” catalysts carried

out during my international short-term stay at the Center for Functional Nanomaterials (Brookhaven National Laboratory, New York):

- **Acquiring fundamental knowledge on model catalysts aimed at extrapolating it later to real heterogeneous systems** is essential in our research field. As already mentioned, the low stability of metal-based catalysts under operating conditions is a common problem in catalysis. Thus, we will afford this issue from a fundamental point of view by investigating the concept of metal confinement inside host structures. Therefore, Chapter 6 will deal with the study of a model ruthenium-based catalyst composed of a 2D-bilayered aluminosilicate grown over a Ru(0001) surface. The combination of these materials in the same composite allows the creation of a unique confined nanosized space that can be exploited as a nano-reactor, using the water formation as a model reaction. In this chapter, a different application of (NAP)-XPS will be found out: Indeed, confined water formation reaction will be monitored by means of this surface science technique. Experimental results obtained at NSLS-II synchrotron will be combined with theoretical studies (DFT), which will allow us to unveil the mechanism operating in this chemical process.

Finally, this doctoral thesis, presented via a compendium of publications, is conceived as an innovative and challenging approach of synthesizing and investigating new non-conventional catalysts operating in the CO<sub>2</sub> hydrogenation. Innovation in Science means to explore new concepts, which is always a tough and complex task. Indeed, hard work is the only way to tackle (and solving) current problems, such as climate change, in an imaginative manner. To conclude, we can state that the three keywords that form the backbone of this



thesis are: development of innovative materials, energy efficiency, and climate change remediation (Figure 2.1).

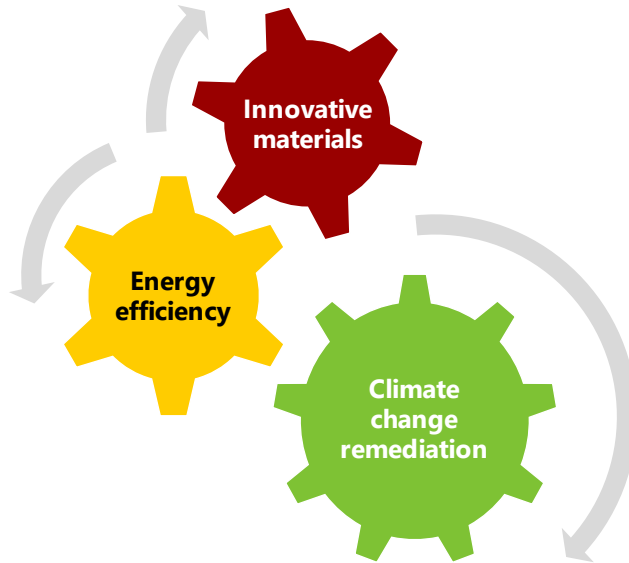
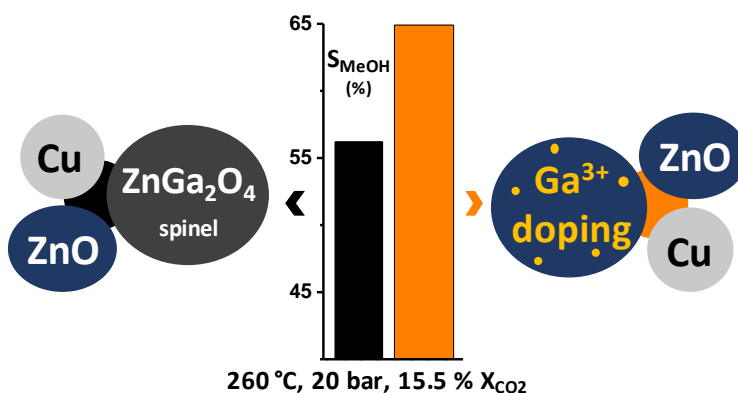


**Figure 2.1** Pillars on which the doctoral thesis is supported.



# CHAPTER 3

## CO<sub>2</sub> hydrogenation to methanol over gallium promoted Cu/ZnO commercial-like catalysts



The content of this chapter was adapted from the following published work:

**“Cu-Ga<sup>3+</sup>-doped wurtzite ZnO interface as driving force for enhanced methanol production in co-precipitated Cu/ZnO/Ga<sub>2</sub>O<sub>3</sub> catalysts”**

Cored, J.; Lopes, C. W.; Liu, L.; Soriano, J.; Agostini, G.; Solsona, B.; Sánchez-Tovar, R.; Concepción, P.

*J. Catal.* **2022**, *407*, 149-161 (Open Access 2022, Elsevier)

*Distributed under the “Creative Commons Attribution License BY-NC-ND 4.0”, which permits unrestricted use, distribution and reproduction as original author.*



### 3.1. Introduction

As it has been mentioned in Chapter 1, industrial methanol synthesis catalysts are bulk systems composed of strongly interacted Cu and ZnO nanoparticles as functional components, and 5-10 mol % Al<sub>2</sub>O<sub>3</sub> as a structural promoter to improve the dispersion of copper and the catalysts thermal stability. In the last years, environmental concerns due to the increased emission of CO<sub>2</sub> and its adverse effects in our planet has attracted much attention toward its capture and use for the production of chemicals and fuels, coupled with the integration of renewable energy. In this sense, the synthesis of methanol using CO<sub>2</sub> as feedstock and H<sub>2</sub> generated from renewable energy represents a sustainable and promising way for CO<sub>2</sub> recycling and hydrogen storage.<sup>[1]</sup> The performance of the current commercial Cu/ZnO/Al<sub>2</sub>O<sub>3</sub> methanol catalysts is not satisfactory for the CO<sub>2</sub> hydrogenation reaction, giving low methanol yields due to thermodynamic limitations and the competitive RWGS reaction, as well as serious catalyst deactivation issues because of the sintering of copper and ZnO components in the presence of water as by-product.<sup>[2]</sup> Thus, the development of highly active, selective and stable catalysts remains a challenge. Extensive studies including new catalyst developments, fundamental understanding of the nature of the active sites, optimization of the reaction conditions and reactor designs have been demonstrated in numerous reviews and publications.<sup>[3-6]</sup> In this direction, different models of active sites are proposed in the literature, where the presence of metal-support interfacial sites are believed to play a key role in the methanol synthesis reaction.<sup>[7]</sup> In addition, many studies are focused on the structural parameters of the Cu species, such as particle size, exposed crystal facets, defects and lattice strains;<sup>[8]</sup> formation of CuZn alloys;<sup>[9,10]</sup> stabilization of Cu<sup>+</sup> sites and migration of

ZnO<sub>x</sub> on the copper surface; and the formation of surface vacancies for stabilization of intermediate species.<sup>[11-15]</sup> The addition of promoters to improve the catalytic performance of commercial-like systems has been widely reported, and among them, Ga<sup>3+</sup> has emerged as a promising candidate.<sup>[9,10,13,16]</sup> The promoting effect depends on the speciation of Ga<sup>3+</sup> in the final catalyst, which is influenced by the synthetic conditions. Thus, some authors suggested that the promoting effect of gallium depends on the size of Ga<sub>2</sub>O<sub>3</sub> nanoparticles, in the sense that the presence of highly dispersed Ga<sub>2</sub>O<sub>3</sub> particles favors the formation of Cu<sup>+</sup> species.<sup>[13,14]</sup> Other authors reported the formation of a ZnGa<sub>2</sub>O<sub>4</sub> spinel phase, which can create an electronic heterojunction with excess of ZnO, facilitating the reduction of ZnO to Zn<sup>0</sup>.<sup>[8-10]</sup> Then, reduced Zn adatoms migrate and decorate step sites in the CuNP, resulting in CuZn alloy species. Other authors found that the addition of gallium generates new active sites, where the adsorption energies of intermediate species are modified, decreasing the apparent activation energy for methanol formation, but not for the RWGS.<sup>[17]</sup> Furthermore, Behrens et al. reported an electronic promoting effect of Ga<sup>3+</sup>, in analogy to that observed in Al promoted Cu/ZnO catalysts at low Al<sup>3+</sup> concentrations (<3.5 wt %).<sup>[18]</sup> In that work, the partial substitution of Zn<sup>2+</sup> with Al<sup>3+</sup> and their effect on the redox and structural properties of the catalyst has been studied and extrapolated to Ga<sup>3+</sup> and Cr<sup>3+</sup>.

On the other hand, the doping of ZnO with other elements such as N<sup>3+</sup>, Al<sup>3+</sup>, In<sup>3+</sup> or Ga<sup>3+</sup> has attracted great interest in the field of optoelectronics as a way of modulating the conductivity of ZnO as n-type semiconductor. In this direction, the role of Ga<sup>3+</sup> doped in the ZnO wurtzite structure has sustained great expectatives for its use in electronic devices.<sup>[19,20]</sup> In line with these works, the goal

of our study is to explore the doping effect of ZnO with Ga<sup>3+</sup> in the methanol synthesis from CO<sub>2</sub> hydrogenation, working on complex commercial-like Cu/ZnO/Ga<sub>2</sub>O<sub>3</sub> systems. To do so, a combination of catalytic studies with in situ/operando characterization techniques will be needed, in order to evaluate the structural, electronic and catalytic promoting effects of Ga<sup>3+</sup> in two selected samples: one of them (CZG-sp) presents a zinc gallate phase, whereas the second (CZG-ox) exhibits a Ga<sup>3+</sup>-doped ZnO lattice. These systems will also face a benchmark catalyst (i.e., Cu/ZnO/Al<sub>2</sub>O<sub>3</sub>, CZA), which has been prepared on purpose for this study.

## 3.2. Materials and methods

### 3.2.1. Preparation of catalytic samples and references

#### *Synthesis of CZG-sp and CZG-ox (CuO/ZnO/Ga<sub>2</sub>O<sub>3</sub>)*

Catalysts were prepared by co-precipitation method. In particular for a CuO/ZnO/Ga<sub>2</sub>O<sub>3</sub> chemical composition of 70:24:6 (Cu:Zn:Ga wt % ratio); Cu(NO<sub>3</sub>)<sub>2</sub>·2.5H<sub>2</sub>O (7.90 g, Sigma Aldrich, >98%), Zn(NO<sub>3</sub>)<sub>2</sub>·6H<sub>2</sub>O (3.69 g, Fluka, >99%), and Ga(NO<sub>3</sub>)<sub>3</sub>·xH<sub>2</sub>O (0.26 g, Alfa Aesar, 99.9%) metallic precursors dissolved in deionized water (41.99 g) were pumped at 0.5 mL·min<sup>-1</sup> (kd Scientific, KDS-200 syringe pump) to a round bottom flask containing 200 mL of deionized water at 65 °C and under stirring. Simultaneously, a 1.4 M basic solution of a precipitating agent (~80 mL) was pipetted to the flask in order to keep the pH constant at 6.5. In detail, NH<sub>4</sub>HCO<sub>3</sub> (Aldrich, 99.5%) and NaOH (Scharlab, >98%) aqueous solutions were used to synthesize CZG-sp and CZG-ox samples, respectively. Then, the suspension was aged under stirring at 65 °C for 2 h. Afterwards, the precipitate was filtered, washed with hot deionized water until pH=7 and dried overnight at 100 °C to yield a colored solid (4.98 g, turquoise for

CZG-sp; 3.39 g, dark brown for CZG-ox). The resulting solid was calcined in a muffle furnace as follows: from 25 °C to 200 °C (2 °C·min<sup>-1</sup>; dwell time: 1 h), from 200 °C to 360 °C (2 °C·min<sup>-1</sup>; dwell time: 1 h), and finally kept at 360 °C for 9.5 h. After calcination, a dark solid was obtained (3.78 g for CZG-sp; 3.22 g for CZG-ox).

#### *Synthesis of CZG-ox (CuO/ZnO/Ga<sub>2</sub>O<sub>3</sub>) at variable gallium loadings*

CZG-ox samples at variable Ga content were additionally prepared following the synthetic procedure described above for CZA-ox (see Table 3.1 for experimental details).

**Table 3.1** Selected experimental details for the CZG-ox samples preparation at variable gallium loadings. The rest of experimental conditions were kept constant in all synthetic procedures.

Ga % wt ratio	M <sup>x+</sup> (NO <sub>3</sub> ) <sub>x</sub> precursor (g)			g H <sub>2</sub> O	g after drying	g after calcination
	Cu	Zn	Ga			
1.0	8.39	4.26	0.11	44.93	3.90	3.72
1.3	8.19	4.05	0.14	43.55	3.88	3.73
4.0	7.59	3.32	0.41	40.09	3.54	3.35
7.5	6.70	2.92	0.70	36.55	3.15	2.96

#### *Synthesis of CZGA-ox*

Catalyst was prepared by co-precipitation. In particular, Cu(NO<sub>3</sub>)<sub>2</sub>·3H<sub>2</sub>O (7.90 g, Sigma Aldrich, >98%), Zn(NO<sub>3</sub>)<sub>2</sub>·6H<sub>2</sub>O (1.93 g, Fluka, >99%), Ga(NO<sub>3</sub>)<sub>3</sub>·xH<sub>2</sub>O (0.29 g, Alfa Aesar, 99.9%), and Al(NO<sub>3</sub>)<sub>3</sub>·9H<sub>2</sub>O (2.30 g, Aldrich, >98%) metallic precursors dissolved in deionized water (41.92 g) were pumped at 0.5 mL·min<sup>-1</sup> (kd Scientific, KDS-200 syringe pump) to a round bottom flask containing 200 mL of deionized water at 70 °C and under stirring. Simultaneously, a 1.4 M basic solution of a precipitating agent (~80 mL) was pipetted to the flask in order to



keep the pH constant at 6.5. In detail, NaOH (Scharlab, >98%) aqueous solution was used to synthesize CZGA-ox sample. Then, the suspension was aged under stirring at 65 °C for 2 h. Afterwards, the precipitate was filtered, washed with hot deionized water until pH=7 and dried overnight at 100 °C to yield a colored solid (3.98 g, dark brown). The resulting solid was calcined in a muffle furnace as follows: from 25 °C to 200 °C (2 °C·min<sup>-1</sup>; dwell time: 1 h), from 200 °C to 360 °C (2 °C·min<sup>-1</sup>; dwell time: 1 h), and finally kept at 360 °C for 9.5 h. After calcination, a dark solid was obtained (3.92 g). Metallic composition (expressed in wt % ratio) obtained by ICP was 70.0:11.5:6.0:12.5 (Cu/Zn/Ga/Al).

#### *Synthesis of CZA (CuO/ZnO/Al<sub>2</sub>O<sub>3</sub>)*

The catalyst was prepared by a co-precipitation method following the procedure reported by Baltes et al.<sup>[21]</sup> In particular, Cu(NO<sub>3</sub>)<sub>2</sub>·3H<sub>2</sub>O (2.88 g, Aldrich, >99%), Zn(NO<sub>3</sub>)<sub>2</sub>·6H<sub>2</sub>O (1.79 g, Fluka, >99%), and Al(NO<sub>3</sub>)<sub>3</sub>·9H<sub>2</sub>O (0.75 g, Aldrich, >98%) metallic precursors dissolved in MiliQ water (60 mL) were pumped at 5 mL·min<sup>-1</sup> (kdScientific, KDS-200 syringe pump) to a round bottom flask containing 200 mL of MiliQ water at 70 °C and under stirring. Simultaneously, a basic solution of Na<sub>2</sub>CO<sub>3</sub> anhydrous (5.31 g, 50 mL, Aldrich, >99.5%) was pipetted to the flask in order to keep the pH constant at 6.0-6.5. Then, the suspension was aged under stirring at 70 °C for 1 h with pH control (i.e., 7, using the metal precursor or the precipitant agent solutions to adjust it). Afterwards, the precipitate was filtered, washed with deionized water (3×150 mL) and dried overnight at 100 °C (2.01 g brown solid). The resulting solid was calcined in a muffle furnace as follows: from 25 °C to 300 °C (2 °C·min<sup>-1</sup>; dwell time: 3 h). After calcination, a dark solid was obtained (1.61 g).

*Synthesis of ZnGa<sub>2</sub>O<sub>4</sub> spinel*

The reference material was prepared under hydrothermal conditions.<sup>[22]</sup> 10 mmol Ga(NO<sub>3</sub>)<sub>3</sub>·xH<sub>2</sub>O (2.56 g, Alfa Aesar, 99.9%), and 5 mmol Zn(NO<sub>3</sub>)<sub>2</sub>·6H<sub>2</sub>O (1.49 g, Fluka, >99%) were dissolved in deionized water (70 mL). The solution was adjusted to pH=9 with an ammonia solution (25 wt %, Sigma Aldrich). The resulting white suspension was aged under stirring for 2 h at room temperature, transferred into a 200 mL Teflon-lined stainless steel autoclave and heated for 24 h at 100 °C. After reaction, the white precipitate was washed with deionized water and dried at 60 °C, yielding a white solid (0.79 g).

*Synthesis of CuGa<sub>2</sub>O<sub>4</sub> spinel*

The reference was prepared through thermal oxidative decomposition.<sup>[23]</sup> Namely, two aqueous solutions of Cu(NO<sub>3</sub>)<sub>2</sub>·2.5H<sub>2</sub>O (2.32 g in 100 mL, Sigma Aldrich, >98%) and Ga(NO<sub>3</sub>)<sub>3</sub>·xH<sub>2</sub>O (5.11 g, Alfa Aesar, 99.9%) were mixed at room temperature (RT). Triethylamine (16.7 mL, Sigma Aldrich, >99.5%) was added to the metallic precursor solution under stirring and the pH of the solution corrected to 6 by using HNO<sub>3</sub> (Sigma Aldrich, 70%). The light blue suspension was heated at 200 °C until complete dehydration. After 1 h of an oxidative-decomposition at that temperature, the reaction generated a powder that turned from green to brown, releasing orange vapors during the process. Afterwards, the solid was crushed and then calcined at 750 °C for 2 h, yielding a dark-brown solid (1.88 g).

*Other materials*

ZnO (Aldrich, 99.9%) and Ga<sub>2</sub>O<sub>3</sub> (Aldrich, 99.99+%) were used as reference samples in characterization studies.

### 3.2.2. Characterization techniques

Metallic content (Cu, Zn, Ga, Al) was analyzed by inductively coupled plasma optical emission spectrometry (ICP-OES) using a Varian 715-ES spectrometer after solid dissolution of catalysts in aqua regia.

X-ray powder diffraction (XRD) was recorded with a PANalytical Cubix Pro diffractometer with a CuK<sub>α</sub> X-ray source ( $\lambda=0.15406$  nm). Data were collected over a  $2\theta$  range of 5-90° at a scan rate of 2 min<sup>-1</sup>, operating at 40 kV and 35 mA. Diffractograms were compared with the PDF2 database (codes in parentheses) for adequate identification.

Surface areas of solid samples (250 mg) were calculated by applying the Brunauer-Emmett-Teller (BET) model to the range of the N<sub>2</sub> adsorption isotherm where a linear relationship is maintained. These isotherms were obtained from liquid nitrogen adsorption experiments at -196 °C, in a Micromeritics flowsorb instrument.

High-resolution transmission electron microscopy (HR-TEM) measurements were performed in a JEOL-JEM 2100F operating at 200 kV. The instrument was equipped with an EDX X-Max 80 detector, which supplied qualitative chemical information. Samples were prepared by dropping the suspension of the powder catalyst using ethanol (Scharlab, absolute) as the solvent directly onto holey-carbon coated copper grids.

Temperature-programmed reduction (TPR-H<sub>2</sub>) analysis was performed on a Micromeritics Autochem 2910 instrument. About 50 mg of sample was initially cleaned with 30 mL·min<sup>-1</sup> of argon at RT for 30 min, and then a mixture of 10 vol % of H<sub>2</sub> in Ar was passed through the solid at a total flow rate of 50 mL·min<sup>-1</sup>,

while the temperature was increased up to 600 °C (heating rate of 10 °C·min<sup>-1</sup>). The H<sub>2</sub> consumption was measured using a thermal conductivity detector (TCD), previously calibrated using the reduction of CuO as reference.

The amount of surface copper metal sites was measured by N<sub>2</sub>O surface oxidation<sup>[24]</sup> followed by temperature-programmed reduction with H<sub>2</sub> (TPR-H<sub>2</sub>) in a Micromeritics Autochem 2910 instrument, assuming an adsorption stoichiometry of 1:2 (H<sub>2</sub>:Cu<sub>s</sub>). Before measurements, about 50 mg of catalyst was activated in 20 mL·min<sup>-1</sup> H<sub>2</sub> flow (pure H<sub>2</sub>, 3 h, 200 °C for CZG samples; 10 vol % H<sub>2</sub> in Ar, 1 h, 200 °C for CZA). After reduction, the sample was cleaning at the same temperature under argon flow. The temperature was decreased to 25 °C and the surface oxidation using N<sub>2</sub>O (1 vol % in He, 10 mL·min<sup>-1</sup>) from Cu<sup>0</sup> to Cu<sub>2</sub>O was performed for 1 h. After the first treatment, the sample was flushed with argon (15 min) at room temperature. Finally, TPR-H<sub>2</sub> was submitted until 400 °C (10 vol % H<sub>2</sub> in Ar, 50 mL·min<sup>-1</sup>, 10 °C·min<sup>-1</sup>).

Temperature-programmed desorption (TPD-CO<sub>2</sub>) studies over in situ reduced samples were performed using a quartz reactor, connected online to a mass spectrometer (MS) Balzer QMG 220M1. 100 mg of sample was firstly activated in a 20 mL·min<sup>-1</sup> H<sub>2</sub> flow at 200 °C for 3 h (1 h and 10 vol % H<sub>2</sub> in Ar for CZA sample, pure H<sub>2</sub> for the others). Then, the sample was flushed with argon (18 mL·min<sup>-1</sup>) at 230 °C for 1 h and the temperature decreased to RT. After stabilization, CO<sub>2</sub> was pulsed 15 times using a four way-valve (100 µL loop). After the adsorption step, the temperature was increased to 650 °C, maintaining the inert flow (10 °C·min<sup>-1</sup>). CO<sub>2</sub> desorption was followed by MS ( $m/z=44$ ).

Hydrogen/Deuterium (H/D) exchange experiments were carried out in a flow reactor at 25 and 90 °C. The feed gas consisted of 4 mL·min<sup>-1</sup> H<sub>2</sub>, 4 mL·min<sup>-1</sup> D<sub>2</sub> and 18 mL·min<sup>-1</sup> argon, and the total weight of catalyst was 41 mg. The sample was diluted with 360 mg of SiC. Reaction products (H<sub>2</sub>, HD and D<sub>2</sub>) were analyzed with a mass spectrometer (Balzer QMG 220M1). The *m/z* values used were 2 (H<sub>2</sub>), 4 (D<sub>2</sub>) and 3 (HD). The sample was in situ reduced at 200 °C (10 mL·min<sup>-1</sup>; 100 vol % H<sub>2</sub>, 3 h for CZG-sp and CZG-ox; 10 vol % H<sub>2</sub> in Ar, 1 h, for CZA) with a temperature-rising rate of 10 °C·min<sup>-1</sup>. Then, the temperature was decreased to 25 °C and, once stabilized, the H<sub>2</sub> feed was changed to the reactant gas composition. The temperature was kept at 25 °C for about 60 min and then, increased to 90 °C, maintaining 60 min at that temperature.

Electrochemical impedance spectroscopy (EIS) tests were performed in a three-electrode electrochemical cell connected to a potentiostat using the catalyst as working electrode (with an exposed area to the electrolyte of 0.5 cm<sup>2</sup>), an Ag/AgCl (3 M, KCl) reference electrode and a platinum tip as counter electrode. The working electrode was made by the deposition of 30 mg of ex situ reduced catalyst dispersed on 0.5 mL of ethanol (Scharlab, absolute) on a FTO glass. The deposition was carried out using a spin coating at 3000 rpm. EIS experiments were performed at 0 V<sub>Ag/AgCl</sub> and applying a potential perturbation of 10 mV from 10 kHz to 10 mHz. Additionally, Mott-Schottky plots were conducted scanning the potential from 0.2 V to -1.0 V at a rate of 50 mV·s<sup>-1</sup> at 5000 Hz. The electrolyte used for the electrochemical measurements was 0.1 M Na<sub>2</sub>SO<sub>4</sub> (PanReac, 99.0%).

Infrared (IR) spectra were recorded with a Nicolet (Nexus) 8700 FTIR spectrometer using a DTGS detector and acquiring at 4 cm<sup>-1</sup> resolution. An IR cell allowing in situ treatments in controlled atmospheres and temperatures from -176 °C to 500

°C was connected to a vacuum system with gas dosing facility. For IR studies, samples were pressed into self-supported wafers and submitted to hydrogen atmosphere prior to CO titration. For the reduction studies, CZG-sp, CZG-ox and CZA samples were treated at 200 °C in H<sub>2</sub> flow (10 mL·min<sup>-1</sup>; 100 vol % H<sub>2</sub>, 3 h for CZG-sp and CZG-ox; 10 vol % H<sub>2</sub> in N<sub>2</sub>, 1 h, for CZA) followed by evacuation at 10<sup>-4</sup> mbar (using a TBM pump, Pfeiffer) at the same temperature for 1 h and cooling down to -50 °C under dynamic vacuum conditions. CO was dosed at -50 °C and at increasing pressure (2-18 mbar). IR spectra were recorded after each dosage.

Laboratory X-ray photoelectron spectroscopy (XPS) spectra were recorded with a SPECS spectrometer equipped with a Phoibos 150 MCD-9 multichannel analyzer using a non-monochromatic AlK<sub>α</sub> (1486.6 eV) X-ray source. Spectra were recorded with an X-ray power of 50 W, pass energy of 30 eV and under an operating pressure of 10<sup>-9</sup> mbar. The sample (~30-50 mg) was pressed into a pellet and loaded onto a SPECS stainless steel sample holder. Before XPS analysis, CZG samples were submitted to different treatments in a high-pressure cell reactor (HPCR) connected under UHV to the XPS analysis chamber: i) H<sub>2</sub> reduction (10 mL·min<sup>-1</sup> flow) at 200 °C and at atmospheric pressure for 3 h; ii) CO<sub>2</sub> hydrogenation reaction at 220 °C and 280 °C (~2 h), 9 bar pressure in a CO<sub>2</sub>:H<sub>2</sub> mixture (1:3 molar ratio, 8 mL·min<sup>-1</sup> total flow). Gases were flown through two mass flow controllers (Bronkhorst). Reaction evolution was analyzed with a mass spectrometer Balzer QMG 220M1 coupled to the HPCR cell. The *m/z* values used to monitor each product were 44 (CO<sub>2</sub>), 31 (MeOH), 28 (CO), 18 (H<sub>2</sub>O), 15 (CH<sub>4</sub>) and 2 (H<sub>2</sub>). XPS spectra were referenced to the C 1s peak (284.5 eV) and data

treatment was addressed using the CASA XPS software. Shirley-type background and Gaussian/Lorentzian-type curves were used in the spectra fitting.

Near ambient pressure X-ray photoelectron spectroscopy experiments ((NAP)-XPS) were performed at ISSS beamline (HZB/Bessy II Electron Storage Ring, Berlin, Germany), where the photon energy range is 80-2000 eV. The endstation is equipped with a Petersen-type plane grating monochromator (PGM). Data were acquired with a Phoibos HSA 3500 electron energy analyzer (SPECS GmbH), pass energy of 20 eV, a step of 0.1 eV and beamline exit slit of 111  $\mu\text{m}$ . The focus size was 100 $\times$ 80 (H $\times$ V)  $\mu\text{m}^2$ . Incident photon energies of 1200, 1290 and 1600 eV for Cu 2p<sub>3/2</sub>; 1200, 1290 and 1600 eV for Zn 2p<sub>3/2</sub>; 1290, 1386 and 1600 eV for Ga 2p<sub>3/2</sub>; 1200 and 1386 eV for Cu LVV AES and 700 eV for O 1s were used, allowing to probe sample depths between 2.0 and 4.3 nm. The probing depth was obtained using the Tanuma Powell and Penn algorithm (TPP2M), calculating the inelastic mean free path for ZnO model.<sup>[25]</sup> The sample (~30 mg) was pelletized, mounted onto a sapphire sample holder and transferred directly to the analysis chamber with an insertion tool. Gas mixtures for in situ experiments were set in a proper ratio adjusting various mass flow controllers (Bronkhorst) present in a gas manifold that was directly connected to the analysis chamber through a leak valve. CZG-sp, CZG-ox and CZA samples were reduced in situ before performing CO<sub>2</sub> hydrogenation reaction. For that purpose, constant pressure of 0.5 mbar H<sub>2</sub> (10 mL $\cdot$ min<sup>-1</sup>) was kept in the chamber and the temperature raised from 25 to 200 °C (2 °C $\cdot$ min<sup>-1</sup>) for a total reduction time of ~2 hours. After complete reduction of copper, the atmosphere was switched to a 2.5 mbar gas mixture of CO<sub>2</sub> and H<sub>2</sub> (1:3 mol ratio, 12 mL $\cdot$ min<sup>-1</sup>) to perform the CO<sub>2</sub> hydrogenation reaction. XPS data were acquired under reaction conditions at 220 °C (~5-7 h) and at 280 °C (~3-4

h). Products evolution was monitored using a Prisma Balzers Mass Spectrometer, which was connected to the chamber via a leak valve. The  $m/z$  values used in the identification were: 32 (MeOH), 2 (H<sub>2</sub>), 18 (H<sub>2</sub>O), 44 (CO<sub>2</sub>) and 28 (CO). Energy scales of XPS spectra were calibrated using the Fermi edge position. CASA XPS software was used to analyze the data. Shirley-type background and Gaussian/Lorentzian-type curves were used in the spectra fitting.

X-ray absorption experiments at Cu (8979 eV) and Zn (9659 eV) K-edges were performed at the BL22 (CLÆSS) beamline<sup>[26]</sup> of ALBA synchrotron (Cerdanyola del Vallès, Spain). The white beam was monochromatized using a Si(111) double crystal; harmonic rejection was performed using Rh-coated silicon mirrors. Spectra were collected in transmission mode by means of the ionization chambers filled with appropriate gases. Samples in the form of self-supported pellets of optimized thickness were located inside in-house built cells allowing in situ experiments. Several scans were acquired at each measurement step to ensure spectral reproducibility and a good signal-to-noise ratio. Data reduction and extraction of the  $\chi(k)$  function as well as the EXAFS data analysis were performed using the Demeter package.<sup>[27]</sup> Phase and amplitudes were calculated by FEFF6 code.

CO<sub>2</sub> hydrogenation catalytic studies were performed in a stainless steel fixed-bed reactor (inner diameter of 11 mm and 240 mm length), equipped with a back-pressure regulator (BPR, Swagelok) that allows for working at a pressure range of 1-20 bar. Typically, 180 mg of catalyst (particle size 400-600  $\mu\text{m}$ ) was diluted in SiC in a weight ratio 0.12 (Cat/SiC). Samples were in situ reduced at atmospheric pressure prior to catalytic tests (25 mL·min<sup>-1</sup> H<sub>2</sub>, 200 °C, 3 h, 10 °C·min<sup>-1</sup> for CZG samples; 25 mL·min<sup>-1</sup> with 10 vol % H<sub>2</sub> in N<sub>2</sub>, 200 °C, 1 h, 10 °C·min<sup>-1</sup>, for CZA



sample). Tests at constant weight hourly space velocity (WHSV,  $\sim 31000 \text{ mL}\cdot\text{g}_{\text{cat}}^{-1}\cdot\text{h}^{-1}$ ) were performed under concentrated reaction conditions (23.7 vol % CO<sub>2</sub>, 71.3 vol % H<sub>2</sub>, 5.0 vol % N<sub>2</sub>) at 20 and 1 bar. Reaction temperatures varied from 160 to 260 °C. Each temperature was maintained for at least 1.5 h. Catalytic experiments at variable WHSV ( $\sim 24000$ - $134000 \text{ mL}\cdot\text{g}_{\text{cat}}^{-1}\cdot\text{h}^{-1}$ ) were carried out at constant 3:1 H<sub>2</sub> to CO<sub>2</sub> mol ratio and 20 bar. Long-term experiments were conducted at 240 °C and 20 bar over 100 h at constant WHSV ( $\sim 28500 \text{ mL}\cdot\text{g}_{\text{cat}}^{-1}\cdot\text{h}^{-1}$ ) and under the concentrated conditions described above. Direct analysis of the reaction products was done by online gas chromatography (GC), using a SCION-456-GC equipment with TCD (MS-13X column) and FID (BR-Q Plot column) detectors. Blank experiments (in the presence of SiC) shown the absence of a homogeneous contribution to the reaction. Intrinsic activity (expressed as  $\text{mol}_{\text{product}}\cdot\text{mol}_{\text{Cu,S}}^{-1}\cdot\text{s}^{-1}$ ) was calculated through the number of copper exposed sites obtained by N<sub>2</sub>O copper surface oxidation followed by TPR-H<sub>2</sub> studies (see above).

### 3.3. Results and discussion

#### 3.3.1. Synthesis and physico-chemical properties of calcined and reduced CZG catalysts

The importance of synthetic conditions in the stabilization of different crystalline precursor phases influencing the structure of the final catalyst has been reported in many works.<sup>[3]</sup> Commercial-like Cu/ZnO catalysts are usually prepared by coprecipitation of the corresponding metal precursors using carbonates (e.g., Na<sub>2</sub>CO<sub>3</sub>, NH<sub>4</sub>HCO<sub>3</sub>) as precipitating agent at controlled pH ( $\sim 6.5$ ), resulting in the formation of zinc malachite, aurichalcite or hydrotalcite precursor phases.<sup>[9,28]</sup> With the addition of other cations like Al<sup>3+</sup> or Ga<sup>3+</sup>, the composition of the

precursor phases may change. In this direction, Tsang et al. disclosed the formation of a ZnGa<sub>2</sub>O<sub>4</sub> spinel phase in coexistence with ZnO, introducing 5-20 mol % Ga<sup>3+</sup> into a Cu/ZnO precursor mixture, co-precipitated in the presence of Na<sub>2</sub>CO<sub>3</sub>.<sup>[9]</sup> In contrast, the doping of ZnO with other elements such as Al<sup>3+</sup>, Ga<sup>3+</sup> or Cr<sup>3+</sup> has been shown critical if a carbonate route is used, being strongly dependent on the synthesis conditions.<sup>[18]</sup> Therefore, an alternative precipitation route in absence of carbonates, i.e., using NaOH, has been selected in our work.

Thus, two CuO/ZnO/Ga<sub>2</sub>O<sub>3</sub> catalysts (CZG) are prepared by a co-precipitation method at controlled pH and in the presence of different precipitation agents (ammonium hydrogen carbonate for the CZG-sp sample and sodium hydroxide for the CZG-ox sample) (see details in Experimental Section 3.2.1). In the first case, zincian malachite is formed in the as-precipitated sample, whereas in the second case, wurtzite ZnO and CuO are obtained (details in Subsection 3.5.1). The composition of CZG systems has been settled similar to that of the commercial-like CuO/ZnO/Al<sub>2</sub>O<sub>3</sub> catalyst (i.e., 70:24:6 wt % ratio for Cu, Zn, and Ga or Al).<sup>[21,29]</sup> After calcination in air at 360 °C, the samples were reduced in H<sub>2</sub> (25 mL·min<sup>-1</sup>) at 200 °C for 3 h. For comparative purposes, a commercial-like catalyst (Cu/ZnO/Al<sub>2</sub>O<sub>3</sub>, labeled as CZA) with identical chemical composition has also been prepared using a procedure described in the literature<sup>[21]</sup> (details in Experimental Section, 3.2.1).

The structural properties of the reduced catalysts were analyzed by XRD and X-ray absorption spectroscopy (XAS) at the Cu and Zn K-edges, where the identification of ZnO and Cu<sup>0</sup> are confirmed in all samples (see 3.5.1 in SI section). Meanwhile, diffraction peaks associated to any gallium phase are not detected in the XRD patterns, inferring for a high dispersion of the Ga species (Figures 3.12-

3.16). In addition, according to the Scherrer equation, the average particle sizes of Cu<sup>0</sup> in all samples are above the threshold defined in the CO<sub>2</sub> hydrogenation for highest activity.<sup>[30]</sup> Thus, values of ~11 nm in the CZG-sp sample, ~17 nm in CZG-ox, and ~9 nm in the CZA sample are obtained.

Regarding the speciation of gallium, XAS at the Ga K-edge reveals a different local environment around Ga atoms in both CZG catalysts. Normalized XANES spectra at Ga K-edge (10367 eV) of CZG samples and Ga-based standards are shown in Figure 3.1a, where all spectra show similar absorption edge positions (10372 eV), corresponding to Ga<sup>3+</sup> compounds. CZG-ox displays a spectrum with a typical feature beyond the edge (10389 eV, marked with an arrow), which is attributed to Ga atoms involved in a wurtzite-type structure.<sup>[31-33]</sup> According to the chemical composition of our samples, the possible wurtzite structures prone to be formed are GaN or Ga<sup>3+</sup>-doped ZnO phase (replacement of Zn<sup>2+</sup> with Ga<sup>3+</sup>). However, the performed chemical analysis ruled out the formation of GaN, then suggesting that Ga atoms are inserted into zinc oxide crystalline structure. This hypothesis is supported by the comparison made in the inset of Figure 3.1a, in which both Ga and Zn K-edge spectra of CZG-ox are displayed with the same XANES features, which was already reported in the literature as proof of wurtzite structure formation.<sup>[32,33]</sup> On the other hand, CZG-sp catalyst showed a XANES spectrum quite similar to that of ZnGa<sub>2</sub>O<sub>4</sub>. A small undulation noticed before the marked ZnGa<sub>2</sub>O<sub>4</sub> feature could be associated to a minor presence of Ga<sub>2</sub>O<sub>3</sub> or even a percentage of Ga with wurtzite structure as in CZG-ox, once this shoulder lies at the same energy values. The k<sup>2</sup>-weighted  $\chi(k)$  functions and |FT| of Figure 3.1b and 3.1c were useful to further support the features observed in XANES, despite the short k-space (2.0-7.5 Å<sup>-1</sup>), which limits our discussion to the first oscillations

and, consequently, qualitative first shell analysis. The  $\chi(k)$  functions of CZG-sp and ZnGa<sub>2</sub>O<sub>4</sub> present the same in-phase oscillations with higher intensities for the latter (due to its more crystalline character), which resulted in similar EXAFS spectra after applying the Fourier-transform. Conversely, the  $\chi(k)$  function of CZG-ox catalyst is rather different, especially in the 6.0-7.5 Å<sup>-1</sup> range, corresponding to a Ga<sup>3+</sup>-doped ZnO phase.

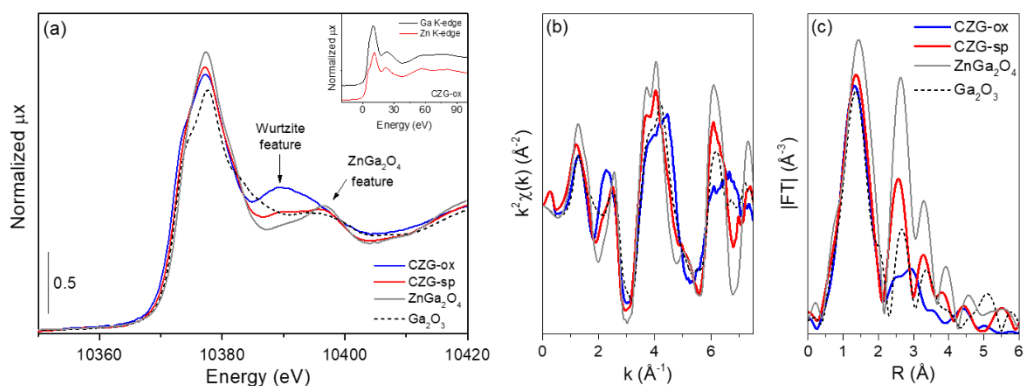


**Figure 3.1** Normalized XANES spectra at Ga K-edge (a), phase-uncorrected,  $k^2$ -weighted  $\chi(k)$  functions (b) and EXAFS spectra (c) of CZG catalysts and Ga-based references. The inset in panel (a) shows a comparison of CZG-ox sample measured at Ga and Zn K-edges.

Analysis of the samples microstructure performed with high-resolution transmission electron microscopy (HR-TEM) imaging shows the coexistence of domains with different composition in both gallium promoted samples. Thus, the integration of Cu ( $d_{111}=0.20$  nm), ZnO ( $d_{101}=0.24$  nm) and ZnGa<sub>2</sub>O<sub>4</sub> ( $d_{111}=0.48$  nm) phases, in close intimacy, are observed in the CZG-sp sample (Figure 3.2a). Similar features of Cu and ZnO phases are observed in the CZG-ox sample (Figure 3.2b), while the identification of the Ga<sup>3+</sup>-doped ZnO phase was hardly visualized from HR-TEM imaging because of the very small variation of the lattice distance due to the Ga doping. From energy dispersive X-ray (EDX) mapping results, Ga

overlaps with Zn in the CZG-ox sample (Figure 3.2c), which could be related to the formation of Ga<sup>3+</sup>-doped ZnO phase in which the Ga species are present as dopants in the ZnO nanoparticles. In contrast, a more homogeneous distribution of all elements (Cu, Zn, and Ga) is visualized in the EDX mapping of CZG-sp sample (Figure 3.2d).

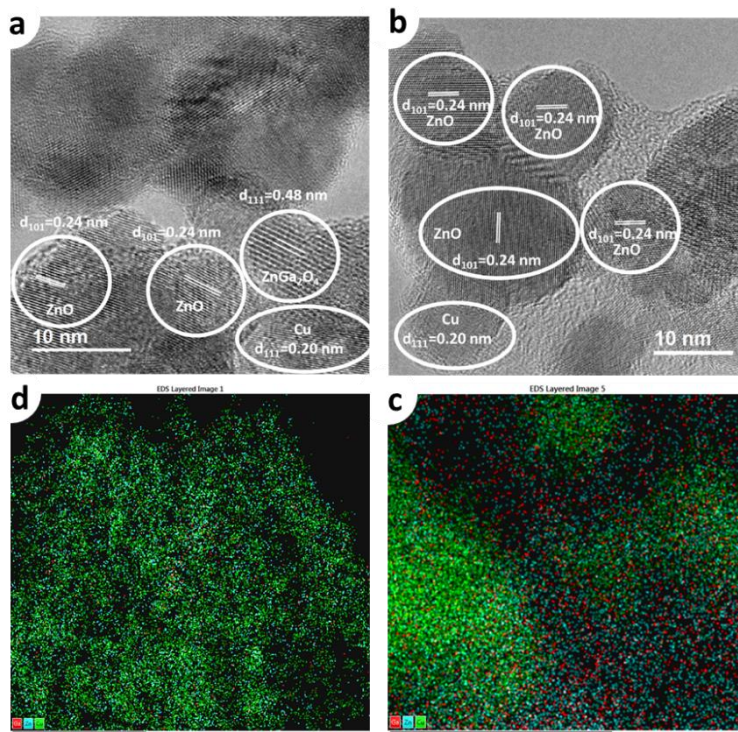


**Figure 3.2** Structural characterization of CZG-ox and CZG-sp samples. High-resolution transmission electron microscopy (HR-TEM) images of CZG-sp (a) and CZG-ox (b) samples. The different phases are marked according to their lattice fringes. STEM-EDX mapping results of CZG-ox (c) and CZG-sp (d). The Ga (red), Zn (cyan) and Cu (green) are indicated by different colors in the images.

Moreover, the electronic properties of the samples under study, presenting different structural features as already discussed, have been proven by electrochemical impedance spectroscopy (EIS) measurements. In particular, the

total resistance of each catalyst can be obtained from the Bode-module plot, reading the impedance module value at low frequencies (Figure 3.3). As shown in Figure 3.3, an increment in the conductivity (i.e., a decrease in the total resistance) of Ga promoted samples (CZG-ox and CZG-sp) versus the undoped commercial-like catalyst (CZA) is clearly observed. This can be explained in view of Al<sub>2</sub>O<sub>3</sub> microstructural role, mainly acting as dispersing agent of the ZnO and Cu nanoparticles. In this sense, the electrical interparticle transport is hindered due to the intrinsic isolating properties of Al<sub>2</sub>O<sub>3</sub>.

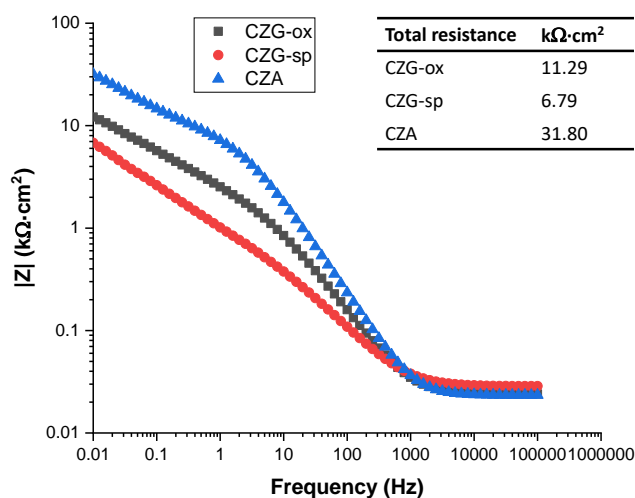


**Figure 3.3** Bode-module plot and total resistance values of the reduced CZG-ox, CZG-sp and CZA samples in 0.1 M Na<sub>2</sub>SO<sub>4</sub> at 0 V<sub>Ag/AgCl</sub>.

In the case of Ga promoted samples, both show similar total electrical resistances, being it slightly lower in the CZG-sp system, which indicates a higher amount of structural defects (according to N<sub>D</sub> values of Figure 3.19: 4.92·10<sup>19</sup> and 1.73·10<sup>19</sup> cm<sup>-3</sup> for CZG-sp and CZG-ox samples, respectively). The low carrier mobility observed in the CZG-ox sample may be due to carrier compensation, where part of the Ga atoms occupy interstitial sites as neutral defects.<sup>[34]</sup> Besides, an excess

of Ga might form a low proportion of Ga<sub>2</sub>O<sub>3</sub>, not detected spectroscopically, which could be somehow responsible for the higher total resistance value of CZG-ox catalyst due to a reduction of the carrier density.<sup>[34-36]</sup> Additionally, the positive slope showed in the Mott-Schottky plots confirms the n-type semiconductor behavior of the catalysts, with oxygen vacancies and Zn<sup>2+</sup> interstitials as main defects (Figure 3.19).

### 3.3.2. Catalytic activity in the CO<sub>2</sub> hydrogenation to methanol

The catalytic performance of the Ga promoted samples (CZG) and that of the commercial CZA sample, as reference, in the CO<sub>2</sub> hydrogenation at 20 bar and at a space velocity (WHSV) of ~31000 mL-g<sub>cat</sub><sup>-1</sup>·h<sup>-1</sup> is included in Table 3.2. The variation of the CO<sub>2</sub> conversion and the selectivity to products at different reaction temperatures are summarized in Figure 3.4a-c.

**Table 3.2** Catalytic results of CZG and CZA samples at 20 bar pressure and at variable temperature (180-260 °C).

T (°C)	Cat.	X <sub>CO<sub>2</sub></sub> (%)	CO <sub>2</sub> selectivity (%)			STY (mol <sub>prod</sub> ·g <sub>cat</sub> <sup>-1</sup> ·h <sup>-1</sup> )		Intrinsic activity (mol <sub>prod</sub> ·mol <sub>Cu,s</sub> <sup>-1</sup> ·s <sup>-1</sup> )	
			MeOH	CO	HCOOMe	MeOH	CO	MeOH	CO
180	CZA	2.9	94.8	4.3	0.9	8.78·10 <sup>-3</sup>	3.98·10 <sup>-4</sup>	8.76·10 <sup>-4</sup>	3.97·10 <sup>-5</sup>
	CZG-sp	3.6	95.9	3.2	0.9	1.08·10 <sup>-2</sup>	3.60·10 <sup>-4</sup>	1.26·10 <sup>-3</sup>	4.20·10 <sup>-5</sup>
	CZG-ox	2.4	97.0	2.0	1.0	7.46·10 <sup>-3</sup>	1.54·10 <sup>-4</sup>	1.63·10 <sup>-3</sup>	3.36·10 <sup>-5</sup>
200	CZA	5.6	89.5	10.1	0.4	1.60·10 <sup>-2</sup>	1.81·10 <sup>-3</sup>	1.60·10 <sup>-3</sup>	1.80·10 <sup>-4</sup>
	CZG-sp	6.2	91.7	7.9	0.4	1.78·10 <sup>-2</sup>	1.53·10 <sup>-3</sup>	2.07·10 <sup>-3</sup>	1.78·10 <sup>-4</sup>
	CZG-ox	4.9	94.6	4.9	0.5	1.48·10 <sup>-2</sup>	7.69·10 <sup>-4</sup>	3.25·10 <sup>-3</sup>	1.68·10 <sup>-4</sup>
220	CZA	10.0	79.9	19.9	0.2	2.55·10 <sup>-2</sup>	6.36·10 <sup>-3</sup>	2.54·10 <sup>-3</sup>	6.34·10 <sup>-4</sup>
	CZG-sp	10.5	84.0	15.8	0.2	2.76·10 <sup>-2</sup>	5.19·10 <sup>-3</sup>	3.21·10 <sup>-3</sup>	6.04·10 <sup>-4</sup>
	CZG-ox	9.0	89.0	10.8	0.2	2.57·10 <sup>-2</sup>	3.11·10 <sup>-3</sup>	5.61·10 <sup>-3</sup>	6.81·10 <sup>-4</sup>
240	CZA	15.9	63.8	36.1	0.1	3.24·10 <sup>-2</sup>	1.83·10 <sup>-2</sup>	3.23·10 <sup>-3</sup>	1.83·10 <sup>-3</sup>
	CZG-sp	15.2	67.4	32.5	0.1	3.20·10 <sup>-2</sup>	1.55·10 <sup>-2</sup>	3.73·10 <sup>-3</sup>	1.80·10 <sup>-3</sup>
	CZG-ox	12.5	79.8	20.1	0.1	3.19·10 <sup>-2</sup>	8.05·10 <sup>-3</sup>	6.99·10 <sup>-3</sup>	1.76·10 <sup>-3</sup>
260	CZA	20.9	45.3	54.7	0.0	3.02·10 <sup>-2</sup>	3.65·10 <sup>-2</sup>	3.02·10 <sup>-3</sup>	3.64·10 <sup>-3</sup>
	CZG-sp	21.1	51.3	48.7	0.0	3.38·10 <sup>-2</sup>	3.21·10 <sup>-2</sup>	3.94·10 <sup>-3</sup>	3.74·10 <sup>-3</sup>
	CZG-ox	15.3	65.0	34.9	0.1	3.18·10 <sup>-2</sup>	1.71·10 <sup>-2</sup>	6.97·10 <sup>-3</sup>	3.74·10 <sup>-3</sup>

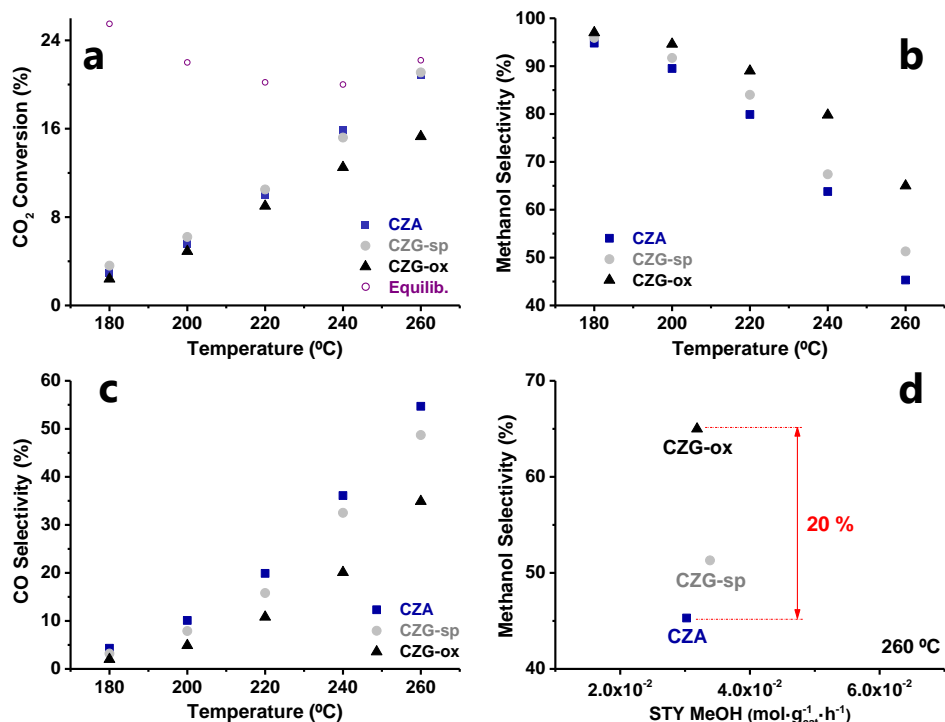


**Figure 3.4** Selected catalytic features for the CO<sub>2</sub> hydrogenation to MeOH on CZG and CZA samples: CO<sub>2</sub> conversion (a), MeOH selectivity (b), and CO selectivity (c) versus temperature; MeOH selectivity versus space-time yield to MeOH at 260 °C (d).

Similar catalytic performance in terms of CO<sub>2</sub> conversion is observed for CZG-sp and CZA samples, being these more active than CZG-ox sample. Normalizing the samples production to MeOH and CO per gram of catalyst (STY), a comparable value is found for the former product at all the temperatures for the three catalysts (Table 3.2). However, a ~2 times higher MeOH production is observed in the CZG-ox system when the normalization is done to square meter of catalyst (Table 3.7). In addition, if the variation of the selectivity to the main product (i.e., MeOH) is plotted versus its productivity (Figure 3.4d), a difference of 20 percentage points is found for the selectivity between CZG-ox and the



commercial CZA systems, and 15 points between CZG-ox and CZG-sp samples. This trend suggests a strong inhibition of CO formation in the gallium promoted samples and, in particular, in CZG-ox catalyst.

An analogous behavior is observed when plotting the variation of the selectivity to methanol with the CO<sub>2</sub> conversion obtained at different contact times. This is displayed in Figure 3.5 at two temperatures (i.e., 220 °C and 240 °C) as examples, and the catalytic data included in Tables 3.8-3.10 and Figure 3.20.

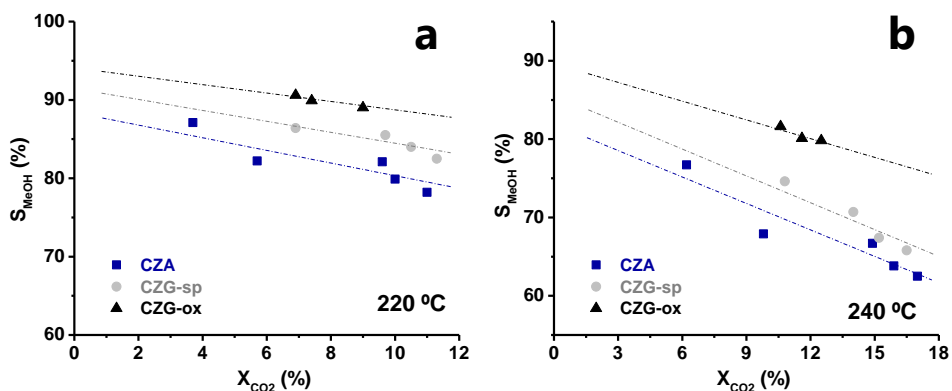


**Figure 3.5** Variation of the methanol selectivity vs. carbon dioxide conversion at 220 °C (a) and 240 °C (b).

In both graphs, a nearly parallel catalytic behavior is found for the CZG and CZA systems, being CZG-ox the most selective one at any operational condition. Thus, at 220 °C and 9.5% CO<sub>2</sub> conversion, an 89.0% methanol selectivity is obtained with CZG-ox catalyst, being higher than the other two (85.5% with CZG-sp and 82.1% with CZA). The enhanced methanol selectivity is even more remarkable at higher temperatures, i.e., 260 °C (Figure 3.21), at which the RWGS reaction becomes predominant. In this case, at a ~15.5% CO<sub>2</sub> conversion, a selectivity to methanol of 65.0% is achieved with the CZG-ox, being 9% and 16% higher than those with the other samples (i.e., 56.2% and 49.0% with CZG-sp and CZA,

respectively). Due to the different amount of exposed copper atoms on the surface of CZG and CZA samples (see Table 3.3), additional normalization of the catalytic activity to the exposed Cu surface area ( $SA_{Cu}$ , measured by N<sub>2</sub>O chemisorption) is done for qualitative analysis, being aware of the controversy about the meaning of this value, particularly for reactions requiring the concerted involvement of metallic and oxide species. Then, the highest intrinsic methanol activity in this project is found for the CZG-ox sample ( $6.99 \cdot 10^{-3} \text{ mol}_{MeOH} \cdot \text{mol}_{Cu,s}^{-1} \cdot \text{s}^{-1}$  at 240 °C), which is 2 times higher than in CZG-sp and CZA samples ( $3.73 \cdot 10^{-3} \text{ mol}_{MeOH} \cdot \text{mol}_{Cu,s}^{-1} \cdot \text{s}^{-1}$  and  $3.23 \cdot 10^{-3} \text{ mol}_{MeOH} \cdot \text{mol}_{Cu,s}^{-1} \cdot \text{s}^{-1}$ , respectively). In view of these results, a promoting effect in methanol production can be concluded for the CZG-ox sample, compared to the CZA and CZG-sp samples.

In the next, in order to define the catalytic role of Ga<sup>3+</sup>-doped in the ZnO lattice of the CZG-ox sample, the performance of the herein studied catalysts has been compared to other gallium-promoted catalysts from the literature. This is collected in Table 3.12, where the methanol production (i.e., STY) and other catalytic features, such as MeOH selectivity, are summarized. Direct comparison is complicated due to the diverse reaction conditions usually used in the literature, being methanol formation favored at high pressures and high space velocities. However, despite these dissimilarities, analyzing the methanol space-time yields ( $STY_{MeOH}$ ) at a selected temperature and contact time (Figure 3.22), the herein reported catalysts appear among the most active ones, with the benefit of a lower working pressure, endowing as promising candidates in the CO<sub>2</sub> hydrogenation to methanol.

The effect of Ga loading on the catalytic performance of the most active sample (i.e., CZG-ox) has been studied, with metal loadings between 1.0 and 7.0 wt %

(details for synthesis and catalytic performance are found in Sections 3.2.1 and 3.5.2, respectively). As shown in Figure 3.23 and Table 3.13, a similar methanol production was obtained regardless the Ga loading in the final catalyst.

### 3.3.3. Determination of catalytic sites involved in MeOH synthesis

In order to understand the effect that the speciation of gallium as promoter has on the properties of active sites, (i.e., copper electronic properties, surface basicity, ZnO decoration, etc.), and trying to correlate them with the catalytic activity of the studied samples, spectroscopic characterization combining state of the art techniques, like near ambient pressure (NAP)-XPS and IR of CO as probe molecule, with TPD-CO<sub>2</sub> and H<sub>2</sub>/D<sub>2</sub> isotopic exchange have been done.

#### *(NAP)-XPS*

The XPS BE of Cu 2p<sub>3/2</sub>, Zn 2p<sub>3/2</sub> and Ga 2p<sub>3/2</sub> core levels acquired at variable sampling depth (between 2.0 and 4.3 nm) and at the different chemical environments (H<sub>2</sub> and CO<sub>2</sub>/H<sub>2</sub>) (see 3.2.2 Subsection for more details) correspond in all cases to Cu<sup>0</sup> (Cu 2p<sub>3/2</sub> ~932.2 ± 0.1 eV and CuL<sub>3</sub>M<sub>45</sub>M<sub>45</sub> 919.5 eV), Zn<sup>2+</sup> (Zn 2p<sub>3/2</sub> ~1021.8 ± 0.3 eV) and Ga<sup>3+</sup> (Ga 2p<sub>3/2</sub> ~1118.0 ± 0.2 eV). The corresponding values are included in Tables 3.14-3.16 and the XPS core level displayed in Figures 3.24-3.26. Those values are similar in all samples and do not demonstrate the differences reflected in the Ga K-edge absorption spectra discussed previously. A similar trend has been observed in other studies, concluding that the Ga 2p core levels were not sensitive enough to the chemical environment around the atoms.<sup>[37]</sup> Some authors, specifically in the case of gallium promoted Cu/ZnO samples, identified a component in the Zn 2p XPS line at 2 eV lower BE than that of ZnO that has been ascribed to Zn<sup>0</sup> species.<sup>[9,10]</sup> However, identification of Zn<sup>0</sup> by XPS is controversial due to the overlapping of the BE of zinc oxide with Zn<sup>0</sup>,<sup>[38-</sup>

<sup>42]</sup> making those assessments doubtful. Analysis at the O 1s XPS core line acquired at the most surface sensitive conditions (i.e., at low X-ray energy (700 eV), Figure 3.27 and Table 3.17) reveals three components at ~530.6 eV, 531.4 eV and 532.9 eV, corresponding to lattice oxygen "O<sup>2-</sup>", oxygen vacancies and/or surface hydroxyl groups (-OH) and carbonate species, respectively.<sup>[43]</sup> The lower percentage found for the 531.4 eV component corresponds to the CZG-ox sample, in agreement with a less defective structure, as determined by EIS measurements.

The surface composition at variable sampling depth in reduced and working catalysts under steady-state conditions is displayed in Figure 3.6 for the three samples under different environments. Significant deviation from the nominal composition determined by ICP-OES for all three measured samples is observed (Tables 3.18-3.20), with Zn enrichment at the surface, in agreement with previous results obtained on Cu/ZnO based catalysts.<sup>[44-47]</sup>

According to Figure 3.6a, a higher surface coverage of ZnO is observed in the reduced CZG-ox sample compared to the other ones (Figure 3.6d for CZG-sp and 3.6g for CZA). As consequence, the number of exposed surface Cu sites ( $SA_{Cu}$ ) determined by N<sub>2</sub>O chemisorption (see Table 3.3) is markedly lower in CZA-ox catalyst. Furthermore, the ZnO coverage does not match with the catalyst reducibility (see Subsection 3.5.1 for TPR-H<sub>2</sub> analysis), while should be related to the dissimilar interaction among the precursor phases in the different synthetic methods used in each case. In addition, from XPS depth profile analysis, it can be observed that the distribution of Ga and Zn species with respect to Cu is different in the reduced CZG-sp (Figure 3.6d) and CZG-ox samples (Figure 3.6a), compared to CZA (Figure 3.6g), which may correspond to dissimilar locations and

interactions of different chemical phases within the catalyst. Thus, the stabilization of distinct copper-metal oxide interfaces, i.e., Cu-Zn (ZnO) in CZA and CZG-sp samples, and Cu-Ga (Ga<sup>3+</sup>-doped ZnO) in CZG-ox sample can be predicted. Undoubtedly, the stabilization of different interfaces influences the electronic properties of the adjacent copper sites, as revealed in the next subsection by IR spectroscopy using CO as probe molecule.

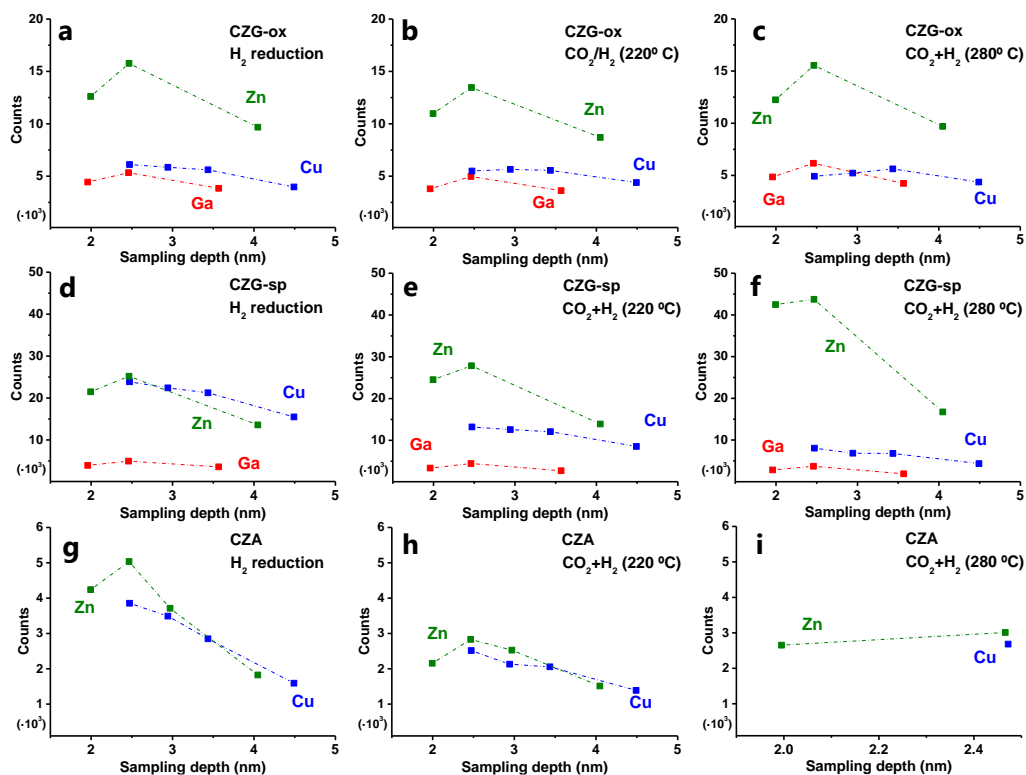


**Figure 3.6** CZG-ox (a,b,c), CZG-sp (d,e,f) and CZA (g,h,i) XPS depth profile spectra at different reaction conditions. Left: spectra of reduced catalysts. Middle: spectra under CO<sub>2</sub>+H<sub>2</sub> atmosphere at 220 °C. Right: spectra under CO<sub>2</sub>+H<sub>2</sub> atmosphere at 280 °C.

Exposing the catalysts to conditions close to the reaction inside the XPS analysis chamber, i.e., 10 mL·min<sup>-1</sup> CO<sub>2</sub>/H<sub>2</sub> flow at 2.5 mbar, a slight migration of ZnO<sub>x</sub> over

the CuNP is observed in the CZG-sp sample at the usual reaction temperatures (i.e., 220 °C, Figure 3.6e and Figure 3.28a), being more prominent at higher reaction temperature (i.e., 280 °C, Figure 3.6f and Figure 3.28b). The dynamic migration of ZnO<sub>x</sub> and the redistribution of interfacial sites under reaction conditions are less pronounced in the CZG-ox (Figure 3.6b,c and Figure 3.29), and practically not detected in the CZA sample (Figure 3.6h,i).

In order to correlate the (NAP)-XPS spectroscopic data obtained in the “mbar range” with the catalytic structural features presented under practical catalytic reaction conditions (i.e., 20 bar), MS analysis of the reaction products in the (NAP)-XPS studies has been tracked, together with catalytic studies performed in the flow reactor at lower pressure (1 bar), and compared to those at 20 bar (Table 3.21 and Figure 3.30). As presented in Figure 3.31, online MS data show that the formation of methanol ( $m/z=32$ ), CO ( $m/z=28$ ), and H<sub>2</sub>O ( $m/z=18$ ) increases with the reaction temperature. Notably, the ratios of CO/CO<sub>2</sub> ( $m/z=28/44$ ) and MeOH/CO<sub>2</sub> ( $m/z=32/44$ ) in the three samples match linearly with the CO and methanol yield obtained at 220 °C and 20 bar in the catalytic flow reactor (see Figure 3.32).

#### *IR-CO probe*

The electron charge density of surface copper species was analyzed by IR spectroscopy using CO as probe molecule. Since the adsorption of CO may cause the reconstruction and sintering of copper particles,<sup>[48]</sup> IR adsorption experiments have been done at low temperature (i.e., -50 °C) in this work.

According to the results shown in Figure 3.7, different types of copper species are distinguished, characterized by dissimilar CO vibration frequencies.

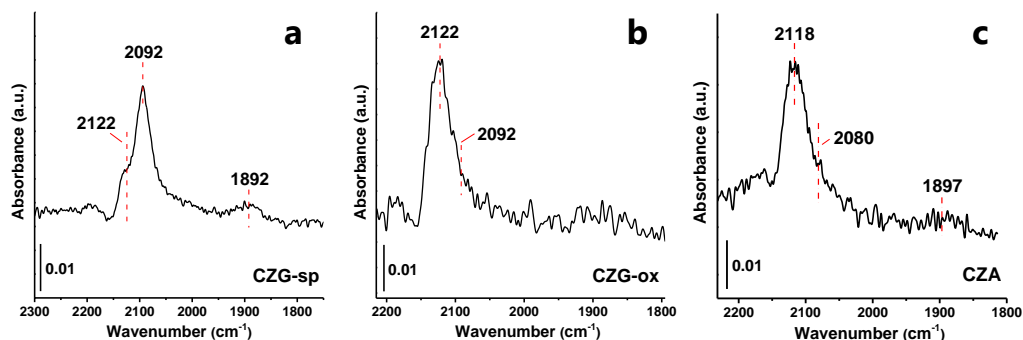


**Figure 3.7** Infrared spectra of CO adsorbed at  $-50\text{ }^{\circ}\text{C}$  on in situ reduced CZG-sp, CZG-ox and CZA samples.

Thus, a band at  $2122\text{ cm}^{-1}$  with a small shoulder at  $2092\text{ cm}^{-1}$  is perceived in the CZG-ox sample. This band is also detected in the CZG-sp sample, in addition to IR bands at  $2092$  and  $1892\text{ cm}^{-1}$ . In the CZA sample, IR bands at  $2118$ ,  $2080$  and  $1897\text{ cm}^{-1}$  are observed. IR bands below  $2100\text{ cm}^{-1}$  are due to CO adsorption on metallic Cu, where the IR bands at  $2092$ – $2080\text{ cm}^{-1}$  are associated to linearly bonded  $\text{Cu}^0$ -CO on high indexed Cu surface planes, and the  $1897$ – $1892\text{ cm}^{-1}$  IR bands to bridging CO species on the Cu(111) surface.<sup>[49,50]</sup> The IR band at  $2118\text{ cm}^{-1}$  is also related to copper species, most probably located at the interface to the metal oxide.<sup>[49]</sup> Regarding the assignation of the IR band at  $2122\text{ cm}^{-1}$ , it has been assigned to linear CO species adsorbed on  $\text{Cu}^+$ <sup>[51-54]</sup> or to positively charged  $\text{Cu}^{\delta+}$ <sup>[49]</sup> or defective  $\text{Zn}^{\delta+}$ . The promoting effect of Ga in stabilizing  $\text{Cu}^+$  species has already been reported in the literature.<sup>[13,14]</sup> In fact, the IR band at  $2122\text{ cm}^{-1}$  is only observed in the gallium promoted samples. Interestingly, metallic copper is detected in minor extent in the CZG-ox sample, which remarkably shows a strong CO inhibiting effect in the catalytic studies. Assuming that copper species, as  $\text{Cu}^0$ , are involved in the activation of  $\text{H}_2$ , this raises a considerable distrust about the effective activation of  $\text{H}_2$  in the CZG-ox sample. In order to address this issue,

H<sub>2</sub>-D<sub>2</sub> isotopic exchange experiments were performed, showing similar exchange ability in all samples (Figure 3.8).

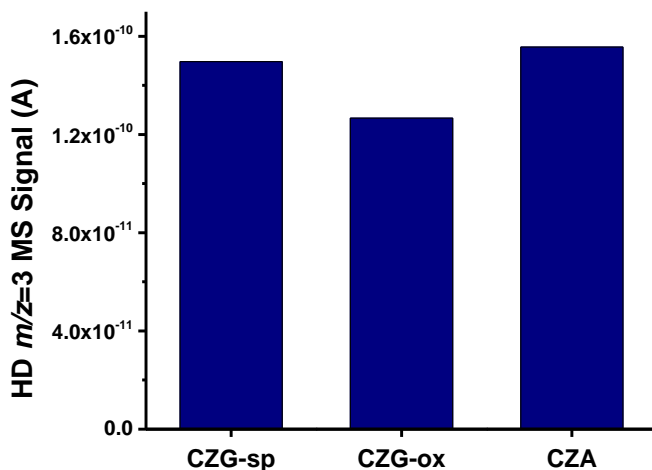


**Figure 3.8** H<sub>2</sub>-D<sub>2</sub> isotopic exchange results for CZG and CZA samples at 90 °C.

#### *TPD-CO<sub>2</sub>*

Surface basic sites have been proposed in several studies to play an important role in the stabilization of different reaction intermediate species, being moderate basic sites<sup>[55-58]</sup> that are critical for enhanced methanol selectivity. Indeed, some authors found a linear correlation between the amount of basic sites and methanol selectivity.<sup>[15,55,56]</sup> In this regard, TPD-CO<sub>2</sub> analysis has been performed, and the corresponding TPD patterns of the herein studied catalysts are displayed in Figure 3.9, and that of reference samples (i.e., ZnO, ZnGa<sub>2</sub>O<sub>4</sub>, CuGa<sub>2</sub>O<sub>4</sub> and Ga<sub>2</sub>O<sub>3</sub>) in Figure 3.39.

Three different regions are clearly observed: <200 °C, 200-400 °C and >400 °C. At low temperature (<200 °C), a peak around 80 °C is distinguished in all samples, ascribed to weakly interacting CO<sub>2</sub> molecules with surface hydroxyl groups. On the other hand, desorption peaks above 400 °C may not contribute to the catalytic



activity due to the high interaction strength with the catalyst surface, and can be considered as spectator species. Therefore, only desorption peaks in the 200-400 °C range can be considered as relevant for the catalytic process, being ascribed to metal-oxygen pairs, surface defects and low coordinated oxygen anions.<sup>[56,57]</sup> In fact, it is in this temperature range where the main differences between catalysts are observed, revealing different nature of basic sites (Figure 3.9).

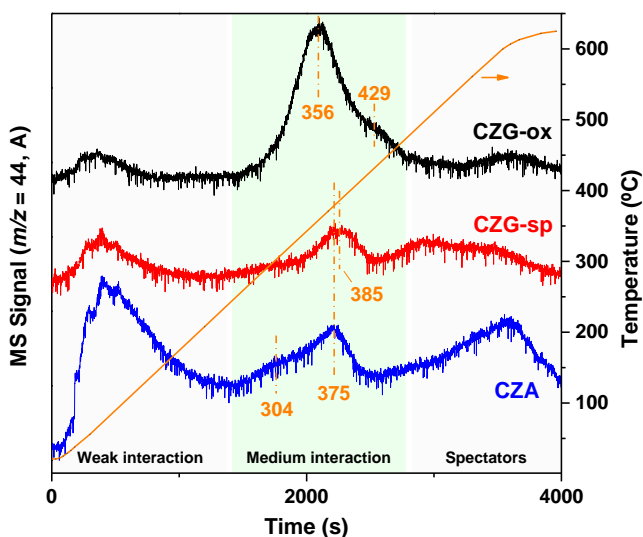


**Figure 3.9** TPD-CO<sub>2</sub> experiments performed on CZG and CZA catalysts.

The amount of basic sites increases in the studied catalysts compared to that of the reference samples (Figure 3.39), where the highest CO<sub>2</sub> desorption is observed in the CZG-ox sample (Table 3.24). In addition, a different desorption pattern is observed in this sample, with a desorption peak at 356 °C, slightly lower than that in CZG-sp and CZA samples (with maxima at ~375-385 °C). In fact, (NAP)-XPS shown a highest amount of surface metal oxide (i.e., ZnO) decorating CuNPs in the CZG-ox sample, which may account for a higher number of surface basic sites.

*Determination of structure-activity correlations*

In the CO<sub>2</sub> hydrogenation to methanol many interrelated parameters are usually involved, making a clear distinction of active components difficult. That is the reason why a multimodal approach is necessary in order to address the complexity of commercial-like catalysts. In our study, Ga<sup>3+</sup>-doped ZnO has been shown as a more efficient promoter than ZnGa<sub>2</sub>O<sub>4</sub>, enhancing methanol selectivity versus CO formation. Different spectroscopic tools have been used in order to unveil the reason behind this promoting effect. It is shown that the presence of gallium increases the conductivity of the catalysts, behaving both CZG-ox and CZG-sp as n-type semiconductors. The concentration of surface defects is higher in CZG-sp sample (containing ZnGa<sub>2</sub>O<sub>4</sub>) than in the Ga<sup>3+</sup>-doped ZnO sample (i.e., CZG-ox). In the CZG-sp sample, the presence of surface vacancies (i.e., defects) with loosely bounded electrons increases the conductivity of the material. These defects have been considered as important active sites in CO<sub>2</sub> activation. Nevertheless, surface basicity is important for the stabilization of intermediate species, directing the selectivity of the reaction. In this work, a higher concentration of moderate surface basicity is observed in the Ga<sup>3+</sup>-doped ZnO sample, (i.e., CZG-ox), behaving this as the most selective sample.

In addition, based on depth profile XPS studies, different interfaces are visualized among the samples, being the copper-gallium interaction favored in the CZG-ox sample. In agreement with other studies, the gallium interface stabilize Cu<sup>+/ $\delta$ +</sup>  ions, which are observed using IR of CO as probe molecule in both gallium promoted samples. The stabilization of Cu<sup>+/ $\delta$ +</sup>  species boosting methanol synthesis has been reported by several authors,<sup>[11-15]</sup> and agrees with the higher selectivity to methanol observed on both CZG samples, compared with the CZA

one. Significantly, metallic copper (Cu<sup>0</sup>) surface species appear as a minor component in the IR studies of the CZG-ox sample. This material exhibits the highest intrinsic activity if methanol production is normalized to the exposed copper surface area determined by N<sub>2</sub>O, which may indicate a different nature of active sites, either at the copper particle or at copper interfacial sites. In particular, depth profile XPS studies show a high surface coverage with zinc oxide species in the CZG-ox sample, which would explain the higher number of surface exposed basic sites observed from TPD-CO<sub>2</sub> studies. Moreover, while it has been generally reported that the presence of dopants in metal oxide lattice modify its surface acid/base properties,<sup>[59-61]</sup> we cannot confirm at this stage if Ga<sup>3+</sup> doping contributes to the acid/base properties of the ZnO support, but we can safely assess that the density of surface sites with moderate basicity has increased compared to the rest of the samples and the pure ZnO. In a recent work of Bonura et al., the methanol formation rate has been discussed as a function of the N<sub>2</sub>O/CO<sub>2</sub> ratio.<sup>[62]</sup> This parameter represents the extent of metal and oxide surface sites, where a balanced amount of both sites has been proposed to promote methanol production. In our case, methanol production is shown to be sensitive to the number of surface basic sites (see Figure 3.40), being enhanced at increasing the number of moderate surface basic centers. This result indicates the importance of surface basic sites in CO<sub>2</sub> activation, in agreement with previous studies in the literature.<sup>[58-61]</sup> Moreover the lower amount of surface metallic copper determined by IR-CO in the CZG-ox may also contribute to the inhibiting effect of CO formation, where metallic copper has been correlated by several authors with the CO production by the RWGS reaction.<sup>[17,63,64]</sup>

*Application at large scale: opportunities and limitations*

Progress in the thermo-catalytic CO<sub>2</sub> reduction through innovative design of new catalysts and process engineering are important aspects in order to accelerate and expand the deployment of these technologies in a circular carbon economy market. In this direction, we are studying a new type of gallium promoted copper-based catalyst containing Ga<sup>3+</sup>-doped ZnO species in this chapter. Here, we found a promoting effect in methanol production on a Ga<sup>3+</sup>-doped ZnO copper-based catalyst (CZG-ox), compared to a reference catalyst with similar formulation containing ZnGa<sub>2</sub>O<sub>4</sub> phase (CZG-sp) and the commercial Cu/ZnO/Al<sub>2</sub>O<sub>3</sub> catalyst (CZA). The CZG-ox system looks promising, with enhanced methanol selectivity, specifically at conditions where the RWGS starts to predominate (260 °C), but it is limited by its low surface area, reducing its activity. In this sense, further studies are ongoing in order to improve the physico-chemical characteristics that definitely affects the methanol production. Despite of it, the catalyst competes well with the most active ones reported in the literature (as already depicted in Figure 3.22).

Another important feature for its potential application at large scale is the long-term stability under reaction conditions. In this respect, catalytic tests over 100 h time-on-stream have been performed at 240 °C, 20 bar and at a space velocity (WHSV) of 28500 mL·g<sub>cat</sub><sup>-1</sup>·h<sup>-1</sup> on the CZG-ox and compared to the commercial-like CZA sample (Figure 3.10).

On both catalysts, a decrease in methanol production is mainly observed in the first ~25 h, remaining then practically stable until the end of the experiment. The initial decrease in methanol production is higher in the CZG-ox sample (~38%) than in the CZA one (~16%).

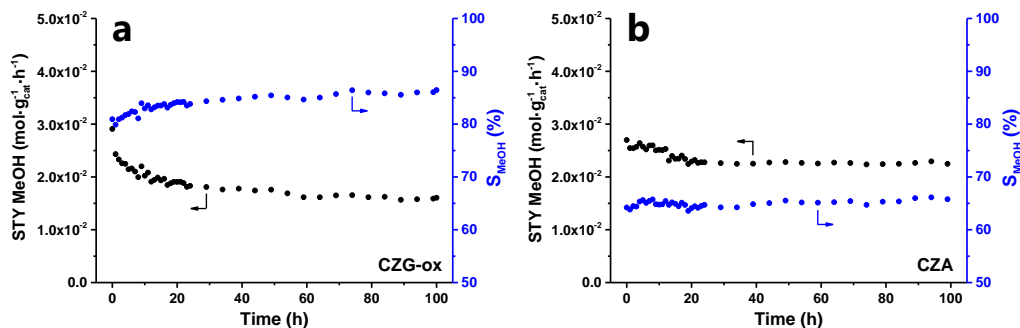


**Figure 3.10** Long-term experiments conducted on CZG-ox and the commercial CZA samples at 240 °C, 20 bar and  $\sim 28500 \text{ mL}\cdot\text{g}_{\text{cat}}^{-1}\cdot\text{h}^{-1}$ .

This deactivation has been usually ascribed to sintering of the copper nanoparticles due to water formation under reaction conditions or due to poisoning of active sites by water adsorption. The XRD analysis of the samples prior and after reaction are shown in Figure 3.15 and Table 3.4, revealing slight change in crystal size. Since the addition of Al<sub>2</sub>O<sub>3</sub> has been reported to enhance catalyst stability, a preliminary study has been done on the CZG-ox sample adding 12.5 % wt ratio Al<sub>2</sub>O<sub>3</sub> (namely, CZGA-ox, details of the synthesis can be found in Subsection 3.2.1). As verified in Figure 3.41a, an improvement in the catalyst stability is achieved, while keeping similar selectivity pattern as in the original CZG-ox sample (Figure 3.41b and Table 3.25). However, further studies are needed in order to investigate the implications that the reformulation of CZG-ox system has in its physico-chemical characteristics, connected to the catalytic performance and the active center operation.

### 3.4. Conclusions

The promoting effect of gallium on the structural, electronic and catalytic properties of two selected CuO/ZnO/Ga<sub>2</sub>O<sub>3</sub> catalysts in the methanol synthesis from CO<sub>2</sub> hydrogenation has been studied in this chapter. Although the

promoting effect of Ga has been subject of many research papers, Ga<sup>3+</sup>-doped wurtzite ZnO has been scarcely studied in the methanol synthesis reaction. In addition, a deeper understanding of the promoting underlying mechanism and interactions among the active components will help in uncovering the complexity of industrial-like Cu/ZnO catalysts, requesting a multimodal spectroscopic-catalytic approach. In this work, we found that Ga<sup>3+</sup>-doped ZnO is a more effective promoter than the already reported ZnGa<sub>2</sub>O<sub>4</sub> phase. The speciation of gallium can be controlled by simply changing the precipitating agent during the co-precipitation of metal precursors, keeping the rest of variables constant. Thus, Ga<sup>3+</sup>-doped ZnO is formed by co-precipitating with NaOH, while ZnGa<sub>2</sub>O<sub>4</sub> appears by using NH<sub>4</sub>HCO<sub>3</sub>. Compared to the reference Cu/ZnO/Al<sub>2</sub>O<sub>3</sub> (CZA) catalyst, an inhibition of CO formation is observed in the gallium promoted samples and, in particular, in the one characterized by the presence of Ga<sup>3+</sup>-doped ZnO domains (CZG-ox). Long-term catalytic test over 100 h time-on-stream shown a decrease in methanol production of ~38% in the first 25 h of reaction, remaining stable until the end of the experiment. This value is higher than that observed in the commercial Cu/ZnO/Al<sub>2</sub>O<sub>3</sub> (CZA) catalyst, where Al<sub>2</sub>O<sub>3</sub> behaves as a structural promoter. In fact, adding 12.5 % wt Al<sub>2</sub>O<sub>3</sub> to the CZG-ox catalyst results in a less marked catalyst deactivation.

As a result of our work, a complex scenario where both the electrochemical potential of the sample and the structural properties of the catalyst are mutually influenced, underlining the need for a multidisciplinary spectroscopic approach for accurate catalytic characterization.

Finally, the promoting effect of Ga<sup>3+</sup>-doped ZnO wurtzite phase for enhanced methanol synthesis found in this work may open new perspectives in the design

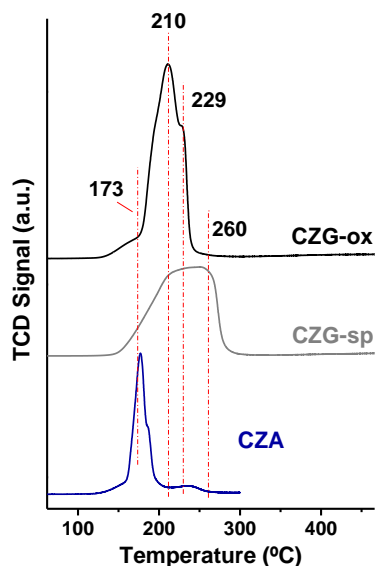
of novel catalytic systems with tailored interfaces, not only in thermal, but also in photo/electro reduction of carbon dioxide. However, further studies are needed in order to be competitive for industrial applications.

### 3.5. Supporting Information

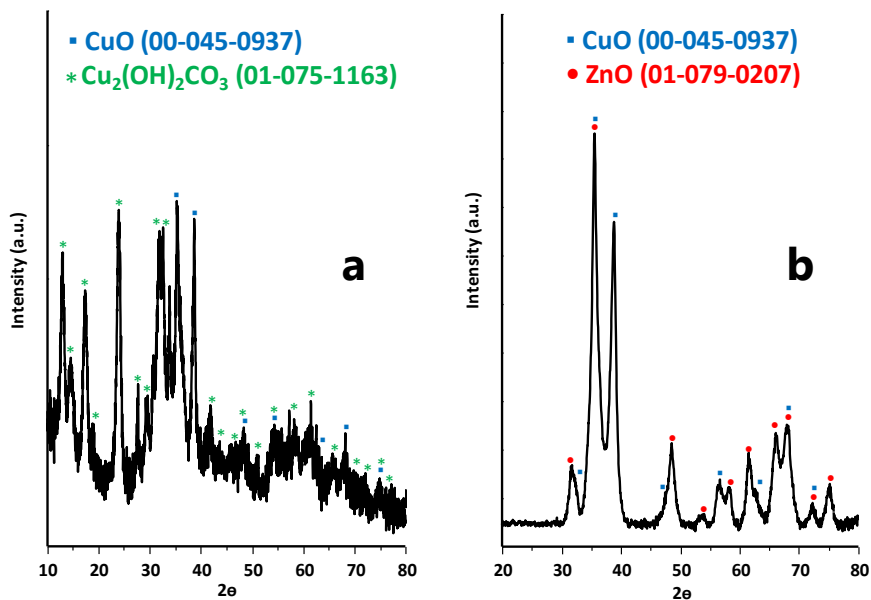
#### 3.5.1. Physico-chemical properties of calcined and reduced CZG catalysts

**Table 3.3** Main physico-chemical properties of studied catalysts.

Cat.	Composition (wt % ratio)			BET surf. m <sup>2</sup> /g <sub>cat</sub>	N <sub>2</sub> O-TPR-H <sub>2</sub>		P. size XRD (nm)
	Cu	Zn	Ga/Al		mL H <sub>2</sub> STP/g <sub>cat</sub>	mol <sub>Cu,s</sub> /g <sub>cat</sub>	
CZG-sp	69.0	25.0	6.0	52	29.2	2.385·10 <sup>-3</sup>	11
CZG-ox	70.5	23.5	6.0	20	15.5	1.269·10 <sup>-3</sup>	17
CZA	66.5	27.0	6.5	49	34.7	2.836·10 <sup>-3</sup>	9



**Figure 3.11** Temperature-programmed reduction (TPR) studies in 10% H<sub>2</sub>/Ar flow, for CZG and CZA catalytic samples.

*X-ray diffraction (XRD)*

**Figure 3.12** Diffractograms of as-prepared (a) and calcined (b) **CZG-sp** sample.

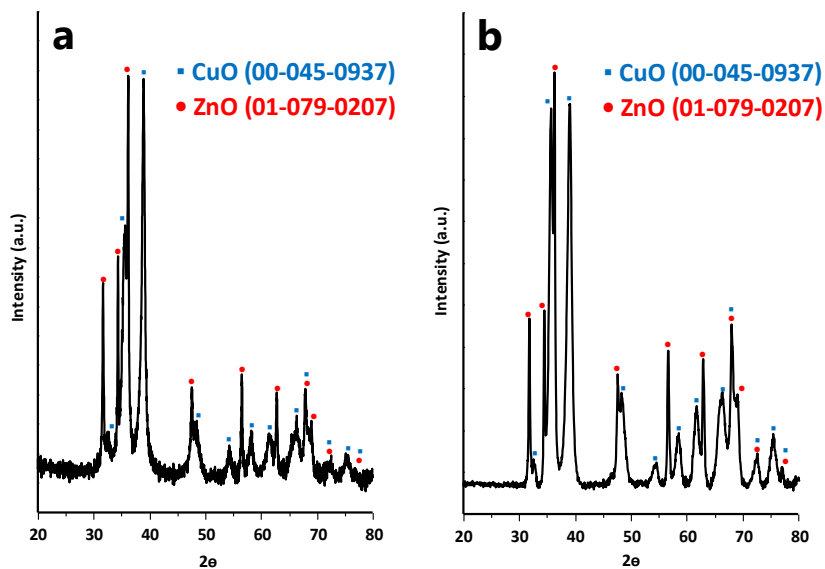


**Figure 3.13** Diffractograms of as-prepared (a) and calcined (b) **CZG-ox** sample.



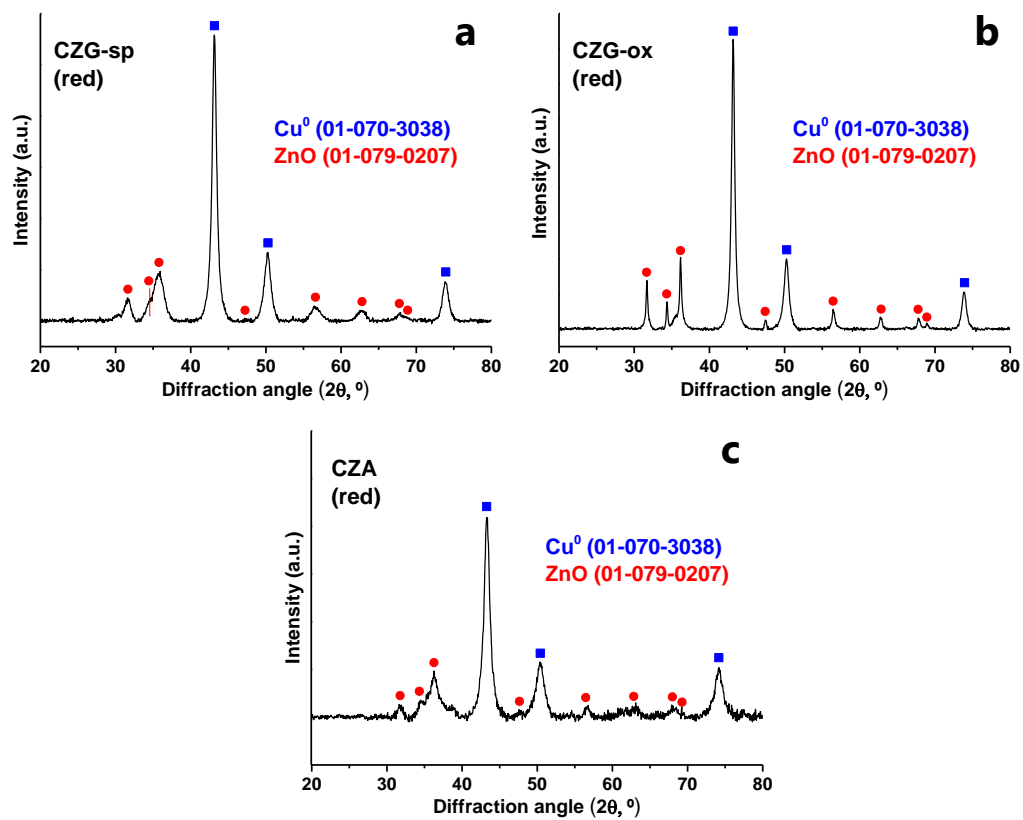
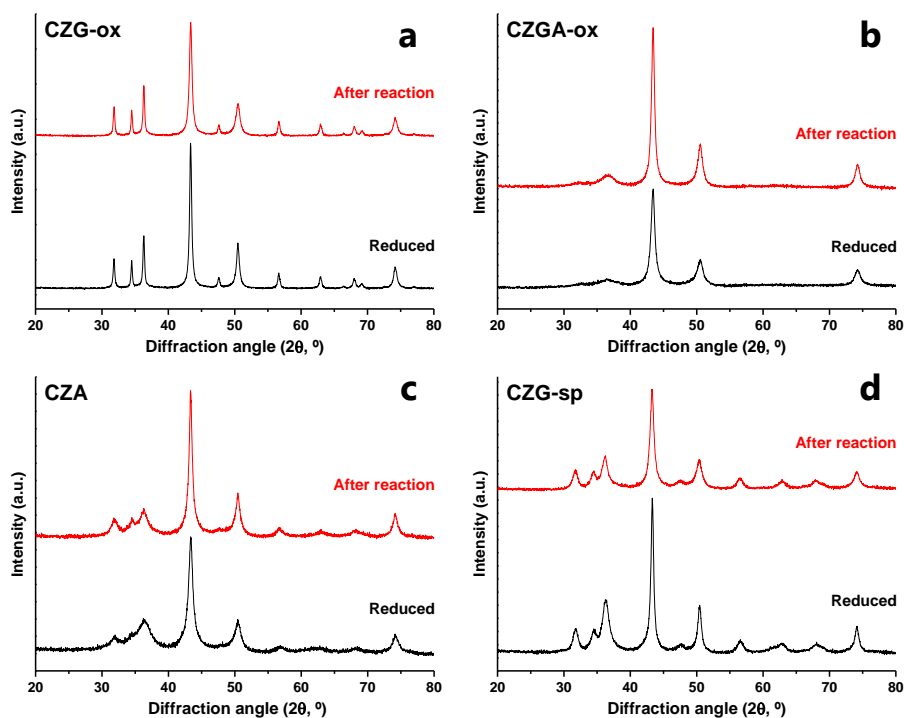


Figure 3.14 Diffractograms of reduced samples.



**Figure 3.15** Comparison between XRD patterns before (black) and after reaction (red).

**Table 3.4** Crystallite size of reduced and spent catalysts by XRD.

Catalyst	Treatment	Cu <sup>0</sup> cryst. size <sup>a</sup> (nm)
CZG-ox	Reduced	17
	After reaction	12
CZGA-ox	Reduced	8
	After reaction	10
CZG-sp	Reduced	11
	After reaction	7
CZA	Reduced	9
	After reaction	12

<sup>a</sup>Average Cu<sup>0</sup> crystallite size (JCPDS: 01-070-3038) was calculated from the main peaks (43.1, 50.2, 73.9; 2 $\theta$ ) using the Scherrer equation and assuming a shape factor  $k=0.9$ .

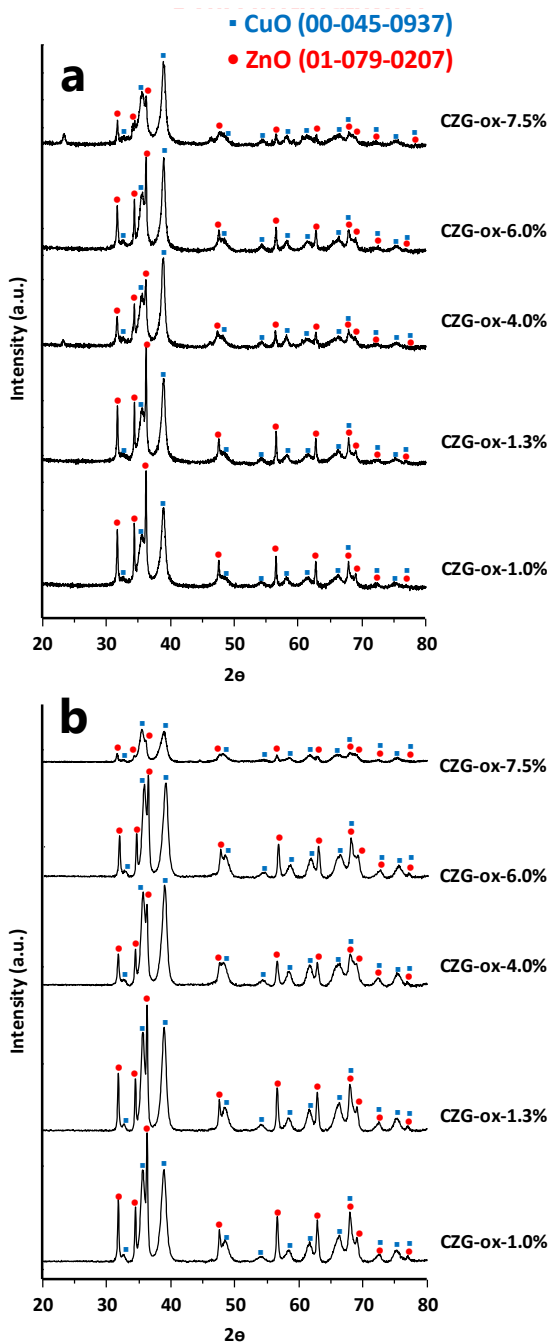


**Figure 3.16** Diffractograms of as-prepared (a) and calcined (b) CZG-ox samples at variable gallium loadings.

*XAS characterization on reduced samples*

Figure 3.17a shows the normalized XANES spectra at Cu K-edge of CZG-ox, CZG-sp and CZA measured at 200 °C during H<sub>2</sub> reduction, as well as those of Cu-based standards measured at room temperature. The absorption edge position (8979 eV) and shape of the spectra in all catalysts resemble those of Cu foil, indicating that the Cu atoms are involved in metallic domains, which is in good agreement with XRD and TEM results. More insights on the size of metallic copper nanoparticles can be obtained from EXAFS data (Figure 3.17b). As already observed in the XANES region, the catalysts spectra present the same features in the moduli of Fourier transform (see inset of Figure 3.17b for data in k-space), with a main contribution between 2-3 Å which is related to the Cu-Cu interatomic distances. Furthermore, the presence of a signal at a higher distance (3-6 Å) suggests a high degree of ordering of the copper nanoparticles. This statement is supported by the quantitative EXAFS results (Table 3.5), which shows Cu-Cu coordination numbers and distances typical of big nanoparticles. It is important to underline that the differences in the magnitude of the |FT| between the Cu foil and the samples are purely related to the increased Debye-Waller factor, as a consequence of the thermal disorder imposed by the reduction treatment (absent in the Cu standards).

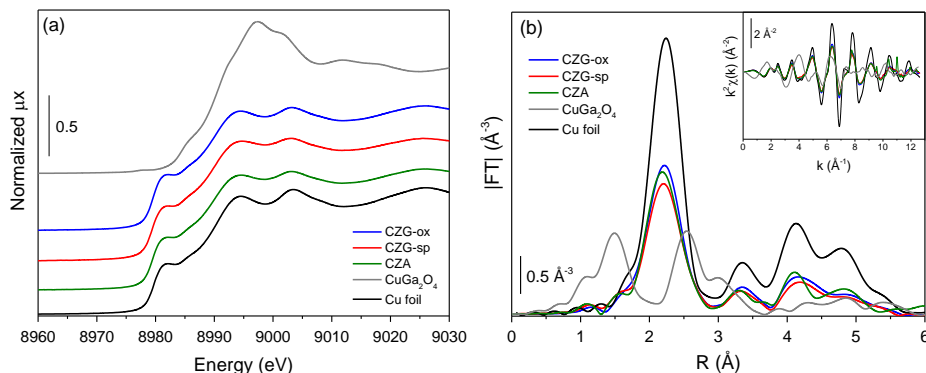


**Figure 3.17** Normalized XANES spectra at Cu K-edge (a) and, phase-uncorrected,  $k^2$ -weighted EXAFS spectra (b) of CZG catalysts and Cu-based references. Inset of (b) reports the corresponding  $k^2$ - $\chi(k)$  functions.

**Table 3.5** Summary of optimized parameters by fitting Cu K-edge EXAFS data of catalysts collected at 200 °C in H<sub>2</sub>.<sup>a</sup>

Sample	$N_{\text{Cu-Cu}}$	$R_{\text{Cu-Cu}}$ (Å)	$\sigma^2$ (Å <sup>2</sup> )	$\Delta E_0$ (eV)	$R_{\text{factor}}$
Cu foil	12	$2.539 \pm 0.002$	$0.0084 \pm 0.0002$	$4.0 \pm 0.3$	0.0034
CZG-ox	$10.3 \pm 0.5$	$2.536 \pm 0.002$	$0.0126 \pm 0.0006$		0.0074
CZG-sp	$10.2 \pm 0.5$	$2.535 \pm 0.003$	$0.0126 \pm 0.0008$		0.0052
CZA	$9.7 \pm 0.9$	$2.533 \pm 0.003$	$0.0125 \pm 0.0010$		0.0225

<sup>a</sup>Fits were performed on the first coordination shell ( $\Delta R=1.0$ - $3.0$  Å) over FT of the  $k^1k^2k^3$ -weighted  $\chi(k)$  functions performed in the  $\Delta k=2.6$ - $13.0$  Å<sup>-1</sup> interval.  $S_0^2=0.87$  from Cu foil (collected at RT).

Figure 3.18a shows the normalized XANES spectra at Zn K-edge of CZG samples, CZA and Zn-based standards. According to the position of the absorption edge (ca. 9662 eV) and the shape of XANES spectra, the Zn atoms in the bulk of CZG-ox, CZG-sp and CZA are involved in the same oxidation state and local environment, more specifically, as ZnO ensembles.

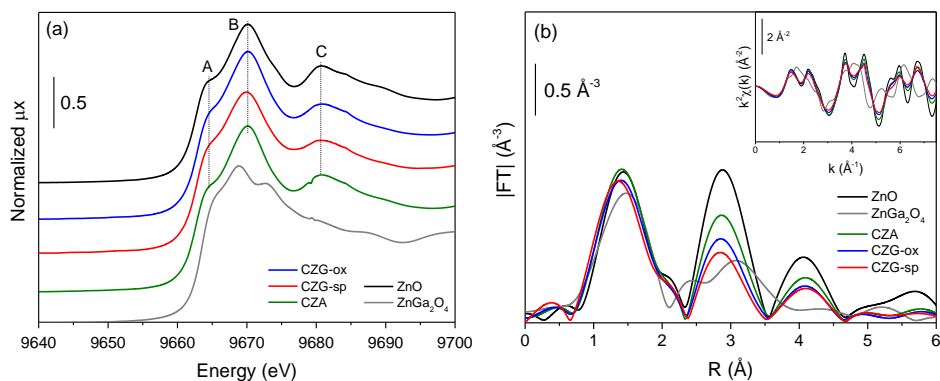


**Figure 3.18** Normalized XANES spectra at Zn K-edge (a) and, phase-uncorrected,  $k^2$ -weighted EXAFS spectra (b) of CZG catalysts and Zn-based references. Inset of (b) reports the  $k^2$ -weighted phase-uncorrected  $\chi(k)$  functions.

The three peaks marked as A, B and C are characteristic of electronic transitions  $1s \rightarrow 4p$  along the  $c$ ,  $a$ , and  $b$  axes of the ZnO hexagonal unit cell, respectively.<sup>[65]</sup> No features regarding the presence of ZnGa<sub>2</sub>O<sub>4</sub> spinel are observed, which if present, should be in small percent. The first feature on the absorption edge is less defined in the samples in comparison with ZnO standard, pointing towards a less crystalline character in the catalysts than in the bulk counterpart, which is typical of nanosized species. EXAFS spectra (Figure 3.18b) confirm this hypothesis once higher Zn coordination shells (at 2.9 and 4.0 Å, respectively) show lower intensities for the H<sub>2</sub>-reduced CZG and CZA samples in comparison with ZnO standard, while the first shell (typical of Zn tetrahedrally coordinated to four oxygen atoms) maintains similar intensities. Unfortunately, due to the limited  $k$ -space ( $2\text{--}8 \text{ \AA}^{-1}$ ) in this dataset (see inset of Figure 3.18b), a quantitative analysis of the EXAFS data was hindered and only a qualitative analysis of ZnO species can be given.

### Electrical properties

**Table 3.6** Metallic species identified in CZA and CZG reduced samples.

CZA	CZG-sp	CZG-ox
ZnO	ZnGa <sub>2</sub> O <sub>4</sub> spinel	Ga <sup>3+</sup> -ZnO doped
Al <sub>2</sub> O <sub>3</sub>	ZnO	ZnO
Cu	Cu	Cu

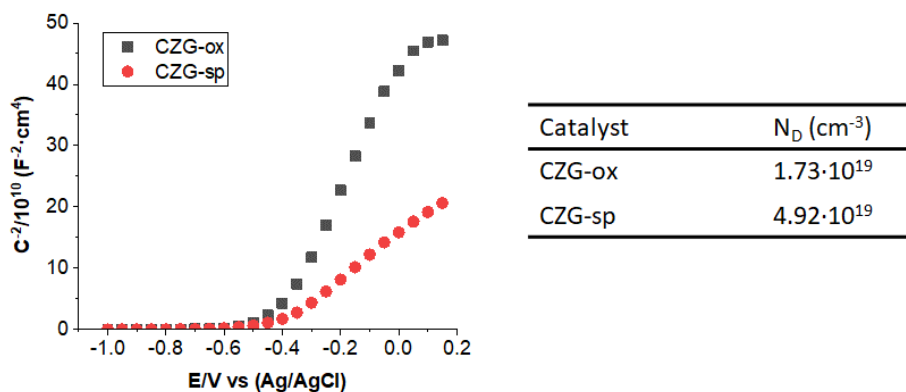


**Figure 3.19** Mott-Schottky plots and  $N_D$  values of the CZG-ox and CZG-sp catalysts.

Capacitance values were calculated from EIS data. Then, Mott-Schottky plots were constructed (Figure 3.19). The charge carrier density can be calculated from the slope of the Mott-Schottky plots according to the following equation:

$$\text{Slope} = \frac{2}{e \cdot \epsilon \cdot \epsilon_0 \cdot N_D} \quad \text{Eq. 3.1}$$

Where:  $e$  is the electron charge ( $1.6 \cdot 10^{-19}$  C);  $\epsilon$  is the dielectric constant of wurtzite ZnO;<sup>[66]</sup>  $\epsilon_0$  is the vacuum permittivity ( $8.85 \cdot 10^{-14}$  F/cm); and  $N_D$  is the donor density.

3.5.2. Catalytic activity in the CO<sub>2</sub> hydrogenation to methanol**Table 3.7** Extended catalytic results at constant WHSV (~31000 mL·g<sub>cat</sub><sup>-1</sup>·h<sup>-1</sup>) at 20 bar.

T (°C)	Cat.	X <sub>CO2</sub> (%)	CO <sub>2</sub> selectivity (%)			STY (mol <sub>prod</sub> ·g <sub>cat</sub> <sup>-1</sup> ·h <sup>-1</sup> )		STY <sub>2</sub> (mol <sub>prod</sub> ·[m <sup>2</sup> ·cat] <sup>-1</sup> ·h <sup>-1</sup> )	
			MeOH	CO	HCOOMe	MeOH	CO	MeOH	CO
180	CZA	2.9	94.8	4.3	0.9	8.78·10 <sup>-3</sup>	3.98·10 <sup>-4</sup>	1.79·10 <sup>-4</sup>	8.13·10 <sup>-6</sup>
	CZG-sp	3.6	95.9	3.2	0.9	1.08·10 <sup>-2</sup>	3.60·10 <sup>-4</sup>	2.08·10 <sup>-4</sup>	6.93·10 <sup>-6</sup>
	CZG-ox	2.4	97.0	2.0	1.0	7.46·10 <sup>-3</sup>	1.54·10 <sup>-4</sup>	3.73·10 <sup>-4</sup>	7.69·10 <sup>-6</sup>
200	CZA	5.6	89.5	10.1	0.4	1.60·10 <sup>-2</sup>	1.81·10 <sup>-3</sup>	3.27·10 <sup>-4</sup>	3.69·10 <sup>-5</sup>
	CZG-sp	6.2	91.7	7.9	0.4	1.78·10 <sup>-2</sup>	1.53·10 <sup>-3</sup>	3.42·10 <sup>-4</sup>	2.95·10 <sup>-5</sup>
	CZG-ox	4.9	94.6	4.9	0.5	1.48·10 <sup>-2</sup>	7.69·10 <sup>-4</sup>	7.42·10 <sup>-4</sup>	3.84·10 <sup>-5</sup>
220	CZA	10.0	79.9	19.9	0.2	2.55·10 <sup>-2</sup>	6.36·10 <sup>-3</sup>	5.21·10 <sup>-4</sup>	1.30·10 <sup>-4</sup>
	CZG-sp	10.5	84.0	15.8	0.2	2.76·10 <sup>-2</sup>	5.19·10 <sup>-3</sup>	5.30·10 <sup>-4</sup>	9.98·10 <sup>-5</sup>
	CZG-ox	9.0	89.0	10.8	0.2	2.57·10 <sup>-2</sup>	3.11·10 <sup>-3</sup>	1.28·10 <sup>-3</sup>	1.56·10 <sup>-4</sup>
240	CZA	15.9	63.8	36.1	0.1	3.24·10 <sup>-2</sup>	1.83·10 <sup>-2</sup>	6.61·10 <sup>-4</sup>	3.74·10 <sup>-4</sup>
	CZG-sp	15.2	67.4	32.5	0.1	3.20·10 <sup>-2</sup>	1.55·10 <sup>-2</sup>	6.16·10 <sup>-4</sup>	2.97·10 <sup>-4</sup>
	CZG-ox	12.5	79.8	20.1	0.1	3.19·10 <sup>-2</sup>	8.05·10 <sup>-3</sup>	1.60·10 <sup>-3</sup>	4.02·10 <sup>-4</sup>
260	CZA	20.9	45.3	54.7	0.0	3.02·10 <sup>-2</sup>	3.65·10 <sup>-2</sup>	6.17·10 <sup>-4</sup>	7.45·10 <sup>-4</sup>
	CZG-sp	21.1	51.3	48.7	0.0	3.38·10 <sup>-2</sup>	3.21·10 <sup>-2</sup>	6.51·10 <sup>-4</sup>	6.18·10 <sup>-4</sup>
	CZG-ox	15.3	65.0	34.9	0.1	3.18·10 <sup>-2</sup>	1.71·10 <sup>-2</sup>	1.59·10 <sup>-3</sup>	8.55·10 <sup>-4</sup>

**Table 3.8** Catalytic results at variable WHSV and 20 bar for the CZA sample.

T (°C)	W/F (mg·min·mL <sup>-1</sup> )	WHSV (mL·g <sub>cat</sub> <sup>-1</sup> ·h <sup>-1</sup> )	X <sub>CO2</sub> (%)	CO <sub>2</sub> selectivity (%)			STY (mol·g <sub>cat</sub> <sup>-1</sup> ·h <sup>-1</sup> )	
				MeOH	CO	HCOOMe	MeOH	CO
180	1.52	39430	3.0	95.3	3.5	1.2	1.15·10 <sup>-2</sup>	4.24·10 <sup>-4</sup>
	1.92	31216	2.9	94.8	4.3	0.9	8.77·10 <sup>-3</sup>	3.98·10 <sup>-4</sup>
	2.28	26287	3.7	94.8	4.2	1.0	9.43·10 <sup>-3</sup>	4.18·10 <sup>-4</sup>
200	0.45	134118	1.9	92.0	6.7	1.3	2.40·10 <sup>-2</sup>	1.75·10 <sup>-3</sup>
	0.90	66511	3.6	91.2	8.0	0.8	2.23·10 <sup>-2</sup>	1.96·10 <sup>-3</sup>
	1.52	39430	5.5	91.0	8.5	0.5	2.02·10 <sup>-2</sup>	1.89·10 <sup>-3</sup>
	1.92	31216	5.6	89.5	10.1	0.4	1.60·10 <sup>-2</sup>	1.81·10 <sup>-3</sup>
220	2.28	26287	6.7	89.4	10.2	0.4	1.61·10 <sup>-2</sup>	1.84·10 <sup>-3</sup>
	0.45	134118	3.7	87.1	12.2	0.7	4.42·10 <sup>-2</sup>	6.19·10 <sup>-3</sup>
	0.90	66511	5.7	82.2	17.4	0.4	3.19·10 <sup>-2</sup>	6.75·10 <sup>-3</sup>
	1.52	39430	9.6	82.1	17.7	0.2	3.18·10 <sup>-2</sup>	6.85·10 <sup>-3</sup>
	1.92	31216	10.0	79.9	19.9	0.2	2.55·10 <sup>-2</sup>	6.36·10 <sup>-3</sup>
240	2.28	26287	11.0	78.2	21.6	0.2	2.31·10 <sup>-2</sup>	6.39·10 <sup>-3</sup>
	0.45	134118	6.2	76.7	22.9	0.4	6.50·10 <sup>-2</sup>	1.95·10 <sup>-2</sup>
	0.90	66511	9.8	67.9	32.0	0.1	4.53·10 <sup>-2</sup>	2.13·10 <sup>-2</sup>
	1.52	39430	14.9	66.7	33.2	0.1	4.01·10 <sup>-2</sup>	2.00·10 <sup>-2</sup>
	1.92	31216	15.9	63.8	36.1	0.1	3.24·10 <sup>-2</sup>	1.83·10 <sup>-2</sup>
	2.28	26287	17.0	62.5	37.4	0.1	2.86·10 <sup>-2</sup>	1.71·10 <sup>-2</sup>
260	0.90	66511	15.4	49.0	51.0	0.0	5.13·10 <sup>-2</sup>	5.34·10 <sup>-2</sup>
	1.52	39430	20.3	47.6	52.4	0.0	3.90·10 <sup>-2</sup>	4.29·10 <sup>-2</sup>
	1.92	31216	20.9	45.3	54.7	0.0	3.02·10 <sup>-2</sup>	3.65·10 <sup>-2</sup>
	2.28	26287	21.7	44.9	55.1	0.0	2.62·10 <sup>-2</sup>	3.22·10 <sup>-2</sup>



**Table 3.9** Catalytic results at variable WHSV and 20 bar for the CZG-sp sample.

T (°C)	W/F (mg·min·mL <sup>-1</sup> )	WHSV (mL·g <sub>cat</sub> <sup>-1</sup> ·h <sup>-1</sup> )	X <sub>CO2</sub> (%)	CO <sub>2</sub> selectivity (%)			STY (mol·g <sub>cat</sub> <sup>-1</sup> ·h <sup>-1</sup> )	
				MeOH	CO	HCOOMe	MeOH	CO
180	0.99	60317	2.3	96.4	2.3	1.3	1.37·10 <sup>-2</sup>	3.26·10 <sup>-4</sup>
	1.62	36997	3.1	96.2	2.8	1.0	1.13·10 <sup>-2</sup>	3.29·10 <sup>-4</sup>
	1.96	30563	3.6	95.9	3.2	0.9	1.08·10 <sup>-2</sup>	3.60·10 <sup>-4</sup>
	2.49	24129	4.0	95.8	3.3	0.9	9.46·10 <sup>-3</sup>	3.26·10 <sup>-4</sup>
200	0.99	60317	4.2	93.8	5.5	0.7	2.43·10 <sup>-2</sup>	1.43·10 <sup>-3</sup>
	1.62	36997	5.6	92.6	6.9	0.5	1.96·10 <sup>-2</sup>	1.46·10 <sup>-3</sup>
	1.96	30563	6.2	91.7	7.9	0.4	1.78·10 <sup>-2</sup>	1.53·10 <sup>-3</sup>
	2.49	24129	6.9	91.3	8.3	0.4	1.56·10 <sup>-2</sup>	1.41·10 <sup>-3</sup>
220	0.99	60317	6.9	86.4	13.2	0.4	3.68·10 <sup>-2</sup>	5.62·10 <sup>-3</sup>
	1.62	36997	9.7	85.5	14.3	0.2	3.14·10 <sup>-2</sup>	5.25·10 <sup>-3</sup>
	1.96	30563	10.5	84.0	15.8	0.2	2.76·10 <sup>-2</sup>	5.19·10 <sup>-3</sup>
	2.49	24129	11.3	82.5	17.4	0.1	2.30·10 <sup>-2</sup>	4.85·10 <sup>-3</sup>
240	0.99	60317	10.8	74.6	25.3	0.1	4.97·10 <sup>-2</sup>	1.69·10 <sup>-2</sup>
	1.62	36997	14.0	70.7	29.2	0.1	3.75·10 <sup>-2</sup>	1.55·10 <sup>-2</sup>
	1.96	30563	15.2	67.4	32.5	0.1	3.20·10 <sup>-2</sup>	1.54·10 <sup>-2</sup>
	2.49	24129	16.5	65.8	34.1	0.1	2.68·10 <sup>-2</sup>	1.39·10 <sup>-2</sup>
260	0.99	60317	15.6	56.2	43.8	0.0	5.41·10 <sup>-2</sup>	4.22·10 <sup>-2</sup>
	1.62	36997	19.1	50.4	49.6	0.0	3.64·10 <sup>-2</sup>	3.59·10 <sup>-2</sup>
	1.96	30563	21.1	51.3	48.7	0.0	3.38·10 <sup>-2</sup>	3.21·10 <sup>-2</sup>
	2.49	24129	21.2	47.2	52.7	0.1	2.47·10 <sup>-2</sup>	2.76·10 <sup>-2</sup>

**Table 3.10** Catalytic results at variable WHSV and 20 bar for the CZG-ox sample.

T (°C)	W/F (mg·min·mL <sup>-1</sup> )	WHSV (mL·g <sub>cat</sub> <sup>-1</sup> ·h <sup>-1</sup> )	X <sub>CO2</sub> (%)	CO <sub>2</sub> selectivity (%)			STY (mol·g <sub>cat</sub> <sup>-1</sup> ·h <sup>-1</sup> )	
				MeOH	CO	HCOOMe	MeOH	CO
180	1.46	41186	1.8	97.2	1.6	1.2	7.37·10 <sup>-3</sup>	1.21·10 <sup>-4</sup>
	1.92	31301	2.4	97.0	2.0	1.0	7.46·10 <sup>-3</sup>	1.54·10 <sup>-4</sup>
	2.43	24712	4.2	95.0	4.4	0.6	1.01·10 <sup>-2</sup>	4.67·10 <sup>-4</sup>
200	1.46	41186	3.9	95.0	4.4	0.6	1.56·10 <sup>-2</sup>	7.23·10 <sup>-4</sup>
	1.92	31301	4.9	94.6	4.9	0.5	1.48·10 <sup>-2</sup>	7.69·10 <sup>-4</sup>
	2.43	24712	7.4	89.9	9.8	0.3	1.68·10 <sup>-2</sup>	1.83·10 <sup>-3</sup>
220	1.46	41186	6.9	90.6	9.1	0.3	2.63·10 <sup>-2</sup>	2.65·10 <sup>-3</sup>
	1.92	31301	9.0	89.0	10.8	0.2	2.57·10 <sup>-2</sup>	3.11·10 <sup>-3</sup>
	2.43	24712	11.6	80.1	19.8	0.1	2.35·10 <sup>-2</sup>	5.81·10 <sup>-3</sup>
240	1.46	41186	10.6	81.6	18.2	0.2	3.64·10 <sup>-2</sup>	8.13·10 <sup>-3</sup>
	1.70	35294	11.6	80.1	19.8	0.1	3.34·10 <sup>-2</sup>	7.91·10 <sup>-3</sup>
	1.92	31301	12.5	79.8	20.1	0.1	3.19·10 <sup>-2</sup>	8.05·10 <sup>-3</sup>
260	1.46	41186	14.2	71.4	28.5	0.1	3.91·10 <sup>-2</sup>	1.57·10 <sup>-2</sup>
	1.92	31301	15.3	65.0	34.9	0.1	3.18·10 <sup>-2</sup>	1.71·10 <sup>-2</sup>
	2.43	24712	14.9	70.0	29.9	0.1	2.43·10 <sup>-2</sup>	1.04·10 <sup>-2</sup>

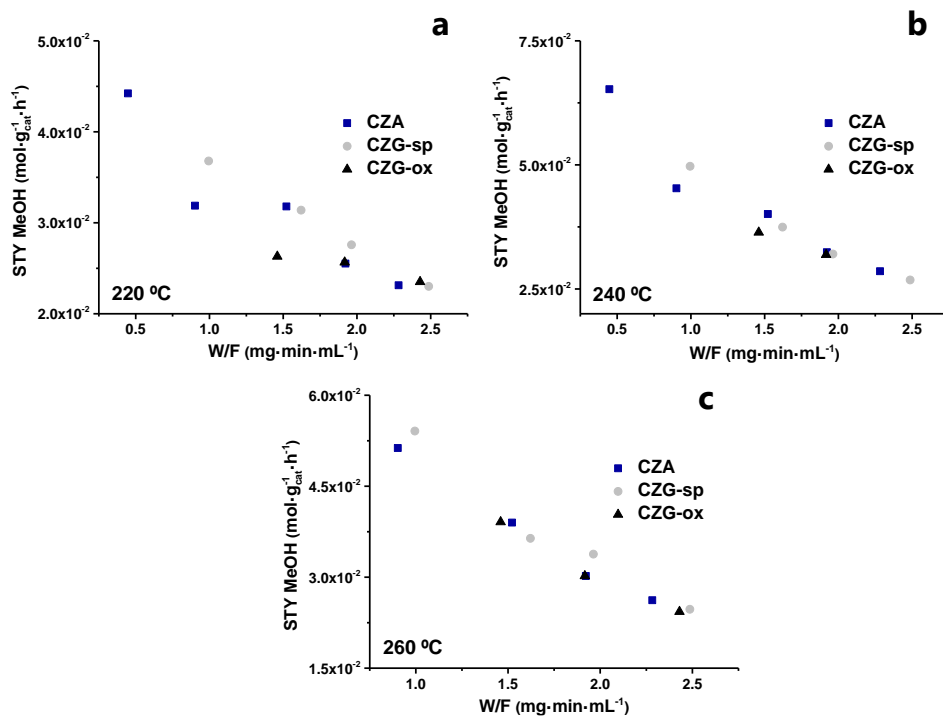


Figure 3.20 STY vs W/F at 220 °C (a) and 240 °C (b) for CZA and CZG systems.

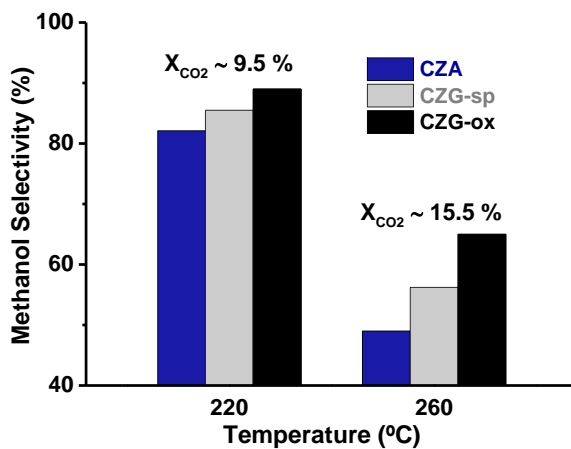


Figure 3.21 MeOH selectivity under iso-conversion conditions at 220 and 260 °C.

**Table 3.11** Analysis of the apparent activation energy ( $E_{a,app}$ ) (Arrhenius plot).

$E_{a,app}$ MeOH (kJ·mol <sup>-1</sup> ) <sup>a</sup>		$E_{a,app}$ CO (kJ·mol <sup>-1</sup> ) <sup>a</sup>	
<b>CZA</b>	49.0 ± 1.8	<b>CZA</b>	140.6 ± 1.1
<b>CZG-sp</b>	47.7 ± 3.4	<b>CZG-sp</b>	137.6 ± 4.9
<b>CZG-ox</b>	45.1 ± 2.6	<b>CZG-ox</b>	123.9 ± 3.5

<sup>a</sup>Apparent activation energy corresponding to MeOH and CO are an average of catalytic results obtained at different weight hourly space velocities (WHSV). In detail, the reaction conditions were the following: Temperature (160-240 °C); Pressure (20 bar); Ratio H<sub>2</sub>/CO<sub>2</sub> (3:1); WHSV (24000-134000 mL·g<sub>cat</sub><sup>-1</sup>·h<sup>-1</sup>).

The apparent activation energy values are of 45-49 kJ·mol<sup>-1</sup> for methanol, and of 123-140 kJ·mol<sup>-1</sup> for CO (Table 3.11), being in the range of those described in the literature.<sup>[16,17,67-69]</sup> Regardless of the small differences among the catalysts, the lowest values are notoriously obtained on CZG-ox sample. However, it is difficult to define any correlation, specifically taking into account that these values rely not only on the nature of the active sites but also on the reaction mechanism.

**Table 3.12** State of the art of Cu-based catalysts in the CO<sub>2</sub> hydrogenation to methanol.

Entry Fig. 3.22	Catalyst	Preparation	H <sub>2</sub> /CO <sub>2</sub> mol ratio	T (°C)	P (Bar)	GHSV or WHSV	Space Velocity <sup>a</sup>	X <sub>CO2</sub> (%)	S <sub>MeOH</sub> (%)	STY (mol <sub>MeOH</sub> ·g <sub>cat</sub> <sup>-1</sup> ·h <sup>-1</sup> )	TOF (s <sup>-1</sup> )	REF
-	CuZn@UiO-bpy	In situ reduction	3:1	250	40	G	18000	3.3	100	-	2.6·10 <sup>0</sup>	[70]
-	CuZnZr <b>Ga</b> Y	Co-precipitation	3:1	240	20	W	120000	5.0	-	-	2.0·10 <sup>-2</sup>	[8]
1	Cu-ZnO-ZrO <sub>2</sub>	Reverse co-precip.	3:1	240	50	W	55000	9.7	62	3.8·10 <sup>-2</sup>	-	[71]
<b>2</b>	<b>CZA</b>	<b>Co-precipitation</b>	<b>3:1</b>	<b>240</b>	<b>20</b>	<b>W</b>	<b>31200</b>	<b>15.9</b>	<b>63.8</b>	<b>3.24·10<sup>-2</sup></b>	<b>3.23·10<sup>-3</sup></b>	<b>Our work</b>
<b>3</b>	<b>CZG-sp</b>	<b>Co-precipitation</b>	<b>3:1</b>	<b>240</b>	<b>20</b>	<b>W</b>	<b>30500</b>	<b>15.2</b>	<b>67.4</b>	<b>3.20·10<sup>-2</sup></b>	<b>3.73·10<sup>-3</sup></b>	<b>Our work</b>
<b>4</b>	<b>CZG-ox</b>	<b>Co-precipitation</b>	<b>3:1</b>	<b>240</b>	<b>20</b>	<b>W</b>	<b>31300</b>	<b>12.5</b>	<b>79.8</b>	<b>3.19·10<sup>-2</sup></b>	<b>6.99·10<sup>-3</sup></b>	<b>Our work</b>
5	<b>Ga</b> -Cu-ZnO-ZrO <sub>2</sub>	Co-precipitation	3:1	250	70	W	15000	22	72	2.2·10 <sup>-2</sup>	-	[16]
6	Cu/ZnO/Al <sub>2</sub> O <sub>3</sub>	Co-precipitation	3:1	250	50	W	18000	19.7	48.1	2.0·10 <sup>-2</sup>	-	[72]
7	CuZnLDH30 <b>Ga</b>	AMOST <sup>b</sup>	3:1	270	45	W	18000	18.8	47.8	1.8·10 <sup>-2</sup>	-	[10]
8	CuZnZr <b>Ga</b> Y	Co-precipitation	3:1	240	20	W	30000	-	-	1.7·10 <sup>-2</sup>	-	[8]
9	Cu/Zn/Al/Y	Co-precipitation	3:1	250	50	W	12000	26.9	52.4	1.6·10 <sup>-2</sup>	-	[73]
-	Cu/ZnO/ZrO <sub>2</sub> / <b>Ga</b> <sub>2</sub> O <sub>3</sub>	Citric complexing	3:1	250	80	G	3300	-	70	1.2·10 <sup>-2</sup>	-	[47]
10	Cu/ <b>Ga</b> /ZnO	Co-impregnation	3:1	270	20	W	18000	6.0	88.0	1.2·10 <sup>-2</sup>	-	[13]
-	Cu/ZrO <sub>2</sub>	Depos.+Co-precip.	3:1	240	20	G	5400	6.3	48.8	1.1·10 <sup>-2</sup>	-	[74]
11	Cu/Zn/ <b>Ga</b> /hydrophobic SiO <sub>2</sub>	Co-impregnation	3:1	270	20	W	18000	5.6	99.5	1.1·10 <sup>-2</sup>	-	[14]
-	Cu/ZnO/ZrO <sub>2</sub> / <b>Ga</b> <sub>2</sub> O <sub>3</sub>	Co-precipitation	3:1	250	80	G	3300	-	75	1.0·10 <sup>-2</sup>	-	[47]
12	Cu <sub>11</sub> In <sub>9</sub> -In <sub>2</sub> O <sub>3</sub>	Co-precipitation	3:1	280	30	W	7500	11.4	80.5	6.1·10 <sup>-3</sup>	-	[75]
13	M-CZZ (16)	Co-precipitation	3:1	240	30	W	6000	9.7	91.4	5.4·10 <sup>-3</sup>	2.1·10 <sup>-2</sup>	[40]
-	Cu/ <b>Ga</b> <sub>2</sub> O <sub>3</sub> /NC ZrO <sub>2</sub>	Depos.+Co-precip.	3:1	250	20	G	2500	13.7	75.6	1.9·10 <sup>-3</sup>	-	[76]

<sup>a</sup>GHSV is expressed in h<sup>-1</sup>; WHSV is expressed in mL·g<sub>cat</sub><sup>-1</sup>·h<sup>-1</sup>. <sup>b</sup>Aqueous miscible organic solvent treatment.

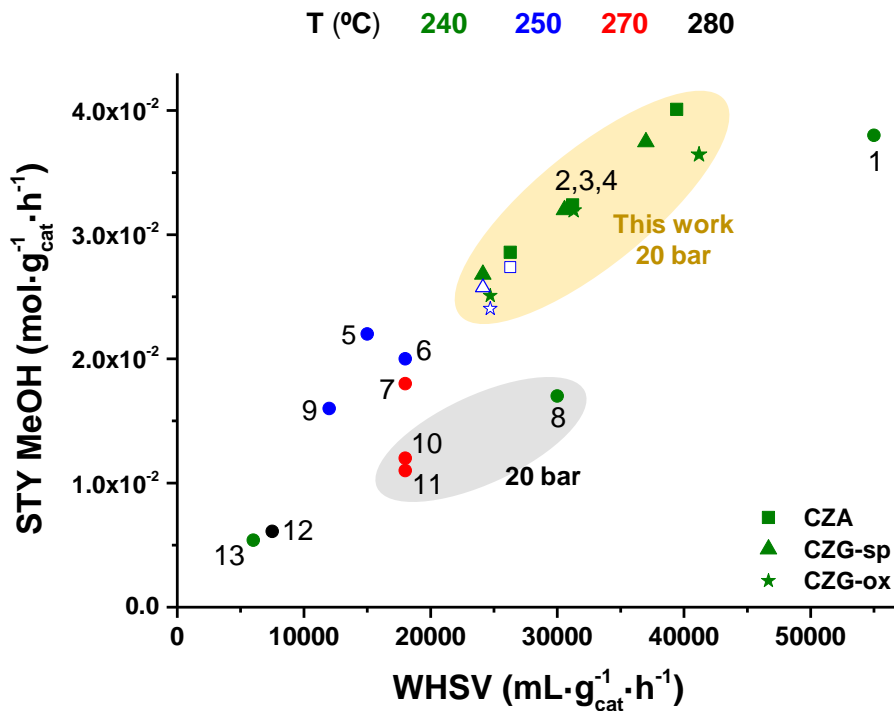


**Figure 3.22** Comparison of the catalytic performance of studied CZG and CZA samples at different temperatures in the CO<sub>2</sub> hydrogenation to methanol with other Cu-based catalysts in the literature. Numbers refer to the entries placed at Table 3.12 (first column).

Points located within the yellowish area correspond to CZG and CZA systems at selected WHSVs and 20 bar (see Tables 3.8-3.10). The gray area corresponds to literature values at 20 bar (i.e., operational pressure used in this work). Generally, literature catalysts operate at higher pressures (30-80 bar). Unfilled blue symbols are interpolated points for our catalytic samples at 250 °C, included for comparative purposes.

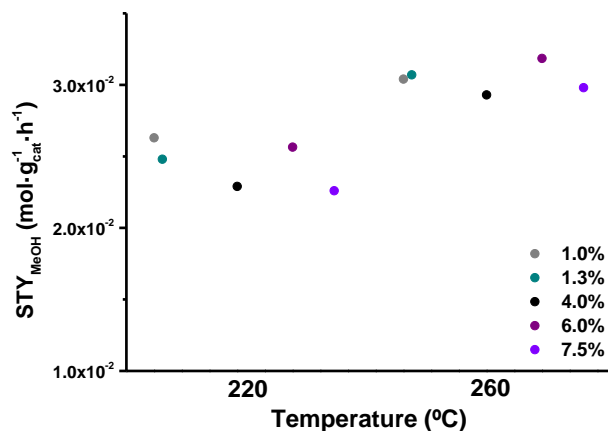


**Figure 3.23** STY at 220 and 260 °C in CZG-ox samples at different levels of Ga doping.

**Table 3.13** Catalytic performance of CZG-ox series at different levels of Ga doping.

T (°C)	Ga wt % ratio	X <sub>CO<sub>2</sub></sub> (%)	CO <sub>2</sub> selectivity (%)			STY (mol·g <sub>cat</sub> <sup>-1</sup> ·h <sup>-1</sup> )		Intrinsic act. MeOH (mol·mol <sub>Cu<sub>2</sub>S</sub> <sup>-1</sup> ·s <sup>-1</sup> )
			MeOH	CO	HCOOMe	MeOH	CO	
180	1.0	2.3	96.7	2.4	0.9	7.38·10 <sup>-3</sup>	1.42·10 <sup>-4</sup>	1.23·10 <sup>-3</sup>
	1.3	1.8	97.4	1.7	0.9	5.83·10 <sup>-3</sup>	7.90·10 <sup>-5</sup>	1.00·10 <sup>-3</sup>
	4.0	2.1	96.7	2.5	0.8	6.75·10 <sup>-3</sup>	1.35·10 <sup>-4</sup>	1.25·10 <sup>-3</sup>
	6.0	2.4	97.0	2.0	1.0	7.46·10 <sup>-3</sup>	1.54·10 <sup>-4</sup>	1.63·10 <sup>-3</sup>
	7.0	2.3	96.5	2.6	0.9	6.47·10 <sup>-3</sup>	1.74·10 <sup>-4</sup>	1.15·10 <sup>-3</sup>
200	1.0	4.7	94.2	5.3	0.5	1.47·10 <sup>-2</sup>	7.51·10 <sup>-4</sup>	2.42·10 <sup>-3</sup>
	1.3	4.2	94.7	4.8	0.5	1.32·10 <sup>-2</sup>	6.10·10 <sup>-4</sup>	2.24·10 <sup>-3</sup>
	4.0	4.3	94.2	5.3	0.5	1.35·10 <sup>-2</sup>	6.89·10 <sup>-4</sup>	2.48·10 <sup>-3</sup>
	6.0	4.9	94.6	4.9	0.5	1.48·10 <sup>-2</sup>	7.69·10 <sup>-4</sup>	3.25·10 <sup>-3</sup>
	7.0	4.7	94.1	5.4	0.5	1.30·10 <sup>-2</sup>	7.40·10 <sup>-4</sup>	2.28·10 <sup>-3</sup>
220	1.0	9.0	88.4	11.4	0.2	2.63·10 <sup>-2</sup>	3.04·10 <sup>-3</sup>	4.35·10 <sup>-3</sup>
	1.3	8.4	89.3	10.5	0.2	2.48·10 <sup>-2</sup>	2.62·10 <sup>-3</sup>	4.23·10 <sup>-3</sup>
	4.0	7.9	87.8	12.0	0.2	2.29·10 <sup>-2</sup>	2.81·10 <sup>-3</sup>	4.24·10 <sup>-3</sup>
	6.0	9.0	89.0	10.8	0.2	2.57·10 <sup>-2</sup>	3.11·10 <sup>-3</sup>	5.61·10 <sup>-3</sup>
	7.0	8.8	87.9	11.9	0.2	2.26·10 <sup>-2</sup>	3.05·10 <sup>-3</sup>	3.99·10 <sup>-3</sup>
240	1.0	11.6	79.0	20.9	0.1	3.13·10 <sup>-2</sup>	7.83·10 <sup>-3</sup>	5.19·10 <sup>-3</sup>
	1.3	11.3	80.5	19.4	0.1	3.12·10 <sup>-2</sup>	7.12·10 <sup>-3</sup>	5.31·10 <sup>-3</sup>
	4.0	10.7	79.4	20.5	0.1	2.91·10 <sup>-2</sup>	7.10·10 <sup>-3</sup>	5.38·10 <sup>-3</sup>
	6.0	12.5	79.8	20.1	0.1	3.19·10 <sup>-2</sup>	8.05·10 <sup>-3</sup>	6.99·10 <sup>-3</sup>
	7.0	11.8	78.9	21.0	0.1	2.71·10 <sup>-2</sup>	7.23·10 <sup>-3</sup>	4.81·10 <sup>-3</sup>
260	1.0	15.5	63.4	36.5	0.1	3.04·10 <sup>-2</sup>	1.72·10 <sup>-2</sup>	5.05·10 <sup>-3</sup>
	1.3	15.0	66.0	33.9	0.1	3.07·10 <sup>-2</sup>	1.55·10 <sup>-2</sup>	5.24·10 <sup>-3</sup>
	4.0	14.4	65.6	34.3	0.1	2.93·10 <sup>-2</sup>	1.51·10 <sup>-2</sup>	5.42·10 <sup>-3</sup>
	6.0	15.3	65.0	34.9	0.1	3.18·10 <sup>-2</sup>	1.71·10 <sup>-2</sup>	6.97·10 <sup>-3</sup>
	7.0	15.8	64.6	35.3	0.1	2.98·10 <sup>-2</sup>	1.63·10 <sup>-2</sup>	5.27·10 <sup>-3</sup>

### 3.5.3. Determination of catalytic sites involved in MeOH synthesis

(NAP)-XPS

**Table 3.14** BE (eV) of the Cu 2p<sub>3/2</sub>, Zn 2p<sub>3/2</sub> and Ga 2p<sub>3/2</sub> core levels of **CZG-sp** sample under different conditions.

Treatment	KE (eV)	Depth (nm)	Cu 2p <sub>3/2</sub> <sup>a</sup>	Zn 2p <sub>3/2</sub> <sup>a</sup>	Ga 2p <sub>3/2</sub> <sup>a</sup>
<b>H<sub>2</sub></b>	174	2.0	-	1021.7	-
	267	2.5	932.2	1021.6	1117.7
	362	3.0	-	-	-
	459	3.5	932.1	-	1117.7
	623	4.3	932.2	1021.6	-
<b>CO<sub>2</sub>+H<sub>2</sub> 220 °C 5 h</b>	174	2.0	-	1021.8	1118.1
	267	2.5	932.2	1021.9	1117.9
	362	3.0	932.2	-	-
	459	3.5	932.1	-	1118.1
	623	4.3	932.3	1021.9	-
<b>CO<sub>2</sub>+H<sub>2</sub> 280 °C 4 h</b>	174	2.0	-	1021.9	1118.1
	267	2.5	932.3	1021.8	1118.0
	362	3.0	932.3	-	-
	459	3.5	932.1	-	1118.0
	623	4.3	932.2	1021.8	-

<sup>a</sup>All BE are corrected to the fermi level.

**Table 3.15** BE (eV) of the Cu 2p<sub>3/2</sub>, Zn 2p<sub>3/2</sub> and Ga 2p<sub>3/2</sub> core levels of **CZG-ox** sample under different conditions.

Treatment	KE (eV)	Depth (nm)	Cu 2p <sub>3/2</sub> <sup>a</sup>	Zn 2p <sub>3/2</sub> <sup>a</sup>	Ga 2p <sub>3/2</sub> <sup>a</sup>
<b>H<sub>2</sub></b>	174	2.0	-	1021.7	1118.0
	267	2.5	932.1	1021.8	1118.0
	362	3.0	-	-	-
	459	3.5	932.2	-	1118.8
	623	4.3	932.2	1021.8	-
<b>CO<sub>2</sub>+H<sub>2</sub> 220 °C 7 h</b>	174	2.0	-	1021.9	1118.0
	267	2.5	932.2	1021.8	1118.0
	362	3.0	932.1	-	-
	459	3.5	932.3	-	1118.0
	623	4.3	932.2	1021.9	-
<b>CO<sub>2</sub>+H<sub>2</sub> 280 °C 3 h</b>	174	2.0	-	1021.9	1118.0
	267	2.5	932.2	1021.8	1118.1
	362	3.0	932.1	-	-
	459	3.5	932.3	-	1118.0
	623	4.3	932.1	1021.9	-

<sup>a</sup>All BE are corrected to the fermi level.



**Table 3.16** BE (eV) of the Cu 2p<sub>3/2</sub> and Zn 2p<sub>3/2</sub> core levels of **CZA** sample under different conditions.

Treatment	KE (eV)	Depth (nm)	Cu 2p <sub>3/2</sub> <sup>a</sup>	Zn 2p <sub>3/2</sub> <sup>a</sup>
<b>H<sub>2</sub></b>	174	2.0	-	1021.9
	267	2.5	932.2	1022.1
	362	3.0	932.2	-
	459	3.5	-	-
	623	4.3	932.2	1021.9
<b>CO<sub>2</sub>+H<sub>2</sub> 220 °C</b>	174	2.0	-	1021.9
	267	2.5	932.3	1022.0
	362	3.0	932.2	-
	459	3.5	932.3	-
	623	4.3	932.2	1021.9
<b>CO<sub>2</sub>+H<sub>2</sub> 280 °C</b>	174	2.0	-	1021.8
	267	2.5	932.1	1021.8
	362	3.0	-	-
	459	3.5	-	-
	623	4.3	932.2	1021.8

<sup>a</sup>All BE are corrected to the fermi level.

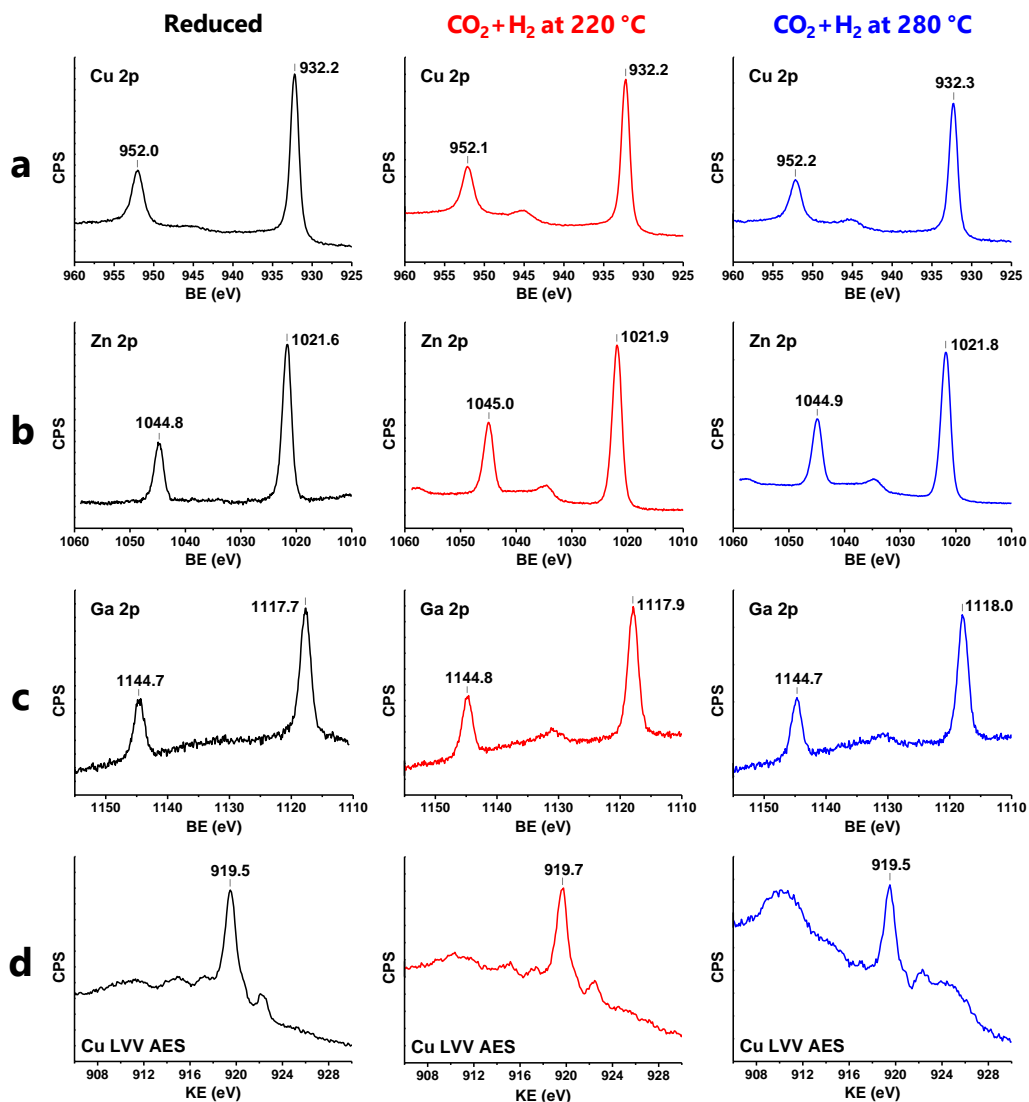


**Figure 3.24** (NAP)-XPS spectra of **CZG-sp** catalyst acquired at different reaction conditions. Core lines of Cu 2p (a), Zn 2p (b), Ga 2p (c) at KE=268 eV and Cu LVV AES (d) at  $h\nu=1290$  eV are shown.

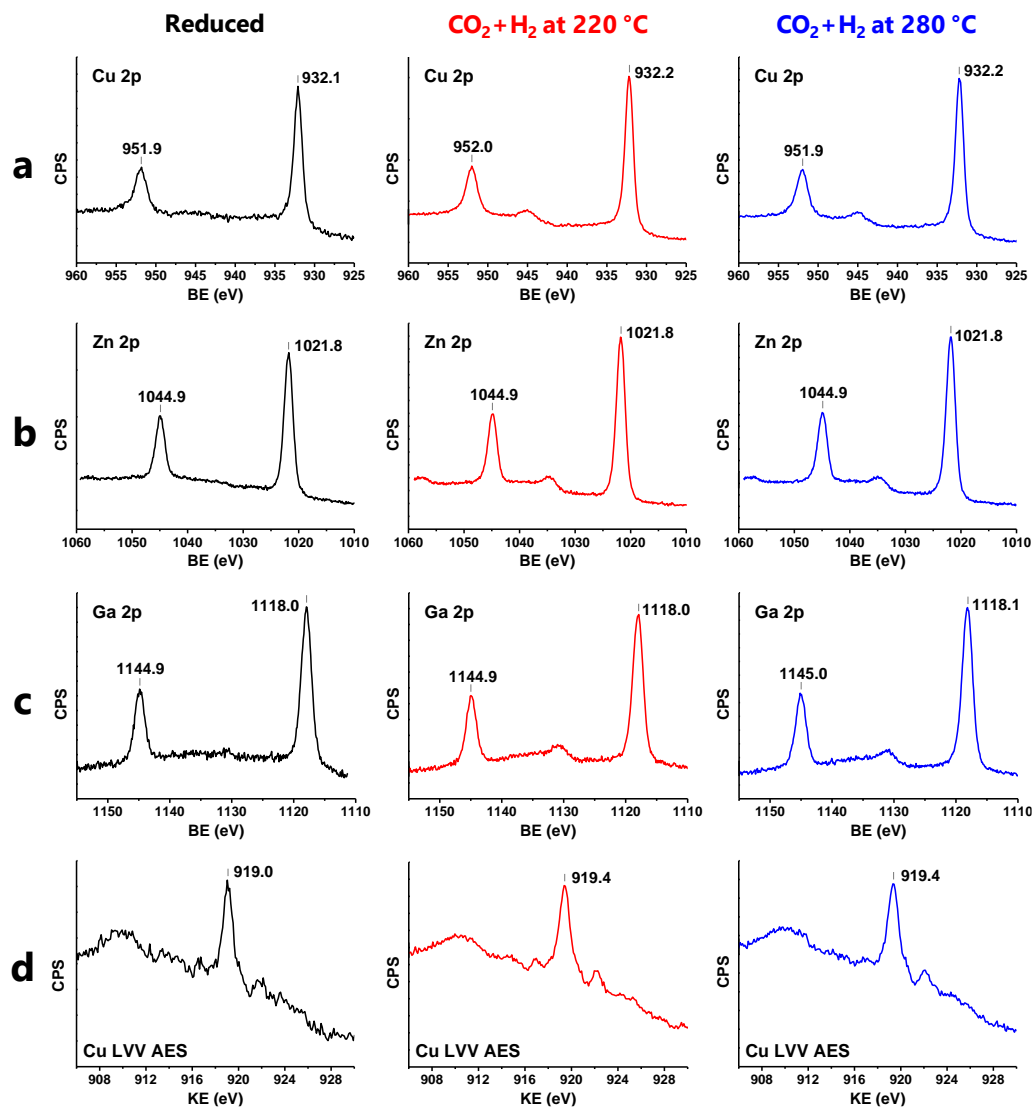


**Figure 3.25** (NAP)-XPS spectra of **CZG-ox** catalyst acquired at different reaction conditions. Core lines of Cu 2p (a), Zn 2p (b), Ga 2p (c) at KE=268 eV and Cu LVV AES (d) at  $h\nu=1290$  eV are shown.

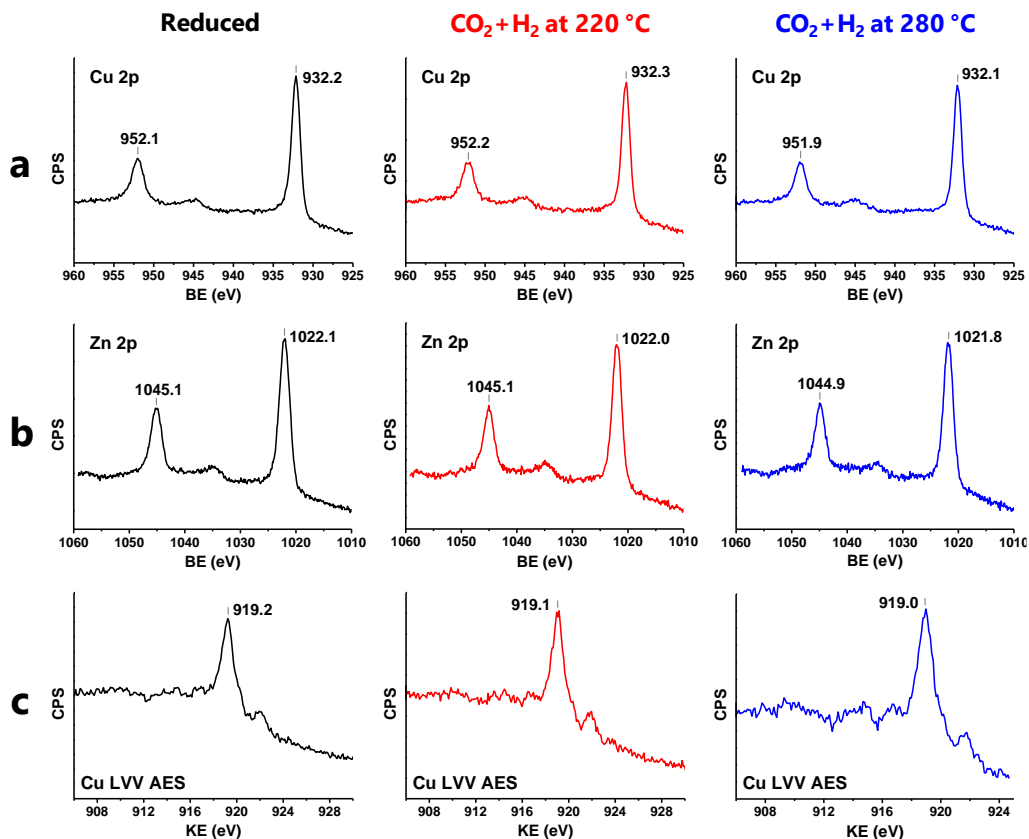


**Figure 3.26** (NAP)-XPS spectra of **CZA** catalyst acquired at different reaction conditions. Core lines of Cu 2p (a) and Zn 2p (b) at KE=268 eV and Cu LVV AES (c) at  $h\nu=1290$  eV are shown.

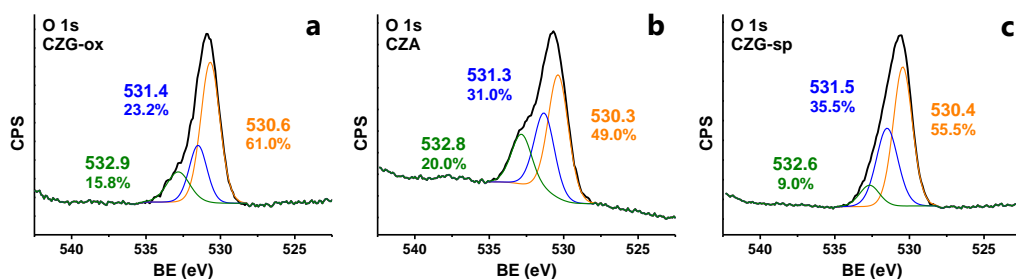


**Figure 3.27** Deconvoluted spectra of the O 1s core level under CO<sub>2</sub>+H<sub>2</sub> reaction at 220 °C on CZG-ox (a), CZA (b), and CZG-sp (c) samples.

**Table 3.17** Deconvolution of O 1s core level under different gaseous conditions.

Sample	H <sub>2</sub> reduced			CO <sub>2</sub> +H <sub>2</sub> at 220 °C			CO <sub>2</sub> +H <sub>2</sub> at 280 °C		
	530.6 62.5%	531.7 22.8%	532.9 14.7%	530.6 61.0%	531.4 23.2%	532.9 15.8%	530.6 65.3%	531.2 22.9%	532.9 11.8%
CZG-ox	530.6	531.7	532.9	530.6	531.4	532.9	530.6	531.2	532.9
	62.5%	22.8%	14.7%	61.0%	23.2%	15.8%	65.3%	22.9%	11.8%
CZA	530.5	531.3	532.6	530.3	531.3	532.8	530.3	531.1	532.8
	51.4%	37.8%	10.8%	49.0%	31.0%	20.0%	46.9%	34.0%	19.1%
CZG-sp	-	-	-	530.4	531.5	532.6	530.3	531.5	532.2
				55.5%	35.5%	9.0%	64.6%	27.6%	7.8%

**Table 3.18** Chemical composition of **CZG-sp** catalyst at different sampling depth and under different conditions (ICP at % ratio: Cu:Zn:Ga = 70.0/24.5/5.5).

Treatment	KE (eV)	Depth (nm)	% mol		
			Cu	Zn	Ga
H <sub>2</sub>	268	2.5	44.2	46.6	9.2
	358	2.9	46.1	44.8	9.1
	467	3.5	49.4	42.3	8.3
CO <sub>2</sub> +H <sub>2</sub> 220 °C 5 h	268	2.5	29.0	61.2	9.8
	358	2.9	31.4	59.3	9.3
	467	3.5	36.0	55.9	8.1
CO <sub>2</sub> +H <sub>2</sub> 280 °C 4 h	268	2.5	14.5	78.8	6.7
	358	2.9	15.0	78.6	6.4
	467	3.5	19.4	75.2	5.4

**Table 3.19** Chemical composition of **CZG-ox** catalyst at different sampling depth and under different conditions (ICP at % ratio: Cu:Zn:Ga = 71.5/23.0/5.5).

Treatment	KE (eV)	Depth (nm)	% mol		
			Cu	Zn	Ga
H <sub>2</sub>	268	2.5	22.4	58.0	19.6
	358	2.9	23.8	57.0	19.2
	467	3.5	26.4	55.6	18.0
CO <sub>2</sub> +H <sub>2</sub> 220 °C 7 h	268	2.5	23.0	56.3	20.7
	358	2.9	25.6	54.6	19.8
	467	3.5	28.4	53.1	18.5
CO <sub>2</sub> +H <sub>2</sub> 280 °C 3 h	268	2.5	18.5	58.4	23.1
	358	2.9	21.4	56.7	21.9
	467	3.5	26.0	54.4	19.6

**Table 3.20** Chemical composition of **CZA** catalyst at different sampling depth and under different conditions (ICP at % ratio: Cu:Zn = 71.7/28.3).

Treatment	KE (eV)	Depth (nm)	% mol	
			Cu	Zn
H <sub>2</sub>	267	2.5	43.4	56.6
	362	3.0	48.5	51.5
	454	3.4	49.5	50.5
CO <sub>2</sub> +H <sub>2</sub> 220 °C	267	2.5	47.0	53.0
	362	3.0	45.7	54.3
	454	3.4	49.5	50.5
CO <sub>2</sub> +H <sub>2</sub> 280 °C	267	2.5	47.1	52.9

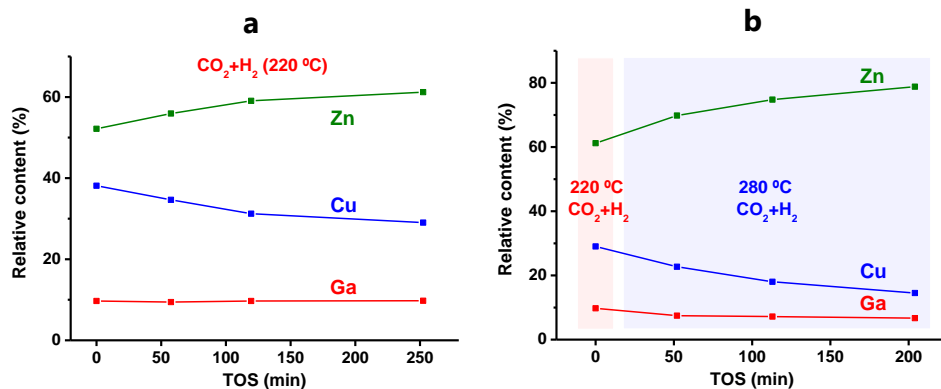


**Figure 3.28** Time-dependent dynamic surface migration under reaction conditions on the reduced **CZG-sp** sample at 220 °C (a) and 280 °C (b) acquired at a depth of 2.5 nm (268 eV KE).

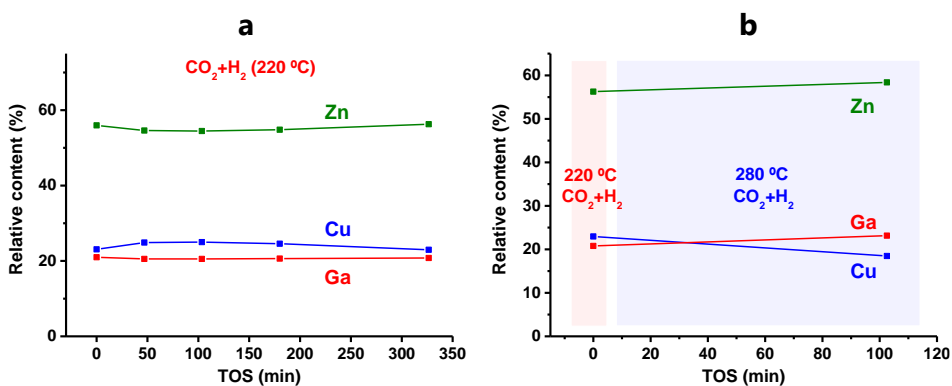


**Figure 3.29** Time-dependent dynamic surface migration under reaction conditions on the reduced **CZG-ox** sample at 220 °C (a) and 280 °C (b) acquired at a depth of 2.5 nm (268 eV KE).

**Table 3.21** Influence of pressure in the CO<sub>2</sub> hydrogenation to methanol. Comparison between 1 and 20 bar at the same temperature.

P (bar)	T (°C)	Cat.	X <sub>CO<sub>2</sub></sub> (%)	CO <sub>2</sub> selectivity (%)			STY (mol·g <sub>cat</sub> <sup>-1</sup> ·h <sup>-1</sup> )		STY <sub>2</sub> (mol·[m <sup>2</sup> <sub>cat</sub> ] <sup>-1</sup> ·h <sup>-1</sup> )	
				MeOH	CO	HCOOMe	MeOH	CO	MeOH	CO
20 <sup>a</sup>	220	CZA	10.0	79.9	19.9	0.2	2.55·10 <sup>-2</sup>	6.36·10 <sup>-3</sup>	5.20·10 <sup>-4</sup>	1.30·10 <sup>-4</sup>
		CZG-sp	10.5	84.0	15.8	0.2	2.76·10 <sup>-2</sup>	5.19·10 <sup>-3</sup>	5.31·10 <sup>-4</sup>	9.98·10 <sup>-5</sup>
		CZG-ox	9.0	89.0	10.8	0.2	2.57·10 <sup>-2</sup>	3.11·10 <sup>-3</sup>	1.29·10 <sup>-3</sup>	1.56·10 <sup>-4</sup>
1 <sup>b</sup>	220	CZA	1.7	39.9	60.1	-	2.45·10 <sup>-3</sup>	3.70·10 <sup>-3</sup>	5.00·10 <sup>-5</sup>	7.55·10 <sup>-5</sup>
		CZG-sp	2.1	38.9	61.1	-	2.83·10 <sup>-3</sup>	4.44·10 <sup>-3</sup>	5.44·10 <sup>-5</sup>	8.54·10 <sup>-5</sup>
		CZG-ox	1.2	65.0	35.0	-	2.74·10 <sup>-3</sup>	1.47·10 <sup>-3</sup>	1.37·10 <sup>-4</sup>	7.35·10 <sup>-5</sup>

Reaction conditions: <sup>a</sup>n(CO<sub>2</sub>):n(H<sub>2</sub>)=1:3, 31000 mL·g<sub>cat</sub><sup>-1</sup>·h<sup>-1</sup>; <sup>b</sup>n(CO<sub>2</sub>):n(H<sub>2</sub>)=1:3, 33700 mL·g<sub>cat</sub><sup>-1</sup>·h<sup>-1</sup>.

As observed in Table 3.21, CZG-ox catalyst is slightly less active than CZG-sp and CZG samples at 1 and 20 bar. At both pressure ranges, CZG-ox is more selective to methanol than the other catalysts. Finally, STY to MeOH per square meter of catalyst is higher in the CZG-ox sample at atmospheric pressure and at 20 bar.

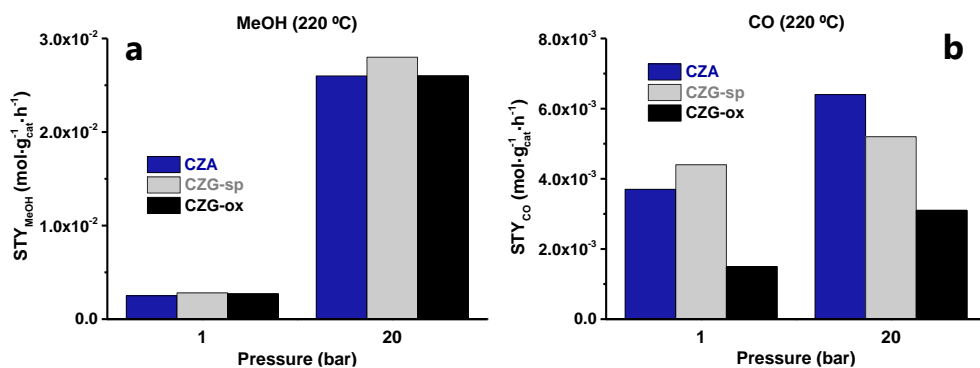


**Figure 3.30** Influence of pressure in the CO<sub>2</sub> hydrogenation to methanol (a) and CO (b). Increasing the pressure (1 to 20 bar) positively affects the productivity of MeOH, keeping the CO yield constant (at least at low-mid temperatures, i.e., 220 °C).



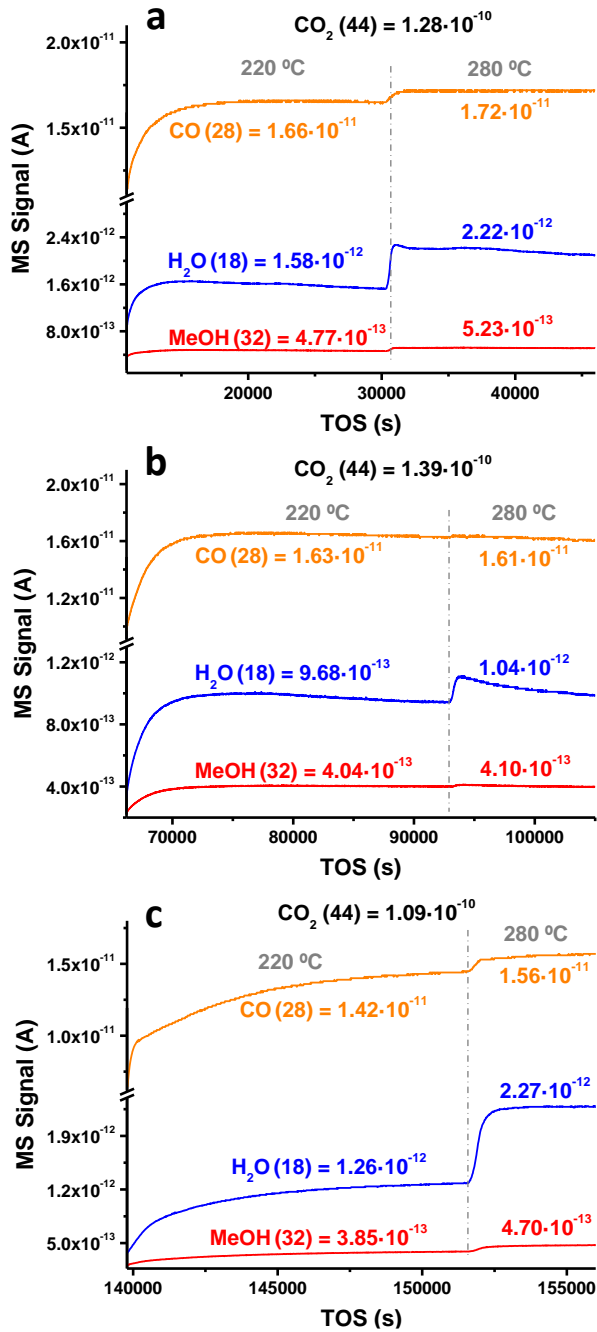


**Figure 3.31** Mass spectra analysis in (NAP)-XPS experiments on CZG-sp (a), CZG-ox (b) and CZA catalysts (c).

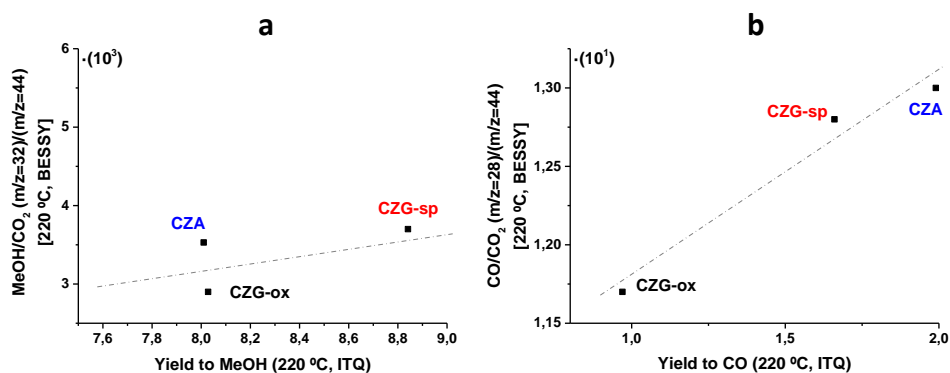


**Figure 3.32** Catalytic correlation between (NAP)-XPS (+MS coupled) experiments performed at Bessy II Synchrotron and catalytic experiments carried out in the 20 bar fixed-bed reactor. A linear correlation for MeOH (a) and CO (b) productivity is observed for the three samples under study.

*XPS at a laboratory scale + HPCR (9 bar)*

Pressure gap is an important handicap in (NAP)-XPS studies, especially when spectroscopic data has to be correlated with the catalytic performance of the samples operating under high-pressure conditions, as in this case. In order to overcome this limitation, laboratory XPS studies have been done on post reacted samples after being exposed to reaction conditions at 9 bar in a high-pressure cell reactor (HPCR) connected under UHV to the XPS analysis chamber (more details in Experimental Section 3.2.2).

The BE of Cu 2p<sub>3/2</sub>, Zn 2p<sub>3/2</sub> and Ga 2p<sub>3/2</sub> core levels and the corresponding auger parameters ( $\alpha'$ ) are given in Table 3.22, and the respective core lines plotted in Figures 3.33-3.36. The BE of the elements corresponds to Cu<sup>0</sup>, Zn<sup>2+</sup> and Ga<sup>3+</sup>. In addition, the  $\alpha'$  of Zn (~2009.9 eV) and Ga (~2180.2 eV) in all samples are slightly lower than that of reference ZnO (2010.1 eV), Ga<sub>2</sub>O<sub>3</sub> (2181.3 eV) or ZnGa<sub>2</sub>O<sub>4</sub> (2010.1 eV (Zn  $\alpha'$ ) and 2181.3 eV (Ga  $\alpha'$ )). This may correspond to surface oxygen vacancies, as already evidenced in (NAP)-XPS studies. The higher sampling depth in the laboratory XPS studies (~4-6 nm) does not allow the accurate detection of surface oxygen vacancies based on the O 1s core line. On the other hand, ZnL<sub>3</sub>M<sub>4,5</sub>M<sub>4,5</sub> auger line (Figure 3.37) shows a shoulder at ~3 eV higher kinetic energy (KE=990.7 eV) from the main peak (KE~987.3 eV), which may be originated from both oxygen vacancies and Zn<sup>0</sup>. The last one cannot be discarded, however no additional proofs of alloy formation could be observed in our work.

Based on the chemical composition of the samples determined from the XPS data, the surface enrichment in ZnO is not as clear as in (NAP)-XPS. However, as above, the distribution of Ga respect to Cu species differs between samples, being close to 1.0 (Cu:Ga atomic ratio) in the CZG-ox, while higher ~1.6 in the CZG-sp sample.

Moreover, migration of ZnO species over the CuNP under reaction conditions is also detected in the CZG-sp sample. Altogether shows a good correlation between the XPS data acquired after sample exposure at reaction conditions at 9 bar (Figure 3.38) and under in situ conditions at 2.5 mbar.

**Table 3.22** Laboratory scale XPS results in reduced CZG samples and after 9 bar reaction at HPCR.

Cat.	Treatment	Cu 2p <sub>3/2</sub>		Zn 2p <sub>3/2</sub>		Ga 2p <sub>3/2</sub>		% mol		
		BE (eV)	α' (eV)	BE (eV)	α' (eV)	BE (eV)	α' (eV)	Cu	Zn	Ga
CZG <sup>sp</sup>	H <sub>2</sub>	932.7	1851.1	1022.4	2009.9	1118.7	2180.2	27.1	55.7	17.2
	CO <sub>2</sub> +H <sub>2</sub>	932.4	1851.2	1022.4	2009.9	1118.5	2179.9	21.8	61.2	17.0
CZG <sup>ox</sup>	H <sub>2</sub>	932.7	1851.3	1022.4	2009.8	1118.6	2180.3	21.0	58.5	20.5
	CO <sub>2</sub> +H <sub>2</sub>	932.7	1851.2	1022.4	2009.8	1118.7	2180.3	20.2	59.3	20.4

**Table 3.23** Laboratory scale XPS results in the reduced CZA sample.

Cat.	Treatment	Cu 2p <sub>3/2</sub>		Zn 2p <sub>3/2</sub>		Al 2p	% mol		
		BE (eV)	α' (eV)	BE (eV)	α' (eV)	BE (eV)	Cu	Zn	Ga
CZA	H <sub>2</sub>	932.7	1851.2	1022.6	2009.5	74.9	23.1	28.6	48.3
	CO <sub>2</sub> +H <sub>2</sub>	-	-	-	-	-	-	-	-

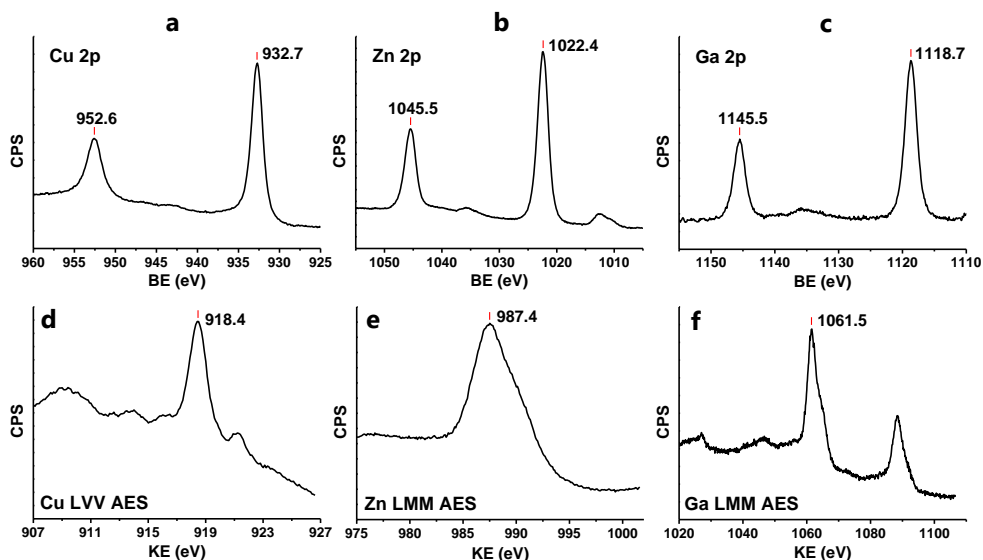


**Figure 3.33** XPS core lines of Cu 2p (a), Zn 2p (b), Ga 2p (c), Cu LVV AES (d), Zn LMM AES (e), and Ga LMM AES (f) at  $h\nu=1486.6$  eV excitation energy of the **reduced CZG-sp** sample.

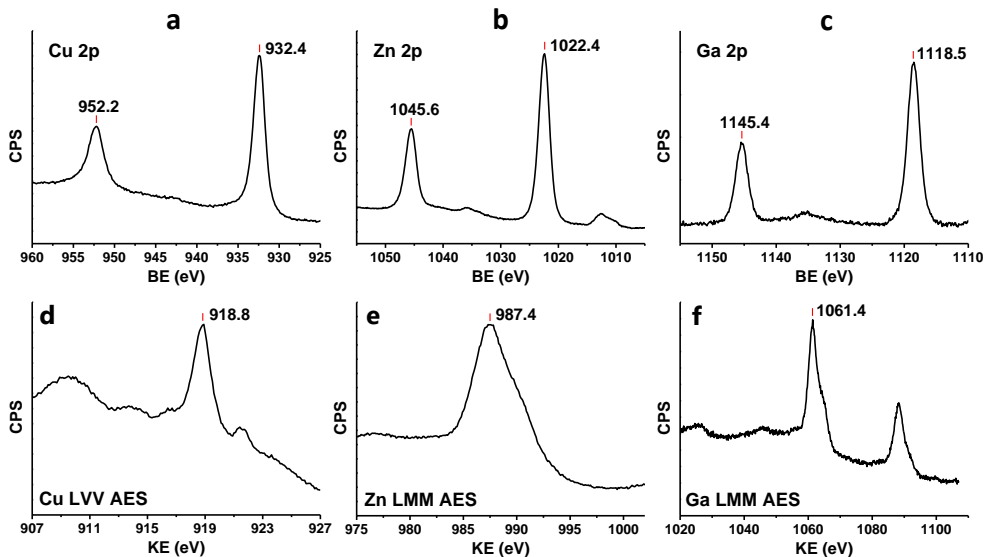


**Figure 3.34** XPS core lines of Cu 2p (a), Zn 2p (b), Ga 2p (c), Cu LVV AES (d), Zn LMM AES (e), and Ga LMM AES (f) at  $h\nu=1486.6$  eV excitation energy of the **CZG-sp** sample **after 9 bar CO<sub>2</sub> hydrogenation** in HPCR.

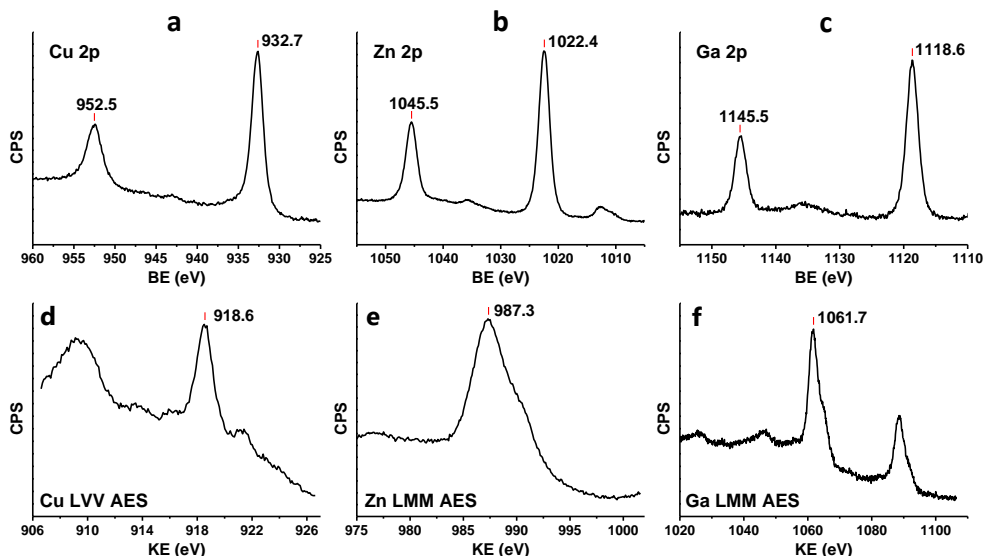


**Figure 3.35** XPS core lines of Cu 2p (a), Zn 2p (b), Ga 2p (c), Cu LVV AES (d), Zn LMM AES (e), and Ga LMM AES (f) at  $h\nu=1486.6$  eV excitation energy of the **reduced CZG-ox** sample.

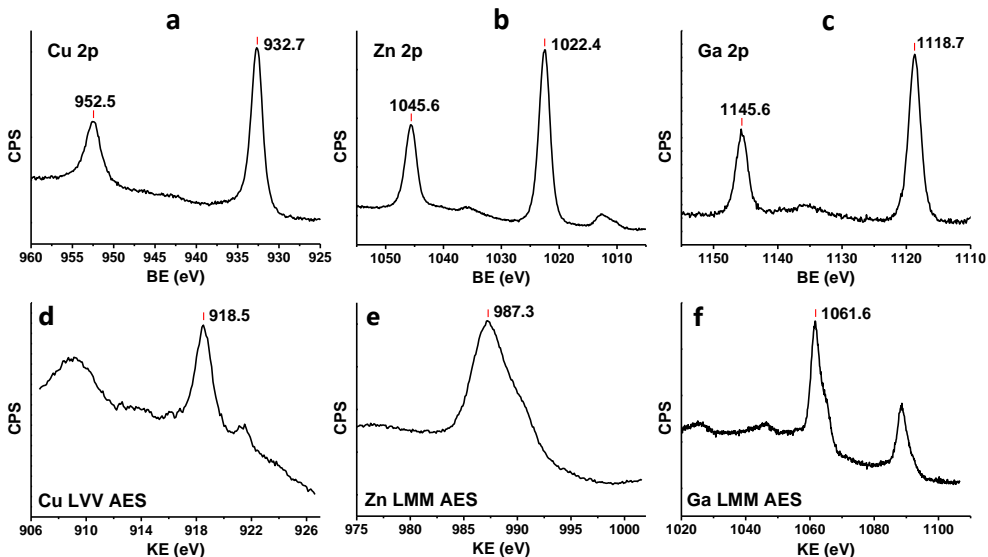


**Figure 3.36** XPS core lines of Cu 2p (a), Zn 2p (b), Ga 2p (c), Cu LVV AES (d), Zn LMM AES (e), and Ga LMM AES (f) at  $h\nu=1486.6$  eV excitation energy of the **CZG-ox** sample **after 9 bar CO<sub>2</sub> hydrogenation** in HPCR.

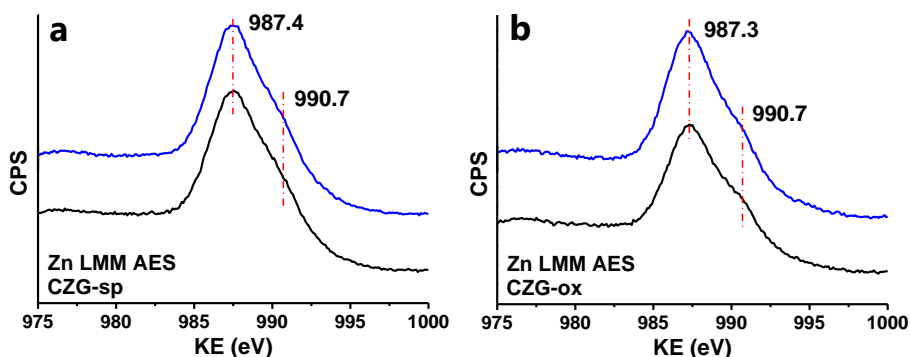


**Figure 3.37** Zn LMM AES line of CZG-sp (a) and CZG-ox (b) reduced samples (black) and after being exposed to CO<sub>2</sub>+H<sub>2</sub> reaction at 9 bar (blue). Spectra were acquired at  $h\nu=1486.6$  eV.

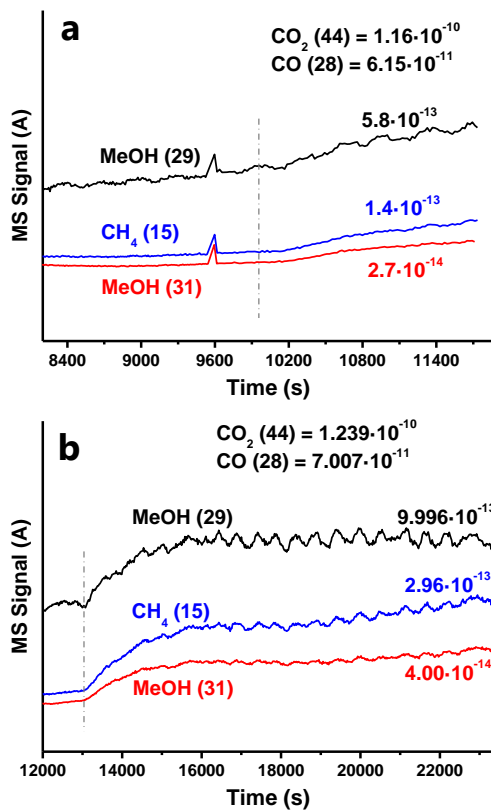


**Figure 3.38** MS of CZG-sp (a) and CZG-ox (b) catalysts during the CO<sub>2</sub> hydrogenation at 9 bar performed in the HPCR unit. Numbers in parentheses correspond to  $m/z$  values.

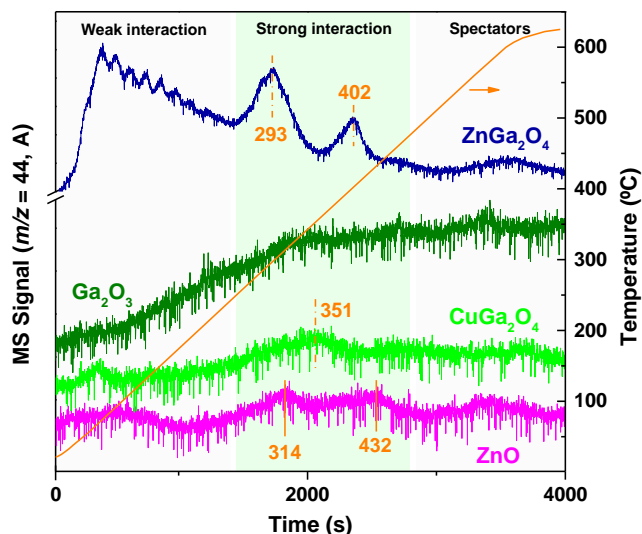
TPD-CO<sub>2</sub>

Figure 3.39 TPD-CO<sub>2</sub> on reference samples.

Reference samples show desorption peaks at 293 and 402 °C for ZnGa<sub>2</sub>O<sub>4</sub> (blue), 314 and 432 °C for ZnO (pink), 351 °C for CuGa<sub>2</sub>O<sub>4</sub> (light green), and a broad peak in the range 230–350 °C for Ga<sub>2</sub>O<sub>3</sub> (dark green). All pure metal oxide supports, except ZnGa<sub>2</sub>O<sub>4</sub>, show low amount of surface basic sites (i.e., low desorption peak area).

Table 3.24 TPD-CO<sub>2</sub> integrated peaks for CZG and CZA samples.

Catalyst	Peak area (A·s)			Total Area (A·s)	% Area (A·s)		
	Weak	Medium	Spectators		Weak	Medium	Spectators
CZG-ox	7.01·10 <sup>-11</sup>	5.21·10 <sup>-10</sup>	6.92·10 <sup>-11</sup>	6.60·10 <sup>-10</sup>	10.6	78.9	10.5
CZG-sp	1.52·10 <sup>-10</sup>	6.49·10 <sup>-11</sup>	1.03·10 <sup>-10</sup>	3.20·10 <sup>-10</sup>	47.5	20.4	32.1
CZA	5.55·10 <sup>-10</sup>	1.51·10 <sup>-10</sup>	2.86·10 <sup>-10</sup>	9.93·10 <sup>-10</sup>	55.9	15.3	28.8



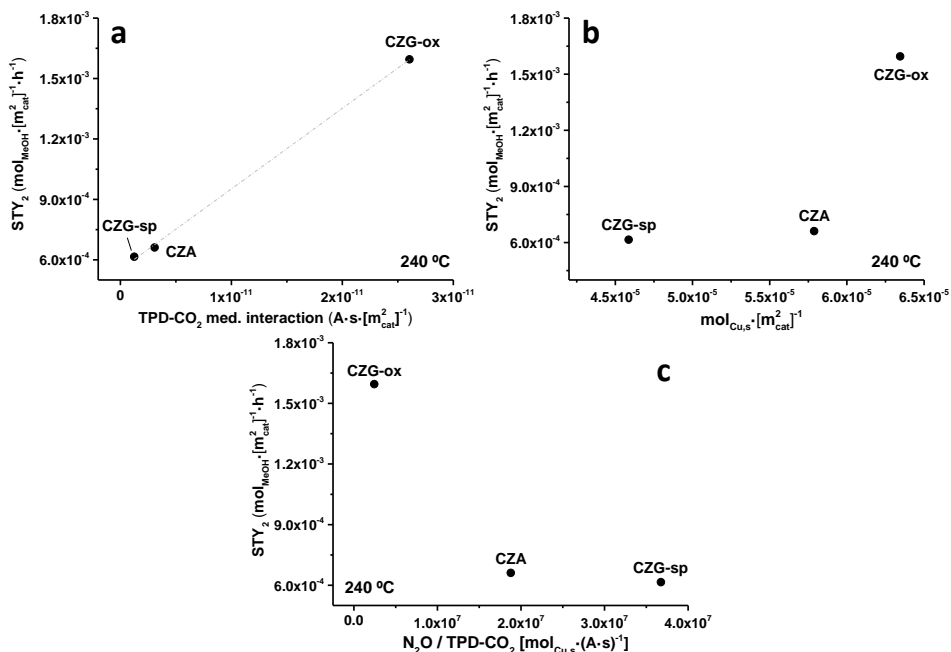


**Figure 3.40** Correlation of STY<sub>2</sub> with medium basicity (a), exposed copper (b), and the ratio of both properties (c).

### *Preliminary catalytic features of reformulated CZGA-ox*

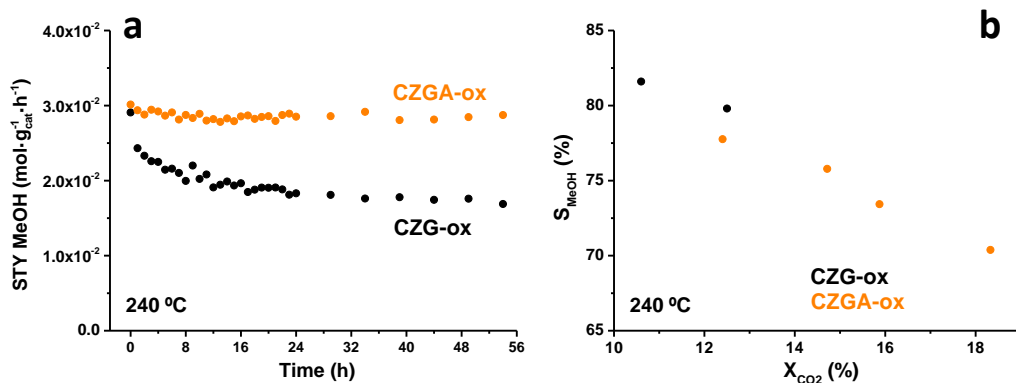


**Figure 3.41** Long-term experiments performed on CZG-ox and CZGA-ox samples at 240 °C, 20 bar and 28500 mL · g<sub>cat</sub><sup>-1</sup> · h<sup>-1</sup> (a) and comparison of catalytic features at that temperature (b).

**Table 3.25** Catalytic results at variable WHSV on the CZGA-ox sample at 20 bar.

T (°C)	W/F (mg·min·mL <sup>-1</sup> )	WHSV (mL·g <sub>cat</sub> <sup>-1</sup> ·h <sup>-1</sup> )	X <sub>CO<sub>2</sub></sub> (%)	CO <sub>2</sub> selectivity (%)			STY (mol·g <sub>cat</sub> <sup>-1</sup> ·h <sup>-1</sup> )	
				MeOH	CO	HCOOMe	MeOH	CO
240	1.41	42686	12.4	77.8	22.2	-	4.08·10 <sup>-2</sup>	1.16·10 <sup>-2</sup>
	2.10	28457	14.7	75.8	24.2	-	3.14·10 <sup>-2</sup>	1.00·10 <sup>-2</sup>
	2.81	21343	15.9	73.4	26.6	-	2.47·10 <sup>-2</sup>	8.91·10 <sup>-3</sup>
	4.22	14229	18.3	70.4	29.6	-	1.82·10 <sup>-2</sup>	7.64·10 <sup>-3</sup>
260	1.41	42686	16.3	63.9	36.1	-	4.40·10 <sup>-2</sup>	2.48·10 <sup>-2</sup>
	2.10	28457	19.3	60.7	39.3	-	3.30·10 <sup>-2</sup>	2.13·10 <sup>-2</sup>
	2.81	21343	20.8	58.4	41.6	-	2.57·10 <sup>-2</sup>	1.83·10 <sup>-2</sup>
	4.22	14229	22.7	54.4	45.6	-	1.74·10 <sup>-2</sup>	1.46·10 <sup>-2</sup>

### 3.6. References

- [1] Meunier, N.; Chauvy, R.; Mouhoubi, S.; Thomas, D.; De Weireld, G. Alternative production of methanol from industrial CO<sub>2</sub>. *Renew. Energy* **2020**, *146*, 1192-1203. DOI: 10.1016/j.renene.2019.07.010.
- [2] Liang, B.; Ma, J.; Su, X.; Yang, C.; Duan, H.; Zhou, H.; Deng, S.; Li, L.; Huang, Y. Investigation on Deactivation of Cu/ZnO/Al<sub>2</sub>O<sub>3</sub> Catalyst for CO<sub>2</sub> Hydrogenation to Methanol. *Ind. Eng. Chem. Res.* **2019**, *58*, 9030-9037. DOI: 10.1021/acs.iecr.9b01546.
- [3] Zhong, J.; Yang, X.; Wu, Z.; Liang, B.; Huang, Y.; Zhang, T. State of the art and perspectives in heterogeneous catalysis of CO<sub>2</sub> hydrogenation to methanol. *Chem. Soc. Rev.* **2020**, *49*, 1385-1413. DOI: 10.1039/C9CS00614A.
- [4] Centi, G.; Quadrelli, E. A.; Perathoner, S. Catalysis for CO<sub>2</sub> conversion: a key technology for rapid introduction of renewable energy in the value chain of chemical industries. *Energy Environ. Sci.* **2013**, *6*, 1711-1731. DOI: 10.1039/C3EE00056G.
- [5] Wang, W.; Wang, S.; Ma, X.; Gong, J. Recent advances in catalytic hydrogenation of carbon dioxide. *Chem. Soc. Rev.* **2011**, *40*, 3703-3727. DOI: 10.1039/C1CS15008A.
- [6] Goepfert, A.; Czaun, M.; Jones, J. P.; Prakash, G. K. S.; Olah, G. A. Recycling of carbon dioxide to methanol and derived products - closing the loop. *Chem. Soc. Rev.* **2014**, *43*, 7995-8048. DOI: 10.1039/C4CS00122B.
- [7] Kattel, S.; Ramírez, P. J.; Chen, J. G.; Rodriguez, J. A.; Liu, P. Active sites for CO<sub>2</sub> hydrogenation to methanol on Cu/ZnO catalysts. *Science* **2017**, *355*, 1296-1299. DOI: 10.1126/science.aal3573.
- [8] Natesakhawat, S.; Lekse, J. W.; Baltrus, J. P.; Ohodnicki Jr., P. R.; Howard, B. H.; Deng, X.; Matranga, C. Active Sites and Structure-Activity Relationships of Copper-Based Catalysts for Carbon Dioxide Hydrogenation to Methanol. *ACS. Catal.* **2012**, *2*, 1667-1676. DOI: 10.1021/cs300008g.

- [9] Li, M. M. J.; Zeng, Z.; Liao, F.; Hong, X.; Tsang, S. C. E. Enhanced CO<sub>2</sub> hydrogenation to methanol over CuZn nanoalloy in Ga modified Cu/ZnO catalysts. *J. Catal.* **2016**, *343*, 157-167. DOI: 10.1016/j.jcat.2016.03.020.
- [10] Li, M. M. J.; Chen, C.; Ayvali, T.; Suo, H.; Zheng, J.; Teixeira, I. F.; Ye, L.; Zou, H.; O'Hare, D.; Tsang, S. C. E. CO<sub>2</sub> Hydrogenation to Methanol over Catalysts Derived from Single Cationic Layer CuZnGa LDH Precursors. *ACS Catal.* **2018**, *8*, 4390-4401. DOI: 10.1021/acscatal.8b00474.
- [11] Saito, M.; Fujitani, T.; Takeuchi, M.; Watanabe, T. Development of copper/zinc oxide-based multicomponent catalysts for methanol synthesis from carbon dioxide and hydrogen. *Appl. Catal. A: Gen.* **1996**, *138*, 311-318. DOI: 10.1016/0926-860X(95)00305-3.
- [12] Gao, P.; Li, F.; Xiao, F.; Zhao, N.; Sun, N.; Wei, W.; Zhong, L.; Sun, Y. Preparation and activity of Cu/Zn/Al/Zr catalysts *via* hydrotalcite-containing precursors for methanol synthesis from CO<sub>2</sub> hydrogenation. *Catal. Sci. Technol.* **2012**, *2*, 1447-1454. DOI: 10.1039/C2CY00481J.
- [13] Toyir, J.; Ramírez de la Piscina, P.; Fierro, J. L. G.; Homs, N. Catalytic performance for CO<sub>2</sub> conversion to methanol of gallium-promoted copper-based catalysts: influence of metallic precursors. *Appl. Catal. B: Environ.* **2001**, *34*, 255-266. DOI: 10.1016/S0926-3373(01)00203-X.
- [14] Toyir, J.; Ramírez de la Piscina, P.; Fierro, J. L. G.; Homs, N. Highly effective conversion of CO<sub>2</sub> to methanol over supported and promoted copper-based catalysts: influence of support and promoter. *Appl. Catal. B: Environ.* **2001**, *29*, 207-215. DOI: 10.1016/S0926-3373(00)00205-8.
- [15] Dong, X.; Li, F.; Zhao, N.; Xiao, F.; Wang, J.; Tan, Y. CO<sub>2</sub> hydrogenation to methanol over Cu/ZnO/ZrO<sub>2</sub> catalysts prepared by precipitation-reduction method. *Appl. Catal. B: Environ.* **2016**, *191*, 8-17. DOI: 10.1016/j.apcatb.2016.03.014.
- [16] Ladera, R.; Pérez-Alonso, F. J.; González-Carballo, J. M.; Ojeda, M.; Rojas, S.; Fierro, J. L. G. Catalytic valorization of CO<sub>2</sub> *via* metanol synthesis with Ga-promoted Cu-ZnO-ZrO<sub>2</sub> catalysts. *Appl. Catal. B: Environ.* **2013**, *142-143*, 241-248. DOI: 10.1016/j.apcatb.2013.05.019.
- [17] Medina, J. C.; Figueroa, M.; Manrique, R.; Pereira, J. R.; Srinivasan, P. D.; Bravo-Suárez, J. J.; Baldovino-Medrano, V. G.; Jiménez, R.; Karelavic, A. Catalytic consequences of Ga promotion on Cu for CO<sub>2</sub> hydrogenation to methanol. *Catal. Sci. Technol.* **2017**, *7*, 3375-3387. DOI: 10.1039/C7CY01021D.
- [18] Behrens, M.; Zander, S.; Kurr, P.; Jacobsen, N.; Senker, J.; Koch, G.; Ressler, T.; Fischer, R. W.; Schlögl, R. Performance Improvement of Nanocatalysts by Promoter-Induced Defects in the Support Material: Methanol Synthesis over Cu/ZnO:Al. *J. Am. Chem. Soc.* **2013**, *135*, 6061-6068. DOI: 10.1021/ja310456f.
- [19] Mishra, P. K.; Ayaz, S.; Srivastava, T.; Tiwari, S.; Meena, R.; Kissinquincker, B.; Biring, S.; Sen, S. Role of Ga-substitution in ZnO on defect states, carrier density, mobility and UV sensing. *J. Mater. Sci.: Mater. Electron.* **2019**, *30*, 18686-1869. DOI: 10.1007/s10854-019-02221-z.

- [20] Liao, F.; Benedict, T. W.; Tsang, E. The Applications of Nano-Hetero-Junction in Optical and Thermal Catalysis. *Eur. J. Inorg. Chem.* **2016**, 1924-1938. DOI: 10.1002/ejic.201501213.
- [21] Baltes, C.; Vukojevic, S.; Schüth, F. Correlations between synthesis, precursor, and catalyst structure and activity of a large set of CuO/ZnO/Al<sub>2</sub>O<sub>3</sub> catalysts for methanol synthesis. *J. Catal.* **2008**, *258*, 334-344. DOI: 10.1016/j.jcat.2008.07.004.
- [22] Zhang, X.; Huang, J.; Ding, K.; Hou, Y.; Wang, X.; Fu, X. Photocatalytic Decomposition of Benzene by Porous Nanocrystalline ZnGa<sub>2</sub>O<sub>4</sub> with High Surface Area. *Environ. Sci. Technol.* **2009**, *43*, 5947-5951. DOI: 10.1021/es900403a.
- [23] Biswas, S. K.; Sarkar, A.; Pathak, A.; Pramanik, P. Studies on the sensing behaviour of Nanocrystalline CuGa<sub>2</sub>O<sub>4</sub> towards hydrogen, liquefied petroleum gas and ammonia. *Talanta* **2010**, *81*, 1607-1612. DOI: 10.1016/j.talanta.2010.03.010.
- [24] Hinrichsen, O.; Genger, T.; Muhler, M. Chemisorption of N<sub>2</sub>O and H<sub>2</sub> for the Surface Determination of Copper Catalysts. *Chem. Eng. Technol.* **2000**, *23*, 956-959. DOI: 10.1002/1521-4125(200011)23:11<956::AID-CEAT956>3.0.CO;2-L.
- [25] Tougaard, S. "QUASES: Software packages to characterize surface nano-structures by analysis of electron spectra"; <http://www.quases.com/products/quases-imfp-tp2m/>
- [26] Simonelli, L.; Marini, C.; Olszewski, W.; Ávila Pérez, M.; Ramanan, N.; Guilera, G.; Cuarteto, V.; Klementiev, K.; Saini, N. L. CLAEISS: The hard X-ray absorption beamline of the ALBA CELLS synchrotron. *Cogent Physics* **2016**, *3*, 1231987. DOI: 10.1080/23311940.2016.1231987.
- [27] Ravel, B.; Newville, M. ATHENA, ARTEMIS, HEPHAESTUS: data analysis for X-ray absorption spectroscopy using IFFFIT. *J. Synchrotron Radiat.* **2005**, *12*, 537-541. DOI: 10.1107/S0909049505012719.
- [28] Guil-López, R.; Mota, N.; Llorente, J.; Millán, E.; Pawelec, B.; García, R.; Fierro, J. L. G.; Navarro, R. M. Structure and activity of Cu/ZnO catalysts co-modified with aluminium and gallium for methanol synthesis. *Catal. Today* **2020**, *355*, 870-881. DOI: 10.1016/j.cattod.2019.03.034.
- [29] Tountas, A. A.; Peng, X.; Tavasoli, A. V.; Duchesne, P. N.; Dingle, T. L.; Dong, Y.; Hurtado, L.; Mohan, A.; Sun, W.; Ulmer, U.; Wang, L.; Wood, T. E.; Maravelias, C. T.; Sain, M. M.; Ozin, G. A. Towards Solar Methanol: Past, Present, and Future. *Adv. Sci.* **2019**, *6*, 1801903. DOI: 10.1002/adv.201801903.
- [30] Van der Berg, R.; Prieto, G.; Korpershoek, G.; Van der Wal, L. I.; Van Bunningen, A. J.; Laegsgaard-Jorgensen, S.; de Jongh, P. E.; de Jong, K. P. Structure sensitivity of Cu and CuZn catalysts relevant to industrial methanol synthesis. *Nat. Commun.* **2016**, *7*, 13057. DOI: 10.1038/ncomms13057.
- [31] Boppana, V. B. R.; Doren, D. J.; Lobo, R. F. Analysis of Ga coordination environment in novel spinel zinc gallium oxy-nitride photocatalysts. *J. Mater. Chem.* **2010**, *20*, 9787-9797. DOI: 10.1039/C0JM01928C.

- [32] Sans, J. A.; Martínez-Criado, G.; Pellicer-Porres, J.; Sánchez-Royo, J. F.; Segura, A. Thermal instability of electrically active centers in heavily Ga-doped ZnO thin films: X-ray absorption study of the Ga-site configuration. *Appl. Phys. Lett.* **2007**, *91*, 221904. DOI: 10.1063/1.2802554.
- [33] Ward, M. J.; Han, W. Q.; Sham, T. K. 2D XAFS-XEOL Mapping of Ga<sub>1-x</sub>Zn<sub>x</sub>N<sub>1-x</sub>O<sub>x</sub> Nanostructured Solid Solutions. *J. Phys. Chem. C* **2011**, *115*, 20507-20514. DOI: 10.1021/jp207545a.
- [34] Shinde, S. S.; Shinde, P. S.; Oh, Y. W.; Haranath, D.; Bhosale, C. H.; Rajpure, K. Y. Structural, optoelectronic, luminescence and thermal properties of Ga-doped zinc oxide thin films. *Appl. Surf. Sci.* **2012**, *258*, 9969-9976. DOI: 10.1016/j.apsusc.2012.06.058.
- [35] Ye, J. D.; Gu, S. L.; Zhu, S. M.; Liu, S. M.; Zheng, Y. D.; Zhang, R.; Shi, Y.; Yu, H. Q.; Ye, Y. D. Gallium doping dependence of single-crystal n-type ZnO grown by metal organic chemical vapor deposition. *J. Cryst. Growth.* **2005**, *283*, 279-285. DOI: 10.1016/j.jcrysgro.2005.06.030.
- [36] Phan, D. T.; Chung, G. S. Effects of defects in Ga-doped ZnO nanorods formed by a hydrothermal method on CO sensing properties. *Sensor Actuat. B: Chem.* **2013**, *187*, 191-197. DOI: 10.1016/j.snb.2012.10.080.
- [37] Turczyniak, S.; Luo, W.; Papaefthimiou, V.; Ramgir, N. S.; Haevecker, M.; Machocki, A.; Zafeirotos, S. A Comparative Ambient Pressure X-ray Photoelectron and Absorption Spectroscopy Study of Various Cobalt-Based Catalysts in Reactive Atmospheres. *Top. Catal.* **2016**, *59*, 532-542. DOI: 10.1007/s11244-015-0531-5.
- [38] Biesinger, M. C.; Lau, L. W. M.; Gerson, A. R.; Smart, R. St. C. Resolving surface chemical states in XPS analysis of first row transition metals, oxides and hydroxides: Sc, Ti, V, Cu and Zn. *Appl. Surf. Sci.* **2010**, *257*, 887-898. DOI: 10.1016/j.apsusc.2010.10.051.
- [39] Wöll, C. The chemistry and physics of zinc oxide surfaces. *Prog. Surf. Sci.* **2007**, *82*, 55-120. DOI: 10.1016/j.progsurf.2006.12.002.
- [40] Wang, Y.; Kattel, S.; Gao, W.; Li, K.; Liu, P.; Chen, J. G.; Wang, H. Exploring the ternary interactions in Cu-ZnO-ZrO<sub>2</sub> catalysts for efficient CO<sub>2</sub> hydrogenation to methanol. *Nat. Commun.* **2019**, *10*, 1166. DOI: 10.1038/s41467-019-09072-6.
- [41] Kuld, S.; Conradsen, C.; Moses, P. G.; Chorkendorff, I.; Sehested, J. Quantification of Zinc Atoms in a Surface Alloy on Copper in an Industrial-Type Methanol Synthesis Catalyst. *Angew. Chem. Int. Ed.* **2014**, *53*, 5941-5945. DOI: 10.1002/ange.201311073.
- [42] Schott, V.; Oberhofer, H.; Birkner, A.; Xu, M.; Wang, Y.; Muhler, M.; Reuter, K.; Wöll, C. Chemical Activity of Thin Oxide Layers: Strong Interactions with the Support Yield a New Thin-Film Phase of ZnO. *Angew. Chem. Int. Ed.* **2013**, *52*, 11925-11929. DOI: 10.1002/anie.201302315.
- [43] Dupin, J. C.; Gonbeau, D.; Vinatier, P.; Levasseur, A. Systematic XPS studies of metal oxides, hydroxides and peroxides. *Phys. Chem. Chem. Phys.* **2000**, *2*, 1319-1324. DOI: 10.1039/A908800H.

- [44] Behrens, M.; Studt, F.; Kasatkin, I.; Kühl, S.; Hävecker, M.; Abild-Pedersen, F.; Zander, S.; Girgsdies, F.; Kurr, P.; Knief, B. L.; Tovar, M.; Fischer, R. W.; Norskov, J. K.; Schlögl, R. The Active Site of Methanol Synthesis over Cu/ZnO/Al<sub>2</sub>O<sub>3</sub> Industrial Catalysts. *Science* **2012**, *336*, 893-897. DOI: 10.1126/science.1219831.
- [45] Zander, S.; Kunkes, E. L.; Schuster, M. E.; Schumann, J.; Weinberg, G.; Teschner, D.; Jacobsen, N.; Schlögl, R.; Behrens, M. The Role of the Oxide Component in the Development of Copper Composite Catalysts for Methanol Synthesis. *Angew. Chem. Int. Ed.* **2013**, *52*, 6536-6540. DOI: 10.1002/anie.201301419.
- [46] Jansen, W. P. A.; Beckers, J.; v. d. Heuvel, J. C.; Denier v. d. Gon, A. W.; Blik, A.; Brongersma, H. H. Dynamic Behavior of the Surface Structure of Cu/ZnO/SiO<sub>2</sub> Catalysts. *J. Catal.* **2002**, *210*, 229-236. DOI: 10.1006/jcat.2002.3679.
- [47] Sloczynski, J.; Grabowski, R.; Olszewski, P.; Kozłowska, A.; Stoch, J.; Lachowska, M.; Skrzypek, J. Effect of metal oxide additives on the activity and stability of Cu/ZnO/ZrO<sub>2</sub> catalysts in the synthesis of methanol from CO<sub>2</sub> and H<sub>2</sub>. *Appl. Catal. A: Gen.* **2006**, *310*, 127-137. DOI: 10.1016/j.apcata.2006.05.035.
- [48] Baber, A. E.; Xu, F.; Dvorak, F.; Mudiyansele, K.; Soldemo, M.; Weissenrieder, J.; Senanayake, S. D.; Sadowski, J. T.; Rodriguez, J. A.; Matolín, V.; White, M. G.; Stacchiola, D. J. *In situ* Imaging of Cu<sub>2</sub>O under Reducing Conditions: Formation of Metallic Fronts by Mass Transfer. *J. Am. Chem. Soc.* **2013**, *135*, 16781-16784. DOI: 10.1021/ja408506y.
- [49] Schumann, J.; Kröhnert, J.; Frei, E.; Schlögl, R.; Trunschke, A. IR-Spectroscopic Study on the Interface of Cu-Based Methanol Synthesis Catalysts: Evidence for the Formation of a ZnO Overlayer. *Top. Catal.* **2017**, *60*, 1735-1743. DOI: 10.1007/s11244-017-0850-9.
- [50] Topsoe, N. Y.; Topsoe, H. On the nature of surface structural changes in Cu/ZnO methanol synthesis catalysts. *Top. Catal.* **1999**, *8*, 267-270. DOI: 10.1023/A:1019133832569.
- [51] Sanguineti, P. B.; Baltanás, M. A.; Bonivardi, A. L. Copper-gallia interaction in Cu-Ga<sub>2</sub>O<sub>3</sub>-ZrO<sub>2</sub> catalysts for methanol production from carbon oxide(s) hydrogenation. *Appl. Catal. A: Gen.* **2015**, *504*, 476-481. DOI: 10.1016/j.apcata.2014.11.021.
- [52] Clarke, D. B.; Suzuki, I.; Bell, A. T. An Infrared Study of the Interactions of CO and CO<sub>2</sub> with Cu/SiO<sub>2</sub>. *J. Catal.* **1993**, *142*, 27-36. DOI: 10.1006/jcat.1993.1186.
- [53] Xu, F.; Mudiyansele, K.; Baber, A. E.; Soldemo, M.; Weissenrieder, J.; White, M. G.; Stacchiola, D. J. Redox-Mediated Reconstruction of Copper during Carbon Monoxide Oxidation. *J. Phys. Chem. C* **2014**, *118*, 15902-15909. DOI: 10.1021/jp5050496.
- [54] Dulaurent, O.; Courtois, X.; Perrichon, V.; Bianchi, D. Heats of Adsorption of CO on a Cu/Al<sub>2</sub>O<sub>3</sub> Catalyst Using FTIR Spectroscopy at High Temperatures and under Adsorption Equilibrium Conditions. *J. Phys. Chem. B* **2000**, *104*, 6001-6011. DOI: 10.1021/jp9943629.

- [55] Dasireddy, V. D. B. C.; Likozar, B. The role of copper oxidation state in Cu/ZnO/Al<sub>2</sub>O<sub>3</sub> catalysts in CO<sub>2</sub> hydrogenation and methanol productivity. *Renew. Energy* **2019**, *140*, 452-460. DOI: 10.1016/j.renene.2019.03.073.
- [56] Chen, S.; Zhang, J.; Wang, P.; Wang, X.; Song, F.; Bai, Y.; Zhang, M.; Wu, Y.; Xie, H.; Tan, Y. Effect of Vapor-phase-treatment to CuZnZr Catalyst on the Reaction Behaviors in CO<sub>2</sub> Hydrogenation into Methanol. *Chem. Cat. Chem.* **2019**, *11*, 1448-1457. DOI: 10.1002/cctc.201801988.
- [57] Gao, P.; Li, F.; Zhan, H.; Zhao, N.; Xiao, F.; Wei, W.; Zhong, L.; Wang, H.; Sun, Y. Influence of Zr on the performance of Cu/Zn/Al/Zr catalysts via hydrotalcite-like precursors for CO<sub>2</sub> hydrogenation to methanol. *J. Catal.* **2013**, *298*, 51-60. DOI: 10.1016/j.jcat.2012.10.030.
- [58] Guo, X.; Mao, D.; Lu, G.; Wang, S.; Wu, G. The influence of La doping on the catalytic behavior of Cu/ZrO<sub>2</sub> for methanol synthesis from CO<sub>2</sub> hydrogenation. *J. Mol. Catal. A: Chem.* **2011**, *345*, 60-68. DOI: 10.1016/j.molcata.2011.05.019.
- [59] Rossi, J. S.; Perrone, O. M.; Siqueira, M. R.; Volanti, D. P.; Gomes, E.; Da-Silva, R.; Boscolo, M. Effect of lanthanide ion doping on Mg-Al mixed oxides as active acid-base catalysts for fatty acid ethyl ester synthesis. *Renew. Energy* **2019**, *133*, 367-372. DOI: 10.1016/j.renene.2018.10.038.
- [60] Chen, Y.; Lin, J.; Chen, X.; Fan, S.; Zheng, Y. Engineering multicomponent metal-oxide units for efficient methane combustion over palladium-based catalysts. *Catal. Sci. Technol.* **2021**, *11*, 152-161. DOI: 10.1039/D0CY01742F.
- [61] Bou-Orm, N.; Iorgu, A.; Daniele, S.; Guilhaume, N. Modification of acid-base properties of TiO<sub>2</sub> by Nb and Mg dopants: Influence on the activity of Pd-Cu/(Mg,Nb)-TiO<sub>2</sub> catalysts for nitrate hydrogenation. *Appl. Catal. A: Gen.* **2013**, *467*, 414-420. DOI: 10.1016/j.apcata.2013.07.038.
- [62] Frusteri, L.; Cannilla, C.; Todaro, S.; Frusteri, F.; Bonura, G. Tailoring of Hydrotalcite-Derived Cu-Based Catalysts for CO<sub>2</sub> Hydrogenation to Methanol. *Catalysts* **2019**, *9*, 1058. DOI: 10.3390/catal9121058.
- [63] Karelovic, A.; Galdames, G.; Medina, J. C.; Yévenes, C.; Barra, Y.; Jiménez, R. Mechanism and structure sensitive of methanol synthesis from CO<sub>2</sub> over SiO<sub>2</sub>-supported Cu nanoparticles. *J. Catal.* **2019**, *369*, 415-426. DOI: 10.1016/j.jcat.2018.11.012.
- [64] Yang, Y.; Mims, C. A.; Disselkamp, R. S.; Mei, D.; Kwak, J. H.; Szanyi, J.; Peden, C. H. F.; Campbell, C. T. Isotopic Effects in Methanol Synthesis and the Reactivity of Copper Formates on a Cu/SiO<sub>2</sub> Catalyst. *Catal. Lett.* **2008**, *125*, 201-208. DOI: 10.1007/s10562-008-9592-4.
- [65] Haug, J.; Chassé, A.; Dubiel, M.; Eisenschmidt, C.; Khalid, M.; Esquinazi, P. Characterization of lattice defects by x-ray absorption spectroscopy at the Zn K-edge in ferromagnetic, pure ZnO films. *J. Appl. Phys.* **2011**, *110*, 063507. DOI: 10.1063/1.3631774.
- [66] Bakhtiargonbadi, F.; Esfahani, H.; Moakhar, R. S.; Dabir, F. Fabrication of novel electrospun Al and Cu doped ZnO thin films and evaluation of photoelectrical and sunlight-driven

- photoelectrochemical properties. *Mater. Chem. Phys.* **2020**, *252*, 123270. DOI: 10.1016/j.matchemphys.2020.123270.
- [67] Schumann, J.; Eichelbaum, M.; Lunkenbein, T.; Thomas, N.; Álvarez Galván, M. C.; Schlögl, R.; Behrens, M. Promoting Strong Metal Support Interaction: Doping ZnO for Enhanced Activity of Cu/ZnO:M (M = Al, Ga, Mg) Catalysts. *ACS Catal.* **2015**, *5*, 3260-3270. DOI: 10.1021/acscatal.5b00188.
- [68] Yoshihara, J.; Parker, S. C.; Schafer, A.; Campbell, C. T. Methanol Synthesis and Reverse Water-Gas Shift Kinetics over Clean Polycrystalline Copper. *Catal. Lett.* **1995**, *31*, 313-324. DOI: 10.1007/BF00808595.
- [69] Kim, J.; Sarma, B. B.; Andrés, E.; Pfänder, N.; Concepción, P.; Prieto, G. Surface Lewis Acidity of Periphery Oxide Species as a General Kinetic Descriptor for CO<sub>2</sub> Hydrogenation to Methanol on Supported Copper Nanoparticles. *ACS Catal.* **2019**, *9*, 10409-10417. DOI: 10.1021/acscatal.9b02412.
- [70] An, B.; Zhang, J. Z.; Cheng, K.; Ji, P. F.; Wang, C.; Lin, W. B. Confinement of Ultrasmall Cu/ZnO<sub>x</sub> Nanoparticles in Metal-Organic Frameworks for Selective Methanol Synthesis from Catalytic Hydrogenation of CO<sub>2</sub>. *J. Am. Chem. Soc.* **2017**, *139*, 3834-3840. DOI: 10.1021/jacs.7b00058.
- [71] Arena, F.; Mezzatesta, G.; Zafarana, G.; Trunfio, G.; Frusteri, F.; Spadaro, L. Effects of oxide carriers on surface functionality and process performance of the Cu-ZnO system in the synthesis of methanol via CO<sub>2</sub> hydrogenation. *J. Catal.* **2013**, *300*, 141-151. DOI: 10.1016/j.jcat.2012.12.019.
- [72] Fujitani, T.; Saito, M.; Kanai, Y.; Takeuchi, M.; Moriya, K.; Watanabe, T.; Kawai, M.; Kakumoto, T. Methanol Synthesis from CO<sub>2</sub> and H<sub>2</sub> over Cu/ZnO/Ga<sub>2</sub>O<sub>3</sub> Catalyst. *Chem. Lett.* **1993**, *22*, 1079-1080. DOI: 10.1246/cl.1993.1079.
- [73] Gao, P.; Li, F.; Zhao, N.; Xiao, F. K.; Wei, W.; Zhong, L. S.; Sun, Y. H. Influence of modifier (Mn, La, Ce, Zr and Y) on the performance of Cu/Zn/Al catalysts via hydrotalcite-like precursors for CO<sub>2</sub> hydrogenation to methanol. *Appl. Catal. A: Gen.* **2013**, *468*, 442-452. DOI: 10.1016/j.apcata.2013.09.026.
- [74] Liu, J. Y.; Shi, J. L.; He, D. H.; Zhang, Q. J.; Wu, X. H.; Liang, Y.; Zhu, Q. M. Surface active structure of ultra-fine Cu/ZrO<sub>2</sub> catalysts used for the CO<sub>2</sub>+H<sub>2</sub> to methanol reaction. *Appl. Catal. A: Gen.* **2001**, *218*, 113-119. DOI: 10.1016/S0926-860X(01)00625-1.
- [75] Shi, Z. S.; Tan, Q. Q.; Tian, C.; Pan, Y.; Sun, X. W.; Zhang, J. X.; Wu, D. F. CO<sub>2</sub> hydrogenation to methanol over Cu-In intermetallic catalysts: Effect of reduction temperature. *J. Catal.* **2019**, *379*, 78-89. DOI: 10.1016/j.jcat.2019.09.024.
- [76] Liu, X. M.; Lu, G. Q.; Yan, Z. F. Nanocrystalline zirconia as catalyst support in methanol synthesis. *Appl. Catal. A: Gen.* **2005**, *279*, 241-245. DOI: 10.1016/j.apcata.2004.10.040.

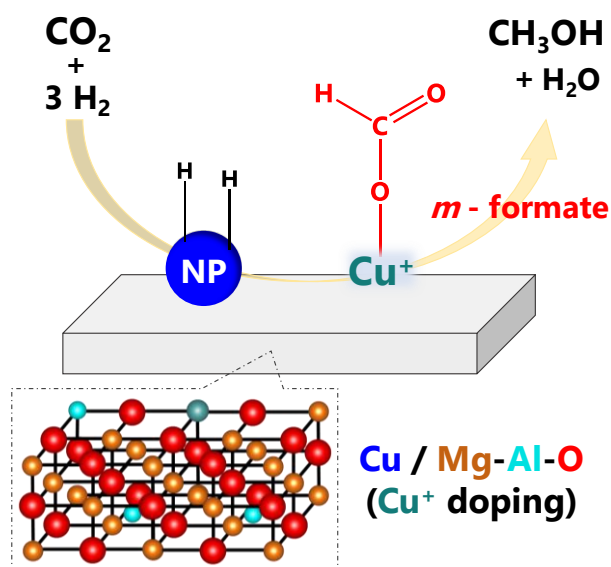






# CHAPTER 4

## Enhanced methanol production over non-promoted 2 nm Cu particles on Cu-MgO-Al<sub>2</sub>O<sub>3</sub> materials



The content of this chapter was adapted with permission from the submitted work:

**“Enhanced methanol production over non-promoted Cu-MgO-Al<sub>2</sub>O<sub>3</sub> materials with ex-solved 2 nm Cu particles: Insights from an Operando spectroscopic study”**

Cored, J.; Mazarío, J.; Cerdá-Moreno, C.; Lustemberg, P. G.; Ganduglia-Pirovano, M. V.; Domine, M. E.; Concepción, P.

*Under revision in ACS Catal.* **2022** (Copyright © 2022, American Chemical Society)



## 4.1. Introduction

Establishing a carbon-neutral economy is going to be one of the main targets in our near-future society. In this context, greenhouse gas recycling, where the carbon dioxide released into the atmosphere is captured and converted into chemicals and fuels, represents a hotspot in catalysis research as a means to close the carbon cycle.<sup>[1-4]</sup> Accordingly, the methanol synthesis from CO/CO<sub>2</sub> hydrogenation is attracting widespread interest since this product is a platform chemical with a total annual production of 95 million tonnes per year in 2019, as mentioned in Chapter 1.<sup>[5,6]</sup> On this point, high catalyst efficiency is one of the most pursued challenges researchers are dealing with. One appealing way to enhance the catalytic performance in many processes is to decrease the size of the active component to the nano- or sub-nanometer range, thus increasing the number of exposed surface atoms and the density of low-coordinated surface sites. This results in most cases in greater activity for smaller particle sizes.<sup>[7]</sup> However, an opposite trend has been reported in the methanol synthesis from CO/CO<sub>2</sub> hydrogenation, where the activity decreases significantly for Cu particles smaller than 8 nm,<sup>[8]</sup> specifically when using inert or non-redox supports in the absence of promoters.<sup>[9,10]</sup> Additionally, it has been reported that, with decreasing particle sizes, CO formation by the reverse water-gas shift reaction (RWGS) starts to dominate versus methanol synthesis,<sup>[11]</sup> resulting in a low catalytic efficiency. In this sense, the possibility to develop new synthetic strategies, whereby it might be possible to modify the selectivity and inactivity of small particle size catalysts, is of particular significance from an economic efficiency viewpoint. This becomes especially interesting when using non redox supports, low metal loadings (<10%) and in the absence of promoters. In this respect, Yu et al. reported on the

possibility of enhancing methanol production by stabilizing Cu<sup>+</sup> ions in a shattuckite-like structure in a 17 wt % Cu/SiO<sub>2</sub> catalysts containing highly dispersed 2.6-3.8 nm copper particles prepared by flame spray pyrolysis.<sup>[12]</sup> Methanol yield of  $\sim 1.1 \cdot 10^{-3}$  mol<sub>MeOH</sub>·g<sub>cat</sub><sup>-1</sup>·h<sup>-1</sup> at 230 °C and 30 bar (CO<sub>2</sub>:H<sub>2</sub> molar ratio 1 to 3; GHSV=2040 h<sup>-1</sup>) is obtained, surpassing that of conventional Cu/SiO<sub>2</sub> catalysts, which have been usually considered as inert catalysts.<sup>[9-11]</sup> In other studies, Cu/Al<sub>2</sub>O<sub>3</sub> catalysts containing other metal oxides like MgO, CaO, SrO and BaO with a Cu:M:Al molar ratio of 50:30:20 and prepared by a co-precipitation method have been investigated. Methanol yield of  $5.1 \cdot 10^{-4}$  mol<sub>MeOH</sub>·g<sub>cat</sub><sup>-1</sup>·h<sup>-1</sup> and 31% selectivity to methanol at 200 °C and 20 bar (CO<sub>2</sub>:H<sub>2</sub> molar ratio 1 to 2.8; GHSV=2000 h<sup>-1</sup>) have been reported for the most active Cu/MgO/Al<sub>2</sub>O<sub>3</sub> catalyst.<sup>[13]</sup> In analogy, low methanol selectivity (29.8% at 4.3% CO<sub>2</sub> conversion) has been reported for copper catalysts supported on MgO-modified by TiO<sub>2</sub>,<sup>[14]</sup> and for Cu-doped MgAl<sub>2</sub>O<sub>4</sub> catalysts containing nano-sized (1-5 nm) CuNPs (displaying methanol selectivity below 20% at 2% CO<sub>2</sub> conversion).<sup>[15]</sup> In summary, all these results converge in an insufficient activity when non-promoted catalysts using non-redox supports are considered.

Aiming at enhancing the activity of small CuNPs, Copéret et al., using a surface organometallic chemistry method, obtained well dispersed and narrowly distributed CuNPs (2-4 nm) on a SiO<sub>2</sub> support decorated with different types of promoters acting as Lewis acid sites (i.e., Ti<sup>4+</sup>, Zr<sup>4+</sup>, Ga<sup>3+</sup>, and Zn<sup>2+</sup>).<sup>[16-19]</sup> Without a promoter, the catalyst shown poor activity, being enhanced after adding a second metal. In that case, methanol formation rates up to  $1.7 \cdot 10^{-4}$  mol<sub>MeOH</sub>·g<sub>cat</sub><sup>-1</sup>·h<sup>-1</sup> with 86% methanol selectivity are obtained at 230 °C, 25 bar (CO<sub>2</sub>:H<sub>2</sub> molar

ratio 1 to 3 and WHSV=24000 mL·g<sub>cat</sub><sup>-1</sup>·h<sup>-1</sup>) on a Cu-Zn<sup>II</sup>@SiO<sub>2</sub> catalyst, composed of 4 nm CuNPs, containing 4.16 wt % Cu and 1.62 wt % Zn.<sup>[19]</sup>

As a precursor of well dispersed metal species, layered double hydroxides (LDH) with hydrotalcite-like structure and a general formula  $[M^{2+}_{1-x}M^{3+}_x(OH)_2]^{z+} \cdot [A^{n-}_{z/n} \cdot mH_2O]^{z-}$  have shown great interest in catalysis. Although most of the material comprises low-cost earth available elements (Mg-Al), the possibility to introduce a wide range of chemical compositions and structural features have made them suitable catalysts in many organic transformations.<sup>[20]</sup> Especially, due to their basicity, they proved to be excellent candidates for CO<sub>2</sub> capture and utilization.<sup>[21,22]</sup> In this regard, many catalysts formulations, including divalent (Ni<sup>2+</sup>, Co<sup>2+</sup>, Mg<sup>2+</sup>, Cu<sup>2+</sup>, Zn<sup>2+</sup>) and trivalent (Fe<sup>3+</sup>, Ga<sup>3+</sup>, Al<sup>3+</sup>, Mn<sup>3+</sup>) cations have been reported, resulting in complex bi- and multimetallic systems with interesting CO<sub>2</sub> hydrogenation activity to methanol.<sup>[21-24]</sup> In the simplest formulation, containing only one metal besides Mg<sup>2+</sup> and Al<sup>3+</sup>, most studies have been focused on Ni<sup>2+</sup> and Co<sup>2+</sup>,<sup>[21]</sup> and recently on Cu<sup>2+</sup>, giving in all cases CO and CH<sub>4</sub> as main reaction products.<sup>[25]</sup> In the latter case, a reduced Cu-Mg-Al LDH-derived catalyst, with basicity and operating conditions selected explicitly for the RWGS reaction, displayed an enhanced specific activity towards CO due to the improved CO<sub>2</sub> adsorption on the material.

Consequently, seeking cost-efficient and non-promoted copper-based catalysts with high atom efficiency in the CO<sub>2</sub> hydrogenation to methanol, hydrotalcite-derived materials seem to be a promising alternative. Therefore, and supported on our previous experience in hydrotalcite-like materials,<sup>[26]</sup> a Cu-MgO-Al<sub>2</sub>O<sub>3</sub> mixed oxide catalyst containing small ex-solved CuNPs (2 nm) derived from a Mg-Al-Cu hydrotalcite precursor (HT) will be explored in this chapter. Despite the

absence of promoters and the redox inertness of the support, this catalyst appears as an appealing candidate, exhibiting a methanol formation rate of  $2.6 \cdot 10^{-3} \text{ mol}_{\text{MeOH}} \cdot \text{g}_{\text{cat}}^{-1} \cdot \text{h}^{-1}$  at 230 °C and 20 bar, with 71% methanol selectivity (mol ratio  $\text{H}_2/\text{CO}_2=3$ ,  $\text{WHSV}=28500 \text{ mL} \cdot \text{g}_{\text{cat}}^{-1} \cdot \text{h}^{-1}$ ). As it will be further discussed, this catalyst presents high thermal and temporal stability, outperforming other analogous non-promoted nano-sized copper-based catalysts performance. Moreover, the beneficial role of the HT-derived structures will be puzzle out by comparing our aforementioned systems with a Cu/Al<sub>2</sub>O<sub>3</sub>/MgO sample that does not derive from a hydrotalcite structure (together with a Cu/SiO<sub>2</sub> reference) at a catalytic level. Finally, IR-mass spectrometry experiments at variable pressure, combined with IR surface titration experiments, will let us disentangle the effect of Cu<sup>+</sup> in enhancing methanol formation. In this way, concepts such as operando catalyst restructuring, HT-memory effect or the role of formate intermediates in Cu<sup>+</sup> promoted methanol synthesis will be thoroughly addressed, shining light on the ambiguity of literature studies.

## 4.2. Materials and methods

### 4.2.1. Preparation of catalytic samples and references

#### *Synthesis of CuHT-230 and CuHT-450*

Hydrotalcite-type materials were prepared by a co-precipitation through a mesoscale flow synthesis procedure described elsewhere.<sup>[27-29]</sup> Besides, and to maximize the yield and bring forth a material with satisfactory physico-chemical properties, synthesis and aging conditions (i.e., pH, temperature, time) were selected according to a recent optimization described in reference [26]. The synthesis method started from two different aqueous solutions. On the one hand, solution A, containing the metallic species (i.e., Mg, Al, Cu) in the desired molar



ratios to achieve a  $M^{2+}/M^{3+}$  mol ratio  $\sim 4$  as nitrates (i.e.,  $Mg(NO_3)_2 \cdot 6H_2O$ ,  $Al(NO_3)_3 \cdot 9H_2O$  and  $Cu(NO_3)_2 \cdot 2.5H_2O$ , from Sigma-Aldrich) and 1.5 M of total cationic concentration. On the other hand, solution B, with the same total mass as solution A, but containing sodium carbonate (Fisher) and sodium hydroxide (Scharlab) in adequate amounts to accomplish a  $CO_3^{2-}$  / (sol. A total cationic number) molar ratio equal to 0.66 and  $OH^-$  / (sol. A overall positive charge) molar ratio equal to 1, respectively. These solutions were added at the same rate (20 mL·h<sup>-1</sup>) to an empty beaker with continuous stirring at 200 rpm and room temperature (RT). After that, the precipitates were aged at 60 °C overnight under sealed conditions, without agitation. The resulting solids were filtered, washed with Milli-Q water until pH  $\sim 7$ , and dried overnight at 100 °C. Finally, the hydrotalcite was calcined at 550 °C for 6 h under static air to attain the corresponding mixed oxide. Before their use in catalysis and for spectroscopic measurements, the mixed oxides were in situ reduced under an H<sub>2</sub> flow (20 mL·min<sup>-1</sup>) at either 230 °C (CuHT-230) or 450 °C (CuHT-450), always using a ramp rate of 5 °C·min<sup>-1</sup> and for 3 h at maximum temperature.

#### *Synthesis of Cu/HT (w) and Cu/HT (ACN)*

Initially, the pure hydrotalcite-derived material used as support (HT; just containing Mg and Al as metallic species) was synthesized following the same procedure above described for the Cu-Mg-Al hydrotalcite-derived materials. Nonetheless, in this case, the hydrotalcite was calcined at 450 °C (2 °C·min<sup>-1</sup>, for a total time of 10 h) under an airflow (100 mL·min<sup>-1</sup>) to attain the corresponding Mg-Al mixed oxide, as usually performed for simple Mg-Al hydrotalcites.<sup>[27,30]</sup> The incorporation of copper onto this support was carried out by the incipient wetness impregnation method using a solution of  $Cu(NO_3)_2 \cdot 2.5H_2O$  in water (w)

or in acetonitrile (ACN) at an adequate concentration to achieve a metal loading of ~10 wt % in the final solid. The latter solvent (i.e., ACN) was used alternatively to avoid the presence of water during the impregnation process, minimizing the HT memory effect. The impregnated solid was dried in a stove at 100 °C for 24 h (Cu/HT (w)) or in a fume hood at room temperature for 6 h (Cu/HT (ACN)). Afterwards, the catalytic system was calcined at 550 °C (3 °C·min<sup>-1</sup>, 5 h) under air. Finally, the catalyst was thermally reduced at 230 °C (5 °C·min<sup>-1</sup>) under a H<sub>2</sub> flow (20 mL·min<sup>-1</sup>) for 3 h, prior to their use in catalytic experiments.

#### *Synthesis of Cu/(Al<sub>2</sub>O<sub>3</sub>/MgO)*

An intimate physical mixture of Al<sub>2</sub>O<sub>3</sub> and MgO was used to support Cu nanoparticles for comparative purposes. This composite was prepared by incorporating Al(NO<sub>3</sub>)<sub>3</sub>·9H<sub>2</sub>O onto a high surface area MgO (MgO Nanoactive Plus, Nanoscale Corp.) by incipient wetness impregnation, followed by a calcination program analogous to that used for the pure Mg-Al hydrotalcites. The amount of Al(NO<sub>3</sub>)<sub>3</sub>·9H<sub>2</sub>O was calculated to keep the M<sup>2+</sup>/M<sup>3+</sup> at the same value used throughout this work (i.e., ~4), aiming at achieving acid-base properties analogous to those obtained for the HT-derived materials. Afterwards, copper was incorporated onto this support by incipient wetness impregnation using an aqueous solution of Cu(NO<sub>3</sub>)<sub>2</sub>·2.5H<sub>2</sub>O, at an adequate concentration to achieve a metal loading of ~10 wt % in the final solid. Finally, the catalyst was thermally reduced at 230 °C (5 °C·min<sup>-1</sup>) under a H<sub>2</sub> flow (20 mL·min<sup>-1</sup>) for 3 h, prior to their use in catalytic experiments.

#### *Synthesis of Cu/SiO<sub>2</sub>*

Nonporous silica spheres were synthesized via a technique reported by Stöber et al.<sup>[31]</sup> Then, copper was deposited via incipient wetness impregnation, followed

by drying and calcination. Before impregnation, the SiO<sub>2</sub> support was dried at 150 °C under vacuum for 1 h to remove adsorbed water. After that, the support was impregnated with an aqueous solution (0.1 M HNO<sub>3</sub>) of copper nitrate (Cu(NO<sub>3</sub>)<sub>2</sub>·3H<sub>2</sub>O, Sigma-Aldrich) with the adequate concentration to achieve 1.5 wt % of Cu in the final material. The material was dried overnight under vacuum, at room temperature. Subsequently, the sample (~1 g) was heated at 350 °C (2 °C·min<sup>-1</sup>) in a flow reactor with 750 mL·min<sup>-1</sup> of N<sub>2</sub>.

#### 4.2.2. Characterization techniques

Copper content, and hydrotalcite/mixed oxide compositions were characterized by inductively coupled plasma optical emission spectrometry (ICP-OES), with a Varian 715-ES spectrometer, after sample digestion in an HNO<sub>3</sub>/HCl aqueous solution for those materials containing Mg, and HNO<sub>3</sub>/HCl/HF aqueous solution for the Cu/SiO<sub>2</sub> sample.

X-ray powder diffraction (XRD) measurements were performed using a PANalytical Cubix Pro diffractometer with a CuK<sub>α</sub> X-ray source ( $\lambda=0.15406$  nm), provided with a variable divergence slit and working in fixed irradiated area mode. Data were collected over a 2 $\theta$  range of 5-90° at a scan rate of 2 min<sup>-1</sup>, operating at 40 kV and 35 mA. Diffractograms were compared with the PDF2 database (codes in parentheses) for adequate identification.

Surface areas of solid samples (250 mg) were calculated by applying the Brunauer-Emmett-Teller (BET) model to the range of the N<sub>2</sub> adsorption isotherm where a linear relationship is maintained. These isotherms were obtained from liquid nitrogen adsorption experiments at -196 °C, in a Micromeritics flowsorb instrument.

High-resolution transmission electron microscopy (HR-TEM) images were collected on a 200 kV Jeol JEM-2100F instrument. The microscope was also equipped with a high-angle annular dark-field (HAADF) detector to be run in a STEM mode, thereby achieving better compositional contrast between CuNPs and the oxide support. In this manner, the particle size distribution for each reduced sample was obtained with its statistical parameters (the  $\pm \sigma$  value). In all cases, a minimum number of 200 particles was considered. This study was done employing an image analyzer software (ImageJ). The instrument also had an EDX X-Max 80 detector, with a resolution of 127 eV, which supplied qualitative information about which elements were in the sample. Therefore, maps with different colors depending on the element were obtained. These analyses allowed us to confirm the presence of copper nanoparticles as the bright dots in the STEM images. Additionally, Field Emission Scanning Electron Microscopy images were collected on a Zeiss Gemini SEM 500 instrument for the sample Cu/SiO<sub>2</sub> to check that the Stöber silica support was prepared correctly.

Temperature-programmed reduction (TPR-H<sub>2</sub>) analysis was performed on a Micromeritics Autochem 2910 instrument. About 50 mg of sample was initially cleaned with 30 mL·min<sup>-1</sup> of Ar at room temperature for 30 min. Then, a mixture of 10 vol % of H<sub>2</sub> in Ar was passed through the solid at a total flow rate of 50 mL·min<sup>-1</sup>, while the temperature was increased up to 800 °C at a heating rate of 10 °C·min<sup>-1</sup>. The H<sub>2</sub> consumption was measured using a thermal conductivity detector (TCD), previously calibrated using the reduction of CuO as a reference.

The amount of surface copper metal sites was measured by N<sub>2</sub>O surface oxidation<sup>[32,33]</sup> followed by TPR-H<sub>2</sub> analysis in a Micromeritics Autochem 2910 instrument assuming an adsorption stoichiometry of 1:2 (H<sub>2</sub>:Cu<sub>s</sub>). Before

measurements, about 50 mg of catalyst was activated in 20 mL·min<sup>-1</sup> H<sub>2</sub> flow (3 h, 230 °C for CuHT-230 sample). After reduction, the sample was cleaned at the same temperature under Ar flow. Then, the temperature was decreased to 25 °C and the surface oxidation from Cu<sup>0</sup> to Cu<sub>2</sub>O using N<sub>2</sub>O (1 vol % in He, 10 mL·min<sup>-1</sup>) was performed for 1 h. After this, the sample was cleaned with Ar (15 min) at room temperature. Finally, TPR-H<sub>2</sub> was submitted until 400 °C (10 vol % H<sub>2</sub> in Ar, 50 mL·min<sup>-1</sup>, 10 °C·min<sup>-1</sup>) to reduce the previously oxidized Cu<sub>2</sub>O to Cu<sup>0</sup>.

The copper surface area was calculated as:  $Cu_{surf,area} (m^2_{Cu}/g_{cat}) = (\frac{mol_{Cu,surf}}{g_{cat}} N_A / C_M)$ , and the mass of exposed copper has been calculated as:  $Mass_{Cu,surf} (g_{Cu}/g_{cat}) = (\frac{mol_{Cu,surf}}{g_{cat}} 63.546 \text{ g/mol})$ , where  $\frac{mol_{Cu,surf}}{g_{cat}}$  is determined from the amount of H<sub>2</sub> consumed to reduce the surface of copper particles (Cu<sub>2</sub>O→Cu<sup>0</sup>) that have been previously oxidized by N<sub>2</sub>O, applying a factor considering the 1:2 (H<sub>2</sub>:Cu) stoichiometry. N<sub>A</sub> is the Avogadro's number; C<sub>M</sub> is the number of surface Cu atoms per unit surface area (1.47·10<sup>19</sup> at/m<sup>2</sup>); 63.546 g/mol is the atomic weight of copper.

Temperature-programmed desorption (TPD-CO<sub>2</sub>) studies over in situ reduced samples were performed using a quartz reactor, connected online to a mass spectrometer Balzer QMG 220M1. 100 mg of sample was first activated in a 20 mL·min<sup>-1</sup> H<sub>2</sub> flow at 230 °C (5 °C·min<sup>-1</sup>) for 3 h. Then, the sample was flushed with Ar (18 mL·min<sup>-1</sup>) and the temperature decreased to RT. After stabilization, CO<sub>2</sub> was pulsed 19 times using a four way-valve (100 μL loop). After the adsorption, the temperature was increased to 600 °C, maintaining the inert flow (10 °C·min<sup>-1</sup>). CO<sub>2</sub> desorption was followed by MS ( $m/z=44$ ).

Infrared (IR) spectra were recorded with a Nicolet (Nexus) 8700 FTIR spectrometer using a DTGS detector and acquiring at 4 cm<sup>-1</sup> resolution. For IR measurements, samples were pressed into self-supported wafers and submitted to activation conditions prior to each experiment.

IR characterization of reduced materials using carbon monoxide as probe molecule was carried out by treating the samples at 230 °C (or 450 °C for CuHT-450 sample) in H<sub>2</sub> flow (10 mL·min<sup>-1</sup>, 2.5 h), followed by evacuation at 10<sup>-4</sup> mbar (using a TBM pump, Pfeiffer) at 150 °C for 1.5 h. After that, the sample was cooled down to -170 °C under dynamic vacuum conditions. CO was dosed at -170 °C and at increasing pressure (up to 5 mbar). IR spectra were recorded after each dosage. Spectra deconvolution has been done using the Origin software. In a first instance, derived curves and the parameters involved in the Gaussian fitting (i.e.,  $y_0$ ,  $x_c$ ,  $w$ , and  $A$ ) associated to the support were obtained. With these values, the IR spectra of the copper containing samples were deconvoluted. Additional titration experiments at RT were performed on selected reduced samples using CD<sub>3</sub>CN as a probe molecule (see Subsection 4.5.4).

Operando CO<sub>2</sub> hydrogenation IR studies at atmospheric pressure were performed in a homemade IR catalytic cell connected online to a mass spectrometer (Balzer QMG 220M1). The IR cell allows in situ treatments in controlled atmospheres and temperatures from -176 °C to 500 °C, connected to a vacuum system with a gas dosing facility. Samples were firstly reduced in H<sub>2</sub> flow (see above). After activation, the temperature was decreased to 160 °C, and the gas feed switched to reaction conditions (20 mL·min<sup>-1</sup> total flow, 5 mL·min<sup>-1</sup> CO<sub>2</sub>, and 15 mL·min<sup>-1</sup> H<sub>2</sub>). After 15 min of stabilization monitored by MS, the temperature was increased to 200 °C and kept there for 30 min. After this reaction step, the temperature was

set at 230 °C for another 30 min. IR spectra were acquired after all the experimental steps and every 15 min during catalysis. Additional offline GC analysis was also performed at all the temperatures. After reaction, the temperature was decreased to 180 °C, followed by evacuation at 10<sup>-1</sup> mbar (primary pump, Leybold). Once the sample was at RT, the system was cooled down to -170 °C under dynamic vacuum conditions (10<sup>-4</sup> mbar, using a TBM pump, Pfeiffer). CO was dosed at -170 °C and at increasing pressure (up to 5 mbar). IR spectra were recorded after each dosage.

Operando CO<sub>2</sub> hydrogenation IR studies at high pressure (9 bar) were performed in a commercial IR catalytic cell (model #2000-A, Aabspec) connected online to a mass spectrometer (Balzer QMG 220M1). This type of experiment initially presents the same two first steps that the IR-operando CO<sub>2</sub> hydrogenation at atmospheric pressure (activation + reaction at 1 bar, see the previous procedure above). After 1 bar reaction, the temperature was decreased to 160 °C, removing CO<sub>2</sub> from the gas mixture and fixing 25 mL·min<sup>-1</sup> pure H<sub>2</sub>. Then, a back-pressure regulator (BPR, Swagelok), connected in the outlet port of the IR cell, was constrained to increase the pressure to 9 bar. After pressurization, the reaction mixture (20 mL·min<sup>-1</sup> total flow, 5 mL·min<sup>-1</sup> CO<sub>2</sub> and 15 mL·min<sup>-1</sup> H<sub>2</sub>) was submitted into the cell and stabilized for 15-30 min. Then, the temperature was increased to 230 °C and kept there for 2 h. IR spectra were acquired after all the experimental steps and every 15 min during catalysis. The reaction was monitored by online MS and by offline GC. A three-way valve was installed before the MS instrument, to extract the downstream gas through a plastic syringe to the latter tracking. After 2 h on stream, the temperature was decreased to 180 °C and the cell was depressurized.

The cell evacuation and the CO titration experiment were performed by following the previous procedure at a temperature of -170 °C.

Hydrogenation experiments after operando IR CO<sub>2</sub>+H<sub>2</sub> reaction were performed at 1 and 9 bar. The experimental procedure until the hydrogenation step has already been explained above for both pressures. After reaction, the temperature was decreased to 100 °C and the gas mixture switched to 30 mL·min<sup>-1</sup>; 10 vol % H<sub>2</sub>/N<sub>2</sub>. Then, a progressive hydrogenation at increasing temperatures and H<sub>2</sub> % vol concentrations was carried out. Further details can be found in Subsection 4.5.6.

Mass analysis was performed using a mass spectrometer Balzer (QMG 220M1) coupled to IR reaction cells. The *m/z* values used to monitor each compound were: 44 (CO<sub>2</sub>), 31 (MeOH), 29 (HCOH), 28 (CO), 18 (H<sub>2</sub>O), 15 (CH<sub>4</sub>) and 2 (H<sub>2</sub>). Additionally, *m/z* values of 3 (HD), 4 (D<sub>2</sub>), 34 (CH<sub>2</sub>DOD), 19 (CHD<sub>3</sub>) and 20 (CD<sub>4</sub>) were monitored during IR isotopic experiments (see Subsection 4.5.6).

Laboratory X-ray photoelectron spectroscopy (XPS) experiments were performed on a SPECS spectrometer equipped with a Phoibos 150 MCD-9 multichannel analyzer using a non-monochromatic AlK<sub>α</sub> (1486.6 eV) X-ray source, an X-ray power of 50 W, pass energy of 30 eV, and under an operating pressure of 10<sup>-9</sup> mbar. The sample (~30-50 mg) was pressed into a pellet and loaded onto a SPECS stainless steel sample holder. Before XPS analysis, samples were submitted to different treatments in a high-pressure cell reactor (HPCR) connected under UHV to the XPS analysis chamber: i) H<sub>2</sub> reduction (10 mL·min<sup>-1</sup> flow) at 230 °C and atmospheric pressure for 3 h; ii) CO<sub>2</sub> hydrogenation reaction at 230 °C and 1 and 9 bar pressures in a CO<sub>2</sub>:H<sub>2</sub> mixture (1:3 molar ratio, 8 mL·min<sup>-1</sup> total flow) for 2 h.



Gases were flown through two mass flow controllers (Bronkhorst). XPS spectra were referenced to the Mg 1s peak (1303.9 eV) and Si 2p peak (103.5 eV). Data treatment was addressed using the CASA XPS software. Shirley-type background and Gaussian/Lorentzian-type curves were used in the spectra fitting.

UV-VIS spectra were acquired in a Cary 5000 spectrometer equipped with a diffuse reflectance accessory (Praying Mantis Harrick). Calcined and ex situ reduced (20 mL·min<sup>-1</sup> H<sub>2</sub>, 230 °C, 3 h, 5 °C·min<sup>-1</sup>) samples were both measured in the 200-800 nm range.

Density functional theory (DFT) calculations were carried out in collaboration with Dr. Ganduglia-Pirovano's group (ICP) using the slab-supercell approach,<sup>[34]</sup> with the Vienna Ab-initio Simulation Package (VASP version 5.4.4).<sup>[35,36]</sup> We explicitly treated the Mg (2p, 3s), O (2s, 2p), Cu(3p, 3d, 4s) and C (2s, 2p) electrons as valence states within the projector augmented wave (PAW) method, whereas the remaining electrons were considered as part of the atomic cores, with a plane-wave cutoff energy of 525 eV and the Perdew, Burke and Ernzerhof (PBE) generalized gradient approximation (GGA) functional.<sup>[37]</sup> Long-range dispersion corrections were considered with DFT lattice constants, employing the so-called DFT-D3 approach.<sup>[38,39]</sup> In this study, the Cu<sub>2</sub>O bulk has been modeled with the nonlocal HSE06 hybrid functional<sup>[40]</sup> and standard PBE-D3 approaches with a 6×6×6 k-point mesh sampling and optimized lattice constant of 4.25 and 4.24 Å, respectively. No long-range dispersion corrections were included in the hybrid calculations. The Cu<sub>2</sub>O(110) surface was modeled with (1×1) periodicity and a Cu<sub>2</sub>O slab consisting of 6 alternating Cu–O and Cu layers (see Figure 4.33). Cu<sub>2</sub>O slabs were repeated in z-direction and separated by vacuum layers of 15 Å. The two bottom layers were kept fixed during geometry optimization. The Cu bulk has

been modeled with the PBE-D3 approach with optimized lattice constant of 3.61 Å and a 12×12×12 k-point mesh sampling. The MgO bulk has been modeled with a unit cell containing four Mg and O atoms and a 15×15×15 k-point mesh sampling. The calculated lattice parameter of 4.217 Å is in excellent agreement with the experimental value of 4.213 Å.<sup>[41]</sup> The MgO(100) surface has been modeled with (2×2) periodicity and a three-layers slab with eight Mg and O atoms per layer (Mg<sub>24</sub>O<sub>24</sub>, see Figure 4.33) with a vacuum separation of 15 Å. During geometry optimization, only the bottom layer of the slab has been fixed according to the MgO bulk structure. As for the interaction with Cu with the MgO surface, it was considered that Cu species may dope the MgO surface or adsorb on it. In the first case, one Mg<sup>2+</sup> was replaced by two Cu (formally Cu<sup>+</sup>) atoms, while in the second case, Cu<sub>m</sub> (m = 2, 5) clusters were adsorbed on the oxide surface (see Figure 4.33). The adsorption energy of CO per molecule was calculated according to the following equation:  $E_{\text{ads}} = [E[n\text{CO}/\text{Surf.}] - E[\text{Surf.}] - nE[\text{CO}_{\text{gas}}]]/n$ , where  $E[n\text{CO}/\text{Surf.}]$  is the total energy of  $n=2, 8$  CO adsorbed molecules on the surface model;  $E[\text{Surf.}]$  is the total energy of the surface without the adsorbates; and  $E[\text{CO}_{\text{gas}}]$  is the energy of one CO molecule in gas phase. Vibrational frequencies and normal modes were obtained by diagonalization of the Hessian matrix, calculated from finite differences with atomic displacements of ±0.015 Å. Infrared (IR) intensities for each normal mode were calculated as the square of the first derivative of the z component of the dynamic dipole moment. The in-phase CO stretching vibrational frequency has been scaled by the factor  $\lambda = v^{\text{exp}}/v^{\text{calc}}$ , being  $v^{\text{exp}} = 2143 \text{ cm}^{-1}$  for the PBE and HSE functionals ( $\lambda^{\text{PBE}} = 2127 \text{ cm}^{-1}$  and  $\lambda^{\text{HSE06}} = 2235 \text{ cm}^{-1}$ ).

CO<sub>2</sub> hydrogenation catalytic tests were performed in a stainless-steel fixed-bed reactor (inner diameter of 11 mm and 240 mm length), equipped with a back-pressure regulator (BPR, Swagelok) that allows working at a pressure range of 1-20 bar. Typically, 200 mg of catalyst (particle size 400-600 μm) was diluted in SiC in a weight ratio 0.13 (Cat/SiC). Samples were in situ reduced at atmospheric pressure prior to catalytic tests (20 mL·min<sup>-1</sup> H<sub>2</sub>, 230 °C, 3 h, 5 °C·min<sup>-1</sup> for all samples; 450 °C for CuHT-450 sample). Experiments at a constant weight hourly space velocity (WHSV~28500 mL·g<sub>cat</sub><sup>-1</sup>·h<sup>-1</sup>) were performed under concentrated reaction conditions (23.7 vol % CO<sub>2</sub>, 71.3 vol % H<sub>2</sub>, 5 vol % N<sub>2</sub>) at 20 bar and reaction temperatures from 230 to 280 °C. Each temperature was maintained for at least 1.5 h. Catalytic experiments were also performed at different contact times (WHSV~570 to 134000 mL·g<sub>cat</sub><sup>-1</sup>·h<sup>-1</sup>), maintaining the 3:1 H<sub>2</sub> to CO<sub>2</sub> molar ratio at 20 bar pressure. The thermal stability of CuHT-230 sample was evaluated at 230 °C after 3 high temperature steps at 280 °C (45, 90 and 90 min) and 20 bar (WHSV~5700 mL·g<sub>cat</sub><sup>-1</sup>·h<sup>-1</sup>). In addition, a long-term stability experiment was carried out at 230 °C and 20 bar (WHSV~5700 mL·g<sub>cat</sub><sup>-1</sup>·h<sup>-1</sup>) for 85 h. Direct analysis of the reaction products was done by online gas chromatography (GC), using a SCION-456-GC equipment with TCD (MS-13X column) and FID (BR-Q Plot column) detectors. Blank experiments (in the presence of SiC) shown the absence of a homogeneous contribution to the reaction.

### **4.3. Results and discussion**

#### **4.3.1. Synthesis, characterization and catalytic properties of calcined-reduced catalysts**

Two Cu-Mg-Al mixed oxide catalysts containing 10 wt % Cu have been prepared starting from a Cu-Mg-Al hydrotalcite (HT) precursor (details in Subsection 4.2.1).

In this study, the molar ratio Cu<sup>2+</sup>/Mg<sup>2+</sup>/Al<sup>3+</sup> has been fixed to 6/74/20, which, based on our previous work,<sup>[26]</sup> results in materials of large surface area ( $S_{\text{BET}} \sim 200$  m<sup>2</sup>/g), high metal dispersion and moderate basic sites. These features, which are critical for an enhanced CO<sub>2</sub> hydrogenation activity and methanol selectivity, are found in the range of previously reported catalysts<sup>[24,42]</sup> and that of a commercial-like Cu/ZnO/Al<sub>2</sub>O<sub>3</sub> sample (i.e., CZA, see Chapter 3) synthesized as reference catalyst (see Figure 4.18). The co-precipitated Cu-Mg-Al-hydroxalite catalysts were first calcined at 550 °C under an air atmosphere, and then reduced in H<sub>2</sub> at two temperatures: 230 and 450 °C. After this procedure, two ex-solved copper-based systems are obtained, labeled as CuHT-230 and CuHT-450, respectively.

Catalysts properties derived from physico-chemical characterization techniques are included in Table 4.1 (together with those of reference samples) and discussed in the Supporting Information (Section 4.5).

**Table 4.1** Main physico-chemical properties of Cu-based materials.

Catalyst	M <sup>2+</sup> /M <sup>3+</sup> (mol ratio) <sup>a</sup>	Mg/Al (wt %)	Cu content (wt %) <sup>a</sup>	Surf. area (m <sup>2</sup> /g) <sup>b</sup>	P. size (nm) <sup>d</sup>	Cu exp. area (m <sup>2</sup> Cu·g <sup>cat</sup> <sup>-1</sup> ) <sup>h</sup>
CuHT-230	4.1	40.1/11.7	9.4	180	1.9	35.7 [5.5·10 <sup>-2</sup> ]
CuHT-450	4.1	40.1/11.7	9.4	180	2.3	29.8 [4.6·10 <sup>-2</sup> ]
Cu/HT (w)	4.1	33.7/10.0	8.8	169	2.3 <sup>e</sup>	26.0 [4.0·10 <sup>-2</sup> ]
Cu/HT (ACN)	4.4	28.3/7.8	7.1	147	-	-
Cu/(Al <sub>2</sub> O <sub>3</sub> /MgO)	3.6	38.8/13.0	8.3	144	2.6 <sup>f</sup>	19.1 [2.9·10 <sup>-2</sup> ]
Cu/SiO <sub>2</sub>	-	-	1.5	162 <sup>c</sup>	3.3 <sup>g</sup>	-

<sup>a</sup>Measured by ICP. <sup>b</sup>Values calculated from the N<sub>2</sub> adsorption isotherm by applying the BET method. <sup>c</sup>Surface area of the bare support. <sup>d</sup>Average Cu particle size by HR-TEM (a minimum of 200 particles was considered) for the reduced material. <sup>e</sup>Considering >60% particles (see Subsection 4.5.1). <sup>f</sup>Considering >70% particles (see Subsection 4.5.1). <sup>g</sup>Considering >90% particles (see Subsection 4.5.1). <sup>h</sup>Cu surface area determined by N<sub>2</sub>O and mass of exposed copper [g<sub>Cu</sub>·g<sub>cat</sub><sup>-1</sup>] in brackets.

Firstly, XRD provides convincing proof of the formation of the desired hydrotalcite phase in as-prepared samples and the corresponding mixed metal oxide in calcined and reduced samples (see Figure 4.9). Diffraction peaks associated with other phases (like MgAl<sub>2</sub>O<sub>4</sub> spinel or Al<sub>2</sub>O<sub>3</sub>) or copper related species are not detected, suggesting a high copper dispersion (see Subsection 4.5.1). Indeed, in the reduced samples, the ex-solution of small and narrowly distributed CuNPs with a particle size of ~2.0 nm has been confirmed by high-resolution transmission electron microscopy (HR-TEM), independently of the reduction temperature, ascertaining a remarkable stability of the so-formed CuNPs (Figure 4.1). Elemental EDX analyses were used to properly distinguish CuNPs from the support (see Figure 4.13).

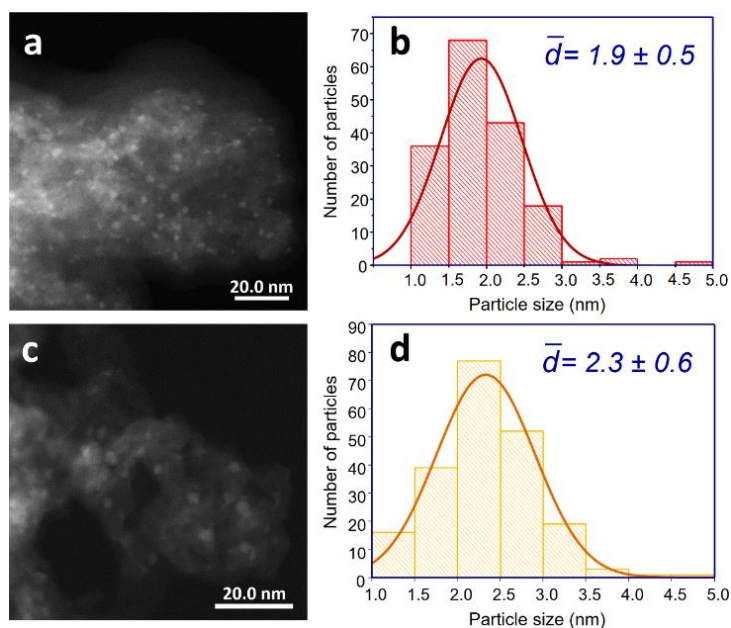


**Figure 4.1** Left, HR-STEM images of CuHT-230 (a) and CuHT-450 catalysts (c). Right, particle size distribution for CuHT-230 (b) and CuHT-450 catalysts (d). More than 200 particles have been measured in each sample.

It has been reported that nano-sized copper NPs (<4 nm), supported on non-redox supports and in the absence of promoters, result in low methanol formation.<sup>[9-14]</sup> This behavior is not observed in our study (Tables 4.2-4.4). In particular, the methanol yield at 230 °C, 20 bar and WHSV of ~28500 mL·g<sub>cat</sub><sup>-1</sup>·h<sup>-1</sup> over the CuHT-230 catalyst is  $2.6 \cdot 10^{-3}$  mol<sub>MeOH</sub>·g<sub>cat</sub><sup>-1</sup>·h<sup>-1</sup>, which normalized by the amount of exposed copper determined by N<sub>2</sub>O titration ( $5.5 \cdot 10^{-2}$  g<sub>Cu</sub>·g<sub>cat</sub><sup>-1</sup>, see Table 4.1) results in  $4.7 \cdot 10^{-2}$  mol<sub>MeOH</sub>·g<sub>Cu</sub><sup>-1</sup>·h<sup>-1</sup> with 71% methanol selectivity (Table 4.3). This value surpasses that of a previously reported Cu/MgO/Al<sub>2</sub>O<sub>3</sub> catalyst,<sup>[13]</sup> where 8.2 mg<sub>MeOH</sub>·mL<sub>cat</sub><sup>-1</sup>·h<sup>-1</sup> ( $5.1 \cdot 10^{-4}$  mol<sub>MeOH</sub>·g<sub>cat</sub><sup>-1</sup>·h<sup>-1</sup>) at 20 bar, 200 °C and GHSV of 2000 h<sup>-1</sup> has been found. Moreover, the catalytic activity of the herein reported Cu-HT-derived catalysts outperforms that referred in the literature with similar particle size (Figure 4.20), including Cu-M@SiO<sub>2</sub> promoted catalysts reported by Copéret et al.,<sup>[18,19]</sup> when working at high contact time. In opposition to these previously reported catalysts, the ones in this study do not need expensive promoters or a complicated air sensitive synthesis methodology, thus leading to promising cost-efficient catalysts.

In order to figure out if the hydrotalcite precursor plays a critical role in the catalytic performance of the final material, an alternative Cu/(Al<sub>2</sub>O<sub>3</sub>/MgO) catalyst was prepared. In this case, the support does not derive from a HT precursor, although displaying similar acid-base properties as the HT-derived catalysts (Figure 4.19). In this sample, copper has been added using the incipient wetness impregnation methodology onto an Al<sub>2</sub>O<sub>3</sub>/MgO support, resulting in a heterogeneous particle size distribution, with most particles around 2.6 nm (Figure 4.16). Using the same synthetic approach, two Cu impregnated Mg-Al HT catalysts (Cu/HT (w) and Cu/HT (ACN), where "w" and "ACN" denote impregnation

in either water or acetonitrile) were also prepared, resulting in similar particle size distributions as the Cu/(Al<sub>2</sub>O<sub>3</sub>/MgO) sample (Figure 4.15). Finally, the performance of these catalysts in the CO<sub>2</sub> hydrogenation has been compared to that of a Cu/SiO<sub>2</sub> catalyst of 3.3 nm particle size (Figure 4.17), prepared as in refs. [31, 43, 44]. More details are found in Subsection 4.2.1 and Table 4.1.

As shown in Figure 4.2, and according to the data in Table 4.3, the methanol yield (STY) increases in the order: Cu/SiO<sub>2</sub> < Cu/(Al<sub>2</sub>O<sub>3</sub>/MgO) << CuHT-450 < Cu/HT (ACN) ~ Cu/HT (w) < CuHT-230. Notoriously, all HT-based samples show significantly higher methanol production than the other catalysts, highlighting the positive role of the HT-type precursor.

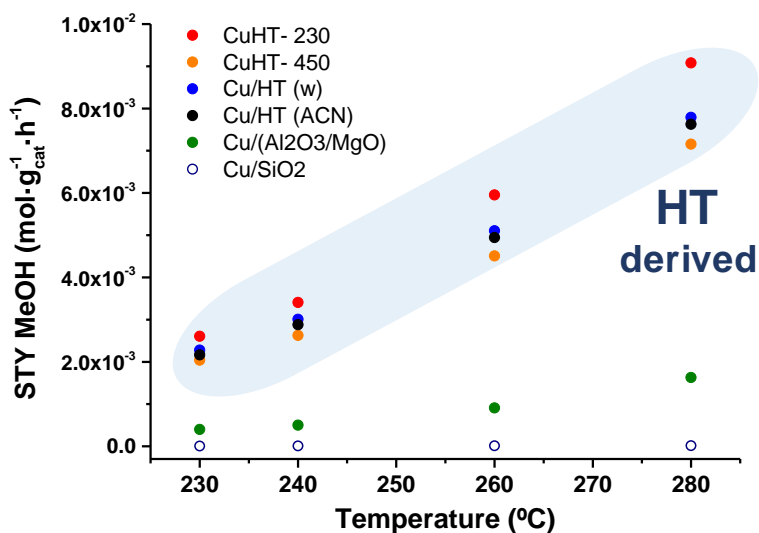


**Figure 4.2** Methanol productivity of studied Cu-based samples at variable temperature and 20 bar pressure (3:1 H<sub>2</sub>/CO<sub>2</sub> vol % ratio, WHSV ~28500 mL·g<sub>cat</sub><sup>-1</sup>·h<sup>-1</sup>).

The effect of the contact time on the catalytic activity and selectivity has been studied on three selected samples (CuHT-230, Cu/(Al<sub>2</sub>O<sub>3</sub>/MgO), and Cu/SiO<sub>2</sub>, details in Table 4.4). Firstly, the variation of the selectivity to methanol with the

CO<sub>2</sub> conversion obtained at 230 °C is given in Figure 4.3a. A higher selectivity is observed in CuHT-230 catalyst, with a methanol selectivity around 67-70% at conversions <22%, while it is lower in the case of Cu/(Al<sub>2</sub>O<sub>3</sub>/MgO) and Cu/SiO<sub>2</sub> samples (i.e., 50-57% and 5-8%, respectively). Interestingly, the CuHT-230 sample maintains a remarkable methanol selectivity when the CO<sub>2</sub> conversion is risen up to the equilibrium level (i.e., ~22%), an unusual behavior in conventional Cu/ZnO-based samples, where the methanol selectivity tends to drop as the CO<sub>2</sub> conversion increases (Figure 4.3b).

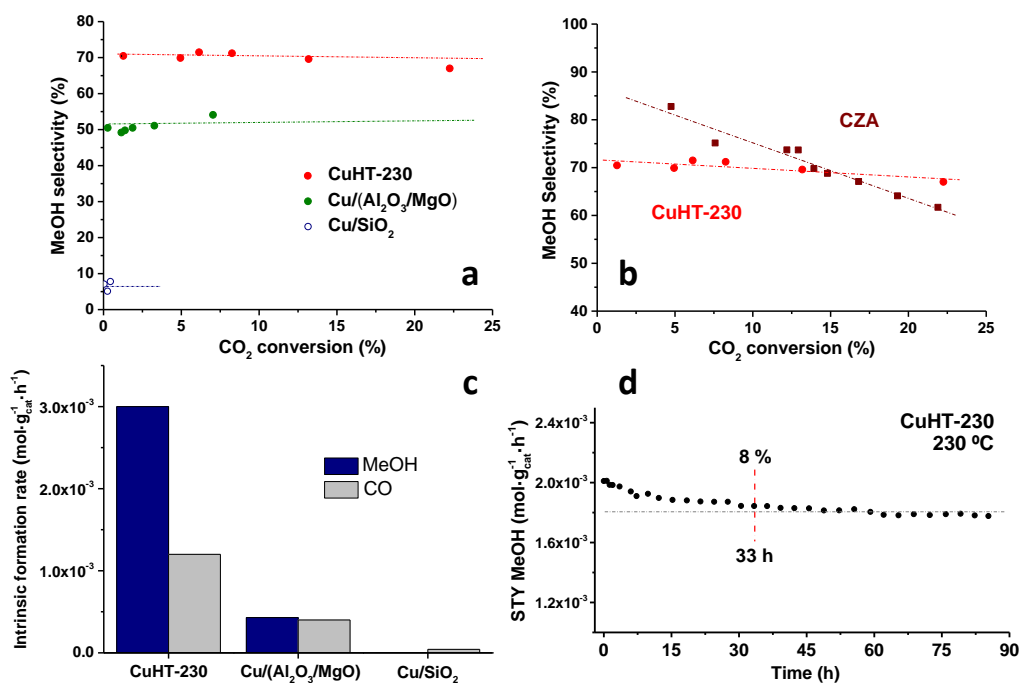


**Figure 4.3** Variation of the MeOH selectivity versus CO<sub>2</sub> conversion at 230 °C and 20 bar on samples under study (a) and comparison between a commercial Cu/ZnO/Al<sub>2</sub>O<sub>3</sub> catalyst (CZA) and CuHT-230 sample under the same catalytic conditions (b). CZA was prepared according to the work of Baltés et al.<sup>[47]</sup> and discussed in Chapter 3. Intrinsic formation rates of methanol and CO for representative catalytic systems (c). Long-term stability of CuHT-230 system at 230 °C, 20 bar and 5700 mL·g<sub>cat</sub><sup>-1</sup>·h<sup>-1</sup> (d).



Analyzing the initial formation rates of methanol and CO (obtained by extrapolating the respective rates to zero contact time, Figure 4.21), both CO and methanol appear as primary products in all three catalysts (Figure 4.3c). In CuHT-230 catalyst, methanol formation is favored over CO formation. In contrast, CO predominates over methanol formation in Cu/(Al<sub>2</sub>O<sub>3</sub>/MgO) sample and, particularly, in Cu/SiO<sub>2</sub> system. This last behavior has been reported for non-promoted nano-sized Cu catalysts, being more active for the RWGS than for methanol synthesis.<sup>[11,45,46]</sup> According to this, the opposite trend observed in the CuHT-230 sample may indicate a different active site condition, as determined later.

In catalysts for methanol synthesis, long-term and thermal stabilities are crucial for practical applications. Significantly, CuHT-230 catalyst shows high long-term stability with ~85 h of time-on-stream (TOS) (Figure 4.3d) operating at 20 bar, 230 °C, and 5700 mL·g<sub>cat</sub><sup>-1</sup>·h<sup>-1</sup>. An initial decrease in methanol formation (8%) is observed during the first ~33 h, remaining stable until the end of the experiment. It is worth noting that conventional Cu-based catalysts in the absence of Al<sub>2</sub>O<sub>3</sub> as stabilizer tend to deactivate when operating at high temperatures (280-300 °C). In contrast, CuHT-230 catalyst displays high thermal resistance against alternating cycles of temperatures between 230 and 280 °C (Figure 4.22), without apparent deactivation.

In this direction, the stability of the CuNPs in CuHT-230 material has been evaluated by HR-TEM on the spent catalyst (Figure 4.23), reflecting a change in the particle size from 1.9 to 3.2 after one catalytic cycle, and then remaining quite stable reaching 4.1 nm after four high-temperature steps at 280 °C. Such particle stability is likely induced by the stable ex-solution sites, at which the particles are

tightly anchored.<sup>[48]</sup> Interestingly, lattice fringes corresponding to the laminar structure of the hydrotalcite are observed in CuHT-230 sample after being submitted to several cycles of temperature. This feature corresponds to the “HT-memory effect”, a behavior later discussed.

In order to understand the reason behind the outstanding activity of the herein Cu-HT derived samples, spectroscopic studies using surface sensitive tools have been performed (i.e., X-ray photoelectron spectroscopy (XPS) and operando IR-MS studies combined with IR-CO titration experiments).

### 4.3.2. Spectroscopic catalyst characterization

#### *Laboratory XPS and IR-CO experiments*

The chemical state of CuNPs has been studied by XPS and IR-CO. XPS spectra show the presence of Cu<sup>0</sup> in all reduced samples, characterized by BE of ~932.5 eV at the Cu 2p<sub>3/2</sub> core line and a Cu L<sub>3</sub>VV auger peak maxima at around 918.4 eV KE (Figure 4.24 and Tables 4.6-4.8). Throughout XPS and auger peaks analysis, the presence of minority Cu<sup>+</sup> species is hard to detect. However, by IR spectroscopy using CO as probe molecule, a higher surface sensitivity is obtained, and Cu<sup>+</sup> species (IR band at 2138-2135 cm<sup>-1</sup>), together with Cu<sup>0</sup> (IR bands at 2100-1990 cm<sup>-1</sup>) and Lewis acid sites and OH groups of the support (~2168 and ~2150 cm<sup>-1</sup>) can be observed on reduced samples (Figure 4.4).<sup>[49-51]</sup> The amount of Cu<sup>+</sup> in the HT-derived samples follows the order: CuHT-230 ≥ CuHT-450 >> Cu/HT (w) ~ Cu/HT (ACN) (Figure 4.4e); being absent in Cu/(Al<sub>2</sub>O<sub>3</sub>/MgO) and Cu/SiO<sub>2</sub> samples (details in Subsection 4.5.4). Furthermore, Cu<sup>+</sup> ions are unexpectedly observed in the Cu/HT (w) sample, prepared by impregnation of a calcined Mg-Al HT support with an aqueous solution of a copper salt. It is known that the presence of water

promotes the so-called “HT-memory effect” (as observed in the XRD pattern of Figure 4.11), favoring the relocation of Cu<sup>2+/+</sup> ions in lattice positions.<sup>[52]</sup>

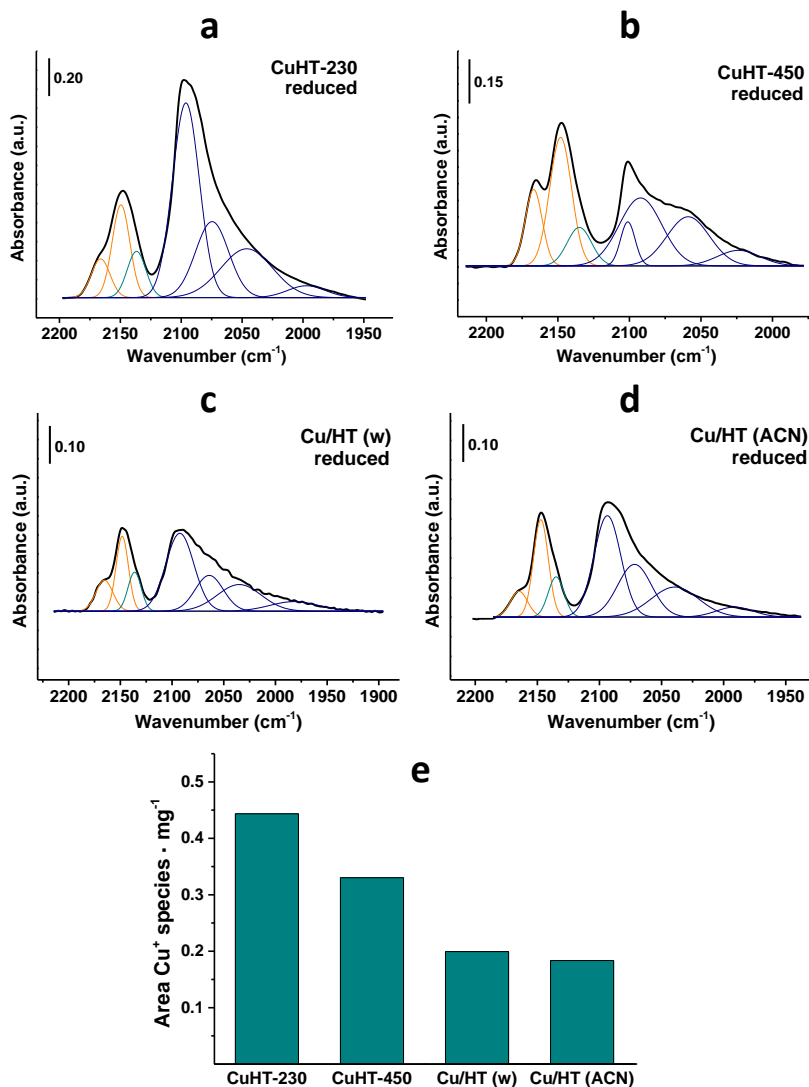


**Figure 4.4** IR of CO adsorption at -170 °C and saturation coverage on reduced Cu-HT-derived samples: CuHT-230 (a), CuHT-450 (b), Cu/HT (w) (c), Cu/HT (ACN) (d). Color code for deconvoluted components: orange (HT support), dark cyan (Cu<sup>+</sup> species), navy (Cu<sup>0</sup> species). Comparison between the amount of Cu<sup>+</sup> species normalized to sample weight analyzed at saturation coverage (e).

Especially, it has been reported that the reconstruction of the hydrotalcite structure has a beneficial effect on maximizing the Cu<sup>+</sup>/Cu<sup>0</sup> ratio in the corresponding reduced materials.<sup>[53]</sup> Indeed, even when performing the same impregnation procedure with an organic solution using acetonitrile, a reversion toward the HT structure is again detected from the XRD pattern, although to less extent, together with the stabilization of lattice Cu<sup>+</sup> ions in the IR-CO spectra.

Concerning the nature of Cu<sup>+</sup> ions, a detailed analysis of the IR data, supported by DFT simulations and combined with UV-VIS studies, allows for assigning the IR band at ~2137 cm<sup>-1</sup> to highly dispersed Cu<sup>+</sup> ions in metal oxide lattice positions. Indeed, when CO interacts with Cu<sub>2</sub>O, its frequency appears around 2118-2127 cm<sup>-1</sup>,<sup>[49,54-57]</sup> while when it coordinates with isolated Cu<sup>+</sup> ions, it has been reported at 2137 cm<sup>-1</sup>.<sup>[58-60]</sup> Similar shifts in the CO frequencies with respect to the gas phase molecule have been retrieved from the DFT simulations (see Subsection 4.5.5), where the IR band at 2137 cm<sup>-1</sup> has been correlated to dopant Cu ions in the metal oxide lattice. In addition, the presence of isolated Cu<sup>2+</sup> and Cu<sup>+</sup> ions in the metal oxide lattice is confirmed by diffuse reflectance UV-VIS analysis (bands at 265 and 227 nm, respectively, see Figure 4.32) being the amount of Cu<sup>+</sup> ions enhanced in the reduced CuHT-230 sample. In conclusion, the above reported results reveal the coexistence of CuNPs and Cu<sup>+</sup> ions likely located in lattice positions of the reduced HT-derived mixed oxide catalysts. The fact that Cu<sup>+</sup> ions are only observed in HT-derived samples and not in Cu/(Al<sub>2</sub>O<sub>3</sub>/MgO) or Cu/SiO<sub>2</sub> systems could explain the different catalytic performance of the materials, considering that Cu<sup>+</sup> has been reported in several works to enhance methanol production.<sup>[12,61,62]</sup>

It must be highlighted that water is formed under reaction conditions, and as indicated above, this by-product promotes the reconstruction of the metal oxide structure allowing the relocation of Cu<sup>+</sup> ions in lattice positions. At the same time, it may also behave as an oxidant competing with the reducing effect of H<sub>2</sub> in the reaction feed or even assisting the desorption of the so-formed methanol or methoxy species during reaction. Thus, it is not surprising that operational conditions (as the reaction pressure) strongly influence the identification of copper species (Cu<sup>0</sup>, Cu<sub>2</sub>O, CuO), as well as the stabilization of lattice Cu<sup>+</sup> ions, feature confirmed through operando spectroscopic studies, as detailed in the next subsection.

#### *Operando IR studies combined with titration experiments*

From infrared studies, significant transformations have been identified on the catalyst surface depending on the working pressure. This is revealed on the quenched sample after 2 h of reaction at 230 °C and 1 or 9 bar, submitted to CO titration at low temperature (-170 °C) (see Subsection 4.2.2 for more experimental details). For instance, while similar trends are observed in all samples, a titration experiment performed on the most active CuHT-230 sample after reaction at 1 bar reveals slight oxidation of copper nanoparticles with the formation of surface Cu<sub>2</sub>O species, whereas at 9 bar the copper nanoparticles appear fully reduced (Figure 4.35). In addition, compared to the reduced catalyst, a decrease in the IR band ascribed to Cu<sup>0</sup> sites, especially those appearing at lower  $\nu(\text{C}\equiv\text{O})$  frequencies, is observed at both pressures. This decrease is due to the poisoning of the copper surface by species involved in the process, as will be demonstrated later. Simultaneously, an increase in surface doped Cu<sup>+</sup> ions (IR band at ~2137 cm<sup>-1</sup>) is detected. This is particularly observed when working at 9 bar, (Figure 4.36

and 4.37), and it is linked to the higher reactivity of the samples (and, accordingly, water formation) at increasing reaction pressure. This feature is confirmed by online MS analysis and is aligned with catalytic studies performed at different pressures (Figure 4.38 and Table 4.14 and 4.15).

In the next, considering all samples studied in this work, we calculated the concentration of Cu<sup>0</sup> and surface doped Cu<sup>+</sup> sites, before and after operando IR reaction at 9 bar, which is given in Figure 4.5 (the corresponding spectra and their respective deconvolution are shown in Figure 4.4, 4.25-4.28, 4.36). Notably, the concentration of Cu<sup>+</sup> increases after reaction in all CuHT samples (Figure 4.5a), reaching a final value of 0.55-0.65 in all of them. In addition, a decrease in the Cu<sup>0</sup> sites is observed in all samples (Figure 4.5b), being ~70% in the CuHT-230 sample, for instance.

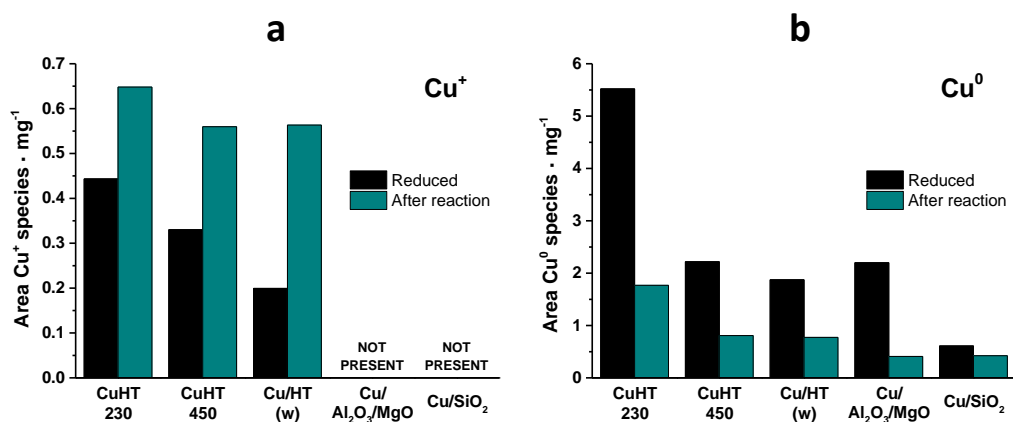


**Figure 4.5** Normalized area of the IR component associated with CO coordinated to Cu<sup>+</sup> (IR band at ~2135 cm<sup>-1</sup>) (a); and Cu<sup>0</sup> (IR bands between 2115-1990 cm<sup>-1</sup>) (b); before (i.e., reduced samples) and after CO<sub>2</sub> hydrogenation at 9 bar.

In order to establish structure-activity correlations and identify the nature of active sites, IR-CO titration experiments after high pressure operando IR reaction

at 9 bar have been compared with the catalytic performance of the samples in the fixed-bed reactor. On the one hand, the amount of unblocked Cu<sup>0</sup> sites has been correlated with catalytic activity and/or selectivity.

In general, it is widely accepted that Cu<sup>0</sup> sites are needed for CO<sub>2</sub> hydrogenation,<sup>[63-67]</sup> in particular for H<sub>2</sub> dissociation. Some authors reported a linear relationship<sup>[11,25,33]</sup> between the methanol yield and the copper surface area, while other studies did not convey such a linear correlation.<sup>[18,44,68]</sup> In other cases, metallic copper has been associated with the RWGS reaction.<sup>[69]</sup> In our case, we do not find a clear correlation between the amount of Cu<sup>0</sup> and the CO or methanol production (Figure 4.39). In contrast, when representing the amount of surface doped Cu<sup>+</sup> species under operando IR conditions at 9 bar versus the methanol yield (STY), a good linear correlation is obtained despite the pressure gap (Figure 4.6), thus highlighting the positive role of Cu<sup>+</sup> in methanol production.

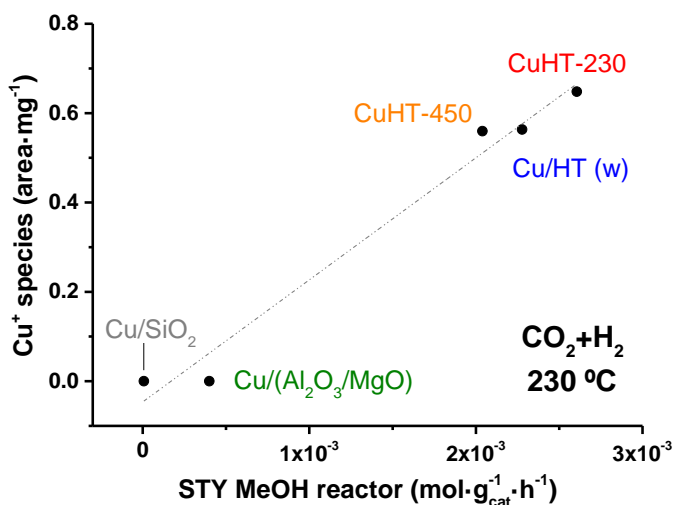


**Figure 4.6** Correlation between methanol production at 20 bar in a fixed-bed reactor (STY MeOH, X axis) and the amount of Cu<sup>+</sup> species normalized to sample weight obtained in the operando IR studies at 9 bar (Y axis).

In definitive, while Cu<sup>0</sup> is necessary for catalytic activity, the controlling step in methanol production is determined by the presence of Cu<sup>+</sup> sites in the mixed metal oxide surface.

Going one step further and aiming to gain mechanistic insights into the type of intermediate reaction species involved in the CO<sub>2</sub> hydrogenation to methanol, and the role of Cu<sup>+</sup> in the mechanism, temperature resolved IR-MS studies have been done. In these experiments, the evolution of surface species in the infrared spectra are monitored on the most active CuHT-230 sample, together with the reaction products tracked by online MS.

Working at 9 bar and in the temperature range from 160 to 230 °C, a complex set of IR bands growing in intensity in the 1670-1200 cm<sup>-1</sup> region, associated with the contribution of different types of carbonate and formate species, are observed (see Figure 4.40A-C). Thus, IR bands<sup>[70-75]</sup> due to monodentate (*m*) formate ( $\nu_{\text{as}}(\text{COO})$  1670-1650 cm<sup>-1</sup>,  $\delta(\text{C-H})$  1355-1340 cm<sup>-1</sup>,  $\nu_{\text{s}}(\text{COO})$  1310-1300 cm<sup>-1</sup>); bridge (*b*) formate ( $\nu_{\text{as}}(\text{COO})$  1587-1579 cm<sup>-1</sup>,  $\delta(\text{C-H})$  1398-1395 cm<sup>-1</sup>,  $\nu_{\text{s}}(\text{COO})$  1374-1369 cm<sup>-1</sup>); bidentate carbonate ( $\nu_{\text{as}}(\text{COO})$  1536-1524 cm<sup>-1</sup>,  $\nu_{\text{s}}(\text{COO})$  1330-1327 cm<sup>-1</sup>); and bicarbonate species ( $\nu_{\text{as}}(\text{COO})$  1638-1621 cm<sup>-1</sup>,  $\nu_{\text{s}}(\text{COO})$  1442-1440 cm<sup>-1</sup>,  $\delta(\text{OH})$  1248-1237 cm<sup>-1</sup>) are observed. Cu<sup>0</sup>-bonded formate (characterized by an IR band at 1350 cm<sup>-1</sup>) and methoxy species ( $\nu(\text{C-O})$  1087-1080 cm<sup>-1</sup>) are also detected (Figure 4.40A-C). At this point, identifying kinetically relevant intermediate species is challenging since no correlation between the MS and a parallel disappearance in the IR bands could be detected. This may be caused by the high working pressure, which enhances the rate of the sequential reaction steps and, accordingly, inhibits the detection of short-lived intermediate species. In fact, by performing isotopic studies replacing part of the H<sub>2</sub> flow by D<sub>2</sub>



under steady-state conditions at 230 °C and 9 bar, the whole set of IR bands in the 1670-1200 cm<sup>-1</sup> remains unaltered, and only the detection of OD bands (2630 cm<sup>-1</sup>), and a very weak IR band at 1019 cm<sup>-1</sup>, associated with  $\delta(\text{C-D})$  vibration, are observed (Figure 4.41). Based on these results, it becomes evident that most of the identified IR species are not directly involved in the reaction mechanism, behaving as spectators, and blocking active sites of the copper surface, as described above. Further confirmation has been attained by exposing the sample after IR operando conditions (i.e., in a CO<sub>2</sub>/H<sub>2</sub> flow at 9 or 1 bar and 230 °C) to a H<sub>2</sub>/N<sub>2</sub> flow at 230 °C during 4.5 h, followed by a subsequent IR-CO titration experiment. As shown in Figure 4.42, the intensity of the Cu<sup>0</sup>-CO signal is restored, confirming that most of these species are blocking the copper surface under reaction conditions. Remarkably, hydrogenation of those adsorbed species results in CH<sub>4</sub> and CO formation, disregarding them as intermediate species in the methanol synthesis and behaving mostly as spectators (Figure 4.43, 4.44 and Table 4.16). Noticeably, the poisoning of the Cu surface by a high coverage of adsorbed species has been reported by other authors as one of the reasons causing the low activity of small CuNPs.<sup>[76]</sup>

Therefore, with the aim of slowing down the reaction kinetics, operando IR studies at lower pressure (i.e., 1 bar) have been carried out. At these conditions and through temperature resolved IR-MS experiments, accurate identification of reaction intermediate species in methanol, methane and CO formation is attained (Figure 4.7). Thus, by increasing the temperature from 160 to 200 °C, the disappearance of IR bands at 2934, 1660, 1348 and 1319 cm<sup>-1</sup>, associated with  $\nu_{\text{stretch}}(\text{C-H})$ ,  $\nu_{\text{as}}(\text{COO})$ ,  $\delta(\text{C-H})$ , and  $\nu_{\text{s}}(\text{COO})$  vibrations of monodentate (*m*)

formate species,<sup>[72,74,77]</sup> respectively, parallels with the exclusive detection of methanol in the MS (Figure 4.7 and Figure 4.45, left side).

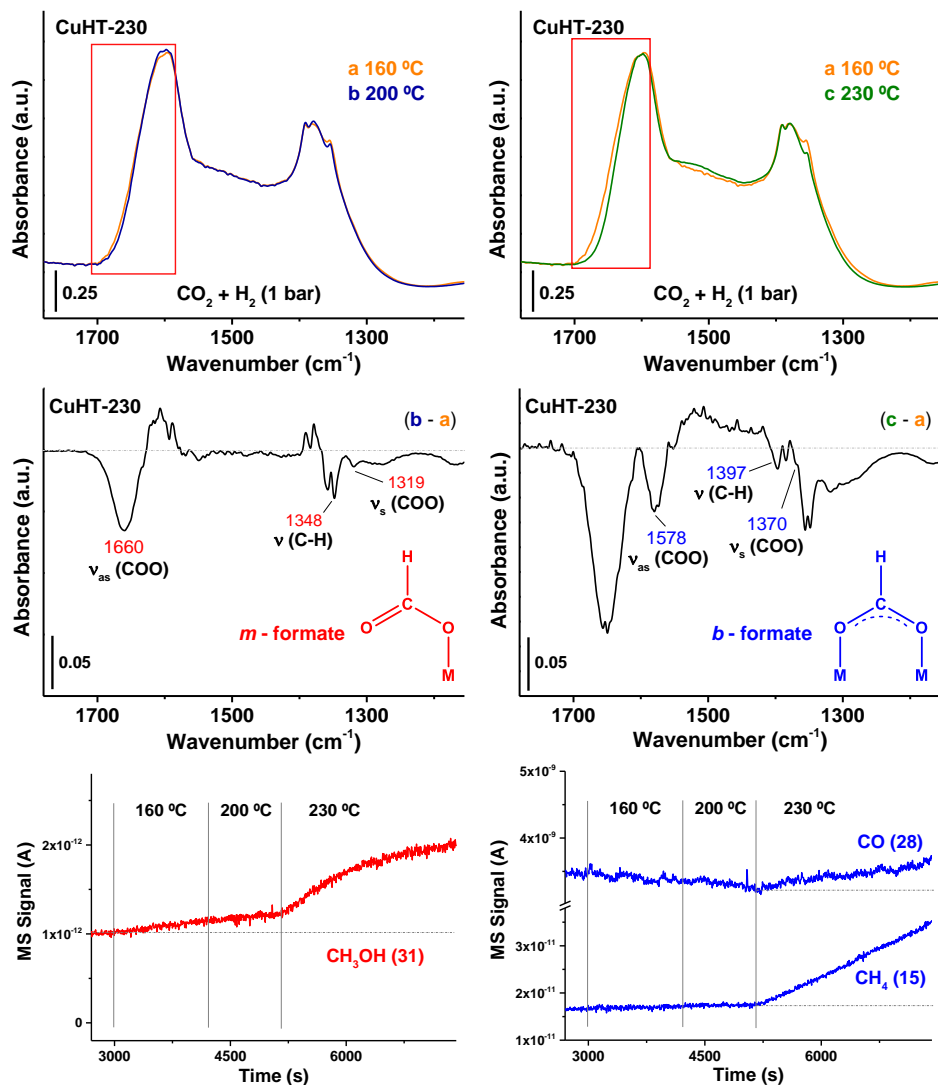


**Figure 4.7** Temperature-resolved IR studies under operando conditions at 1 bar in CO<sub>2</sub>/H<sub>2</sub> flow over CuHT-230 catalyst. Sequential steps at 200 and 230 °C are displayed on the left and on the right side, respectively. First row panels show IR spectra at indicated temperatures. Middle row panels exhibit the subtracted spectra. Third row panels show the reaction products evolution monitored by online MS.

A concomitant vanishing of the IR bands at 2853 and 1350 cm<sup>-1</sup> assigned to formate species onto the copper surface<sup>[78]</sup> is also observed, whereas its participation in the reaction can be ruled out.<sup>[77]</sup> A further increase in the reaction temperature to 230 °C results in the disappearance of additional IR bands at around 2872 cm<sup>-1</sup>, 1578 cm<sup>-1</sup>, 1397 cm<sup>-1</sup> and 1370 cm<sup>-1</sup>, associated with the  $\nu_{\text{stretch}}(\text{C-H})$ ,  $\nu_{\text{as}}(\text{COO})$ ,  $\delta(\text{C-H})$  and  $\nu_{\text{s}}(\text{COO})$  vibrations of bridge (*b*) formate species, respectively, paralleling the detection of methane and CO in the MS, confirmed by offline GC analysis (right panels in Figure 4.7, Figure 4.46, 4.47 and Table 4.17, 4.18). Assignment of both formate species is supported by their dissimilar  $\Delta\nu_{\text{as-s}}(\text{COO})$  splitting, i.e., 341 cm<sup>-1</sup> for monodentate and 208 cm<sup>-1</sup> of bridge formate species.<sup>[79]</sup>

These findings allow us to associate *m*-formate and *b*-formate species as intermediate in methanol and methane/CO formation, respectively. These correlations have been controversially discussed previously in the literature and scarcely supported experimentally. Moreover, the earlier detection of methanol (onset temperature of 160 °C) in comparison to methane and CO (onset temperature of 230 °C) sustains the higher reactivity of *m*-formate species, in agreement with previous literature studies.<sup>[70,80]</sup>

#### 4.4. Conclusions

In this chapter, a copper-based catalyst, mainly composed of inexpensive earth abundant MgO and prepared by an easy synthetic procedure in the absence of promoters, has demonstrated to be a potential candidate for the CO<sub>2</sub> hydrogenation to methanol. This copper mixed oxide catalyst was obtained after calcination and further reduction of a Mg-Al-Cu hydrotalcite precursor. The

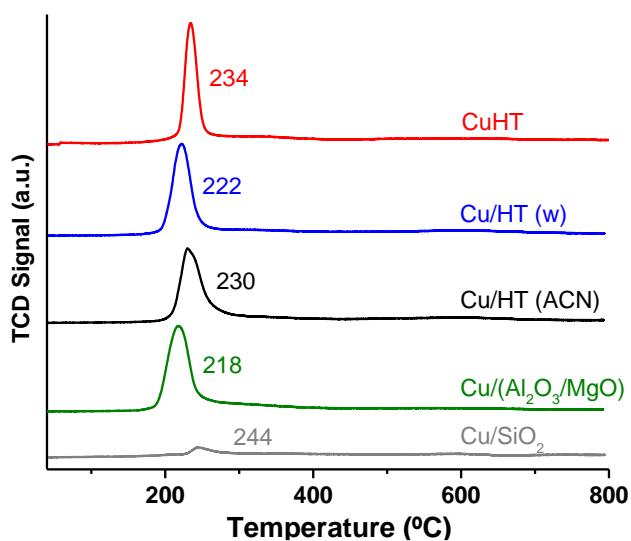
striking activity of our CuHT systems compared to conventional Cu/Al<sub>2</sub>O<sub>3</sub>/MgO catalysts has been ascribed to the stabilization of Cu<sup>+</sup> ions in lattice positions. This stabilization seems to be promoted under reaction conditions, which results in partial reconstruction of the metal oxide lattice linked to the “HT-memory effect” in the presence of water. This feature confers high resistance to the catalyst during alternative sequential temperature cycles, overcoming usual deactivation, one of the most critical drawbacks in methanol synthesis via CO<sub>2</sub> hydrogenation. Operando temperature resolved IR-MS experiments have enabled the discernment of monodentate formate species as the intermediate in methanol synthesis. These *m*-formate species are much more reactive than *b*-formate species, behaving the latter ones as intermediates in methane and CO formation. By combining spectroscopic and catalytic studies, we found that the stabilization of *m*-formate species is ascribed to surface doped Cu<sup>+</sup> ions, thereby explaining the superior catalytic performance of the Cu-based HT-derived materials. In addition, other essential aspects that remained ambiguous in the literature have been clarified in this study. Thus, high coverage of adsorbed species blocking preferentially low coordinated sites in the CuNPs has been visualized. Especially predominant in small copper nanoparticles, these species behave mostly as non-intermediate species (i.e., spectators), whose hydrogenation results in undesired methane and CO formation.

In conclusion, this study represents a step further in unraveling fundamental aspects that could help in the design of a new generation of efficient catalysts for CO<sub>2</sub> valorization.

## 4.5. Supporting Information

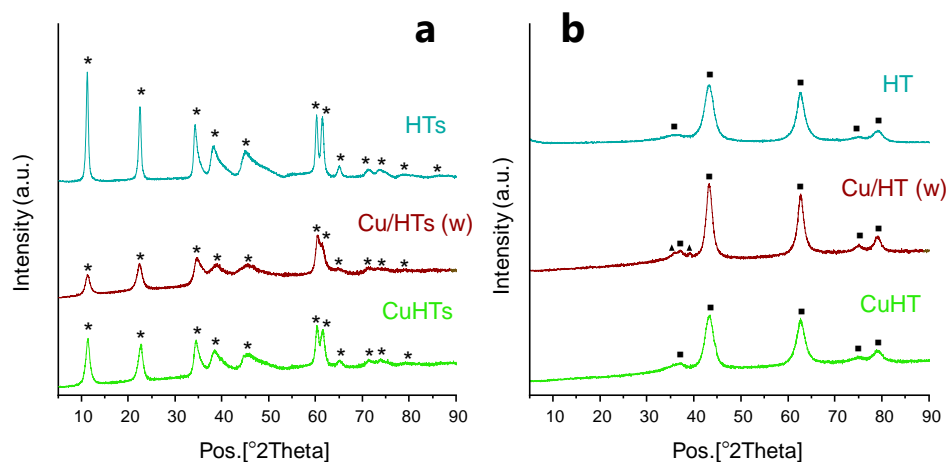
### 4.5.1. Physico-chemical properties of calcined-reduced catalysts

*TPR-H<sub>2</sub> experiments*



**Figure 4.8** Temperature-programmed reduction studies in 10% H<sub>2</sub>/Ar flow.

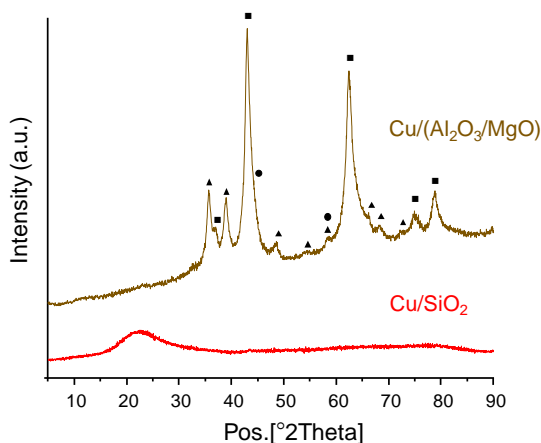
A reduction peak around 218-244 °C is observed in all the catalytic samples, associated with the reduction of highly dispersed and/or nano-sized CuO.<sup>[81-83]</sup>

*X-ray diffraction (XRD)*

\* Mg/Al hydrotalcite (PDF2: 00-022-0700)    ■ MgO (PDF2: 00-004-0829)    ▲ CuO (PDF2: 00-002-1040)

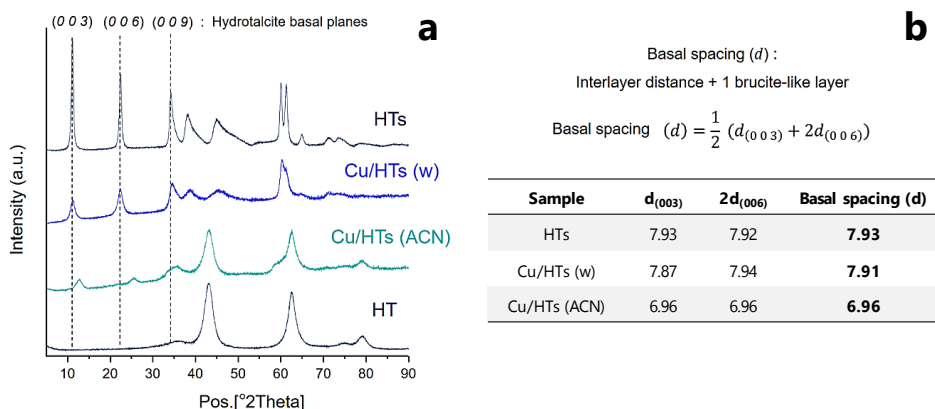
**Figure 4.9** XRD patterns of HT-type samples under study before (a) and after (b) calcination. “s” label in left panel refers to synthesized/as-prepared hydrotalcites.

A hydrotalcite phase is observed before calcination (Figure 4.9a). This crystalline phase collapses into a mixed oxide with a MgO-like structure after the thermal treatment (Figure 4.9b).



■ MgO (PDF2: 00-004-0829)    ▲ CuO (PDF2: 00-002-1040)    • Al<sub>2</sub>O<sub>3</sub> (PDF2: 00-001-1243)

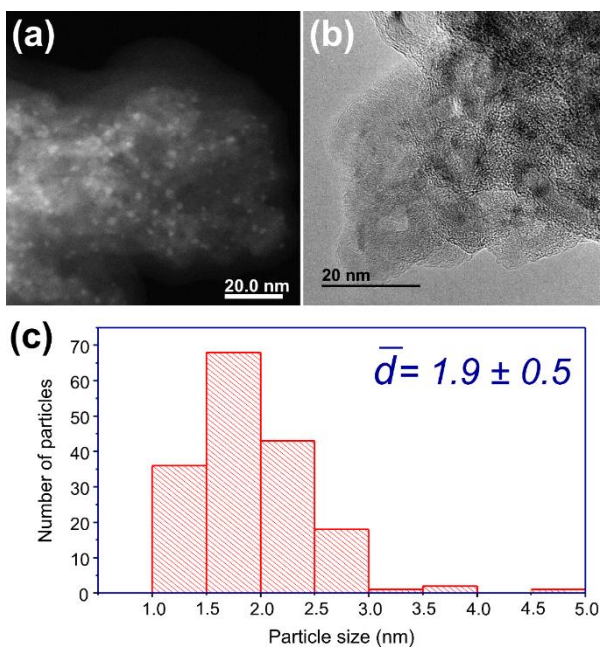
**Figure 4.10** XRD patterns of non-HT-derived samples after calcination.



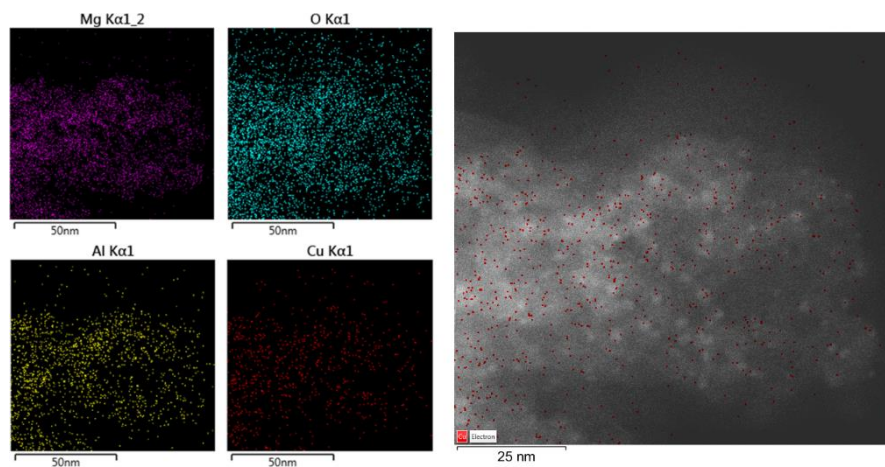
**Figure 4.11** “Memory effect” observed in the HT-derived materials. XR diffractograms for Cu/HTs (w) and Cu/HTs (ACN) after impregnation and comparison with as-prepared Mg-Al hydrotalcite (labeled as HTs) and collapsed Mg-Al-mixed oxide (labeled as HT) (a). Basal spacing calculations and results (b).

Figure 4.11 shows the influence of the impregnation with water or organic solvent (ACN) on the formation of hydrotalcite, mixed oxide and intermediate crystalline structures. The reversion from the oxide to the hydrotalcite occurs for both impregnated systems (Cu/HTs (w) and Cu/HTs (ACN)). Nonetheless, the transformation is slightly higher when using water as the solvent during the synthesis, as indicated by a higher basal spacing in the Cu/HTs (w) sample.

## Microscopy images

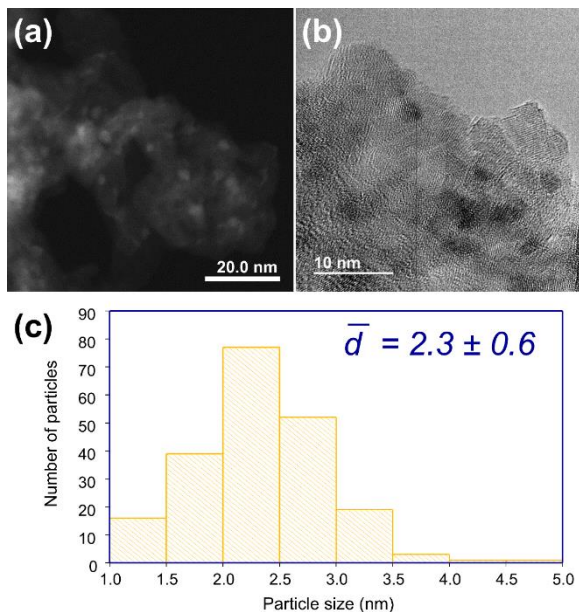


**Figure 4.12** HR-STEM (a) and HR-TEM (b) micrographs, and particle size distribution (c) for reduced CuHT-230 sample.

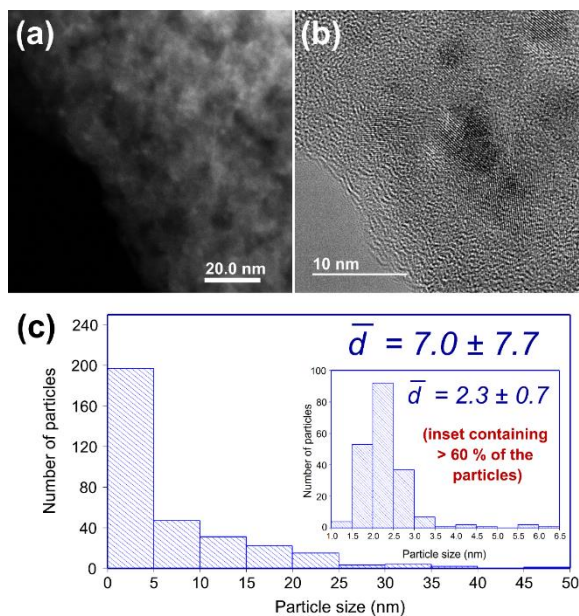


**Figure 4.13** Illustration of Cu nanoparticle identification by EDX mapping in STEM mode for reduced CuHT-230 sample.

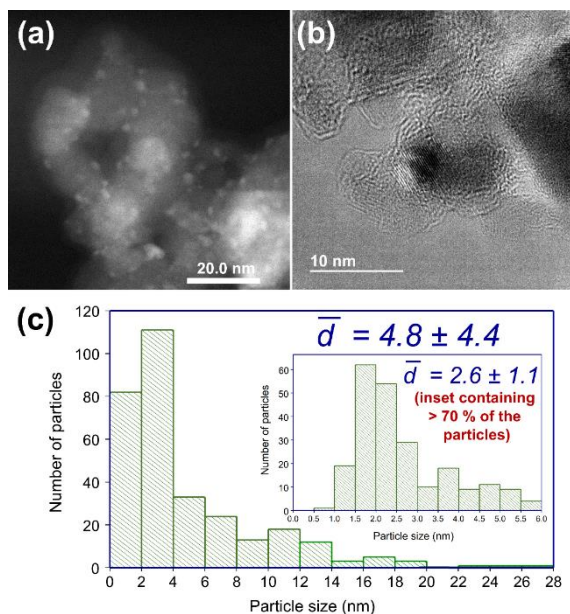




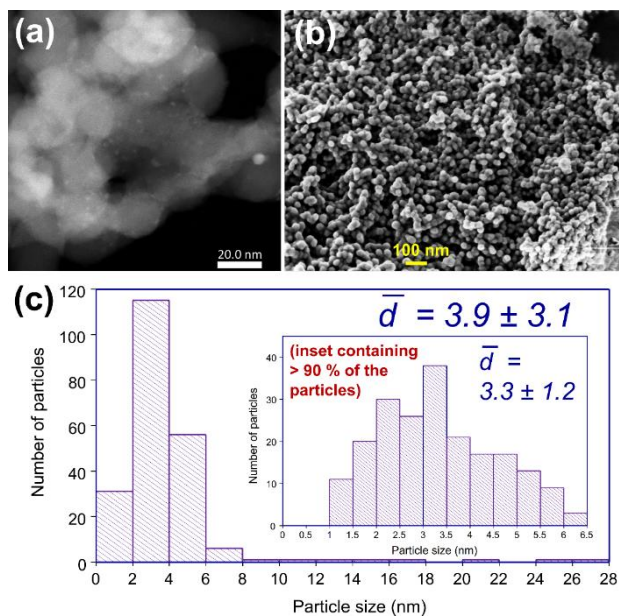
**Figure 4.14** HR-STEM (a) and HR-TEM (b) micrographs, and particle size distribution (c) for reduced CuHT-450 sample.



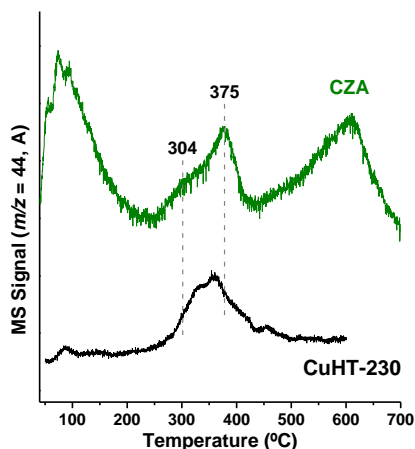
**Figure 4.15** HR-STEM (a) and HR-TEM (b) micrographs, and particle size distribution (c) for reduced Cu/HT (w) sample.



**Figure 4.16** HR-STEM (a), HR-TEM (b) micrographs, and particle size distribution (c) for reduced Cu/(Al<sub>2</sub>O<sub>3</sub>/MgO) sample.



**Figure 4.17** HR-STEM (a), HR-TEM (b) micrographs, and particle size distribution (c) for reduced Cu/SiO<sub>2</sub> sample.

*TPD-CO<sub>2</sub> experiments*

**Figure 4.18** TPD-CO<sub>2</sub> patterns of CuHT-230 and the commercial-like sample (CZA).

As already discussed in Chapter 3, surface basic sites have been proposed in several studies to play an important role in the stabilization of different reaction intermediate species, being moderate basic sites critical for enhanced methanol selectivity.<sup>[24,84,85]</sup> In particular, Gao et al. reported that strong/moderate basic sites are related with methanol formation, while medium basic sites give CO.<sup>[24]</sup> In fact, a weak CO<sub>2</sub> adsorption on the catalyst surface prevents the sequential hydrogenation via C-O bond dissociation, enhancing the parallel RWGS reaction with CO formation.<sup>[42,86,87]</sup> Thus, an adequate control of basic sites is key in this reaction. In this sense, CuHT-230 sample shows moderate basic sites with TPD-CO<sub>2</sub> desorption peaks in the range to that of the commercial-like CZA sample (see Figure 4.18).

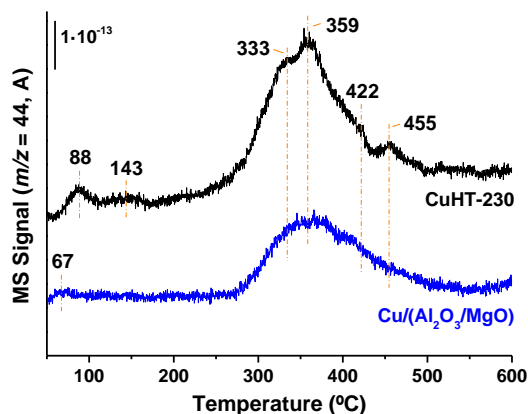


**Figure 4.19** TPD-CO<sub>2</sub> performed on reduced CuHT-230 and Cu/(Al<sub>2</sub>O<sub>3</sub>/MgO) samples.

#### 4.5.2. Catalytic activity in the CO<sub>2</sub> hydrogenation to methanol

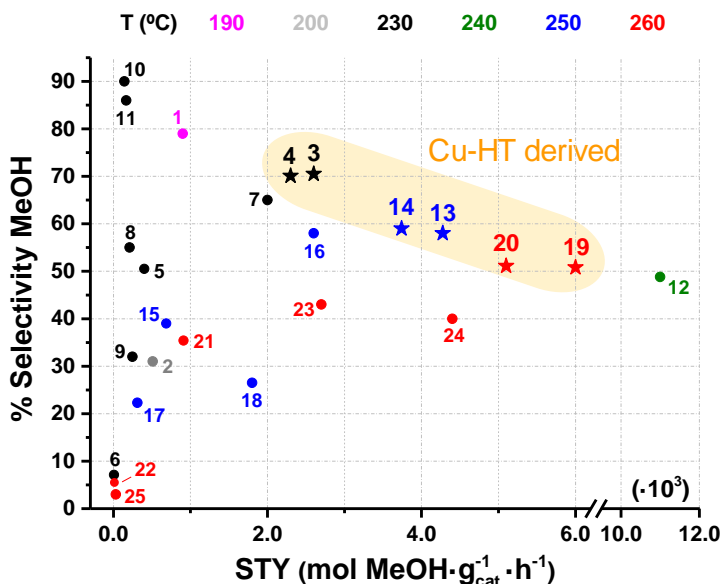


**Figure 4.20** Comparison of the catalytic performance of the herein reported Cu-HT-derived samples at different temperatures in the CO<sub>2</sub> hydrogenation with other nano-sized Cu-based catalysts in the literature. Numbers refer to the entries placed in Table 4.2 (first column). Entries 13-15 represent interpolated values of CuHT-230, Cu/HT (w) and Cu/Al<sub>2</sub>O<sub>3</sub>/MgO samples at 250 °C and ~28500 mL·g<sub>cat</sub><sup>-1</sup>·h<sup>-1</sup>, respectively (included for comparative purpose).

**Table 4.2** State of the art of nano size Cu-based catalysts in the CO<sub>2</sub> hydrogenation to methanol.

Entry Fig. 4.20	Catalyst	Preparation	Cu loading (% wt)	CuNP size (nm)*	H <sub>2</sub> /CO <sub>2</sub> mol ratio	T (°C)	P (bar)	GHSV (h <sup>-1</sup> )	WHSV (mL·g <sub>cat</sub> <sup>-1</sup> ·h <sup>-1</sup> )	X <sub>CO2</sub> (%)	S <sub>MeOH</sub> (%)	STY (mol <sub>MeOH</sub> ·g <sub>cat</sub> <sup>-1</sup> ·h <sup>-1</sup> )	TOF (s <sup>-1</sup> )	REF
1	Cu/SiO <sub>2</sub> (shattuckite)	Flame spray pyrolysis	17.8	3.8 (c)	3:1	190	30	2040	-	5.2	79	9.0·10 <sup>-4</sup>	3.3·10 <sup>-4</sup>	[12]
2	Cu/MgO/Al <sub>2</sub> O <sub>3</sub>	Co-precipitation	51	29 (b)	2.8:1	200	20	2000	-	3.6	31	5.1·10 <sup>-4</sup> 8.2 mg <sub>MeOH</sub> ·mL <sub>cat</sub> <sup>-1</sup> ·h <sup>-1</sup>	1.3·10 <sup>-3</sup>	[13]
-	Cu/TiO <sub>2</sub> (C/T)	Impregnation	10	30.9 (b)	3:1	220	30	4800	-	4.3	29.8	-	6.8·10 <sup>-3</sup>	[14]
-	Cu/MgO/TiO <sub>2</sub> (C/1%MT)	Impregnation	10	30.8 (b)	3:1	220	30	4800	-	5.2	37.9	-	6.9·10 <sup>-3</sup>	[14]
<b>3</b>	<b>CuHT-230</b>	<b>Co-precipitation</b>	<b>10.2</b>	<b>1.9 (a)</b>	<b>3:1</b>	<b>230</b>	<b>20</b>	<b>14963</b>	<b>28429</b>	<b>1.3</b>	<b>70.5</b>	<b>2.6·10<sup>-3</sup></b> <b>1.5 g<sub>MeOH</sub>·g<sub>Cu</sub><sup>-1</sup>·h<sup>-1</sup></b>	-	<b>Our work</b>
-	<b>CuHT-230</b>	<b>Co-precipitation</b>	<b>10.2</b>	<b>1.9 (a)</b>	<b>3:1</b>	<b>230</b>	<b>20</b>	<b>1425</b>	<b>2849</b>	<b>8.3</b>	<b>71.2</b>	<b>1.7·10<sup>-3</sup></b> <b>1.0 g<sub>MeOH</sub>·g<sub>Cu</sub><sup>-1</sup>·h<sup>-1</sup></b>	-	<b>Our work</b>
4	Cu/HT (w)	Impregnation	8.8	2.3 (a)	3:1	230	20	14978	28457	1.1	70.1	2.3·10 <sup>-3</sup>	-	Our work
5	Cu/(Al <sub>2</sub> O <sub>3</sub> /MgO)	Impregnation	8.3	2.6 (a)	3:1	230	20	22894	28274	0.3	50.5	4.0·10 <sup>-4</sup>	-	Our work
-	Cu/(Al <sub>2</sub> O <sub>3</sub> /MgO)	Impregnation	8.3	2.6 (a)	3:1	230	20	2193	2851	1.9	50.5	2.8·10 <sup>-4</sup>	-	Our work
6	Cu/SiO <sub>2</sub>	Impregnation	1.5	3.3 (a)	3:1	230	20	11888	27104	<0.1	7.1	7.1·10 <sup>-6</sup>	-	Our work

\*Nanoparticle size calculated through microscopy (a), XRD (b), chemisorption (c).

Entry Fig. 4.20	Catalyst	Preparation	Cu loading (% wt)	CuNP size (nm)*	H <sub>2</sub> /CO <sub>2</sub> mol ratio	T (°C)	P (bar)	GHSV (h <sup>-1</sup> )	WHSV (mL·g <sub>cat</sub> <sup>-1</sup> ·h <sup>-1</sup> )	X <sub>CO2</sub> (%)	S <sub>MeOH</sub> (%)	STY (mol <sub>MeOH</sub> ·g <sub>cat</sub> <sup>-1</sup> ·h <sup>-1</sup> )	TOF (s <sup>-1</sup> )	REF
7	Cu/a-ZrO <sub>2</sub>	Impregnation (IW)	10	~2 (a)	3:1	230	30	-	7200	4.0	65	2.0·10 <sup>-3</sup>	-	[88]
8	Cu/ZrO <sub>2</sub>	Grafting	0.8	2.2 (a)	3:1	230	25	-	1908	2.1	55	2.1·10 <sup>-4</sup>	-	[89]
-	Cu/ZrO <sub>2</sub>	Grafting	0.8	2.2 (a)	3:1	230	25	-	7400	~0.7	72	-	7.3·10 <sup>-4</sup>	[89]
-	Cu/SiO <sub>2</sub>	Grafting	2.3	2.1 (a)	3:1	230	25	-	Extrapolated to 0	-	49	-	1.7·10 <sup>-4</sup>	[89]
9	Cu/SiO <sub>2</sub>	Grafting	2.3	2.1 (a)	3:1	230	25	-	3276	2.1	32	2.5·10 <sup>-4</sup>	-	[89]
-	Cu/SiO <sub>2</sub>	Grafting	2.3	2.1 (a)	3:1	230	25	-	7400	~0.7	42	-	1.6·10 <sup>-4</sup>	[89]
-	Cu/SiO <sub>2</sub> (shattuckite)	Flame spray pyrolysis	17.8	3.8 (c)	3:1	230	30	2040	-	-	-	1.1·10 <sup>-3</sup>	-	[12]
-	Cu/SiO <sub>2</sub>	Surf. organom. chemistry	20	2.8 (a)	3:1	230	25	-	-	<10	49.0	-	2.3·10 <sup>-4</sup>	[17]
10	Cu-Zn/SiO <sub>2</sub>	Surf. organom. chemistry	4.16	3.9 (a)	3:1	230	25	-	24000	1.5	86	1.7·10 <sup>-4</sup> 1.6 g <sub>MeOH</sub> ·g <sub>Cu</sub> <sup>-1</sup> ·h <sup>-1</sup>	-	[19]
-	Cu-Zn/SiO <sub>2</sub>	Surf. organom. chemistry	4.16	3.9 (a)	3:1	230	25	-	2400	4.4	72	4.1·10 <sup>-5</sup> 0.4 g <sub>MeOH</sub> ·g <sub>Cu</sub> <sup>-1</sup> ·h <sup>-1</sup>	-	[19]

\*Nanoparticle size calculated through microscopy (a), XRD (b), chemisorption (c).

Entry Fig. 4.20	Catalyst	Preparation	Cu loading (% wt)	CuNP size (nm)*	H <sub>2</sub> /CO <sub>2</sub> mol ratio	T (°C)	P (bar)	GHSV (h <sup>-1</sup> )	WHSV (mL·g <sub>cat</sub> <sup>-1</sup> ·h <sup>-1</sup> )	X <sub>CO2</sub> (%)	S <sub>MeOH</sub> (%)	STY (mol <sub>MeOH</sub> ·g <sub>cat</sub> <sup>-1</sup> ·h <sup>-1</sup> )	TOF (s <sup>-1</sup> )	REF
11	Cu-Ga/SiO <sub>2</sub>	Surf. organom. chemistry	3.88	4.6 (a)	3:1	230	25	-	24000	0.8	90	1.4·10 <sup>-4</sup> 1.3 g <sub>MeOH</sub> ·g <sub>Cu</sub> <sup>-1</sup> ·h <sup>-1</sup>	-	[18]
-	Cu-Ga/SiO <sub>2</sub>	Surf. organom. chemistry	3.88	4.6 (a)	3:1	230	25	-	2400	2.7	81	4.2·10 <sup>-5</sup> 0.4 g <sub>MeOH</sub> ·g <sub>Cu</sub> <sup>-1</sup> ·h <sup>-1</sup>	-	[18]
12	Cu/ZrO <sub>2</sub> (DP3)	Deposition / co-precipitation	30.0	16	3:1	240	20	5400	-	6.3	48.8	1.1·10 <sup>-2</sup>	-	[90]
16	Cu/Ga <sub>2</sub> O <sub>3</sub> (IW)	Impregnation (IW)	2	-	3.4:1	250	30	20000	-	1.09	58	2.6·10 <sup>-3</sup>	-	[54]
17	Cu/m-SiO <sub>2</sub>	Impregnation	12.1	30.5 (b)	3:1	250	50	-	6000	2.1	22.3	3.1·10 <sup>-4</sup>	-	[9]
18	Cu@m-SiO <sub>2</sub>	Sol-Gel	12.0	4.7 (b)	3:1	250	50	-	6000	10.2	26.5	1.8·10 <sup>-3</sup>	-	[9]
<b>19</b>	<b>CuHT-230</b>	<b>Co-precipitation</b>	<b>10.2</b>	<b>1.9 (a)</b>	<b>3:1</b>	<b>260</b>	<b>20</b>	<b>14963</b>	<b>28429</b>	<b>4.0</b>	<b>50.8</b>	<b>6.0·10<sup>-3</sup></b> <b>3.4 g<sub>MeOH</sub>·g<sub>Cu</sub><sup>-1</sup>·h<sup>-1</sup></b>	-	<b>Our work</b>
<b>20</b>	<b>Cu/HT (w)</b>	<b>Impregnation</b>	<b>8.8</b>	<b>2.3 (a)</b>	<b>3:1</b>	<b>260</b>	<b>20</b>	<b>14978</b>	<b>28457</b>	<b>3.4</b>	<b>51.1</b>	<b>5.1·10<sup>-3</sup></b>	-	<b>Our work</b>
<b>21</b>	<b>Cu/(Al<sub>2</sub>O<sub>3</sub>/MgO)</b>	<b>Impregnation</b>	<b>8.3</b>	<b>2.6 (a)</b>	<b>3:1</b>	<b>260</b>	<b>20</b>	<b>22894</b>	<b>28274</b>	<b>0.9</b>	<b>35.4</b>	<b>9.1·10<sup>-4</sup></b>	-	<b>Our work</b>
<b>22</b>	<b>Cu/SiO<sub>2</sub></b>	<b>Impregnation</b>	<b>1.5</b>	<b>3.3 (a)</b>	<b>3:1</b>	<b>260</b>	<b>20</b>	<b>11888</b>	<b>27104</b>	<b>0.1</b>	<b>5.5</b>	<b>1.2·10<sup>-5</sup></b>	-	<b>Our work</b>

\*Nanoparticle size calculated through microscopy (a), XRD (b), chemisorption (c).

Entry Fig. 4.20	Catalyst	Preparation	Cu loading (% wt)	CuNP size (nm)*	H <sub>2</sub> /CO <sub>2</sub> mol ratio	T (°C)	P (bar)	GHSV (h <sup>-1</sup> )	WHSV (mL·g <sub>cat</sub> <sup>-1</sup> ·h <sup>-1</sup> )	X <sub>CO2</sub> (%)	S <sub>MeOH</sub> (%)	STY (mol <sub>MeOH</sub> ·g <sub>cat</sub> <sup>-1</sup> ·h <sup>-1</sup> )	TOF (s <sup>-1</sup> )	REF
23	Cu/a-ZrO <sub>2</sub>	Impregnation (IW)	10	~2 (a)	3:1	260	30	-	7200	8.0	43	2.7·10 <sup>-3</sup>	4.5·10 <sup>-3</sup>	[88]
24	Cu/SiO <sub>2</sub> -AE	Ammonia evaporation	10.7	2.1 (a)	4:1	260	30	-	16000	~8.0	40	4.4·10 <sup>-3</sup>	-	[10]
25	Cu-4.2/SiO <sub>2</sub>	Water-in-oil microemulsion	9.9	4.2 (a)	3:1	260	8	-	2000-4500	-	1-3	3.0·10 <sup>-5</sup>	3.0·10 <sup>-5</sup>	[11]
-	Cu/SiO <sub>2</sub>	Water-in-oil microemulsion	9.9	5.0 (a)	3:1	260	8	-	2000-10000	1.4	6.5	-	2.2·10 <sup>-5</sup>	[45]
-	Cu/TiO <sub>2</sub> (C/T)	Impregnation	10	30.9 (b)	3:1	260	30	4800	-	9.5	21	-	-	[14]
-	Cu/MgO/TiO <sub>2</sub> (C/1%MT)	Impregnation	10	30.8 (b)	3:1	260	30	4800	-	10.2	24	-	-	[14]

\*Nanoparticle size calculated through microscopy (a), XRD (b), chemisorption (c).



**Table 4.3** Catalytic results of samples under study at 20 bar pressure and variable temperature (230-280 °C). WHSV~28500 mL·g<sub>cat</sub><sup>-1</sup>·h<sup>-1</sup> (27104 mL·g<sub>cat</sub><sup>-1</sup>·h<sup>-1</sup> for Cu/SiO<sub>2</sub>).

T (°C)	Catalyst	X <sub>CO<sub>2</sub></sub> (%)	CO <sub>2</sub> selectivity (%)				STY (mol <sub>prod</sub> ·g <sub>cat</sub> <sup>-1</sup> ·h <sup>-1</sup> )	
			MeOH	CO	HCOOMe	CH <sub>4</sub>	MeOH	CO
230	CuHT-230	1.3	70.5	28.6	0.8	0.1	2.6·10 <sup>-3</sup>	1.1·10 <sup>-3</sup>
	CuHT-450	1.1	61.8	36.6	0.7	0.9	2.0·10 <sup>-3</sup>	1.2·10 <sup>-3</sup>
	Cu/HT (w)	1.1	70.1	28.8	0.9	0.2	2.3·10 <sup>-3</sup>	9.4·10 <sup>-4</sup>
	Cu/HT (ACN)	1.1	69.1	25.4	0.9	4.6	2.2·10 <sup>-3</sup>	8.0·10 <sup>-4</sup>
	Cu/(Al <sub>2</sub> O <sub>3</sub> /MgO)	0.3	50.5	43.7	0.9	4.9	4.0·10 <sup>-4</sup>	3.5·10 <sup>-4</sup>
	Cu/SiO <sub>2</sub>	<0.1	7.1	79.6	0.0	13.3	7.1·10 <sup>-6</sup>	8.0·10 <sup>-5</sup>
240	CuHT-230	1.8	64.2	35.1	0.5	0.2	3.4·10 <sup>-3</sup>	1.9·10 <sup>-3</sup>
	CuHT-450	1.6	57.6	41.3	0.5	0.6	2.6·10 <sup>-3</sup>	1.9·10 <sup>-3</sup>
	Cu/HT (w)	1.6	64.6	34.5	0.6	0.3	3.0·10 <sup>-3</sup>	1.6·10 <sup>-3</sup>
	Cu/HT (ACN)	1.5	64.9	31.8	0.6	2.7	2.9·10 <sup>-3</sup>	1.4·10 <sup>-3</sup>
	Cu/(Al <sub>2</sub> O <sub>3</sub> /MgO)	0.4	44.6	49.9	0.7	4.8	5.0·10 <sup>-4</sup>	5.6·10 <sup>-4</sup>
	Cu/SiO <sub>2</sub>	<0.1	6.8	81.3	0.0	11.9	9.5·10 <sup>-6</sup>	1.1·10 <sup>-4</sup>
260	CuHT-230	4.0	50.8	48.9	0.2	0.1	6.0·10 <sup>-3</sup>	5.7·10 <sup>-3</sup>
	CuHT-450	3.3	46.7	52.7	0.2	0.4	4.5·10 <sup>-3</sup>	5.1·10 <sup>-3</sup>
	Cu/HT (w)	3.4	51.1	48.4	0.2	0.3	5.1·10 <sup>-3</sup>	4.8·10 <sup>-3</sup>
	Cu/HT (ACN)	3.2	52.6	46.1	0.2	1.1	4.9·10 <sup>-3</sup>	4.3·10 <sup>-3</sup>
	Cu/(Al <sub>2</sub> O <sub>3</sub> /MgO)	0.9	35.4	60.3	0.3	4.0	9.1·10 <sup>-4</sup>	1.5·10 <sup>-3</sup>
	Cu/SiO <sub>2</sub>	0.1	5.5	80.3	0.0	14.2	1.2·10 <sup>-5</sup>	1.7·10 <sup>-4</sup>
280	CuHT-230	8.5	36.7	63.2	0.0	0.1	9.1·10 <sup>-3</sup>	1.6·10 <sup>-2</sup>
	CuHT-450	7.1	34.8	64.8	0.1	0.3	7.2·10 <sup>-3</sup>	1.3·10 <sup>-2</sup>
	Cu/HT (w)	7.1	37.8	62.0	0.1	0.1	7.8·10 <sup>-3</sup>	1.3·10 <sup>-2</sup>
	Cu/HT (ACN)	6.7	39.1	60.3	0.1	0.5	7.6·10 <sup>-3</sup>	1.2·10 <sup>-2</sup>
	Cu/(Al <sub>2</sub> O <sub>3</sub> /MgO)	2.0	28.9	67.8	0.1	3.2	1.6·10 <sup>-3</sup>	3.8·10 <sup>-3</sup>
	Cu/SiO <sub>2</sub>	0.1	4.5	79.5	0.0	16.0	1.6·10 <sup>-5</sup>	2.9·10 <sup>-4</sup>

**Table 4.4** Catalytic results of selected samples at 230 °C, 20 bar and variable WHSV. Selectivity to minor products (i.e., HCOOMe and CH<sub>4</sub>) not shown.

Catalyst	W/F (mg·min·mL <sup>-1</sup> )	WHSV (mL·g <sub>cat</sub> <sup>-1</sup> ·h <sup>-1</sup> )	X <sub>CO<sub>2</sub></sub> (%)	CO <sub>2</sub> selectivity (%)		STY (mol·g <sub>cat</sub> <sup>-1</sup> ·h <sup>-1</sup> )	
				MeOH	CO	MeOH	CO
CuHT-230	2.1	28429	1.3	70.5	28.6	2.6·10 <sup>-3</sup>	1.1·10 <sup>-3</sup>
	10.5	5695	4.9	69.9	29.5	2.0·10 <sup>-3</sup>	8.5·10 <sup>-4</sup>
	14.0	4271	6.1	71.5	28.0	1.9·10 <sup>-3</sup>	7.5·10 <sup>-4</sup>
	21.1	2849	8.3	71.2	28.3	1.7·10 <sup>-3</sup>	6.8·10 <sup>-4</sup>
	42.1	1424	13.2	69.6	29.9	1.3·10 <sup>-3</sup>	5.7·10 <sup>-4</sup>
	105.1	571	22.3	67.0	32.5	8.7·10 <sup>-4</sup>	4.2·10 <sup>-4</sup>
Cu/SiO <sub>2</sub>	2.2	27104	<0.1	7.1	79.6	7.1·10 <sup>-6</sup>	8.0·10 <sup>-5</sup>
	6.2	9653	0.25	5.1	90.9	1.3·10 <sup>-5</sup>	2.3·10 <sup>-4</sup>
	7.8	7722	0.44	7.8	89.8	2.7·10 <sup>-5</sup>	3.1·10 <sup>-4</sup>
Cu/ (Al <sub>2</sub> O <sub>3</sub> /MgO)	2.1	28429	0.3	50.5	43.7	4.0·10 <sup>-5</sup>	3.5·10 <sup>-4</sup>
	10.5	5700	1.1	49.2	46.5	3.3·10 <sup>-4</sup>	3.1·10 <sup>-4</sup>
	14.0	4274	1.4	49.8	46.0	3.0·10 <sup>-4</sup>	2.8·10 <sup>-4</sup>
	21.0	2851	1.9	50.5	45.3	2.8·10 <sup>-4</sup>	2.5·10 <sup>-4</sup>
	42.1	1426	3.3	51.1	44.9	2.4·10 <sup>-4</sup>	2.1·10 <sup>-4</sup>
	105.0	571	7.0	54.1	42.4	2.2·10 <sup>-4</sup>	1.7·10 <sup>-4</sup>
CZA	0.4	134118	4.8	82.8	16.1	5.4·10 <sup>-2</sup>	1.0·10 <sup>-2</sup>
	0.9	66511	7.6	75.2	24.2	3.9·10 <sup>-2</sup>	1.2·10 <sup>-2</sup>
	1.5	39430	12.2	73.7	24.4	3.6·10 <sup>-2</sup>	1.2·10 <sup>-2</sup>
	1.9	31216	12.9	73.7	26.3	3.0·10 <sup>-2</sup>	1.1·10 <sup>-2</sup>
	2.3	26287	13.9	69.8	28.9	2.6·10 <sup>-2</sup>	1.1·10 <sup>-2</sup>
	2.5	24255	14.8	68.8	30.8	2.5·10 <sup>-2</sup>	1.1·10 <sup>-2</sup>
	2.8	21195	16.8	67.1	32.8	2.4·10 <sup>-2</sup>	1.2·10 <sup>-2</sup>
	4.2	14130	19.3	64.1	35.9	1.8·10 <sup>-2</sup>	1.0·10 <sup>-2</sup>
	8.5	7065	21.9	61.7	37.9	9.8·10 <sup>-3</sup>	6.0·10 <sup>-3</sup>

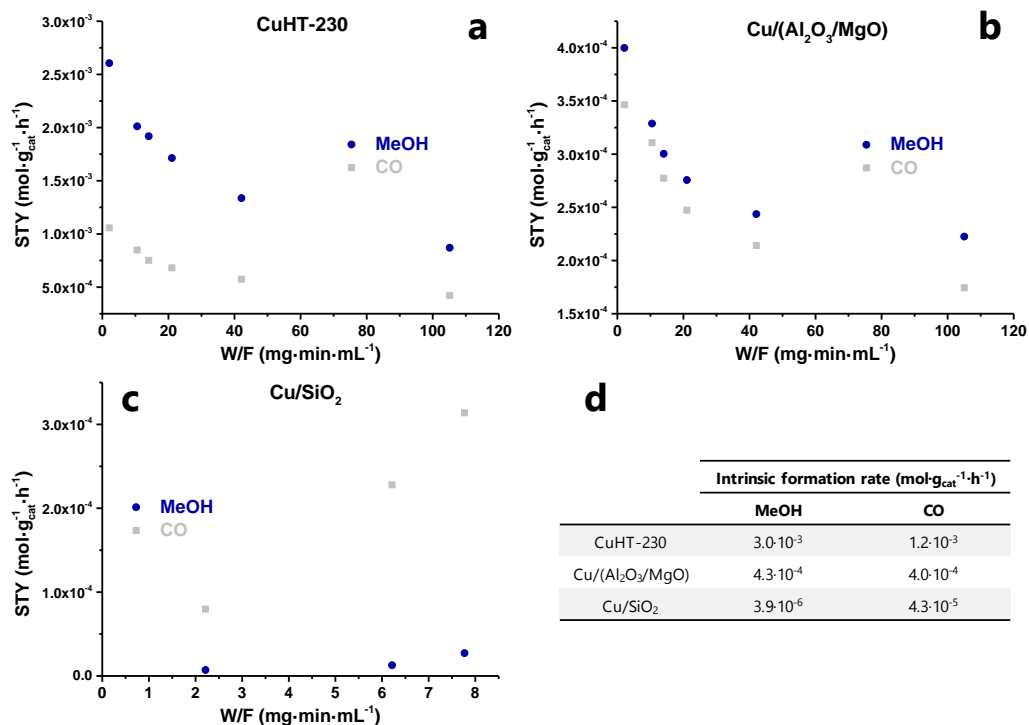


**Figure 4.21** Extrapolation to “zero contact time” conditions at 230 °C and 20 bar in selected samples: CuHT-230 (a), Cu/(Al<sub>2</sub>O<sub>3</sub>/MgO) (b), and Cu/SiO<sub>2</sub> (c). MeOH and CO intrinsic formation rates obtained for catalysts under study (d).

For CuHT-230 and Cu/(Al<sub>2</sub>O<sub>3</sub>/MgO) catalysts, both methanol and CO formation rates decrease at increasing contact time, behavior already observed in other catalysts such as the commercial-like Cu/ZnO/Al<sub>2</sub>O<sub>3</sub> catalyst.<sup>[19]</sup>

**Table 4.5** Analysis of the apparent activation energy ( $E_{a,app}$ ) (Arrhenius plot).

Catalyst	$E_{a,app}$ MeOH (kJ·mol <sup>-1</sup> )	$E_{a,app}$ CO (kJ·mol <sup>-1</sup> )
CuHT-230	61.6	125.0
CuHT-450	58.6	111.8
Cu/HT (w)	57.2	121.6
Cu/(Al <sub>2</sub> O <sub>3</sub> /MgO)	65.8	111.9
Cu/SiO <sub>2</sub>	45.0	64.7

The values of  $E_{a,app}$  calculated for MeOH and CO production at 20 bar are in the range of those reported on similar Cu catalytic systems.<sup>[91]</sup>

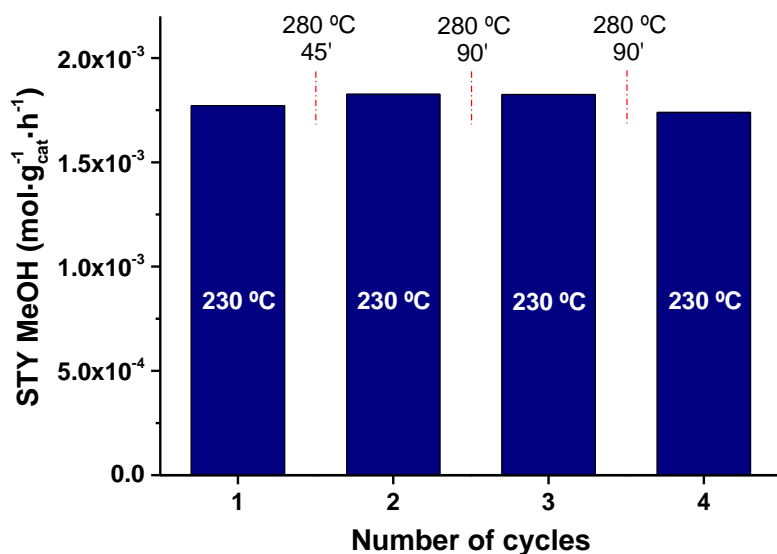


**Figure 4.22** Methanol production on the CuHT-230 catalyst after alternating cycles of CO<sub>2</sub> hydrogenation at 230 and 280 °C (20 bar and WHSV of 5700 mL·g<sub>cat</sub><sup>-1</sup>·h<sup>-1</sup>). The intervals placed between blue bars correspond to the time in minutes at which the catalyst has been exposed to high temperature (i.e., 280 °C) MeOH synthesis conditions.

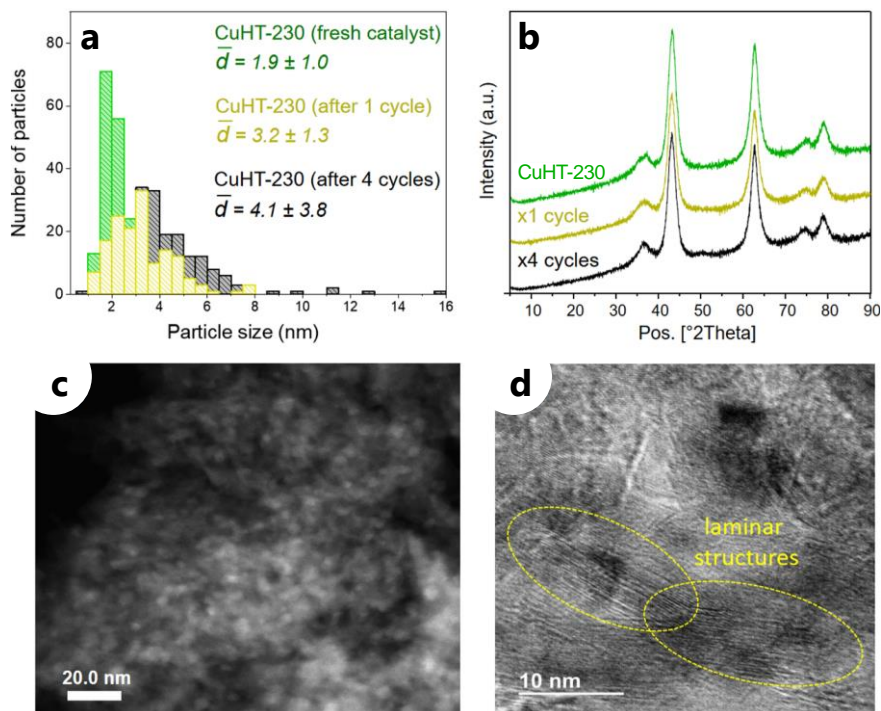


**Figure 4.23** Stability of CuNPs in the CuHT-230 catalyst under long term (85 h) reaction conditions at 230 °C, 20 bar and 5700 mL $_{\text{cat}}^{-1}\cdot\text{h}^{-1}$ , followed by alternating cycles of temperature between 230 and 280 °C (1 and 4 cycles): Cu particle size evolution throughout the catalytic processes calculated by STEM imaging by measuring at least 200 particles (a), X-ray powder diffraction pattern for CuHT-230 sample before and after reaction, STEM (c) and TEM (d) images for CuHT-230 after the catalytic processes.

After the long-term experiment (Figure 4.3d), CuHT-230 sample presented a slight increase in particle size from 1.9 to 3.2 and 4.1 nm (for 1 and 4 thermal cycles, respectively). In addition, microscopy performed on the spent sample revealed laminar structures, characteristic of LDH. This observation indicates a partial surface reversion from the collapsed oxide to the hydrotalcite phase during catalysis.

## 4.5.3. X-ray photoelectron spectroscopy (XPS) characterization

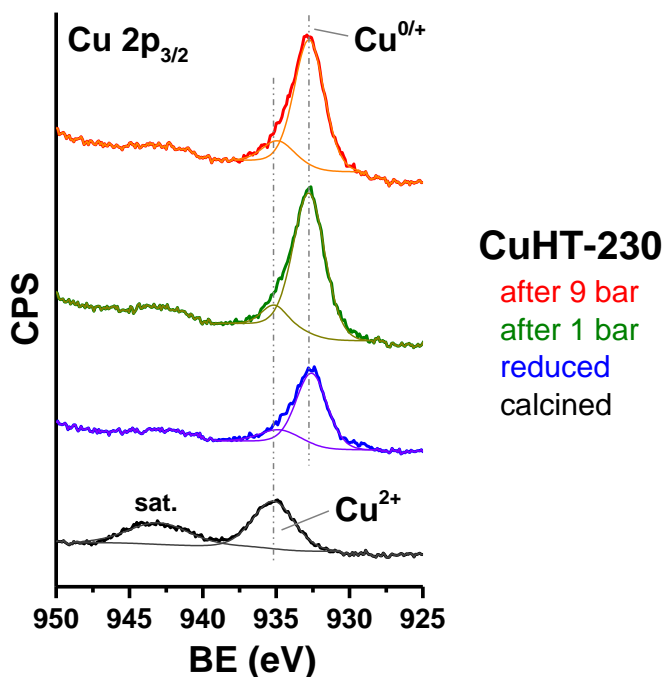


**Figure 4.24** XPS core lines of Cu  $2p_{3/2}$  at  $h\nu=1486.6$  eV excitation energy of CuHT-230 sample at different reaction conditions.

**Table 4.6** XPS core levels and surface chemical composition of CuHT-230 sample under different reaction conditions ( $h\nu=1486.6$  eV excitation energy).

CuHT-230 treatment	Cu $2p_{3/2}$			Mg 1s	Al 2s	% mol				Mg/Al ratio	Cu/Al ratio
	BE <sub>1</sub> (eV) <sup>a</sup>	BE <sub>2</sub> (eV) <sup>a</sup>	$\alpha'$ (eV)	BE (eV)	BE (eV)	Cu	Mg	Al	O		
Calcined	935.1	-	1851.4	1303.9	119.4	2.03	22.90	11.85	63.22	1.93	0.17
Reduced	934.8	932.5	1850.8	1303.9	119.4	1.50	23.72	13.10	61.68	1.81	0.11
After 1 bar	935.1	932.7	1850.0	1303.9	119.4	1.45	24.77	12.48	61.30	1.98	0.11
After 9 bar	934.8	932.7	1850.0	1303.9	119.4	1.34	24.35	12.92	61.39	1.88	0.10

<sup>a</sup>BE<sub>1</sub> corresponds to Cu<sup>2+</sup>, which appears as minor fraction in the reduced and in the working catalysts; BE<sub>2</sub> corresponds to Cu<sup>0</sup>.

**Table 4.7** XPS core levels and surface chemical composition of the reduced samples ( $h\nu=1486.6$  eV excitation energy).

Catalyst	Cu 2p <sub>3/2</sub>			Mg 1s	Al 2s	% mol				Mg/Al ratio	Cu/Al ratio
	BE <sub>1</sub> (eV) <sup>a</sup>	BE <sub>2</sub> (eV) <sup>a</sup>	α' (eV)	BE (eV)	BE (eV)	Cu	Mg	Al	O		
CuHT-230	934.8	932.5	1850.8	1303.9	119.4	1.50	23.72	13.10	61.68	1.81	0.11
Cu/HT (w)	-	932.6	1851.1	1303.9	119.6	2.13	14.23	8.28	75.36	1.72	0.26
Cu/(Al <sub>2</sub> O <sub>3</sub> /MgO)	935.2	932.7	1850.9	1303.9	119.4	2.99	18.03	14.51	64.47	1.24	0.21

<sup>a</sup>BE<sub>1</sub> corresponds to Cu<sup>2+</sup>, which appears as minor fraction in the reduced working catalysts; BE<sub>2</sub> corresponds to Cu<sup>0</sup>.

**Table 4.8** XPS core levels and surface chemical composition of the reduced Cu/SiO<sub>2</sub> sample ( $h\nu=1486.6$  eV excitation energy).

Catalyst	Cu 2p <sub>3/2</sub>		Si 2p	% mol			Cu/Si ratio
	BE <sub>1</sub> (eV) <sup>a</sup>	α' (eV)	BE (eV)	Cu	Si	O	
Cu/SiO <sub>2</sub>	932.0	1850.4	103.5	0.47	41.05	58.48	0.01

<sup>a</sup>BE<sub>1</sub> corresponds to Cu<sup>0</sup>.

#### 4.5.4. Infrared characterization: Identification of Cu<sup>+</sup> species

##### *FTIR using CO as probe molecule*

CO has been widely utilized as probe molecule in IR spectroscopy due to its high sensitivity to the oxidation and coordination state of the metal ions.<sup>[51]</sup> Then, the FTIR spectra of CO adsorption on the **reduced supports** and on the corresponding **copper-based catalysts** are discussed below.

- **Reduced supports**

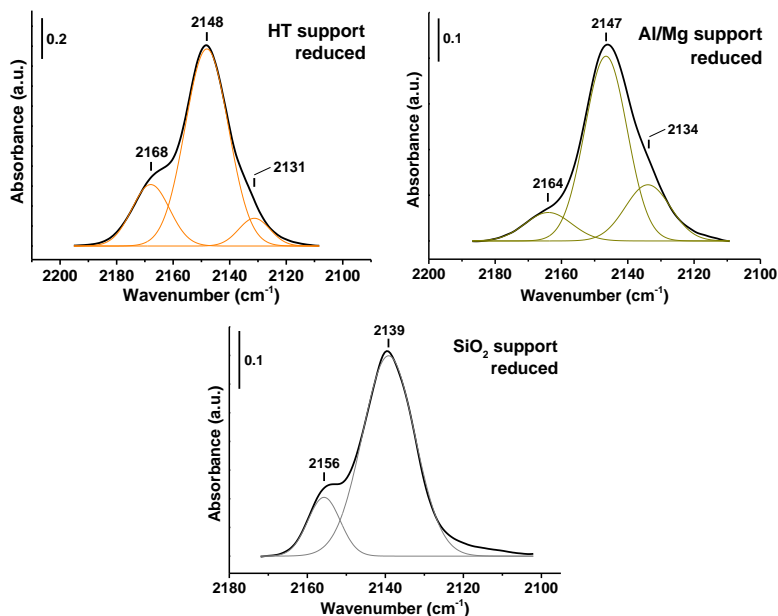


**Figure 4.25** IR-CO deconvoluted spectra of reduced supports.

HT and Al/Mg supports: Three same features are observed in both spectra. The two bands at higher wavenumbers are ascribed to Mg<sup>2+</sup> under-coordinated Lewis acid sites and OH groups.<sup>[50,92-94]</sup> The band placed at a lower frequency (2131 cm<sup>-1</sup> for HT and 2134 cm<sup>-1</sup> for Al/Mg) corresponds to a CO multilayer, which is in direct interaction with the surface.<sup>[92]</sup>

SiO<sub>2</sub> support: On the one hand, the band placed at 2156 cm<sup>-1</sup> is ascribed to hydroxyl (OH) groups.<sup>[51]</sup> The band that appears at lower wavenumbers (2139 cm<sup>-1</sup>) is assigned to a CO multilayer interacting with the surface, as in the other supports.<sup>[92]</sup>

- **Copper-based catalysts**

CuHT-230 samples: In Figure 4.25, the reduced HT support presents a minor component at 2131 cm<sup>-1</sup>. A similar band at ~2137 cm<sup>-1</sup> (but more intense)



appears in the reduced CuHT-230 derived samples, increasing in intensity after 9 bar reaction (see Figure 4.26 and Table 4.9). In the literature, similar IR bands have been ascribed to isolated Cu<sup>+</sup> ions in Cu-ZSM-5<sup>[58]</sup> and to Cu<sup>+</sup> ions strongly interacting with the support in a Cu/TiO<sub>2</sub>-SiO<sub>2</sub> catalyst.<sup>[59]</sup> In the last case, a band around 2140 cm<sup>-1</sup> has been assigned to the  $\nu_s$  modes of Cu<sup>+</sup>(CO)<sub>2</sub> species, being the asymmetric mode around 2100 cm<sup>-1</sup>. In other studies, a band at 2135 cm<sup>-1</sup> has been assigned to Cu<sup>+</sup> cations interacting with CO.<sup>[60]</sup> The presence of Cu<sup>+</sup> species in the reduced and reacted samples is supported by the shift in the copper auger parameter to lower values (Table 4.6) observed from XPS data on the CuHT-230 sample. A more detailed analysis of the IR band at 2137 cm<sup>-1</sup> and its assignation to Cu<sup>+</sup> species combining UV-VIS and DFT simulation is found in Subsection 4.5.5.

Cu/(Al<sub>2</sub>O<sub>3</sub>/MgO) sample: In this case, the IR band at ~2137 cm<sup>-1</sup> is also present in the reduced Al/Mg support. The area of this IR band (normalized by the respective sample weight) is higher in the reduced Al/Mg support than in the reduced and reacted Cu/(Al<sub>2</sub>O<sub>3</sub>/MgO) samples (Figure 4.27 and Table 4.10).

Cu/SiO<sub>2</sub> sample: Similar to the above discussed Cu/(Al<sub>2</sub>O<sub>3</sub>/MgO) sample, the component at 2139 cm<sup>-1</sup> in the Cu/SiO<sub>2</sub> catalyst, remains constant in intensity after different treatments, and analogous than in the SiO<sub>2</sub> support. (Figure 4.28 and Table 4.11).

Thus, the assignation of these bands to Cu<sup>+</sup>, in both cases is unclear. Therefore, an additional probe molecule (i.e., CD<sub>3</sub>CN) has been selected and discussed to reinforce our hypothesis.

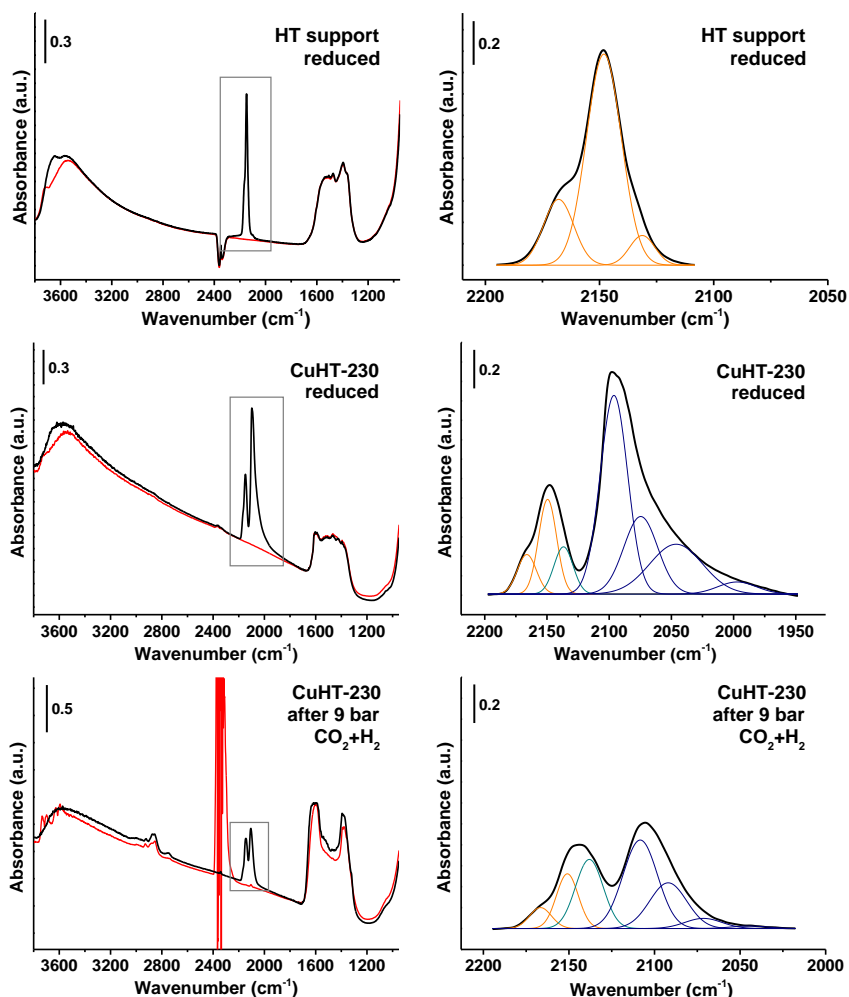


**Figure 4.26** IR-CO spectra of reduced HT support (first row), and CuHT-230 catalyst before (middle row) and after (third row) 9 bar CO<sub>2</sub> hydrogenation. Left panels contain full range spectra before (red) and after (black) CO adsorption. Right panels exhibit the deconvoluted  $\nu(\text{C}\equiv\text{O})$  region.

**Table 4.9** Quantification of Cu<sup>+</sup> species on the reduced HT support and CuHT-230 catalyst under different reaction conditions.

	HT support	Reduced	9 bar
Area comp. 2135 cm <sup>-1</sup>	1.92	4.66	6.67
mg pellet	8.7	10.5	10.3
Area-mg <sup>-1</sup>	0.22	0.44	0.65

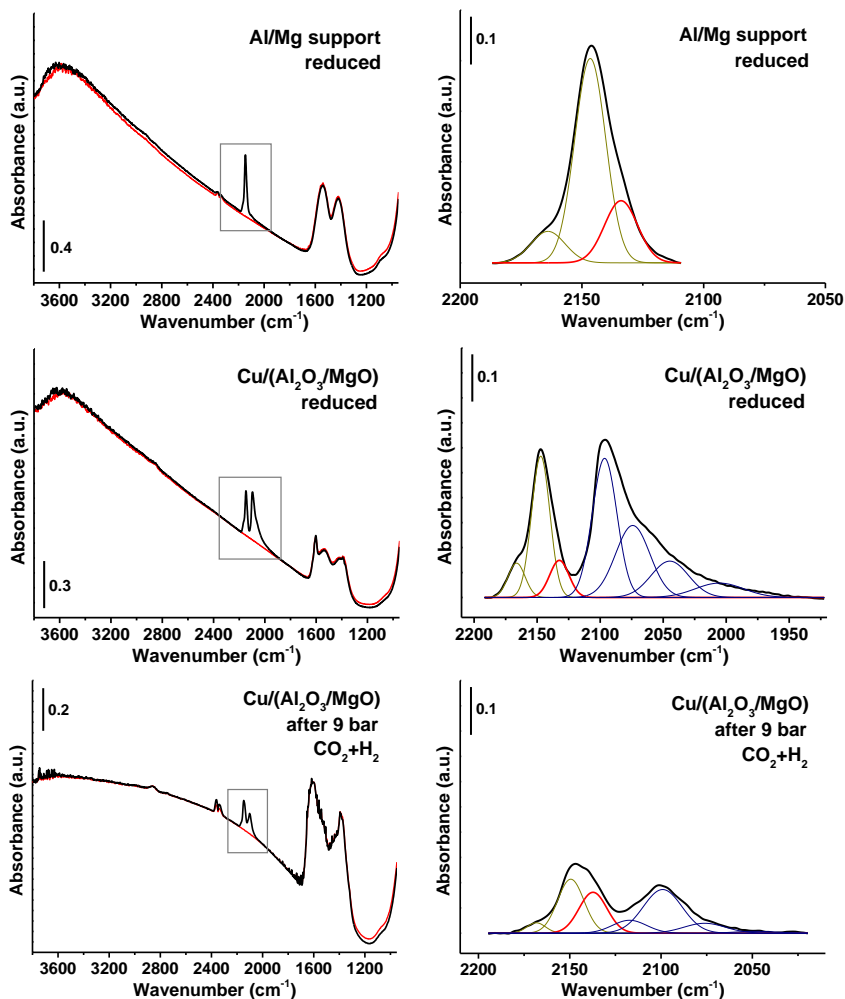


**Figure 4.27** IR-CO spectra of reduced Al/Mg support (first row), and Cu/(Al<sub>2</sub>O<sub>3</sub>/MgO) catalyst before (middle row) and after (third row) 9 bar CO<sub>2</sub> hydrogenation. Left panels contain full range spectra before (red) and after (black) CO adsorption. Right panels exhibit the deconvoluted  $\nu(\text{C}\equiv\text{O})$  region.

**Table 4.10** Quantification of Cu<sup>+</sup> species on the reduced Al/Mg support and Cu/(Al<sub>2</sub>O<sub>3</sub>/MgO) catalyst under different reaction conditions.

	Al/Mg support	Reduced	9 bar
Area comp. 2134 cm <sup>-1</sup>	2.09	1.42	1.55
mg pellet	6.5	7.2	8.7
Area·mg <sup>-1</sup>	0.32	0.20	0.18

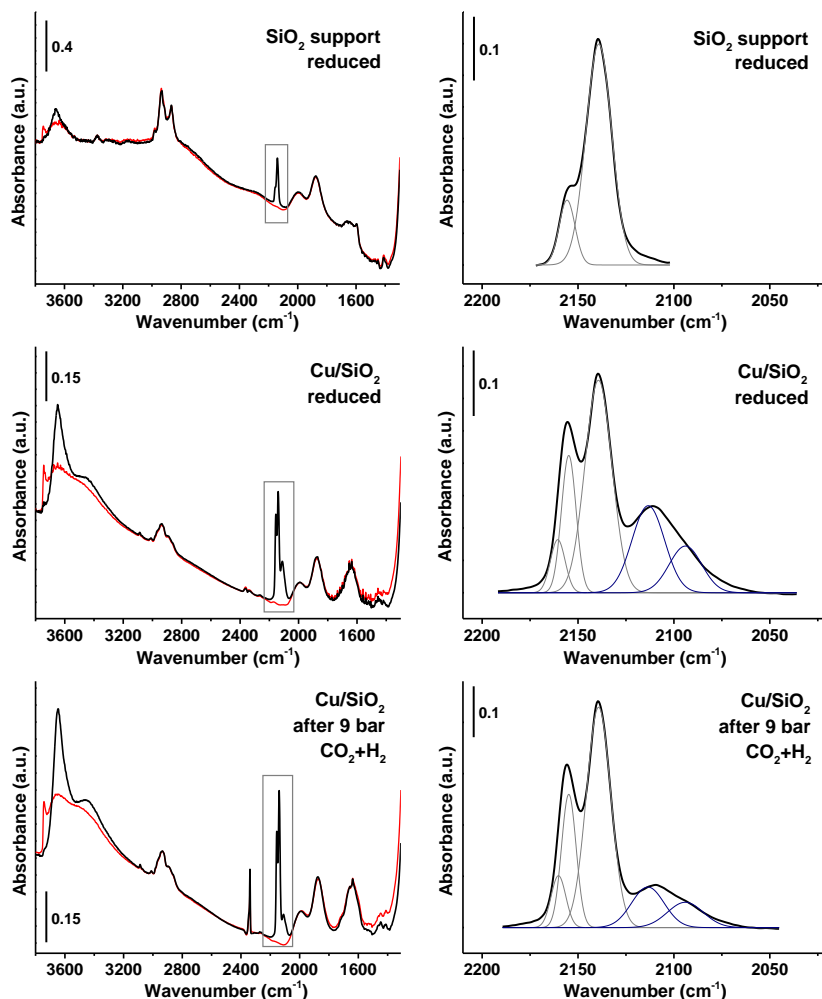


**Figure 4.28** IR-CO spectra of reduced SiO<sub>2</sub> support (first row), and Cu/SiO<sub>2</sub> catalyst before (middle row) and after (third row) 9 bar CO<sub>2</sub> hydrogenation. Left panels contain full range spectra before (red) and after (black) CO adsorption. Right panels exhibit the deconvoluted  $\nu(\text{C}\equiv\text{O})$  region.

**Table 4.11** Quantification of Cu<sup>+</sup> species on the reduced SiO<sub>2</sub> support and Cu/SiO<sub>2</sub> catalyst under different reaction conditions.

	SiO <sub>2</sub> support	Reduced	9 bar
Area comp. 2139 cm <sup>-1</sup>	5.88	5.77	6.85
mg pellet	6.1	7.2	6.7
Area-mg <sup>-1</sup>	0.96	0.80	1.02

*FTIR using CD<sub>3</sub>CN as probe molecule*

- **Cu/(Al<sub>2</sub>O<sub>3</sub>/MgO) sample:** Adsorption of CD<sub>3</sub>CN at increasing dosing (0.05 to 8.2 mbar) results in one band at 2260 cm<sup>-1</sup> due to physisorbed CD<sub>3</sub>CN (Figure 4.29). No band characteristic of CD<sub>3</sub>CN interacting with Cu<sup>+</sup> ions (2297 cm<sup>-1</sup>) is observed.<sup>[95]</sup>

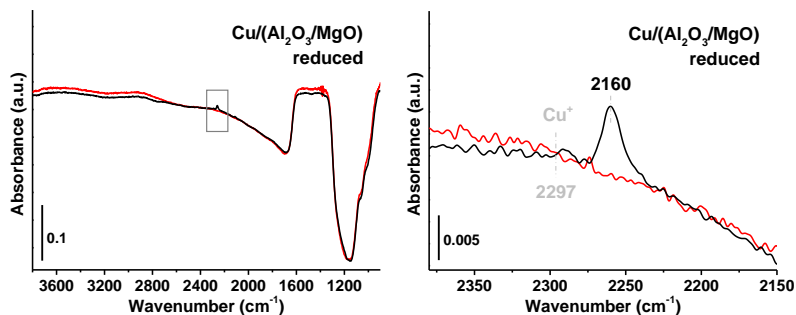


**Figure 4.29** IR-ACN spectra adsorbed at 25 °C on the reduced Cu/(Al<sub>2</sub>O<sub>3</sub>/MgO) sample. Left panel contains full range spectra before (red) and after (black) CD<sub>3</sub>CN adsorption. Right panel exhibits the zone marked by the gray square.

- **Cu/SiO<sub>2</sub> sample:** Adsorption of CD<sub>3</sub>CN at increasing dosing (0.05 to 8.2 mbar) results in one band at 2273 cm<sup>-1</sup> due to CD<sub>3</sub>CN interacting with the OH of syanol groups<sup>[96]</sup> (Figure 4.30). Similarly to the Cu/(Al<sub>2</sub>O<sub>3</sub>/MgO) sample, no band associated with Cu<sup>+</sup> is observed in the Cu/SiO<sub>2</sub> system.

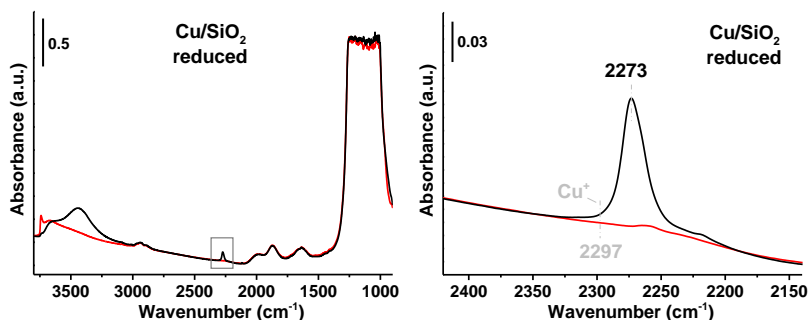


**Figure 4.30** IR-ACN spectra adsorbed at 25 °C on the reduced Cu/SiO<sub>2</sub> sample. Left panel contains full range spectra before (red) and after (black) CD<sub>3</sub>CN adsorption. Right panel exhibits the zone marked by the gray square.

- CuHT-230 sample:** In this case, a strong overlapping of IR bands associated with the copper-free HT support at 2293 and 2261 cm<sup>-1</sup> is observed (Figure 4.31), impeding the identification of Cu<sup>+</sup> species at 2297 cm<sup>-1</sup>. Therefore, in the HT-based catalysts CO is a more suitable probe molecule for identification of Cu<sup>+</sup> ions.

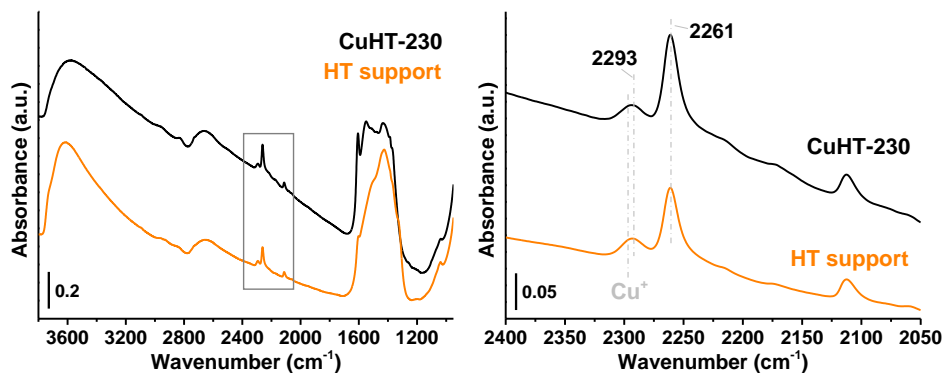


**Figure 4.31** IR-ACN spectra adsorbed at 25 °C on the reduced CuHT-230 (black) and HT support (orange) samples. Left panel contains full range spectra after CD<sub>3</sub>CN titration. Right panel exhibits the zone marked by the gray square for both systems.

#### 4.5.5. Assignment of the IR band at 2137 cm<sup>-1</sup> to Cu<sup>+</sup> ions in metal oxide lattice positions

As discussed above, the IR band at 2137 cm<sup>-1</sup> has been ascribed in the literature to CO interacting with Cu<sup>+</sup> ions.<sup>[59,60]</sup> In order to reinforce the assignment of this type of Cu<sup>+</sup> species, UV-VIS studies and theoretical (DFT) simulation of CO frequencies interacting with different types of Cu ions have been done.

##### UV-VIS

The substitution of Mg atoms by copper in the hydrotalcite structure and the corresponding Cu-based Mg-Al-O mixed oxide derived from decomposition of

the layered double hydroxalite structure has been confirmed by several authors using high resolved <sup>27</sup>Al MAS NMR and diffuse reflectance UV-VIS spectroscopy.<sup>[97-100]</sup> An in depth structural characterization of Cu ions in mixed metal oxides has been done by Chaudhari et al.<sup>[100]</sup> allowing discriminate between highly dispersed isolated Cu<sup>2+</sup> ions in octahedral coordination (band at 260 nm) in the metal oxide lattice, Cu<sup>2+</sup> in oligomeric (Cu-O-Cu)<sub>x</sub> species in octahedral and distorted octahedral coordination (410 and 360 nm, respectively) and bulk-like CuO (620 nm). Additionally, a band at 230 nm had been assigned by Schmal et al., to isolated Cu<sup>+</sup> species.<sup>[99]</sup> In our study, the UV-VIS spectra of the calcined and reduced CuHT-230 sample is shown in Figure 4.32.

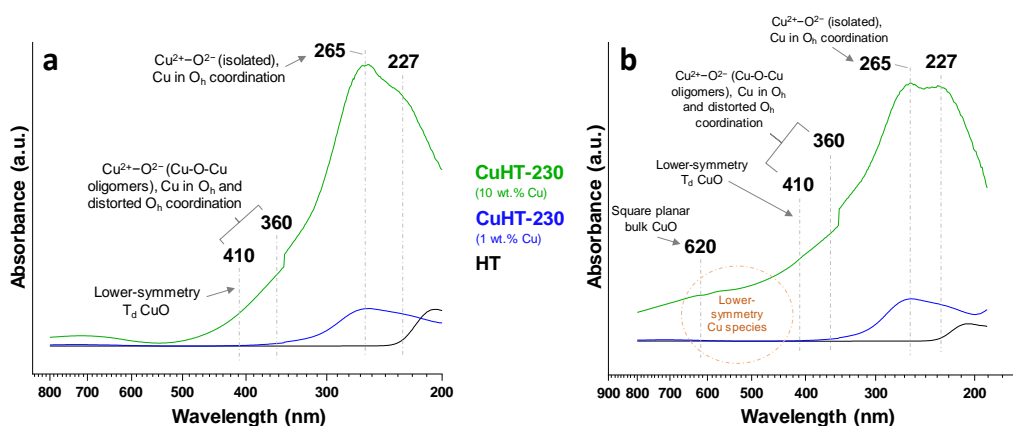


**Figure 4.32** UV-VIS spectra of (a) calcined and (b) ex situ reduced systems. A CuHT-230 sample with 1 wt % Cu (blue line) has been synthesized for comparative purposes following the synthetic procedure indicated in Subsection 4.2.1 (adjusting the amount of copper precursor).

According to the literature, the band at 227 nm, whose intensity increases in the reduced sample, can be ascribed to isolated Cu<sup>+</sup> species,<sup>[99]</sup> and the band at 265 nm is associated to LMCT from O<sup>2-</sup> to an isolated Cu<sup>2+</sup> ion in octahedral coordination.<sup>[100]</sup> Both ions can be considered to be doping the MgO lattice. In

addition, a shoulder at 410 and 360 nm, which may be ascribed to Cu<sup>2+</sup>-O-Cu<sup>2+</sup> oligomers, is observed in both calcined and reduced CuHT-230 (10 wt % Cu) samples (green line), while absent in the reference Cu HT-230 (1 wt % Cu) samples (blue line). From these results we can confirm the presence of Cu<sup>+</sup> ions in metal oxide lattice positions.

*DFT simulations (collaboration with Dr. Ganduglia-Pirovano's group from ICP)*

- **Cu oxidation state**

To determine the oxidation state of Cu species in the different models considered, the Bader charges of metallic Cu and Cu<sub>2</sub>O bulks were first calculated. In Cu bulk, each atom is Cu<sup>0</sup> with a Bader charge of 17 (see Table 4.12) that matches the number of valence electrons: 3p<sup>6</sup> 3d<sup>10</sup> 4s<sup>1</sup>. Instead, in Cu<sub>2</sub>O, we have formally Cu<sup>+</sup> and a Bader charge of 16.442, which is 0.558 less than Cu<sup>0</sup>. On the other hand, when doping with one Cu atom the MgO(100) surface, we replace a Mg<sup>2+</sup> by a Cu<sup>2+</sup> and it turns out that the calculated charge of Cu<sup>2+</sup> is close to 16. By using these data as a reference, we conclude on the oxidation state of Cu ions in the other model systems considered in this work.

On one hand, when replacing one Mg<sup>2+</sup> ion at the MgO(100) surface by two Cu ions (see Figure 4.33f), the latter are formally in the +1 oxidation state. This is corroborated by the calculated Bader charge of the Cu atoms, since they differ by only 0.032 and 0.058, respectively, from the Bader charge of Cu in Cu<sub>2</sub>O bulk (see Table 4.12). On the other hand, the Bader charges of Cu species when they are adsorbed and in direct contact with the MgO surface, as it is the case of the Cu<sub>2</sub>/MgO(100) system (see Figure 4.33g), indicate a slight increase of the charges compared to Cu<sup>0</sup> species in bulk Cu (Table 4.12), defining these species as Cu<sup>δ</sup>.



**Table 4.12** Cu Bader charge values for each model studied. The differences with respect to Cu ( $\text{Cu}_i\text{-Cu}_{\text{bulk}}$ ) and Cu<sub>2</sub>O ( $\text{Cu}_i\text{-Cu}_2\text{O}$ ) bulks are also indicated.

Model	Cu charge	$\Delta(\text{Cu}_i\text{-Cu}_{\text{bulk}})$	$\Delta(\text{Cu}_i\text{-Cu}_2\text{O})$
<b>Cu bulk</b>	17.000	0.000	0.558
<b>Cu<sub>2</sub>O.HSE bulk</b>	16.442	-0.558	<b>0.000</b>
<b>Cu<sub>2</sub><sup>doping</sup></b>	16.474	-0.526	<b>0.032</b>
	16.500	-0.500	<b>0.058</b>
<b>Cu<sub>2</sub><sup>ads</sup></b>	17.109	0.109	0.667
	17.132	0.132	0.690
<b>Cu<sub>5</sub><sup>ads</sup></b>	17.174	0.174	0.732
	16.954	<b>-0.046</b>	0.512
	16.978	<b>-0.022</b>	0.536
	17.174	0.174	0.732
	16.973	<b>-0.027</b>	0.531

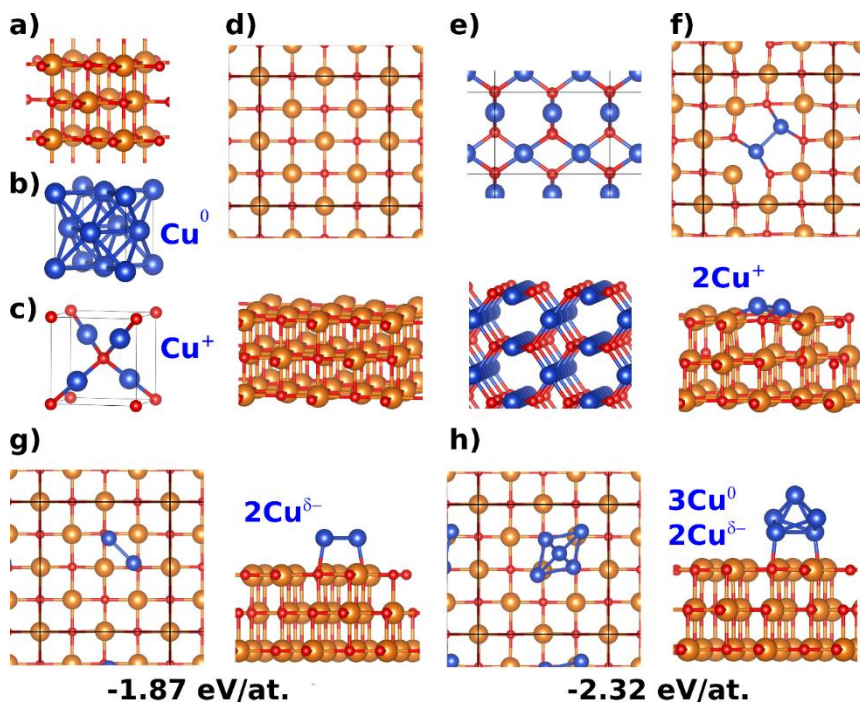


**Figure 4.33** MgO (a), Cu (b) and Cu<sub>2</sub>O (c) bulk unit cells. Top and side view of: MgO(100) (d), Cu<sub>2</sub>O(110) (e), Cu<sub>2</sub>-doped MgO(100) (f), Cu<sub>2</sub> (g), and Cu<sub>5</sub> (h) adsorbed nanoparticles on MgO(100). For each Cu-containing model, the Cu oxidation state is indicated. The adsorption energies of the Cu clusters per atom with respect to atomic Cu<sub>gas</sub> of the models (g,h) are indicated. Color code: Mg (orange), O (red), and Cu (blue).

When the size of the adsorbed Cu nanoparticles is larger, as for the example of Cu<sub>5</sub><sup>ads</sup>, it can be observed that only two Cu atoms are bound to oxygen atoms of the MgO support, while the others are bound only to Cu atoms. The Bader charges of the three Cu atoms that are not in direct contact with the MgO support are formally Cu<sup>0</sup>, since their charge differ by only 0.022, 0.027 and 0.046 from that of Cu in metallic Cu bulk (Table 4.12). Figure 4.33 also indicates the adsorption energy per Cu atom in the Cu<sub>m</sub><sup>ads</sup> models (m = 2, 5). These results suggest that Cu tends to form compact nanoparticles and that the formation of Cu-Cu bonds is favored, which is in good agreement with the structure reported by Geudtner et al.<sup>[101]</sup>

- **CO adsorption**

The objective is here to demonstrate that the CO stretch frequencies of CO molecule adsorbed on the model systems described above are not only sensitive to charge state but configuration-dependent.

Recently, Zhang et al. studied the morphology-dependent reduction kinetics and the surface copper species evolution of a Cu<sub>2</sub>O catalyst under a reductive CO atmosphere. They reported DRIFT results at 123 K where CO, bound to Cu<sup>+</sup>, has a stretch vibrational frequency of 2107 ( $\Delta\nu = -36$  with respect to gas phase CO) and 2109 cm<sup>-1</sup> ( $\Delta\nu = -34$ ) in nanocrystals with orientations (110) and (111), respectively, while for the (100) orientation, CO would not adsorb.<sup>[102]</sup> Moreover, Soon et al. reported a theoretical shift of -26 cm<sup>-1</sup> for Cu<sup>+</sup> in Cu<sub>2</sub>O(111).<sup>[103]</sup> For metallic surfaces of Cu (Cu<sup>0</sup>), there is also a dependence with the surface orientation, as summarized by Braglia et al.,<sup>[104]</sup> with experimental redshifts of -49, -55 and -71 cm<sup>-1</sup> for high CO coverage on the three most stable (110), (100) and (111) surfaces, respectively. Generalizing these results might be an oversimplification of the

complexity of the systems, but they undoubtedly demonstrate how the oxidation state and chemical environment of Cu could affect the CO stretch frequency.

The one monolayer adsorption (saturation coverage) of CO molecules on the (1×1)-Cu<sub>2</sub>O(110) surface was simulated with two CO. The formation of di-carbonyls, (CO)<sub>2</sub>, was found to be energetically preferred compared to that of two mono-carbonyls, 2(CO), -0.23 and -0.02 eV, respectively (Figure 4.34b). The calculation of frequencies and corresponding intensities allowed us to discard those frequencies with zero (or very low) intensity. Table 4.13 reports the calculated frequencies as obtained from the simulations as well as the scaled values and the corresponding shifts with respect to the stretching frequency of CO in gas phase. For Cu<sup>+</sup> in the surface layer of Cu<sub>2</sub>O(110) is -22 cm<sup>-1</sup>, which lies within the -16 to -36 cm<sup>-1</sup> range of experimental shifts reported in the literature for systems with Cu<sup>+</sup> as Cu<sub>2</sub>O, including Cu<sub>2</sub>O surfaces,<sup>[56,102]</sup> and Cu nanoparticles partially oxidized interacting with ZnO,<sup>[49]</sup> MgO,<sup>[50]</sup> Ga<sub>2</sub>O<sub>3</sub>,<sup>[54]</sup> SiO<sub>2</sub>,<sup>[55]</sup> and Al<sub>2</sub>O<sub>3</sub>.<sup>[57]</sup>

**Table 4.13** CO vibrational frequency and corresponding shift.

Model	CO ads. type	E <sub>ads</sub> (eV/molec.)	Cu oxid. state	Frequency (cm <sup>-1</sup> )		
				Calculated	Scaled	Shift
CO <sub>gas</sub> PBE	-	-	-	2127	2143	<b>0</b>
CO <sub>gas</sub> HSE	-	-	-	2235	2143	<b>0</b>
MgO	8CO	-0.18	-	2134	2150	<b>+7</b>
Cu <sub>2</sub> O(110)	(CO) <sub>2</sub>	-0.23	Cu <sup>+</sup>	2213	2122	<b>-22</b>
Cu <sub>2</sub> doping	CO <sub>brg</sub>	-0.54	Cu <sup>+</sup>	2118	2134	<b>-9</b>
Cu <sub>2</sub> <sup>ads</sup>	2(CO) <sub>2</sub>	-1.25	Cu <sup>δ-</sup>	1928	1943	<b>-200</b>
	2(CO) <sub>2</sub> + CO <sub>brg</sub>	-1.25	Cu <sup>δ-</sup>	1859	1873	<b>-270</b>
Cu <sub>5</sub> <sup>ads</sup>	(CO) <sub>m</sub>	-1.03	Cu <sup>δ-}/Cu<sup>0</sup></sup>	2062	2078	<b>-65</b>

The adsorption energy and stretching frequencies for full CO coverage has also been calculated for a number of Cu-containing (2×2)-MgO(100) surfaces. We

assumed that full coverage is achieved by considering 8 CO molecules since the surface unit cell has 8 Mg atoms in its top most layer. In Figure 4.34, the most stable states of 8 CO adsorbed on MgO(100), Cu<sub>2</sub>-doped MgO(100), and Cu<sub>m</sub><sup>ads</sup>/MgO(100) (m = 2, 5) are shown. The results indicate a red shift when the catalysts contain Cu, in contrast to a blue shift of +7 cm<sup>-1</sup> on the clean MgO(100) surface (Figure 4.34 and Table 4.13). When CO is adsorbed on the Cu-containing surfaces, it is observed that dicarbonyls, Cu-(CO)<sub>2</sub>, tend to form, as it has been suggested in previous experimental publications on supported silica.<sup>[59,60,105]</sup> In the case of the Cu<sub>2</sub>-doped MgO(100) (2Cu<sup>+</sup>), in the most stable state (hereinafter referred to as called CO<sub>brg</sub> state, Figure 4.34c), it is observed that CO significantly displaces Cu from their equilibrium position in the pristine surface, and a CO is bound to the two Cu atoms and another CO is bound to a single Cu. In the case of Cu<sup>+</sup> dopants, the CO stretch frequency shift with respect to gas phase CO is -9 cm<sup>-1</sup>, in line with the experimentally observed -8 cm<sup>-1</sup> in this work.

In the Cu<sub>2</sub><sup>ads</sup>/MgO(100) system, two iso-energetic states were found (Figure 4.34d and 4.34e, where a (CO)<sub>2</sub> species was adsorbed on each Cu. The difference between the two states is that in one of them, one CO binds to both Cu atoms (CO<sub>brg</sub>). These calculations allow us to affirm that if the copper species were adsorbed in direct contact with the MgO(100) support, such interfacial species would have a Cu<sup>δ-</sup> oxidation state, and the CO vibration would be greatly redshifted, as it is the case for Cu<sub>2</sub><sup>ads</sup>/MgO(100) systems with shifts in the -200 to -270 cm<sup>-1</sup>, something that in no case was observed in our experiments. Furthermore, if somewhat larger 3D Cu clusters would form, those Cu atoms that are not in direct contact with the MgO support would retain their metallic character, Cu<sup>0</sup>, and the redshift would be about eight times larger than what was

observed in the experiments ( $-8\text{ cm}^{-1}$ ), as it is the case for  $\text{Cu}_5^{\text{ads}}/\text{MgO}(100)$  system with a  $-65\text{ cm}^{-1}$  frequency shift, for which a more complex adsorbate structure with  $\text{CO}_{\text{brg}}$  and  $(\text{CO})_2$  appears. The shift is in line with those reported for metallic Cu surfaces with experimentally observed shifts between  $-71$  and  $-49\text{ cm}^{-1}$ .<sup>[106-111]</sup> It should be noted that since Cu tends to form 3D nanoparticles, the existence of  $\text{Cu}_2^{\text{ads}}$  is unlikely compared to larger nanoparticles such as  $\text{Cu}_5^{\text{ads}}$ , therefore the  $200\text{--}270\text{ cm}^{-1}$  shifts are not expected to be observed experimentally.

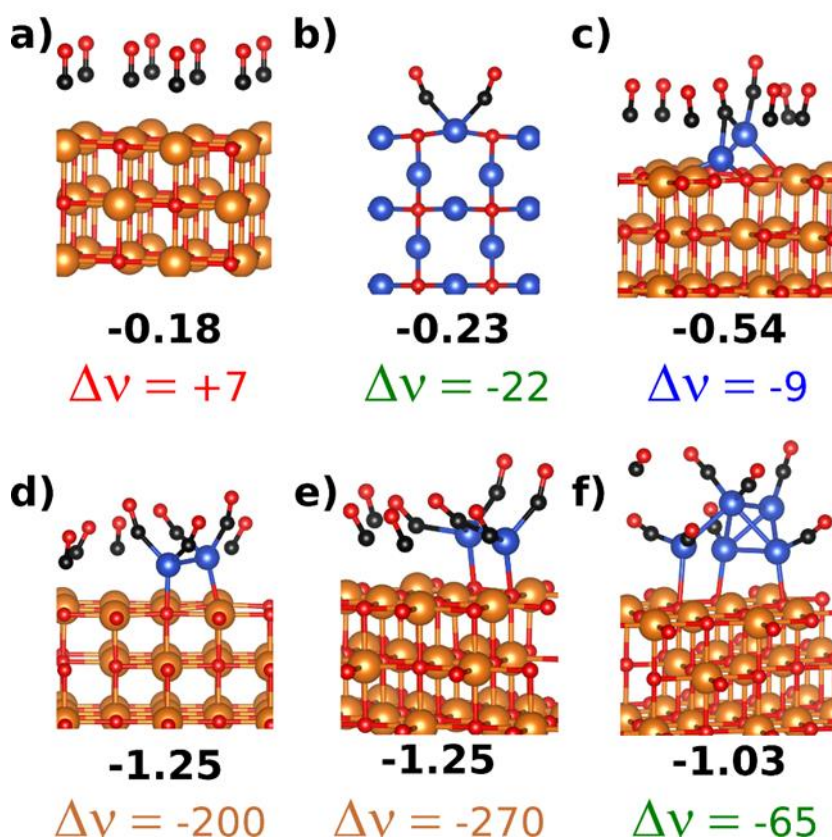


**Figure 4.34** Eight adsorbed CO molecules on MgO (a),  $\text{Cu}_2\text{O}(110)$  (b),  $\text{Cu}_2$ -doped MgO(100) (c),  $\text{Cu}_2^{\text{ads}}$  (d,e), and  $\text{Cu}_5^{\text{ads}}$  (f). The adsorption energy in eV for each state is indicated (bold-type numbers) and also the frequency shifts ( $\Delta\nu$ ) in  $\text{cm}^{-1}$ . Colors refer to Table 4.13 values.

The calculated frequencies allow us to conclude that when CO is adsorbed on the surface of a Cu<sup>+</sup>-doped catalyst, there is a blue shift of  $-9\text{ cm}^{-1}$ , in line with the experimental data, which is about 2.3 times smaller than that of CO adsorbed on the Cu<sub>2</sub>O(110) surface. In addition, when copper is metallic (Cu<sup>0</sup>), as it is the case of Cu atoms in 3D Cu nanoparticles on MgO that are not interfacial, the redshift is about 7.2 times larger.

#### 4.5.6. Operando Infrared studies and structural-activity correlations

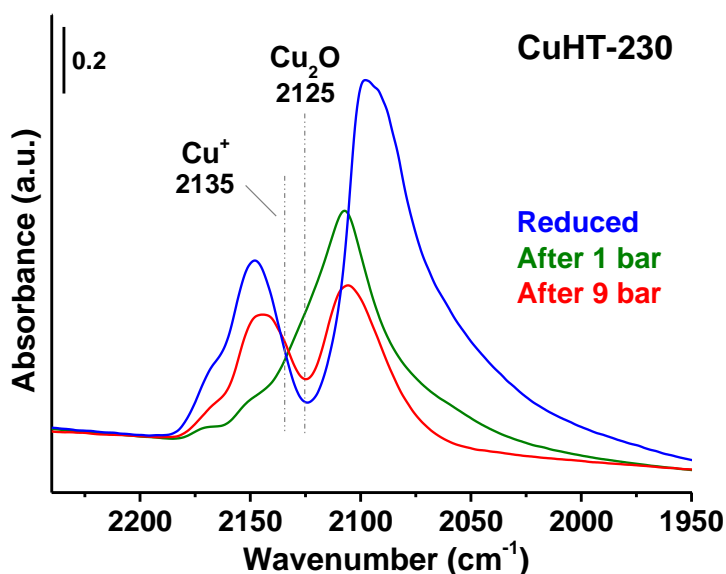


**Figure 4.35** IR-CO titration study on the CuHT-230 sample after reduction (blue), and after quenching the operando IR reaction (2 h at 230 °C), at 1 bar (green) or 9 (red) bar pressure. All spectra are normalized by sample weight.

After reaction at 1 bar, a shoulder at  $2125\text{ cm}^{-1}$  is observed in the CO-IR spectra corresponding to surface Cu<sub>2</sub>O species, while it is absent at increasing reaction pressure to 9 bar. In addition, compared to the reduced catalyst, a decrease in the IR band ascribed to Cu<sup>0</sup> sites is observed at both pressures, together with an increase in the amount of surface Cu<sup>+</sup> species ( $2135\text{ cm}^{-1}$ ).

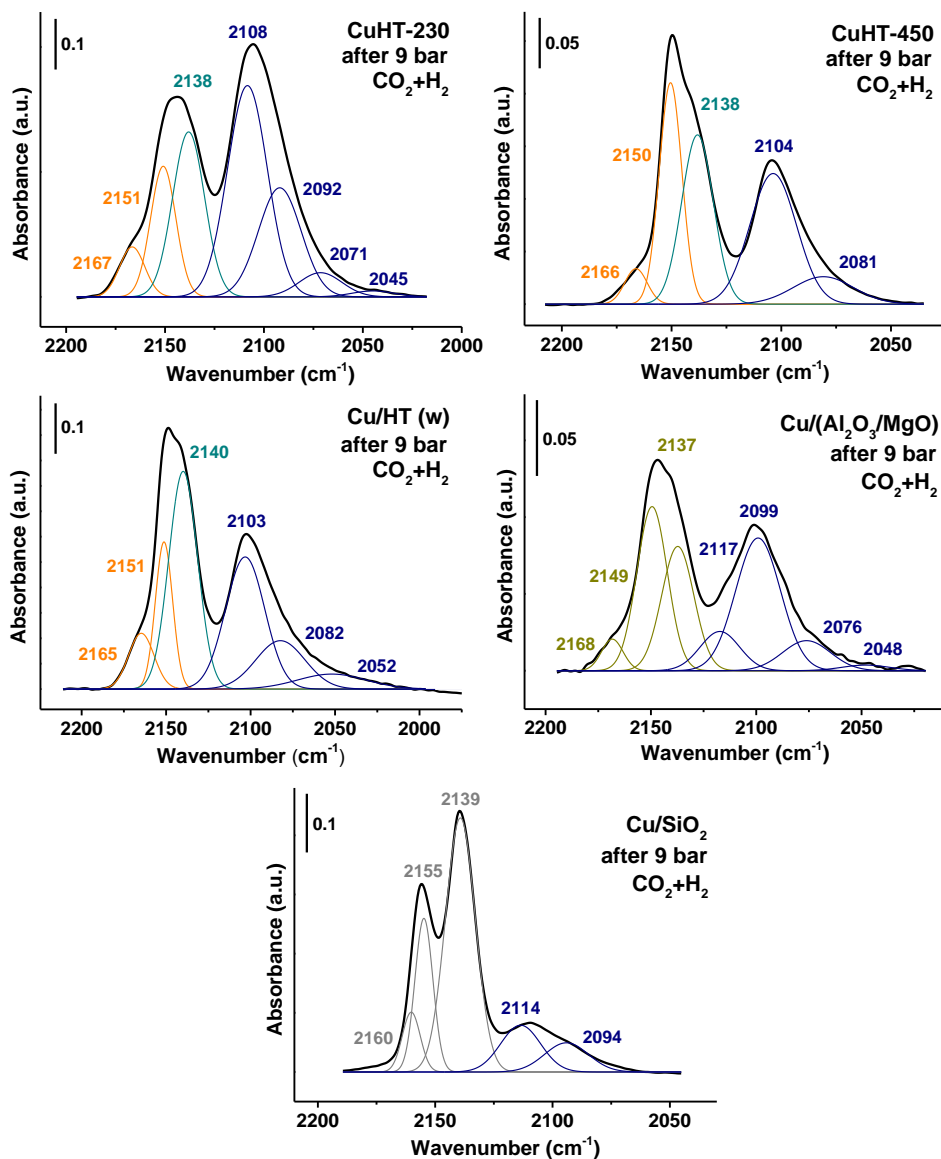


**Figure 4.36** IR-CO deconvoluted spectra of spent samples after 9 bar reaction. Color code for deconvoluted components: orange (HT support), dark yellow (Al/Mg support), gray (SiO<sub>2</sub> support), cyan (Cu<sup>+</sup> species) and navy (Cu<sup>0</sup> species). All spectra correspond to CO saturation at -170 °C.

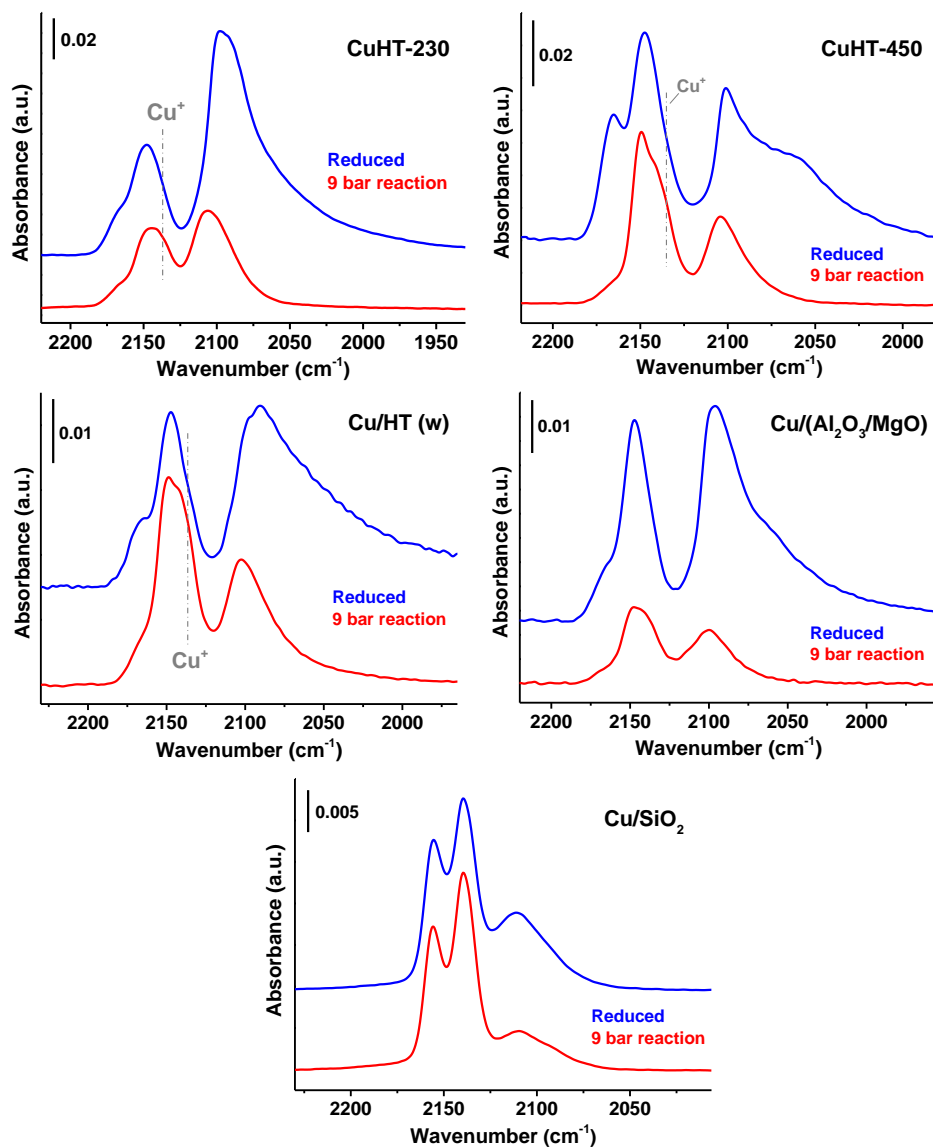


**Figure 4.37** IR-CO spectra at saturation conditions at -170 °C of in situ H<sub>2</sub>-reduced catalysts (blue spectra) and after exposing them to 9 bar reaction conditions (red spectra). For comparison purposes, spectra are normalized by sample weight.



### Pressure gap influence

A positive influence of reaction pressure in MeOH production is observed in Table 4.14, where online MS analysis ( $m/z=31$ ) coupled to the IR cell shown an increased methanol formation at 230 °C and 9 bar versus atmospheric pressure.

**Table 4.14** Pressure effect on MeOH formation in the IR cell.

Pressure (bar)	$\Delta(\text{MeOH})/\text{CO}_2$
1	$6.508 \cdot 10^{-6}$
9	$1.558 \cdot 10^{-5}$

This behavior is in good correlation with catalytic studies performed at different pressures (1, 14 and 20 bar) and at identical temperature (i.e., 230 °C) in the fixed-bed reactor, where a linear trend is found (see Table 4.15 and Figure 4.38).

**Table 4.15** Pressure effect on MeOH formation in the fixed-bed reactor.

Pressure (bar)	STY MeOH ( $\text{mol} \cdot \text{g}_{\text{cat}}^{-1} \cdot \text{h}^{-1}$ )
1	$1.5 \cdot 10^{-4}$
14	$1.9 \cdot 10^{-3}$
20	$2.6 \cdot 10^{-3}$

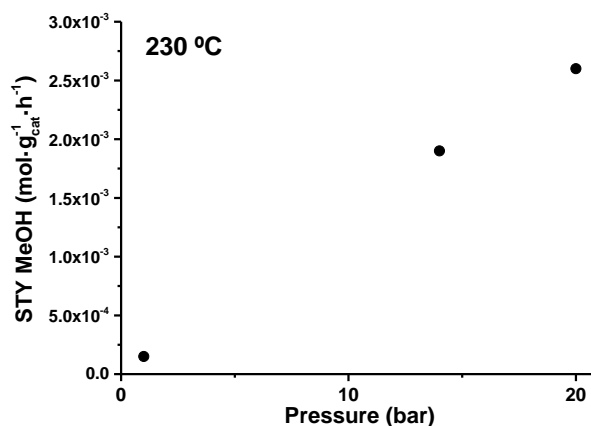


**Figure 4.38** Correlation between pressure and MeOH production in the reactor.

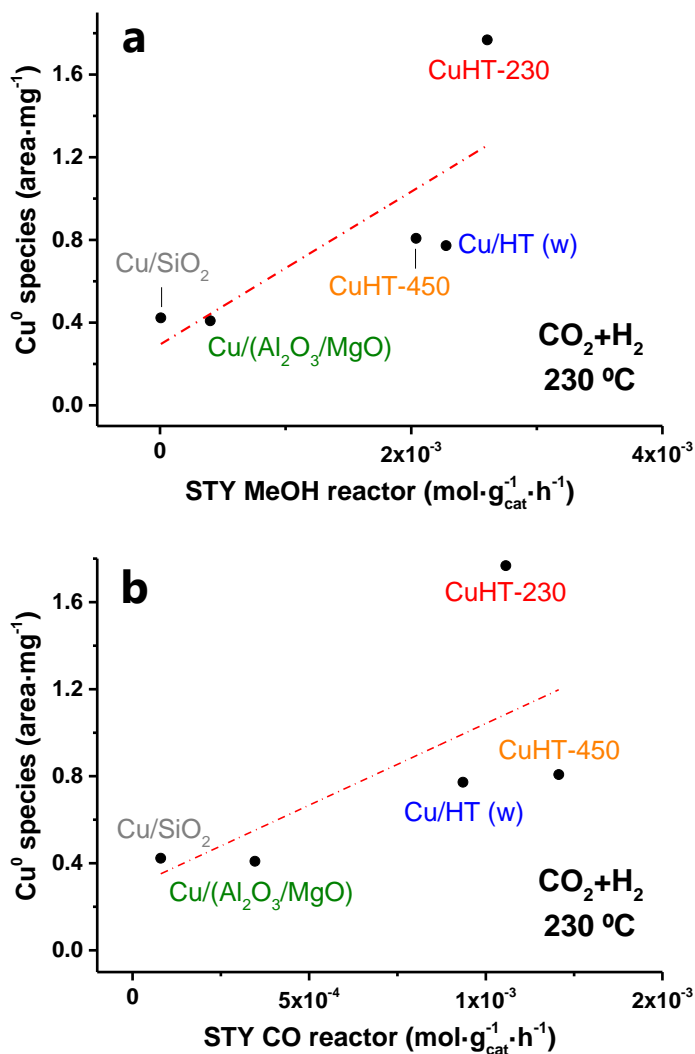


**Figure 4.39** Correlation between the amount of exposed Cu<sup>0</sup> sites (determined by IR titration experiments after operando IR reaction at 9 bar and 230 °C) and MeOH (a) and CO (b) productivity obtained in the catalytic studies.

As depicted in both graphs, there is no clear correspondence between metallic copper sites (Cu<sup>0</sup>) and the formation of MeOH and CO.

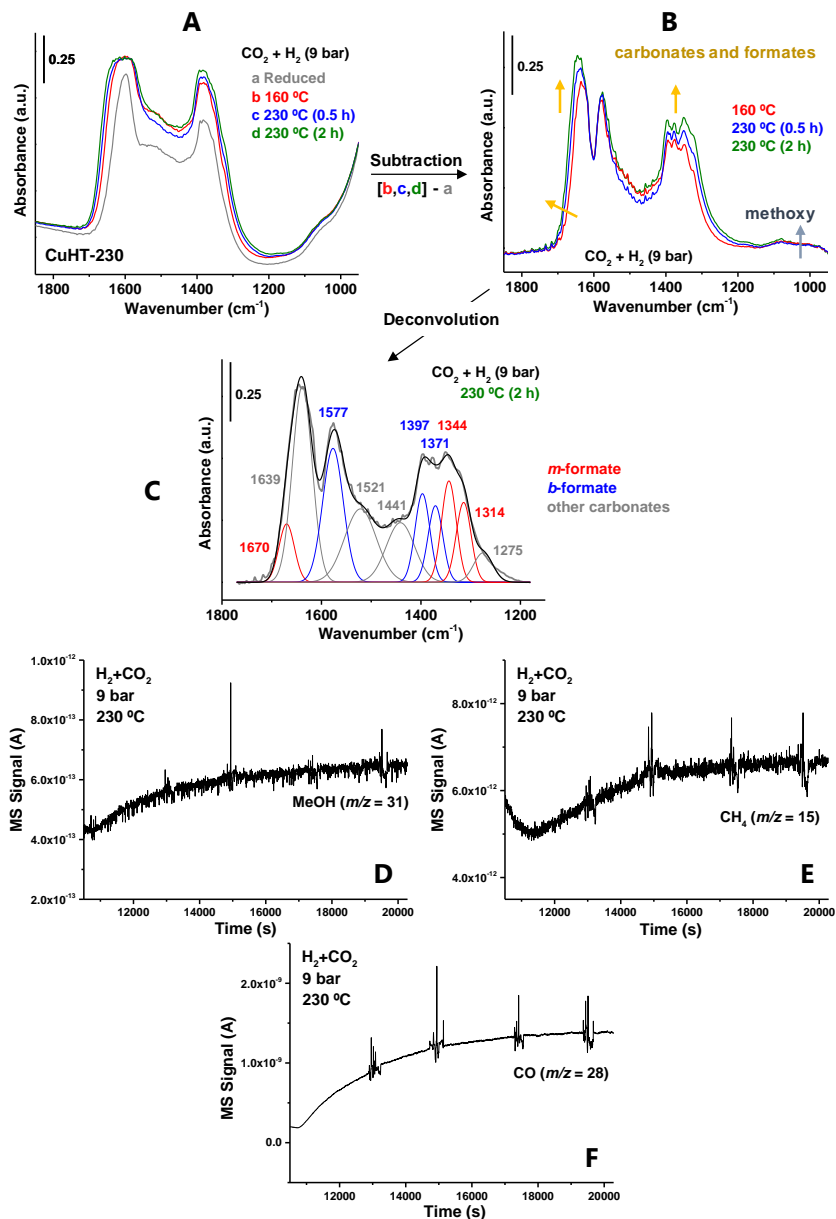


**Figure 4.40** Evolution in the 1800-1000 cm<sup>-1</sup> spectral region during IR operando CO<sub>2</sub> hydrogenation at 9 bar and at increasing temperatures for CuHT-230 sample: original spectra (A), subtracted spectra respect to the reduced starting point (B), deconvolution of the subtracted spectra at steady-state reaction conditions (C). Online MS profile of methanol (D, *m/z* = 31), methane (E, *m/z* = 15) and CO (F, *m/z* = 28) formation.

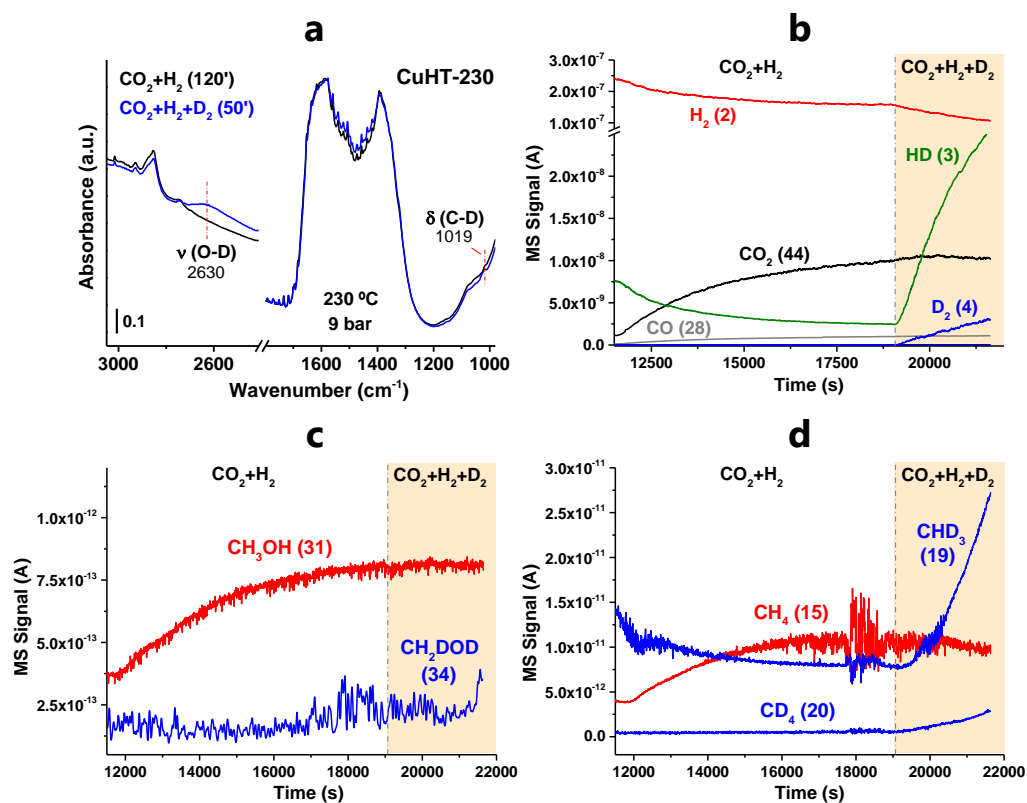


**Figure 4.41** IR-MS isotopic studies, where part of the H<sub>2</sub> flow is replaced by D<sub>2</sub> under steady-state conditions (CO<sub>2</sub>:H<sub>2</sub> 1:3 molar ratio), at 230 °C and 9 bar, on the CuHT-230 sample.

The isotopic experiment performed under steady-state conditions at 230 °C and 9 bar in an IR cell (MS coupled) reveals that the whole set of IR bands in the 1670–1200 cm<sup>-1</sup> range remains unaltered when D<sub>2</sub> replaces part of the H<sub>2</sub> flow.

In detail, after 2 hours of experiment, D<sub>2</sub> is submitted in the reaction mixture, and OD bands (2630 cm<sup>-1</sup>) and a very weak band at 1019 cm<sup>-1</sup> (associated with δ(C-D)) appear in the IR spectrum (blue line in Figure 4.41a). Regarding the MS information, during the first part of the experiment until ~19000 s (CO<sub>2</sub>+H<sub>2</sub> gas mixture), the production of CO (*m/z*=28, gray line in Figure 4.41b), methanol

( $m/z=31$ , red line in Figure 4.41c) and CH<sub>4</sub> ( $m/z=15$ , red line in Figure 4.41d) are observed. After 2 hours on stream, D<sub>2</sub> is also submitted in the gas mixture (CO<sub>2</sub>+H<sub>2</sub>+D<sub>2</sub>, shaded region). At that moment, a fast response in the  $m/z=3$  (HD) is found (green line in Figure 4.41b), due to H<sub>2</sub>/D<sub>2</sub> isotopic exchange. Moreover, the MS signal of deuterated products derived from CH<sub>4</sub> (i.e., CD<sub>4</sub>,  $m/z=20$ ; CHD<sub>3</sub>,  $m/z=19$ , blue lines in Figure 4.41d) grows in the same manner. On the other hand, deuterated methanol starts to be formed at the end of the experiment (CH<sub>2</sub>DOD)  $m/z=34$ , blue line in Figure 4.41c). Based on these results, it becomes clear that a different kinetic isotopic effect is observed for methane and methanol formation, pointing that the two reactions do not proceed through a common intermediate.

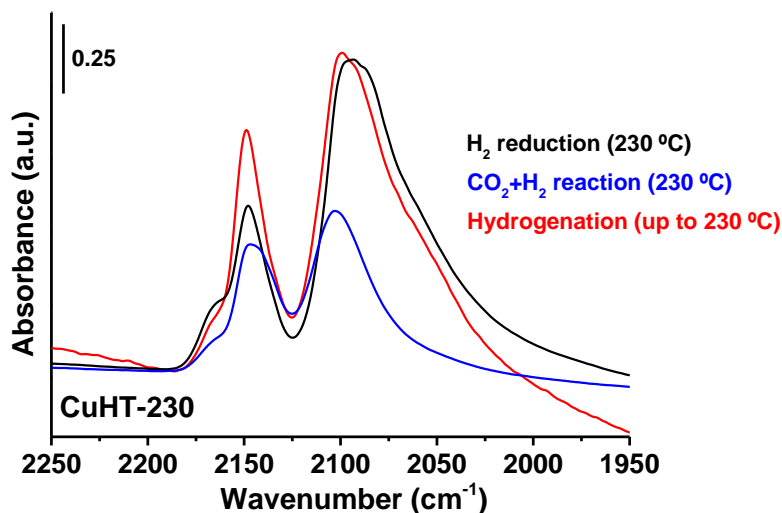


**Figure 4.42** IR-CO spectra at saturation conditions (acquired at -170 °C) of CuHT-230: reduced sample (black); quenched sample after operando IR studies in a CO<sub>2</sub>/H<sub>2</sub> flow at 9 bar and 230 °C for 40 min (blue); sample after IR operando conditions and later exposed to a H<sub>2</sub>/N<sub>2</sub> flow at the same temperature for ~4.5 h (red). As observed, the intensity of the Cu<sup>0</sup>-CO signal is restored after hydrogenation of the spent catalysts.

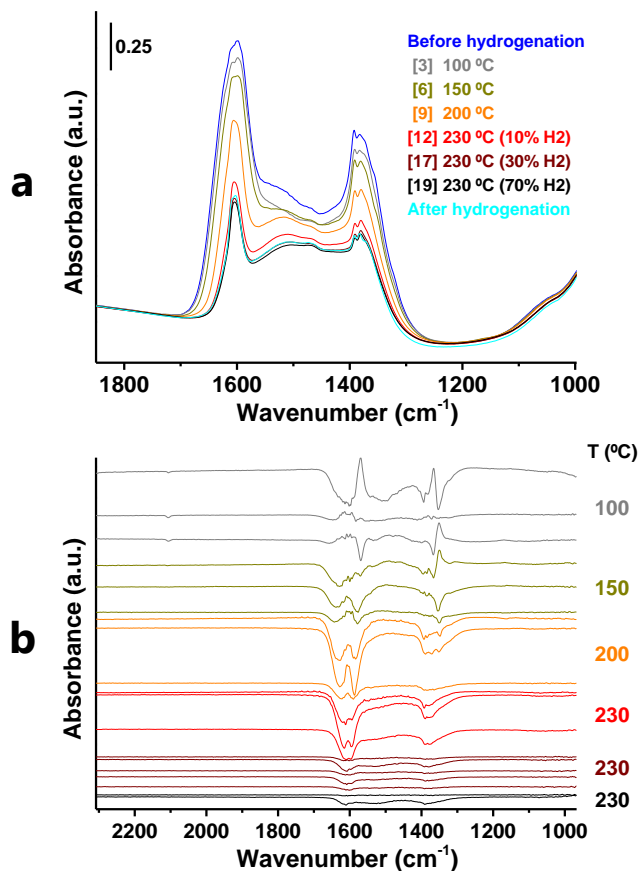


**Figure 4.43** Hydrogenation of CuHT-230 after operando IR CO<sub>2</sub>+H<sub>2</sub> reaction at 1 bar and 230 °C: IR spectra at different steps (in brackets, see Table 4.16 below) of the hydrogenation process (a). Subtracted IR spectra at each step versus the one before starting the treatment.

**Table 4.16** Experimental steps followed in the hydrogenation of CuHT-230 at 1 bar.

Spectrum	T (°C)	% vol H <sub>2</sub>	Time (min)	Spectrum	T (°C)	% vol H <sub>2</sub>	Time (min)
1	100	10	0	10	230	10	152
2	100	10	15	11	230	10	167
3	100	10	60	12	230	10	192
4	150	10	71	13	230	30	198
5	150	10	86	14	230	30	218
6	150	10	96	15	230	30	228
7	200	10	120	16	230	30	243
8	200	10	135	17	230	30	253
9	200	10	145	18	230	75	259
				19	230	75	299

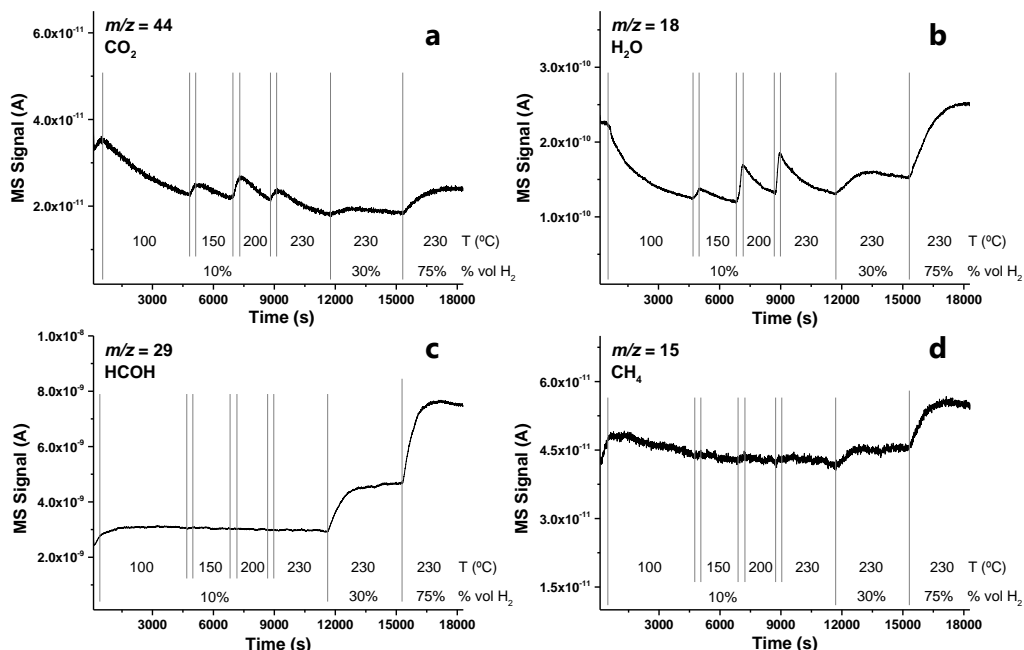


**Figure 4.44** Evolution of products detected by MS during the hydrogenation treatment of CuHT-230 after operando IR CO<sub>2</sub>+H<sub>2</sub> reaction at 1 bar and 230 °C.

Up to 230 °C, CO<sub>2</sub> ( $m/z=44$ ) and water ( $m/z=18$ ) are detected in MS (Figure 4.44a-b), due to carbonates desorption. In fact, IR bands that disappear during low temperature steps (1587 and 1325 cm<sup>-1</sup>; 1567 and 1366 cm<sup>-1</sup>) are assigned to bidentate carbonates (Figure 4.43).<sup>[70,71]</sup> Then, at 230 °C, formaldehyde ( $m/z=29$ ) and methane ( $m/z=15$ ) are formed (Figure 4.44c-d). In the IR spectra, these products are associated with formate-like intermediates (i.e., bridge formates), presenting characteristic bands at 1596 and 1378 cm<sup>-1</sup>.<sup>[70,71]</sup> Finally, methanol ( $m/z=31$ ) was not detected at any temperature during the experiment.

After finishing the hydrogenation treatment, some species were still adsorbed onto the support, as observed in cyan spectrum in Figure 4.43a.

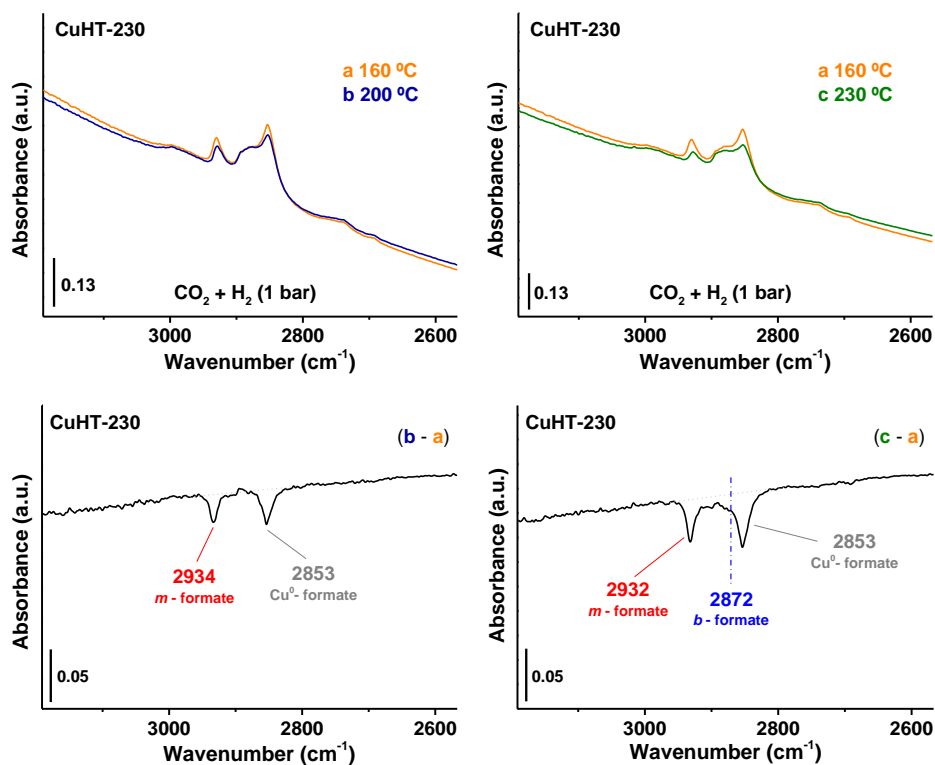


**Figure 4.45** C-H stretching region corresponding to the temperature-resolved IR studies under operando conditions at 1 bar in CO<sub>2</sub>/H<sub>2</sub> flow over CuHT-230 catalyst shown in Figure 4.7. Sequential steps at 200 and 230 °C are displayed on the left and on the right side, respectively. First row panels show IR spectra at specific temperatures. Second row panels exhibit the subtracted spectra.



### Dual tracking of operando IR by MS and GC

In order to double check the representativeness of catalytic data obtained during the IR operando CO<sub>2</sub> hydrogenation, two techniques were used to monitor the reaction evolution: online MS and offline GC. As an example, we will discuss the operando IR study performed at atmospheric pressure in Figure 4.7.

Firstly, Table 4.17 summarizes representative MS values for the main reaction products in the operando study and their normalization to CO<sub>2</sub> MS intensity:

**Table 4.17** Selected MS values (in A) for the operando IR study at 1 bar.

Mass Spectrometry									
t (s)	t' (s) <sup>a</sup>	T (°C)	CH <sub>4</sub> (A)	CH <sub>3</sub> OH (A)	CO (A)	CO <sub>2</sub> (A)	CH <sub>4</sub> /CO <sub>2</sub>	CH <sub>3</sub> OH/CO <sub>2</sub>	CO/CO <sub>2</sub>
3000	0	160	1.669·10 <sup>-11</sup>	1.019·10 <sup>-12</sup>	3.740·10 <sup>-9</sup>	3.694·10 <sup>-8</sup>	4.517·10 <sup>-4</sup>	2.758·10 <sup>-5</sup>	1.012·10 <sup>-1</sup>
3600	600	160	1.682·10 <sup>-11</sup>	1.073·10 <sup>-12</sup>	3.677·10 <sup>-9</sup>	3.666·10 <sup>-8</sup>	4.588·10 <sup>-4</sup>	2.926·10 <sup>-5</sup>	1.003·10 <sup>-1</sup>
4200	1200	160	1.719·10 <sup>-11</sup>	1.148·10 <sup>-12</sup>	3.670·10 <sup>-9</sup>	3.670·10 <sup>-8</sup>	4.684·10 <sup>-4</sup>	3.128·10 <sup>-5</sup>	9.999·10 <sup>-2</sup>
4700	1700	200	1.739·10 <sup>-11</sup>	1.149·10 <sup>-12</sup>	3.678·10 <sup>-9</sup>	3.686·10 <sup>-8</sup>	4.719·10 <sup>-4</sup>	3.117·10 <sup>-5</sup>	9.980·10 <sup>-2</sup>
5200	2200	200	1.740·10 <sup>-11</sup>	1.268·10 <sup>-12</sup>	3.623·10 <sup>-9</sup>	3.647·10 <sup>-8</sup>	4.771·10 <sup>-4</sup>	3.475·10 <sup>-5</sup>	9.932·10 <sup>-2</sup>
6500	3500	230	2.734·10 <sup>-11</sup>	1.834·10 <sup>-12</sup>	3.735·10 <sup>-9</sup>	3.658·10 <sup>-8</sup>	7.475·10 <sup>-4</sup>	5.013·10 <sup>-5</sup>	1.021·10 <sup>-1</sup>
7600	4600	230	3.598·10 <sup>-11</sup>	2.010·10 <sup>-12</sup>	3.839·10 <sup>-9</sup>	3.659·10 <sup>-8</sup>	9.831·10 <sup>-4</sup>	5.493·10 <sup>-5</sup>	1.049·10 <sup>-1</sup>

<sup>a</sup>Time correction considering t<sub>0</sub>=3000 s.

If X/CO<sub>2</sub> ratios (X = CH<sub>4</sub>, CH<sub>3</sub>OH, CO) are plotted versus time (Figure 4.46a-c), we obtain analogous trends to that obtained in Figure 4.7. As it can be seen below, CO/CO<sub>2</sub> MS ratio remains stable up to 200 °C, increasing its value when the temperature is set at 230 °C (Figure 4.46c). Since the mass signal of CO (*m/z* = 28) overlaps with CO<sub>2</sub> fragmentation, accurate analysis of CO formation by MS is challenging. Then, an additional analysis of the evolved products in the operando IR studies by using an external GC was performed (Figure 4.47 and Table 4.18). A good correlation is found by comparing the CO/CO<sub>2</sub> and CH<sub>4</sub>/CO<sub>2</sub> ratios obtained in the MS with that of the simultaneous analysis in the GC.

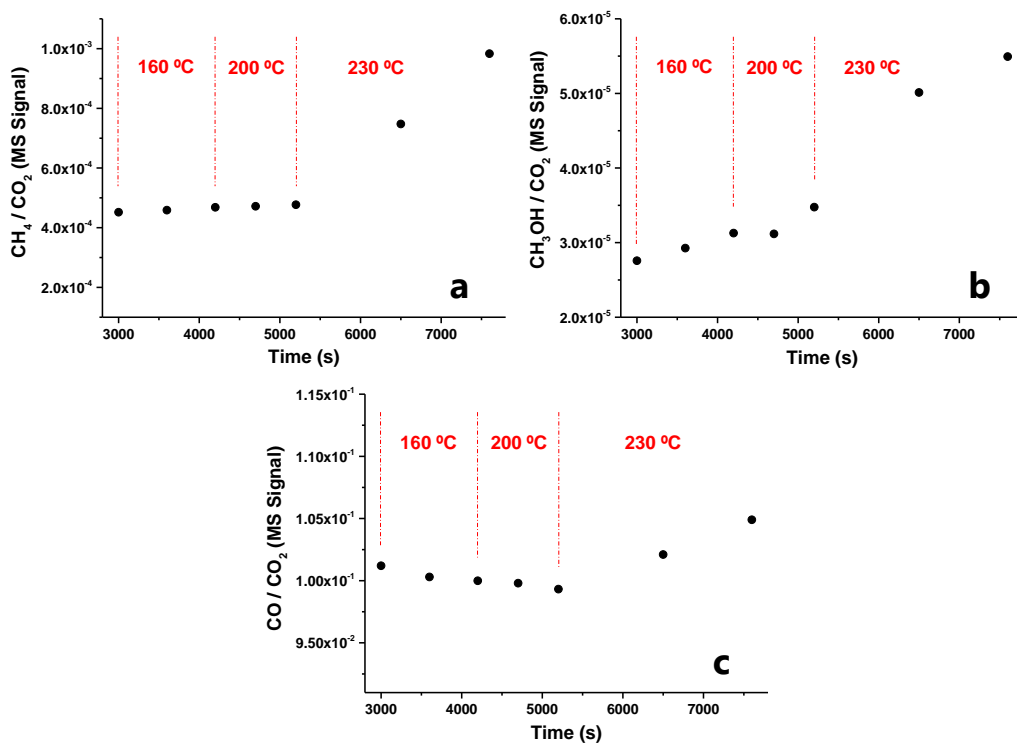


**Figure 4.46** Evolution of reaction products in operando IR CO<sub>2</sub> hydrogenation: methane (a), methanol (b), carbon monoxide (c). Values in Y axis are normalized to CO<sub>2</sub> MS signal.

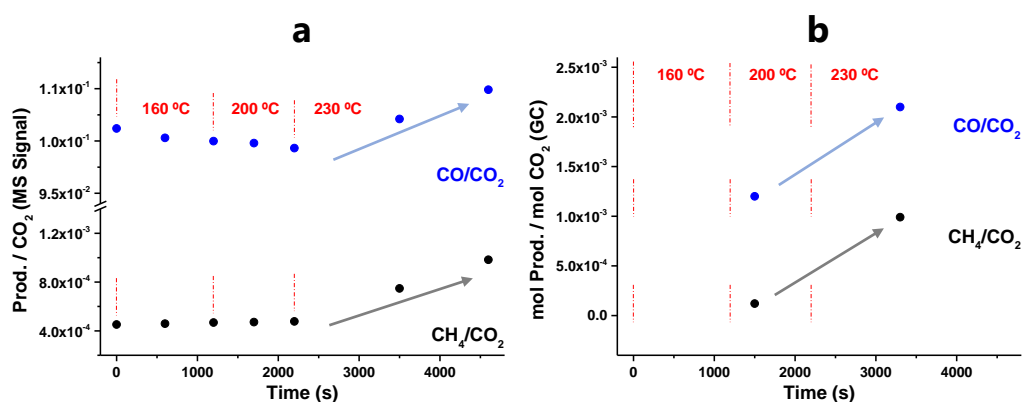


**Figure 4.47** By-products formation (CO and CH<sub>4</sub>) observed under operando IR conditions in online MS (a) and in offline GC (b). Values in Y axis are normalized to CO<sub>2</sub> signal.

**Table 4.18** Selected GC values for the operando IR study at 1 bar.

t (s)	t' (s) <sup>a</sup>	T (°C)	Gas Chromatography	
			CH <sub>4</sub> /CO <sub>2</sub> (mol/mol)	CO/CO <sub>2</sub> (mol/mol)
4500	1500	200	1.2·10 <sup>-4</sup>	1.2·10 <sup>-3</sup>
6300	3300	230	9.9·10 <sup>-4</sup>	2.1·10 <sup>-3</sup>

<sup>a</sup>Time correction considering t<sub>0</sub>=3000 s.

## 4.6. References

- [1] Ye, R. P.; Ding, J.; Gong, W.; Argyle, M. D.; Zhong, Q.; Wang, Y.; Russell, C. K.; Xu, Z.; Russell, A. G.; Li, Q.; Fan, M.; Yao, Y. G. CO<sub>2</sub> hydrogenation to high-value products via heterogeneous catalysis. *Nat. Commun.* **2019**, *10*, 5698. DOI: 10.1038/s41467-019-13638-9.
- [2] Centi, G.; Quadrelli, E. A.; Perathoner, S. Catalysis for CO<sub>2</sub> conversion: a key technology for rapid introduction of renewable energy in the value chain of chemical industries. *Energy Environ. Sci.* **2013**, *6*, 1711-1731. DOI: 10.1039/C3EE00056G.
- [3] Roy, S.; Cherevotan, A.; Peter, S. C. Thermochemical CO<sub>2</sub> Hydrogenation to Single Carbon Products: Scientific and Technological Challenges. *ACS Energy Lett.* **2018**, *3*, 1938-1966. DOI: 10.1021/acsenerylett.8b00740.
- [4] Grim, R. G.; Huang, Z.; Guarnieri, M. T.; Ferrell, J. R.; Tao, L.; Schaidle, J. A. Transforming the carbon economy: challenges and opportunities in the convergence of low-cost electricity and reductive CO<sub>2</sub> utilization. *Energy Environ. Sci.* **2020**, *13*, 472-494. DOI: 10.1039/C9EE02410G.
- [5] Kajaste, R.; Hurme, M.; Oinas, P. Methanol-Managing greenhouse gas emissions in the production chain by optimizing the resource base. *AIMS Energy* **2018**, *6*, 1074-1102. DOI: 10.3934/energy.2018.6.1074.
- [6] Sheldon, D. Methanol Production - A Technical History. *Johnson Matthey Technol. Rev.* **2017**, *61*, 172-182. DOI: 10.1595/205651317X695622.
- [7] Liu, L.; Corma, A. Metal Catalysts for Heterogeneous Catalysis: From Single Atoms to Nanoclusters and Nanoparticles. *Chem. Rev.* **2018**, *118*, 4981-5079. DOI: 10.1021/acs.chemrev.7b00776.
- [8] Van der Berg, R.; Prieto, G.; Korpershoek, G.; Van der Wal, L. I.; Van Bunningen, A. J.; Laegsgaard-Jorgensen, S.; De Jongh, P. E.; De Jong, K. P. Structure sensitivity of Cu and CuZn catalysts relevant to industrial methanol synthesis. *Nat. Commun.* **2016**, *7*, 13057. DOI: 10.1038/ncomms13057.

- [9] Yang, H.; Gao, P.; Zhang, C.; Zhong, L.; Li, X.; Wang, S.; Wang, H.; Wei, W.; Sun, Y. Core-shell structured Cu@m-SiO<sub>2</sub> and Cu/ZnO@m-SiO<sub>2</sub> catalysts for methanol synthesis from CO<sub>2</sub> hydrogenation. *Catal. Commun.* **2016**, *84*, 56-60. DOI: 10.1016/j.catcom.2016.06.010.
- [10] Wang, Z. Q.; Xu, Z. N.; Peng, S. Y.; Zhang, M. J.; Lu, G.; Chen, Q. S.; Chen, Y.; Guo, G. C. High-Performance and Long-Lived Cu/SiO<sub>2</sub> Nanocatalyst for CO<sub>2</sub> Hydrogenation. *ACS Catal.* **2015**, *5*, 4255-4259. DOI: 10.1021/acscatal.5b00682.
- [11] Karelavic, A.; Galdames, G.; Medina, J. C.; Yévenes, C.; Barra, Y.; Jiménez, R. Mechanism and structure sensitive of methanol synthesis from CO<sub>2</sub> over SiO<sub>2</sub>-supported Cu nanoparticles. *J. Catal.* **2019**, *369*, 415-426. DOI: 10.1016/j.jcat.2018.11.012.
- [12] Yu, J.; Yang, M.; Zhang, J.; Ge, Q.; Zimina, A.; Pruessmann, T.; Zheng, L.; Grunwaldt, J. D.; Sun, J. Stabilizing Cu<sup>+</sup> in Cu/SiO<sub>2</sub> Catalysts with a Shattuckite-Like Structure Boosts CO<sub>2</sub> Hydrogenation into Methanol. *ACS Catal.* **2020**, *10*, 14694-14706. DOI: 10.1021/acscatal.0c04371.
- [13] Dasireddy, V. D. B. C.; Stenfancic, N. S.; Lizokar, B. Correlation between synthesis pH, structure and Cu/MgO/Al<sub>2</sub>O<sub>3</sub> heterogeneous catalyst activity and selectivity in CO<sub>2</sub> hydrogenation to methanol. *J. CO<sub>2</sub> Util.* **2018**, *28*, 189-199. DOI: 10.1016/j.jcou.2018.09.002.
- [14] Liu, C.; Guo, X.; Guo, Q.; Mao, D.; Yu, J.; Lu, G. Methanol synthesis from CO<sub>2</sub> hydrogenation over copper catalysts supported in MgO-modified TiO<sub>2</sub>. *J. Mol. Catal. A Chem.* **2016**, *425*, 86-93. DOI: 10.1016/j.molcata.2016.09.032.
- [15] Tada, S.; Otsuka, F.; Fujiwara, K.; Moularas, C.; Deligiannakis, Y.; Kinoshita, Y.; Uchida, S.; Honma, T.; Nishijima, M.; Kikuchi, R. Development of CO<sub>2</sub>-to-Methanol Hydrogenation Catalyst by Focusing on the Coordination Structure of the Cu species in Spinel-Type Oxide Mg<sub>1-x</sub>Cu<sub>x</sub>Al<sub>2</sub>O<sub>4</sub>. *ACS Catal.* **2020**, *10*, 15186-15194. DOI: 10.1021/acscatal.0c02868.
- [16] Lam, E.; Larmier, K.; Wolf, P.; Tada, S.; Safonova, O. V.; Copéret, C. Isolated Zr Surface Sites on Silica Promote Hydrogenation of CO<sub>2</sub> to CH<sub>3</sub>OH in Supported Cu Catalysts. *J. Am. Chem. Soc.* **2018**, *140*, 10530-10535. DOI: 10.1021/jacs.8b05595.
- [17] Noh, G.; Lam, E.; Alfke, J. L.; Larmier, K.; Searles, K.; Wolf, P.; Copéret, C. Selective Hydrogenation of CO<sub>2</sub> to CH<sub>3</sub>OH on Supported Cu Nanoparticles Promoted by Isolated Ti<sup>IV</sup> Surface Sites on SiO<sub>2</sub>. *ChemSusChem* **2019**, *12*, 968-972. DOI: 10.1002/cssc.201900134.
- [18] Lam, E.; Noh, G.; Chan, K. W.; Larmier, K.; Lebedev, D.; Searles, K.; Wolf, P.; Safonova, O. V.; Copéret, C. Enhanced CH<sub>3</sub>OH selectivity in CO<sub>2</sub> hydrogenation using Cu-based catalysts generated *via* SOMC from Ga<sup>III</sup> single-sites. *Chem. Sci.* **2020**, *11*, 7593-7598. DOI: 10.1039/D0SC00465K.
- [19] Lam, E.; Noh, G.; Larmier, K.; Safonova, O. V.; Copéret, C. CO<sub>2</sub> hydrogenation on Cu-catalysts generated from Zn<sup>II</sup> single-sites: Enhanced CH<sub>3</sub>OH selectivity compared to Cu/ZnO/Al<sub>2</sub>O<sub>3</sub>. *J. Catal.* **2021**, *394*, 266-272. DOI: 10.1016/j.jcat.2020.04.028.

- [20] Sels, B. F.; De Vos, D. E.; Jacobs, P. A. Hydrotalcite-like anionic clays in catalytic organic reactions. *Catal. Rev.* **2001**, *43*, 443-488. DOI: 10.1081/CR-120001809.
- [21] Dewangan, N.; Hui, W. M.; Jayaprakash, S.; Bawah, A. R.; Poerjoto, A. J.; Jie, T.; Jangam, A.; Hidajat, K.; Kawi, S. Recent progress on layered double hydroxide (LDH) derived metal-based catalysts for CO<sub>2</sub> conversion to valuable chemicals. *Catal. Today* **2020**, *356*, 490-513. DOI: 10.1016/j.cattod.2020.06.020.
- [22] Fang, X.; Chen, C.; Jia, H.; Li, Y.; Liu, J.; Wang, Y.; Song, Y.; Du, T.; Liu, L. Progress in Adsorption-Enhanced Hydrogenation of CO<sub>2</sub> on Layered Double Hydroxide (LDH) Derived Catalysts. *J. Ind. Eng. Chem.* **2021**, *95*, 16-27. DOI: 10.1016/j.jiec.2020.12.027.
- [23] Gao, P.; Li, F.; Xiao, F.; Zhao, N.; Sun, N.; Wei, W.; Zhong, L.; Sun, Y. Preparation and activity of Cu/Zn/Al/Zr catalysts *via* hydrotalcite-containing precursors for methanol synthesis from CO<sub>2</sub> hydrogenation. *Catal. Sci. Technol.* **2012**, *2*, 1447-1454. DOI: 10.1039/C2CY00481J.
- [24] Gao, P.; Li, F.; Zhan, H.; Zhao, N.; Xiao, F.; Wei, W.; Zhong, L.; Wang, H.; Sun, Y. Influence of Zr on the performance of Cu/Zn/Al/Zr catalysts *via* hydrotalcite-like precursors for CO<sub>2</sub> hydrogenation to methanol. *J. Catal.* **2013**, *298*, 51-60. DOI: 10.1016/j.jcat.2012.10.030.
- [25] Chen, Y.; Hong, H.; Cai, J.; Li, Z. Highly Efficient CO<sub>2</sub> to CO Transformation over Cu-Based Catalyst Derived from a CuMgAl-Layered Double Hydroxide (LDH). *Chem. Cat. Chem.* **2021**, *13*, 656-663. DOI: 10.1002/cctc.202001611.
- [26] Mazarío, J.; Concepción, P.; Ventura, M.; Domine, M. E. Continuous catalytic process for the selective dehydration of glycerol over Cu-based mixed oxide. *J. Catal.* **2020**, *385*, 160-175. DOI: 10.1016/j.jcat.2020.03.010.
- [27] Climent, M. J.; Corma, A.; De Frutos, P.; Iborra, S.; Noy, M.; Veltý, A.; Concepción, P. Chemicals from biomass: Synthesis of glycerol carbonate by transesterification and carbonylation with urea with hydrotalcite catalysts. The role of acid-base pairs. *J. Catal.* **2010**, *269*, 140-149. DOI: 10.1016/j.jcat.2009.11.001.
- [28] Blanch-Raga, N.; Palomares, A. E.; Martínez-Triguero, J.; Fetter, G.; Bosch, P. Cu Mixed Oxides Based on Hydrotalcite-Like Compounds for the Oxidation of Trichloroethylene. *Ind. Eng. Chem. Res.* **2013**, *52*, 15772-15779. DOI: 10.1021/ie4024935.
- [29] Yaseneva, P.; An, N.; Finn, M.; Tiedemann, N.; Jose, N.; Voutchkova-Kostal, A.; Lapkin, A. Continuous synthesis of doped layered double hydroxides in a meso-scale flow reactor. *Chem. Eng. J.* **2019**, *360*, 190-199. DOI: 10.1016/j.cej.2018.11.197.
- [30] Dumitriu, E.; Hulea, V.; Chelaru, C.; Catrinescu, C.; Tichit, D.; Durand, R. Influence of the acid-base properties of solid catalysts derived from hydrotalcite-like compounds on the condensation of formaldehyde and acetaldehyde. *Appl. Catal. A: Gen.* **1999**, *178*, 145-157. DOI: 10.1016/S0926-860X(98)00282-8.

- [31] Stöber, W.; Fink, A.; Bohn, E. Controlled growth of monodisperse silica spheres in the micron size range. *J. Colloid Interface Sci.* **1968**, *26*, 62-69. DOI: 10.1016/0021-9797(68)90272-5.
- [32] Hinrichsen, O.; Genger, T.; Muhler, M. Chemisorption of N<sub>2</sub>O and H<sub>2</sub> for the Surface Determination of Copper Catalysts. *Chem. Eng. Technol.* **2000**, *23*, 956-959. DOI: 10.1002/1521-4125(200011)23:11<956::AID-CEAT956>3.0.CO;2-L.
- [33] Luo, W.; Jing, F. L.; Yu, X. P.; Sun, S.; Luo, S. Z.; Chu, W. Synthesis of 2-Methylpyrazine Over Highly Dispersed Copper Catalysts. *Catal. Lett.* **2012**, *142*, 492-500. DOI: 10.1007/s10562-012-0782-8.
- [34] Payne, M. C.; Teter, M. P.; Allan, D. C.; Arias, T. A.; Joannopoulos, J. D. Iterative minimization techniques for ab initio total-energy calculations: molecular dynamics and conjugate gradients. *Rev. Mod. Phys.* **1992**, *64*, 1045-1097. DOI: 10.1103/RevModPhys.64.1045.
- [35] Kresse, G.; Furthmüller, J. Efficient iterative schemes for ab initio total-energy calculations using a plane-wave basis set. *Phys. Rev. B* **1996**, *54*, 11169-11186. DOI: 10.1103/PhysRevB.54.11169.
- [36] Kresse, G.; Joubert, D. From ultrasoft pseudopotentials to the projector augmented-wave method. *Phys. Rev. B* **1999**, *59*, 1758-1775. DOI: 10.1103/PhysRevB.59.1758.
- [37] Perdew, J. P.; Burke, K.; Ernzerhof, M. Generalized Gradient Approximation Made Simple. *Phys. Rev. Lett.* **1996**, *77*, 3865-3868. DOI: 10.1103/PhysRevLett.77.3865.
- [38] Grimme, S.; Antony, J.; Ehrlich, S.; Krieg, H. A consistent and accurate ab initio parametrization of density functional dispersion correction (DFT-D) for the 94 elements H-Pu. *J. Chem. Phys.* **2010**, *132*, 154104. DOI: 10.1063/1.3382344.
- [39] Grimme, S.; Ehrlich, S.; Goerigk, L. Effect of the damping function in dispersion corrected density functional theory. *J. Comput. Chem.* **2011**, *32*, 1456-1465. DOI: 10.1002/jcc.21759.
- [40] Krukau, A. V.; Vydrov, O. A.; Izmaylov, A. F.; Scuseria, G. E. Influence of the exchange screening parameter on the performance of screened hybrid functionals. *J. Chem. Phys.* **2006**, *125*, 224106. DOI: 10.1063/1.2404663.
- [41] Fei, Y. Effects of temperature and composition on the bulk modulus of (Mg,Fe)O. *Am. Min.* **1999**, *84*, 272-276. DOI: 10.2138/am-1999-0308.
- [42] Frusteri, L.; Cannilla, C.; Todaro, S.; Frusteri, F.; Bonura, G. Tailoring of Hydrotalcite-Derived Cu-Based Catalysts for CO<sub>2</sub> Hydrogenation to Methanol. *Catalysts* **2019**, *9*, 1058. DOI: 10.3390/catal9121058.
- [43] Oliveira, R. L.; Kiyohara, P. K.; Rossi, L. M. High performance magnetic separation of gold nanoparticles for catalytic oxidation of alcohols. *Green Chem.* **2010**, *12*, 144-149. DOI: 10.1039/B916825G.

- [44] Jacinto, M. J.; Kiyohara, P. K.; Masunaga, S. H.; Jardim, R. F.; Rossi, L. M. Recoverable rhodium nanoparticles: Synthesis, characterization and catalytic performance in hydrogenation reactions. *Appl. Catal. A: Gen.* **2008**, *338*, 52-57. DOI: 10.1016/j.apcata.2007.12.018.
- [45] Medina, J. C.; Figueroa, M.; Manrique, R.; Pereira, J. R.; Srinivasan, P. D.; Bravo-Suárez, J. J.; Baldovino-Medrano, V. G.; Jiménez, R.; Karelavic, A. Catalytic consequences of Ga promotion on Cu for CO<sub>2</sub> hydrogenation to methanol. *Catal. Sci. Technol.* **2017**, *7*, 3375-3387. DOI: 10.1039/C7CY01021D.
- [46] Yang, Y.; Mims, C. A.; Disselkamp, R. S.; Mei, D.; Kwak, J. H.; Szanyi, J.; Peden, C. H. F.; Campbell, C. T. Isotopic Effects in Methanol Synthesis and the Reactivity of Copper Formates on a Cu/SiO<sub>2</sub> Catalyst. *Catal. Lett.* **2008**, *125*, 201-208. DOI: 10.1007/s10562-008-9592-4.
- [47] Baltes, C.; Vukojevic, S.; Schüth, F. Correlation between synthesis, precursor, and catalyst structure and activity of a large set of CuO/ZnO/Al<sub>2</sub>O<sub>3</sub> catalysts for methanol synthesis. *J. Catal.* **2008**, *258*, 334-344. DOI: 10.1016/j.jcat.2008.07.004.
- [48] Jo, Y. R.; Koo, B.; Seo, M. J.; Kim, J. K.; Lee, S.; Kim, K.; Han, J. W.; Jung, W.; Kim, B. J. Growth Kinetics of Individual Co Particles Ex-solved on SrTi<sub>0.75</sub>Co<sub>0.25</sub>O<sub>3-δ</sub> Polycrystalline Perovskite Thin Films. *J. Am. Chem. Soc.* **2019**, *141*, 6690-6697. DOI: 10.1021/jacs.9b01882.
- [49] Schumann, J.; Kröhnert, J.; Frei, E.; Schlögl, R.; Trunschke, A. IR-Spectroscopic Study on the Interface of Cu-Based Methanol Synthesis Catalysts: Evidence for the Formation of a ZnO Overlayer. *Top. Catal.* **2017**, *60*, 1735-1743. DOI: 10.1007/s11244-017-0850-9.
- [50] Pacchioni, G.; Cogliandro, G.; Bagus, P. S. Characterization of oxide surfaces by infrared spectroscopy of adsorbed carbon monoxide: a theoretical investigation of the frequency shift of CO on MgO and NiO. *Surf. Sci.* **1991**, *255*, 344-354. DOI: 10.1016/0039-6028(91)90691-K.
- [51] Hadjiivanov, K. I.; Vayssilov, G. N. Characterization of oxide surfaces and zeolites by carbon monoxide as an IR probe molecule. *Adv. Catal.* **2002**, *47*, 307-511. DOI: 10.1016/S0360-0564(02)47008-3.
- [52] Miyata, S. Physico-Chemical Properties of Synthetic Hydrotalcites in Relation to Composition. *Clays Clay Miner.* **1980**, *28*, 50-56. DOI: 10.1346/CCMN.1980.0280107.
- [53] Gao, P.; Li, F.; Xiao, F.; Zhao, N.; Wei, W.; Zhong, L.; Sun, T. Effect of hydrotalcite-containing precursors on the performance of Cu/Zn/Al/Zr catalysts for CO<sub>2</sub> hydrogenation: Introduction of Cu<sup>2+</sup> at different formation stages of precursors. *Catal. Today* **2012**, *194*, 9-15. DOI: 10.1016/j.cattod.2012.06.012.
- [54] Sanguineti, P. B.; Baltanás, M. A.; Bonivardi, A. L. Copper-gallia interaction in Cu-Ga<sub>2</sub>O<sub>3</sub>-ZrO<sub>2</sub> catalysts for methanol production from carbon oxide(s) hydrogenation. *Appl. Catal. A: Gen.* **2015**, *504*, 476-481. DOI: 10.1016/j.apcata.2014.11.021.

- [55] Clarke, D. B.; Suzuki, I.; Bell, A. T. An Infrared Study of the Interactions of CO and CO<sub>2</sub> with Cu/SiO<sub>2</sub>. *J. Catal.* **1993**, *142*, 27-36. DOI: 10.1006/jcat.1993.1186.
- [56] Xu, F.; Mudiyansele, K.; Baber, A. E.; Soldemo, M.; Weissenrieder, J.; White, M. G.; Stacchiola, D. J. Redox-Mediated Reconstruction of Copper during Carbon Monoxide Oxidation. *J. Phys. Chem. C* **2014**, *118*, 15902-15909. DOI: 10.1021/jp5050496.
- [57] Dulaurent, O.; Courtois, X.; Perrichon, V.; Bianchi, D. Heats of Adsorption of CO on a Cu/Al<sub>2</sub>O<sub>3</sub> Catalyst Using FTIR Spectroscopy at High Temperatures and under Adsorption Equilibrium Conditions. *J. Phys. Chem. B* **2000**, *104*, 6001-6011. DOI: 10.1021/jp9943629.
- [58] Meng, T.; Ren, N.; Ma, Z. Silicalite-1@Cu-ZSM-5 core-shell catalyst for N<sub>2</sub>O decomposition. *J. Mol. Catal. A Chem.* **2015**, *404-405*, 233-239. DOI: 10.1016/j.molcata.2015.05.006.
- [59] Meng, X.; Yuan, L.; Guo, H.; Hou, B.; Chen, C.; Sun, D.; Wang, J.; Li, D. Carbonylation of methanol to methyl acetate over Cu/TiO<sub>2</sub>-SiO<sub>2</sub> catalysts: Influence of copper precursors. *Mol. Catal.* **2018**, *456*, 1-9. DOI: 10.1016/j.mcat.2018.06.022.
- [60] Hadjiivanov, K.; Knözinger, H. FTIR study of CO and NO adsorption and coadsorption on a Cu/SiO<sub>2</sub> catalyst: Probing the oxidation state of copper. *Phys. Chem. Chem. Phys.* **2001**, *3*, 1132-1137. DOI: 10.1039/B009649K.
- [61] Toyir, J.; Ramírez de la Piscina, P.; Fierro, J. L. G.; Homs, N. Catalytic performance for CO<sub>2</sub> conversion to methanol of gallium-promoted copper-based catalysts: influence of metallic precursors. *Appl. Catal. B: Environ.* **2001**, *34*, 255-266. DOI: 10.1016/S0926-3373(01)00203-X.
- [62] Wang, Y.; Zhong, Z.; Liu, T.; Liu, G.; Hong, X. Cu@UiO-66 Derived Cu<sup>+</sup>-ZrO<sub>2</sub> Interfacial Sites for Efficient CO<sub>2</sub> Hydrogenation to Methanol. *Acta Phys.-Chim. Sin.* **2021**, *37*, 2007089. DOI: 10.3866/PKU.WHXB202007089.
- [63] Olah, G. A. Beyond oil and gas: the methanol economy. *Angew. Chem. Int. Ed.* **2005**, *44*, 2636-2639. DOI: 10.1002/anie.200462121.
- [64] Porosoff, M. D.; Yan, B.; Chen, J. G. Catalytic reduction of CO<sub>2</sub> by H<sub>2</sub> for synthesis of CO, methanol and hydrocarbons: challenges and opportunities. *Energy Environ. Sci.* **2016**, *9*, 62-73. DOI: 10.1039/C5EE02657A.
- [65] Zhang, Y.; Zhong, L.; Wang, H.; Gao, P.; Li, X.; Xiao, S.; Ding, G.; Wei, W.; Sun, Y. Catalytic performance of spray-dried Cu/ZnO/Al<sub>2</sub>O<sub>3</sub>/ZrO<sub>2</sub> catalysts for slurry methanol synthesis from CO<sub>2</sub> hydrogenation. *J. CO<sub>2</sub> Util.* **2016**, *15*, 72-82. DOI: 10.1016/j.jccou.2016.01.005.
- [66] Schumann, J.; Tarasov, A.; Thomas, N.; Schlögl, R.; Behrens, M. Cu,Zn-based catalysts for methanol synthesis: On the effect of calcination conditions and the part of residual carbonates. *Appl. Catal. A: Gen.* **2016**, *516*, 117-126. DOI: 10.1016/j.apcata.2016.01.037.



- [67] Tisseraud, C.; Comminges, C.; Belin, T.; Ahouari, H.; Soualah, A.; Pouilloux, Y.; Le Valant, A. The Cu-ZnO synergy in methanol synthesis from CO<sub>2</sub>, Part 2: Origin of the methanol and CO selectivities explained by experimental studies and a sphere contact quantification model in randomly packed binary mixtures on Cu-ZnO coprecipitate catalysts. *J. Catal.* **2015**, *330*, 533-544. DOI: 10.1016/j.jcat.2015.04.035.
- [68] Dasireddy, V. D. B. C.; Likozar, B.; The role of copper oxidation state in Cu/ZnO/Al<sub>2</sub>O<sub>3</sub> catalysts in CO<sub>2</sub> hydrogenation and methanol productivity. *Renew. Energy* **2019**, *140*, 452-460. DOI: 10.1016/j.renene.2019.03.073.
- [69] Chen, Y.; Hong, H.; Cai, J.; Li, Z. Highly Efficient CO<sub>2</sub> to CO Transformation over Cu-Based Catalyst Derived from a CuMgAl-Layered Double Hydroxide (LDH). *Chem. Cat. Chem.* **2021**, *13*, 656-663. DOI: 10.1002/cctc.202001611.
- [70] Collins, S. E.; Baltanás, M. A.; Bonivardi, A. L. An infrared study of the intermediates of methanol synthesis from carbon dioxide over Pd/ $\beta$ -Ga<sub>2</sub>O<sub>3</sub>. *J. Catal.* **2004**, *226*, 410-421. DOI: 10.1016/j.jcat.2004.06.012.
- [71] Solis-Garcia, A.; Fierro-Gonzalez, J. C. Mechanistic Insights into the CO<sub>2</sub> Methanation Catalyzed by Supported Metals: A Review. *J. Nanosci. Nanotechnol.* **2019**, *19*, 3110-3123. DOI: 10.1166/jnn.2019.16606.
- [72] Calatayud, M.; Collins, S. E.; Baltanás, M. A.; Bonivardi, A. L. Stability of formate species on  $\beta$ -Ga<sub>2</sub>O<sub>3</sub>. *Phys. Chem. Chem. Phys.* **2009**, *11*, 1397-1405. DOI: 10.1039/B800519B.
- [73] Borchert, H.; Jürgens, B.; Zielasek, V.; Rupprechter, G.; Giorgio, S.; Henry, C. R.; Bäumer, M. Pd nanoparticles with highly defined structure on MgO as model catalysts: An FTIR study of the interaction with CO, O<sub>2</sub>, and H<sub>2</sub> under ambient conditions. *J. Catal.* **2007**, *247*, 145-154. DOI: 10.1016/j.jcat.2007.02.002.
- [74] Collins, S. E.; Baltanás, M. A.; Bonivardi, A. L. Infrared Spectroscopic Study of the Carbon Dioxide Adsorption on the Surface of Ga<sub>2</sub>O<sub>3</sub> Polymorphs. *J. Phys. Chem. B* **2006**, *110*, 5498-5507. DOI: 10.1021/jp055594c.
- [75] Zhao, K.; Wang, L.; Calizzi, M.; Moiola, E.; Züttel, A. In Situ Control of the Adsorption Species in CO<sub>2</sub> Hydrogenation: Determination of Intermediates and Byproducts. *J. Phys. Chem. C* **2018**, *122*, 20888-20893. DOI: 10.1021/acs.jpcc.8b06508.
- [76] Van Rensburg, W. J.; Petersen, M. A.; Datt, M. S.; Van der Berg, J. A.; Van Helden, P. On the Kinetic Interpretation of DFT-Derived Energy Profiles: Cu-Catalyzed Methanol Synthesis. *Catal. Lett.* **2015**, *145*, 559-568. DOI: 10.1007/s10562-014-1407-1.
- [77] Clarke, D. B.; Bell, A. T. An Infrared Study of Methanol Synthesis from CO<sub>2</sub> on Clean and Potassium-Promoted Cu/SiO<sub>2</sub>. *J. Catal.* **1995**, *154*, 314-328. DOI: 10.1006/jcat.1995.1173.

- [78] Bando, K. K.; Sayama, K.; Kusama, H.; Okabe, K.; Arakawa, H. In-situ FT-IR study on CO<sub>2</sub> hydrogenation over Cu catalysts supported on SiO<sub>2</sub>, Al<sub>2</sub>O<sub>3</sub>, and TiO<sub>2</sub>. *Appl. Catal. A: Gen.* **1997**, *165*, 391-409. DOI: 10.1016/S0926-860X(97)00221-4.
- [79] Busca, G.; Lorenzelli, V. Infrared spectroscopic identification of species arising from reactive adsorption of carbon dioxide on metal oxide surfaces. *Mater. Chem.* **1982**, *7*, 89-126. DOI: 10.1016/0390-6035(82)90059-1.
- [80] Yang, Y.; Mims, C. A.; Disselkamp, R. S.; Kwak, J. H.; Peden, C. H. F.; Campbell, C. T. (Non)formation of Methanol by Direct Hydrogenation of Formate on Copper Catalysts. *J. Phys. Chem. C* **2010**, *114*, 17205-17211. DOI: 10.1021/jp104068k.
- [81] Dow, W. P.; Wang, Y. P.; Huang, T. J. TPR and XRD studies of yttria-doped ceria/γ-alumina-supported copper oxide catalyst. *Appl. Catal. A: Gen.* **2000**, *190*, 25-34. DOI: 10.1016/S0926-860X(99)00286-0.
- [82] Kovanda, F.; JirátoVá, K.; Rymeš, J.; Koloušek, D. Characterization of activated Cu/Mg/Al hydrotalcites and their catalytic activity in toluene combustion. *Appl. Clay Sci.* **2001**, *18*, 71-80. DOI: 10.1016/S0169-1317(00)00032-6.
- [83] Tu, C. H.; Wang, A. Q.; Zheng, M. Y.; Wang, X. D.; Zhang, T. Factors influencing the catalytic activity of SBA-15-supported copper nanoparticles in CO oxidation. *Appl. Catal. A: Gen.* **2006**, *297*, 40-47. DOI: 10.1016/j.apcata.2005.08.035.
- [84] Chen, S.; Zhang, J.; Wang, P.; Wang, X.; Song, F.; Bai, Y.; Zhang, M.; Wu, Y.; Xie, H.; Tan, Y. Effect of Vapor-phase-treatment to CuZnZr Catalyst on the Reaction Behaviors in CO<sub>2</sub> Hydrogenation into Methanol. *Chem. Cat. Chem.* **2019**, *11*, 1448-1457. DOI: 10.1002/cctc.201801988.
- [85] Guo, X.; Mao, D.; Lu, G.; Wang, S.; Wu, G. The influence of La doping on the catalytic behavior of Cu/ZrO<sub>2</sub> for methanol synthesis from CO<sub>2</sub> hydrogenation. *J. Mol. Catal. A: Chem.* **2011**, *345*, 60-68. DOI: 10.1016/j.molcata.2011.05.019.
- [86] Daza, Y. A.; Kuhn, J. N. CO<sub>2</sub> conversion by reverse water gas shift catalysis: comparison of catalysts, mechanisms and their consequences for CO<sub>2</sub> conversion to liquid fuels. *RSC Adv.* **2016**, *6*, 49675-49691. DOI: 10.1039/C6RA05414E.
- [87] Pastor-Pérez, L.; Shah, M.; Le Saché, E.; Ramirez Reina, T. Improving Fe/Al<sub>2</sub>O<sub>3</sub> Catalysts for the Reverse Water-Gas Shift Reaction: On the Effect of Cs as Activity/Selectivity Promoter. *Catalysts* **2018**, *8*, 608. DOI: 10.3390/catal8120608.
- [88] Witoon, T.; Chalorngtham, J.; Dumrongbunditkul, P.; Chareonpanich, M.; Limtrakul, J. CO<sub>2</sub> hydrogenation to methanol over Cu/ZrO<sub>2</sub> catalysts: Effects of zirconia phases. *Chem. Eng. J.* **2016**, *293*, 327-336. DOI: 10.1016/j.cej.2016.02.069.
- [89] Larmier, K.; Liao, W. C.; Tada, S.; Lam, E.; Verel, R.; Bansode, A.; Urakawa, A.; Comas-Vives, A.; Copéret, C. CO<sub>2</sub>-to-Methanol Hydrogenation on Zirconia-Supported Copper Nanoparticles:

- Reaction Intermediates and the Role of the Metal-Support Interface. *Angew. Chem. Int. Ed.* **2017**, *56*, 2318-2323. DOI: 10.1002/anie.201610166.
- [90] Liu, J.; Shi, J.; He, D.; Zhang, Q.; Wu, X.; Liang, Y.; Zhu, Q. Surface active structure of ultra-fine Cu/ZrO<sub>2</sub> catalysts used for the CO<sub>2</sub>+H<sub>2</sub> to methanol reaction. *Appl. Catal. A: Gen.* **2001**, *218*, 113-119. DOI: 10.1016/S0926-860X(01)00625-1.
- [91] Kim, J.; Sarma, B. B.; Andrés, E.; Pfänder, N.; Concepción, P.; Prieto, G. Surface Lewis Acidity of Periphery Oxide Species as a General Kinetic Descriptor for CO<sub>2</sub> Hydrogenation to Methanol on Supported Copper Nanoparticles. *ACS Catal.* **2019**, *9*, 10409-10417. DOI: 10.1021/acscatal.9b02412.
- [92] Signorile, M.; Zamirri, L.; Tsuchiyama, A.; Ugliengo, P.; Bonino, F.; Martra, G. On the Surface Acid-Base Properties of Amorphous and Crystalline Mg<sub>2</sub>SO<sub>4</sub> as Probed by Adsorbed CO, CO<sub>2</sub>, and CD<sub>3</sub>CN. *ACS Earth Space Chem.* **2020**, *4*, 345-354. DOI: 10.1021/acsearthspacechem.9b00271.
- [93] Zakharov, V. A.; Paukshtis, E. A.; Mikenas, T. B.; Volodin, A. M.; Vitus, E. N.; Potapov, A. G. Surface acidic sites of highly disperse magnesium chloride: IR and ESR spectroscopy studies. *Macromolecular Symp.* **1995**, *89*, 55-61. DOI: 10.1002/masy.19950890108.
- [94] Sterrer, M.; Risse, T.; Freund, H. J. CO adsorption on the surface of Mg(001) thin films. *Appl. Catal. A: Gen.* **2006**, *307*, 58-61. DOI: 10.1016/j.apcata.2006.03.007.
- [95] Szanyi, J.; Paffett, M. T. FTIR investigation of the co-adsorption of acetonitrile and carbon monoxide on Cu-ZSM-5. *J. Chem. Soc. Faraday Trans.* **1996**, *92*, 5165-5175. DOI: 10.1039/FT9969205165.
- [96] Boronat, M.; Concepción, P.; Corma, A.; Navarro, M. T.; Renz, M.; Valencia, S. Reactivity in the confined spaces of zeolites: the interplay between spectroscopy and theory to develop structure-activity relationships for catalysis. *Phys. Chem. Chem. Phys.* **2009**, *11*, 2876-2884. DOI: 10.1039/B821297J.
- [97] Hosoglu, F.; Faye, J.; Mareseanu, K.; Tesquet, G.; Miquel, P.; Capron, M.; Gardoll, O.; Lamonier, J. F.; Lamonier, C.; Dumeignil, F. High resolution NMR unraveling Cu substitution of Mg in hydrotalcites-ethanol reactivity. *Appl. Catal. A: Gen.* **2015**, *504*, 533-541. DOI: 10.1016/j.apcata.2014.10.005.
- [98] Crivello, M.; Pérez, C.; Herrero, E.; Ghione, G.; Casuscelli, S.; Rodríguez-Castellón. Characterization of Al-Cu and Al-Cu-Mg mixed oxides and their catalytic activity in dehydrogenation of 2-octanol. *Catal. Today* **2005**, *107-108*, 215-222. DOI: 10.1016/j.cattod.2005.07.168.
- [99] Nunes Amorim de Carvalho, M. C.; Barboza Passos, F.; Schmal, M. The behavior of Cu/ZSM-5 in the oxide and reduced form in the presence of NO and methanol. *Appl. Catal. A: Gen.* **2000**, *193*, 265-276. DOI: 10.1016/S0926-860X(99)00444-5.

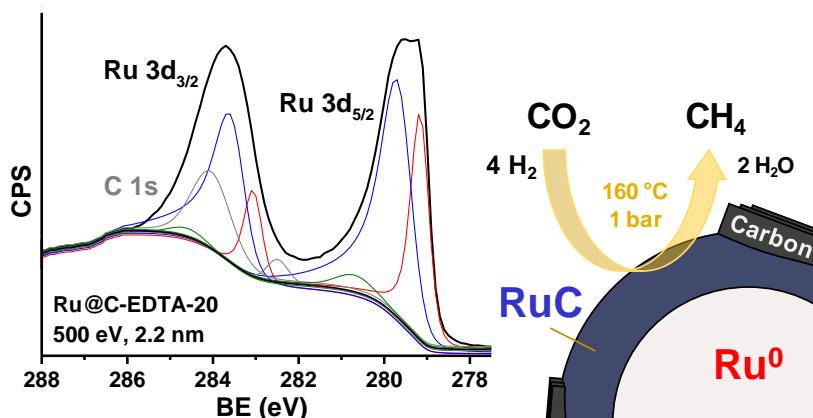
- [100] Bravo-Suárez, J. J.; Subramaniam, B.; Chaudhari, R. V. Ultraviolet-Visible Spectroscopy and Temperature-Programmed Techniques as Tools for Structural Characterization of Cu in CuMgAlO<sub>x</sub> Mixed Metal Oxides. *J. Phys. Chem. C* **2012**, *116*, 18207-18221. DOI: 10.1021/jp303631v.
- [101] Geudtner, G.; Jug, K.; Köster, A. M. Cu adsorption on the MgO(100) surface. *Surf. Sci.* **2000**, *467*, 98-106. DOI: 10.1016/S0039-6028(00)00720-2.
- [102] Zhang, Z.; Zhang, J.; Jia, A. P.; Lu, J. Q.; Huang, W. Morphology-Dependent CO Reduction Kinetics and Surface Copper Species Evolution of Cu<sub>2</sub>O Nanocrystals. *J. Phys. Chem. C* **2020**, *124*, 21568-21576. DOI: 10.1021/acs.jpcc.0c06425.
- [103] Soon, A.; Söhnle, T.; Idriss, H. Plane-wave pseudopotential density functional theory periodic slab calculations of CO adsorption on Cu<sub>2</sub>O(111) surface. *Surf. Sci.* **2005**, *579*, 131-140. DOI: 10.1016/j.susc.2005.01.038.
- [104] Braglia, L.; Borfecchia, E.; Maddalena, L.; Øien, S.; Lomachenko, K. A.; Bugaev, A. L.; Bordiga, S.; Soldatov, A. V.; Lillerud, K. P.; Lamberti, C. Exploring structure and reactivity of Cu sites in functionalized UiO-67 MOF. *Catal. Today* **2017**, *283*, 89-103. DOI: 10.1016/j.cattod.2016.02.039.
- [105] Scarano, D.; Bordiga, S.; Lamberti, G.; Spoto, G.; Ricchiardi, A.; Zecchina, A.; Otero Areán, C. FTIR study of the interaction of CO with pure and silica-supported copper (I) oxide. *Surf. Sci.* **1998**, *411*, 272-285. DOI: 10.1016/S0039-6028(98)00331-8.
- [106] Greeley, J.; Gokhale, A. A.; Kreuser, J.; Dumesic, J. A.; Topsøe, H.; Topsøe, N. Y.; Mavrikakis, M. CO vibrational frequencies on methanol synthesis catalysts: a DFT study. *J. Catal.* **2003**, *213*, 63-72. DOI: 10.1016/S0021-9517(02)00040-4.
- [107] Horn, K.; Pritchard, J. Infrared spectrum of CO chemisorbed on Cu(100). *Surf. Sci.* **1976**, *55*, 701-704. DOI: 10.1016/0039-6028(76)90267-3.
- [108] Nishiyama, H.; Inoue, Y. IRAS study of surface acoustic wave effects on CO adsorbed on Cu surfaces. *Surf. Sci.* **2005**, *594*, 156-162. DOI: 10.1016/j.susc.2005.07.021.
- [109] Pritchard, J.; Catterick, T.; Gupta, R. K. Infrared spectroscopy of chemisorbed carbon monoxide on copper. *Surf. Sci.* **1975**, *53*, 1-20. DOI: 10.1016/0039-6028(75)90113-2.
- [110] Hirschmugl, C. J.; Chabal, Y. J.; Hoffmann, F. M.; Williams, G. P. Low-frequency dynamics of CO/Cu breakdown of Born–Oppenheimer approximation. *J. Vac. Sci. Technol.* **1994**, *12*, 2229-2234. DOI: 10.1116/1.579120.
- [111] Roiaz, M.; Falivene, L.; Rameshan, C.; Cavallo, L.; Kozlov, S. M.; Rupprechter, G. Roughening of Copper (100) at Elevated CO Pressure: Cu Adatom and Cluster Formation Enable CO Dissociation. *J. Phys. Chem. C* **2019**, *123*, 8112-8121. DOI: 10.1021/acs.jpcc.8b07668.





# CHAPTER 5

## Low-temperature carbon dioxide hydrogenation to methane over hydrothermal Ru@C catalysts



The content of this chapter was adapted with permission from the published work:

**“Hydrothermal Synthesis of Ruthenium Nanoparticles with a Metallic Core and a Ruthenium Carbide Shell for Low-Temperature Activation of CO<sub>2</sub> to Methane”**

Cored, J.; García-Ortiz, A.; Iborra, S.; Climent, M. J.; Liu, L.; Chuang, C. H.; Chan, T. S.; Escudero, C.; Concepción, P.; Corma, A.

*J. Am. Chem. Soc.* **2019**, *141*, 19304-19311 (Copyright © 2019 American Chemical Society)





## 5.1. Introduction

Among the processes discussed in Chapter 1 for carbon dioxide capture and use, CO<sub>2</sub> methanation reaction (the so-called Sabatier reaction) has received renewed interest in the last years as a way to store surplus renewable energy in the form of CH<sub>4</sub>, which is easily stored, transported, and used in the actual industrial infrastructure.<sup>[1]</sup> Carbon dioxide methanation is a simple reaction, favored thermodynamically at low temperatures ( $\text{CO}_2 + 4 \text{H}_2 \rightleftharpoons \text{CH}_4 + 2 \text{H}_2\text{O}$ ;  $\Delta H_{298\text{K}}^0 = -164.6 \text{ kJ}\cdot\text{mol}^{-1}$ ), but limited kinetically because of the high stability of CO<sub>2</sub>. The catalysts proposed in patents and in the literature for producing CH<sub>4</sub> from CO<sub>2</sub> are based on metals like Ni, Ru, Pd, Rh, mono- or multimetallic, with or without promoters (Na, K, Cs, rare-earth elements, etc.) on different supports (TiO<sub>2</sub>, SiO<sub>2</sub>, Al<sub>2</sub>O<sub>3</sub>, CeO<sub>2</sub>, ZrO<sub>2</sub>, carbon nanotube (CNT) doped with N).<sup>[2-4]</sup> In all cases, high temperatures (300-500 °C) are employed, which results in large energy input, high operational costs for large-scale production, and negative impact on catalyst stability. Ruthenium is a highly active metal for CO<sub>2</sub> methanation at lower temperature; however, the highest space-time yield to methane reported up to now does not exceed  $0.9 \mu\text{mol}_{\text{CH}_4}\cdot\text{g}_{\text{cat}}^{-1}\cdot\text{s}^{-1}$  at 165 °C and  $2.6 \mu\text{mol}_{\text{CH}_4}\cdot\text{g}_{\text{cat}}^{-1}\cdot\text{s}^{-1}$  at 200 °C and atmospheric pressure, obtained at a  $1.6 \text{ mL}\cdot\text{g}_{\text{cat}}^{-1}\cdot\text{s}^{-1}$  gas feed rate on a Ru/TiO<sub>2</sub> catalyst, still too low for industrial application.<sup>[5,6]</sup> Therefore, a breakthrough in the CO<sub>2</sub> methanation reaction will require a highly active and selective catalyst able to operate under mild reaction conditions.

Transition-metal carbides appear as appealing catalytic alternatives with interesting properties for many processes, such as isomerization of *n*-heptane,<sup>[7]</sup> steam reforming of methanol,<sup>[8]</sup> dry reforming of methane,<sup>[9]</sup> CO hydrogenation,<sup>[10-12]</sup> and CO<sub>2</sub> hydrogenation.<sup>[13-17]</sup> Molybdenum carbide ( $\beta$ -

Mo<sub>2</sub>C)<sup>[13]</sup> and metal-supported carbides (M/Mo<sub>2</sub>C,<sup>[16]</sup> Me=Ni, Co, Cu, or M/TiC,<sup>[15]</sup> M=Cu, Ni, Au) have shown high activity for CO<sub>2</sub> hydrogenation (i.e., 6-8% CO<sub>2</sub> conversion at 200 °C, 20 bar and 2.5 mL·g<sub>cat</sub><sup>-1</sup>·s<sup>-1</sup> gas feed rate),<sup>[16]</sup> being 3-5 times higher than the corresponding metals supported on conventional oxide supports. However, the selectivity to the target product is relatively low (29% and 42% CH<sub>4</sub> at 200 °C on β-Mo<sub>2</sub>C and Ni/Mo<sub>2</sub>C, respectively)<sup>[16]</sup> due to CO formation (39% and 37%, respectively). The high activity has been ascribed to the intrinsic activity of metal carbides to adsorb and activate the CO<sub>2</sub> molecule through a net charge transfer from carbide to the CO<sub>2</sub> molecule.<sup>[14,18]</sup> The reactivity, i.e., C-O bond cleavage of the CO<sub>2</sub> molecule, strongly depends on the carbon/metal ratio. Thus, CO<sub>2</sub> dissociation occurs spontaneously on a Mo-terminated β-Mo<sub>2</sub>C surface, yielding CO and O, while on a carbon-rich surface (i.e., δ-MoC) a hydrocarboxyl (HOCO) intermediate is formed, resulting in different product selectivity.

In an early study, Moreno-Castilla et al.<sup>[19]</sup> reported the formation of ruthenium carbide (RuC) in a Ru-activated carbon catalyst prepared by sublimating Ru<sub>3</sub>(CO)<sub>12</sub> on a carbon support, followed by thermal decarbonylation in He at 150 °C. On the basis of CO and H<sub>2</sub> chemisorption data, they argued the formation of a Ru<sup>4+</sup> active phase, which according to the authors has been assigned to RuC. This result has to be reviewed considering the low tendency of ruthenium to form carbides or a solid solution with carbon, those usually requiring elevated pressure (5 GPa) and temperatures (1700-2500 °C) for their synthesis.<sup>[20-23]</sup> Moreover, the reported yield of methane in the CO<sub>2</sub>/H<sub>2</sub> reaction was not higher (~1.4-1.0 times) than that of a similar sample without carbide species, which makes the assignation to RuC doubtful.

In the present chapter, we show the possibility of synthesizing ruthenium carbide catalysts (labeled as Ru@C) by an easy and mild hydrothermal method instead of using the harsh treatments previously reported. Most importantly, the as-synthesized Ru@C catalysts show unprecedented activity for the low temperature (160-200 °C) CO<sub>2</sub> hydrogenation reaction to CH<sub>4</sub>. Methane yields up to 3.5  $\mu\text{mol}_{\text{CH}_4}\cdot\text{g}_{\text{cat}}^{-1}\cdot\text{s}^{-1}$  at 160 °C and 13.8  $\mu\text{mol}_{\text{CH}_4}\cdot\text{g}_{\text{cat}}^{-1}\cdot\text{s}^{-1}$  at 200 °C are achieved at atmospheric pressure and at 7.9  $\text{mL}\cdot\text{g}_{\text{cat}}^{-1}\cdot\text{s}^{-1}$  feed rate, surpassing by far the most active Ru catalyst reported up to now.<sup>[4,5,6,24,25]</sup> The catalysts also show good stability under operational conditions with CH<sub>4</sub> selectivity above 99.9%. Finally, we will demonstrate that the formation of CH<sub>4</sub> is taken place by direct activation and hydrogenation of CO<sub>2</sub>.

## 5.2. Materials and methods

### 5.2.1. Preparation of catalytic samples and references

#### *Synthesis of Ru@C-EDTA-X*

Samples with different Ru contents were prepared using the same synthetic procedure but modifying the amount of Ru precursor. In general, G (G = 1.5, 3.1, 5.3 and 6.6) g of Ru(acac)<sub>3</sub> (acac=acetylacetonate) (Aldrich, >97%), 1.77 g Na<sub>2</sub>EDTA·2H<sub>2</sub>O (EDTA=ethylenediaminetetraacetic acid derived salt) (Aldrich, 99%) and 0.39 g NaOH (Acros, 98%) were dissolved in 8 mL of deionized water. Then, 4 mL of methanol was added to the mixed aqueous solution with stirring at room temperature (RT), resulting in a red suspension, which was transferred into a 35 mL Teflon-coated stainless steel autoclave followed by static hydrothermal processing at 200 °C for 24 h. Afterward, the autoclave was taken out of the oven and cooled down to RT over 3 h. The generated precipitate was filtered and washed with deionized water and acetone five times. Samples were labeled as

Ru@C-EDTA-X, where X corresponds to the ruthenium loading, determined by ICP (Table 5.3 in Subsection 5.5.1).

#### *Synthesis of Ru@C-Glucose*

A 120 mg portion of glucose (Aldrich, 99%) dissolved in 7 mL of deionized water was stirred at RT for 0.5 h. Then, 100 mg of RuO<sub>2</sub> (Aldrich, 99.9%, particle size 32 nm, determined by XRD) was added and the mixture was ultrasonicated (Branson 3510 operating at 40 Hz) for 0.5 h, obtaining a black suspension. The so-obtained suspension was transferred into a Teflon-coated stainless steel autoclave of 12.5 mL. The autoclave was introduced in an oven at 175 °C and kept under static conditions for 18 h. Afterward, the autoclave was taken out of the oven and cooled down to RT over 2 h. The content of the autoclave was then filtrated under vacuum conditions, recovering a black solid. The solid was washed five times, first with water and later with acetone. Finally, it was dried in an oven at 60 °C for 12 h. The loading of ruthenium in the sample was 24.3 wt %, according to ICP analysis.

#### *Synthesis of Ru/C-WI*

The sample was prepared by a wet impregnation method as follows: 396 mg of Ru(acac)<sub>3</sub> was dissolved in 20 mL of toluene for 0.5 h. Then, 900 mg of carbon (activated charcoal Norit, Aldrich) was added and the mixture stirred for 15 h at RT. The final suspension was evaporated under vacuum, resulting in a black solid. The solid was reduced in 50 mL·min<sup>-1</sup> H<sub>2</sub> at 250 °C for 3 h with a heating ramp of 10 °C·min<sup>-1</sup>, followed by cooling down in N<sub>2</sub> to 25 °C. After this, it was oxidized in 50 mL·min<sup>-1</sup> O<sub>2</sub> flow at 400 °C for 3 h. The loading of ruthenium in the sample was 3.0 wt %, according to ICP analysis. XRD analysis is shown in Figure 5.12, Subsection 5.5.1).

### *Synthesis of Ru/C-Ar800*

A 58 mg portion of Ru(acac)<sub>3</sub> was dissolved in 20 mL of acetone and stirred at 50 °C. Subsequently, 1.47 g of Na<sub>2</sub>EDTA and 120 mg NaOH were dissolved in water (20 mL), and the resulting aqueous solution was added to the metal solution and stirred at 50 °C for 0.5 h. Then, 1.60 g of carbon (activated charcoal Norit, Aldrich) was added and the mixture was refluxed at 50 °C for 24 h. After cooling, the suspension was rotoevaporated, washed with water, filtered, and dried at 100 °C overnight. The black solid was pyrolyzed in an Ar flow (10 mL·min<sup>-1</sup>) at 800 °C for 5 h (5 °C·min<sup>-1</sup>). XRD analysis is shown in Figure 5.12 (Subsection 5.5.1).

### *Synthesis of Ru@C/NG*

The catalyst was synthesized according to reference [26]. Briefly, graphene oxide (GO) support was prepared following the improved Hummers method. GO was doped with nitrogen using formaldehyde (37% in water, Aldrich) and melamine (Acros, 99%), and the suspension was transferred into a Teflon-coated stainless steel autoclave (12.5 mL) and kept at 180 °C for 12 h. The gel obtained was submitted to pyrolysis in a N<sub>2</sub> flow at 750 °C for 5 h. The nitrogen-doped graphene (NG) support was dispersed in a phosphate-buffered solution with the metal precursor (RuCl<sub>3</sub>·3H<sub>2</sub>O, Johnson Matthey, 99%), dopamine hydrochloride (Aldrich, 98%), and cetyltrimethylammonium bromide (CTAB) (Acros, +99%) and hydrothermally treated at 140 °C for 6 h. The resulting suspension was centrifuged and the solid was washed with water and dried. The catalyst was obtained after a high-temperature treatment in argon (800 °C, 10 mL·min<sup>-1</sup>) for 3 h.

### *Synthesis of Ru<sub>3</sub>(CO)<sub>12</sub>/C*

The catalyst was synthesized according to reference [19], following a sublimation technique. First, Ru<sub>3</sub>(CO)<sub>12</sub> (27 mg, Aldrich, 99%) and carbon (490 mg, activated

charcoal Norit, Aldrich) were physically mixed in a glass ampoule. Afterwards, vacuum (5 mbar) was made at RT for 4 h. After this step, the temperature was decreased with liquid N<sub>2</sub> to obtain a pressure of 1 mbar and the ampoule was sealed. Then, the sealed vial was mechanically rotated at 70 °C for 4 h, to encourage the carbonyl compound to sublime onto the support.

#### *Ruthenium references*

Commercial Ru on carbon (Ru/C-com; Acros Organics, 5 wt % Ru) and Ru-black (Aldrich, >98%) were used as reference samples in catalytic and spectroscopic studies. XRD are shown in Figure 5.12 (Subsection 5.5.1).

#### **5.2.2. Characterization techniques**

The Ru content was analyzed by inductively coupled plasma optical emission spectrometry (ICP-OES) using a Varian 715-ES spectrometer. The samples were dissolved in aqua regia at 60 °C for 20 h.

X-ray powder diffraction (XRD) was recorded with a PANalytical Cubix Pro diffractometer with a CuK<sub>α</sub> X-ray source ( $\lambda=0.15406$  nm). Data were collected over a  $2\theta$  range of 5-90° at a scan rate of 2 min<sup>-1</sup>, operating at 40 kV and 35 mA. Average particle size was calculated from the main peaks (38.4, 42.2, 44.0, 58.3, 69.4, 78.4;  $2\theta$ ) of Ru<sup>0</sup> (JCPDS: 00-006-0663) using the Scherrer equation.

High-resolution transmission electron microscopy (HR-TEM) measurements were performed on a JEOL-JEM 2100F operating at 200 kV. Samples were prepared by dropping a suspension of the powder catalyst using ethanol (Scharlab, absolute) as the solvent directly onto holey-carbon coated Cu grids.

The amount of surface ruthenium metal sites was measured by CO chemisorption at 25 °C on a Quantachrome Autosorb-1C instrument by extrapolating the total

gas uptakes in the adsorption isotherms at zero pressure and assuming an adsorption stoichiometry of 1:1 (Ru:CO).<sup>[19]</sup> Before measurements, about 300 mg of catalyst was activated in a helium flow at 100 °C (2 h) and in a vacuum at the same temperature (1 h).

Temperature-programmed reduction (TPR-H<sub>2</sub>) studies were performed using a quartz reactor, connected online to a mass spectrometer (Balzer QMG 220M1). A 120 mg portion of catalyst was flushed with argon at 25 °C for 30 min and then switched to a 70 vol % H<sub>2</sub> in Ar flow (14 mL·min<sup>-1</sup>). The reaction was carried out at increasing temperatures (160, 180, 200, 220, 260 and 280 °C, 10 °C·min<sup>-1</sup>). The *m/z* values used to monitor each product were 44 (CO<sub>2</sub>), 28 (CO and CO<sub>2</sub>), 2 (H<sub>2</sub>), 15 (CH<sub>4</sub>), 16 (CH<sub>4</sub>) and 18 (H<sub>2</sub>O).

Raman studies were performed using a Renishaw "In via" spectrometer connected to an Olympia microscope. The instrument is equipped with a He-Ne green laser (514 nm), a diode laser (785 nm), and a CCD detector.

Laboratory X-ray photoelectron spectroscopy (XPS) experiments were performed on a SPECS equipment with a Phoibos 150 MCD-9 multichannel analyzer and using non-monochromatic AlK<sub>α</sub> (1486.6 eV) X-ray radiation. The pass energy was 20 eV and the X-ray power was 100 W. The sample (~30-50 mg) was pressed into a pellet and loaded onto a SPECS stainless steel sample holder. Binding energies (BE) were calibrated with respect to C 1s signal settled at 284.5 eV. CASA XPS software was used to analyze the data. Shirley-type background and Lorentzian-type curves were used in the spectra fitting.

Synchrotron X-ray photoelectron spectroscopy (XPS) experiments were performed at beamline BL24-CIRCE (NAPP branch) at ALBA Synchrotron Light

Source (Cerdanyola del Vallès, Barcelona, Spain). CIRCE is an undulator beamline with a photon energy range of 100-2000 eV. Data acquisition was performed using a PHOIBOS 150NAP electron energy analyzer (SPECS GmbH). The spectra were acquired with an exit slit of 20  $\mu\text{m}$  and a pass energy of 20 eV. The X-ray spot size was 100 $\times$ 65 (H $\times$ V)  $\mu\text{m}^2$ . Incident photon energies of 500 and 1150 eV for Ru 3d and C 1s were used to record the XPS spectra. The sample (50 mg) was pelletized, mounted onto the sample holder, and measured at room temperature at a 10<sup>-9</sup> mbar pressure without previous activation. Binding energies (BE) were calibrated with respect to C 1s signal settled at 284.5 eV. Shirley-type background and Lorentzian-type curves were used in the spectra fitting.

Near-edge X-ray absorption fine structure (NEXAFS) spectra at the Ru L<sub>2</sub>/L<sub>3</sub>-edges were collected by the total fluorescence yield via a Lytle detector at beamline 16A1 at the Taiwan Light Source. The spot size was 500 $\times$ 500 (H $\times$ V)  $\mu\text{m}^2$ , where probed at the Ru powder sample at an incident angle of 45°. X-ray energy from Si (111) monochromator was calibrated using the energy jump of standard Mo foil at L<sub>3</sub>-edge.

Isotopic <sup>13</sup>CO/<sup>12</sup>CO<sub>2</sub>/H<sub>2</sub> experiments with carbon-labeled species were performed in a homemade stainless steel cell connected online with a mass spectrometer (Balzer QMG 220M1). The catalyst (15 mg) was pelletized and kept in a vacuum at 120 °C for 0.5 h. In the case of Ru/C-com, the sample was additionally reduced in situ with a H<sub>2</sub> flow (280 °C, 1 h, 10 mL·min<sup>-1</sup>) before reaction. After activation, a mixture of <sup>13</sup>CO/<sup>12</sup>CO<sub>2</sub>/H<sub>2</sub> (1:1:6 vol %) was fed continuously at 15 mbar total pressure. Then, the temperature was increased to 160 °C, and finally, the pressure was set at 25 mbar. The reaction evolution was monitored by mass spectrometry



(MS) with  $m/z$  values of 44 (<sup>12</sup>CO<sub>2</sub>), 45 (<sup>13</sup>CO<sub>2</sub>), 28 (<sup>12</sup>CO), 29 (<sup>13</sup>CO), 15 (<sup>12</sup>CH<sub>4</sub>), 17 (<sup>13</sup>CH<sub>4</sub>), 18 (H<sub>2</sub>O) and 2 (H<sub>2</sub>).

CO<sub>2</sub> hydrogenation catalysis was performed in a stainless steel fixed-bed reactor with an inner diameter of 11 mm and 240 mm length. Typically, 210 mg of catalyst (particle size 400-600 μm) was diluted in SiC in a weight ratio of 0.14 (cat./SiC). Ru@C-EDTA and Ru@C-Glucose were not activated before reaction. Ru<sub>3</sub>(CO)<sub>12</sub> was in situ activated in a N<sub>2</sub> flow (25 mL·min<sup>-1</sup>) at 400 °C (2°C·min<sup>-1</sup> heating ramp) for 12 hours. The other samples were in situ reduced prior to catalytic tests (25 mL·min<sup>-1</sup> H<sub>2</sub>, 280 °C, 1 h, 10 °C·min<sup>-1</sup>). The reaction took place at atmospheric pressure, and the reaction temperatures were 160, 180, and 200 °C. Each temperature was maintained for at least 1.5 h. The reaction was carried out at 21428 h<sup>-1</sup> GHSV under concentrated (23.7 vol % CO<sub>2</sub>, 71.3 vol % H<sub>2</sub>, 5.0 vol % N<sub>2</sub>) or diluted (5.0 vol % CO<sub>2</sub>, 20.0 vol % H<sub>2</sub>, 75.0 % vol N<sub>2</sub>) conditions. Direct analysis of the reaction products was done by online gas chromatography (GC), using a SCION-456-GC equipment with TCD (MS-13X column) and FID (BR-Q Plot column) detectors. Blank experiments (in the presence of SiC) showed the absence of a homogeneous contribution to the reaction. Turnover frequency values (TOFs) were obtained from CO chemisorption data.

CO hydrogenation catalysis was performed in the CO<sub>2</sub> hydrogenation reactor setup described before. In this case, the inlet gas mixture was 30.0 % vol CO, 60.0 % vol H<sub>2</sub>, and 10.0 % vol Ar with identical total flow (100 mL·min<sup>-1</sup>). The process took place at atmospheric pressure and in a temperature range of 160-240 °C, using 210 mg of catalyst.

Reactants partial pressure influence study was also performed in the CO<sub>2</sub> hydrogenation reactor setup described above. In particular, 212.5 mg of Ru@C-EDTA were loaded and the total flow was 100 mL·min<sup>-1</sup>. The experiment was carried out at 160 °C. To monitor the H<sub>2</sub> influence, 5 mL·min<sup>-1</sup> CO<sub>2</sub> was kept constant, and the H<sub>2</sub> proportion was varied. To monitor the CO<sub>2</sub> influence, 30 mL·min<sup>-1</sup> H<sub>2</sub> was kept constant while varying the CO<sub>2</sub> proportion. N<sub>2</sub> was used to balance in both series.

### 5.3. Results and discussion

#### 5.3.1. Synthesis and characterization of Ru@C-EDTA catalysts

Ru@C-EDTA samples are prepared under hydrothermal conditions (details in Subsection 5.2.1), modifying the amount of Ruthenium(III) acetylacetonate (Ru(acac)<sub>3</sub>) in the synthesis gel, while the ethylenediaminetetraacetic acid disodium salt dihydrate (Na<sub>2</sub>EDTA·2H<sub>2</sub>O) is kept constant. The synthesis takes place at autogenous pressure at 200 °C for 24 h. The ruthenium loading in the as-prepared samples, determined from ICP analysis, takes values between 6 and 28 wt % (Table 5.3). Representative TEM images obtained from the Ru@C-EDTA samples are presented in Figure 5.1 and Figures 5.6-5.9, which show the presence of Ru<sup>0</sup> nanoparticles (RuNPs) embedded in a carbon matrix. A homogeneous distribution of small RuNPs with average particle sizes of 2-5 nm is observed in the Ru@C-EDTA-6, -12, and -20 samples. However, a more heterogeneous size distribution of small (2-5 nm) and bigger (10-15 nm) Ru nanoparticles can be detected in the Ru@C-EDTA-28 sample (Figure 5.9).

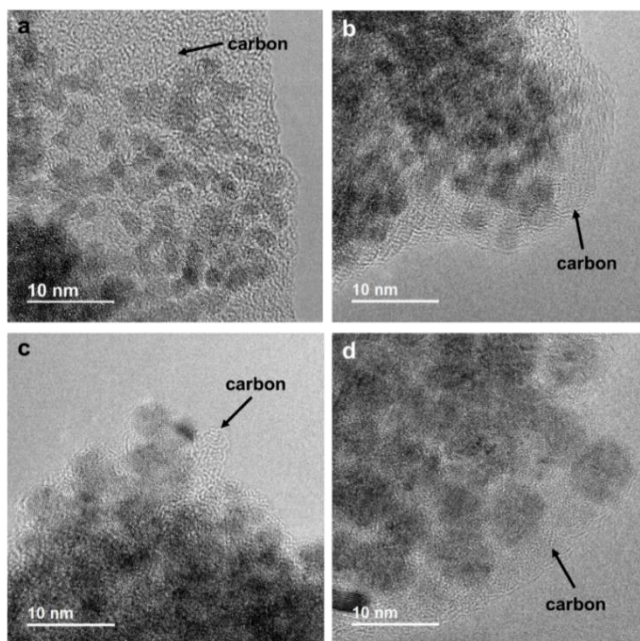


**Figure 5.1** TEM images of Ru@C-EDTA samples prepared by hydrothermal synthesis with different ratios of Ru/EDTA: Ru@C-EDTA-6 (a), Ru@C-EDTA-12 (b), Ru@C-EDTA-20 (c), and Ru@C-EDTA-28 (d).

This is in accordance with the bulk information extracted from X-ray diffractograms (Figure 5.12), where the peak broadening observed in samples Ru@C-EDTA-6, -12, and -20 samples corresponds to a small crystallite size, whereas some sharp peaks are visualized in the Ru@C-EDTA-28 sample, corresponding to crystalline Ru<sup>0</sup> (hexagonal, JCPDS: 00-006-0663). The nature of the carbon matrix studied by Raman spectroscopy shows a graphitic structure (1600 cm<sup>-1</sup>) with defects (1371 cm<sup>-1</sup>) and some amorphous carbon (1506 cm<sup>-1</sup>)<sup>[28]</sup> (Figure 5.11). In addition, concerning the nature of the ruthenium species, XPS studies performed in a laboratory-scale spectrometer using AlK<sub>α</sub> (1486.6 eV) X-ray energy (Figure 5.13) displays the presence of Ru<sup>0</sup> (279.3 eV) and RuO<sub>2</sub> (281.0 eV). However, high-resolution XPS using synchrotron radiation allowed us to

obtain surface-sensitive information of the Ru@C-EDTA samples working at variable X-ray excitation energy. In fact, at low X-ray excitation energy (500 eV) with a probing depth of around 2.2 nm,<sup>[29]</sup> an additional ruthenium specie at 279.6 eV, together with Ru<sup>0</sup> (at 279.1 eV) and RuO<sub>2</sub> (281.0–280.4 eV), is clearly observed (Figure 5.2a). The surface concentration of this new specie slightly increases from ~56% to ~70% upon decreasing the Ru content in the samples (Figure 5.2b).

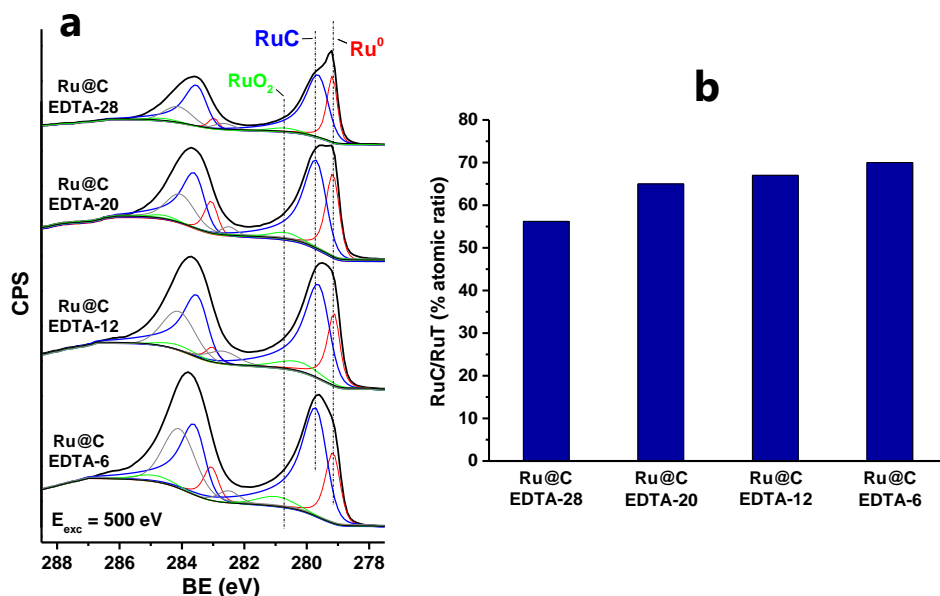


**Figure 5.2** Synchrotron XPS of the C 1s and Ru 3d core levels at 500 eV X-ray excitation energy on fresh Ru@C-EDTA samples (a). Color code for components: Ru<sup>0</sup> (red), RuC (blue), RuO<sub>2</sub> (green), and C (gray). Surface concentration of the ruthenium carbide phase (RuC) relative to the total ruthenium (RuT) (b).

On the basis of XPS depth profile analysis, at a sample depth of 4.4 nm, the contribution of the new component at 279.6 eV to the total Ru peak intensity decreases ~30–40% in all samples at the expense of the Ru<sup>0</sup> component (Figure 5.13), meaning that the new Ru specie identified by synchrotron XPS is preferentially located on the upper surface layers of the catalyst. This new

component is ascribed in our work to ruthenium carbide (RuC) species. However, its assignment is not straightforward, due to the lack of reference data associated with RuC and uncertainties that exist in the literature regarding to the assignment of ruthenium chemical states.<sup>[30]</sup> Our assignment has been made based on previous studies, where a +0.5 eV shift with respect to the metal was related to carbide species,<sup>[31]</sup> and is also supported by HR-TEM analysis (Figure 5.3a and Figure 5.10), where lattice fringes at 0.21 and 0.31 nm, corresponding to Ru<sup>0</sup> and RuO<sub>x</sub>, respectively,<sup>[32]</sup> and at 0.25 and 0.28 nm, due to RuC (JCPDS: 01-089-3016) are detected.

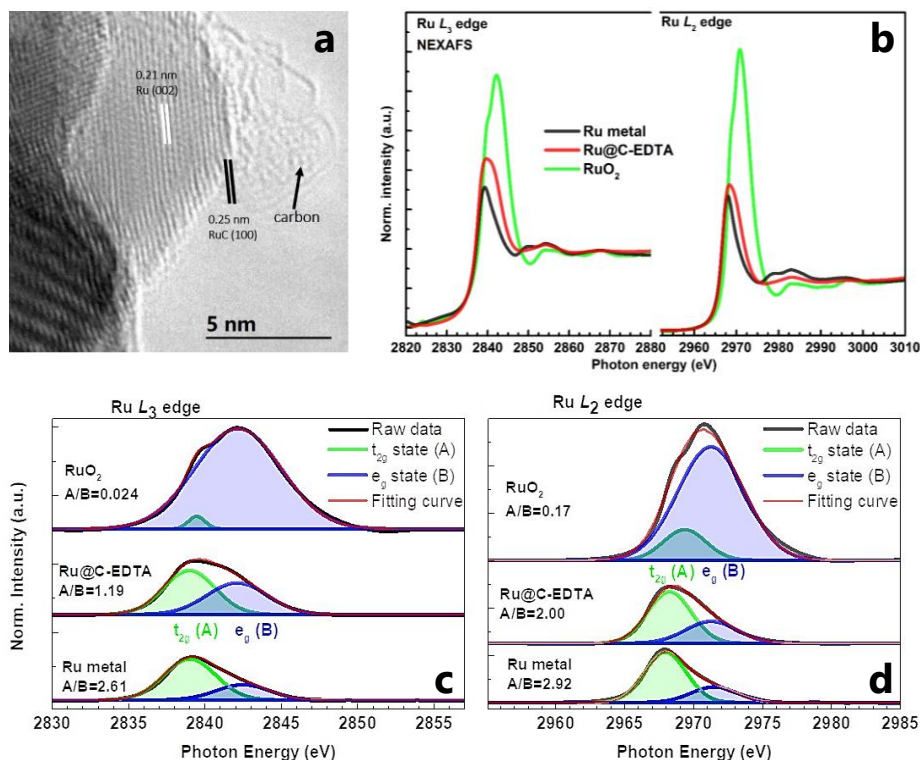


**Figure 5.3** HR-TEM image of the Ru@C-EDTA-20 sample (a). The L<sub>3</sub>-edge spectra (left panel) and L<sub>2</sub>-edge spectra (right panel) of Ru<sup>0</sup>, Ru@C-EDTA-20, and RuO<sub>2</sub> (b). Curve-fitting simulation from the NEXAFS spectra at L<sub>3</sub>- (c) and L<sub>2</sub>- (d) edges on RuO<sub>2</sub>, Ru@C-EDTA-20 and Ru<sup>0</sup>.

In addition to XPS and HR-TEM analysis, the assignment of the new detected specie to RuC is supported by NEXAFS analysis performed on the Ru@C-EDTA-20 sample at the Ru L<sub>2</sub>/L<sub>3</sub>-edges, which is compared with that of RuO<sub>2</sub> and Ru<sup>0</sup> references (Figure 5.3b). The spectra reflect the electronic structure of surface Ru species and their local environment, which do not correspond to RuO<sub>2</sub> nor Ru<sup>0</sup>. Indeed, the Ru L-edge white lines of Ru@C-EDTA-20 (located around 2840 and 2969 eV for the L<sub>3</sub> and L<sub>2</sub>, respectively) are shifted to higher photon energy compared to that of Ru metal, and to lower energy with respect to that of RuO<sub>2</sub>, while they are compatible with the RuC phase.<sup>[33]</sup> Moreover, the global spectral shapes characteristic of Ru<sup>0</sup> and RuO<sub>2</sub> are incompatible with the spectra collected on the Ru@C-EDTA-20 sample, where both the double-peak structure around 2850 (L<sub>3</sub>) / 2980 (L<sub>2</sub>) eV (characteristic of the metal phase) and the one broadened peak structure of the white line (characteristic of the RuO<sub>2</sub> phase) are absent (details in Figure 5.15a,b). Curve-fitting simulation from the NEXAFS spectra at L<sub>3</sub>/L<sub>2</sub> edges is shown in Figure 5.3c,d, representing two peaks corresponding to the electronic transition 2p → 4d-t<sub>2g</sub> (A) and 4d-e<sub>g</sub> (B) states. The A/B ratios in RuO<sub>2</sub> and Ru metal at L<sub>3</sub>-edge (L<sub>2</sub>) are 0.024 (0.17) and 2.61 (2.92), respectively, which are the opposite of that expected from their electronic configurations (4d<sup>4</sup> and 4d<sup>8</sup> electrons). In the Ru@C-EDTA-20 sample, the A/B ratios result at the L<sub>3</sub>- and L<sub>2</sub>-edge, 1.19 and 2.00, respectively, is between that of RuO<sub>2</sub> and Ru metal, reflecting a different feature symmetry and ligand environment in the Ru@C-EDTA-20 sample. This agrees with the previous results and indicates that the upper surface of our catalysts is most likely ascribed to RuC. To our knowledge, this is the first time that a ruthenium carbide phase is formed under mild

conditions (hydrothermal synthesis at 200 °C) as opposed to the harsh conditions (5 GPa and 1000-2500 °C) usually required for its synthesis.<sup>[20-23]</sup>

### 5.3.2. Catalytic properties and active site elucidation in the Sabatier reaction.

From the point of view of their application in the CO<sub>2</sub> hydrogenation reaction, an important issue to deal with is the thermal stability of the Ru@C-EDTA catalytic systems under H<sub>2</sub>-rich conditions, which is proved by a TPR-H<sub>2</sub> study. In this experiment, performed in H<sub>2</sub> flow at atmospheric pressure, the CH<sub>4</sub> formation (due to carbide and/or carbon hydrogenation) is followed by online MS. Under these conditions, CH<sub>4</sub> MS signal ( $m/z=15$ ) clearly evolves above 240 °C (Figure 5.16), limiting the catalytic studies to this temperature.

The herein reported Ru@C-EDTA catalysts show markedly high activity at low temperature (160-200 °C) and atmospheric pressure for the CO<sub>2</sub> hydrogenation reaction, with 99.9% selectivity to methane, operating at 21428 h<sup>-1</sup> GHSV (details in Subsection 5.2.2). The CO<sub>2</sub> conversion and the methane space-time yield (STY<sub>CH<sub>4</sub></sub>) in the 160-180 °C temperature range at concentrated reaction conditions is summarized in Table 5.1 where an increase in the catalytic activity is observed at increasing Ru loading in the samples.

**Table 5.1** Catalytic activity in the CO<sub>2</sub> hydrogenation reaction at concentrated reaction conditions<sup>a</sup> on the Ru@C-EDTA samples.

Catalyst	160 °C		180 °C	
	X <sub>CO<sub>2</sub></sub> (%)	STY <sub>CH<sub>4</sub></sub> ( $\mu\text{mol}_{\text{CH}_4}\cdot\text{g}_{\text{cat}}^{-1}\cdot\text{s}^{-1}$ )	X <sub>CO<sub>2</sub></sub> (%)	STY <sub>CH<sub>4</sub></sub> ( $\mu\text{mol}_{\text{CH}_4}\cdot\text{g}_{\text{cat}}^{-1}\cdot\text{s}^{-1}$ )
Ru@C-EDTA-28	4.9	3.8	13.2	10.1
Ru@C-EDTA-20	4.6	3.5	9.8	7.6
Ru@C-EDTA-12	2.7	2.2	6.5	5.3
Ru@C-EDTA-6	1.3	1.8	2.5	3.5

<sup>a</sup>Conditions: 1 bar, GHSV 21428 h<sup>-1</sup>, and reactant feed composed of 23.7 vol % CO<sub>2</sub>, 71.3 vol % H<sub>2</sub>, 5.0 vol % N<sub>2</sub>.

The catalyst stability of Ru@C-EDTA-20 sample tested over a period of ~15 h reaction time at 160 °C is plotted in Figure 5.4. A decrease in activity (~8%) is observed in the first 12 h of reaction, while it remains stable in the last 3 h.

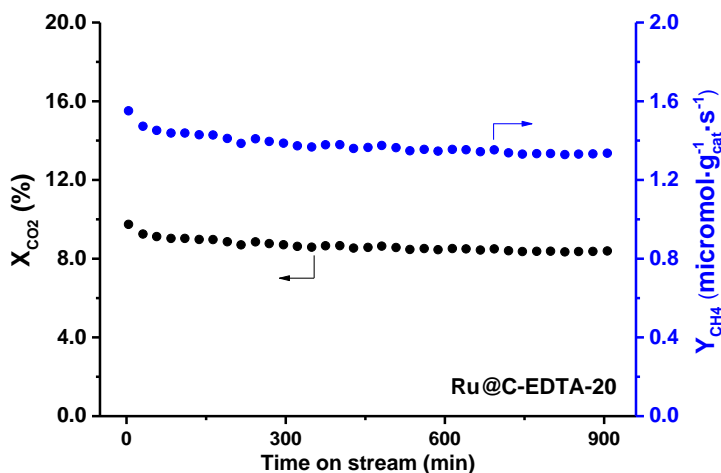


**Figure 5.4** CO<sub>2</sub> conversion (left axis, black) and methane STY (right axis, blue) on the Ru@C-EDTA-20 catalyst at 160 °C, 21428 h<sup>-1</sup> GHSV, and 5.0 % vol CO<sub>2</sub>, 20.0 % vol H<sub>2</sub>, and 75.0 % vol N<sub>2</sub>.

The observed loss of activity corresponds to a partial removal of surface ruthenium carbide species under reaction conditions, as evidenced from XPS studies using synchrotron radiation performed on the spent catalysts (Figure 5.17a), while the carbonaceous matrix where the RuNPs are embedded is maintained (see Raman spectra of the spent catalysts in Figure 5.11). In fact, a loss of RuC species is observed in all samples according to the XPS spectra acquired at 500 eV X-ray excitation energy, being on the order of 23-31% on the Ru@C-EDTA-6, -12, and -20 samples and of 5% on the Ru@C-EDTA-28 sample (Figure 5.17b). Based on this data, a fairly good correlation between the amount of surface RuC of the spent Ru@C-EDTA catalysts and the STY<sub>CH<sub>4</sub></sub> at 160 °C (Table 5.1) is found, as displayed in Figure 5.5. These results suggest that the RuC species



should play a key role in the catalytic activity of the Ru@C-EDTA samples, as discussed later.

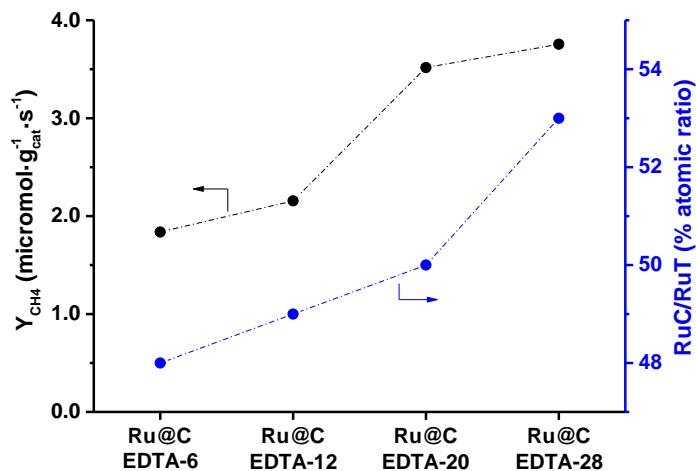


**Figure 5.5** Methane STY (left axis, black) at 160 °C, 21428 h<sup>-1</sup> GHSV, and 23.7% CO<sub>2</sub>, 71.3% H<sub>2</sub>, 5.0% N<sub>2</sub> (% vol). On the right axis (blue) is the RuC/RuT atomic ratio obtained from XPS analysis on the spent Ru@C-EDTA catalysts at 500 eV X-ray excitation energy (Figure 5.17).

The activity of the Ru@C-EDTA samples surpasses by far that of other synthesized ruthenium carbon catalysts, as shown in Table 5.2, and is markedly higher than that of most active ruthenium catalysts we found in the literature (Table 5.4). Being aware that the CO<sub>2</sub> methanation on Ru catalysts has been reported to be size-dependent, where large particles were found to be more active than smaller ones,<sup>[34]</sup> reference catalysts with different particle sizes have been considered. All catalysts prepared by different synthesis strategies, some of them reproducing those of the literature,<sup>[19,26,35]</sup> and the commercial-type catalysts (such as Ru/C-com and Ru-black) show negligible activity under the mild operation conditions considered in this work. Moreover, the selectivity to methane is almost 100 % on the Ru@C-EDTA samples, while other by-products like CO or C<sub>x</sub>H<sub>y</sub> are formed on the other samples (Figure 5.18). Altogether this indicates a very promising catalyst

for the Sabatier reaction. In addition, the synthesis of this type of catalyst can be also achieved starting from other precursors, like RuO<sub>2</sub> and glucose, using water as solvent (see Subsection 5.2.1 and Figure 5.19). The similar catalytic activity achieved in the Ru@C-Glucose catalyst (see Table 5.5) allows one to discard the notion that the enhanced catalytic activity of the Ru@C-EDTA catalysts is due to the presence of nitrogen or Na<sup>+</sup> additives coming from the Na<sub>2</sub>EDTA precursor.

**Table 5.2** Catalytic activity in the CO<sub>2</sub> hydrogenation to methane at 160 °C and concentrated reaction conditions<sup>a</sup> of the Ru@C-EDTA-20 sample compared to that of other reference ruthenium carbon samples.

Catalyst	wt % Ru [p. size (nm)] <sup>f</sup>	X <sub>CO<sub>2</sub></sub> (%)	STY <sub>CH<sub>4</sub></sub> (μmol <sub>CH<sub>4</sub></sub> ·g <sub>cat</sub> <sup>-1</sup> ·s <sup>-1</sup> )	CO <sub>2</sub> selectivity (%)		
				CH <sub>4</sub>	CO	C <sub>2</sub> H <sub>6</sub>
Ru@C-EDTA-20	20.2 [2-5] <sup>g</sup>	4.6	3.5	99.9	-	0.1
Ru/C-WI <sup>b</sup>	3.0 [17]	<0.1	4.0·10 <sup>-2</sup>	38.3	61.5	0.2
Ru/C-com	5.0 [2] <sup>g</sup>	<0.1	7.0·10 <sup>-2</sup>	92.7	6.8	0.5
Ru/C-Ar800 <sup>c</sup>	4.0 [-]	0.1	<10 <sup>-2</sup>	73.4	25.6	1.0
Ru@C/NG <sup>d</sup>	13.0 <sup>27</sup> [-]	<0.1	-	-	-	-
Ru <sub>3</sub> (CO) <sub>12</sub> /C <sup>e</sup>	2.5 [1.2] <sup>20</sup>	<0.1	<10 <sup>-2</sup>	-	100.0	0.0
Ru-black (Aldrich)	100 [20]	0.3	0.2	99.9	-	0.1

<sup>a</sup>Conditions: 1 bar, GHSV 21428 h<sup>-1</sup>, and reactant feed composed of 23.7 vol % CO<sub>2</sub>, 71.3 vol % H<sub>2</sub>, 5.0 vol % N<sub>2</sub>. <sup>b</sup>Prepared by wet impregnation of Ru(acac)<sub>3</sub> on a carbon support. <sup>c</sup>Prepared by pyrolysis of the metal precursors according to ref. [35]; <sup>d</sup>Prepared through thermal annealing of polydopamine (PDA)-coated RuNPs supported on a three-dimensional N-doped graphene layer as in ref. [26]; <sup>e</sup>Prepared from Ru<sub>3</sub>(CO)<sub>12</sub> precursor as described in ref. [19]; <sup>f</sup>Calculated by XRD; <sup>g</sup>Calculated by HR-TEM.

Regarding the ruthenium surface speciation in the samples, Ru<sup>0</sup> is the only specie present in all reference catalysts (Table 5.2). However, in Ru@C-EDTA materials, a combination of Ru<sup>0</sup> and RuC (that predominates in upper layers) exists, together with a carbon coating, which could explain their much superior performance. In fact, if the RuC phase in Ru@C-EDTA-20 is removed by treating the catalyst in H<sub>2</sub>

at 280 °C, the catalytic activity strongly decreases (Figure 5.20). This result reinforces our previous assumption of RuC species as a key component responsible for the high catalytic reactivity obtained in the CO<sub>2</sub> methanation reaction at low temperature.

The reaction mechanism (direct CO<sub>2</sub> hydrogenation, via RWGS, or through direct C-O bond cleavage) of the Ru@C-EDTA samples has been studied by combining catalytic studies feeding a CO/H<sub>2</sub> mixture with isotopic studies using a <sup>13</sup>CO/<sup>12</sup>CO<sub>2</sub>/H<sub>2</sub> (1:1:6) reactant feed. For this purpose, the Ru@C-EDTA-20 catalyst is selected as the reference sample that presents surface RuC species, and its behavior is compared to that of a sample containing only Ru<sup>0</sup> (i.e., commercial Ru/C-com). Catalytic studies show negligible CO conversion (<0.05%) on the Ru@C-EDTA-20 sample in the 180-240 °C temperature range, while CO reacts on the commercial Ru/C sample (Table 5.6). Isotopic studies in the presence of <sup>13</sup>CO/<sup>12</sup>CO<sub>2</sub> show a very high preferential <sup>12</sup>CO<sub>2</sub> hydrogenation versus <sup>13</sup>CO on the Ru@C-EDTA-20 sample, since only <sup>12</sup>CH<sub>4</sub> is detected (Figure 5.21a). Meanwhile, <sup>13</sup>CO is preferentially hydrogenated versus <sup>12</sup>CO<sub>2</sub> on the Ru/C-com sample, resulting in <sup>13</sup>CH<sub>4</sub> formation (Figure 5.21b). Combining both results, and taking into account the different selectivity to CO obtained during the CO<sub>2</sub> hydrogenation (CO is not detected for the Ru@C-EDTA-20 sample, while it is formed as the major by-product in the Ru/C-com sample; see Figure 5.18), we can conclude that a direct CO<sub>2</sub> hydrogenation path to CH<sub>4</sub> takes place on the Ru@C-EDTA-20 sample, while contribution of a RWGS reaction mechanism occurs on the Ru/C-com sample in the presence of Ru<sup>0</sup>, in agreement with previous studies.<sup>[34,36-41]</sup> Moreover, the fact that <sup>13</sup>CH<sub>4</sub> is not observed in the isotopic studies of the Ru@C-EDTA-20 sample allows one to disregard the

coexistence of Ru<sup>0</sup> species on the catalyst surface or, if present, they should be exist in a very low amount, being that the activity is ascribed predominately to the presence of RuC species. Finally, the influence of CO<sub>2</sub> and H<sub>2</sub> partial pressure on the initial reaction rate has also been evaluated (Figure 5.22). On the basis of it, a core-shell structure containing a metallic core and an upper shell of ruthenium carbide and carbon species can be proposed for our catalysts. The RuC phase has been proven to be the active species in the CO<sub>2</sub> hydrogenation, which in accordance with the literature<sup>[14,18]</sup> favors CO<sub>2</sub> binding and activation.

#### 5.4. Conclusions

We have described an easy hydrothermal synthesis method that allows the stabilization of surface ruthenium carbide species on a metallic ruthenium core. Advanced surface-sensitive characterization techniques, such as synchrotron XPS, NEXAFS, and HR-TEM, were required to elucidate the presence of these carbidic species, which are not present in other catalysts previously reported. Surface RuC enables CO<sub>2</sub> activation, which is hydrogenated to methane in a direct reaction pathway, yielding 100% selectivity to CH<sub>4</sub>. The high activity at low temperature (160-200 °C) and the absence of CO in the gas effluent make the herein synthesized Ru@C-EDTA and Ru@C-Glucose samples very promising candidates for the Sabatier reaction.

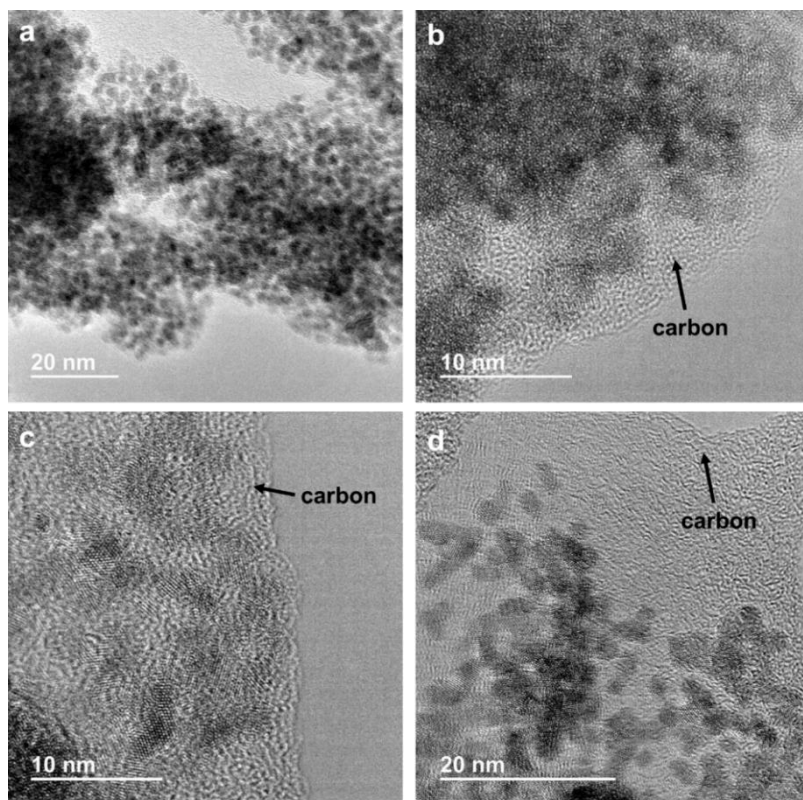
## 5.5. Supporting Information

### 5.5.1. Synthesis and characterization of Ru@C-EDTA catalysts

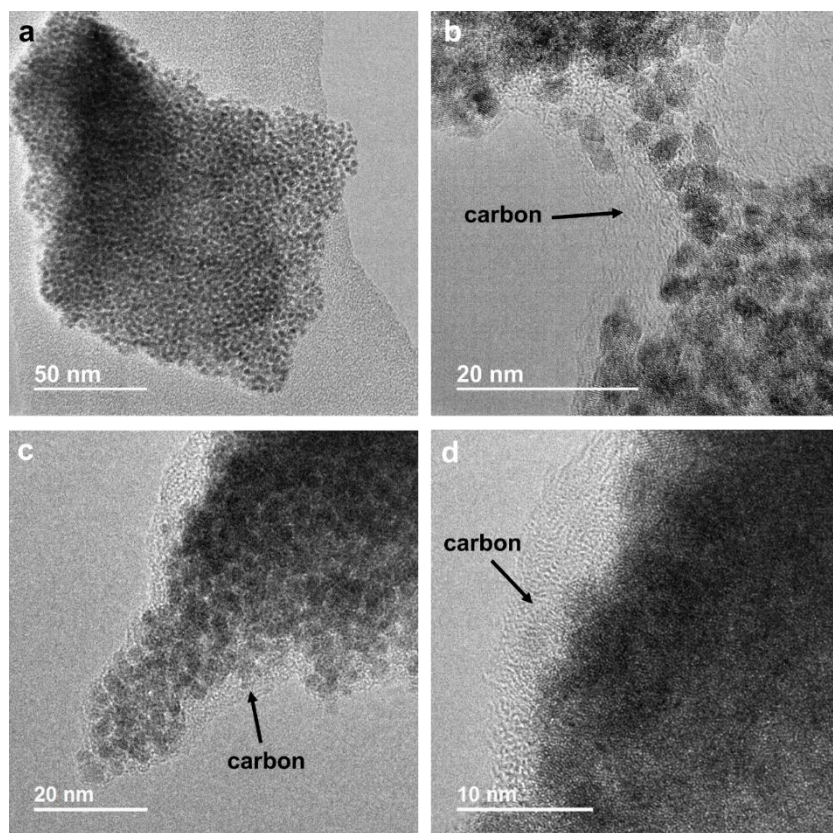
**Table 5.3** Ru@C-EDTA-X synthetic details and ruthenium loading on final catalysts.

Catalyst	Ru(acac) <sub>3</sub> [g]	Ru(acac) <sub>3</sub> /Na <sub>2</sub> EDTA [mol ratio]	Ru loading ICP [wt %]
Ru@C-EDTA-28	6.6	3.4	28.1
Ru@C-EDTA-20	5.3	2.7	20.2
Ru@C-EDTA-12	3.1	1.6	12.0
Ru@C-EDTA-6	1.5	0.8	5.7

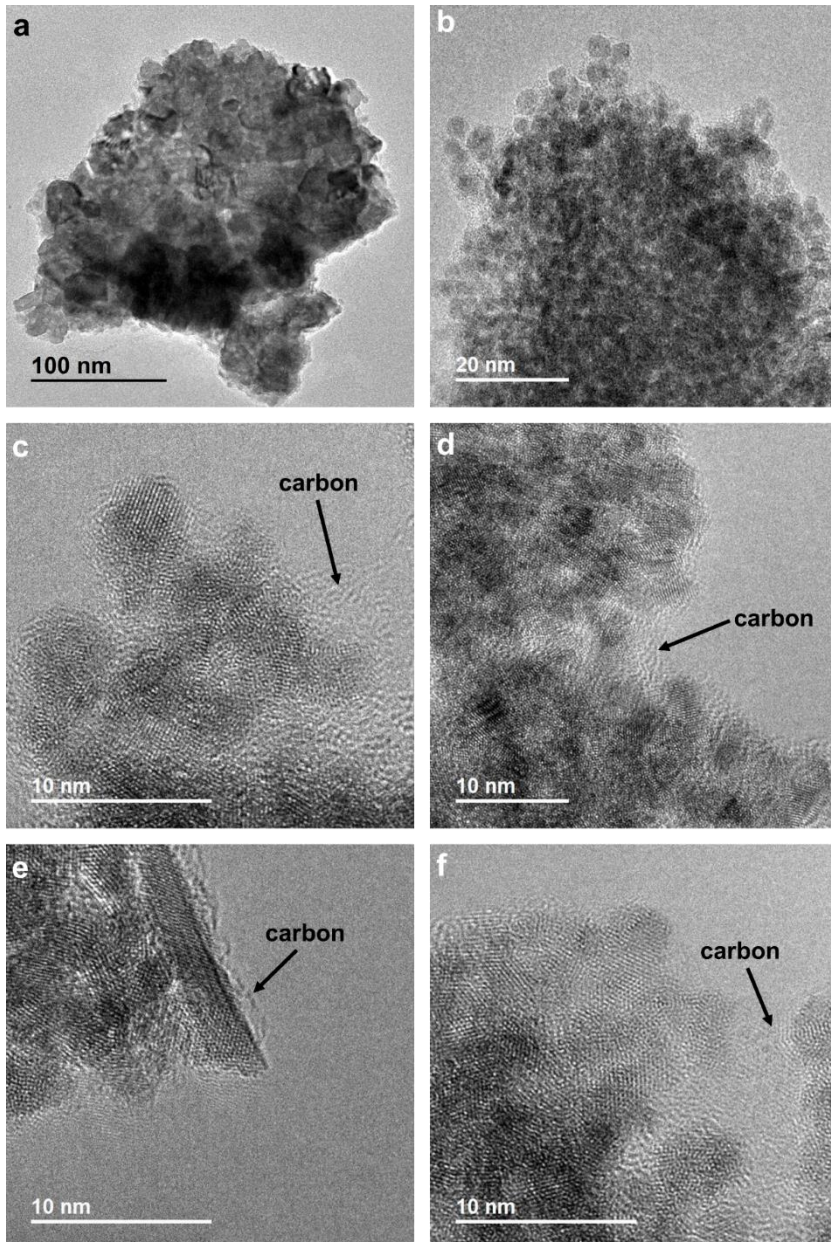
#### *Microscopy images*



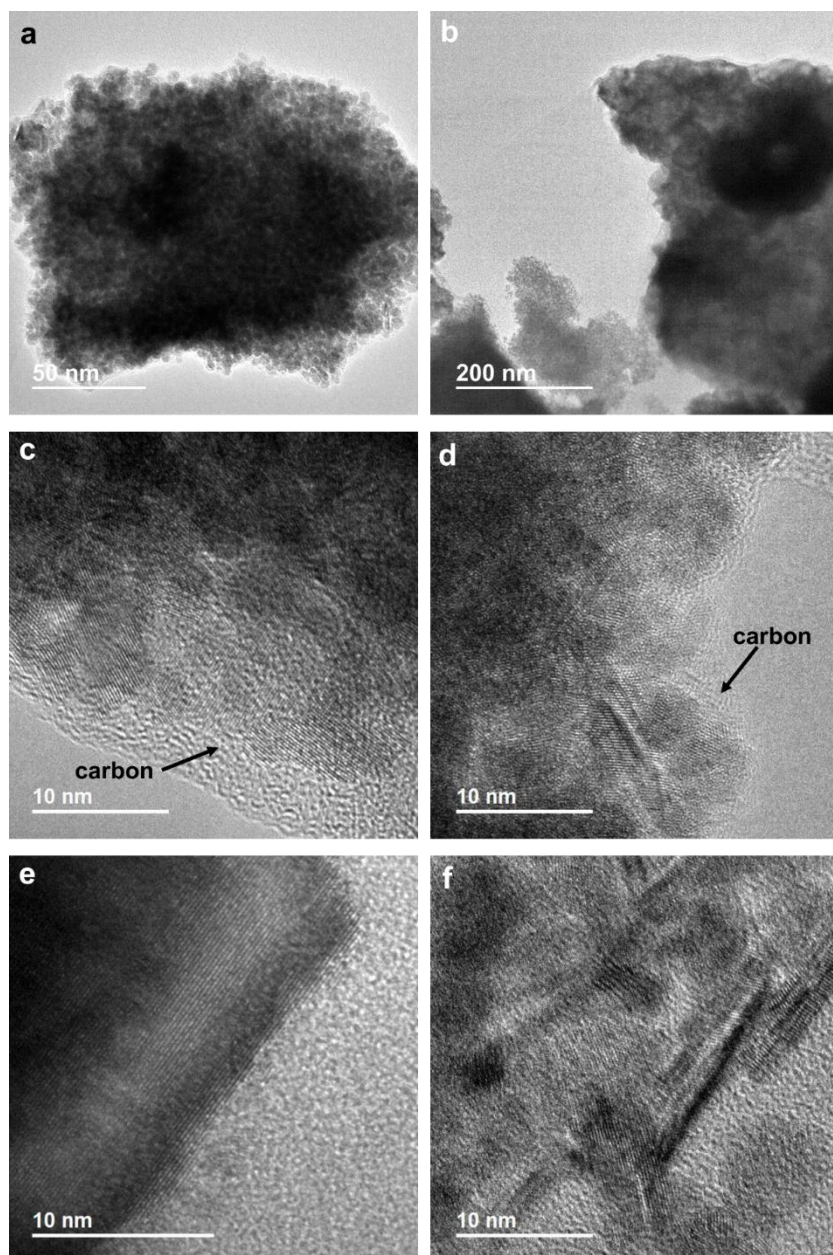
**Figure 5.6** TEM images of Ru@C-EDTA-6 catalyst. Ru nanoparticles of 2-5 nm encapsulated by thin carbon layers can be seen in this sample.



**Figure 5.7** TEM images of Ru@C-EDTA-12 catalyst. Ru nanoparticles of 2-5 nm encapsulated by thin carbon layers can be seen in this sample.

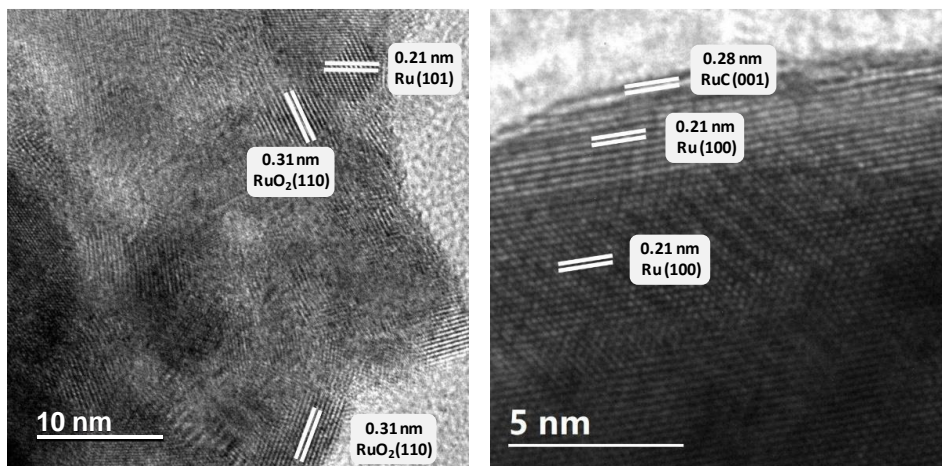


**Figure 5.8** TEM images of Ru@C-EDTA-20 catalyst. Small Ru nanoparticles of 2-5 nm encapsulated by thin carbon layers can be seen in this sample, in addition to few bigger Ru particles.



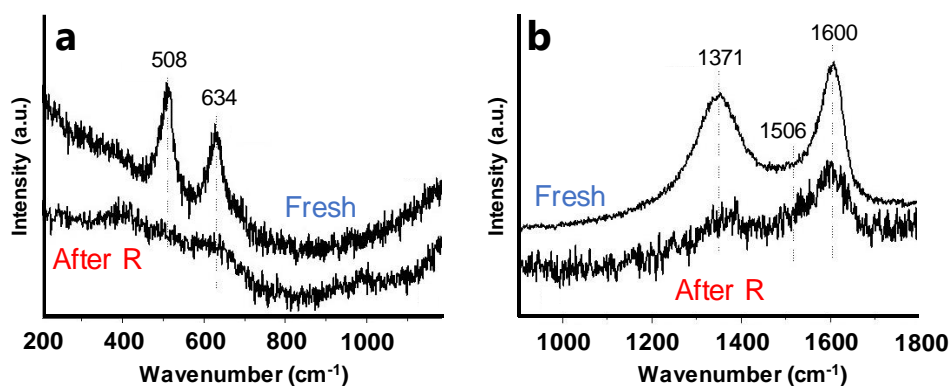
**Figure 5.9** TEM images of Ru@C-EDTA-28 catalyst. Both small Ru nanoparticles of 2-5 nm encapsulated by thin carbon layers and big Ru nanoparticles can be seen in this sample.





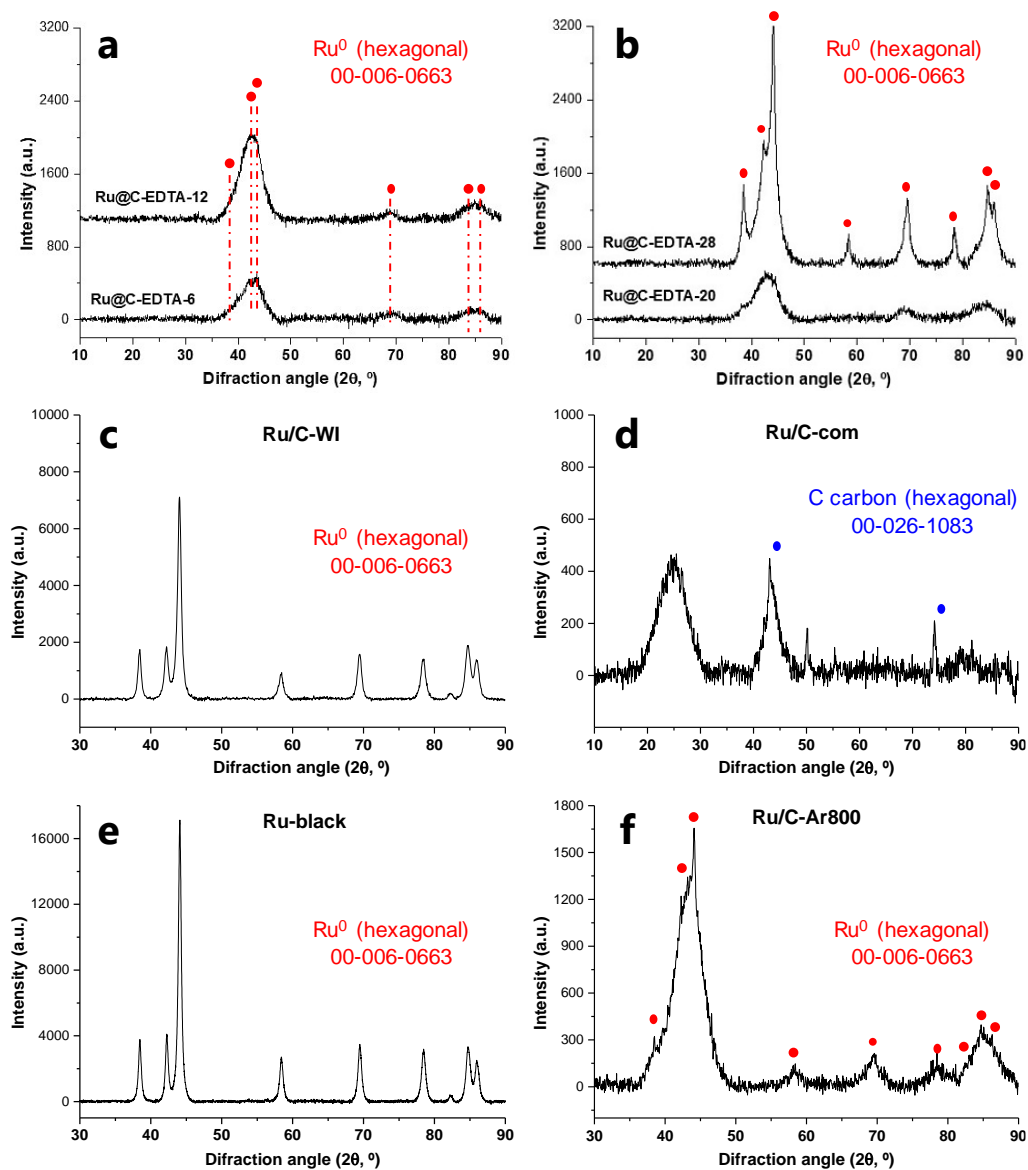
**Figure 5.10** HR-TEM images of Ru@C-EDTA-20 sample, showing the presence of Ru<sup>0</sup>, RuO<sub>2</sub> and RuC phases.

### Raman spectroscopy

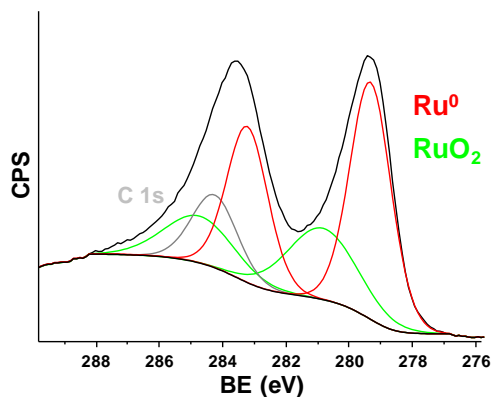


**Figure 5.11** Raman spectra of Ru@C-EDTA-20 acquired with 785 nm laser. Color code: Fresh sample (blue); after catalytic test sample (red).

The lower intensity of the Raman bands at 634 and 508 cm<sup>-1</sup> (ascribed to RuO<sub>2</sub>) in the spent catalyst is in accordance to the XPS data of Figure 5.17, where a lesser amount of RuO<sub>2</sub> is detected on the Ru@C-EDTA-20 sample.

*X-ray diffraction (XRD)*

**Figure 5.12** XRD patterns of Ru@C-EDTA-6 and Ru@C-EDTA-12 (a), Ru@C-EDTA-20 and Ru@C-EDTA-28 (b), Ru/C-WI (c), Ru/C-com (d), Ru-Black (e), and Ru/C-Ar800 (f).

*X-ray photoelectron spectroscopy (XPS)*

**Figure 5.13** Laboratory XPS spectra of the C 1s and Ru 3d core levels of the Ru@C-EDTA-20 sample. ( $AlK_{\alpha}$ =1486.6 eV).

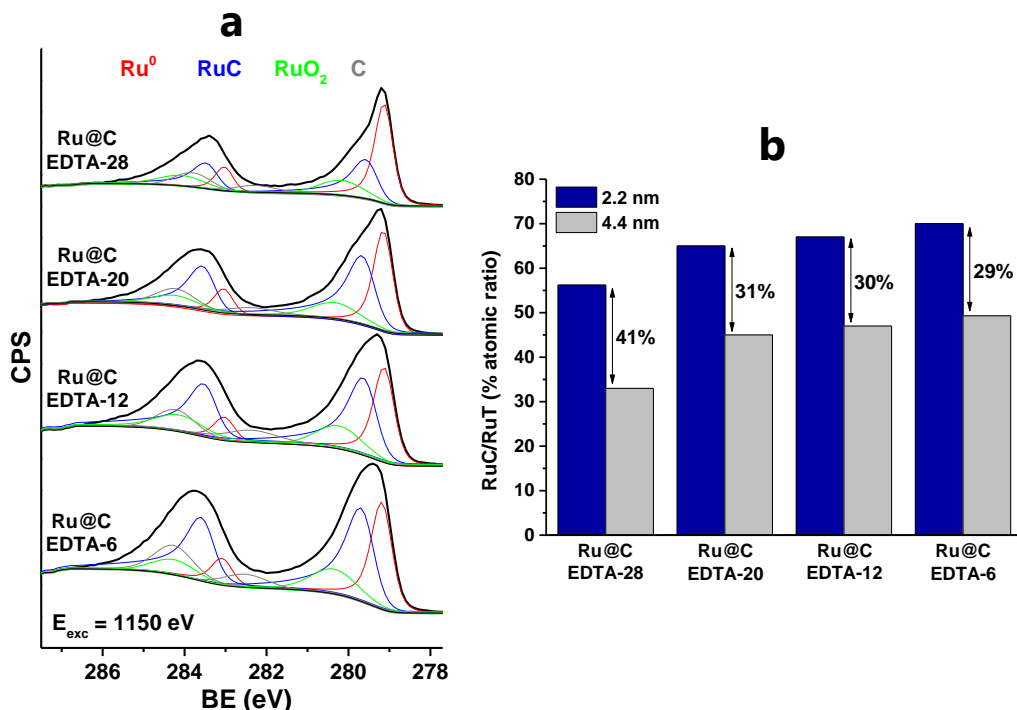


**Figure 5.14** Synchrotron XPS of the C 1s and Ru 3d core levels at  $E_{exc}=1150$  eV (4.4 nm depth) on fresh Ru@C-EDTA samples (a). Surface concentration of ruthenium carbide (RuC) relative to the total ruthenium (RuT) species compared at two sample depths.

## NEXAFS

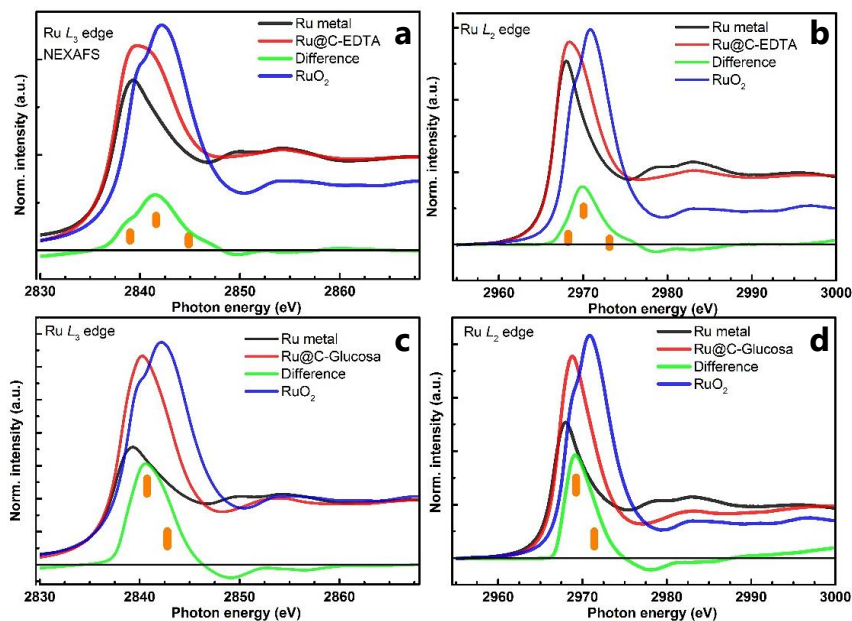


**Figure 5.15** X-ray absorption spectra of Ru@C-EDTA-20, Ru metal, and RuO<sub>2</sub> at L<sub>2</sub>/L<sub>3</sub>-edges (a,b). Spectra of Ru@C-Glucose and Ru references at L<sub>2</sub>/L<sub>3</sub>-edges (c,d). The “difference” spectra is the spectral intensity of Ru metal subtracted from Ru@C samples.

To confirm the oxidation state of Ru@C samples, we could compare their NEXAFS spectra to that of RuO<sub>2</sub> at Ru L<sub>2</sub>/L<sub>3</sub>-edges, subtracting the Ru<sup>0</sup> contribution. Because the white line of Ru metal has lower photon energy position than that of RuO<sub>2</sub>, the method to subtract Ru metal contribution, owing to the core-shell shape (Ru-RuC), is to set the zero intensity around the pre-edge range. In Figure 5.15a,b, the difference spectra (green curve) of Ru@C-EDTA-20 show three features (orange bars). It characterizes the crystal-field splitting of Ru@C-EDTA-20 different from the orbitals hybridization in RuO<sub>2</sub> (blue), respective of the similar L<sub>2</sub>/L<sub>3</sub>-edge observation. In Figure 5.15c,d, the difference spectra of Ru@C-Glucose at Ru L<sub>2</sub>/L<sub>3</sub>-edge behaves the asymmetric shape (orange bar), leading to other orbital splitting condition.

### 5.5.2. Catalytic properties and active site elucidation in the Sabatier reaction.

TPR-H<sub>2</sub>

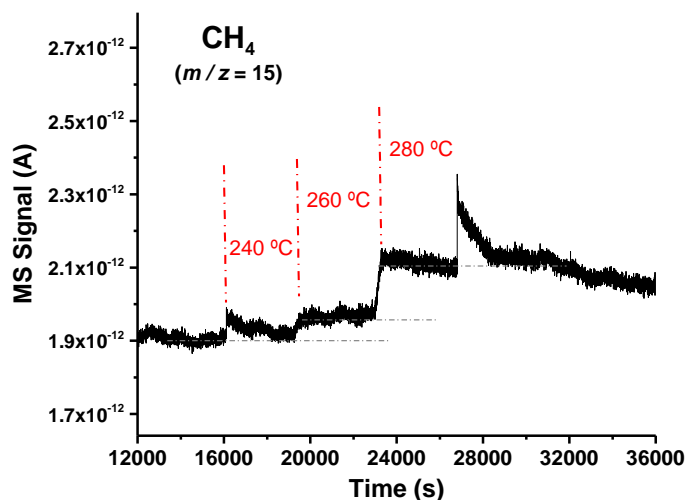


Figure 5.16 TPR-H<sub>2</sub> of Ru@C-EDTA-20 catalyst.

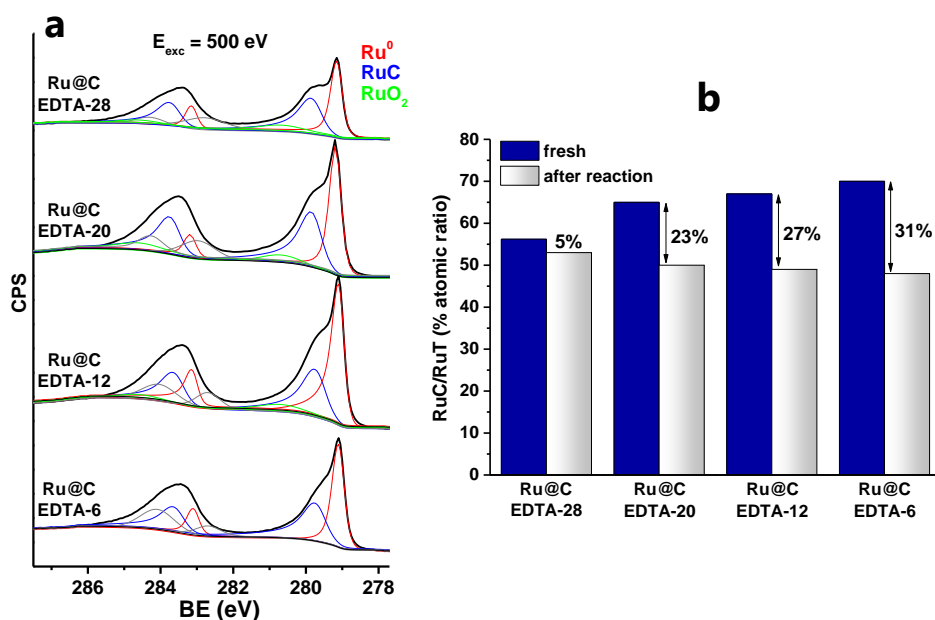
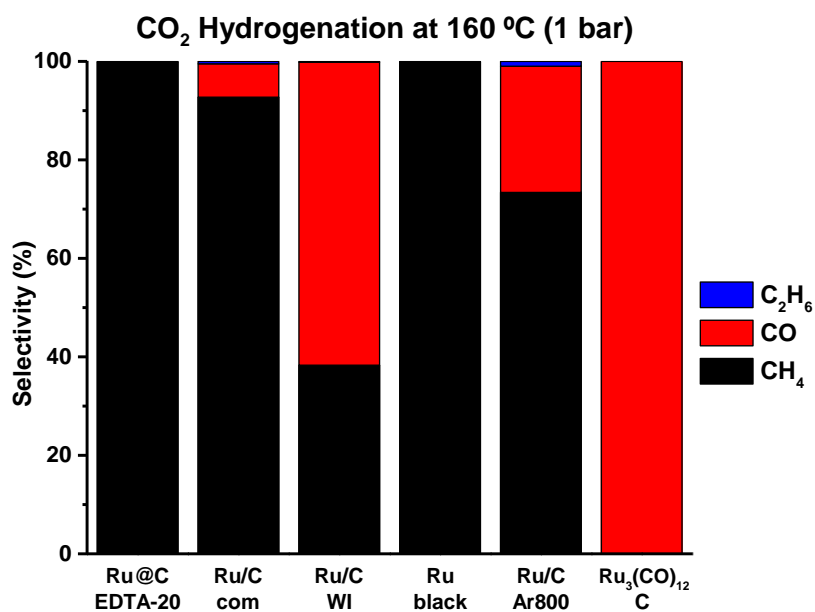


Figure 5.17 Synchrotron XPS of the C 1s and Ru 3d core levels at  $E_{exc}=500$  eV (2.2 nm depth) on the spent Ru@C-EDTA samples (a). Surface concentration of RuC relative to total ruthenium (RuT) species on the fresh catalysts compared to the spent ones (b).



**Figure 5.18** Product selectivity in the CO<sub>2</sub>/H<sub>2</sub> reaction at 160 °C (1 bar, 7.9 mL·g<sub>cat</sub><sup>-1</sup>·s<sup>-1</sup>, Gas mixture: 23.7 % vol CO<sub>2</sub>, 71.3 % vol H<sub>2</sub>, 5.0 % vol N<sub>2</sub>).

**Table 5.4** State of the art of Ru and/or carbon-based catalysts in the CO<sub>2</sub> to CH<sub>4</sub> reaction.

Catalyst	P (bar)	T (°C)	WHSV (mL·g <sub>cat</sub> <sup>-1</sup> ·s <sup>-1</sup> )	STY <sub>CH<sub>4</sub></sub> (μmol·g <sub>cat</sub> <sup>-1</sup> ·s <sup>-1</sup> )	S <sub>CH<sub>4</sub></sub> (%)	TOF (s <sup>-1</sup> )	Ref
β-Mo <sub>2</sub> C	20	200	2.5	0.2	29	-	[13]
Ni/Mo <sub>2</sub> C	20	200	2.5	0.5	42	-	[13]
Ru <sub>3</sub> (CO) <sub>12</sub> /C (5.6 wt % Ru)	1	250	-	4.4	94.7	1.35·10 <sup>-2</sup>	[19]
Ru/TiO <sub>2</sub> -P25 (2.6 wt % Ru)	20	165	1.6	0.9	~100	-	[5]
Ru/TiO <sub>2</sub> -P25 (2.6 wt % Ru)	20	200	1.6	2.6	~100	-	[5]
Ru/TiO <sub>2</sub> (5 wt % Ru)	1	160	20.8	-	-	6.0·10 <sup>-3</sup>	[6]
Ru/TiO <sub>2</sub> (0.8 wt % Ru)	1	160	0.24	-	~100	1.5·10 <sup>-2</sup>	[24]
Ru@C-EDTA-20 (20.2 wt % Ru)	1	160	7.9	3.5	~100	1.4·10 <sup>-1</sup>	Our work
Ru@C-EDTA-20 (20.2 wt % Ru)	1	200	7.9	13.8	~100	5.4·10 <sup>-1</sup>	Our work

**Table 5.5** Catalytic activity of studied samples at concentrated reaction conditions (reactant feed composed of 23.7% CO<sub>2</sub>, 71.3% H<sub>2</sub>, and 5.0% N<sub>2</sub> (% vol), GHSV=21428 h<sup>-1</sup>).

Catalyst	T (°C)	X <sub>CO<sub>2</sub></sub> (%)	STY <sub>CH<sub>4</sub></sub> (μmol·g <sub>cat</sub> <sup>-1</sup> ·s <sup>-1</sup> )	TOF (s <sup>-1</sup> )
Ru@C-EDTA-20	160	4.6	3.5	1.4·10 <sup>-1</sup>
	180	9.8	7.6	2.9·10 <sup>-1</sup>
	200	17.8	13.8	5.4·10 <sup>-1</sup>
Ru@C-Glucose	160	6.0	4.8	8.6·10 <sup>-2</sup>
	180	-	-	-
	200	12.0	9.8	1.8·10 <sup>-1</sup>

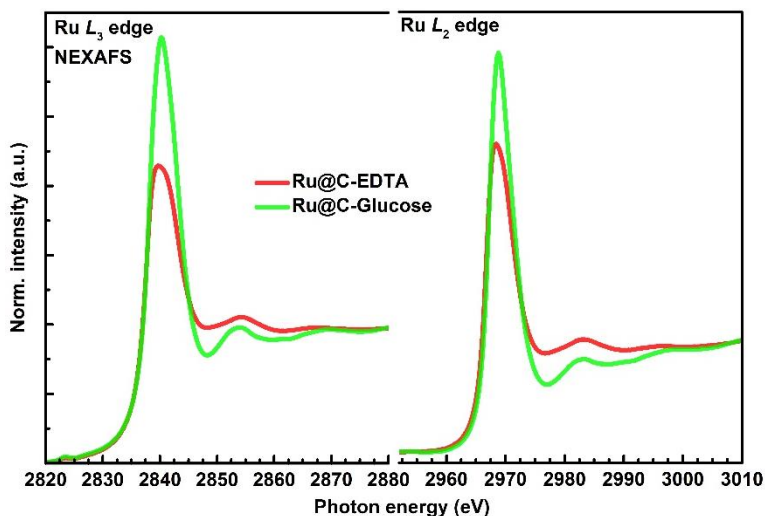


**Figure 5.19** NEXAFS spectra of Ru@C catalysts (EDTA-20 and Glucose) at L<sub>3</sub>, L<sub>2</sub>-edges.

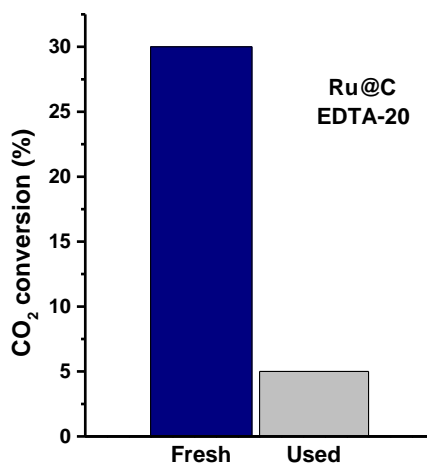


**Figure 5.20** Activity of the as-prepared Ru@C-EDTA-20 sample (fresh), and after being exposed to 280 °C reaction temperature (used) catalyst. Reaction conditions: 180 °C, 5.0% CO<sub>2</sub>, 20.0% H<sub>2</sub>, and 75.0% N<sub>2</sub> (% vol), GHSV of 21428 h<sup>-1</sup>.



**Table 5.6** Catalytic activity of Ru@C-EDTA-20 and Ru/C-com samples on the CO hydrogenation reaction (30.0%, 60.0% and 10.0% (vol %), 1 bar, WHSV=7.9 mL·g<sub>cat</sub><sup>-1</sup>·s<sup>-1</sup>).

Catalyst	T (°C)	X <sub>CO</sub> (%)	CO <sub>2</sub> selectivity (%)						
			CO <sub>2</sub>	CH <sub>4</sub>	C <sub>2</sub> H <sub>6</sub>	C <sub>2</sub> H <sub>4</sub>	C <sub>3</sub> H <sub>8</sub>	C <sub>3</sub> H <sub>6</sub>	Others
Ru@C EDTA-20	180	0.01	27.4	68.3	4.3	-	-	-	-
	200	0.01	24.2	70.8	5.0	-	-	-	-
	220	0.02	27.6	66.9	5.5	-	-	-	-
	240	0.05	26.1	67.5	6.4	-	-	-	-
Ru/C com	160	0.02	79.0	15.5	1.9	0.2	0.8	0.8	1.8
	200	0.05	42.6	42.4	5.1	0.4	2.3	2.2	5.0
	240	0.44	7.3	68.5	8.3	0.7	3.8	3.6	7.8

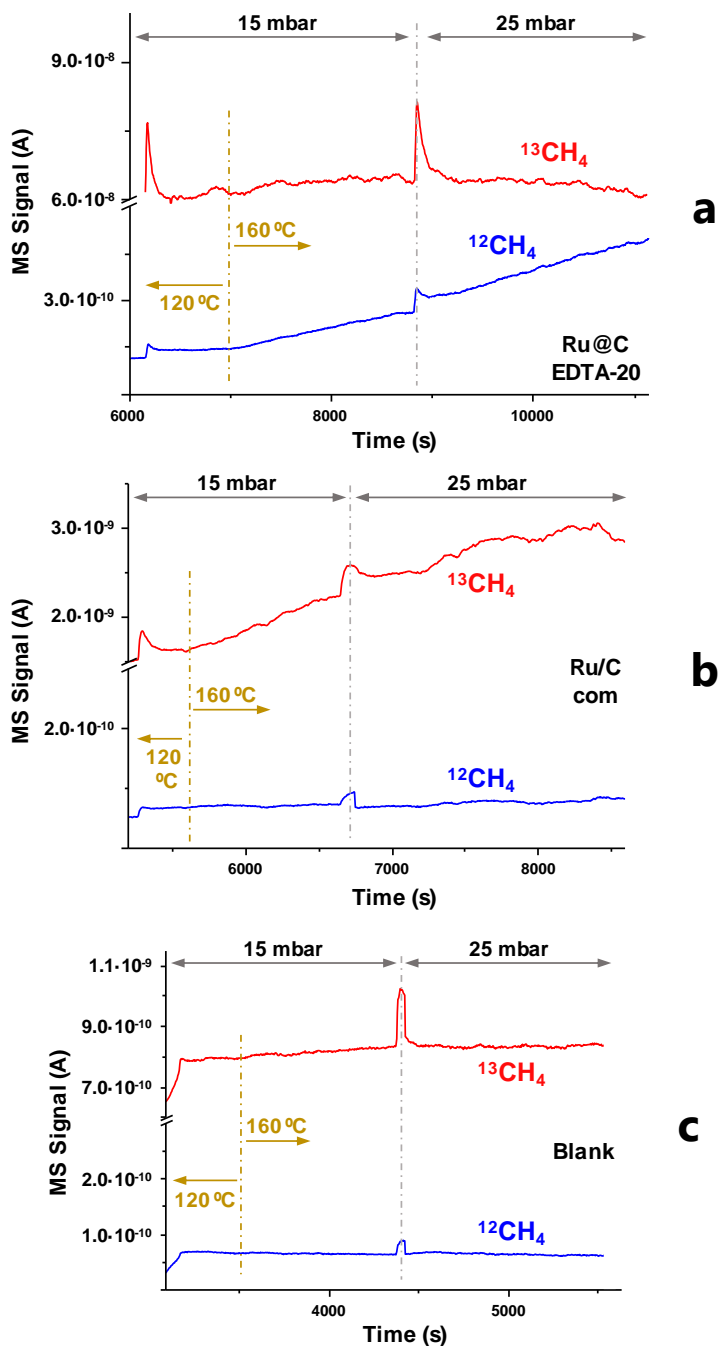


**Figure 5.21** Combined catalytic+MS studies with reactant feed  $^{13}\text{CO}/^{12}\text{CO}_2/\text{H}_2$  on Ru@C-EDTA-20 (a) and Ru/C-com samples (b). Blank experiment (c).

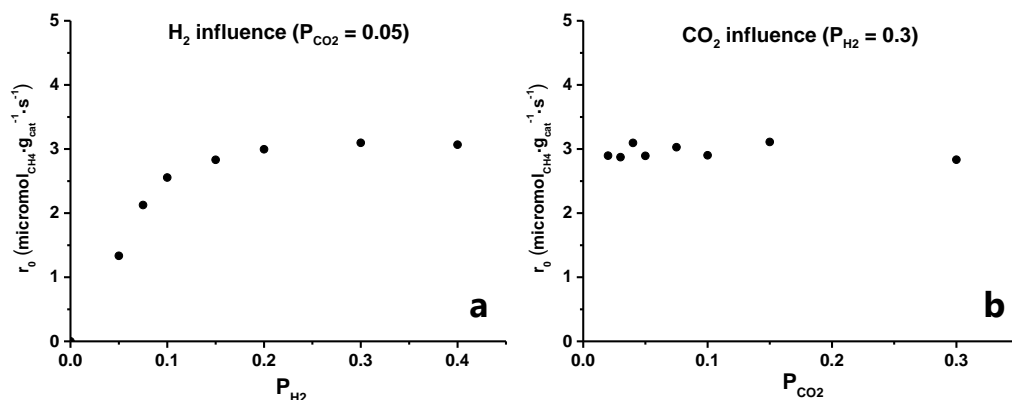


**Figure 5.22** Influence of reactants on the initial reaction rate in the CO<sub>2</sub> hydrogenation to methane. Experiments were carried out at 160 °C. 5 mL·min<sup>-1</sup> CO<sub>2</sub> (constant) varying H<sub>2</sub> proportion (a). 30 mL·min<sup>-1</sup> H<sub>2</sub> (constant) varying CO<sub>2</sub> proportion (b). N<sub>2</sub> was used to balance in both series.

According to Figure 5.22 a dependence between the CH<sub>4</sub> formation and the H<sub>2</sub> partial pressure is observed, while no influence is found for the CO<sub>2</sub> partial pressure. This behavior may indicate that the controlling step of the reaction would be in some way related to the presence of active hydrogen species. Indeed, in most Ru-based catalysts, the hydrogenation of the CO intermediate specie has been considered as rate-determining step in the CO<sub>2</sub> methanation,<sup>[34,36-40]</sup> rather than CO<sub>2</sub> activation.<sup>[41]</sup>

## 5.6. References

- [1] Stangeland, K.; Kalai, D.; Li, H.; Yu, Z. CO<sub>2</sub> Methanation: The Effect of Catalysts and Reaction Conditions. *Energy Procedia* **2017**, *105*, 2022-2027. DOI: 10.1016/j.egypro.2017.03.577.
- [2] Solis-García, A.; Fierro-González, J. C. Mechanistic Insights into the CO<sub>2</sub> Methanation Catalyzed by Supported Metals: A review. *J. Nanosci. Nanotechnol.* **2019**, *19*, 3110-3123. DOI: 10.1166/jnn.2019.16606.
- [3] Panagiotopoulou, P. Hydrogenation of CO<sub>2</sub> over supported noble metal catalysts. *Appl. Catal. A: Gen.* **2017**, *542*, 63-70. DOI: 10.1016/j.apcata.2017.05.026.

- [4] Qin, Z.; Zhou, Y.; Jiang, Y.; Liu, Z.; Ji, H. Recent advances in heterogeneous Catalytic Hydrogenation of CO<sub>2</sub> to methane: Chapter 4. In *New Advances in Hydrogenation Processes-Fundamentals and Applications*; DOI: 10.5772/65407 Intechopen: **2017**; pp 57-82.
- [5] Kim, A.; Sanchez, C.; Patriarche, G.; Ersen, O.; Moldovan, S.; Wisnet, A.; Sassoie, C.; Debecker, D. P. Selective CO<sub>2</sub> methanation on Ru/TiO<sub>2</sub> catalysts: unravelling the decisive role of the TiO<sub>2</sub> support crystal structure. *Catal. Sci. Technol.* **2016**, *6*, 8117-8128. DOI: 10.1039/C6CY01677D.
- [6] Lin, Q.; Liu, X. Y.; Jiang, Y.; Wang, Y.; Huang, Y.; Zhang, T. Crystal phase effects on the structure and performance of ruthenium nanoparticles for CO<sub>2</sub> hydrogenation. *Catal. Sci. Technol.* **2014**, *4*, 2058-2063. DOI: 10.1039/C4CY00030G.
- [7] Lamic, A. F.; Pham, T. L. H.; Potvin, C.; Manoli, J. M.; Mariadassou, G. D. Kinetics of bifunctional isomerization over carbides (Mo, W). *J. Mol. Catal. A: Chem.* **2005**, *237*, 109-114. DOI: 10.1016/j.molcata.2005.03.041.
- [8] Ma, Y.; Guan, G.; Hao, X.; Zuo, Z.; Huang, W.; Phanthong, P.; Kusakabe, K.; Abudula, A. Highly-efficient steam reforming of methanol over copper modified molybdenum carbide. *RSC Adv.* **2014**, *4*, 44175-44184. DOI: 10.1039/C4RA05673F.
- [9] Shi, C.; Zhang, A.; Li, X.; Zhang, S.; Zhu, A.; Ma, Y.; Au, C. Ni-modified Mo<sub>2</sub>C catalysts for methane dry reforming. *Appl. Catal. A: Gen.* **2012**, *431-432*, 164-170. DOI: 10.1016/j.apcata.2012.04.035.
- [10] Christensen, J. M.; Duchstein, L. D. L.; Wagner, J. B.; Jensen, P. A.; Temel, B.; Jensen, A. D. Catalytic Conversion of Syngas into Higher Alcohols over Carbide Catalysts. *Ind. Eng. Chem. Res.* **2012**, *51*, 4161-4172. DOI: 10.1021/ie2018417.
- [11] Liu, C.; Lin, M.; Jiang, D.; Fang, K.; Sun, Y. Preparation of Promoted Molybdenum Carbides Nanowire for CO Hydrogenation. *Catal. Lett.* **2014**, *144*, 567-573. DOI: 10.1007/s10562-013-1163-7.
- [12] Yin, K.; Shou, H.; Ferrari, D.; Jones, C. W.; Davis, R. J. Influence of Cobalt on Rubidium-Promoted Alumina-Supported Molybdenum Carbide Catalysts for Higher Alcohol Synthesis from Syngas. *Top. Catal.* **2013**, *56*, 1740-1751. DOI: 10.1007/s11244-013-0110-6.
- [13] Xu, W.; Ramirez, P. J.; Stacchiola, D.; Rodriguez, J. A. Synthesis of  $\alpha$ -MoC<sub>1-x</sub> and  $\beta$ -MoC<sub>y</sub> Catalysts for CO<sub>2</sub> Hydrogenation by Thermal Carburization of Mo-oxide in Hydrocarbon and Hydrogen Mixtures. *Catal. Lett.* **2014**, *144*, 1418-1424. DOI: 10.1007/s10562-014-1278-5.
- [14] Posada-Pérez, S.; Viñes, F.; Ramirez, P. J.; Vidal, A. B.; Rodriguez, J. A.; Illas, F. The bending machine: CO<sub>2</sub> activation and hydrogenation on  $\delta$ -MoC(001) and  $\beta$ -Mo<sub>2</sub>C(001) surfaces. *Phys. Chem. Chem. Phys.* **2014**, *16*, 14912-14921. DOI: 10.1039/C4CP01943A.
- [15] Rodriguez, J. A.; Evans, J.; Feria, L.; Vidal, A. B.; Liu, P.; Nakamura, K.; Illas, F. CO<sub>2</sub> hydrogenation on Au/TiC, Cu/TiC, and Ni/TiC catalysts: Production of CO, methanol, and methane. *J. Catal.* **2013**, *307*, 162-169. DOI: 10.1016/j.jcat.2013.07.023.

- [16] Xu, W.; Ramírez, P. J.; Stacchiola, D.; Brito, J. L.; Rodriguez, J. A. The carburization of transition metal molybdates (M<sub>x</sub>MoO<sub>4</sub>, M=Cu, Ni or Co) and the generation of highly active metal/carbide catalysts for CO<sub>2</sub> hydrogenation. *Catal. Lett.* **2015**, *145*, 1365-1373. DOI: 10.1007/s10562-015-1540-5.
- [17] Liu, X.; Song, Y.; Geng, W.; Li, H.; Xiao, L.; Wu, W. Cu-Mo<sub>2</sub>C/MCM-41: An Efficient Catalyst for the Selective Synthesis of Methanol from CO<sub>2</sub>. *Catalysts* **2016**, *6*, 75. DOI: 10.3390/catal6050075.
- [18] Nagai, M.; Oshikawa, K.; Kurakami, T.; Miyao, T.; Omi, S. Surface Properties of Carbided Molybdena-Alumina and Its Activity for CO<sub>2</sub> Hydrogenation. *J. Catal.* **1998**, *180*, 14-23. DOI: 10.1006/jcat.1998.2262.
- [19] Moreno-Castilla, C.; Salas-Peregrín, M. A.; López-Garzón, F. J. Hydrogenation of carbon oxides by Ru/activated carbon catalysts obtained from Ru<sub>3</sub>(CO)<sub>12</sub>: effect of pretreatment on their dispersion, composition and activity. *J. Mol. Catal. A: Chem.* **1995**, *95*, 223-233. DOI: 10.1016/1381-1169(94)00023-9.
- [20] Jiménez-Villacorta, F.; Álvarez-Fraga, L.; Bartolomé, J.; Climent-Pascual, E.; Salas-Colera, E.; Aguilar-Pujol, M. X.; Ramírez-Jiménez, R.; Cremades, A.; Prieto, C.; Andrés, A. Nanocrystalline cubic ruthenium carbide formation in the synthesis of graphene on ruthenium ultrathin films. *J. Mater. Chem. C* **2017**, *5*, 10260-10269. DOI: 10.1039/C7TC02855E.
- [21] Zhao, Z.; Meng, C.; Li, P.; Zhu, W.; Wang, Q.; Ma, Y.; Shen, G.; Bai, L.; He, H.; He, D.; Yu, D.; He, J.; Xu, B.; Tian, Y. Carbon coated face-centered cubic Ru-C nanoalloys. *Nanoscale* **2014**, *6*, 10370-10376. DOI: 10.1039/C4NR02632B.
- [22] Sun, W.; Chakraborty, S.; Ahuja, R. Stabilizing a hexagonal Ru<sub>2</sub>C via Lifshitz transition under pressure. *Appl. Phys. Lett.* **2013**, *103*, 251901. DOI: 10.1063/1.4850195.
- [23] Sanjay Kumar, N. R.; Chandra Shekar, N. V.; Chandra, S.; Basu, J.; Divakar, R.; Sahu, P. C. Synthesis of novel Ru<sub>2</sub>C under high pressure-high temperature conditions. *J. Phys.: Condens. Matter* **2012**, *24*, 362202. DOI: 10.1088/0953-8984/24/36/362202.
- [24] Abe, T.; Tanizawa, M.; Watanabe, K.; Taguchi, A. CO<sub>2</sub> methanation property of Ru nanoparticle-loaded TiO<sub>2</sub> prepared by a polygonal barrel-sputtering method. *Energy Environ. Sci.* **2009**, *2*, 315-321. DOI: 10.1039/B817740F.
- [25] Li, D.; Ichikuni, N.; Shimazu, S.; Uematsu, T. Hydrogenation of CO<sub>2</sub> over sprayed Ru/TiO<sub>2</sub> fine particles and strong metal-support interaction. *Appl. Catal. A: Gen.* **1990**, *180*, 227-235. DOI: 10.1016/S0926-860X(98)00335-4.
- [26] Li, Y.; Zhang, L. A.; Qin, Y.; Chu, F.; Kong, Y.; Tao, Y.; Li, Y.; Bu, Y.; Ding, D.; Liu, M. Crystallinity Dependence of Ruthenium Nanocatalyst toward Hydrogen Evolution Reaction. *ACS Catal.* **2018**, *8*, 5714-5720. DOI: 10.1021/acscatal.8b01609.

- [27] Martínez Tejada, L. M.; Muñoz, A.; Centeno, M. A.; Odriozola, J. A. In-situ Raman spectroscopy study of Ru/TiO<sub>2</sub> catalyst in the selective methanation of CO. *J. Raman Spectrosc.* **2016**, *47*, 189-197. DOI: 10.1002/jrs.4774.
- [28] Sadezky, A.; Muckenhuber, H.; Grothe, H.; Niessner, R.; Pöschl, U. Raman microspectroscopy of soot and related carbonaceous materials: Spectral analysis and structural information. *Carbon* **2005**, *43*, 1731-1742. DOI: 10.1016/j.carbon.2005.02.018.
- [29] Tougaard, S. QUASES: Software packages to characterize surface nano-structures by analysis of electron spectra. <http://www.quases.com/products/quases-imfp-tpp2m/>
- [30] Morgan, D. J. Resolving ruthenium: XPS studies of common ruthenium materials. *Surf. Interface Anal.* **2015**, *47*, 1072-1079. DOI: 10.1002/sia.5852.
- [31] Teschner, D.; Borsodi, J.; Woosch, A.; Révay, Z.; Hävecker, M.; Knop-Gericke, A.; Jackson, S. D.; Schlögl, R. The Roles of Subsurface Carbon and Hydrogen in Palladium-Catalyzed Alkyne Hydrogenation. *Science* **2008**, *320*, 86-89. DOI: 10.1126/science.1155200.
- [32] Park, J.; Lee, J. W.; Ye, B. U.; Chun, S. H.; Joo, S. H.; Park, H.; Lee, H.; Jeong, H. Y.; Kim, M. H.; Baik, J. M. Structural Evolution of Chemically-Driven RuO<sub>2</sub> Nanowires and 3-Dimensional Design for Photo-Catalytic Applications. *Sci. Rep.* **2015**, *5*, 11933. DOI: 10.1038/srep11933.
- [33] Liu, J.; Zhang, L. L.; Zhang, J.; Liu, T.; Zhao, X. S. Bimetallic ruthenium-copper nanoparticles embedded in mesoporous carbon as an effective hydrogenation catalyst *Nanoscale* **2013**, *5*, 11044-11050. DOI: 10.1039/C3NR03813K.
- [34] Wang, X.; Hong, Y.; Shi, H.; Szanyi, J. Kinetic modeling and transient DRIFTS-MS studies of CO<sub>2</sub> methanation over Ru/Al<sub>2</sub>O<sub>3</sub> catalysts. *J. Catal.* **2016**, *343*, 185-195. DOI: 10.1016/j.jcat.2016.02.001.
- [35] Hertrich, M. F.; Scharnagl, F. K.; Pews-Davtyan, A.; Kreyenschulte, C. R.; Lund, H.; Bartling, S.; Jackstell, R.; Beller, M. Supported Cobalt Nanoparticles for Hydroformylation Reactions. *Chem. Eur. J.* **2019**, *25*, 5534-5538. DOI: 10.1002/chem.201806282.
- [36] Marwood, M.; Doepper, R.; Renken, A. In-situ surface and gas phase analysis for kinetic studies under transient conditions: The catalytic hydrogenation of CO<sub>2</sub>. *Appl. Catal. A: Gen.* **1997**, *151*, 223-246. DOI: 10.1016/S0926-860X(96)00267-0.
- [37] Panagiotopoulou, P.; Kondarides, D. I.; Verykios, X. E. Mechanistic aspects of the selective methanation of CO over Ru/TiO<sub>2</sub> catalyst. *Catal. Today* **2012**, *181*, 138-147. DOI: 10.1016/j.cattod.2011.05.030.
- [38] Sachtler, J. W. A.; Kool, J. M.; Ponec, V. The role of carbon in methanation by cobalt and ruthenium. *J. Catal.* **1979**, *56*, 284-286. DOI: 10.1016/0021-9517(79)90116-7.

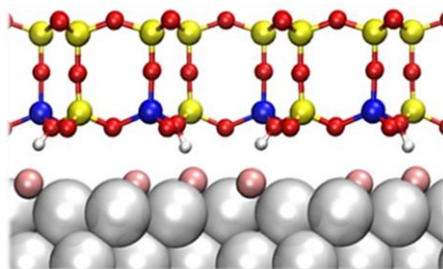
- [39] Panagiotopoulou, P.; Verykios, X. E. Mechanistic Study of the Selective Methanation of CO over Ru/TiO<sub>2</sub> Catalysts: Effect of Metal Crystallite Size on the Nature of Active Surface Species and Reaction Pathways. *J. Phys. Chem. C* **2017**, *121*, 5058-5068. DOI: 10.1021/acs.jpcc.6b12091.
- [40] Zhao, K.; Wang, L.; Calizzi, M.; Moiola, E.; Züttel, A. In Situ Control of the Adsorption Species in CO<sub>2</sub> Hydrogenation: Determination of Intermediates and Byproducts. *J. Phys. Chem. C* **2018**, *122*, 20888-20893. DOI: 10.1021/acs.jpcc.8b06508.
- [41] Eckle, S.; Anfang, H. G.; Behm R. J. Reaction Intermediates and Side Products in the Methanation of CO and CO<sub>2</sub> over Supported Ru Catalysts in H<sub>2</sub>-Rich Reformate Gases. *J. Phys. Chem. C* **2011**, *115*, 1361-1367. DOI: 10.1021/jp108106t.





# CHAPTER 6

## Water formation reaction under interfacial confinement over AlSiO<sub>2</sub>/Ru(0001) model system



The content of this chapter was adapted from the following published work:

**“Water Formation Reaction under Interfacial Confinement: Al<sub>0.25</sub>Si<sub>0.75</sub>O<sub>2</sub> on O-Ru(0001)”**

Cored, J.; Wang, M.; Akter, N.; Darbari, Z.; Xu, Y.; Karagoz, B.; Waluyo, I.; Stacchiola, D.; Head, A. R.; Concepción, P.; Lu, D.; Boscoboinik, J. A.

*Nanomaterials* **2022**, *12*, 183. (Open Access 2022, MDPI)

*Distributed under the “Creative Commons Attribution License BY 4.0”, which permits unrestricted use, distribution and reproduction in any medium.*



## 6.1. Introduction

The effects of nanoscale confinement are common in nature, and their importance is becoming increasingly recognized in different chemical research areas.<sup>[1,2]</sup> Depending on the size and shape of the confined space, the “molecule-host material” or “molecule-molecule” interactions can be altered or even controlled, which can have a fundamental impact in a variety of fields, especially in catalysis.<sup>[3-6]</sup> Some ordered nanoporous materials, such as zeolites or metal-organic frameworks (MOF), have been used to explore confinement effects in heterogeneous catalysis. In addition to the sort of interaction of molecules with the material, the extent of the confinement can affect the activity and the selectivity of a chemical process, introducing steric requirements for substrates participating in the reaction.<sup>[7]</sup> For instance, carbon-derived materials (such as carbon nanotubes, CNTs) have been used to drive reactions with improved formation rates, favoring the activation of stable chemical functionalities, such as C-H bonds.<sup>[8,9]</sup> Moreover, the combination of CNTs with metallic nanoparticles (i.e., copper) has been shown as a good strategy to improve the catalytic performance in the hydrogenation of methyl acetate to methanol and ethanol. In that work, the selectivity to the C<sub>2</sub> alcohol was found to be dependent on the inner diameter of the CNT, being the nano-confinement also responsible for the improved long-term stability of the catalyst.<sup>[10]</sup> On the other hand, zeolitic materials have been applied in a wide variety of industrial processes (Fischer-Tropsch, partial oxidation of aromatic molecules, C-C coupling, etc.) because of their structural versatility and outstanding thermal and chemical stabilities.<sup>[11]</sup>

Another type of architecture that attracted growing attention in past decades is the confined space that appears in weakly bound composites formed by a metal

substrate and a thin film or layered 2D structure. In this sense, the interfacial confinement existing in these materials can also alter the mechanism operating in a particular chemical process.<sup>[12,13]</sup> For example, it is well known that carbonaceous deposits formed during hydrogenation reactions involving carbon-based compounds can poison metallic surfaces, blocking active sites. However, the adequate use of 2D-graphene covering a Pt(111) surface creates a unique confined interface that reduces the activation energy for the CO oxidation reaction by 0.15 eV, compared to a bare platinum surface.<sup>[14]</sup> Furthermore, it is possible to promote the hydrogen evolution reaction (HER) on a nickel surface by depositing graphene. As a consequence, the initial dissociative adsorption of H<sub>2</sub> molecules at the metal/graphene interface is ~0.2 eV weaker compared to the bare Ni. Other side phenomena taking place during HER can be enhanced due to this confinement, such as H<sub>2</sub> spillover, to increase the reaction rate.<sup>[15]</sup>

Additionally, porous thin-film silicates weakly interacting with metallic supports (via van der Waals forces, vdW) have been applied for the same purpose. These materials, considered 2D models (or simplified mimics) of zeolitic structures, consist of a ~0.5 nm thick bilayer SiO<sub>2</sub> scaffold of hexagonal prisms. The parallel -(Si-O-Si)- sheets that form the bilayer are interconnected by oxygen atoms, generating pores of about 5 Å.<sup>[16,17]</sup> Different crystallinities can be obtained depending on the synthetic procedure, including vitreous<sup>[18]</sup> or mixed vitreous-crystalline arrangements.<sup>[19,20]</sup> The structure of these composites can be characterized using surface science tools and theoretical approaches.<sup>[12,21-23]</sup>

Due to the crystalline porous structure of 2D bilayer silica, the permeation of small molecules or atoms (such as CO, O<sub>2</sub>, H<sub>2</sub>, H<sub>2</sub>O, Ar, Au, Pd) through the 2D nano-space is feasible, permitting in this manner the interaction of these adsorbates

with the bilayer or with the metallic surface.<sup>[24-30]</sup> Furthermore, the structural and electric features of these SiO<sub>2</sub>/metal heterojunctions (and subsequently, the nature of the interfacial space that is created) can be tuned by modifying the surface where the silicate is grown (e.g., Pd(111) and (100),<sup>[31,32]</sup> Pt(111),<sup>[33]</sup> and Ru(0001)<sup>[16,21]</sup>). Additionally, it is possible to control the magnitude of the interfacial distance by replacing some of the Si atoms with Al during the synthesis<sup>[34]</sup> or by introducing chemisorbed species into the nano-space,<sup>[35]</sup> inducing electrostatic interactions. Some examples of reactions affected by this confinement, such as CO oxidation<sup>[17]</sup> or furfuryl alcohol evolution to different furan derivatives,<sup>[36]</sup> have been recently published by our group, highlighting the importance of exploring this novel chemistry at a subnanometric scale.<sup>[24]</sup>

The structures that will be the subject of study in Chapter 6 are presented in Figure 6.1. Side views of bilayer silica (Figure 6.1a), bilayer aluminosilicate (6.1b), and hydroxylated bilayer aluminosilicate (6.1c) supported on Ru(0001) are shown, together with the top view of the hydroxylated aluminosilicate bilayer (6.1d). All of them are based on density functional theory (DFT) calculations described in more detail below.

On the other hand, the chemical process selected to carry out this study is the water formation reaction (WFR,  $1/2 \text{O}_2 + \text{H}_2 \rightleftharpoons \text{H}_2\text{O}$ ,  $\Delta H^0 = -285.8 \text{ kJ}\cdot\text{mol}^{-1}$ ). Despite its apparent simplicity, the mechanism of WFR has been the object of investigation because the individual steps involved in the reaction pathway (i.e., dissociative adsorption of H<sub>2</sub> or O<sub>2</sub> molecules onto a metal, or the combination of \*H and \*O to yield the hydroxyl intermediate) are common to very diverse catalytic transformations. For instance, the oxidation of fuel molecules (H<sub>2</sub>) is a key electrochemical process that takes place in solid oxide fuel cells (SOFC).<sup>[37]</sup>

Some of the aforementioned steps also occur in hydrogen or oxygen evolution reactions (HER and OER, respectively).<sup>[38]</sup> Therefore, significant efforts have been made to understand the fundamentals of this process, in order to discover new active centers that compete with platinum-based materials.<sup>[39]</sup>

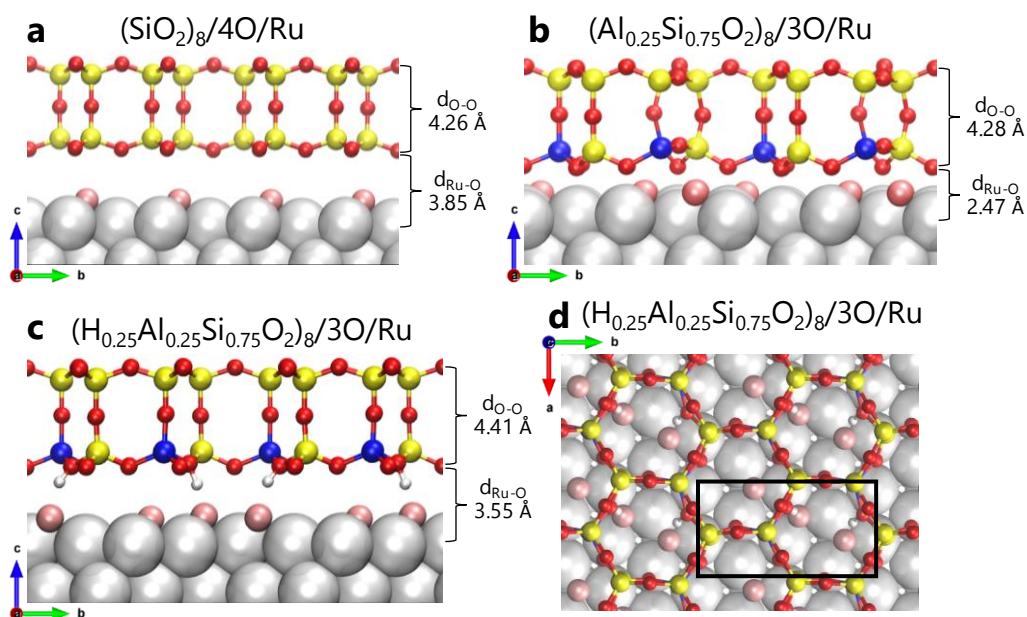


**Figure 6.1** Atomic structures of (SiO<sub>2</sub>)<sub>8</sub>/4O/Ru (a) and (Al<sub>0.25</sub>Si<sub>0.75</sub>O<sub>2</sub>)<sub>8</sub>/3O/Ru(0001) (b). Side (c) and top (d) views of the bilayer aluminosilicate film growth on Ru(0001) with two H<sup>+</sup> bound to the bridging O in (Al-O)-Si to compensate the framework charge [i.e., (H<sub>0.25</sub>Al<sub>0.25</sub>Si<sub>0.75</sub>O<sub>2</sub>)<sub>8</sub>/3O/Ru(0001)]. The black rectangle on the top view (panel d) indicates the unit cell. Color code: Ru (silver), Si (yellow), Al (blue), H (white), O in aluminosilicate (red), and O chemisorbed on Ru (pink).

In fact, the WFR has been studied on the Pt(111) surface over a wide temperature range: i.e., below 150 K<sup>[40-42]</sup> and 250-450 K.<sup>[43-45]</sup> Based on DFT studies,<sup>[46]</sup> combined with high-resolution electron energy loss spectroscopy (HREELS) and scanning tunneling microscope (STM) experiments,<sup>[47]</sup> Figure 6.2 shows the dual-path mechanism suggested for the WFR on Pt(111) substrate.

The WFR mechanism starts with the H<sub>2</sub> molecule adsorption and dissociation onto the metallic surface (TS1). Afterward, the rate-limiting step, i.e., hydroxyl group formation, occurs. As marked in Figure 6.2, \*OH intermediate formation can be produced via two alternative pathways: (a) a direct hydrogen addition (\*H + \*O ⇌ \*OH; TS2, blue line) or (b) a disproportionation pathway (\*H<sub>2</sub>O + \*O ⇌ 2 \*OH; TS2', red arrow).<sup>[47]</sup> In the latter option, a \*H<sub>2</sub>O molecule that has already been synthesized combines with a chemisorbed oxygen to form two \*OH. The “activation” of one or the other pathway depends on both the reaction temperature and the desorption temperature of water on the material. For Pt(111), this temperature is found around 150 K. Then, below that point, the disproportionation pathway (TS2') dominates, with a low activation energy of ~0.33 eV.<sup>[46]</sup> However, above the water desorption temperature, \*OH formation occurs via direct H addition (TS2), exhibiting higher activation energy (~1 eV).<sup>[46]</sup>

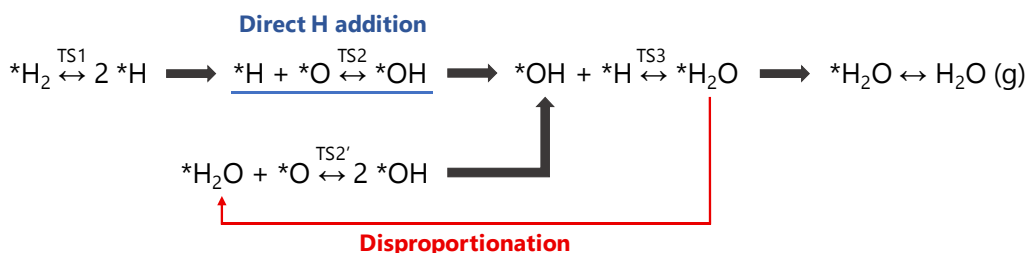


**Figure 6.2** Dual-path reaction mechanism of water formation reaction (WFR) reported on the Pt(111) surface. (\*) indicates the species adsorbed on the platinum surface.

Besides platinum, ruthenium (Ru(0001)) can also catalyze the WFR.<sup>[48,49]</sup> Hence, since bilayer silicates and aluminosilicates are well studied on Ru(0001), this architecture lends itself as an ideal model to study the effect of interfacial confinement in the reactivity of this surface. In this system, O<sub>2</sub> molecules can permeate through the silicate and chemisorb dissociatively on the Ru(0001)

surface. There, \*O can be reduced by H<sub>2</sub> under mild conditions to generate water, which finally desorbs from the interface as a product.<sup>[34,35,50,51]</sup> In prior work by our group (using (NAP)-XPS) and by Prieto et al. (using LEEM), the WFR was studied under confinement at the BL-silica/Ru(0001), reporting a comparable decrease of the apparent activation energy ( $E_{a,app}$ ) by 0.38 eV and 0.32 eV, respectively, with respect to the Ru(0001) case.<sup>[52,53]</sup> Moreover, temperature-programmed desorption (TPD) experiments and HREELS characterization demonstrated that the dual-path WFR mechanism proposed for Pt(111) in Figure 6.2 also operates on bare Ru(0001).<sup>[48,49]</sup> Finally, a detailed study of the kinetic aspects of confinement aiming at understanding the distribution of species across the reaction fronts and the differences in the  $E_{a,app}$  have been recently reported by Prieto et al.<sup>[54]</sup> In that work, carried out at 540 K and low H<sub>2</sub> pressure ( $\sim 10^{-7}$  Torr) on a crystalline BL-SiO<sub>2</sub>/Ru(0001) sample, they reported that the H-adsorption step is strongly affected by the presence of the silica bilayer, influencing the propagation of the reaction cascade.

In the present study, synchrotron-based near ambient pressure X-ray photoelectron spectroscopy was used to determine the  $E_{a,app}$  of the WFR through the reduction of chemisorbed oxygen at elevated H<sub>2</sub> pressures on the BL-aluminosilicate/Ru(0001) interface. The reaction order with respect to H<sub>2</sub> was also determined experimentally. Moreover, DFT was used to examine the WFR at this confined interface, considering both discussed reaction pathways to produce the \*OH intermediate, namely: the direct hydrogenation (TS2) and the disproportionation (TS2'). The energy profiles for both alternatives were compared to understand the effect of doping the silicate with Al in the WFR under confinement.



## 6.2. Materials and methods

### 6.2.1. Material synthesis

The Ru(0001) single crystal surface was cleaned with several cycles of Ar<sup>+</sup> sputtering and annealing at 1200 K (e-beam heating). The temperature was measured by a K-type thermocouple attached to the side of the sample. The surface was then exposed to  $3 \cdot 10^{-6}$  Torr O<sub>2</sub> at 1200 K in order to form a (2×2)-3O/Ru(0001) surface. The aluminosilicate bilayer film was grown on the (2×2)-3O/Ru(0001) surface as described in detail elsewhere.<sup>[21]</sup> Briefly, Si and Al were thermally evaporated onto the (2×2)-3O/Ru(0001) surface at room temperature under  $2 \cdot 10^{-7}$  Torr O<sub>2</sub>, followed by oxidation at 1200 K in  $3 \cdot 10^{-6}$  Torr O<sub>2</sub> for 10 min. Then, the temperature was decreased to 300 K, keeping the O<sub>2</sub> pressure constant. The bilayer nature of the aluminosilicate was verified using infrared reflection absorption spectroscopy (IRRAS). The IRRAS system is home-built, using a Bruker Vertex 80 V spectrometer. After synthesis, the sample was transported through air to the near ambient pressure XPS system (NAP)-XPS at the 23-ID-2 (IOS) beamline of the National Synchrotron Light Source II (NSLS-II, Upton, New York, USA). To clean the surface from airborne carbonaceous contamination, the surface was firstly annealed to 700 K in  $5 \cdot 10^{-2}$  Torr O<sub>2</sub>, followed by annealing to 373 K in 1.0 Torr of H<sub>2</sub>. The sample cleaning procedure was monitored in situ by (NAP)-XPS. The annealing in H<sub>2</sub> was performed to remove the chemisorbed oxygen formed during the previous step.<sup>[50]</sup>

### 6.2.2. Water formation reaction procedure

Catalytic experiments were performed at the beamline 23-ID-2 (IOS, APPES branch) of NSLS-II. IOS beamline offers ultrabright X-rays ranging from 250 to 2000 eV, delivered by a pair of identical elliptical polarized undulators (EPU49),

with a variable line spacing plane grating monochromator (VLS-PGM). Data acquisition was performed using a PHOIBOS 150NAP electron energy analyzer with a 1D-DLD detector (SPECS GmbH). The spectra were acquired with a pass energy of 10 eV and a step of 0.05 eV. The X-ray spot size was 80×20 (H×V) μm<sup>2</sup>. Incident photon energy of 650 eV was used to acquire alternatively the Si 2p and O 1s core levels during catalysis. Two type of experiments were carried out in the analysis chamber: WFR at constant pressure (0.1 Torr) and variable temperature (380, 400, 420 and 450 K); and WFR at fixed temperature (420 K) and variable pressure (0.1, 0.2, and 0.5 Torr). Binding energies (BE) were calibrated with respect to C 1s signal settled at 284.5 eV. CASA XPS software was used to analyze the data. Shirley-type background and Gaussian/Lorentzian-type curves were used in the spectra fitting.

### 6.2.3. Computational methods

DFT calculations were performed using the projector augmented wave method implemented in the Vienna Ab initio simulation package (VASP).<sup>[55,56]</sup> The non-local vdW interactions were described by the optB86b-vdW functional.<sup>[57-59]</sup> The system consists of the BL-aluminosilicate film adsorbed on Ru(0001) in a 5.392 Å × 9.339 Å × 27 Å super cell, which includes five layers of Ru atoms in the slab model, the bilayer aluminosilicate, and O atoms adsorbed at the BL/Ru surface. A kinetic energy cutoff of 800 eV was used and the Brillouin zone was sampled with an 8×4×1 mesh. The reaction pathways and energy barriers were calculated using the climbing image nudged elastic band method (CI-NEB)<sup>[60]</sup> implemented in VASP. The BL-aluminosilicate, chemisorbed O atoms, and top two layers of Ru atoms were allowed to relax until forces were smaller than 0.02 eV/Å in the structural optimization and smaller than 0.05 eV/Å in the CI-NEB calculations.

## 6.3. Results and discussion

### 6.3.1. Kinetic study of the water formation reaction at constant pressure (0.1

#### Torr H<sub>2</sub>) by (NAP)-XPS

For all the experiments shown in this work, the starting coverage of chemisorbed oxygen (\*O) is estimated to be 0.375 ML, based on the O 1s peak area ratio between chemisorbed oxygen (\*O) and the framework oxygen of the BL-aluminosilicate. The initial coverage was obtained by annealing the sample in oxygen atmosphere ( $3 \cdot 10^{-6}$  Torr) at 823 K for 30 min. The WFR was first studied in situ by (NAP)-XPS at a H<sub>2</sub> pressure of 0.1 Torr by acquiring alternatively the Si 2p and the O 1s core level spectra as a function of time to follow the \*O consumption evolution. This was done at four different temperatures: 380, 400, 420, and 450 K. Figure 6.3a,b show respectively the XPS Si 2p and O 1s core level spectra before (black line) and after (blue line) the WFR at the 2D-aluminosilicate/Ru(0001) interface at 450 K. In prior work, for the all-Si silica bilayer, the consumption of O 1s component corresponding to chemisorbed O was used to quantitatively follow the progress of the water formation reaction. In the current paper, the presence of Al in the framework complicated the reliable use of this method, given the additional component of framework oxygen bridging between Si and Al, and the fact that this O atom can also be in the hydroxylated (Figure 6.1c) and non-hydroxylated (Figure 6.1b) forms. The complexity of deconvoluting these components is shown in Figure 6.3c, where four peaks are used to deconvolute the O 1s region before the start of the reaction, at 450 K. This region can be deconvoluted into four peaks located at 533.5, 531.9, 531.3, and 530.0 eV, corresponding to O atoms in OH-Al<sup>3+</sup> groups, Si-O-Si and Si-O-Al environments, and O chemisorbed on the Ru(0001) surface (\*O), respectively. Given this, and the

fact that four components can easily fit an elephant, we have chosen to use the shift of the Si 2p spectrum as a measure of the reaction progress. Note that in prior work,<sup>[52]</sup> it has already been determined that the magnitude of the blueshift of Si 2p is proportional to the consumption of chemisorbed O, as the Ru-O dipoles are removed during the reaction. Figure 6.9 in Section 6.5 shows the plot of Si 2p shift vs. change in coverage that is used for reference.

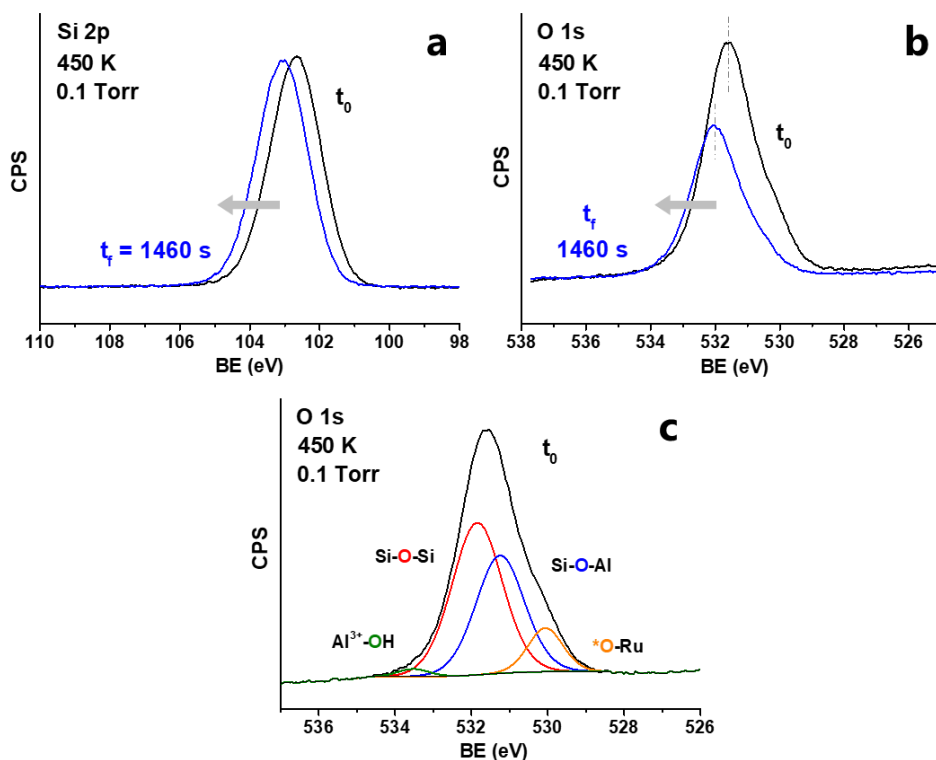


**Figure 6.3** Si 2p (a) and O 1s (b) core level spectra before and after reaction at 450 K in 0.1 Torr of H<sub>2</sub>. Deconvolution of the O 1s core level spectrum before reaction (c).

Figure 6.4 shows the shifts of Si 2p and O 1s (Si-O-Si and Si-O-Al) core levels (left axis, solid symbols) as a function of time at 450 K and 0.1 Torr of H<sub>2</sub>. The open circles (right axis) show the corresponding coverage of chemisorbed oxygen. As

it was for the all-SiO<sub>2</sub> bilayer, there is an induction period before the reaction starts taking place. Additionally, as the temperature stabilizes at the beginning of the reaction, the current in the filament that heats up the sample takes a few minutes to stabilize. As the filament current is changing in this brief period, there are changes in the induced electric field, resulting in artifacts in the peak position. For this reason, we have chosen to discard these initial data points, and the plot starts at 400 s. The full plot for all temperatures is included in Figure 6.10 (see Section 6.5).

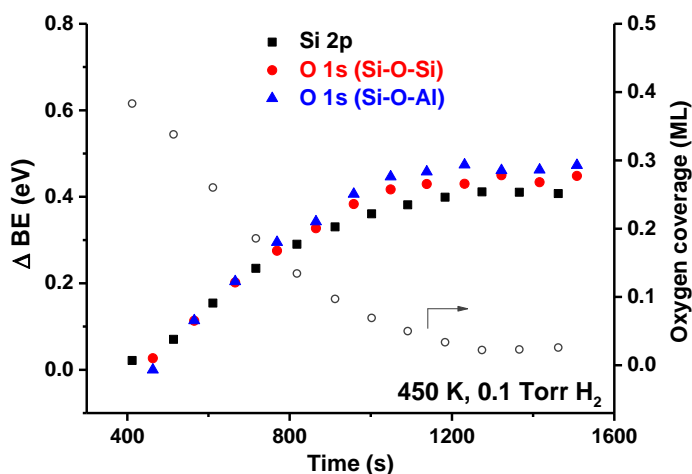


**Figure 6.4** Core level shifts (solid symbols) for Si 2p and O 1s (Si-O-Si and Si-O-Al components) as a function of time at 450 K in 0.1 Torr of H<sub>2</sub>. The coverage of chemisorbed O (open circles) is also shown for comparison.

In Figure 6.5a, we plot the linear part of the coverage (after the induction period) vs. time, in order to obtain the initial rate of reaction at four different temperatures, namely 380, 400, 420, and 450 K. This temperature range was chosen so that obtained rates of consumption of chemisorbed oxygen could be tracked by near ambient pressure XPS considering the constraints of our time resolution. This rate was then used to obtain the Arrhenius plot shown in Figure

6.5b (blue triangles). An apparent activation energy of 55 kJ·mol<sup>-1</sup> was obtained. This was much higher than the case of the all-Si bilayer, but lower than the case of bare Ru. The Arrhenius plots for these cases (reproduced from reference [52]) are also included in Figure 6.5b for comparison.

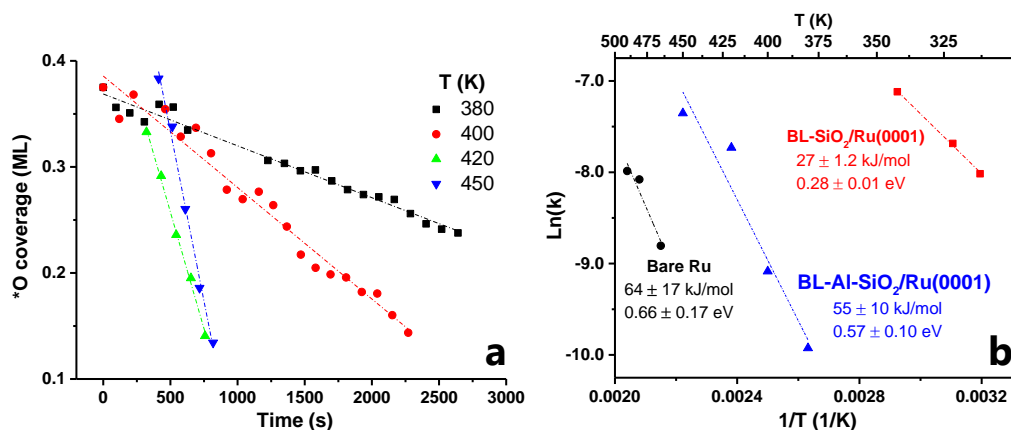


**Figure 6.5** Plot of \*O coverage vs. time at 380, 400, 420, and 450 K (a). Arrhenius plots for WFR at the BL-aluminosilicate/Ru(0001) interface (this work, blue triangles), compared to similar prior work on bare Ru(0001) (black circles) and BL-SiO<sub>2</sub>/Ru(0001) (b).

### 6.3.2. DFT calculations

DFT calculations revealed that the rate-limiting step of the WFR is the formation of \*OH on the Ru(0001) surface via the first hydrogen addition step ( $*\text{H} + *\text{O} \rightleftharpoons *\text{OH}$ ).<sup>[46,52]</sup> Bilayer silica films (Figure 6.1a) create a large desorption barrier that trap water molecules at the interface ( $d_{\text{Ru-O}} = 3.85 \text{ \AA}$ ) and activate an alternative disproportionation reaction pathway ( $*\text{H}_2\text{O} + *\text{O} \rightleftharpoons 2 *\text{OH}$ ; TS2' in Figure 6.2) to form \*OH groups, with a barrier of 0.25 eV lower than the first hydrogen addition step.<sup>[52]</sup> The structure of aluminosilicate film is similar to that of the bilayer silica film, and thus it is expected to also trap water molecules at the interface. Here,

we perform DFT calculations to study both reaction pathways to determine the energy barriers for WFR at the aluminosilicate/Ru interface.

Figure 6.1b shows the super cell of the bilayer aluminosilicate/3O/Ru(0001) system including two aluminosilicate nano-cages, eight surface Ru atoms, and three O atoms adsorbed on the Ru surface. The O coverage corresponds to 0.375 monolayers (ML) in the experiment. The Al concentration in the BL-aluminosilicate is 25%: two Al atoms are included in a unit cell  $[(\text{Al}_{0.25}\text{Si}_{0.75}\text{O}_2)_8]$ . The substitution of Si with Al results in an  $[\text{AlO}_4]^-$  center that attracts an extra electron to saturate one O to form four Al-O bonds. The negative charge on  $[\text{AlO}_4]^-$  is locally compensated by a proton or another cation. Our previous studies have shown that this charge compensation can also be supplied by the Ru substrate.<sup>[34]</sup> Upon H<sub>2</sub> adsorption, we found that the adsorption energy of two H atoms is much larger in magnitude at the bottom layer of the BL-aluminosilicate than on the Ru surface, indicating that charge compensation from the H atoms is more stable than the Ru substrate. Therefore, our studies on the water formation reaction (WFR) start from a new substrate  $[(\text{Al}_{0.25}\text{Si}_{0.75}\text{O}_2)_8-2\text{H}/3\text{O}/\text{Ru}]$  (Figure 6.1c,d) where two H atoms are bonded to two O atoms in the bottom layer of the BL-aluminosilicate. Due to the adsorption of H, the interface space ( $d_{\text{Ru-O}} = 3.55 \text{ \AA}$ ) is much larger than the aluminosilicate/3O/Ru system ( $d_{\text{Ru-O}} = 2.47 \text{ \AA}$  in Figure 6.1b). Figure 6.6a shows the reaction pathway for first hydrogen addition reaction ( $*\text{H} + *\text{O} \rightleftharpoons *\text{OH}$ ), where a  $*\text{H}$  atom migrates to bond to an  $*\text{O}$  atom on Ru. The activation energy is 1.12 eV, which is close to the bare Ru and silica/Ru interface.<sup>[52]</sup> The water molecules formed from the initial first hydrogen addition reaction can be stabilized by the BL-aluminosilicate film, which activates the disproportionation pathway.

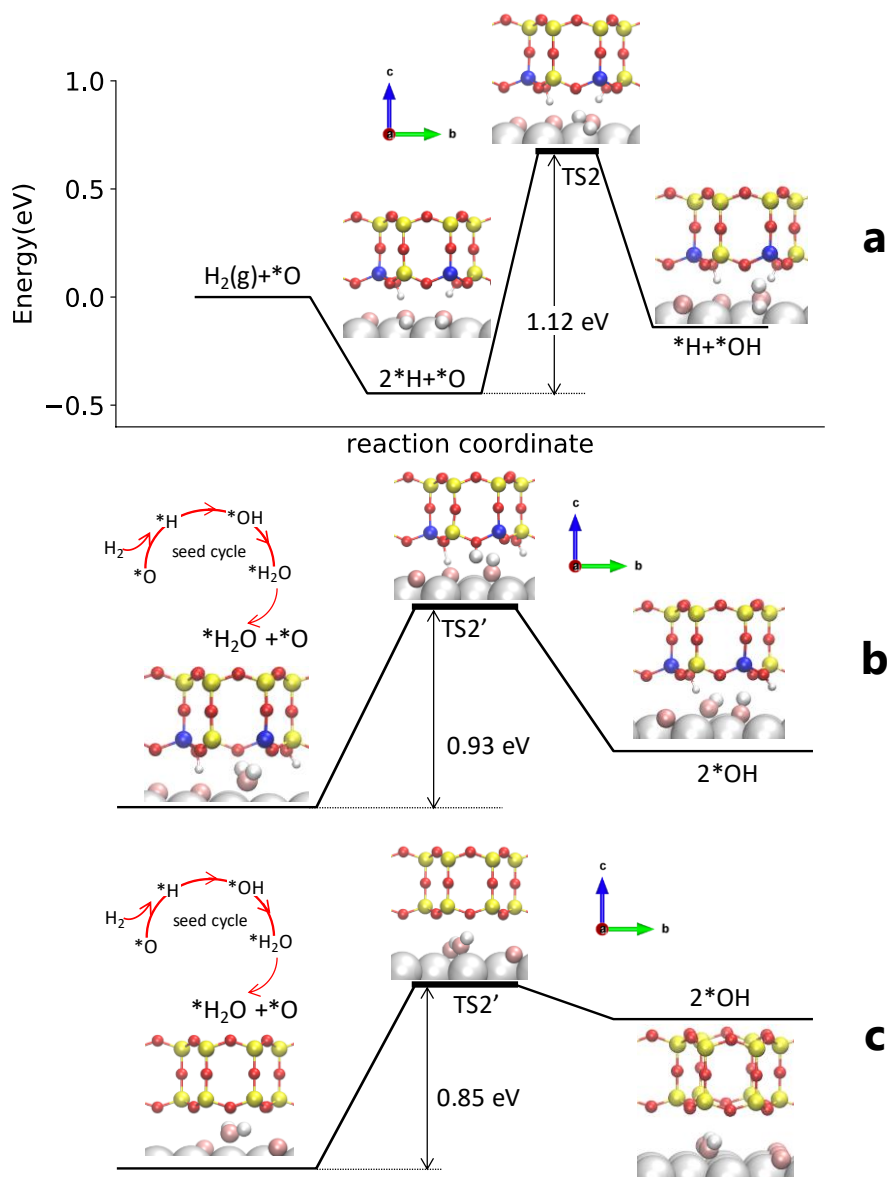


**Figure 6.6** Potential energy diagram for the WFR at the BL-AlSiO<sub>2</sub>/Ru(0001) interface via first hydrogen addition step ( $*\text{H} + *\text{O} \rightleftharpoons *\text{OH}$ , TS2) (a) and disproportionation pathway ( $*\text{H}_2\text{O} + *\text{O} \rightleftharpoons 2*\text{OH}$ , TS2') (b). Potential energy diagram for the disproportionation pathway (TS2') at the silica/Ru(0001) interface (c). Color code: Ru (silver), Si (yellow), Al (blue), H adsorbed on BL-AlSiO<sub>2</sub> (small white), O in BL-AlSiO<sub>2</sub> (red),  $*\text{O}$  chemisorbed on Ru (pink), and  $*\text{H}$  adsorbed at the BL-AlSiO<sub>2</sub>/Ru(0001) interface that react with  $*\text{O}$  (large white).



The initial state of the disproportionation pathway involves a water molecule adsorbed at the interface. Figure 6.6b shows that one of the \*H atoms of \*H<sub>2</sub>O migrates to combine with a nearby \*O atom (\*H<sub>2</sub>O + \*O ⇌ 2 \*OH) with an activation energy of 0.93 eV, which is lower than the hydrogen addition reaction.

To compare with the disproportionation reaction at the silica/Ru interface, we also show this pathway in Figure 6.6c. The activation energy of \*H<sub>2</sub>O + \*O ⇌ 2 \*OH at the aluminosilicate/Ru interface (0.93 eV) is slightly higher than the silica/Ru interface (0.85 eV in Figure 6.6c).<sup>[52]</sup> Moreover, the disproportionation reaction at the silica/Ru interface only involves \*H and \*O atoms migrating on Ru. In the aluminosilicate case, one \*H atom dissociates from the water molecule, and its migration to the nearby \*O atom, is facilitated by a framework O atom bridging between Si and Al, as seen in the transition state in Figure 6.6b.

### 6.3.3. Reaction order with respect to H<sub>2</sub>

Another interesting feature to analyze in the WFR under interfacial confinement is the impact of H<sub>2</sub> pressure during the catalytic process. In Subsection 6.3.1., 0.1 Torr H<sub>2</sub> was set at a constant pressure, and the temperature was varied from 380 to 450 K. In this second set of experiments, the pre-activation of the sample was identical (3·10<sup>-6</sup> Torr O<sub>2</sub> at 823 K, 30 min). The initial O coverages were also 0.375 ML. Based on the results obtained at variable temperature, 420 K was chosen to carry out the experiments, and three H<sub>2</sub> pressures were used, namely: 0.1, 0.2, and 0.5 Torr. Figure 6.7 shows the θ<sub>\*O</sub> evolution for these three pressures. For 0.1 Torr H<sub>2</sub>, the endpoint of the reaction is reached in ~27 min (~1600 s). Increasing the pressure increases the reaction rate, reaching the final coverage at approximately 17 min (~1050 s) at 0.2 Torr and 12 min (~750 s) at 0.5 Torr H<sub>2</sub>.

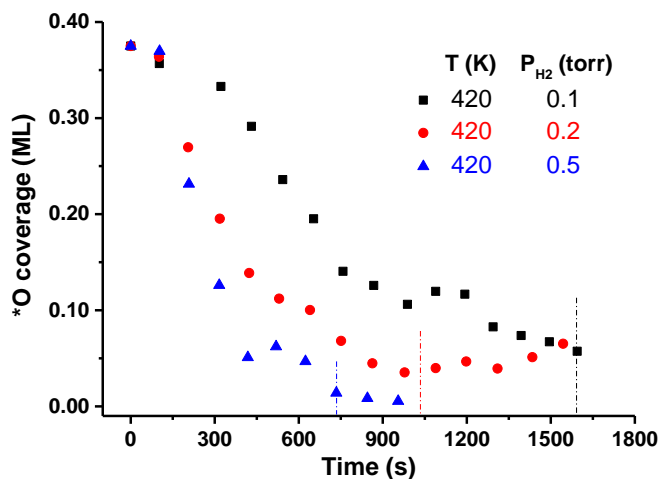


**Figure 6.7** WFR reaction evolution at 420 K and variable pressure conditions (0.1-0.5 Torr  $H_2$ ). Vertical lines indicate the endpoint of the reaction at each working pressure.

Examining the initial catalytic evolution, we observe that  $\theta_{*O}$  decreases linearly with time at all pressure ranges after the induction period. This linear region is shown in Figure 6.8a.

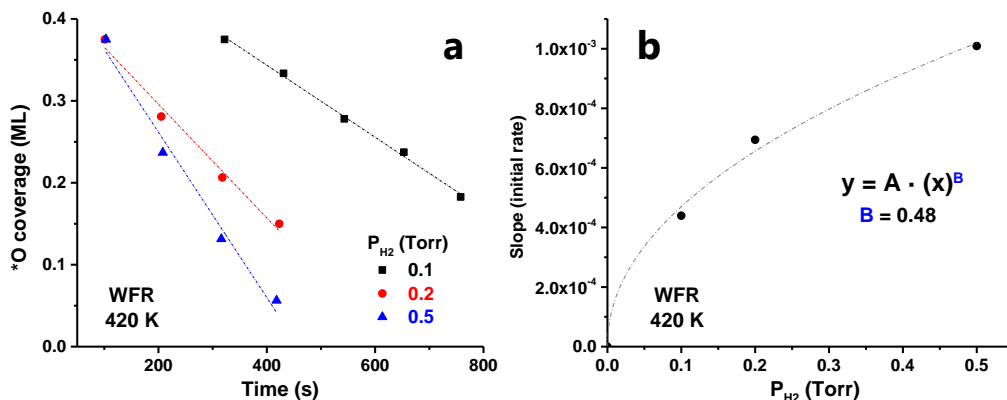


**Figure 6.8** Initial WFR reaction evolution at different temperatures (380-450 K) at 0.1 torr  $H_2$  (a) and dependence between the initial rate and the  $H_2$  pressure (b).

Then, the kinetic constant ( $k$ ) can be calculated by assuming a zero-order kinetics with respect to  $\theta_{*O}$ , as done in Subsection 6.3.1. By plotting the value of the kinetic

constant ( $k$ ) vs. H<sub>2</sub> pressure, an exponential fitting can be proposed, obtaining a reaction order of  $\sim 0.5$  with respect to H<sub>2</sub> (Figure 6.8b). Note that this reaction order of 0.5 is based on only three data points and, while it provided a reasonable approximation, further experiments would be needed to obtain a more accurate value.

#### 6.4. Conclusions

In this chapter, we studied the water formation reaction at the confined interface between an aluminosilicate bilayer and Ru(0001) surface (i.e., Al<sub>0.25</sub>Si<sub>0.75</sub>O<sub>2</sub>/Ru(0001)). The system can be thought of as a nano-reactor. The reaction kinetics were followed by synchrotron-based near ambient pressure XPS, complemented by DFT calculations.

First, a catalytic study on the model system at constant H<sub>2</sub> pressure (0.1 Torr) and at variable temperature (380-450 K) was performed. In all cases, the initial \*O coverage was 0.375 ML. The temporal evolution of chemisorbed oxygen on the Ru(0001) surface during the reaction was monitored by (NAP)-XPS at each temperature. These data were used to obtain rate constants from the initial reaction rates to produce an Arrhenius plot. An apparent activation energy of 55 kJ·mol<sup>-1</sup> was determined. This value is similar to that obtained for the bare Ru (64 kJ·mol<sup>-1</sup>) and surprisingly higher than the  $E_{a,app}$  value recently reported by our group in the pure BL-SiO<sub>2</sub>/Ru(0001) (i.e., 27 kJ·mol<sup>-1</sup>).

The presence of aluminum in the doped-bilayer introduces negative charges in the framework that are likely compensated by a proton bound to a bridging O (Si-O-Al). Therefore, the substrate used to carry out the theoretical calculations was [(H<sub>0.25</sub>Al<sub>0.25</sub>Si<sub>0.75</sub>O<sub>2</sub>)<sub>8</sub>/3O/Ru], exhibiting a slightly smaller interfacial space

( $d_{\text{Ru-O}} = 3.55 \text{ \AA}$ ) than its pure silicate ( $d_{\text{Ru-O}} = 3.85 \text{ \AA}$ ) counterpart. While the confinement at such an interface favors the disproportionation pathway, as was the case for bilayer silica (at the conditions used in our work), the activation energy for the hydrogen is higher than in the pure silica (0.93 eV for the BL-AlSiO<sub>2</sub> vs. 0.85 eV for the BL-SiO<sub>2</sub>). This agrees with the experimentally obtained apparent activation energy lower than that of bare Ru(0001) but higher than that of bilayer silica.

Finally, the impact of H<sub>2</sub> pressure in the water formation reaction was evaluated. The (H<sub>0.25</sub>Al<sub>0.25</sub>Si<sub>0.75</sub>O<sub>2</sub>)<sub>8</sub>/3O/Ru was kept at a temperature of 420 K, while the kinetic experiment was run at different pressures. This allowed us to determine a reaction order with respect to H<sub>2</sub> of 0.5.

## 6.5. Supporting Information

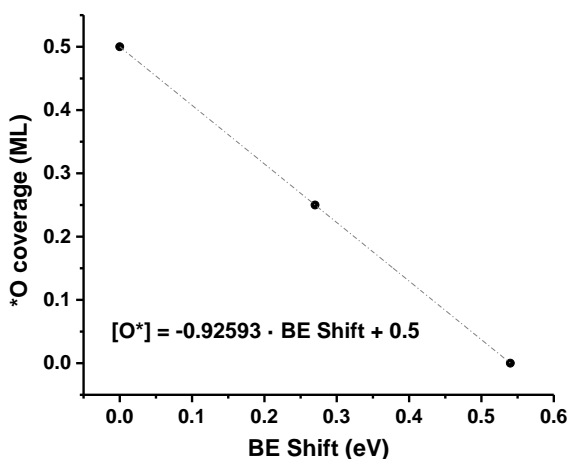


**Figure 6.9** Correlation between the Si 2p core level shift (in (NAP)-XPS) and the change in chemisorbed oxygen (\*O) coverage.<sup>[35,52]</sup>

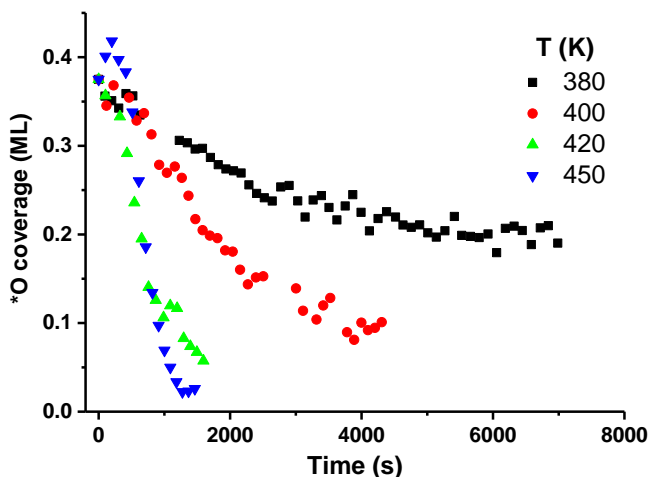


**Figure 6.10** Full plot of \*O coverage evolution at 380–450 K corresponding to Figure 6.5.

## 6.6. References

- [1] Haywood, D. G.; Saha-Shah, A.; Baker, L. A.; Jacobson, S. C. Fundamental Studies of Nanofluidics: Nanopores, Nanochannels, and Nanopipets. *Anal. Chem.* **2015**, *87*, 172–187. DOI: 10.1021/ac504180h.
- [2] Lee, S. A.; Ponjavic, A.; Siv, C.; Lee, S. F.; Biteen, J. S. Nanoscopic Cellular Imaging: Confinement Broadens Understanding. *ACS Nano* **2016**, *10*, 8143–8153. DOI: 10.1021/acsnano.6b02863.
- [3] Anduix-Canto, C.; Kim, Y. Y.; Wang, Y. W.; Kulak, A.; Meldrum, F. C.; Christenson, H. K. Effect of Nanoscale Confinement on the Crystallization of Potassium Ferrocyanide. *Cryst. Growth Des.* **2016**, *16*, 5403–5411. DOI: 10.1021/acs.cgd.6b00894.
- [4] Ha, J. M.; Hamilton, B. D.; Hillmyer, M. A.; Ward, M. D. Alignment of Organic Crystals under Nanoscale Confinement. *Cryst. Growth Des.* **2012**, *12*, 4494–4504. DOI: 10.1021/cg3006635.
- [5] Chavan, K. S.; Calabrese Barton, S. Simulation of Intermediate Channeling by Nanoscale Confinement. *J. Phys. Chem. C* **2018**, *122*, 14474–14480. DOI: 10.1021/acs.jpcc.8b01922.
- [6] Shifa, T. A.; Vomiero, A. Confined Catalysis: Progress and Prospects in Energy Conversion. *Adv. Energy Mater.* **2019**, *9*, 1902307. DOI: 10.1002/aenm.201902307.
- [7] Miners, S. A.; Rance, G. A.; Khlobystov, A. N. Regioselective control of aromatic halogenation reactions in carbon nanotube nanoreactors. *Chem. Commun.* **2013**, *49*, 5586–5588. DOI: 10.1039/C3CC42414F.

- [8] Shao, J.; Yuan, L.; Hu, X.; Wu, Y.; Zhang, Z. The Effect of Nano Confinement on the C-H Activation and its Corresponding Structure-Activity Relationship. *Sci. Rep.* **2014**, *4*, 7225. DOI: 10.1038/srep07225.
- [9] Pan, X.; Bao, X. The Effects of Confinement inside Carbon Nanotubes on Catalysis. *Acc. Chem. Res.* **2011**, *44*, 553-562. DOI: 10.1021/ar100160t.
- [10] Wang, D.; Yang, G.; Ma, Q.; Wu, M.; Tan, Y.; Yoneyama, Y.; Tsubaki, N. Confinement Effect of Carbon Nanotubes: Copper Nanoparticles Filled Carbon Nanotubes for Hydrogenation of Methyl Acetate. *ACS Catal.* **2012**, *2*, 1958-1966. DOI: 10.1021/cs300234e.
- [11] Dai, J.; Zhang, H. Recent Advances in Catalytic Confinement Effect within Micro/Meso-Porous Crystalline Materials. *Small* **2021**, *17*, 2005334. DOI: 10.1002/sml.202005334.
- [12] Li, H.; Xiao, J.; Fu, Q.; Bao, X. Confined Catalysis under Two-Dimensional Materials. *Proc. Natl. Acad. Sci.* **2017**, *114*, 5930-5934. DOI: 10.1073/pnas.1701280114.
- [13] Fu, Q.; Bao, X. Surface Chemistry and Catalysis Confined under Two-Dimensional Materials. *Chem. Soc. Rev.* **2017**, *46*, 1842-1874. DOI: 10.1039/C6CS00424E.
- [14] Yao, Y.; Fu, Q.; Zhang, Y. Y.; Weng, X.; Li, H.; Chen, M.; Jin, L.; Dong, A.; Mu, R.; Jiang, P.; Liu, L.; Bluhm, H.; Liu, Z.; Zhang, S. B.; Bao, X. Graphene Cover-Promoted Metal-Catalyzed Reactions. *Proc. Natl. Acad. Sci.* **2014**, *111*, 17023-17028. DOI: 10.1073/pnas.1416368111.
- [15] Zhou, Y.; Chen, W.; Cui, P.; Zeng, J.; Lin, Z.; Kaxiras, E.; Zhang, Z. Enhancing the Hydrogen Activation Reactivity of Nonprecious Metal Substrates Via Confined Catalysis Underneath Graphene. *Nano Lett.* **2016**, *16*, 6058-6063. DOI: 10.1021/acs.nanolett.6b02052.
- [16] Löffler, D.; Uhlrich, J. J.; Baron, M.; Yang, B.; Yu, X.; Lichtenstein, L.; Heinke, L.; Büchner, C.; Heyde, M.; Shaikhutdinov, S. Growth and Structure of Crystalline Silica Sheet on Ru(0001). *Phys. Rev. Lett.* **2010**, *105*, 146104. DOI: 10.1103/PhysRevLett.105.146104.
- [17] Eads, C. N.; Boscoboinik, J. A.; Head, A. R.; Hunt, A.; Waluyo, I.; Stacchiola, D. J.; Tenney, S. A. Enhanced Catalysis under 2D Silica: a CO Oxidation Study. *Angew. Chem. Int. Ed.* **2020**, *60*, 10888-10894. DOI: 10.1002/anie.202013801.
- [18] Lichtenstein, L.; Büchner, C.; Yang, B.; Shaikhutdinov, S.; Heyde, M.; Sierka, M.; Włodarczyk, R.; Sauer, J.; Freund, H. J. The Atomic Structure of a Metal-Supported Vitreous Thin Silica Film. *Angew. Chem. Int. Ed.* **2012**, *51*, 404-407. DOI: 10.1002/anie.201107097.
- [19] Büchner, C.; Lichtenstein, L.; Yu, X.; Boscoboinik, J. A.; Yang, B.; Kaden, W. E.; Heyde, M.; Shaikhutdinov, S. K.; Włodarczyk, R.; Sierka, M. Ultrathin Silica Films: The Atomic Structure of Two-Dimensional Crystals and Glasses. *Chem. Eur. J.* **2014**, *20*, 9176-9183. DOI: 10.1002/chem.201402452.

- [20] Klemm, H. W.; Prieto, M. J.; Xiong, F.; Hassine, G. B.; Heyde, M.; Menzel, D.; Sierka, M.; Schmidt, T.; Freund, H. J. A Silica Bilayer Supported on Ru(0001): Following the Crystalline to Vitreous Transformation in Real Time with Spectro-Microscopy. *Angew. Chem.* **2020**, *132*, 10674-10680. DOI: 10.1002/ange.202002514.
- [21] Boscoboinik, J. A.; Yu, X.; Yang, B.; Fischer, F. D.; Włodarczyk, R.; Sierka, M.; Shaikhutdinov, S.; Sauer, J.; Freund, H. J. Modeling Zeolites with Metal-Supported Two-Dimensional Aluminosilicate Films. *Angew. Chem. Int. Ed.* **2012**, *51*, 6005-6008. DOI: 10.1002/anie.201201319.
- [22] Boscoboinik, J. A.; Yu, X.; Shaikhutdinov, S.; Freund, H. J. Preparation of an Ordered Ultra-Thin Aluminosilicate Framework Composed of Hexagonal Prisms Forming a Percolated Network. *Microporous Mesoporous Mater.* **2014**, *189*, 91-96. DOI: 10.1016/j.micromeso.2013.10.023.
- [23] Boscoboinik, J. A.; Shaikhutdinov, S. Exploring Zeolite Chemistry with the Tools of Surface Science: Challenges, Opportunities, and Limitations. *Catal. Lett.* **2014**, *144*, 1987-1995. DOI: 10.1007/s10562-014-1369-3.
- [24] Boscoboinik, J. A. Chemistry in Confined Space through the Eyes of Surface Science-2D Porous Materials. *J. Phys.: Condens. Matter* **2019**, *31*, 063001. DOI: 10.1088/1361-648X/aaf2ce.
- [25] Yao, B.; Mandrà, S.; Curry, J. O.; Shaikhutdinov, S.; Freund, H. J.; Schrier, J. Gas Separation through Bilayer Silica, the Thinnest Possible Silica Membrane. *ACS Appl. Mater. Interfaces* **2017**, *9*, 43061-43071. DOI: 10.1021/acsami.7b13302.
- [26] Schlexer, P.; Pacchioni, G.; Włodarczyk, R.; Sauer, J. CO Adsorption on a Silica Bilayer Supported on Ru(0001). *Surf. Sci.* **2016**, *648*, 2-9. DOI: 10.1016/j.susc.2015.10.027.
- [27] Büchner, C.; Lichtenstein, L.; Stuckenholtz, S.; Heyde, M.; Ringleb, F.; Sterrer, M.; Kaden, W. E.; Giordano, L.; Pacchioni, G.; Freund, H. J. Adsorption of Au and Pd on Ruthenium-Supported Bilayer Silica. *J. Phys. Chem. C* **2014**, *118*, 20959-20969. DOI: 10.1021/jp5055342.
- [28] Akter, N.; Wang, M.; Zhong, J. Q.; Liu, Z.; Kim, T.; Lu, D.; Boscoboinik, J. A.; Stacchiola, D. J. Stabilization of Oxidized Copper Nanoclusters in Confined Spaces. *Top. Catal.* **2018**, *61*, 419-427. DOI: 10.1007/s11244-017-0879-9.
- [29] Zhong, J. Q.; Wang, M.; Akter, N.; Kestell, J. D.; Boscoboinik, A. M.; Kim, T.; Stacchiola, D. J.; Lu, D.; Boscoboinik, J. A. Immobilization of Single Argon Atoms in Nano-Cages of Two-Dimensional Zeolite Model Systems. *Nat. Commun.* **2017**, *8*, 16118. DOI: 10.1038/ncomms16118.
- [30] Zhong, J. Q.; Wang, M.; Akter, N.; Kestell, J. D.; Niu, T.; Boscoboinik, A. M.; Kim, T.; Stacchiola, D. J.; Wu, Q.; Lu, D. Ionization-Facilitated Formation of 2D (Alumino) Silicate-Noble Gas Clathrate Compounds. *Adv. Funct. Mater.* **2019**, *29*, 1806583. DOI: 10.1002/adfm.201806583.
- [31] Jhang, J. H.; Zhou, C.; Dagdeviren, O. E.; Hutchings, G. S.; Schwarz, U. D.; Altman, E. I. Growth of Two Dimensional Silica and Aluminosilicate Bilayers on Pd(111): From Incommensurate to

- Commensurate Crystalline. *Phys. Chem. Chem. Phys.* **2017**, *19*, 14001-14011. DOI: 10.1039/C7CP02382K.
- [32] Altman, E. I.; Götzen, J.; Samudrala, N.; Schwarz, U. D. Growth and Characterization of Crystalline Silica Films on Pd(100). *J. Phys. Chem. C* **2013**, *117*, 26144-26155. DOI: 10.1021/jp4101152.
- [33] Yu, X.; Yang, B.; Boscoboinik, J. A.; Shaikhutdinov, S.; Freund, H. J. Support Effects on the Atomic Structure of Ultrathin Silica Films on Metals. *Appl. Phys. Lett.* **2012**, *100*, 151608. DOI: 10.1063/1.3703609.
- [34] Wang, M.; Zhong, J. Q.; Stacchiola, D. J.; Boscoboinik, J. A.; Lu, D. First-Principles Study of Interface Structures and Charge Rearrangement at the Aluminosilicate/Ru(0001) Heterojunction. *J. Phys. Chem. C* **2019**, *123*, 7731-7739. DOI: 10.1021/acs.jpcc.8b05853.
- [35] Wang, M.; Zhong, J. Q.; Kestell, J.; Waluyo, I.; Stacchiola, D. J.; Boscoboinik, J. A.; Lu, D. Energy Level Shifts at the Silica/Ru(0001) Heterojunction Driven by Surface and Interface Dipoles. *Top. Catal.* **2017**, *60*, 481-491. DOI: 10.1007/s11244-016-0704-x.
- [36] Mark, L. O.; Chen, W.; Eads, C. N.; Lu, D.; Boscoboinik, J. A.; Stacchiola, D.; Will Medlin, J.; Tenney, S. A. Confinement Effects on Furfuryl Alcohol Reactions over Porous Bilayer Silica-Modified Pd(111). *J. Phys. Chem. C* **2020**, *124*, 25437-25446. DOI: 10.1021/acs.jpcc.0c09095.
- [37] Shishkin, M.; Ziegler, T. Hydrogen Oxidation at the Ni/Yttria-Stabilized Zirconia Interface: A Study Based on Density Functional Theory. *J. Phys. Chem. C* **2010**, *114*, 11209-11214. DOI: 10.1021/jp1030575.
- [38] Ohyama, J.; Sato, T.; Yamamoto, Y.; Arai, S.; Satsuma, A. Size Specifically High Activity of Ru Nanoparticles for Hydrogen Oxidation Reaction in Alkaline Electrolyte. *J. Am. Chem. Soc.* **2013**, *135*, 8016-8021. DOI: 10.1021/ja4021638.
- [39] Alia, S. M.; Pivovar, B. S.; Yan, Y. Platinum-Coated Copper Nanowires with High Activity for Hydrogen Oxidation Reaction in Base. *J. Am. Chem. Soc.* **2013**, *135*, 13473-13478. DOI: 10.1021/ja405598a.
- [40] Fisher, G. B.; Gland, J. L.; Schmiege, S. J. The Spectroscopic Observation of Water Formation. *J. Vac. Sci. Technol.* **1982**, *20*, 518-521. DOI: 10.1116/1.571421.
- [41] Germer, T. A.; Ho, W. Direct Characterization of the Hydroxyl Intermediate During Reduction of Oxygen on Pt(111) by Time-Resolved Electron Energy Loss Spectroscopy. *Chem. Phys. Lett.* **1989**, *163*, 449-454. DOI: 10.1016/0009-2614(89)85166-8.
- [42] Ogle, K.; White, J. M. The Low Temperature Water Formation Reaction on Pt(111): A Static SIMS and TDS Study. *Surf. Sci.* **1984**, *139*, 43-62. DOI: 10.1016/0039-6028(84)90007-4.



- [43] Gland, J. L.; Fisher, G. B.; Kollin, E. B. The Hydrogen-Oxygen Reaction over the Pt(111) Surface: Transient Titration of Adsorbed Oxygen with Hydrogen. *J. Catal.* **1982**, *77*, 263-278. DOI: 10.1016/0021-9517(82)90167-1.
- [44] Hellsing, B.; Kasemo, B.; Zhdanov, V. P. Kinetics of the Hydrogen-Oxygen Reaction on Platinum. *J. Catal.* **1991**, *132*, 210-228. DOI: 10.1016/0021-9517(91)90258-6.
- [45] Verheij, L. K.; Freitag, M.; Hugenschmidt, M. B.; Kempf, I.; Poelsema, B.; Comsa, G. Autocatalytic Behavior and Role of Oxygen Diffusion in the Hydrogen-Oxygen Reaction on Pt(111). *Surf. Sci.* **1992**, *272*, 276-282. DOI: 10.1016/0039-6028(92)91450-P.
- [46] Michaelides, A.; Hu, P. Catalytic Water Formation on Platinum: A First-Principles Study. *J. Am. Chem. Soc.* **2001**, *123*, 4235-4242. DOI: 10.1021/ja003576x.
- [47] Völkening, S.; Bedürftig, K.; Jacobi, K.; Wintterlin, J.; Ertl, G. Dual-Path Mechanism for Catalytic Oxidation of Hydrogen on Platinum Surfaces. *Phys. Rev. Lett.* **1999**, *83*, 2672. DOI: 10.1103/PhysRevLett.83.2672.
- [48] Koch, M. H.; Jakob, P.; Menzel, D. The Influence of Steps on the Water-Formation Reaction on Ru(001). *Surf. Sci.* **1996**, *367*, 293-306. DOI: 10.1016/S0039-6028(96)00811-4.
- [49] Schick, M.; Xie, J.; Mitchell, W. J.; Weinberg, W. H. Interaction of Gas-Phase Atomic Deuterium with the Ru(001)-p(1×2)-O Surface: Kinetics of Hydroxyl and Water Formation. *J. Chem. Phys.* **1996**, *104*, 7713-7718. DOI: 10.1063/1.471452.
- [50] Zhong, J. Q.; Kestell, J.; Waluyo, I.; Wilkins, S.; Mazzoli, C.; Barbour, A.; Kaznatcheev, K.; Shete, M.; Tsapatsis, M.; Boscoboinik, J. A. Oxidation and Reduction under Cover: Chemistry at the Confined Space between Ultrathin Nanoporous Silicates and Ru(0001). *J. Phys. Chem. C* **2016**, *120*, 8240-8245. DOI: 10.1021/acs.jpcc.6b02851.
- [51] Emmez, E.; Boscoboinik, J. A.; Tenney, S.; Sutter, P.; Shaikhdudinov, S.; Freund, H. J. Oxidation of the Ru(0001) Surface Covered by Weakly Bound, Ultrathin Silicate Films. *Surf. Sci.* **2016**, *646*, 19-25. DOI: 10.1016/j.susc.2015.06.019.
- [52] Wang, M.; Zhou, C.; Akter, N.; Tysøe, W. T.; Boscoboinik, J. A.; Lu, D. Mechanism of the Accelerated Water Formation Reaction under Interfacial Confinement. *ACS Catal.* **2020**, *10*, 6119-6128. DOI: 10.1021/acscatal.9b05289.
- [53] Prieto, M. J.; Klemm, H. W.; Xiong, F.; Gottlob, D. M.; Menzel, D.; Schmidt, T.; Freund, H. J. Water Formation under Silica Thin Films: Real-Time Observation of a Chemical Reaction in a Physically Confined Space. *Angew. Chem. Int. Ed.* **2018**, *57*, 8749-8753. DOI: 10.1002/anie.201802000.
- [54] Prieto, M. J.; Mullan, T.; Schlutow, M.; Gottlob, D. M.; Tanase, L. C.; Menzel, D.; Sauer, J.; Usvyat, D.; Schmidt, T.; Freund, H. J. Insights into Reaction Kinetics in Confined Space: Real Time Observation of Water Formation under a Silica Cover. *J. Am. Chem. Soc.* **2021**, *143*, 8780-8790. DOI: 10.1021/jacs.1c03197.

- [55] Kresse, G.; Furthmüller, J. Efficient Iterative Schemes for Ab Initio Total-Energy Calculations Using a Plane-Wave Basis Set. *Phys. Rev. B* **1996**, *54*, 11169. DOI: 10.1103/PhysRevB.54.11169.
- [56] Kresse, G.; Furthmüller, J. Efficiency of Ab-Initio Total Energy Calculations for Metals and Semiconductors Using a Plane-Wave Basis Set. *Comput. Mater. Sci.* **1996**, *6*, 15-50. DOI: 10.1016/0927-0256(96)00008-0.
- [57] Klimeš, J.; Bowler, D. R.; Michaelides, A. Chemical Accuracy for the Van Der Waals Density Functional. *J. Phys.: Condens. Matter* **2009**, *22*, 022201. DOI: 10.1088/0953-8984/22/2/022201.
- [58] Klimeš, J.; Bowler, D. R.; Michaelides, A. Van Der Waals Density Functionals Applied to Solids. *Phys. Rev. B* **2011**, *83*, 195131. DOI: 10.1103/PhysRevB.83.195131.
- [59] Lee, K.; Murray, É. D.; Kong, L.; Lundqvist, B. I.; Langreth, D. C. Higher-Accuracy Van Der Waals Density Functional. *Phys. Rev. B* **2010**, *82*, 081101. DOI: 10.1103/PhysRevB.82.081101.
- [60] Henkelman, G.; Uberuaga, B. P.; Jónsson, H. A Climbing Image Nudged Elastic Band Method for Finding Saddle Points and Minimum Energy Paths. *J. Chem. Phys.* **2000**, *113*, 9901-9904. DOI: 10.1063/1.1329672.





# CHAPTER 7

## General Conclusions





The results presented in the different chapters of this Doctoral Thesis have led to the following general conclusions:

### *Chapter 3*

- Gallium is an effective promoter in commercial-like Cu/ZnO catalysts in the CO<sub>2</sub> hydrogenation to methanol.
- The nature of gallium species in Cu/ZnO systems can be easily tuned by selecting the appropriate precipitating agent. The use of NH<sub>4</sub>HCO<sub>3</sub> and NaOH resulted in zinc gallate (ZnGa<sub>2</sub>O<sub>4</sub>) and Ga<sup>3+</sup>-doped ZnO wurtzite, respectively.
- Methanol production via CO<sub>2</sub> hydrogenation is promoted doping Ga<sup>3+</sup> ions in ZnO in a commercial-like Cu/ZnO system (CZG-ox). This results in a methanol selectivity of 65.0% at 260 °C and ~15.5% CO<sub>2</sub> conversion, being 9% and 16% higher than those of the ZnGa<sub>2</sub>O<sub>4</sub> (CZG-sp) and a commercial Cu/ZnO/Al<sub>2</sub>O<sub>3</sub> (CZA) catalysts (i.e., selectivity of 56.2% and 49.0%, respectively, at iso-conversion).
- Despite the promising higher methanol selectivity of the Ga<sup>3+</sup> doped Cu/ZnO (CZG-ox) catalyst, its activity per gram of catalyst is lower, due to its lower surface area. However, when normalizing it to surface area, it presents a two-fold higher activity compared to the other samples (CZG-sp and CZA catalysts).
- The industrial application of the Ga<sup>3+</sup> doped Cu/ZnO (CZG-ox) catalyst is hampered by its reduced long-term stability, with an initial decrease (~38%) in methanol production over the first 25 h time-on-stream. A preliminary reformulation including Al<sub>2</sub>O<sub>3</sub> let us obtain a more stable temporal profile, avoiding deactivation. However, further studies are needed in the future to understand the fundamental implications of this catalyst modification.

- Operando spectroscopic studies revealed surface basic sites, the stabilization of  $\text{Cu}^+$  surface species, and a low amount of surface metallic copper due to ZnO migration over CuNPs as fundamental features for enhanced methanol production versus CO formation in the  $\text{Ga}^{3+}$ -doped Cu/ZnO (CZG-ox) catalyst.

#### *Chapter 4*

- High methanol production has been obtained on copper-based catalysts containing small particle size (2 nm). The reported low activity of small copper particles has been overcome by the stabilization of doped  $\text{Cu}^+$  ions in the metal oxide lattice of a Cu-Mg-Al catalyst derived from a hydrotalcite precursor.
- Supported on operando IR studies performed under relevant reaction conditions, a linear correlation between the  $\text{STY}_{\text{MeOH}}$  and the amount of  $\text{Cu}^+$  species has been observed.
- The partial reconstruction under reaction conditions observed on the metal oxide due to the “HT-memory effect” in presence of water conferred thermal and temporal stability to the Cu-Mg-Al mixed oxide catalyst system (CuHT-230), avoiding a massive sintering that usually causes the catalyst deactivation.
- Advanced IR operando  $\text{CO}_2$  hydrogenation experiments at variable pressure (1-9 bar) revealed that the presence of  $\text{Cu}^+$  doped ions favors the stabilization of *m*-formate intermediates, responsible for the methanol formation. Less reactive *b*-formate species were also detected in transient experiments, yielding CO and methane.



### Chapter 5

- An innovative core-shell structure formed by a core of metallic ruthenium and a shell of ruthenium carbide, embedded in a carbon matrix, was synthesized via hydrothermal treatment (Ru@EDTA-20). This catalyst exhibited unprecedented activity in a non-usual reactivity window for the Sabatier reaction (i.e., below 200 °C and at atmospheric pressure), outperforming the state of the art catalysts operating above ~350 °C.
- Due to its innovative conceptual design, exceptional catalytic performance and potential application as an industrial catalyst operating in the low temperature Sabatier reaction, this system was recently patented at national (ES2828458 A1) and international (WO/2021/105537 A1) level.
- Ruthenium carbide species are responsible for CO<sub>2</sub> activation, which is subsequently hydrogenated to methane in a direct reaction pathway (in contrast to conventional catalysts that usually follow the RWGS mechanism), yielding 100% selectivity to CH<sub>4</sub>.

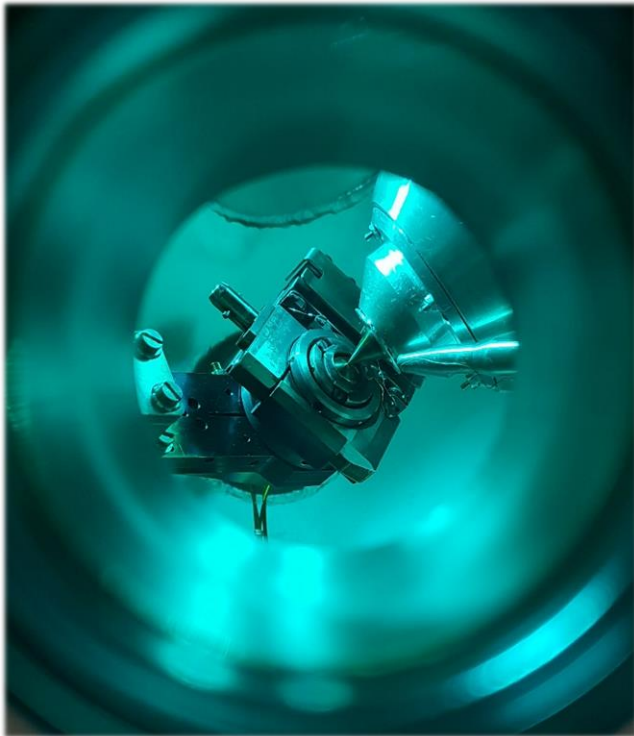
### Chapter 6

- A 2D bilayer Al<sub>0.25</sub>Si<sub>0.75</sub>O<sub>2</sub>/Ru(0001) model was selected to study the water formation reaction under interfacial confinement. The nano-space generated by the combination of the 2D aluminosilicate and the Ru crystal “activates” the disproportionation pathway (TS2'), as it was already reported in the pure silicate. However, the introduction of Al<sup>3+</sup> in the system caused a small nano-space contraction of 0.3 Å, which is not beneficial to the progress of the reaction, as confirmed by DFT calculations (0.93 eV TS2'<sub>Al-Si</sub> vs. 0.85 eV TS2'<sub>Si</sub>).



# CHAPTER 8

## Appendices





## 8.1. List of abbreviations and acronyms

a.u.: arbitrary unit

Å: angstrom

acac: Acetylacetonate

ACN: Acetonitrile

AES: Auger electron spectroscopy

at: Atomic

b: Bridge (also brg)

BE: Binding energy

BET: Brunauer-Emmett-Teller

BL: Beamline

BPR: Back-pressure regulator

bpy: 2,2'-Bipyridine

Cat: Catalyst

CC BY-NC-ND: Creative Commons BY Non-commercial No-derivatives

CC-BY: Creative Commons BY

CCS: Carbon Capture and Storage

CCU: Carbon Capture and Utilization

CFC: Chloroflourocarbons

CNT: Carbon nanotube

CO<sub>2</sub>e: Carbon dioxide equivalent

CO<sub>2</sub>R: CO<sub>2</sub> reductive transformation

CPS: Counts per second

CTAB: Cetyltrimethylammonium bromide

DFT: Density Functional Theory

DME: Dimethyl ether

DMF: Dimethylformamide

DTGS: Deuterated triglycine sulfate detector

e.g.: For example (*exempli gratia*)

E<sub>a,app</sub>: Apparent activation energy

E<sub>ads</sub>: Adsorption energy

EDTA: Ethylenediaminetetraacetic acid derived salt

EDX: Energy-dispersive X-ray detector

E<sub>exc</sub>: Excitation energy

EIS: Electrochemical impedance spectroscopy

EOR: Enhanced oil recovery

EU: European Union

eV: Electron-volt

EXAFS: Extended X-ray absorption fine structure spectroscopy  
FID: Flame ionization detector  
FT: Fourier-transform  
FTS: Fischer-Tropsch synthesis  
GC: Gas chromatography  
GGA: Generalized gradient approximation  
GHG: Greenhouse gas  
GHSV: Gas Hourly Space Velocity  
HER: Hydrogen evolution reaction  
HPCR: High-pressure cell reactor  
HREELS: High-resolution electron energy loss spectroscopy  
HR-TEM: High-resolution transmission electron microscopy  
HT: Hydrotalcite  
i.e.: That is (id est)  
ICP-OES: Inductively coupled plasma optical emission spectrometry  
IEA: International Energy Agency  
IMFP: Inelastic mean free path  
IPCC: Intergovernmental Panel on Climate Change  
IRENA: International Renewable Energy Agency  
IRRAS: Infrared reflection absorption spectroscopy  
JCPDS: Joint Committee on Powder Diffraction Standards  
k: Kinetic constant  
KE: Kinetic energy  
LCM: Low carbon methanol  
LDH: Layered double hydroxide  
LPMEOH: Liquid-phase methanol synthesis process  
m/z: Mass-to-charge ratio  
M: Metal  
m: Monodentate  
MCD: Multi channeltron detector  
MEA: Monoethanolamine  
MES: Microbial electrosynthesis  
ML: Monolayer  
MOF: Metal-organic framework  
MRF: Multi-stage radial flow  
MS: Mass spectrometry (or spectrometer)  
MTBE: Methyl tert-butyl ether  
MTG: Methanol-to-gasoline  
MTO: Methanol-to-olefins

NAP-XPS: Near-ambient pressure X-ray photoelectron spectroscopy  
NEXAFS: Near-edge X-ray absorption fine structure  
NP: Nanoparticle  
NTP: Non-thermal plasma  
OER: Oxygen evolution reaction  
P: Pressure  
P2G: Power-to-gas  
PAW: projector augmented wave  
PBE: Perdew, Burke and Ernzerhof  
PDA: Polydopamine  
PGM: Plane grating monochromator  
Ref: Reference  
RT: Room temperature  
RWGS: Reverse water-gas shift reaction  
S: Selectivity  
 $S_A$ : Surface area  
SBCR: Slurry bubble column reactor  
SI: Supporting information  
SMR: Steam methane reforming  
SOFC: Solid oxide fuel cell  
STM: Scanning tunneling microscope  
STY: Space-time yield  
T: Temperature  
TBM: Turbomolecular pump  
TCD: Thermal conductivity detector  
TOF: Turnover frequency  
TOS: Time-on-stream  
TPD: Temperature-programmed desorption  
TPP2M: Tanuma Powell and Penn algorithm  
TPR: Temperature-programmed reduction  
TS: Transition state  
UNFCCC: United Nations Framework Convention on Climate Change  
UV-VIS: Ultraviolet-visible  
VASP: Vienna ab-initio simulation package  
vdW: Van der Waals  
vol: Volume  
w: Water  
WFR: Water formation reaction  
WHSV: Weight hourly space velocity

WI: Wet impregnation

wt: Weight

X: Conversion

XANES: X-ray absorption near-edge spectroscopy

XAS: X-ray absorption spectroscopy

XRD: X-ray diffraction

$\alpha'$ : Auger parameter

$\delta$ : Symmetric bending vibration

$\theta$ : Coverage

$\nu_{as}$ : Asymmetric stretching vibration

$\nu_s$ : Symmetric stretching vibration

2D: Two-dimensional



## 8.2. List of Figures

**Figure 1.1** Total Solar Irradiance (in watts per square meter) received from the Sun compared with global surface temperature changes since 1880. Thinner lines correspond to yearly levels. Thicker lines show the 11-year average trends. *Author credits: NASA/JPL-Caltech. No copyright intended.<sup>[4]</sup>*

**Figure 1.2** Global greenhouse gas emissions by gas in 2016 (converted to CO<sub>2</sub>e). *Author credits: Ritchie, H. Open access under a CC-BY License.<sup>[9]</sup>*

**Figure 1.3** Global CO<sub>2</sub> production-based emissions in 2017. *Author credits: Ritchie, H. Open access under a CC-BY License.<sup>[10]</sup>*

**Figure 1.4** Total GHG emissions (EU-27+UK) over the period 1990-2019 in billion tCO<sub>2</sub>e. International transport contribution is included.<sup>[11]</sup> *Author credits: Cored, J. No copyright intended.*

**Figure 1.5** Distribution of CO<sub>2</sub> emissions by origin (EU-27+UK). Comparison of 1990 (outer ring) and 2019 (inner ring) situations.<sup>[12]</sup> *Author credits: Cored, J. No copyright intended.*

**Figure 1.6** Color code nomenclature commonly used to denominate the way hydrogen is produced. (SMR = Steam methane reforming). *Author credits: International Renewable Energy Agency (IRENA). No copyright intended.<sup>[22]</sup>*

**Figure 1.7** The phase diagram of carbon dioxide. *Author credits: Rothwild-Wikimedia Commons. No copyright intended.<sup>[25]</sup>*

**Figure 1.8** Current CCS commercial facilities in the world. *Author credits: Global CCS Institute. Open access under a CC BY-NC-ND 4.0 License.<sup>[33]</sup>*

**Figure 1.9** CO<sub>2</sub> chemical network to obtain diverse products of industrial interest via thermocatalytic hydrogenation. *Author credits: Concepción, P. and Cored, J. No copyright intended.*

**Figure 1.10** Equilibrium CO<sub>2</sub> conversion and methanol selectivity at different temperatures and at increasing pressures: (a) 10 bar, (b) 30 bar, (c) 100 bar, (d) 200 bar, (e) 300 bar, (f) 400 bar, and (g) 500 bar. Initial H<sub>2</sub>/CO<sub>2</sub> molar ratio mixtures of 3 (left panels) and 10 (right panels) are used. *Reprinted with permission from ACS Catal. 2020, 10, 14147-14185. Copyright 2020 American Chemical Society.<sup>[43]</sup>*

**Figure 1.11** Proposed reaction network for methanol synthesis from CO<sub>2</sub> hydrogenation. (\*) indicates adsorbed species. *Reproduced from Chem. Soc. Rev. 2020, 49, 1325-1616 with permission from the Royal Society of Chemistry (Copyright 2020).*

**Figure 1.12** Companies and institutions involved in the production of sustainable MeOH. Adapted from reference [107]. *Author credits: Methanol Institute/ATA insights. No copyright intended.*

**Figure 1.13** Effect of pressure and temperature in CO<sub>2</sub> conversion (a) and CH<sub>4</sub> selectivity (b) at a H<sub>2</sub>/CO<sub>2</sub> molar ratio of 4; and influence of H<sub>2</sub>/CO<sub>2</sub> molar ratio and temperature at 1 atm (1.013 bar) and 30 atm (30.397 bar) in CO<sub>2</sub> conversion (c) and CH<sub>4</sub> selectivity (d). *Reproduced from RSC Advances 2012, 2, 2358-2368 with permission from the Royal Society of Chemistry (Copyright 2012).*

**Figure 1.14** Reaction pathways of CO<sub>2</sub> hydrogenation to CH<sub>4</sub> (CH<sub>3</sub>OH and CO products are also included). (\*) indicates adsorbed species. *Reprinted with permission of J. Am. Chem. Soc. 2017, 139, 9739-9754. Copyright 2017 American Chemical Society.*

**Figure 1.15** CO<sub>2</sub> methanation projects under different stages of development. Numbers in brackets refer to the capacity/power of the plant, expressed in kW. <sup>a</sup>First module will go into operation in 2022, full capacity in 2028. <sup>b</sup>This plant will start operations in 2024. *Author credits: Cored, J. No copyright intended.*

**Figure 2.1** Pillars on which the doctoral thesis is supported.

**Figure 3.1** Normalized XANES spectra at Ga K-edge (a), phase-uncorrected, k<sup>2</sup>-weighted  $\chi(k)$  functions (b) and EXAFS spectra (c) of CZG catalysts and Ga-based references. The inset in panel (a) shows a comparison of CZG-ox sample measured at Ga and Zn K-edges.

**Figure 3.2** Structural characterization of CZG-ox and CZG-sp samples. High-resolution transmission electron microscopy (HR-TEM) images of CZG-sp (a) and CZG-ox (b) samples. The different phases are marked according to their lattice fringes. STEM-EDX mapping results of CZG-ox (c) and CZG-sp (d). The Ga (red), Zn (cyan) and Cu (green) are indicated by different colors in the images.

**Figure 3.3** Bode-module plot and total resistance values of the reduced CZG-ox, CZG-sp and CZA samples in 0.1 M Na<sub>2</sub>SO<sub>4</sub> at 0 V<sub>Ag/AgCl</sub>.

**Figure 3.4** Selected catalytic features for the CO<sub>2</sub> hydrogenation to MeOH on CZG and CZA samples: CO<sub>2</sub> conversion (a), MeOH selectivity (b), and CO selectivity (c) versus temperature; MeOH selectivity versus space-time yield to MeOH at 260 °C (d).

**Figure 3.5** Variation of the methanol selectivity vs. carbon dioxide conversion at 220 °C (a) and 240 °C (b).

**Figure 3.6** CZG-ox (a,b,c), CZG-sp (d,e,f) and CZA (g,h,i) XPS depth profile spectra at different reaction conditions. Left: spectra of reduced catalysts. Middle: spectra under CO<sub>2</sub>+H<sub>2</sub> atmosphere at 220 °C. Right: spectra under CO<sub>2</sub>+H<sub>2</sub> atmosphere at 280 °C.

**Figure 3.7** Infrared spectra of CO adsorbed at -50 °C on in situ reduced CZG-sp, CZG-ox and CZA samples.

**Figure 3.8** H<sub>2</sub>-D<sub>2</sub> isotopic exchange results for CZG and CZA samples at 90 °C.

**Figure 3.9** TPD-CO<sub>2</sub> experiments performed on CZG and CZA catalysts.

**Figure 3.10** Long-term experiments conducted on CZG-ox and the commercial CZA samples at 240 °C, 20 bar and ~28500 mL·g<sub>cat</sub><sup>-1</sup>·h<sup>-1</sup>.

**Figure 3.11** Temperature-programmed reduction (TPR) studies in 10% H<sub>2</sub>/Ar flow, for CZG and CZA catalytic samples.

**Figure 3.12** Diffractograms of as-prepared (a) and calcined (b) CZG-sp sample.

**Figure 3.13** Diffractograms of as-prepared (a) and calcined CZG-ox sample (b).

**Figure 3.14** Diffractograms of reduced samples.

**Figure 3.15** Comparison between XRD patterns before (black) and after reaction (red).

**Figure 3.16** Diffractograms of as-prepared (a) and calcined (b) CZG-ox samples at variable gallium loadings.

**Figure 3.17** Normalized XANES spectra at Cu K-edge (a) and, phase-uncorrected,  $k^2$ -weighted EXAFS spectra (b) of CZG catalysts and Cu-based references. Inset of (b) reports the corresponding  $k^2$ - $\chi(k)$  functions.

**Figure 3.18** Normalized XANES spectra at Zn K-edge (a) and, phase-uncorrected,  $k^2$ -weighted EXAFS spectra (b) of CZG catalysts and Zn-based references. Inset of (b) reports the  $k^2$ -weighted phase-uncorrected  $\chi(k)$  functions.

**Figure 3.19** Mott-Schottky plots and  $N_D$  values of the CZG-ox and CZG-sp catalysts.

**Figure 3.20** STY vs W/F at 220 °C (a) and 240 °C (b) for CZA and CZG systems.

**Figure 3.21** MeOH selectivity under iso-conversion conditions at 220 and 260 °C.

**Figure 3.22** Comparison of the catalytic performance of studied CZG and CZA samples at different temperatures in the CO<sub>2</sub> hydrogenation to methanol with other Cu-based catalysts in the literature. Numbers refer to the entries placed at Table 3.12 (first column).

**Figure 3.23** STY at 220 and 260 °C in CZG-ox samples at different levels of Ga doping.

**Figure 3.24** (NAP)-XPS spectra of CZG-sp catalyst acquired at different reaction conditions. Core lines of Cu 2p (a), Zn 2p (b), Ga 2p (c) at KE=268 eV and Cu LVV AES (d) at  $h\nu=1290$  eV are shown.

**Figure 3.25** (NAP)-XPS spectra of CZG-ox catalyst acquired at different reaction conditions. Core lines of Cu 2p (a), Zn 2p (b), Ga 2p (c) at KE=268 eV and Cu LVV AES (d) at  $h\nu=1290$  eV are shown.

**Figure 3.26** (NAP)-XPS spectra of CZA catalyst acquired at different reaction conditions. Core lines of Cu 2p (a) and Zn 2p (b) at KE=268 eV and Cu LVV AES (c) at  $h\nu=1290$  eV are shown.

**Figure 3.27** Deconvoluted spectra of the O 1s core level under CO<sub>2</sub>+H<sub>2</sub> reaction at 220 °C on CZG-ox (a), CZA (b), and CZG-sp (c) samples.

**Figure 3.28** Time-dependent dynamic surface migration under reaction conditions on the reduced CZG-sp sample at 220 °C (a) and 280 °C (b) acquired at a depth of 2.5 nm (268 eV KE).

**Figure 3.29** Time-dependent dynamic surface migration under reaction conditions on the reduced CZG-ox sample at 220 °C (a) and 280 °C (b) acquired at a depth of 2.5 nm (268 eV KE).

**Figure 3.30** Influence of pressure in the CO<sub>2</sub> hydrogenation to methanol (a) and CO (b).

**Figure 3.31** Mass spectra analysis in (NAP)-XPS experiments on CZG-sp (a), CZG-ox (b) and CZA catalysts (c).

**Figure 3.32** Catalytic correlation between (NAP)-XPS (+MS coupled) experiments performed at Bessy II Synchrotron and catalytic experiments carried out in the 20 bar fixed-bed reactor. A linear correlation for MeOH (a) and CO (b) productivity is observed for the three samples under study.

**Figure 3.33** XPS core lines of Cu 2p (a), Zn 2p (b), Ga 2p (c), Cu LVV AES (d), Zn LMM AES (e), and Ga LMM AES (f) at  $h\nu=1486.6$  eV excitation energy of the reduced CZG-sp sample.

**Figure 3.34** XPS core lines of Cu 2p (a), Zn 2p (b), Ga 2p (c), Cu LVV AES (d), Zn LMM AES (e), and Ga LMM AES (f) at  $h\nu=1486.6$  eV excitation energy of the CZG-sp sample after 9 bar CO<sub>2</sub> hydrogenation in HPCR.

**Figure 3.35** XPS core lines of Cu 2p (a), Zn 2p (b), Ga 2p (c), Cu LVV AES (d), Zn LMM AES (e), and Ga LMM AES (f) at  $h\nu=1486.6$  eV excitation energy of the reduced CZG-ox sample.

**Figure 3.36** XPS core lines of Cu 2p (a), Zn 2p (b), Ga 2p (c), Cu LVV AES (d), Zn LMM AES (e), and Ga LMM AES (f) at  $h\nu=1486.6$  eV excitation energy of the CZG-ox sample after 9 bar CO<sub>2</sub> hydrogenation in HPCR.

**Figure 3.37** Zn LMM AES line of CZG-sp (a) and CZG-ox (b) reduced samples (black) and after being exposed to CO<sub>2</sub>+H<sub>2</sub> reaction at 9 bar (blue). Spectra were acquired at  $h\nu=1486.6$  eV.

**Figure 3.38** MS of CZG-sp (a) and CZG-ox (b) catalysts during the CO<sub>2</sub> hydrogenation at 9 bar performed in the HPCR unit. Numbers in parentheses correspond to  $m/z$  values.

**Figure 3.39** TPD-CO<sub>2</sub> on reference samples.

**Figure 3.40** Correlation of STY<sub>2</sub> with medium basicity (a), exposed copper (b), and the ratio of both properties (c).

**Figure 3.41** Long-term experiments performed on CZG-ox and CZGA-ox samples at 240 °C, 20 bar and 28500 mL-g<sub>cat</sub><sup>-1</sup>·h<sup>-1</sup> (a) and comparison of catalytic features at that temperature (b).

**Figure 4.1** Left, HR-STEM images of CuHT-230 (a) and CuHT-450 catalysts (c). Right, particle size distribution for CuHT-230 (b) and CuHT-450 catalysts (d). More than 200 particles have been measured in each sample.

**Figure 4.2** Methanol productivity of studied Cu-based samples at variable temperature and 20 bar pressure (3:1 H<sub>2</sub>/CO<sub>2</sub> vol % ratio, WHSV ~28500 mL-g<sub>cat</sub><sup>-1</sup>·h<sup>-1</sup>).

**Figure 4.3** Variation of the MeOH selectivity versus CO<sub>2</sub> conversion at 230 °C and 20 bar on samples under study (a) and comparison between a commercial Cu/ZnO/Al<sub>2</sub>O<sub>3</sub> catalyst (CZA) and CuHT-230 sample under the same catalytic conditions (b). CZA was prepared according to the work of Baltes et al.<sup>[47]</sup> and discussed in Chapter 3. Intrinsic formation rates of methanol and CO for representative

catalytic systems (c). Long-term stability of CuHT-230 system at 230 °C, 20 bar and 5700 mL-g<sub>cat</sub><sup>-1</sup>·h<sup>-1</sup> (d).

**Figure 4.4** IR of CO adsorption at -170 °C and saturation coverage on reduced Cu-HT-derived samples: CuHT-230 (a), CuHT-450 (b), Cu/HT (w) (c), Cu/HT (ACN) (d). Color code for deconvoluted components: orange (HT support), dark cyan (Cu<sup>+</sup> species), navy (Cu<sup>0</sup> species). Comparison between the amount of Cu<sup>+</sup> species normalized to sample weight analyzed at saturation coverage (e).

**Figure 4.5** Normalized area of the IR component associated with CO coordinated to Cu<sup>+</sup> (IR band at ~2135 cm<sup>-1</sup>) (a); and Cu<sup>0</sup> (IR bands between 2115-1990 cm<sup>-1</sup>) (b); before (i.e., reduced samples) and after CO<sub>2</sub> hydrogenation at 9 bar.

**Figure 4.6** Correlation between methanol production at 20 bar in a fixed-bed reactor (STY MeOH, X axis) and the amount of Cu<sup>+</sup> species normalized to sample weight obtained in the operando IR studies at 9 bar (Y axis).

**Figure 4.7** Temperature-resolved IR studies under operando conditions at 1 bar in CO<sub>2</sub>/H<sub>2</sub> flow over CuHT-230 catalyst. Sequential steps at 200 and 230 °C are displayed on the left and on the right side, respectively. First row panels show IR spectra at indicated temperatures. Middle row panels exhibit the subtracted spectra. Third row panels show the reaction products evolution monitored by MS.

**Figure 4.8** Temperature-programmed reduction studies in 10% H<sub>2</sub>/Ar flow.

**Figure 4.9** XRD patterns of HT-type samples under study before (a) and after (b) calcination. "s" label in left panel refers to synthesized/as-prepared hydrotalcites.

**Figure 4.10** XRD patterns of non-HT-derived samples after calcination.

**Figure 4.11** "Memory effect" observed in the HT-derived materials. XRD for Cu/HTs (w) and Cu/HTs (ACN) after impregnation and comparison with as-prepared Mg-Al hydrotalcite (labeled as HTs) and collapsed Mg-Al-mixed oxide (labeled as HT) (a). Basal spacing calculations and results (b).

**Figure 4.12** HR-STEM (a) and HR-TEM (b) micrographs, and particle size distribution (c) for reduced CuHT-230 sample.

**Figure 4.13** Illustration of Cu nanoparticle identification by EDX mapping in STEM mode for reduced CuHT-230 sample.

**Figure 4.14** HR-STEM (a) and HR-TEM (b) micrographs, and particle size distribution (c) for reduced CuHT-450 sample.

**Figure 4.15** HR-STEM (a) and HR-TEM (b) micrographs, and particle size distribution (c) for reduced Cu/HT (w) sample.

**Figure 4.16** HR-STEM (a), HR-TEM (b) micrographs, and particle size distribution (c) for reduced Cu/(Al<sub>2</sub>O<sub>3</sub>/MgO) sample.

**Figure 4.17** HR-STEM (a), HR-TEM (b) micrographs, and particle size distribution (c) for reduced Cu/SiO<sub>2</sub> sample.

**Figure 4.18** TPD-CO<sub>2</sub> patterns of CuHT-230 and the commercial-like sample (CZA).

**Figure 4.19** TPD-CO<sub>2</sub> performed on reduced CuHT-230 and Cu/(Al<sub>2</sub>O<sub>3</sub>/MgO) samples.

**Figure 4.20** Comparison of the catalytic performance of the herein reported Cu-HT-derived samples at different temperatures in the CO<sub>2</sub> hydrogenation with other nano-sized Cu-based catalysts in the literature. Numbers refer to the entries placed in Table 4.2 (first column). Entries 13-15 represent interpolated values of CuHT-230, Cu/HT (w) and Cu/Al<sub>2</sub>O<sub>3</sub>/MgO samples at 250 °C and ~28500 mL·g<sub>cat</sub><sup>-1</sup>·h<sup>-1</sup>, respectively (included for comparative purpose).

**Figure 4.21** Extrapolation to “zero contact time” conditions at 230 °C and 20 bar in selected samples: CuHT-230 (a), Cu/(Al<sub>2</sub>O<sub>3</sub>/MgO) (b), and Cu/SiO<sub>2</sub> (c). MeOH and CO intrinsic formation rates obtained for catalysts under study (d).

**Figure 4.22** Methanol production on the CuHT-230 catalyst after alternating cycles of CO<sub>2</sub> hydrogenation at 230 and 280 °C (20 bar and WHSV of 5700 mL·g<sub>cat</sub><sup>-1</sup>·h<sup>-1</sup>). The intervals placed between blue bars correspond to the time in minutes at which the catalyst has been exposed to high temperature (i.e., 280 °C) MeOH synthesis conditions.

**Figure 4.23** Stability of CuNPs in the CuHT-230 catalyst under long term (85 h) reaction conditions at 230 °C, 20 bar and 5700 mL·g<sub>cat</sub><sup>-1</sup>·h<sup>-1</sup>, followed by alternating cycles of temperature between 230 and 280 °C (1 and 4 cycles): Cu particle size evolution throughout the catalytic processes calculated by STEM imaging by measuring at least 200 particles (a), X-ray powder diffraction pattern for CuHT-230 sample before and after reaction, STEM (c) and TEM (d) images for CuHT-230 after the catalytic processes.

**Figure 4.24** XPS core lines of Cu 2p<sub>3/2</sub> at hv=1486.6 eV excitation energy of CuHT-230 sample at different reaction conditions.

**Figure 4.25** IR-CO deconvoluted spectra of reduced supports.

**Figure 4.26** IR-CO spectra of reduced HT support (first row), and CuHT-230 catalyst before (middle row) and after (third row) 9 bar CO<sub>2</sub> hydrogenation. Left panels contain full range spectra before (red) and after (black) CO adsorption. Right panels exhibit the deconvoluted ν(C≡O) region.

**Figure 4.27** IR-CO spectra of reduced Al/Mg support (first row), and Cu/(Al<sub>2</sub>O<sub>3</sub>/MgO) catalyst before (middle row) and after (third row) 9 bar CO<sub>2</sub> hydrogenation. Left panels contain full range spectra before (red) and after (black) CO adsorption. Right panels exhibit the deconvoluted ν(C≡O) region.

**Figure 4.28** IR-CO spectra of reduced SiO<sub>2</sub> support (first row), and Cu/SiO<sub>2</sub> catalyst before (middle row) and after (third row) 9 bar CO<sub>2</sub> hydrogenation. Left panels contain full range spectra before (red) and after (black) CO adsorption. Right panels exhibit the deconvoluted ν(C≡O) region.

**Figure 4.29** IR-ACN spectra adsorbed at 25 °C on the reduced Cu/(Al<sub>2</sub>O<sub>3</sub>/MgO) sample. Left panel contains full range spectra before (red) and after (black) CD<sub>3</sub>CN adsorption. Right panel exhibits the zone marked by the gray square.

**Figure 4.30** IR-ACN spectra adsorbed at 25 °C on the reduced Cu/SiO<sub>2</sub> sample. Left panel contains full range spectra before (red) and after (black) CD<sub>3</sub>CN adsorption. Right panel exhibits the zone marked by the gray square.

**Figure 4.31** IR-ACN spectra adsorbed at 25 °C on the reduced CuHT-230 (black) and HT support (orange) samples. Left panel contains full range spectra after CD<sub>3</sub>CN titration. Right panel exhibits the zone marked by the gray square for both systems.

**Figure 4.32** UV-VIS spectra of (a) calcined and (b) ex situ reduced systems. A CuHT-230 sample with 1 wt % Cu (blue line) has been synthesized for comparative purposes following the synthetic procedure indicated in Subsection 4.2.1 (adjusting the amount of copper precursor).

**Figure 4.33** MgO (a), Cu (b) and Cu<sub>2</sub>O (c) bulk unit cells. Top and side view of: MgO(100) (d), Cu<sub>2</sub>O(110) (e), Cu<sub>2</sub>-doped MgO(100) (f), Cu<sub>2</sub> (g), and Cu<sub>5</sub> (h) adsorbed nanoparticles on MgO(100). For each Cu-containing model, the Cu oxidation state is indicated. The adsorption energies of the Cu clusters per atom with respect to atomic Cu<sub>gas</sub> of the models (g,h) are indicated. Color code: Mg (orange), O (red), and Cu (blue).

**Figure 4.34** Eight adsorbed CO molecules on MgO (a), Cu<sub>2</sub>O(110) (b), Cu<sub>2</sub>-doped MgO(100) (c), Cu<sub>2</sub><sup>ads</sup> (d,e), and Cu<sub>5</sub><sup>ads</sup> (f). The adsorption energy in eV for each state is indicated (bold-type numbers) and also the frequency shifts ( $\Delta\nu$ ) in cm<sup>-1</sup>. Colors refer to Table 4.13 values.

**Figure 4.35** IR-CO titration study on the CuHT-230 sample after reduction (blue), and after quenching the operando IR reaction (2 h at 230 °C), at 1 bar (green) or 9 (red) bar pressure. All spectra are normalized by sample weight.

**Figure 4.36** IR-CO deconvoluted spectra of spent samples after 9 bar reaction. Color code for deconvoluted components: orange (HT support), dark yellow (Al/Mg support), gray (SiO<sub>2</sub> support), cyan (Cu<sup>+</sup> species) and navy (Cu<sup>0</sup> species). All spectra correspond to CO saturation at -170 °C.

**Figure 4.37** IR-CO spectra at saturation conditions at -170 °C of in situ H<sub>2</sub>-reduced catalysts (blue spectra) and after exposing them to 9 bar reaction conditions (red spectra). For comparison purposes, spectra are normalized by sample weight.

**Figure 4.38** Correlation between pressure and MeOH production in the reactor.

**Figure 4.39** Correlation between the amount of exposed Cu<sup>0</sup> sites (determined by IR titration experiments after operando IR reaction at 9 bar and 230 °C) and MeOH (a) and CO (b) productivity obtained in the catalytic studies.

**Figure 4.40** Evolution in the 1800-1000 cm<sup>-1</sup> spectral region during IR operando CO<sub>2</sub> hydrogenation at 9 bar and at increasing temperatures for CuHT-230 sample: original spectra (A), subtracted spectra

respect to the reduced starting point (B), deconvolution of the subtracted spectra at steady-state reaction conditions (C). Online MS profile of methanol (D,  $m/z=31$ ), methane (E,  $m/z=15$ ) and CO (F,  $m/z=28$ ) formation.

**Figure 4.41** IR-MS isotopic studies, where part of the H<sub>2</sub> flow is replaced by D<sub>2</sub> under steady-state conditions (CO<sub>2</sub>:H<sub>2</sub> 1:3 molar ratio), at 230 °C and 9 bar, on the CuHT-230 sample.

**Figure 4.42** IR-CO spectra at saturation conditions (acquired at -170 °C) of CuHT-230: reduced sample (black); quenched sample after operando IR studies in a CO<sub>2</sub>/H<sub>2</sub> flow at 9 bar and 230 °C for 40 min (blue); sample after IR operando conditions and later exposed to a H<sub>2</sub>/N<sub>2</sub> flow at the same temperature for ~4.5 h (red). As observed, the intensity of the Cu<sup>0</sup>-CO signal is restored after hydrogenation of the spent catalysts.

**Figure 4.43** Hydrogenation of CuHT-230 after operando IR CO<sub>2</sub>+H<sub>2</sub> reaction at 1 bar and 230 °C: IR spectra at different steps (in brackets, see Table 4.16 below) of the hydrogenation process (a). Subtracted IR spectra at each step versus the one before starting the treatment.

**Figure 4.44** Evolution of products detected by MS during the hydrogenation treatment of CuHT-230 after operando IR CO<sub>2</sub>+H<sub>2</sub> reaction at 1 bar and 230 °C.

**Figure 4.45** C-H stretching region corresponding to the temperature-resolved IR studies under operando conditions at 1 bar in CO<sub>2</sub>/H<sub>2</sub> flow over CuHT-230 catalyst shown in Figure 4.7. Sequential steps at 200 and 230 °C are displayed on the left and on the right side, respectively. First row panels show IR spectra at indicated temperatures. Middle row panels exhibit the subtracted spectra.

**Figure 4.46** Evolution of reaction products in operando IR CO<sub>2</sub> hydrogenation: methane (a), methanol (b), carbon monoxide (c). Values in Y axis are normalized to CO<sub>2</sub> MS signal.

**Figure 4.47** By-products formation (CO and CH<sub>4</sub>) observed under operando IR conditions in online MS (a) and in offline GC (b). Values in Y axis are normalized to CO<sub>2</sub> signal.

**Figure 5.1** TEM images of Ru@C-EDTA samples prepared by hydrothermal synthesis with different ratios of Ru/EDTA: Ru@C-EDTA-6 (a), Ru@C-EDTA-12 (b), Ru@C-EDTA-20 (c), and Ru@C-EDTA-28 (d).

**Figure 5.2** Synchrotron XPS of the C 1s and Ru 3d core levels at 500 eV X-ray excitation energy on fresh Ru@C-EDTA samples (a). Color code for components: Ru<sup>0</sup> (red), RuC (blue), RuO<sub>2</sub> (green), and C (gray). Surface concentration of the ruthenium carbide phase (RuC) relative to the total ruthenium (RuT) (b).

**Figure 5.3** HR-TEM image of the Ru@C-EDTA-20 sample (a). The L<sub>3</sub>-edge spectra (left panel) and L<sub>2</sub>-edge spectra (right panel) of Ru<sup>0</sup>, Ru@C-EDTA-20, and RuO<sub>2</sub> (b). Curve-fitting simulation from the NEXAFS spectra at L<sub>3</sub>- (c) and L<sub>2</sub>- (d) edges on RuO<sub>2</sub>, Ru@C-EDTA-20 and Ru<sup>0</sup>.

**Figure 5.4** CO<sub>2</sub> conversion (left axis, black) and methane STY (right axis, blue) on the Ru@C-EDTA-20 catalyst at 160 °C, 21428 h<sup>-1</sup> GHSV, and 5.0 % vol CO<sub>2</sub>, 20.0 % vol H<sub>2</sub>, and 75.0 % vol N<sub>2</sub>.



**Figure 5.5** Methane STY (left axis, black) at 160 °C, 21428 h<sup>-1</sup> GHSV, and 23.7% CO<sub>2</sub>, 71.3% H<sub>2</sub>, 5.0% N<sub>2</sub> (% vol). On the right axis (blue) is the RuC/RuT atomic ratio obtained from XPS analysis on the spent Ru@C-EDTA catalysts at 500 eV X-ray excitation energy (Figure 5.17).

**Figure 5.6** TEM images of Ru@C-EDTA-6 catalyst. Ru nanoparticles of 2-5 nm encapsulated by thin carbon layers can be seen in this sample.

**Figure 5.7** TEM images of Ru@C-EDTA-12 catalyst. Ru nanoparticles of 2-5 nm encapsulated by thin carbon layers can be seen in this sample.

**Figure 5.8** TEM images of Ru@C-EDTA-20 catalyst. Small Ru nanoparticles of 2-5 nm encapsulated by thin carbon layers can be seen in this sample, in addition to few bigger Ru particles.

**Figure 5.9** TEM images of Ru@C-EDTA-28 catalyst. Both small Ru nanoparticles of 2-5 nm encapsulated by thin carbon layers and big Ru nanoparticles can be seen in this sample.

**Figure 5.10** HR-TEM images of Ru@C-EDTA-20 sample, showing the presence of Ru<sup>0</sup>, RuO<sub>2</sub> and RuC phases.

**Figure 5.11** Raman spectra of Ru@C-EDTA-20 acquired with 785 nm laser. Color code: Fresh sample (blue); after catalytic test sample (red).

**Figure 5.12** XRD patterns of Ru@C-EDTA-6 and Ru@C-EDTA-12 (a), Ru@C-EDTA-20 and Ru@C-EDTA-28 (b), Ru/C-WI (c), Ru/C-com (d), Ru-Black (e), and Ru/C-Ar800 (f).

**Figure 5.13** Laboratory XPS spectra of the C 1s and Ru 3d core levels of the Ru@C-EDTA-20 sample. (AlK<sub>α</sub>=1486.6 eV).

**Figure 5.14** Synchrotron XPS of the C 1s and Ru 3d core levels at E<sub>exc</sub>=1150 eV (4.4 nm depth) on fresh Ru@C-EDTA samples (a). Surface concentration of ruthenium carbide (RuC) relative to the total ruthenium (RuT) species compared at two sample depths.

**Figure 5.15** X-ray absorption spectra of Ru@C-EDTA-20, Ru metal, and RuO<sub>2</sub> at L<sub>2</sub>/L<sub>3</sub>-edges (a,b). Spectra of Ru@C-Glucose and Ru references at L<sub>2</sub>/L<sub>3</sub>-edges (c,d). The "difference" spectra is the spectral intensity of Ru metal subtracted from Ru@C samples.

**Figure 5.16** TPR-H<sub>2</sub> of Ru@C-EDTA-20 catalyst.

**Figure 5.17** Synchrotron XPS of the C 1s and Ru 3d core levels at E<sub>exc</sub>=500 eV (2.2 nm depth) on the spent Ru@C-EDTA samples (a). Surface concentration of RuC relative to total ruthenium (RuT) species on the fresh catalysts compared to the spent ones (b).

**Figure 5.18** Product selectivity in the CO<sub>2</sub>/H<sub>2</sub> reaction at 160 °C (1 bar, 7.9 mL·g<sub>cat</sub><sup>-1</sup>·s<sup>-1</sup>, Gas mixture: 23.7 % vol CO<sub>2</sub>, 71.3 % vol H<sub>2</sub>, 5.0 % vol N<sub>2</sub>).

**Figure 5.19** NEXAFS spectra of Ru@C catalysts (EDTA-20 and Glucose) at L<sub>3</sub>, L<sub>2</sub>-edges.

**Figure 5.20** Activity of the as-prepared Ru@C-EDTA-20 sample (fresh), and after being exposed to 280 °C reaction temperature (used) catalyst. Reaction conditions: 180 °C, 5.0% CO<sub>2</sub>, 20.0% H<sub>2</sub>, and 75.0% N<sub>2</sub> (% vol), GHSV of 21428 h<sup>-1</sup>.

**Figure 5.21** Combined catalytic+MS studies with reactant feed <sup>13</sup>CO/<sup>12</sup>CO<sub>2</sub>/H<sub>2</sub> on Ru@C-EDTA-20 (a) and Ru/C-com samples (b). Blank experiment (c).

**Figure 5.22** Influence of reactants on the initial reaction rate in the CO<sub>2</sub> hydrogenation to methane. Experiments were carried out at 160 °C. 5 mL·min<sup>-1</sup> CO<sub>2</sub> (constant) varying H<sub>2</sub> proportion (a). 30 mL·min<sup>-1</sup> H<sub>2</sub> (constant) varying CO<sub>2</sub> proportion (b). N<sub>2</sub> was used to balance in both series.

**Figure 6.1** Atomic structures of (SiO<sub>2</sub>)<sub>8</sub>/4O/Ru (a) and (Al<sub>0.25</sub>Si<sub>0.75</sub>O<sub>2</sub>)<sub>8</sub>/3O/Ru(0001) (b). Side (c) and top (d) views of the bilayer aluminosilicate film growth on Ru(0001) with two H<sup>+</sup> bound to the bridging O in (Al-O)-Si to compensate the framework charge [i.e., (H<sub>0.25</sub>Al<sub>0.25</sub>Si<sub>0.75</sub>O<sub>2</sub>)<sub>8</sub>/3O/Ru(0001)]. The black rectangle on the top view (panel d) indicates the unit cell. Color code: Ru (silver), Si (yellow), Al (blue), H (white), O in aluminosilicate (red), and O chemisorbed on Ru (pink).

**Figure 6.2** Dual-path reaction mechanism of water formation reaction (WFR) reported on the Pt(111) surface. (\*) indicates the species adsorbed on the platinum surface.

**Figure 6.3** Si 2p (a) and O 1s (b) core level spectra before and after reaction at 450 K in 0.1 Torr of H<sub>2</sub>. Deconvolution of the O 1s core level spectrum before reaction (c).

**Figure 6.4** Core level shifts (solid symbols) for Si 2p and O 1s (Si-O-Si and Si-O-Al components) as a function of time at 450 K in 0.1 Torr of H<sub>2</sub>. The coverage of chemisorbed O (open circles) is also shown for comparison.

**Figure 6.5** Plot of \*O coverage vs. time at 380, 400, 420, and 450 K (a). Arrhenius plots for WFR at the BL-aluminosilicate/Ru(0001) interface (this work, blue triangles), compared to similar prior work on bare Ru(0001) (black circles) and BL-SiO<sub>2</sub>/Ru(0001) (red squares) (b).

**Figure 6.6** Potential energy diagram for the WFR at the BL-AlSiO<sub>2</sub>/Ru(0001) interface via first hydrogen addition step (\*H + \*O ⇌ \*OH, TS2) (a) and disproportionation pathway (\*H<sub>2</sub>O + \*O ⇌ 2 \*OH, TS2') (b). Potential energy diagram for the disproportionation pathway (TS2') at the silica/Ru(0001) interface (c). Color code: Ru (silver), Si (yellow), Al (blue), H adsorbed on BL-AlSiO<sub>2</sub> (small white), O in BL-AlSiO<sub>2</sub> (red), \*O chemisorbed on Ru (pink), and \*H adsorbed at the BL-AlSiO<sub>2</sub>/Ru(0001) interface that react with \*O (large white).

**Figure 6.7** WFR reaction evolution at 420 K and variable pressure conditions (0.1-0.5 Torr H<sub>2</sub>). Vertical lines indicate the endpoint of the reaction at each working pressure.

**Figure 6.8** Initial WFR reaction evolution at different temperatures (380-450 K) at 0.1 torr H<sub>2</sub> (a) and dependence between the initial rate and the H<sub>2</sub> pressure (b).

**Figure 6.9** Correlation between the Si 2p core level shift (in AP-XPS) and the change in chemisorbed oxygen (\*O) coverage.

**Figure 6.10** Full plot of \*O coverage evolution at 380-450 K corresponding to Figure 6.5.

### 8.3. List of Tables

**Table 1.1** Effect of human activities on the molar concentration of GHG in the Earth's atmosphere before the Industrial Revolution and nowadays.

**Table 1.2** Performance of representative catalytic systems in the CO<sub>2</sub> hydrogenation to methanol.

**Table 1.3** Performance of representative catalytic systems in the CO<sub>2</sub> hydrogenation to methane.

**Table 2.1** Global strategy to be followed to accomplish the thesis objectives.

**Table 3.1** Selected experimental details for the CZG-ox samples preparation at variable gallium loadings. The rest of experimental conditions were kept constant in all synthetic procedures.

**Table 3.2** Catalytic results of CZG and CZA samples at 20 bar pressure and at variable temperature (180-260 °C).

**Table 3.3** Main physico-chemical properties of studied catalysts.

**Table 3.4** Crystallite size of reduced and spent catalysts by XRD.

**Table 3.5** Summary of optimized parameters by fitting Cu K-edge EXAFS data of catalysts collected at 200 °C in H<sub>2</sub>.

**Table 3.6** Metallic species identified in CZA and CZG reduced samples.

**Table 3.7** Extended catalytic results at constant WHSV (~31000 mL·g<sub>cat</sub><sup>-1</sup>·h<sup>-1</sup>) at 20 bar.

**Table 3.8** Catalytic results at variable WHSV and 20 bar for the CZA sample.

**Table 3.9** Catalytic results at variable WHSV and 20 bar for the CZG-sp sample.

**Table 3.10** Catalytic results at variable WHSV and 20 bar for the CZG-ox sample.

**Table 3.11** Analysis of the apparent activation energy ( $E_{a,app}$ ) (Arrhenius plot).

**Table 3.12** State of the art of Cu-based catalysts in the CO<sub>2</sub> hydrogenation to methanol.

**Table 3.13** Catalytic performance of CZG-ox series at different levels of Ga doping.

**Table 3.14** BE (eV) of the Cu 2p<sub>3/2</sub>, Zn 2p<sub>3/2</sub> and Ga 2p<sub>3/2</sub> core levels of CZG-sp sample under different conditions.

**Table 3.15** BE (eV) of the Cu 2p<sub>3/2</sub>, Zn 2p<sub>3/2</sub> and Ga 2p<sub>3/2</sub> core levels of CZG-ox sample under different conditions.

**Table 3.16** BE (eV) of the Cu 2p<sub>3/2</sub> and Zn 2p<sub>3/2</sub> core levels of CZA sample under different conditions.

**Table 3.17** Deconvolution of O 1s core level under different gaseous conditions.

**Table 3.18** Chemical composition of CZG-sp catalyst at different sampling depth and under different conditions (ICP at % ratio: Cu:Zn:Ga = 70.0/24.5/5.5).

**Table 3.19** Chemical composition of CZG-ox catalyst at different sampling depth and under different conditions (ICP at % ratio: Cu:Zn:Ga = 71.5/23.0/5.5).

**Table 3.20** Chemical composition of CZA catalyst at different sampling depth and under different conditions (ICP at % ratio: Cu:Zn = 71.7/28.3).

**Table 3.21** Influence of pressure in the CO<sub>2</sub> hydrogenation to methanol. Comparison between 1 and 20 bar at the same temperature.

**Table 3.22** Laboratory scale XPS results in reduced CZG samples and after 9 bar reaction at HPCR.

**Table 3.23** Laboratory scale XPS results in the reduced CZA sample.

**Table 3.24** TPD-CO<sub>2</sub> integrated peaks for CZG and CZA samples.

**Table 3.25** Catalytic results at variable WHSV on the CZGA-ox sample at 20 bar.

**Table 4.1** Main physico-chemical properties of Cu-based materials.

**Table 4.2** State of the art of nano size Cu-based catalysts in the CO<sub>2</sub> hydrogenation to methanol.

**Table 4.3** Catalytic results of samples under study at 20 bar pressure and variable temperature (230-280 °C). WHSV~28500 mL·g<sub>cat</sub><sup>-1</sup>·h<sup>-1</sup> (27104 mL·g<sub>cat</sub><sup>-1</sup>·h<sup>-1</sup> for Cu/SiO<sub>2</sub>).

**Table 4.4** Catalytic results of selected samples at 230 °C, 20 bar and variable WHSV. Selectivity to minor products (i.e., HCOOMe and CH<sub>4</sub>) not shown.

**Table 4.5** Analysis of the apparent activation energy ( $E_{a,app}$ ) (Arrhenius plot).

**Table 4.6** XPS core levels and surface chemical composition of CuHT-230 sample under different reaction conditions (hν=1486.6 eV excitation energy).

**Table 4.7** XPS core levels and surface chemical composition of the reduced samples (hν=1486.6 eV excitation energy).

**Table 4.8** XPS core levels and surface chemical composition of the reduced Cu/SiO<sub>2</sub> sample (hν=1486.6 eV excitation energy).

**Table 4.9** Quantification of Cu<sup>+</sup> species on the reduced HT support and CuHT-230 catalyst under different reaction conditions.

**Table 4.10** Quantification of Cu<sup>+</sup> species on the reduced Al/Mg support and Cu/(Al<sub>2</sub>O<sub>3</sub>/MgO) catalyst under different reaction conditions.

**Table 4.11** Quantification of Cu<sup>+</sup> species on the reduced SiO<sub>2</sub> support and Cu/SiO<sub>2</sub> catalyst under different reaction conditions.

**Table 4.12** Cu Bader charge values for each model studied. The differences with respect to Cu (Cu<sub>i</sub>-Cu<sub>bulk</sub>) and Cu<sub>2</sub>O (Cu<sub>i</sub>-Cu<sub>2</sub>O) bulks are also indicated.

**Table 4.13** CO vibrational frequency and corresponding shift.

**Table 4.14** Pressure effect on MeOH formation in the IR cell.

**Table 4.15** Pressure effect on MeOH formation in the fixed-bed reactor.

**Table 4.16** Experimental steps followed in the hydrogenation of CuHT-230 at 1 bar.

**Table 4.17** Selected MS values (in A) for the operando IR study at 1 bar.

**Table 4.18** Selected GC values for the operando IR study at 1 bar.

**Table 5.1** Catalytic activity in the CO<sub>2</sub> hydrogenation reaction at concentrated reaction conditions on the Ru@C-EDTA samples.

**Table 5.2** Catalytic activity in the CO<sub>2</sub> hydrogenation to methane at 160 °C and concentrated reaction conditions of the Ru@C-EDTA-20 sample compared to that of other reference ruthenium carbon samples.

**Table 5.3** Ru@C-EDTA-X synthetic details and ruthenium loading on final catalysts.

**Table 5.4** State of the art of Ru and/or carbon-based catalysts in the CO<sub>2</sub> to CH<sub>4</sub> reaction.

**Table 5.5** Catalytic activity of studied samples at concentrated reaction conditions (reactant feed composed of 23.7% CO<sub>2</sub>, 71.3% H<sub>2</sub>, and 5.0% N<sub>2</sub> (% vol), GHSV=21428 h<sup>-1</sup>).

**Table 5.6** Catalytic activity of Ru@C-EDTA-20 and Ru/C-com samples on the CO hydrogenation reaction (30.0%, 60.0% and 10.0% (vol %), 1 bar, WHSV=7.9 mL·g<sub>cat</sub><sup>-1</sup>·s<sup>-1</sup>).

## 8.4. Fundamentals of selected characterization techniques

### 8.4.1. X-ray diffraction (XRD)

The physical phenomenon of X-ray diffraction occurs when a solid interacts with a monochromatic beam of X-rays of wavelength similar to the interplanar spaces of crystalline structures (in the Å scale). Indeed, the diffraction is the combination of two phenomena: coherent scattering and constructive interference. Diffraction peaks (i.e., diffraction maxima) that appear in the pattern result when coherently scattered X-ray photons of the same wavelength constructively interfere. The technique is mathematically described by the Bragg law, which relates the incident angle of the radiation to the interplanar space for each diffraction peak, according to Eq. 8.1:

$$n \cdot \lambda = 2 \cdot d_{hkl} \cdot \sin(\theta) \quad \text{Eq. 8.1}$$

Where  $d$  is the interplanar space of crystalline planes with Miller indices (hkl);  $\lambda$  is the wavelength of incident X-ray beam;  $\theta$  is the incident angle of X-rays.

This technique provides information about the crystalline (or amorphous) nature of a material, allowing the identification of phases that are present. In this thesis, the experimental XRD patterns were compared with JCPDS crystallographic files through X'Pert HighScore Plus software.

Moreover, XRD allows the estimation of the average crystallite size since the width of the X-ray diffraction signal is related to the imperfections of the crystalline structure of a phase. This degree of imperfection is, in turn, mainly related to the crystal size. Thus, smaller crystals offer wider diffraction signals. This idea is the basis of the Scherrer equation (Eq. 8.2), which relates the width of the diffraction peak at FWHM (Full Width at Half Maximum) to the average crystal size:

$$D = \frac{K \cdot \lambda}{FWHM \cdot \cos(\theta)} \quad \text{Eq. 8.2}$$

Where **D** is the average size of the ordered crystalline domains (considered as particle size); **K** is a dimensionless geometric factor (this value is of about 0.9, assuming sphericity of crystals); **λ** is the wavelength of the incident radiation; **FWHM** is the line broadening at that condition (instrumentally corrected); **θ** is the position of the analyzed diffraction signal. X'Pert HighScore Plus software implements a Scherrer Calculator tool to facilitate this task.

#### 8.4.2. Infrared spectroscopy (IR)

IR spectroscopy is an instrumental technique mainly applied for the structural determination of organic (or organometallic) compounds. It is normally used to identify functional groups, since a molecule absorbs characteristic frequencies of radiation, coinciding with the vibration frequency of their chemical bonds, allowing a vibrational transition.

The harmonic oscillator is the simplest model to describe the vibration of a chemical bond, assuming that the atoms are connected through a "spring" that obeys Hooke's Law (Eq. 8.3):

$$\nu = \frac{1}{2\pi} \cdot \sqrt{\frac{k}{\mu}} \quad \text{Eq. 8.3}$$

Where **ν** is the classic frequency of the oscillator; **k** is the force constant of the spring (which "symbolizes" the chemical bond strength); **μ** is the reduced mass of the system ( $m_1 \cdot m_2 / [m_1 + m_2]$ ). Then, the expression found for the (quantized) vibrational energy after solving the Schrödinger equation for the simplified system is:

$$E(V) = \left(V + \frac{1}{2}\right) \cdot h \cdot \frac{1}{2\pi} \cdot \sqrt{\frac{k}{\mu}} \quad \text{Eq. 8.4}$$

Where **h** is Planck's constant; **k** is the force constant; **μ** is the reduced mass of the system; **V** are the possible vibrational quantum numbers ( $V = 0, 1, 2, \dots$ ). It is important to note that to be "IR active", a vibrational mode must be associated with changes in the permanent dipole. Moreover, in vibrational spectroscopy, it is more usual to express the spectral information in wavenumbers ( $\tilde{\nu}$ ,  $\text{cm}^{-1}$ , which is the inverse of the wavelength), than in frequency units.

The infrared region of the electromagnetic spectrum is divided into three regions: The far-IR ( $400\text{-}10\text{ cm}^{-1}$ ), the mid-IR ( $4000\text{-}400\text{ cm}^{-1}$ ), and the near-IR ( $14000\text{-}4000\text{ cm}^{-1}$ ). Our region of study is the mid-IR, where we can find the fundamental vibrations of typical functional groups.

However, in the area of heterogeneous catalysis, IR can be exploited to obtain surface information from a sample (such as electronic features of active centers or acid-base properties) via adsorption of a probe molecule. The overall idea of this method is using a molecule with certain chemical characteristics that is IR-active. On the one hand, we need to know the position of its fundamental vibrations (IR bands) when the molecule is "free" (i.e., not interacting with the surface). After dosing the probe molecule, we should observe a change (e.g., a band shift or depletion) in the IR spectrum, caused by the probed surface/catalyst.

In the particular case of this thesis, carbon monoxide (CO) has been usually used as a probe molecule because of its permanent dipole, small molecular size and simple spectrum. The frequency of the stretching vibrations of the C-O bond in the gaseous phase occurs at  $2143\text{ cm}^{-1}$ , being altered when the probe interacts



with the catalysts surface. CO is an amphoteric probe able to titrate either acidic or basic sites, depending on the nature of the substrate under study. In Chapters 3 and 4, CO was utilized to examine the electronics of copper surface species present in the catalysts. The binding between CO and the metal (Cu in this thesis) involves a  $\sigma$ -donation from the filled CO  $5\sigma$  molecular orbitals (interacting through the carbon atom) to the unfilled metal d-orbital. At the same time, a back donation from the filled metal d-orbitals to the vacant CO  $\pi^*$ -antibonding orbital can occur. Thus, the weakening or strengthening of the C-O bond (manifested in the IR spectrum as a band shift to lower or higher wavenumbers, respectively) will depend on the combination of these two electronic effects, governed by the nature of the metallic centers (oxidation state, geometry, dispersion, etc.) and the number of CO molecules and the way they interact with the surface (e.g., linear, bridge).



*Dosing CO at -170 °C by cooling down with liquid N<sub>2</sub> in a catalytic cell coupled to a Thermo Nicolet Nexus IR spectrophotometer*

### 8.4.3. X-ray photoelectron spectroscopy (XPS)

XPS is a non-destructive analysis technique that allows to study the surface characteristics (6-10 nm) of solids (such as polymers, catalysts, thin films, etc.). Heterogeneous catalysis is a surface phenomenon, and consequently, XPS is a powerful and versatile spectroscopy that can be applied to obtain quantitative information about surface composition of samples, speciation of chemical elements (it differentiates among different oxidation or coordination states), and also compositional depth profiling.

This technique is based on the concept of photoelectric effect. When a sample is irradiated with photons of a certain energy (20-2000 eV,  $1 \text{ eV} = 1.595 \cdot 10^{-19} \text{ J}$ ), electrons are ejected from its surface. Depending on the energy range, two types of spectroscopies are distinguished: i) ultraviolet photoemission (UPS, below  $\sim 150\text{-}200 \text{ eV}$ ), that allows the emission of electrons from the valence band; and ii) X-ray photoemission (XPS, 200-2000 eV), concerning the liberation of electrons from internal levels. In this thesis, the higher energy range (200-2000 eV) was used at both laboratory and synchrotron levels.

The theoretical model proposed in 1964 by Berglund and Spicer (known as "Three-step model") divides the photoemission process in:

- Photoionization: Firstly, the atom absorbs the energy provided by a photon. If this energy is sufficiently high, the atom can ionize, causing the emission of a core electron from a given orbital (conserving the energy).
- Then, the photoelectron travels from the excitation site to the surface of the solid. Throughout this second step, the electrons whose mean free path is greater than this distance (i.e., excitation site-surface) and have not been

affected by other electrons (elastic scattering) will give rise to the main photoemission peak. However, some electrons can interact to others, undergoing inelastic collisions, losing kinetic energy and altering its momentum. The inelastic scattering affects the background of the XPS spectrum, and can cause additional phenomena: For example, if an electron loses part of its kinetic energy but it still achieves to arrive to the surface maintaining its momentum, we will observe peak broadening or extrinsic satellites. Moreover, an electron could come to the surface but losing the information of initial state because it suffered too many inelastic collisions (these are called secondary electrons).

- Finally, the electrons have to escape into the vacuum. To do so, they have to overcome a potential barrier called "sample work function ( $\phi_s$ )", which is defined as the minimum energy required to move an electron from the Fermi level to the vacuum.

The kinetic energy of the emitted photoelectron (KE), which is the magnitude analyzed by the spectrometer, is given by the following equation:

$$KE = h\nu - BE - \phi_s \quad \text{Eq. 8.5}$$

Where **hν** is the photon energy of the incident X-rays employed; **BE** is the binding energy (needed to remove a particular electron from its nucleus); **φ<sub>s</sub>** (also **φ<sub>s</sub>**) is the sample work function.

In metallic samples, the BE is generally measured with respect to the Fermi level. During a measurement, the sample holder and the analyzer are in electrical contact and grounded to prevent the sample surface from becoming charged. In this configuration, the Fermi level of the sample and the instrument are aligned.

In consequence, to calculate the BE from the KE measured in the XPS analyzer, it is only required to know the work function of the analyzer:

$$KE = h\nu - BE - \varphi_{\text{analyzer}} \quad \text{Eq. 8.6}$$

The BE of an electron depends on its chemical environment, mainly determined by the electrostatic Coulomb interaction force with other electrons and with the atomic nucleus. Changes in the environment of the initial state of the atom prior to the photoemission process would cause a shift into the binding energy. Chemical shifts are observable and interpretable in the XPS spectra. Furthermore, this ability to discriminate between different oxidation states and chemical environments is the reason why XPS is a very useful technique in the field of heterogeneous catalysis to characterize samples, not only before/after reaction, but also under operando conditions.

Although XPS is a surface analysis method, it is possible to use this technique to provide compositional information as a function of depth (see Chapters 3 and 5 of this thesis as examples). This can be achieved by optimizing the geometry of the sample holder during the experiment (usually done at laboratory level with X-ray sources emitting at constant energy, with less depth variation); or by varying significantly the kinetic energy of the emitted electron (which is a consequence of working at variable excitation energy, i.e., at a synchrotron facility). The XPS depth of analysis (in nm) is approximated as:

$$\text{Depth} = 3 \cdot \lambda \cdot \cos(\theta) \quad \text{Eq. 8.7}$$

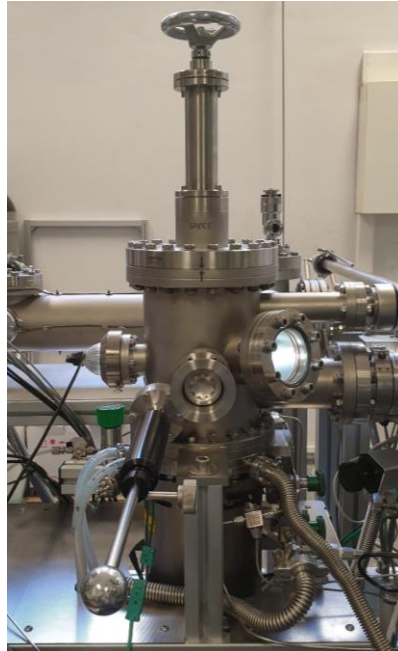
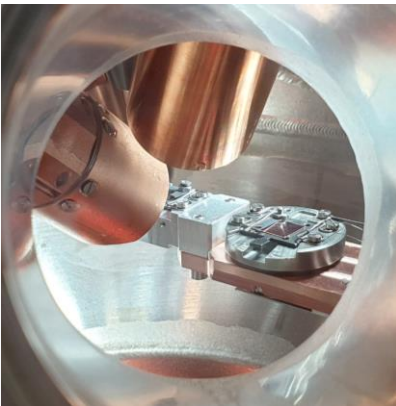
Where  $\lambda$  is the inelastic mean free path of the emitted electron (which expresses the averaged distance that the photoelectron travels through a material before losing energy);  $\theta$  is the angle of emission (between the normal to the sample and

the trajectory of the analyzer axis). The maximum depth is achieved at  $\theta=0^\circ$  (normal emission), where the electron energy analyzer is aligned to the electron emission. QUASES-IMFP-TPP2M software was used in this thesis to obtain the  $\lambda$  value. This tool includes a database with parameters for all chemical elements and many different substrates (such as oxides, polymers, organics, etc.).

In order to avoid the collision of the emitted electrons with the environment, the XPS measurements are usually performed under ultra-high vacuum (UHV) conditions (below  $\sim 10^{-8}$  mbar). This technical requirement is solved by using turbomolecular vacuum pumps (TBMs), which maintain the UHV not only in the analysis chamber, but also in other devices/chambers connected through transfer lines and valves. The components that can be found in a XPS station are (there are multiple options depending on the laboratory and the research area):

- Load lock: chamber where the sample is inserted and depressurized to UHV conditions.
- Preparation chamber: space where different procedures can be carried out (such as thermal treatments, sputtering, evaporation of metals...).
- Analysis chamber: where the XPS measurements actually take place.
- High pressure cell reactor (HPRC): device coupled to the system where a “high-ambient pressure” reaction can be performed (sometimes with MS monitoring capabilities).
- Parking: chamber where samples can be stored under UHV conditions (calibration references, air-sensitive materials under study).

- Other ports: it is possible to couple other instruments to the UHV station (such as an Infrared spectrophotometer) that operate under similar experimental conditions.



*Analysis chamber (left) and HPCR (right) units of the XPS Laboratory at the ITQ*

#### 8.4.4. X-ray absorption spectroscopy (XAS)

XAS is an analysis technique that allows to study the bulk characteristics of solid materials. In particular, it is a unique tool for observing the local structure (at the “atomic” scale) around selected chemical elements that are contained within the material (crystals, films, membranes, solutions, etc.). Important features such as element speciation (differentiating among different oxidation states), the number and nature of neighboring elements, or structural disorder can be revealed by using this technique. In order to acquire XAS spectra, an energy-tunable X-ray source is required. This is the reason why these type of experiments are performed at synchrotron radiation facilities.

When discussing X-ray absorption, we must first define the absorption coefficient ( $\mu$ ), which gives the probability of a photon to be absorbed, according to Beer’s Law:

$$I = I_0 \cdot e^{-\mu x} \quad \text{Eq. 8.8}$$

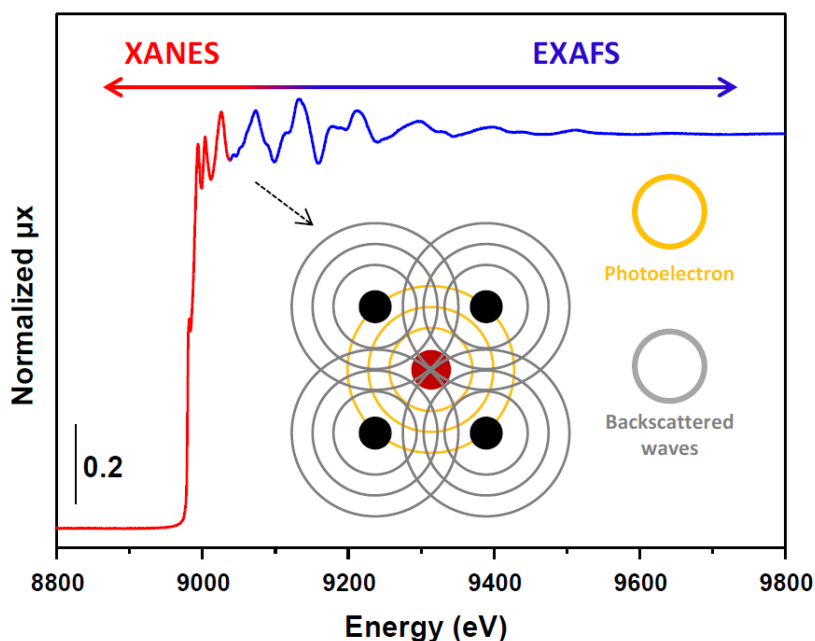
Where **I** is the intensity transmitted through the sample after photon attenuation; **I<sub>0</sub>** is the X-ray intensity incident on a sample; **μ** is the absorption coefficient; **x** is the sample thickness. Moreover, the absorption coefficient depends on the sample composition and the incident energy (E) of X-rays (i.e.,  $\mu(E)$ ). In fact, as the energy increases, a decrease in the absorption coefficient is found:

$$\frac{\mu(E)}{\rho} \approx \frac{Z^4}{A \cdot E^3} \quad \text{Eq. 8.9}$$

Where **ρ** is the sample density; **Z** is the atomic number; **A** is the atomic mass. When the incident X-ray photon has an energy equal to that of the binding energy (BE) of a core level electron, a sharp rise in absorption appears, known as

absorption edge, corresponding to the promotion of this core level electron to the continuum. Since every atom possesses specific core level electrons with well-known BE (usually tabulated), it is possible to study different absorption edges (mainly K and L levels in the hard X-ray regime) tuning the energy of the incident X-rays. Most of the elements can be probed with photons in the range of 5-35 keV, which makes XAFS an “element-specific” technique.

A XAS spectrum can be divided into two regions, with the absorption edge ( $E_0$ ) being a key feature for distinguishing/locating them.



*Graphical example of a XAS spectrum identifying XANES and EXAFS regions*

The region surrounding the  $E_0$  (i.e.,  $E_0 \pm 50$  eV) is known as XANES (X-ray absorption near-edge spectroscopy). This region is important to determine the oxidation state of the element, the ligand types, or the geometry around the absorber. Because of this, XANES is utilized as a “fingerprint” tool, where the



sample under study is compared with references (presenting a particular crystalline structure and oxidation state). On the other hand, the region located beyond the  $E_0$  (up to  $\sim E_0 + 1000$  eV) is called EXAFS (extended X-ray absorption fine structure spectroscopy). The appearance of pronounced oscillations in this part of the spectrum is very characteristic, which is caused by single scattering processes. In particular, these features are due to the interaction between the ejected photoelectron of the absorber and the backscattered radiation produced by the neighboring atoms. Moreover, the crests and the valleys in the EXAFS region are due to constructive and destructive interferences (respectively) of incoming and outgoing waves. The deep analysis of these oscillations gives us information about the local environment of the absorber.

The EXAFS oscillations are defined by the function  $\chi(E)$ , which describes solely the interactions with neighboring atoms:

$$\chi(E) = \frac{\mu(E) - \mu_0(E)}{\Delta\mu_0(E)} \quad \text{Eq. 8.10}$$

Where  $\mu(E)$  is the measured absorption coefficient;  $\mu_0(E)$  is a smooth background function representing the absorption of an isolated atom;  $\Delta\mu_0(E)$  is the measured jump in the absorption coefficient at the threshold energy  $E_0$ .

For a better understanding of EXAFS region, and taking into account the undulating behavior of the photoelectron originated in the absorption process, it is common to convert the X-ray energies to wavenumbers ( $k$ ), whose dimensions are 1/distance, being defined as:

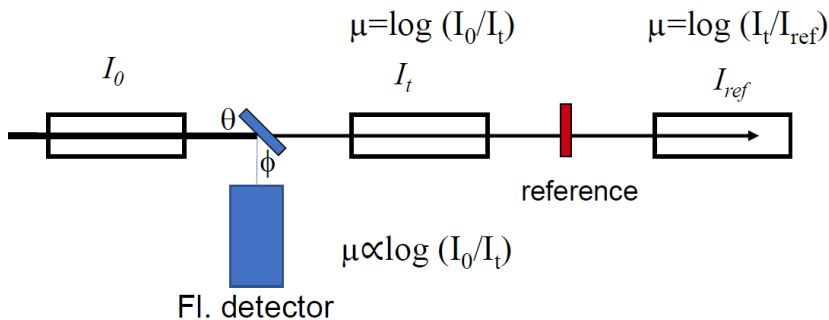
$$k = \sqrt{\frac{2 \cdot m \cdot (E - E_0)}{h^2}} \quad \text{Eq. 8.11}$$

Where  $m$  is the electron mass;  $E$  is the measured energy;  $E_0$  is the energy in the absorption edge;  $h$  is the Planck constant. Finally, the sum of frequencies that compose the EXAFS oscillations correspond to different near-neighbor coordination shells, which can be modeled according to the following equation (as a function of  $k$ ):

$$\chi(k) = \sum_j \frac{N_j \cdot f_j(k) \cdot e^{-2 \cdot k^2 \cdot \sigma_j^2}}{k \cdot R_j^2} \cdot \sin[2 \cdot k \cdot R_j + \delta_j(k)] \quad \text{Eq. 8.12}$$

Where  $f(k)$  and  $\delta(k)$  refer to scattering properties of the neighbor atoms (amplitude and phase-shift, respectively);  $N_j$  is the number of neighbor atoms (i.e., coordination number);  $R_j$  is the distance separating the absorber and the neighbor atom;  $\sigma^2$  represents the disorder in the neighbor distance. All the equations, together with different mathematical tools that allow us to process and interpret XAS spectra (in  $\mu(E)$ ,  $\chi(E)$  and R-space plots), are implemented in a free software package (i.e., Athena).

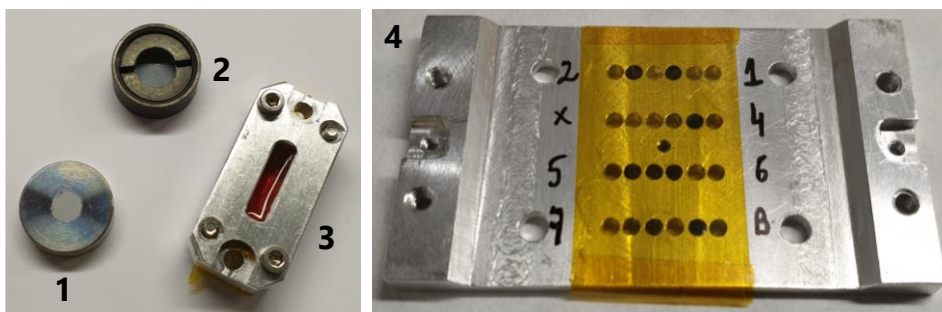
Moving to an experimental point of view, the scheme shown below represents the basic configuration for XAS measurements (transmission and fluorescence modes).



*Schematic representation of a typical experimental setup for XAS measurements*

Although transmission is the most selected mode due to its "easiness" and accuracy, sometimes it cannot be used due to technical issues. For instance, if the amount of absorber is too low (i.e., the metal to be analyzed is too diluted in the sample), fluorescence mode can be applied (with a detector positioned at 90°).

XAS is a powerful spectroscopic technique, however it presents some limitations: On the one hand, it is not possible to distinguish chemical elements with similar atomic numbers (such as C, O, and N). Moreover, if more than one absorber is present in the sample (e.g., bimetallic catalysts, alloys, etc.) the analysis of the spectral information becomes very challenging because XAS is an average technique. Finally, when in situ/operando experiments are performed, the degree of thermal disorder increases ( $\sigma^2$  factor) due to the harsh conditions submitted in the cell (temperature/pressure). This feature makes the data interpretation difficult, introducing uncertainty in the calculation of different parameters (such as coordination number,  $N_j$ ).



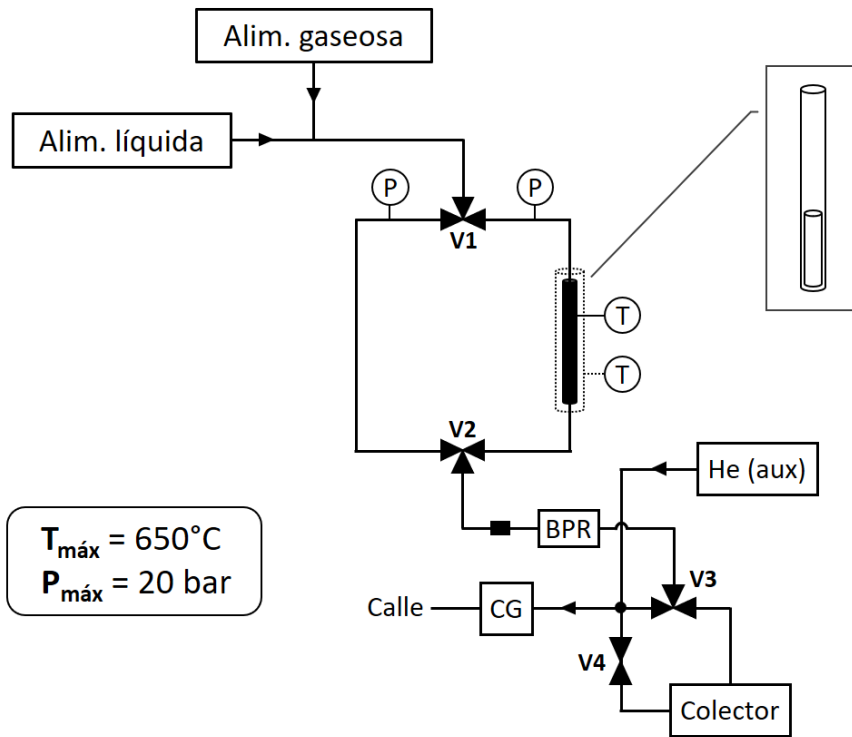
*XAS sample holders containing solid (1, 2, 4-high throughput) and liquid (3) samples*

#### 8.4.5. Catalytic tests in the fixed-bed reactor

The reaction setup designed, built and utilized for the catalytic tests conducted during my predoctoral stage consisted of three parts/zones:

- Feeding system: Gas mixtures (typically CO<sub>2</sub>, H<sub>2</sub> and N<sub>2</sub>) are set in a proper ratio adjusting various mass flow controllers (Bronkhorst). The mixture is then submitted to the reaction zone.
- Reaction system: CO<sub>2</sub> transformations take place in a stainless steel fixed-bed reactor (inner diameter of 11 mm and 240 mm length), equipped with a back-pressure regulator (BPR, Swagelok) that allows for working at a pressure range of 1-20 bar. In parallel to the reactor, a bypass is connected to offer the possibility of isolating the reactor without stopping the flow.
- Analysis system: Analysis of the obtained reaction products is done by online gas chromatography (GC), using a SCION-456-GC equipment with TCD (MS-13X column) and FID (BR-Q Plot column) detectors.

All the lines and valves forming the reaction system are conveniently heated (up to ~150 °C), in order to avoid possible condensation of reaction products. The scheme (and a real image) of the reaction setup is shown below.



*Stainless steel fixed-bed reactor setup (1-20 bar)*

Finally, the main catalytic parameters discussed in the thesis are defined below:

$$\text{CO}_2 \text{ conversion } (X_{\text{CO}_2}, \%) = \frac{\left(\frac{\text{mol}}{\text{h}}\right)_{\text{CO}_2,\text{in}} - \left(\frac{\text{mol}}{\text{h}}\right)_{\text{CO}_2,\text{out}}}{\left(\frac{\text{mol}}{\text{h}}\right)_{\text{CO}_2,\text{in}}} \cdot 100 \quad \text{Eq. 8.13}$$

$$\text{Selectivity to } i (S_i, \%) = \frac{\left(\frac{\text{mol}}{\text{h}}\right)_{i,\text{out}}}{\left(\frac{\text{mol}}{\text{h}}\right)_{\text{CO}_2,\text{in}} - \left(\frac{\text{mol}}{\text{h}}\right)_{\text{CO}_2,\text{out}}} \cdot 100 \quad \text{Eq. 8.14}$$

$$\text{Space time yield } \left(\text{STY}_i, \frac{\text{mol}_i}{\text{g}_{\text{cat}} \cdot \text{h}}\right) = \frac{\left(\frac{\text{mol}}{\text{h}}\right)_{\text{CO}_2,\text{in}} \cdot X_{\text{CO}_2} \cdot S_i}{\text{mass}_{\text{catalyst}}} \quad \text{Eq. 8.15}$$

$$\text{Weight hourly space velocity } \left(\text{WHSV}, \frac{\text{mL}}{\text{g}_{\text{cat}} \cdot \text{h}}\right) = \frac{\left(\frac{\text{mL}}{\text{h}}\right)_{\text{reactants,in}}}{\text{mass}_{\text{catalyst}}} \quad \text{Eq. 8.16}$$

$$\text{Gas hourly space velocity } (\text{GHSV}, \text{h}^{-1}) = \frac{\left(\frac{\text{mL}}{\text{h}}\right)_{\text{reactants,in}}}{\text{mL}_{\text{cat. bed}}} \quad \text{Eq. 8.17}$$

#### 8.4.6. References (for Section 8.4)

- Karge, H. G.; Geidel, E. Vibrational Spectroscopy. In *Molecular Sieves: Science and Technology*. Karge, H. G.; Weitkamp, J., Eds.; Springer: Berlin, 2004; pp 1-200.
- Watts, J. F.; Wolstenholme, J. *An Introduction to Surface Analysis by XPS and AES*; Wiley: Chichester, 2003.
- Newville, M. Fundamentals of XAFS. *Rev. Mineral. Geochem.* **2014**, *78*, 33-74. DOI: 10.2138/rmg.2014.78.2.

- Wittee-Lopes, C. Characterization of metallic species on porous materials by in situ XAS. Doctoral Thesis, Universitat Politècnica de València, July 2018.
- Ruano, D. Caracterización de catalizadores basados en cobre en condiciones de reacción mediante técnicas espectroscópicas in situ. Doctoral thesis, Universitat Autònoma de Barcelona, February 2021.
- Cerdá-Moreno, C. Desarrollo de catalizadores heterogéneos para la producción de metano a partir de la hidrogenación selectiva de CO<sub>2</sub>. Doctoral thesis, Universitat Politècnica de València, September 2019.

## 8.5. Scientific production

### 8.5.1. Publications

- I. Cored, J.; Mazarío, J.; Cerdá-Moreno, C.; Lustemberg, P. G.; Ganduglia-Pirovano, M. V.; Domine, M.; Concepción, P. Enhanced methanol production over non-promoted Cu-MgO-Al<sub>2</sub>O<sub>3</sub> materials with ex-solved 2 nm Cu particles: Insights from an Operando spectroscopic study (*Under revision*).
- II. Cored, J.; Lopes, C. W.; Liu, L.; Soriano, J.; Agostini, G.; Solsona, B.; Sánchez-Tovar, R.; Concepción, P. Cu-Ga<sup>3+</sup>-doped wurtzite ZnO interface as driving force for enhanced methanol production in co-precipitated Cu/ZnO/Ga<sub>2</sub>O<sub>3</sub> catalysts. *J. Catal.* **2022**, *407*, 149-161. [F. I. = 7.92 (2020)]. DOI: [10.1016/j.jcat.2022.01.032](https://doi.org/10.1016/j.jcat.2022.01.032).
- III. Cored, J.; Wang, M.; Akter, N.; Darbari, Z.; Xu, Y.; Karagoz, B.; Waluyo, I.; Stacchiola, D.; Head, A. R.; Concepción, P.; Lu, D.; Boscoboinik, J. A. Water Formation Reaction under Interfacial Confinement: Al<sub>0.25</sub>Si<sub>0.75</sub>O<sub>2</sub> on O-Ru(0001). *Nanomaterials* **2022**, *12*, 183. [F. I. = 5.076 (2020)]. DOI: [10.3390/nano12020183](https://doi.org/10.3390/nano12020183).
- IV. García-Ortiz, A.; Vidal, J. D.; Iborra, S.; Climent, M. J.; Cored, J.; Ruano, D.; Pérez-Dieste, V.; Concepción, P.; Corma, A. Synthesis of a hybrid Pd<sup>0</sup>/Pd-carbide/carbon catalyst material with high selectivity for hydrogenation reactions. *J. Catal.* **2020**, *389*, 706-713. [F. I. = 7.92 (2020)]. DOI: [10.1016/j.jcat.2020.06.036](https://doi.org/10.1016/j.jcat.2020.06.036).

- V. Ruano, D.; [Cored, J.](#); Azenha, C.; Pérez-Dieste, V.; Mendes, A.; Mateos, C.; Concepción, P. Dynamic Structure and Subsurface Oxygen Formation of a Working Copper Catalyst under Methanol Steam Reforming Conditions: An in Situ Time-Resolved Spectroscopic Study. *ACS Catal.* **2019**, *9*, 2922-2930. [F. I. = 13.084 (2020)]. DOI: [10.1021/acscatal.8b05042](https://doi.org/10.1021/acscatal.8b05042).
- VI. [Cored, J.](#); García-Ortiz, A.; Iborra, S.; Climent, M. J.; Liu, L.; Chuang, C. H.; Chan, T. S.; Escudero, C.; Concepción, P.; Corma, A. Hydrothermal Synthesis of Ruthenium Nanoparticles with a Metallic Core and a Ruthenium Carbide Shell for Low-Temperature Activation of CO<sub>2</sub> to Methane. *J. Am. Chem. Soc.* **2019**, *141*, 19304-19311. [F. I. = 15.419 (2020)]. DOI: [10.1021/jacs.9b07088](https://doi.org/10.1021/jacs.9b07088).
- VII. Liu, L.; Puga, A. V.; [Cored, J.](#); Concepción, P.; Pérez-Dieste, V.; García, H.; Corma, A. Sunlight-assisted hydrogenation of CO<sub>2</sub> into ethanol and C<sub>2+</sub> hydrocarbons by sodium-promoted Co@C nanocomposites. *Appl. Catal. B: Environ.* **2018**, *235*, 186-196. [F. I. = 19.503 (2020)]. DOI: [10.1016/j.apcatb.2018.04.060](https://doi.org/10.1016/j.apcatb.2018.04.060).

### 8.5.2. Patents

- VIII. Corma, A.; Concepción, P.; [Cored, J.](#) Catalyst for the hydrogenation of CO<sub>2</sub> to methane at low temperatures. National protection (ES2828458 A1 - 26/05/2021). International protection (WO 2021/105537 A1 - 03/06/2021).

### 8.5.3. Conference contributions

*Reunión Bienal de la Sociedad Española de Catálisis SECAT'19*

*Cordoba, Spain (24<sup>th</sup>-26<sup>th</sup> June 2019)*

- IX. [Cored, J.](#); Mazarío, J.; Domine, M. E.; Concepción, P. Influencia en las propiedades electrónicas de promotores basados en óxidos metálicos en la hidrogenación de CO<sub>2</sub> a metanol. (POSTER)
- X. [Ruano, D.](#); [Cored, J.](#); Pérez-Dieste, V.; Concepción, P. Comportamiento dinámico del catalizador CuO/ZnO/Ga<sub>2</sub>O<sub>3</sub> en condiciones de reformado de metanol con vapor de agua. (ORAL)

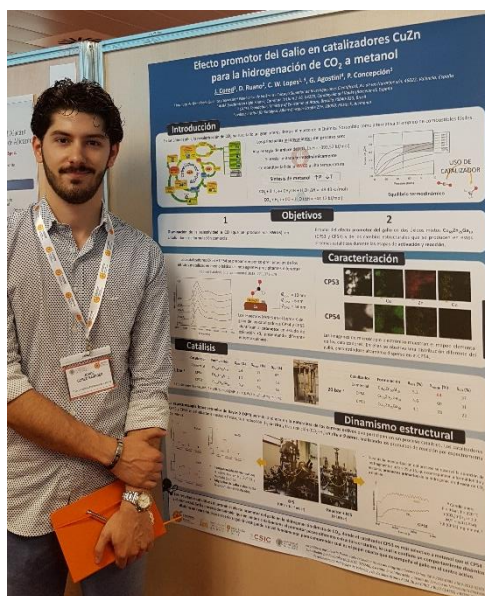


*5<sup>th</sup> Annual Ambient Pressure X-ray Photoelectron Spectroscopy Workshop 2018  
Berlin, Germany (11<sup>th</sup>-14<sup>th</sup> December 2018)*

- XI. Concepción, P.; Cored, J.; Liu, L.; Puga, A. V.; Pérez-Dieste, V.; García, H.; Corma, A. Sunlight-assisted Hydrogenation of CO<sub>2</sub> into ethanol and C<sub>2+</sub> Hydrocarbons by Sodium-promoted Co@C Nanocomposites. (POSTER)

*III Encuentro de Jóvenes Investigadores de la Sociedad Española de Catálisis  
Valencia, Spain (25<sup>th</sup>-27<sup>th</sup> June 2018)*

- XII. Cored, J.; Ruano, D.; Lopes, C. W.; Agostini, G.; Concepción, P. Efecto promotor del Galio en catalizadores CuZn para la hidrogenación de CO<sub>2</sub> a metanol. (POSTER)



*“III Encuentro de Jóvenes Investigadores de la SECAT” in Valencia (2018)*

## 8.6. Synchrotron projects

During my predoctoral period, I participated in about twenty research projects related to industrial catalytic processes as a member of the “Experimental Team”. Consequently, a highly specialized training in this sort of singular facilities has

been obtained, with more than 2000 h of operation at five synchrotrons worldwide.

### 8.6.1. ALBA Synchrotron (Cerdanyola del Vallès, Barcelona, Spain)

2020

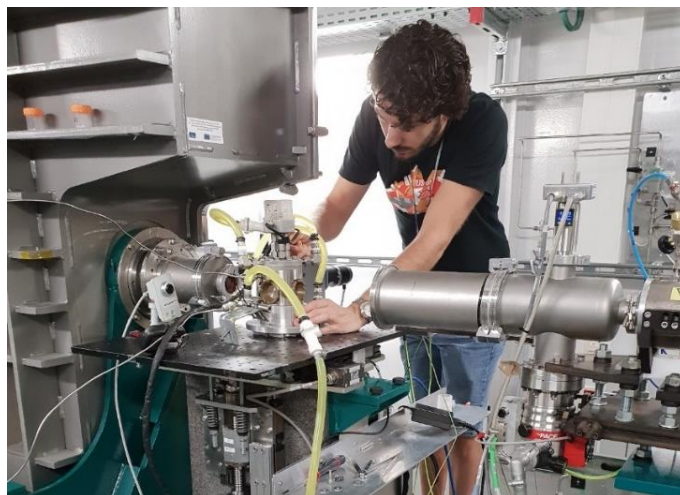
- *"Influence of the reaction conditions on the nature of Ruthenium sites in a Ru@carbon catalyst with unprecedented activity in the low temperature CO<sub>2</sub> hydrogenation reaction" (ID-2020024106, Beamline: BL22-CLAESS, 18 shifts).*
- *"State of the nature of active sites in an ex situ activated Ru carbon catalyst resulting in improved activity in the low temperature CO<sub>2</sub> hydrogenation reaction" (ID-2020024066, Beamline: BL24-CIRCE, 12 shifts).*
- *"Monitoring the In situ formation of active sites in a Ru carbon catalyst with exceptionally high activity in the low temperature CO<sub>2</sub> hydrogenation reaction" (ID-2019093692, Beamline: BL22-CLAESS, 6 shifts).*

2019

- *"XAS studies on the nature of the active species generated under reaction conditions in the hydroformylation of 1-hexene by a ruthenium chitosan nanocomposite" (ID-2019023481, Beamline: BL22-CLAESS, 9 shifts).*
- *"Methanol oxidation on CeO<sub>2</sub>/Cu inverse model catalysts and real catalysts" (IH-2019043587, Beamline: BL24-CIRCE, 9 shifts).*
- *"In-house Experiment" (IH-2019033576, Beamline: BL22-CLAESS, 6 shifts).*

2018

- *"Study on the evolution of subnanometric bimetallic clusters under reaction conditions by in-situ XAS" (AV-2018022706, Beamline: BL22-CLAESS, 15 shifts).*
- *"Methanol oxidation on CeO<sub>2</sub>/Cu inverse model catalysts and real catalysts" (IH-2018052860, Beamline: BL24-CIRCE, 21 shifts).*



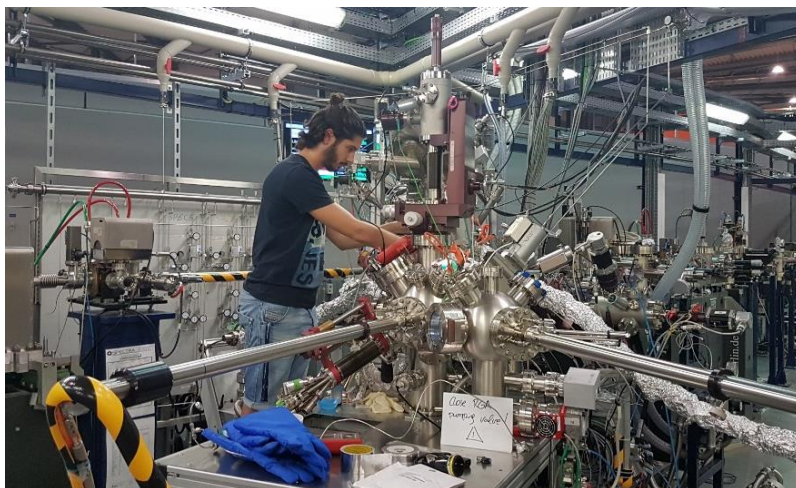
*BL-22 (CLAESS) at ALBA Synchrotron Light Source (2018)*

### 2017

- *“Influence of the support and gas environment on the stabilization of surface cobalt sites in Co-Ru/TiO<sub>2</sub> catalysts and their applications in Fischer-Tropsch” (ID-2017022091, Beamline: BL24-CIRCE, 12 shifts).*
- *“Analysis of the active site of CuZnGa catalysts with enhanced catalytic performance in the low temperature Methanol Steam Reforming” (ID-2017032114, Beamline: BL22-CLAESS, 15 shifts).*
- *“Methanol Oxidation in inverse model and in real catalysts” (IH-2017102522, Beamline: BL24-CIRCE, 12 shifts).*
- *“Analysis of the active site of CuZnGa catalysts with enhanced catalytic performance in the low temperature Methanol Steam Reforming” (ID-2016091943, Beamline: BL24-CIRCE, 12 shifts).*

### 2016

- *“Fundamental knowledge of the Surface properties of metal nanoparticles under reaction conditions by means of NAPP-XPS” (ID-2015021233, Beamline: BL24-CIRCE, 36 shifts).*



*BL-24 (CIRCE) at ALBA Synchrotron Light Source (2016)*

### **8.6.2. NSLS-II (Brookhaven National Laboratory, Upton, NY, United States)**

*2019*

- *"Ambient-Pressure X-ray Photoelectron Spectroscopy for Chemistry in Confined Spaces" (Beamline: 23-ID-2 [IOS], 9 shifts).*

### **8.6.3. European Synchrotron Radiation Facility, ESRF (Grenoble, France)**

*2018*

- *"Time resolved monitoring of the catalytic active sites in Cu-Ga<sub>2</sub>O<sub>3</sub>-ZnO catalyst in the Methanol Steam Reforming reaction" (CH-5285, Beamline: ID24, 18 shifts).*

### **8.6.4. DIAMOND Light Source Ltd. (Didcot, Oxfordshire, United Kingdom)**

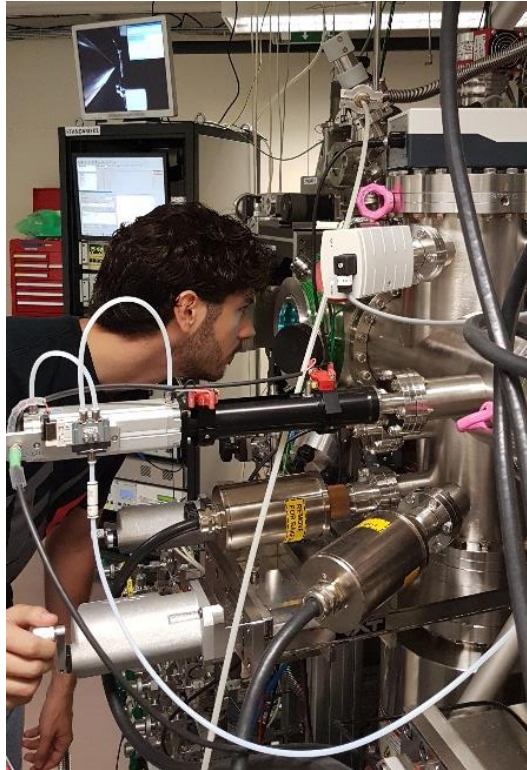
*2018*

- *"Tuning the catalytic properties of Pd Nanoparticles by C dissolution onto and into the Pd particle. Role of the carbon support" (SI-18179-1, Beamline: B07-1, 18 shifts).*

### **8.6.5. BESSY II Photon Source, HZB (Berlin, Germany)**

*2017*

- *"Low temperature NO reduction with CO catalysed by Pt clusters of less than 10 atoms" (16204137-ST-1.1-P, Beamline: BL-ISISS, 21 shifts).*



*BL-ISISS at BESSY II Photon Source (2018)*

## **8.7. Scientific dissemination**

In 2020, I became one of the finalists in the 1<sup>st</sup> National Video Contest for CSIC PhD Students “Yo investigo. Yo soy CSIC”. This activity was an open call announced by the Postgraduate and Specialization Department (DPE) of the Spanish Research Council (CSIC) aimed at predoctoral CSIC researchers. The contest consisted of presenting our doctoral thesis investigation to a non-specialized audience in a three-minute video. I recorded all takes during my short-term stay at Brookhaven National Laboratory (2019).

Youtube Link: <https://www.youtube.com/watch?v=Sx0bfGaDt90>



*Shooting of the documentary at Brookhaven National Laboratory (2019)*

## 8.8. Dr. Patricia Concepción's group



*"Research in times of pandemic". From left to right: J. Soriano, J. M. Salas, C. Tébar, P. Concepción, J. Coreá, C. Cerdá, D. Soriano, A. Muñoz (2021)*